Cranfield University

A. I. KALFAS

TRANSITION TO TURBULENCE IN THE BOUNDARY LAYER OF TURBOMACHINERY BLADING

School of Mechanical Engineering

PhD Thesis

CRANFIELD UNIVERSITY

SCHOOL OF MECHANICAL ENGINEERING

PhD THESIS

ACADEMIC YEAR 1993-1994

A. I. KALFAS

TRANSITION TO TURBULENCE IN THE BOUNDARY LAYER OF TURBOMACHINERY BLADING

Supervisor: Professor R. L. ELDER

APRIL 1994

SYNOPSIS

This thesis is concerned with the investigation of boundary layer transition phenomena in relation to turbomachinery flows. The present study involved the experimental investigation of the flow field around flat plates with various leading edge configurations. This study has also included some theoretical predictions using computational fluid dynamics.

The experimental investigation involved a variety of free stream environments which have attempted to simulate typical turbomachinery flows. Three flat plate configurations with a sharp, a semi-circular and a C4 leading edge shapes have been employed. The effect of free stream turbulence intensity over a range of free stream Reynolds numbers has been examined. Surface flow visualisation techniques have been applied to a total of 36 different experimental conditions in order to define the transitional characteristics of the boundary layer. This flow visualisation method was found to be appropriate for the large range of test cases involved and especially for the flat plate with the cylindrical leading edge. For the cylindrical leading edge configuration, a separation bubble has been detected in the vicinity of the leading edge, under all tested conditions.

Hot-wire investigation of the boundary layer has been undertaken over the flat plate with the C4 leading edge, which has been regarded as the most relevant configuration for turbomachinery applications. This method provided high frequency velocity data which have been analysed in order to obtain information about the spatial distribution of integral parameters of the boundary layer, such as the mean velocity, the turbulence intensity and the skewness and flatness factors. Boundary layer spectra have also been acquired. Statistical analysis of this data has been employed in order to obtain the intermittency distribution. The present results have been found to be in good agreement with existing transition correlations.

Calculations of the flow over flat plates with leading edge shapes similar to the experimental configuration have been undertaken using a two-dimensional elliptic Navier-Stokes solver. A solution of the flow field around a semi-circular and an elliptical leading edge has been obtained. Low Reynolds number k-ε modelling has been applied in order to model the transitional characteristics of the boundary layer flow very near the wall. The use of the Nagano-Hishida version of the low-Reynolds number turbulence model led to predictions of an early start and end of transition.

To my parents

ACKNOWLEDGEMENTS

I would like to express my sincere gratitude to my supervisor Professor Robin L. Elder for his continuous guidance, help and encouragement throughout the course of this study. Also, I would like to thank Dr Archie McKenzie and Mr W.John Calvert for their suggestions on many turbomachinery aerodynamics issues that I have discussed with them. The help and valuable suggestions of Prof. P. Stow and Mr J. Coopeland of the Design Sciences Group of Rolls Royce Plc as well as Mr A. Jones and Mr D. Brierley of the Rolls Royce Applied Science Laboratory is gratefully acknowledged. Thanks are due to Dr K.P. Garry and Mrs J.E. Collis of Cranfield College of Aeronautics for their assistance and valuable suggestions concerning the flow visualisation experiments. Special thanks are also due to Mr Bernard Charnley and the Test Area staff for their technical support. Finally, I am grateful to all my friends and colleagues for their support and encouragement.

I would like to acknowledge the financial support of the Commission of the European Community (CEC). I also wish to thank Dr Dunkler for his involvement in the EURAM-BRITE Aero-0002 research project as well as all of my colleagues in this European project, including Prof. A. Goulas, Prof. S. Nychas and Mrs K. Fotea of Aristotle University of Thessaloniki, Greece and Prof. Ch. Hirsch and Dr B.K. Hazarika of Vrije Universiteit Brussel, Belgium.

I wish to express my gratitude to my mother Φανή, my fiancee Ελένη and the rest of my family for their support, endurance and fortitude during all these years that have made the completion of this thesis possible. I shall always remember my late father Ιωάννης who devoted his life to his family and was such a significant source of inspiration and stamina in my early years. Finally, I would like to thank all my teachers for inspiring and guiding me throughout the years of my education.

Ανέστης Ι. Κάλφας

CONTENTS

SYNOPSIS	ii
ACKNOWLEDGEMENTS	v
CONTENTS	vi
LIST OF TABLES AND FIGURES	xi
NOMENCLATURE	xxvi
CHAPTER 1 INTRODUCTION	1
1.1 Introduction	2
1.2 The Role of Laminar to Turbulent Transition in Turbomachinery Flows	4
1.2.1 A General Discussion	4
1.2.2 The Various Modes of Transition	6
1.2.3 Boundary Layer Flow under Low Free stream Turbulence	7
1.2.4 A Short Note on the Stability Theory of Laminar Flows	8
1.2.5 Bypass Transition	10
1.2.6 A Modern Approach to the Later Stages of Natural Transition and Bypass Transition	12
1.2.7 Separated Flow Transition	16
1.2.8 Effects of the Free-Stream Turbulence	19
1.2.9 Effects of the Pressure Gradient	21
1.2.10 Effects Related to Turbomachinery Blading Aerodynamics	23
1.3 The Scope of this Thesis	26
1.4 Organisation of the Thesis	27
CHAPTER 2 EXPERIMENTAL ARRANGEMENT	33
2.1 Introduction	34
2.2 The Low Speed Wind Tunnel	36
2.2.1 General Layout of the Tunnel	36
2.2.2 Wind Tunnel Characteristics	39
2.3 The Experimental Model Plates	42

2.3.1 Raw Material Specifications 43
2.3.2 Leading Edge Formation 44
2.3.3 Static Pressure Tappings 47
2.4 Turbulence Generating Grids 49
2.5 Instrumentation 53
2.5.1 Pneumatic Probes 53
2.5.2 Hot Wire Probes 54
2.5.3 Hot Film Multisensor Gauge 55
2.5.4 Other Instruments 56
2.6 Concluding Remarks 57

CHAPTER 3 EXPERIMENTAL METHODS 69
3.1 Introduction 70
3.2 Flow Visualisation Techniques 71
3.2.1 A General Discussion 72
3.2.2 Flow Visualisation Methods Employed in this Study 73
3.3 Hot Wire Anemometry 76
3.3.1 Fundamentals of Hot Wire Anemometry 76
3.3.2 Hot Wire Calibration 77
3.3.3 Digital Data Acquisition and Data Reduction 78
3.4 Installation Method and Apparatus Set Up 84
3.5 Accuracy in Measurements 85
3.6 Concluding Remarks 87

CHAPTER 4 THE FLOW VISUALISATION EXPERIMENTS 91
4.1 Introduction 92
4.2 Separated Flow Transition 93
4.2.1 Separated Flow Transition Results 94
4.2.2 Data Analysis and Discussion 95
4.3 Natural and Bypass Transition 99
4.3.1 Results and Discussion 99
4.4 Conclusions 101

CHAPTER 5 HOT WIRE INVESTIGATION OF THE FLOW FIELD 113

5.1 Introduction 114

5.2 Presentation and Statistical Analysis of the Obtained Results 116

5.2.1 Introduction 116

5.2.2 The concept of Intermittency 118

5.2.3 Probability Density Distribution 121

5.2.4 Mean Velocity Profiles 124

5.2.5 Profiles of the Turbulence Intensity 126

5.2.6 Profiles of the Skewness and Flatness Factors 127

5.3 Representation of the Measured Quantities in a Dimensionless Space Domain 130

5.3.1 Introduction 130

5.3.2 Distribution of the Dimensionless Velocity u^+ 131

5.3.3 Distribution of the Turbulence Intensity 132

5.3.4 Distribution of the Skewness and Flatness Factors 133

5.4 Integral Quantities of the Flow Field 135

5.4.1 Introduction 135

5.4.2 Integral Quantities of the Flow Field 135

5.5 Boundary Layer Spectra 138

5.5.1 Introduction 138

5.5.2 Results and Discussion 139

5.6 The Intermittency Distribution 143

5.6.1 Introduction 143

5.6.2 Determination of the Intermittency Function 144

5.6.3 Results and Discussion 147

5.7 Overall Assessment of the Results and Conclusions 152

CHAPTER 6 COMPUTATIONAL APPROACH 205

6.1 Introduction 206

6.2 Computational Methods 208

6.3 The Present Computational Approach 213

6.3.1 Introduction 213

6.3.2 The Numerical Model 214
6.3.3 The Computational Mesh 216
6.3.4 Leading Edge Flow Results 217
6.3.5 Numerical Prediction of Transition 221
6.4 Concluding Remarks 224

CHAPTER 7 CONCLUSIONS AND SUGGESTIONS FOR FUTURE WORK 234
7.1 Conclusions 235
7.2 Suggestions for Future Work 238

BIBLIOGRAPHY 241

APPENDIX A A1
Analytical Plots of the Hot Wire Results A1
Section i A3
Section ii A24
Section iii A46

APPENDIX B B1
On the Correction of Hot-Wire Measurements for Wall Proximity B1
B.1 Introduction B2
B.2 A Brief Review of the Literature B3
B.3 The Present Correction Procedure B4

APPENDIX C C1
On the Determination of the Skin Friction Coefficient C1
C.1 Introduction C2
C.2 Theoretical Considerations C3
C.3 The Determination Procedure C4

APPENDIX D D1

On the Determination of Turbulence Length Scale D1

D.1 Introduction D2

D.2 Theoretical Considerations D3

D.3 Length Scale Determination D5

LIST OF TABLES AND FIGURES

Figure 1.1 : Fundamental Problems in Modern Compressor Flow Field

Figure 1.2 : Reynolds Number Variation Through a Medium Size Gas Turbine

Figure 1.3 : Idealized Sketch of Transition Zone in the Boundary Layer on a Flat Plate at Zero Incidence

Figure 1.4 : Growth of a Turbulent Spot in a Laminar Boundary Layer on a Flat Plate at Zero Incidence

Figure 1.5 : Propagation and Dependence Conelike Regions for a Point P_0

Figure 1.6 : Flow Around a Separation Bubble Including the Corresponding Pressure Distribution

Figure 1.7 : Surface Heat Transfer Measurements on Gas Turbine Blades

Figure 1.8 : Rotor- Mid-Span Hot-Film Results at Design Conditions

Table 2.1 : Location of Pressure Tappings in the X Direction for the Three Plate Configurations

Table 2.2 : Principal Characteristics of the Turbulence Generating Grids

Figure 2.1 : Schematic Representation of the Wind Tunnel

Figure 2.2 : General Layout of Test Facility

Figure 2.3 : Inlet Flare Design

Figure 2.4 : Schematic View of the Working Section Including the Dimensions of the Flat Plate

Figure 2.5 : Picture of the Centrifugal Impeller

Figure 2.6 : Measured Characteristic of the Centrifugal Fan

Figure 2.7 : Flat Plate Suspension Scheme

Figure 2.8 : Comparison Between the Various Leading Edge Shapes

Figure 2.9 : Schematic Representation of the Design and Manufacturing of the Sharp Leading Edge

Figure 2.10 : Static Pressure Tappings Distribution in the Leading Edge Area of the Various Flat Plates

Figure 2.11 : Picture of the PXS Turbulence Generating Grid

Figure 2.12 : Schematic Representation of the Turbulence Generating Grids

Figure 2.13 : Streamwise Decay of Turbulence Downstream PXR and PXS Grids

Figure 2.14 : Pneumatic and Hot-Wire Probe Geometry

Figure 2.15 : Picture of the Plug-In Hot-Wire Probes

Figure 2.16 : Picture of the Hot-Film Multigauge

Figure 2.17 : Data Acquisition Scheme for Calibration and Measurements

Figure 3.1 : A Typical Hot-Wire Calibration Curve

Figure 3.2 : Picture of the Prong Tip of a DANTEC 55P05 Hot Wire Probe Attached to a Microscopic Scale (10 μm Increments)

Figure 3.3 : Static Pressure Coefficient Distribution for the Flat Plate with Cylindrical Leading Edge

Figure 3.4 : Static Pressure Coefficient Distribution for the Flat Plate with C4 Leading Edge

Figure 4.1 : Picture of the Surface Flow Patterns Generated Under Background Turbulence (Tu = 0.8%) and 15 m/s Free Stream Velocity

Figure 4.2 : Picture of the Surface Flow Patterns Generated Under 2.5% Free Stream Turbulence Intensity and 5 m/s Free Stream Velocity

Figure 4.3 : Picture of the Surface Flow Patterns Generated Under 2.5% Free Stream Turbulence Intensity and 15 m/s Free Stream Velocity

Figure 4.4 : Picture of the Surface Flow Patterns Generated Under 2.5% Free Stream Turbulence Intensity and 35 m/s Free Stream Velocity

Figure 4.5 : Picture of the Surface Flow Patterns Generated Under 10% Free Stream Turbulence Intensity and 5 m/s Free Stream Velocity

Figure 4.6 : Picture of the Surface Flow Patterns Generated Under 10% Free Stream Turbulence Intensity and 15 m/s Free Stream Velocity

Figure 4.7 : Picture of the Surface Flow Patterns Generated Under 10% Free Stream Turbulence Intensity and 35 m/s Free Stream Velocity

Figure 4.8 : Picture of the Surface Flow Patterns Generated Under 15% Free Stream Turbulence Intensity and 5 m/s Free Stream Velocity

Figure 4.9 : Picture of the Surface Flow Patterns Generated Under 15% Free Stream Turbulence Intensity and 15 m/s Free Stream Velocity

Figure 4.10 : Picture of the Surface Flow Patterns Generated Under 15% Free Stream Turbulence Intensity and 35 m/s Free Stream Velocity

Figure 4.11 : The Present Results Compared with VUB Hot Wire Data at Background Turbulence

Figure 4.12 : Separated Flow Transition Measurements Using SMR Grid Located at X=-150 mm

Figure 4.13 : Separated Flow Transition Measurements Using PR Grid Located at X=-150 mm

Figure 4.14 : Separated Flow Transition Measurements Using PS Grid Located at X=-150 mm

Figure 4.15 : Variation of Recirculation Length with Free Stream Reynolds Number and Turbulence Intensity

Figure 4.16 : Comparison Between Transition Results for the Sharp and C4 Leading Edge at Tu=2.5%

Figure 4.17 : Comparison Between Transition Results for the Sharp and C4 Leading Edge at Tu=10%

Figure 4.18 : Comparison Between Transition Results for the Sharp and C4 Leading Edge at Tu=15%

Figure 4.19 : Visualisation of the Lateral Misalignment of the Plate Using the Present Technique

Table 5.1 : Theoretically Derived Correlations for the Behaviour of the Integral Quantities in Laminar and Turbulent Boundary Layers

Figure 5.1 : Profiles of the Integral Boundary Layer Quantities (U_∞ = 5 m/s, Tu_∞ = 4 %, X = 100 mm)

Figure 5.2 : Probability Distributions of the Velocity in the Boundary Layer (U_∞ = 5 m/s, Tu_∞ = 4 %, X = 100 mm)

Figure 5.3 : Profiles of the Integral Boundary Layer Quantities (U_∞ = 5 m/s, Tu_∞ = 4 %, X = 200 mm)

Figure 5.4 : Probability Distributions of the Velocity in the Boundary Layer (U_∞ = 5 m/s, Tu_∞ = 4 %, X = 200 mm)

Figure 5.5 : Profiles of the Integral Boundary Layer Quantities (U_∞ = 5 m/s, Tu_∞ = 4 %, X = 300 mm)

Figure 5.6 : Probability Distributions of the Velocity in the Boundary Layer (U_∞ = 5 m/s, Tu_∞ = 4 %, X = 300 mm)

Figure 5.7 : Profiles of the Integral Boundary Layer Quantities
(U_∞ = 5 m/s, Tu_∞ = 4 %, X = 350 mm)

Figure 5.8 : Probability Distributions of the Velocity in the Boundary Layer
(U_∞ = 5 m/s, Tu_∞ = 4 %, X = 350 mm)

Figure 5.9 : Profiles of the Integral Boundary Layer Quantities
(U_∞ = 5 m/s, Tu_∞ = 4 %, X = 550 mm)

Figure 5.10 : Probability Distributions of the Velocity in the Boundary Layer
(U_∞ = 5 m/s, Tu_∞ = 4 %, X = 550 mm)

Figure 5.11 : Profiles of the Integral Boundary Layer Quantities
(U_∞ = 15 m/s, Tu_∞ = 4 %, X = 45 mm)

Figure 5.12 : Probability Distributions of the Velocity in the Boundary Layer
(U_∞ = 15 m/s, Tu_∞ = 4 %, X = 45 mm)

Figure 5.13 : Profiles of the Integral Boundary Layer Quantities
(U_∞ = 15 m/s, Tu_∞ = 4 %, X = 75 mm)

Figure 5.14 : Probability Distributions of the Velocity in the Boundary Layer
(U_∞ = 15 m/s, Tu_∞ = 4 %, X = 75 mm)

Figure 5.15 : Profiles of the Integral Boundary Layer Quantities
(U_∞ = 15 m/s, Tu_∞ = 4 %, X = 118 mm)

Figure 5.16 : Probability Distributions of the Velocity in the Boundary Layer
(U_∞ = 15 m/s, Tu_∞ = 4 %, X = 118 mm)

Figure 5.17 : Profiles of the Integral Boundary Layer Quantities
(U_∞ = 15 m/s, Tu_∞ = 4 %, X = 175 mm)

Figure 5.18 : Probability Distributions of the Velocity in the Boundary Layer
(U_∞ = 15 m/s, Tu_∞ = 4 %, X = 175 mm)

Figure 5.19 : Profiles of the Integral Boundary Layer Quantities
(U_∞ = 15 m/s, Tu_∞ = 1.8 %, X = 150 mm)

Figure 5.20 : Profiles of the Integral Boundary Layer Quantities
(U_∞ = 15 m/s, Tu_∞ = 1.8 %, X = 350 mm)

Figure 5.21 : Profiles of the Integral Boundary Layer Quantities
(U_∞ = 15 m/s, Tu_∞ = 1.8 %, X = 425 mm)

Figure 5.22 : Profiles of the Integral Boundary Layer Quantities
(U_∞ = 15 m/s, Tu_∞ = 1.8 %, X = 650 mm)

Figure 5.23 : Boundary Layer Parameter Distribution on a Re_x - y^+ Plane (U_∞ = 5 m/s, Tu_∞ = 4 %)

Figure 5.24 : Boundary Layer Parameter Distribution on a Re_x - y^+ Plane (U_∞ = 15 m/s, Tu_∞ = 4 %)

Figure 5.25 : Boundary Layer Parameter Distribution on a Re_x - y^+ Plane (U_∞ = 15 m/s, Tu_∞ = 1.8 %)

Figure 5.26 : Universal Velocity Distribution for Turbulent Velocity Profiles Near Smooth Walls (after Clauser, 1954)

Figure 5.27 : Distribution of the Boundary Layer Thickness (U_∞ = 5 m/s, Tu_∞ = 4 %)

Figure 5.28 : Distribution of the Boundary Layer Displacement Thickness (U_∞ = 5 m/s, Tu_∞ = 4 %)

Figure 5.29 : Distribution of the Boundary Layer Momentum Thickness (U_∞ = 5 m/s, Tu_∞ = 4 %)

Figure 5.30 : Distribution of the Boundary Layer Energy Thickness (U_∞ = 5 m/s, Tu_∞ = 4 %)

Figure 5.31 : Shape Factor H_{12} Distribution (U_∞ = 5 m/s, Tu_∞ = 4 %)

Figure 5.32 : Shape Factor H_{23} Distribution (U_∞ = 5 m/s, Tu_∞ = 4 %)

Figure 5.33 : Skin Friction Coefficient Distribution (U_∞ = 5 m/s, Tu_∞ = 4 %)

Figure 5.34 : Momentum Thickness Reynolds Number Distribution (U_∞ = 5 m/s, Tu_∞ = 4 %)

Figure 5.35 : Distribution of the Boundary Layer Thickness (U_∞ = 15 m/s, Tu_∞ = 4 %)

Figure 5.36 : Distribution of the Boundary Layer Displacement Thickness (U_∞ = 15 m/s, Tu_∞ = 4 %)

Figure 5.37 : Distribution of the Boundary Layer Momentum Thickness (U_∞ = 15 m/s, Tu_∞ = 4 %)

Figure 5.38 : Distribution of the Boundary Layer Energy Thickness (U_∞ = 15 m/s, Tu_∞ = 4 %)

Figure 5.39 : Shape Factor H_{12} Distribution (U_∞ = 15 m/s, Tu_∞ = 4 %)

Figure 5.40 : Shape Factor H_{23} Distribution (U_∞ = 15 m/s, Tu_∞ = 4 %)

Figure 5.41 : Skin Friction Coefficient Distribution (U_∞ = 15 m/s, Tu_∞ = 4 %)

Figure 5.42 : Momentum Thickness Reynolds Number Distribution (U_∞ = 15 m/s, Tu_∞ = 4 %)

Figure 5.43 : Distribution of the Boundary Layer Thickness (U_∞ = 15 m/s, Tu_∞ = 1.8 %)

Figure 5.44 : Distribution of the Boundary Layer Displacement Thickness (U_∞ = 15 m/s, Tu_∞ = 1.8 %)

Figure 5.45 : Distribution of the Boundary Layer Momentum Thickness (U_∞ = 15 m/s, Tu_∞ = 1.8 %)

Figure 5.46 : Distribution of the Boundary Layer Energy Thickness (U_∞ = 15 m/s, Tu_∞ = 1.8 %)

Figure 5.47 : Shape Factor H_{12} Distribution (U_∞ = 15 m/s, Tu_∞ = 1.8 %)

Figure 5.48 : Shape Factor H_{23} Distribution (U_∞ = 15 m/s, Tu_∞ = 1.8 %)

Figure 5.49 : Skin Friction Coefficient Distribution (U_∞ = 15 m/s, Tu_∞ = 1.8 %)

Figure 5.50 : Momentum Thickness Reynolds Number Distribution (U_∞ = 15 m/s, Tu_∞ = 1.8 %)

Figure 5.51 : Power Spectral Density on the Frequency and Wave Number Domain (U_∞ = 5 m/s, Tu_∞ = 4 %, Y = 0.2 mm)

Figure 5.52 : Power Spectral Density on the Frequency and Wave Number Domain (U_∞ = 5 m/s, Tu_∞ = 4 %, Y = 1.0 mm)

Figure 5.53 : Power Spectral Density on the Frequency and Wave Number Domain (U_∞ = 15 m/s, Tu_∞ = 4 %, Y = 0.2 mm)

Figure 5.54 : Power Spectral Density on the Frequency and Wave Number Domain (U_∞ = 15 m/s, Tu_∞ = 4 %, Y = 1.0 mm)

Figure 5.55 : Power Spectral Density on the Frequency and Wave Number Domain (U_∞ = 15 m/s, Tu_∞ = 1.8 %, Y = 0.2 mm)

Figure 5.56 : Power Spectral Density on the Frequency and Wave Number Domain (U_∞ = 15 m/s, Tu_∞ = 1.8 %, Y = 1.0 mm)

Figure 5.57 : Velocity Signal Processing for Intermittency Determination (U_∞ = 15 m/s, Tu_∞ = 1.8 %, X = 250 mm, Y = 0.2 mm)

Figure 5.58 : Probability Density Distributions of the Velocity Signals (U_∞ = 15 m/s, Tu_∞ = 1.8 %, X = 250 mm, Y = 0.2 mm)

Figure 5.59 : Velocity Signal Processing for Intermittency Determination
(U_∞ = 15 m/s, Tu_∞ = 1.8 %, X = 300 mm, Y = 1.0 mm)

Figure 5.60 : Probability Density Distributions of the Velocity Signals
(U_∞ = 15 m/s, Tu_∞ = 1.8 %, X = 300 mm, Y = 1.0 mm)

Figure 5.61 : Velocity Signal Processing for Intermittency Determination
(U_∞ = 15 m/s, Tu_∞ = 1.8 %, X = 400 mm, Y = 0.2 mm)

Figure 5.62 : Probability Density Distributions of the Velocity Signals
(U_∞ = 15 m/s, Tu_∞ = 1.8 %, X = 400 mm, Y = 0.2 mm)

Figure 5.63 : Velocity Signal Processing for Intermittency Determination
(U_∞ = 15 m/s, Tu_∞ = 1.8 %, X = 550 mm, Y = 1.0 mm)

Figure 5.64 : Probability Density Distributions of the Velocity Signals
(U_∞ = 15 m/s, Tu_∞ = 1.8 %, X = 550 mm, Y = 1.0 mm)

Figure 5.65 : Intermittency Factor Distribution as a Function of η
(U_∞ = 5 m/s, Tu_∞ = 4 %)

Figure 5.66 : Determination of Transition Inception Using Narasimha Procedure
(U_∞ = 5 m/s, Tu_∞ = 4 %)

Figure 5.67 : Intermittency Factor Distribution in the Physical Plane
(U_∞ = 5 m/s, Tu_∞ = 4 %)

Figure 5.68 : Intermittency Factor Distribution as a Function of ξ
(U_∞ = 5 m/s, Tu_∞ = 4 %)

Figure 5.69 : Intermittency Factor Distribution as a Function of η
(U_∞ = 15 m/s, Tu_∞ = 4 %)

Figure 5.70 : Determination of Transition Inception Using Narasimha Procedure
(U_∞ = 15 m/s, Tu_∞ = 4 %)

Figure 5.71 : Intermittency Factor Distribution in the Physical Plane
(U_∞ = 15 m/s, Tu_∞ = 4 %)

Figure 5.72 : Intermittency Factor Distribution as a Function of ξ
(U_∞ = 15 m/s, Tu_∞ = 4 %)

Figure 5.73 : Intermittency Factor Distribution as a Function of η
(U_∞ = 15 m/s, Tu_∞ = 1.8 %)

Figure 5.74 : Determination of Transition Inception Using Narasimha Procedure
(U_∞ = 15 m/s, Tu_∞ = 1.8 %)

Figure 5.75 : Intermittency Factor Distribution in the Physical Plane (U_∞ = 15 m/s, Tu_∞ = 1.8 %)

Figure 5.76 : Intermittency Factor Distribution as a Function of ξ (U_∞ = 15 m/s, Tu_∞ = 1.8 %)

Table 6.1 : The Low-Reynolds Functions Used in Various k-ε Turbulence Models

Figure 6.1 : General View of the Computational Mesh Employed in the Study of the Flow Around the Cylindrical Leading Edge

Figure 6.2 : Leading Edge Detail of the Computational Mesh Employed in the Study of the Flow Around the Cylindrical Leading Edge

Figure 6.3 : General View of the Computational Mesh Employed in the Study of the Flow Around the Elliptical Leading Edge

Figure 6.4 : Leading Edge Detail of the Computational Mesh Employed in the Study of the Flow Around the Elliptical Leading Edge

Figure 6.5 : Velocity Vector Plot of the Complete Computational Domain Around the Cylindrical Leading Edge

Figure 6.6 : Leading Edge Detail of the Vector Plot Illustrating the Flow Around the Stagnation Point of the Cylindrical Leading Edge

Figure 6.7 : Detail of the Vector Plot Illustrating the Boundary Flow Immediately After the Cylindrical Leading Edge

Figure 6.8 : Detail of the Vector Plot Illustrating the Boundary Flow Further Downstream of the Cylindrical Leading Edge

Figure 6.9 : Velocity Vector Plot of the Complete Computational Domain Around the Elliptical Leading Edge

Figure 6.10 : Leading Edge Detail of the Vector Plot Illustrating the Flow Around the Stagnation Point of the Elliptical Leading Edge

Figure 6.11 : Detail of the Vector Plot Illustrating the Boundary Flow Immediately After the Elliptical Leading Edge

Figure 6.12 : Detail of the Vector Plot Illustrating the Boundary Flow Further Downstream of the Elliptical Leading Edge

Figure 6.13 : Comparison of the Predicted Velocity Profiles Downstream of the Elliptical Leading Edge Against the Present Experimental Results for the C4 Test Case.

Figure 6.14 : General View of the Computational Mesh Employed in the Numerical Prediction of Transition

Figure 6.15 : Inlet Profiles for the Mean Velocity and Turbulent Kinetic Energy

Figure 6.16 : Comparison of the Predicted Skin Friction Coefficient Distribution Against Experimental Results

Figure 6.17 : Nagano-Hishida Model Predictions for Various Initial Dissipation Profiles in ERCOFTAC Case T3A (after Savill, 1991)

Figure A1.1 : Profiles of the Mean Velocity and Turbulence Intensity (C4 Plate, U_∞ = 5 m/s, Tu_∞ = 4 %, X = 50 mm)

Figure A1.2 : Profiles of the Skewness and Flatness Factors (C4 Plate, U_∞ = 5 m/s, Tu_∞ = 4 %, X = 50 mm)

Figure A1.3 : Profiles of the Mean Velocity and Turbulence Intensity (C4 Plate, U_∞ = 5 m/s, Tu_∞ = 4 %, X = 100 mm)

Figure A1.4 : Profiles of the Skewness and Flatness Factors (C4 Plate, U_∞ = 5 m/s, Tu_∞ = 4 %, X = 100 mm)

Figure A1.5 : Profiles of the Mean Velocity and Turbulence Intensity (C4 Plate, U_∞ = 5 m/s, Tu_∞ = 4 %, X = 150 mm)

Figure A1.6 : Profiles of the Skewness and Flatness Factors (C4 Plate, U_∞ = 5 m/s, Tu_∞ = 4 %, X = 150 mm)

Figure A1.7 : Profiles of the Mean Velocity and Turbulence Intensity (C4 Plate, U_∞ = 5 m/s, Tu_∞ = 4 %, X = 200 mm)

Figure A1.8 : Profiles of the Skewness and Flatness Factors (C4 Plate, U_∞ = 5 m/s, Tu_∞ = 4 %, X = 200 mm)

Figure A1.9 : Profiles of the Mean Velocity and Turbulence Intensity (C4 Plate, U_∞ = 5 m/s, Tu_∞ = 4 %, X = 250 mm)

Figure A1.10 : Profiles of the Skewness and Flatness Factors (C4 Plate, U_∞ = 5 m/s, Tu_∞ = 4 %, X = 250 mm)

Figure A1.11 : Profiles of the Mean Velocity and Turbulence Intensity (C4 Plate, U_∞ = 5 m/s, Tu_∞ = 4 %, X = 300 mm)

Figure A1.12 : Profiles of the Skewness and Flatness Factors (C4 Plate, U_∞ = 5 m/s, Tu_∞ = 4 %, X = 300 mm)

Figure A1.13 : Profiles of the Mean Velocity and Turbulence Intensity

(C4 Plate, U_∞ = 5 m/s, Tu_∞ = 4 %, X = 325 mm)

Figure A1.14 : Profiles of the Skewness and Flatness Factors
(C4 Plate, U_∞ = 5 m/s, Tu_∞ = 4 %, X = 325 mm)

Figure A1.15 : Profiles of the Mean Velocity and Turbulence Intensity
(C4 Plate, U_∞ = 5 m/s, Tu_∞ = 4 %, X = 350 mm)

Figure A1.16 : Profiles of the Skewness and Flatness Factors
(C4 Plate, U_∞ = 5 m/s, Tu_∞ = 4 %, X = 350 mm)

Figure A1.17 : Profiles of the Mean Velocity and Turbulence Intensity
(C4 Plate, U_∞ = 5 m/s, Tu_∞ = 4 %, X = 375 mm)

Figure A1.18 : Profiles of the Skewness and Flatness Factors
(C4 Plate, U_∞ = 5 m/s, Tu_∞ = 4 %, X = 375 mm)

Figure A1.19 : Profiles of the Mean Velocity and Turbulence Intensity
(C4 Plate, U_∞ = 5 m/s, Tu_∞ = 4 %, X = 400 mm)

Figure A1.20 : Profiles of the Skewness and Flatness Factors
(C4 Plate, U_∞ = 5 m/s, Tu_∞ = 4 %, X = 400 mm)

Figure A1.21 : Profiles of the Mean Velocity and Turbulence Intensity
(C4 Plate, U_∞ = 5 m/s, Tu_∞ = 4 %, X = 425 mm)

Figure A1.22 : Profiles of the Skewness and Flatness Factors
(C4 Plate, U_∞ = 5 m/s, Tu_∞ = 4 %, X = 425 mm)

Figure A1.23 : Profiles of the Mean Velocity and Turbulence Intensity
(C4 Plate, U_∞ = 5 m/s, Tu_∞ = 4 %, X = 450 mm)

Figure A1.24 : Profiles of the Skewness and Flatness Factors
(C4 Plate, U_∞ = 5 m/s, Tu_∞ = 4 %, X = 450 mm)

Figure A1.25 : Profiles of the Mean Velocity and Turbulence Intensity
(C4 Plate, U_∞ = 5 m/s, Tu_∞ = 4 %, X = 475 mm)

Figure A1.26 : Profiles of the Skewness and Flatness Factors
(C4 Plate, U_∞ = 5 m/s, Tu_∞ = 4 %, X = 475 mm)

Figure A1.27 : Profiles of the Mean Velocity and Turbulence Intensity
(C4 Plate, U_∞ = 5 m/s, Tu_∞ = 4 %, X = 525 mm)

Figure A1.28 : Profiles of the Skewness and Flatness Factors
(C4 Plate, U_∞ = 5 m/s, Tu_∞ = 4 %, X = 525 mm)

Figure A1.29 : Profiles of the Mean Velocity and Turbulence Intensity

(C4 Plate, U_∞ = 5 m/s, Tu_∞ = 4 %, X = 550 mm)

Figure A1.30 : Profiles of the Skewness and Flatness Factors
(C4 Plate, U_∞ = 5 m/s, Tu_∞ = 4 %, X = 550 mm)

Figure A1.31 : Profiles of the Mean Velocity and Turbulence Intensity
(C4 Plate, U_∞ = 5 m/s, Tu_∞ = 4 %, X = 575 mm)

Figure A1.32 : Profiles of the Skewness and Flatness Factors
(C4 Plate, U_∞ = 5 m/s, Tu_∞ = 4 %, X = 575 mm)

Figure A1.33 : Profiles of the Mean Velocity and Turbulence Intensity
(C4 Plate, U_∞ = 5 m/s, Tu_∞ = 4 %, X = 600 mm)

Figure A1.34 : Profiles of the Skewness and Flatness Factors
(C4 Plate, U_∞ = 5 m/s, Tu_∞ = 4 %, X = 600 mm)

Figure A1.35 : Profiles of the Mean Velocity and Turbulence Intensity
(C4 Plate, U_∞ = 5 m/s, Tu_∞ = 4 %, X = 700 mm)

Figure A1.36 : Profiles of the Skewness and Flatness Factors
(C4 Plate, U_∞ = 5 m/s, Tu_∞ = 4 %, X = 700 mm)

Figure A1.37 : Profiles of the Mean Velocity and Turbulence Intensity
(C4 Plate, U_∞ = 5 m/s, Tu_∞ = 4 %, X = 850 mm)

Figure A1.38 : Profiles of the Skewness and Flatness Factors
(C4 Plate, U_∞ = 5 m/s, Tu_∞ = 4 %, X = 850 mm)

Figure A1.39 : Profiles of the Mean Velocity and Turbulence Intensity
(C4 Plate, U_∞ = 5 m/s, Tu_∞ = 4 %, X = 1002 mm)

Figure A1.40 : Profiles of the Skewness and Flatness Factors
(C4 Plate, U_∞ = 5 m/s, Tu_∞ = 4 %, X = 1002 mm)

Figure A2.1 : Profiles of the Mean Velocity and Turbulence Intensity
(C4 Plate, U_∞ = 15 m/s, Tu_∞ = 4 %, X = 35 mm)

Figure A2.2 : Profiles of the Skewness and Flatness Factors
(C4 Plate, U_∞ = 15 m/s, Tu_∞ = 4 %, X = 35 mm)

Figure A2.3 : Profiles of the Mean Velocity and Turbulence Intensity
(C4 Plate, U_∞ = 15 m/s, Tu_∞ = 4 %, X = 40 mm)

Figure A2.4 : Profiles of the Skewness and Flatness Factors
(C4 Plate, U_∞ = 15 m/s, Tu_∞ = 4 %, X = 40 mm)

Figure A2.5 : Profiles of the Mean Velocity and Turbulence Intensity

(C4 Plate, U_∞ = 15 m/s, Tu_∞ = 4 %, X = 45 mm)

Figure A2.6 : Profiles of the Skewness and Flatness Factors
(C4 Plate, U_∞ = 15 m/s, Tu_∞ = 4 %, X = 45 mm)

Figure A2.7 : Profiles of the Mean Velocity and Turbulence Intensity
(C4 Plate, U_∞ = 15 m/s, Tu_∞ = 4 %, X = 50 mm)

Figure A2.8 : Profiles of the Skewness and Flatness Factors
(C4 Plate, U_∞ = 15 m/s, Tu_∞ = 4 %, X = 50 mm)

Figure A2.9 : Profiles of the Mean Velocity and Turbulence Intensity
(C4 Plate, U_∞ = 15 m/s, Tu_∞ = 4 %, X = 55 mm)

Figure A2.10 : Profiles of the Skewness and Flatness Factors
(C4 Plate, U_∞ = 15 m/s, Tu_∞ = 4 %, X = 55 mm)

Figure A2.11 : Profiles of the Mean Velocity and Turbulence Intensity
(C4 Plate, U_∞ = 15 m/s, Tu_∞ = 4 %, X = 65 mm)

Figure A2.12 : Profiles of the Skewness and Flatness Factors
(C4 Plate, U_∞ = 15 m/s, Tu_∞ = 4 %, X = 65 mm)

Figure A2.13 : Profiles of the Mean Velocity and Turbulence Intensity
(C4 Plate, U_∞ = 15 m/s, Tu_∞ = 4 %, X = 75 mm)

Figure A2.14 : Profiles of the Skewness and Flatness Factors
(C4 Plate, U_∞ = 15 m/s, Tu_∞ = 4 %, X = 75 mm)

Figure A2.15 : Profiles of the Mean Velocity and Turbulence Intensity
(C4 Plate, U_∞ = 15 m/s, Tu_∞ = 4 %, X = 83 mm)

Figure A2.16 : Profiles of the Skewness and Flatness Factors
(C4 Plate, U_∞ = 15 m/s, Tu_∞ = 4 %, X = 83 mm)

Figure A2.17 : Profiles of the Mean Velocity and Turbulence Intensity
(C4 Plate, U_∞ = 15 m/s, Tu_∞ = 4 %, X =91 mm)

Figure A2.18 : Profiles of the Skewness and Flatness Factors
(C4 Plate, U_∞ = 15 m/s, Tu_∞ = 4 %, X = 91 mm)

Figure A2.19 : Profiles of the Mean Velocity and Turbulence Intensity
(C4 Plate, U_∞ = 15 m/s, Tu_∞ = 4 %, X = 100 mm)

Figure A2.20 : Profiles of the Skewness and Flatness Factors
(C4 Plate, U_∞ = 15 m/s, Tu_∞ = 4 %, X = 100 mm)

Figure A2.21 : Profiles of the Mean Velocity and Turbulence Intensity

(C4 Plate, U_∞ = 15 m/s, Tu_∞ = 4 %, X = 106 mm)

Figure A2.22 : Profiles of the Skewness and Flatness Factors
(C4 Plate, U_∞ = 15 m/s, Tu_∞ = 4 %, X = 106 mm)

Figure A2.23 : Profiles of the Mean Velocity and Turbulence Intensity
(C4 Plate, U_∞ = 15 m/s, Tu_∞ = 4 %, X = 112 mm)

Figure A2.24 : Profiles of the Skewness and Flatness Factors
(C4 Plate, U_∞ = 15 m/s, Tu_∞ = 4 %, X = 112 mm)

Figure A2.25 : Profiles of the Mean Velocity and Turbulence Intensity
(C4 Plate, U_∞ = 15 m/s, Tu_∞ = 4 %, X = 118 mm)

Figure A2.26 : Profiles of the Skewness and Flatness Factors
(C4 Plate, U_∞ = 15 m/s, Tu_∞ = 4 %, X = 118 mm)

Figure A2.27 : Profiles of the Mean Velocity and Turbulence Intensity
(C4 Plate, U_∞ = 15 m/s, Tu_∞ = 4 %, X = 125 mm)

Figure A2.28 : Profiles of the Skewness and Flatness Factors
(C4 Plate, U_∞ = 15 m/s, Tu_∞ = 4 %, X = 125 mm)

Figure A2.29 : Profiles of the Mean Velocity and Turbulence Intensity
(C4 Plate, U_∞ = 15 m/s, Tu_∞ = 4 %, X = 133 mm)

Figure A2.30 : Profiles of the Skewness and Flatness Factors
(C4 Plate, U_∞ = 15 m/s, Tu_∞ = 4 %, X = 133 mm)

Figure A2.31 : Profiles of the Mean Velocity and Turbulence Intensity
(C4 Plate, U_∞ = 15 m/s, Tu_∞ = 4 %, X = 141 mm)

Figure A2.32 : Profiles of the Skewness and Flatness Factors
(C4 Plate, U_∞ = 15 m/s, Tu_∞ = 4 %, X = 141 mm)

Figure A2.33 : Profiles of the Mean Velocity and Turbulence Intensity
(C4 Plate, U_∞ = 15 m/s, Tu_∞ = 4 %, X = 150 mm)

Figure A2.34 : Profiles of the Skewness and Flatness Factors
(C4 Plate, U_∞ = 15 m/s, Tu_∞ = 4 %, X = 150 mm)

Figure A2.35 : Profiles of the Mean Velocity and Turbulence Intensity
(C4 Plate, U_∞ = 15 m/s, Tu_∞ = 4 %, X = 162.5 mm)

Figure A2.36 : Profiles of the Skewness and Flatness Factors
(C4 Plate, U_∞ = 15 m/s, Tu_∞ = 4 %, X = 162.5 mm)

Figure A2.37 : Profiles of the Mean Velocity and Turbulence Intensity

(C4 Plate, U_∞ = 15 m/s, Tu_∞ = 4 %, X = 175 mm)

Figure A2.38 : Profiles of the Skewness and Flatness Factors
(C4 Plate, U_∞ = 15 m/s, Tu_∞ = 4 %, X = 175 mm)

Figure A2.39 : Profiles of the Mean Velocity and Turbulence Intensity
(C4 Plate, U_∞ = 15 m/s, Tu_∞ = 4 %, X = 200 mm)

Figure A2.40 : Profiles of the Skewness and Flatness Factors
(C4 Plate, U_∞ = 15 m/s, Tu_∞ = 4 %, X = 200 mm)

Figure A2.41 : Profiles of the Mean Velocity and Turbulence Intensity
(C4 Plate, U_∞ = 15 m/s, Tu_∞ = 4 %, X = 250 mm)

Figure A2.42 : Profiles of the Skewness and Flatness Factors
(C4 Plate, U_∞ = 15 m/s, Tu_∞ = 4 %, X = 250 mm)

Figure A3.1 : Profiles of the Mean Velocity and Turbulence Intensity
(C4 Plate, U_∞ = 15 m/s, Tu_∞ = 1.8 %, X = 25 mm)

Figure A3.2 : Profiles of the Mean Velocity and Turbulence Intensity
(C4 Plate, U_∞ = 15 m/s, Tu_∞ = 1.8 %, X = 50 mm)

Figure A3.3 : Profiles of the Mean Velocity and Turbulence Intensity
(C4 Plate, U_∞ = 15 m/s, Tu_∞ = 1.8 %, X = 75 mm)

Figure A3.4 : Profiles of the Mean Velocity and Turbulence Intensity
(C4 Plate, U_∞ = 15 m/s, Tu_∞ = 1.8 %, X = 150 mm)

Figure A3.5 : Profiles of the Mean Velocity and Turbulence Intensity
(C4 Plate, U_∞ = 15 m/s, Tu_∞ = 1.8 %, X = 200 mm)

Figure A3.6 : Profiles of the Mean Velocity and Turbulence Intensity
(C4 Plate, U_∞ = 15 m/s, Tu_∞ = 1.8 %, X = 250 mm)

Figure A3.7 : Profiles of the Mean Velocity and Turbulence Intensity
(C4 Plate, U_∞ = 15 m/s, Tu_∞ = 1.8 %, X = 275 mm)

Figure A3.8 : Profiles of the Mean Velocity and Turbulence Intensity
(C4 Plate, U_∞ = 15 m/s, Tu_∞ = 1.8 %, X = 300 mm)

Figure A3.9 : Profiles of the Mean Velocity and Turbulence Intensity
(C4 Plate, U_∞ = 15 m/s, Tu_∞ = 1.8 %, X = 325 mm)

Figure A3.10 : Profiles of the Mean Velocity and Turbulence Intensity
(C4 Plate, U_∞ = 15 m/s, Tu_∞ = 1.8 %, X = 350 mm)

Figure A3.11 : Profiles of the Mean Velocity and Turbulence Intensity

(C4 Plate, U_∞ = 15 m/s, Tu_∞ = 1.8 %, X = 375 mm)

Figure A3.12 : Profiles of the Mean Velocity and Turbulence Intensity
(C4 Plate, U_∞ = 15 m/s, Tu_∞ = 1.8 %, X = 400 mm)

Figure A3.13 : Profiles of the Mean Velocity and Turbulence Intensity
(C4 Plate, U_∞ = 15 m/s, Tu_∞ = 1.8 %, X = 425 mm)

Figure A3.14 : Profiles of the Mean Velocity and Turbulence Intensity
(C4 Plate, U_∞ = 15 m/s, Tu_∞ = 1.8 %, X = 450 mm)

Figure A3.15 : Profiles of the Mean Velocity and Turbulence Intensity
(C4 Plate, U_∞ = 15 m/s, Tu_∞ = 1.8 %, X = 475 mm)

Figure A3.16 : Profiles of the Mean Velocity and Turbulence Intensity
(C4 Plate, U_∞ = 15 m/s, Tu_∞ = 1.8 %, X = 500 mm)

Figure A3.17 : Profiles of the Mean Velocity and Turbulence Intensity
(C4 Plate, U_∞ = 15 m/s, Tu_∞ = 1.8 %, X = 550 mm)

Figure A3.18 : Profiles of the Mean Velocity and Turbulence Intensity
(C4 Plate, U_∞ = 15 m/s, Tu_∞ = 1.8 %, X = 650 mm)

Figure A3.19 : Profiles of the Mean Velocity and Turbulence Intensity
(C4 Plate, U_∞ = 15 m/s, Tu_∞ = 1.8 %, X = 750 mm)

Figure A3.20 : Profiles of the Mean Velocity and Turbulence Intensity
(C4 Plate, U_∞ = 15 m/s, Tu_∞ = 1.8 %, X = 850 mm)

Figure B.1 : Correction Chart Applied to the Measured Values of Re_w^n for wall proximity (after Wills (1962))

Figure B.2 : The Correction Procedure Applied to a Typical Velocity Profile

Figure C.1 : Dimensionless Representation of the Turbulent Boundary Layer Indicating the Various Regions in the Boundary Layer

Figure C.2 : Determination of the Skin Friction Coefficient According to Clauser Method

Figure D.1 : Autocorrelation of the Axial Turbulence Component
(C4 Plate, U_∞ = 5 m/s, Tu_∞ = 4 %, X = 50 mm)

Figure D.2 : Autocorrelation of the Axial Turbulence Component
(C4 Plate, U_∞ = 5 m/s, Tu_∞ = 4 %, X = 425 mm)

NOMENCLATURE

A	: constant appearing in King's law
B	: constant appearing in King's law
C	: threshold used for the determination of intermittency
C_1, C_2	: constants appearing in k-ε turbulence model
Cf	: skin friction coefficient
Cp	: static pressure coefficient [$Cp = (p_i - p)/(P_0 - p)$]
C_μ	: constant appearing in k-ε turbulence model
D(t)	: detector function
D	: empirical function appearing in k-ε turbulence model
E	: normalised power spectral density
	; empirical function appearing in k-ε turbulence model
F(γ)	: a function of intermittency used in Narasimha procedure
G(u)	: cumulative probability density function of a signal u(t)
H_{12}, H_{23}	: boundary layer shape factors
I(t)	: intermittency function
K	: acceleration parameter [$K = (\nu / U^2)\, du/dx$]
L	: integral length scale of turbulence
M	: Mach number
N	: non-dimensional spot formation rate [$N = n\sigma\theta_t^3 / \nu$]
P	: stagnation pressure
R	: correlation coefficient
	; gas constant [273 Joule/Kg/K]
R_{11}	: non-dimensional correlation coefficient
R_t, R_y	: local Reynolds numbers appearing in k-ε turbulence model
Re	: Reynolds number
U	: velocity in the streamwise direction
S	: skewness factor
T	: flatness factor; time period; temperature
Tu	: turbulence intensity (percent)

X, Y, Z	: cartesian coordinates as defined in figure 3.1
f	: frequency
f_1, f_2, f_μ	: empirical functions appearing in k-ε turbulence model
g(u)	: probability density function of a signal u(t)
k	: wave number
	; turbulent kinetic energy
n	: number of turbulent spot breakdowns per unit time and spanwise distance
	; constant appearing in King's law
p	: static pressure
t	: time
u, v, w	: velocity components in the boundary layer
u′, v′, w′	: fluctuation of the velocity components
u^+	: non-dimensional velocity
u^*	: friction velocity
x	: axial distance measured on the solid surface
y	: normal distance from the wall
y^+	: non-dimensional distance in wall units

Greek

$\Gamma(\kappa)$	: probability density function of the Gamma distribution
Δp	: dynamic head
Δp_{Loss}	: pressure drop in a duct or over a turbulence grid
α	: speed of sound (air)
	; constant
β, β_1, β_2, β_3	: constants
γ	: intermittency factor (probability that the flow is turbulent)
	; specific heat ratio
δ	: boundary layer thickness
	; Dirac's delta function
δ^* (δ_1)	: displacement thickness of the boundary layer

δ_3 : energy dissipation thickness of the boundary layer

ε : turbulent kinetic energy dissipation rate

η : dimensionless distance [$\eta = (x - x_{ST}) / (x_{ET} - x_{ST})$]

; dimensionless length scale

θ (δ_2) : momentum thickness of the boundary layer

λ : distance from 0.25 to 0.75 intermittency [$\lambda = x_{(\gamma=0.75)} - x_{(\gamma=0.25)}$]

λ_θ : pressure gradient parameter [$\lambda_\theta = (\theta^2/\nu) (du/dx)$]

μ : dynamic viscosity (air)

μ_t : eddy viscosity (turbulent)

ν : kinematic viscosity (air)

ν_t : turbulent viscosity defined as μ_t / ρ

ξ : dimensionless distance in transitional area [$\xi = (x-x_t)/\lambda$]

κ : parameter of the Gamma distribution

ρ : density (air)

σ_k, σ_ε : constants appearing in k-ε turbulence model

σ : turbulent spot propagation parameter

τ : time step

$\tau,\tau_{xx},\tau_{yy},\tau_{xy}$: Reynolds stresses

ϕ : power spectral density

ω : circular frequency

Subscripts

B : barometric

; referred to Blasius analytical solution

ET : end of transition [$\gamma = 0.99$]

L : laminar (non-turbulent)

LT : length of transition [from $\gamma = 0.01$ to $\gamma = 0.99$]

S : sampling

ST : start of transition [$\gamma = 0.01$]

T : turbulent

TR : transitional

a	: ambient
e	: value at the edge of the boundary layer
n	: referring to a normalised parameter
r	: reattachment
s	: separation
	; static
	; smoothed
t	: start of transition (Narasimha method)
w	: near wall value
x	: based on the streamwise distance
∞	: free-stream value
0	: reference value
	; value at 0
Γ	: referring to the Gamma distribution
θ	: based on momentum thickness

Superscripts

-	: mean value
^	: most probable value
′	: deviation from the mean
.	: time derivative

General Notes

1. S.I. units should be assumed unless otherwise stated
2. In many cases throughout this thesis, reference has been made to the standard engineering drawing filling system used by the School of Mechanical Engineering of Cranfield University (e.g. PD21200 in figure 2.1)

CHAPTER 1

Introduction

CHAPTER 1

Introduction

1.1 INTRODUCTION

Since their introduction in the late thirties, gas turbines have found a wide range of applications in power generation for land sea and air. Of the group of engines that make use of the chemical energy of hydrocarbons to generate power, the gas turbine engine represents the most compact power source presently available. The historically well established technology of reciprocating engines dominated power generation for aviation before the war (having also been very successful in the automotive industry) although it is based on some design principles with inherent engineering disadvantages. It was only in the years of the second world war that gas turbines were starting their breakthrough into aircraft propulsion and significant advances have been made since.

In recent years, progress in gas-turbine technology has brought about the demand for the development of more accurate calculation procedures in order to facilitate the design and to improve the efficiency of these engines. A number of complicated fluid dynamic issues, including the full understanding of transition to turbulence over the blade surfaces has yet to be resolved. For many years laminar to turbulent transition in the boundary layer of turbomachinery blading has been considered to be short enough to be taken into account as instantaneous. However, the effect of such an assumption in the accuracy of many design procedures can be significant since the correct estimation of the friction losses in the boundary layers as well as heat transfer rates from the blading of various engine components is essential.

Transitional boundary layer flows soon attracted the interest of researchers and a considerable amount of effort has been devoted to the understanding of the physics of transition. It was only in recent years though, that attempts have been made to distinguish between the mechanism of natural transition occurring in the boundary layer of a solid surface in a "clean" flow and other mechanisms that can effectively speed up the transition process or bypass some stages of natural transition.

In general, the flow within a turbomachine is unsteady and turbulent including various coherent structures of vorticity. The fundamental flow problems involved in a modern axial turbomachine are schematically summarised in figure 1.1. A number of flow phenomena can actually influence the conditions under which the boundary layer changes from laminar to turbulent, such as instability in the free stream, background homogenous and isotropic turbulence, shear free stream flow and coherent flow structures including three dimensional flow phenomena. Acoustic noise, mechanical vibrations as well as surface roughness and dimensional accuracy of the solid walls of the flow passage can be considered as important parameters that can affect the boundary layer flow. These effects are more apparent in multistage machines where the interaction between consecutive stages generates an unsteady and highly perturbated flow environment. Even under these circumstances, the flow next to the solid surfaces can be either laminar or turbulent. The Reynolds number variation through a medium size gas turbine engine as given by Hourmouziadis (1989) is presented in figure 1.2. It is usually assumed that the flow undergoes transition from laminar to turbulent when the Reynolds number based on the streamwise distance along the surface is about $3.5\ 10^5$. Thus, it can be considered that in a real turbomachine, transitional flows are very likely to occur in the various gas turbine components.

In the following paragraphs, the present state of knowledge related to turbulent transition will be reviewed in brief. Some of the key issues in transition research will be addressed including the various modes of transition and the generation of turbulent spots. The statistics of turbulence and the description of transition through intermittency will be examined with respect to their impact on the understanding of transition.

1.2 THE ROLE OF LAMINAR TO TURBULENT TRANSITION IN TURBOMACHINERY FLOWS

A close look at the various details of boundary layer development in the light of its influence in gas turbine design soon reveals that laminar to turbulent transition in turbomachinery is a complicated phenomenon that involves a number of difficult fluid dynamics issues. The boundary layer which develops in the various internal flows in a gas turbine is a major contributor towards the total loss production. From the designer's point of view, both the accurate prediction of the transition location and the minimisation of any negative effects that might be produced as a result of the dramatic changes occurring in the boundary layer during transition, bear a lot of importance.

1.2.1 A General Discussion

This section of the thesis deals with the presentation of the flow phenomena involved in laminar to turbulent transition and their impact in turbomachinery flows. The fundamentals of the transition process attracted the interest of scientists from the late nineteenth century. Eventually, Osborne Reynolds conducted his famous dye experiment in a water pipe flow that constituted the first well documented attempt to distinguish between the laminar and turbulent regimes in a pipe flow. In the relevant paper published in the Philosophical Transactions of the Royal Society of London in 1883, Reynolds attempted to define the circumstances which determine when the motion of water shall be "direct" or "sinuous" (according to his own terminology). The fact that the flow in the boundary layer can also undergo transition was actually discovered much later than that of transition in a pipe. The theoretical explanation given to these phenomena at that time was that transition constitutes a problem of stability in laminar flows.

At the beginning of this century, Prandtl's school in Goettingen produced a number of significant scientific achievements including the analytical solution of the Navier Stokes equations for laminar boundary layer flow over a flat plate (Blasius, 1908) and the stability theory accomplished around 1930. Since then, a great deal of theoretical work has been devoted to the clarification of the significance of various parameters governing the process of transition.

In the thirties and the preceding years, the engineering world had been concentrating its efforts in the development of new and more efficient flying machines. The engineering and scientific achievements involved in the development of aircraft design were followed by an intense activity in the aerodynamics concerning the flow characteristics of the developing boundary layer over aircraft wings. In this case, the surrounding environment was considered to be free of large distortions and well structured flow patterns. Consequently, the relevant experimental investigations of the transition phenomena involved experimental layouts that provided very low free stream turbulence characteristics. The transition research of this period produced a quite clear picture of the transition process under low free stream turbulence (usually called natural transition). A comprehensive review of the various phases of the transition process has been incorporated in Schlichting's boundary layer theory that was first published in the early fifties (Schlichting, 1979).

Historically, the need for the scientific investigation of the flow phenomena involved in boundary layer transition under highly perturbated internal flows, arose only when the newly introduced gas turbine started to mature technologically. It is interesting that the aerodynamic design of a gas turbine still involves the use of a lot of empirical design concepts including estimations of the transition location and extent. For many years, designers of gas turbine blading, considered transition to be a "point" phenomenon which involved an infinitesimal transition length and a rough approximation of the transition location. This assumption often led to inaccurate predictions of the aerodynamic performance and the overall characteristics of the designed blading. The obvious reason that forced gas turbine designers to adopt such assumptions, has been

that the already existing experimental data for boundary layer transition under low free stream turbulence predicted transition lengths far too long compared to the actual transition lengths observed on the blading of real gas turbines (Addison and Hodson, 1990a&b, 1991).

The role of transition phenomena in the aerodynamics of turbomachinery has been critically reviewed by Mayle (1991). The existing state of knowledge has been summarised and a significant attempt has been made to utilise the experimental information gathered from any reliable previous data sets. Useful correlations for the transitional characteristics of the flow in the major components of a gas turbine have been produced. Walker (1992) presented an elaborate discussion of the previous work along the lines of Mayle's paper. Walker's review focused on transition in decelerating flows and the implementation of the concept of intermittency in the theoretical studies of transition. This publication raised a lot of questions concerning the appropriate interpretation of the existing data, and in a number of occasions offered alternative approaches for the explanation of transitional phenomena to the ones proposed by Mayle (1991). The differences in the approaches presented in the survey papers of Mayle and Walker largely reflected their different backgrounds, which are mainly in the turbine and compressor fields, respectively.

1.2.2 The Various Modes of Transition

Laminar to turbulent transition can occur in three substantially different ways that are commonly called "modes of transition". The different paths to turbulence can substantially affect the overall characteristics of the boundary layer flow, which eventually defines the macroscopic quantities defining the flow field. From the engineering point of view, the latter bear much more importance than the actual mechanism that induces them. Hence, the various modes of transition are usually studied independently and a clear distinction between the various stages involved in each mode is made.

The most commonly studied mode is the "natural transition" (Schlichting, 1979) that occurs as a result of the amplification of two dimensional Tollmien-Schlichting waves and the subsequent breakdown of turbulent spots. This mode of transition is not very common in the internal flow path of gas turbines. On the contrary, a very common mode of transition is the "bypass mode" (Morkovin, 1978). In this case, boundary layer transition occurs under the influence of strong flow irregularities in the core flow. This path of transition to turbulence involves the direct formation of turbulent spots with a mechanism that bypasses the amplification of Tollmien-Schlichting waves. Finally, the so called "separated flow transition" is also a common feature in gas turbines. This third transition mode involves separation of the laminar boundary layer under a strong adverse pressure gradient and the consecutive flow transition in the separated shear layer. After the start of the transition process the separated shear layer regains significant resistance against separation and the reattachment process is already under way. The end of the transition process has not always been found to be before reattachment (Walker, 1975, 1992). The physics of the separated flow transition presents an extra degree of complexity because it involves two of the most interesting phenomena in fluid mechanics; separated shear layers under turbulence and laminar to turbulent transition. Separated flow transition could occur following either the natural transition path or the bypass transition path to turbulence.

1.2.3 Boundary Layer Flow under Low Free Stream Turbulence

The process of transition in the boundary layer of a flat plate under very low free stream turbulence conditions has been considered by numerous investigators. Dryden (1936) was the first to investigate transition on a flat plate in great detail. Starting from the leading edge, the various stages involved in boundary layer transition on a flat plate can be summarised as follows:

i) Stable laminar flow following the leading edge.

ii) Unstable, laminar flow with two-dimensional Tollmien-Schlichting waves.

iii) Development of unstable, laminar, three-dimensional waves and vortex formation.

iv) Bursts of turbulence in places of very high local vorticity.

v) Formation of turbulent spots in places when the turbulent fluctuations are large.

vi) Coalescence of turbulent spots into a fully developed turbulent boundary layer.

An idealized sketch of the transition zone in the boundary layer on a flat plate at zero incidence that illustrates the various stages involved (fig. 1.3), has been presented by White (1974) (see also Schlichting, 1979).

The above described path to turbulence is often referred to as natural transition and it can only be observed in a boundary layer flow in the presence of an external flow of low turbulence intensity. Various investigators in the past dealt in great detail with the primary two-dimensional instability that develops in the boundary layer in the form of the Tollmien-Schlichting waves. It is now well accepted by the scientific community that this form of instability is lying very close to the "origin of turbulence".

1.2.4 A Short Note on the Stability Theory of Laminar Flows

The following paragraphs discuss in brief the principles of the stability theory that was developed in order to explain the experimental evidence that laminar flows undergo transition to turbulence. Although the stability theory can be applied in any kind of flows the following short analysis is focused on the boundary layer flow stability. The present discussion is primarily based on Gaster's (1974) investigation of the effects of the boundary layer growth on flow stability, and Schlichting's (1979) boundary layer theory.

The theoretical investigations that led to the development of the stability theory were based on the assumption that laminar flows are affected by certain small disturbances caused by a variety of sources including free stream turbulence, wall surface roughness, mechanical vibrations, acoustic noise, etc. In the case that these

disturbances decay in time, the mean flow can be considered as stable. Alternatively, if these small disturbances get amplified with time in the boundary flow, then the boundary layer flow is considered as unstable and the probability of laminar to turbulent transition is increased.

The initial stages of development of any disturbance are described by a set of perturbation equations derived from the Navier-Stokes equations by linearisation. Any general perturbation can split into normal modes and the flow is deemed to be stable or unstable depending on the behaviour of the least stable mode. Thus, in general the determination of the stability of a given flow requires the evaluation of the eigenvalues of a set of partial differential equations. In the case that the mean flow is defined as a function of only one spatial variable, the set of partial differential equations defining the perturbation is separable and the problem reduces to that of solving a set of ordinary differential equations. In boundary layers, the flow field has actually a weak dependence on a second spacial variable. The assumption that is usually made in this case is that the mean flows are almost one-dimensional and that the flow is parallel over some region. The relevant perturbation equation then separates and the ordinary differential equation obtained is known as the Orr-Sommerfeld equation.

Using the assumption of parallel flow Tollmien (1929) and Schlichting (1933) developed a suitable calculation procedure for the flow instability in the boundary layer. They predicted a critical value of the boundary layer Reynolds number above which travelling wave disturbances grow, derived from an asymptotic solution of the Orr-Sommerfeld equation. This theoretical formulation has been verified by a series of remarkable experimental results obtained by Schubauer and Skramstad (1948).

In order to derive the Orr-Sommerfeld equation, the mean laminar flow is assumed to be influenced by a disturbance which can be analysed in a number of partial fluctuations. Each of them consists of a wave that propagates downstream. It is possible then, to introduce a stream function representing a single oscillation of the disturbance in the following form:

$$\psi(x,y,t) = \phi(y)\, e^{i(\alpha x - \beta t)} \tag{1.1}$$

where, $\phi(y)$ represents the amplitude of the oscillation and α, β are constants related to the spacial and time dependence of the phase of the oscillation. By introducing this stream function into a simplified form of the Navier Stokes equations and using some algebra, we can obtain the Orr-Sommerfeld equation which is the fundamental differential equation for the disturbance (stability equation), in the following form:

$$(u - \frac{\beta}{\alpha})(\phi'' - \alpha^2\phi) - u''\phi = -\frac{i}{\alpha Re_\delta}(\phi'''' - 2\alpha^2\phi'' + \alpha^4\phi) \tag{1.2}$$

where, the primes denote differentiation with respect to the non-dimensional parameters y/δ and Re_δ.

The eigenvalue problem of the Orr-Sommerfeld equation has been examined by many investigators including Gaster and Jordinson (1975) in recent years. Very detailed analytical calculations on the stability of laminar flows have been performed for a variety of cases by numerous investigators. A closer investigation of these results and the calculation procedures used, reveals that further calculations were mathematically particularly involved. The theoretical results obtained this way covered the first two stages of transition as described earlier (see also fig. 1.3). Unfortunately, little of the information obtained this way, has been very relevant for gas turbine technology applications.

1.2.5 Bypass Transition

The numerous investigations of laminar to turbulent transition under idealised free stream conditions produced remarkable results and enhanced the understanding of the basic mechanisms that lead to the chaotic motion in the boundary layer flow after transition completion. These theoretical and experimental results though, have had little practical application in gas turbines where the main stream flow conditions are far from ideal. It should be emphasised that transition Reynolds numbers of $Re_{\theta t} = 100$ are not

uncommon in gas turbines, although the equivalent transition Reynolds numbers predicted by laminar stability theory are around 400.

The term bypass transition is usually attributed to Morkovin (1978), who defined as bypass, the path of transition to turbulence that cannot be identified as starting from a known linear instability and subsequent amplification of Tollmien-Schlichting waves. In his review paper, Morkovin (1978) also critically summarised the effect of various sources of instability that could induce transition to turbulence which bypass the idealised Tollmien-Schlichting path. He also argued that the old "Reynolds dye experiment" actually belongs to a larger bypass transition phenomena category. In the pipe flows considered here, it has been observed that the onset of transition may occur before the parabolic flow is established. These ideas were formed in view of the results obtained from the small disturbance experiments which were found not to be in total agreement with linear stability theory.

Another bypass phenomenon that has been described by Charters (1943), is the transition by transverse or lateral contamination. This experimental investigation involved tests under low turbulence in the free stream, in which transition started at some point in a normally laminar layer by an external disturbance. This initial flow irregularity affected the adjacent laminar boundary layer and spread laterally as the flow progressed downstream. The evolution of the lateral spread occurred at a constant rate and once transition started it was independent of the originating cause. Charters also discovered that turbulence grew from the edges of the plate from where it was suspended. Hot wire exploration of the flow field near the solid surface revealed that the turbulent front created due to the corner eddying region was developing laterally at a constant angle of about 9.6°. This behaviour is regarded to be similar to the evolution of strait-sided turbulent fronts generated by the interaction of eddying wake with the boundary layer of downstream solid surfaces.

The effect of two and three dimensional tripping devices on the transition process has been studied in detail by Gibbings et al. (1986) (see also Hall, 1968). The actual

process of transition after tripping devices is considered as a bypass process. The flow phenomena that dominate the transition process in this case, are considered to lay in the complicated structure formations in the wake of the tripping devices. Transition due to surface roughness or artificially introduced roughness elements is studied as a bypass phenomenon, as well. In this case, the physical processes that initiate transition are not very clearly understood up to now although it is usually assumed that the waviness in the microscale of the solid boundary has an immediate effect on the shear flow of the boundary layer.

Observations of the behaviour of the flow at very high Reynolds numbers, revealed that a number of flow particularities, typical of the high speed flows, have the potential of inducing bypass transition to turbulence. These flow phenomena can seriously affect the optimum design and performance of high speed vehicles, such as space shuttles and re-entry capsules. Transition in accelerating flows involves a lot of unclear points including the process of relaminarisation and the subsequent retransition. The transition phenomena under these circumstances have yet to be understood completely, but it is quite clear that they might involve various bypasses. Blair in various publications (e.g. Blair, 1992a&b) reported that in favourable pressure gradients, no Tollmien-Schlichting waves have been detected.

1.2.6 A Modern Approach to the Later Stages of Natural Transition and Bypass Transition

Since the first and possibly the second stages of transition are bypassed in several cases of realistic flow environments, the theory of laminar instability has been regarded as insufficient to explain theoretically the processes involved. The initial steps towards the formulation of a new theoretical approach that would explain the later stages of natural transition as well as bypass transition, have been taken by Emmons (1951). It is very interesting to note that Emmons' ideas for the formation of turbulent spots came about as a result of a flow visualisation experiment in a water channel, similarly to the breakthrough in transition research that came about as a result of the "Reynolds dye

experiment". The new theoretical approach was concerned only with the production, growth and convection of turbulent spots (fig. 1.4) and the eventual completion of transition with the agglomeration of spots.

The turbulent spots actually protrude beyond the already established laminar boundary layer. An isolated spot resembles a downstream pointing arrowhead in plane form (fig. 1.4). The speed of growth of the turbulent spot has been found by Schubauer and Klebanoff (1955) to be directly proportional to the free stream velocity. Actually, the velocity of the leading end of the spot was found to be around 88 % of the free stream velocity and the velocity of the trailing end to be around half (50 %) the free stream velocity (fig. 1.4). The most interesting characteristic of transitional flows is that there is no smooth change in the physics of the boundary layer flow. On the contrary, there is actually an abrupt change from turbulent to non-turbulent motion on the surface that defines the boundaries of a turbulent spot (see also the insert in figure 1.4).

Emmons' theory about transition was based on the principal that on every point on a body, the flow is turbulent for a fraction of time; the rest of time being non-turbulent. Transition to turbulence is thus seen to be essentially intermittent. Each point on the solid surface is covered by a laminar boundary layer, except during those periods of time during which a turbulent spot is moving over it. The fraction of time during which the flow over a particular point on a solid surface subjected to a stream is turbulent, has been defined as the "intermittency" at this point. Intermittency has the value of zero when the flow is laminar and one when the flow is turbulent. In any intermediate point covered with transitional fluid the value of intermittency obtains a value between zero and one. Since the spots grow as they move, the downstream points will be covered by turbulent spots for longer periods. Finally the spots overlap and cover downstream portions continuously.

Emmons initiated the development of a probability transition theory. The probability that a point $P_0(x_0,z_0,t_0)$ in the space-time domain is subjected to turbulent flow, can be calculated by assuming the existence of a function $g(x,z,t)$ of surface area

and time that accounts for the production of turbulent spots at a point P(x,y,t). A related assumption is that the spot is swept away by the main stream in a way that it does not propagate upstream. The physical consideration behind this assumption is that if turbulent spots did propagate upstream then turbulence would have been self-sustaining and as a result the permanent state of any boundary layer flow. All the points P that are likely to affect the flow field at P_0 through the generation of turbulent spots, lay on a conelike volume R upstream point P, called "the dependence volume". Using the same assumptions, a similar conelike volume can be defined downstream a given point $P_0(x_0,z_0,t_0)$. The, so called, "propagation volume" is the locus of points P(x,z,t) which are likely to be affected by a turbulent spot generated at P_0 (fig. 1.5).

Using the above theoretical considerations the turbulent intermittency has been defined as the sum of turbulent spot production, g(P), over a volume of all the points P which are sources of turbulent spots that will pass over the point P_0:

$$\gamma(P_0)=1-e^{-\iiint_R g(P)\,dx\,dz\,dt} \tag{1.3}$$

The hypothesis of random generation of turbulent spots over the transitional region of the boundary layer was not in complete agreement with some experimental observation made by Schubauer and Klebanoff (1955). In order to account for these findings, Narasimha (1957) proposed the hypothesis of "concentrated breakdown" which stated that spots form at a preferred streamwise location (a narrow band compared to the length of transition) randomly in time and crosswise position. This streamwise location is usually identified as the onset of transition x_t. The distribution of turbulent spot production within this narrow band has been shown to be Gaussian. Since Dirac's delta function is the limiting form of the normal distribution as the standard deviation goes to zero, an appropriate idealisation for the longitudinal spacial dependence of the spot production in time-averaged two-dimensional flows is usually assumed to be:

$$g(P) \cong g(x) = n\,\delta(x-x_t) \tag{1.4}$$

where n is the number of turbulent spot breakdowns per unit time and spanwise distance. The corresponding intermittency distribution for $x \geq x_t$ can be expressed as:

$$\gamma = 1 - e^{-\frac{n\sigma}{U}(x-x_t)^2} \tag{1.5}$$

where σ is Emmons' non-dimensional spot propagation parameter which depends on the shape and velocity of the turbulent spots. Measurements by Schubauer and Klebanoff (1955) indicated the value σ to be constant and about 0.27. It should be noted that a first crude approximation by Emmons (1951) suggested a value of 0.1.

Because of the intermittent character of the transitional boundary layer, it can be considered that the mean quantities of the transitional boundary layer in a time averaged flow can be obtained as a superposition of their laminar and turbulent counterparts. In order to calculate the value of any quantity at a streamwise location x, the effect of a laminar boundary layer starting from the leading edge is added to the effect of a turbulent boundary layer originating at x_t, in the proportion 1-γ to γ. For example, the skin friction coefficient could be calculated as:

$$c_{f_{TR}} = (1-\gamma)\, c_{f_L} + \gamma\, c_{f_T} \tag{1.6}$$

Narasimha (1957) and Dhawan and Narasimha (1958) applied the foregoing assumptions in order to obtain the universal intermittency distribution in the form of:

$$\gamma = 1 - e^{-\alpha \xi^2} \tag{1.7}$$

where α is a constant that has been given an empirical value of 0.412 and ξ represents a normalised streamwise coordinate in the transition region:

$$\xi = \frac{x - x_t}{\lambda} \qquad where \qquad \lambda = x_{(\gamma=0.75)} - x_{(\gamma=0.25)} \tag{1.8}$$

They also noted an interesting connection between the transition Reynolds number $Re_{\theta t}$ and the Reynolds number based on the physical extent of the transition zone Re_λ. The correlation originally suggested in order to obtain good agreement with the experimental data available has been of the following form:

$$Re_\lambda = \alpha\, Re_{\theta t}^{\beta} \tag{1.9}$$

where α and β are constants that in the initial publication have been given the empirical values of 5.0 and 0.8 respectively. Narasimha (1985) in his review paper on boundary

layer transition suggested some updated values for α and β, viz. $\alpha = 9.0$ and $\beta = 0.75$. Furthermore, using equation (1.7) and the fact that the value of the intermittency corresponding to $x = x_{ET}$ is $\gamma = 0.99$, the transition length can be calculated as follows:

$$LT = (x_{ET} - x_t) = 3.36\ \lambda \tag{1.10}$$

This result can be used together with equation (1.9) in order to obtain Narasimha's correlation for the transition length:

$$Re_{LT} = 30.2\ Re_{\theta t}^{0.75} \tag{1.11}$$

A similar correlation using the same principals with respect to the transition Reynolds number at the end of transition has been included in Mayle's review paper:

$$Re_{LT} = 75\ Re_{\theta ET}^{1.25} \tag{1.12}$$

Gostelow and Blunden (1988) conducted measurements of intermittency in transitional flows over a wide range of adverse pressure gradients. The location of transition inception has been identified by plotting the intermittency function $F(\gamma) = \sqrt{-\ln(1-\gamma)}$ against a non-dimensional distance $\eta = \frac{x - x_{ST}}{x_{ET} - x_{ST}}$. This technique that has been originally proposed by Narasimha, was found to be adequate for the identification of the universal intermittency distribution in the transition zone by Gostelow and coworkers.

1.2.7 Separated Flow Transition

Separated flow transition occurs under various circumstances in turbomachinery flows. Accordingly, the complete understanding of the flow phenomena involved and the implementation of controlled transition through separation could have a great impact on the overall performance of compressors and low-pressure turbines.

In the past, separated flow phenomena have been studied in great detail regarding mainly the effect of the recirculation area on the pressure distribution in the direction of the main stream over the studied surfaces. The recirculation bubbles are then classified as "long bubbles" or "short bubbles" according to their effect on the pressure distribution. Short bubbles have only local displacement effect in a way that the pressure distribution before and after the bubble can be predicted from the idealised flow without separation. Long bubbles on the other hand, interact with the external flow in such a way that the resultant pressure distribution is significantly different. Small changes in the overall characteristics of the flow field around a short recirculation bubble can cause the bubble to change from short to long with often catastrophic consequences.

Gaster (1969) along with a number of other investigators including Woodward (1967), Owen et al. (1955) and Crabtree (1959), suggested that the structure and behaviour of laminar separation bubbles is mainly dependant on the separation Reynolds number $Re_{\theta s} = \frac{U\theta_s}{\nu}$ and the pressure gradient parameter $\lambda_{\theta s} = \frac{\theta_s^2}{\nu}\frac{dU}{dx}$ at separation.

In an early theoretical study of laminar boundary layer flows, Thwaites (1949) suggested that the value of the pressure gradient parameter at the point of separation is constant (Thwaites laminar separation criterion):

$$\lambda_{\theta s} = \frac{\theta_s^2}{\nu}\frac{\Delta U}{\Delta x} \approx -0.082 \qquad (1.13)$$

where ΔU denotes the velocity change over the separated flow region based on the inviscid pressure distribution and Δx denotes the length of the separation bubble.

Usually, separation bubbles are initiated under the influence of strong adverse pressure gradients, before the start of transition. The transition process starts over the separated shear layer due to the influence of the free stream turbulence. It should be noted that the shear layer is more susceptible to external disturbances than the attached boundary layer. The separated shear layer becomes progressively more stable and eventually reattaches as turbulent boundary layer (fig. 1.6). The location of the transition

end has generated some conflicting arguments in the review papers of Mayle (1991) and Walker (1992). Walker, actually, proposed that the end of transition does not necessarily coincide with the end of the constant pressure region, as implied in figure 1.6. It was also argued that according to some experimental evidence, in certain cases, the transition process continues after reattachment.

Experimental evidence from flow visualisation experiments (Kalfas and Elder, 1991) suggested that the separated shear layer in recirculation bubbles occurring in the flow over a flat plate with semi-circular leading edge, reattaches as a completely turbulent boundary layer. It should be noted that this study was restricted to a particular pressure distribution and the phenomena observed were strongly related to the geometry of the leading edge. These results are also discussed later in this thesis. A quite elaborate experimental set of data concerning the same test configuration has been presented by Hazarika and Hirsch (1991), using hot-wire anemometry. Similar test configurations have been used by Goulas et al. (1992) in order to study the effects of free stream turbulence and coherent structures on the characteristics of the recirculation area. Finally, a recent investigation of the effects of turbomachinery blade incidence on separation bubbles has been presented by Walreavens and Cumpsty (1993). The experimental data produced by the foregoing studies have been incorporated in data sets used by Calvert (1994), in order to set up an inviscid-viscous method to predict the performance of the critical regions for different leading edge shapes.

Summarising the results obtained by Gaster (1969), Roberts (1980) and Bellows (1985), Mayle (1991) proposed a number of empirical correlations for the main characteristics of the separated flow transition. It should be noted that most of these data were obtained under very low free stream turbulence and may not be very appropriate for gas turbine design purposes. In the following correlations, Mayles' notation is used in the formation of the Reynolds numbers (as presented in figure 1.6). The Reynolds number based on the distance between separation and the end of the constant pressure portion of the bubble can be given as a function of the separation Reynolds number as follows:

$$Re_{xsT} = Re_{xT} - Re_{xs} = 700\ Re_{\theta s}^{0.7} \tag{1.14}$$

The Reynolds number based on the distance between separation and the start of transition (Narasimha method) appears to correlate differently with the separation Reynolds number for short and long bubbles:

$$\begin{aligned} Re_{xst} &= 300\ Re_{\theta s}^{0.7} \qquad \textit{Short Bubbles} \\ Re_{xst} &= 1000\ Re_{\theta s}^{0.7} \qquad \textit{Long Bubbles} \end{aligned} \tag{1.15}$$

It has also been noted that the transition length is not dependent on whether the bubble is short or long. The proposed correlation is of the following form:

$$Re_{xLT} = Re_{xT} - Re_{xt} = 400\ Re_{\theta s}^{0.7} \tag{1.16}$$

A critical comparison between the transition lengths predicted for separated and attached flow transition reveals that transition lengths in separation bubbles is much shorter than for attached flow. This behaviour could be used for gas turbine design purposes in order to control the transition process by separation.

1.2.8 Effects of the Free-Stream Turbulence

All the available well documented experimental results have been summarised by Mayle (1991). The evaluation of the existing correlations with respect to their ability to predict the trends of the primary experimental results, offered the opportunity to generate a new set of correlations that are consistent with each other and with the older theoretical considerations.

The influence of turbulence intensity and pressure gradient at low speed has been carefully examined by Hall and Gibbings (1972). The various methods for predicting transition that were available up to that time have been evaluated critically. The experimental results, partly obtained by the same authors (see also Hall, 1968), combined with the various features of the examined computational methods, enabled these authors to summarise the key data and propose a semi-empirical chart describing

the combined effect of pressure gradient and free-stream turbulence upon the beginning of transition.

The effects of free stream turbulence are particularly strong on the early stages of transition. In a free stream environment with zero pressure gradient in the streamwise direction ($\partial p/\partial x = 0$), the main effect of increased turbulence intensity in the free stream is to reduce the momentum thickness Reynolds number at which transition starts. For bypass transition, Mayle (1991) suggested the following correlations for the start of transition:

$$Re_{\theta ST} = 400\ Tu^{-5/8} \tag{1.17}$$

and transition length:

$$Re_{\theta LT} = 75\ (Re_{\theta ET})^{5/4} \tag{1.18}$$

Older correlations presented by other investigators including Hall and Gibbings (1972) which have been updated by Abu-Ghannam and Shaw (1980) have also been successful in predicting the trends in the variation of the critical parameters with turbulence intensity, although a generally applicable model that properly accounts for the effect of the dominant parameters is still under consideration.

Narasimha (1985) suggested that a modified turbulent spot production rate parameter, defined as:

$$N = \frac{n\sigma\theta_t^3}{\nu} \tag{1.19}$$

is more appropriate for the description of turbulence induced transition. The spot formation parameter N is usually evaluated using the following relation:

$$N = 0.412\ \frac{Re_{\theta t}^3}{Re_\lambda^2} \tag{1.20}$$

which is derived using the definition of N and Narasimha's universal intermittency distribution. This expression indicates the strong relationship between the increased spot production rate and the reduction in the transition length.

Narasimha (1985) suggested that N is independent from the free stream turbulence intensity level. Initially, the value given to N was $0.7\ 10^{-3}$. More recent experimental investigations, conducted mainly by Gostelow and co-workers, revealed that the value of N decreases monotonically with increasing free stream turbulence. Actually, Gostelow et al. (1992) suggested a correlation of the following form:

$$N = \alpha\ e^{\beta_1 \ln(Tu)} \tag{1.21}$$

where α and β_1 were given the values $0.86\ 10^{-3}$ and -0.564 respectively. This correlation predicts Narasimha's level of $0.7\ 10^{-3}$, at turbulence intensity level of 1.44%.

1.2.9 Effects of the Pressure Gradient

Experimental investigations of transition phenomena under streamwise pressure gradients are not very common in the literature. Some comprehensive measurements have been taken by Abu-Ghannam and Shaw (1980) in a range of zero, favourable and adverse pressure gradients. A quite detailed study of transition phenomena in accelerating flows has been obtained by Blair (1992a&b, 1983a&b). Gostelow and coworkers (1992, 1988) completed a remarkable set of transition experiments under adverse pressure gradient for a range of free stream turbulence conditions. Both previous studies included measurements of intermittency from which the onset of transition as well as the spot production rate could be determined. An earlier study by Arnal et al. (1979) considered the effect of adverse pressure gradient on transition in a low free stream turbulence intensity environment. This study included intermittency measurements based on the instantaneous velocity record generated with a fast data acquisition system. Arnal and Juillen (1977) presented the basic technique used in order to separate the intermittent signal into its laminar and turbulent portions.

It is worth noting at this point, that there exist two limits to the strength of the longitudinal pressure gradient that can be imposed on a flat plate flow. In an adverse pressure gradient environment, the limit is imposed by Thwaites laminar separation

criterion ($\lambda_{\theta s}$ = -0.082) and in an accelerating flow environment the limit is set by the process of relaminarisation.

In an attempt to estimate the transition length in strongly decelerating flow and to place limits on the possible range of transitional flow lengths, Walker (1987) developed the "minimum transition length model" based on the continuous breakdown hypothesis. The main difference between this model and Narasimha's "concentrated breakdown hypothesis" is that the periodic exchange between the breakdown of turbulent spots and non-turbulent motion is substituted by the continuous breakdown of turbulent spots. It is actually assumed that under strong adverse pressure gradient, the breakdown of turbulence occurs in every circle of primary instability wave, at a frequency approximated by:

$$\frac{\omega \nu}{U^2} = 3.2 \quad Re_{\delta^*}^{-\frac{3}{2}} \tag{1.22}$$

Furthermore, it is assumed that the completion of transition occurs at a streamwise location corresponding to the first longitudinal meeting of neighbouring turbulent spots (Walker and Gostelow, 1990)

The effect of turbulence on transition is much more pronounced in decelerating flows rather than in accelerating flows. Gostelow et al. (1992) studied the effect of the free stream turbulence intensity in a range of adverse pressure gradients. They attempted to formulated a new correlation that accounts for both the effect of turbulence intensity and adverse pressure gradient:

$$N = \alpha \; e^{(\beta_1 \ln(Tu) + \beta_2 \lambda_{\theta x} + \beta_3 \lambda_{\theta x} \ln(Tu))} \tag{1.23}$$

where the values of α and β_1 were kept the same as in equation (1.17) and of the extra factors β_2 and β_3 have been given values of -59.23 and 2.134 respectively. It is very interesting to note that the resistance of the boundary layer against separation is naturally increased by means of the significant changes in the transition process as the flow tends to reach the limit of Thwaites separation criterion (Thwaites, 1949). Finally, the overall

survey of the existing experimental data by Mayle (1991) led him to suggest that above a critical level of turbulence intensity (about 3%) the changes in the transition process are dominated by turbulence intensity, as implied by equation (1.17). Another important observation is that further increase in the free stream turbulence intensity will have minimal influence on the transition Reynolds number.

1.2.10 Effects Related to Turbomachinery Blading Aerodynamics

In the foregoing paragraphs, the individual effects of many gas turbine related flow phenomena on laminar to turbulent transition have been briefly reviewed. The actual flow in a real turbomachine though, involves a very complicated combination of all those effects. An additional phenomenon related to multistage turbomachines is the periodic and unsteady transition caused by the periodic passing of moving wakes generated at the previous stages. Many investigators in the past, including Walker (1974), Turner (1971), Addison and Hodson (1989a&b) and Mayle and Dullenkopf (1989, 1990) attempted measurements in real turbomachinery environment in order to clarify the combined influence and the degree of involvement of the various modes of transition on gas turbine flows.

Mayle and Dullenkopf attempted to generalise the turbulent spot theory arguing that transition to turbulence can occur in multiple modes in a way that more than one mode can actually occur simultaneously. A further assumption incorporated in this model was that turbulent spots generated due to a passing wake, coalesce with each other almost immediately because the production rate is extremely intense. This way they form a turbulent strip that grows and propagates within the surrounding laminar boundary layer.

Decelerating flows are a major source of loss production in axial turbomachine blades. The observation that the transition lengths under strong adverse pressure gradient are substantially reduced in parallel with an increase in the spot production rate is of fundamental importance for the loading capacity of axial flow compressors (Walker,

1987). This behaviour can be partially explained taking into account the increased resistance of turbulent boundary layer against separation.

Figure 1.7 presents some heat transfer results obtained by Turner (1971) on an unswept turbine blade in a two dimensional cascade. On the convex surface transition is detected by a sudden change in the values of the heat transfer coefficient at around 70% to 80% chord for the lower end of the range of free stream turbulence levels. In the upper range of turbulence intensity levels the change in the measured values is more gradual starting at around 10% chord and finishing at around the same location as previously observed. The flow on the concave surface is much more difficult to interpret because there is only gradual variation from the laminar to turbulent values without a distinct point of change.

Hodson (1984) undertook a set of measurements concerning transition and separation near the leading edge of a high-speed turbine blade. The effects of Reynolds number compressibility, incidence and free stream turbulence have been studied using hot-film anemometry (measurements of wall shear stress) in conjunction with a fast data acquisition system. Addison and Hodson (1990a&b, 1991) reported on a series of measurements concerning transition on axial-flow turbines using hot film anemometry techniques as described before. In figure 1.8 a set of measurements at rotor mid-span is presented. At this location the flow is essentially two-dimensional and free from the influences of tip leakage and secondary flows (Hodson and Addison, 1988). In this particular case the stator-rotor axial gap amounts to 50% of the stator axial chord. From figure 1.8 three distinct areas can be identified on the suction surface. The first is identified as the laminar zone which ends before 45% surface length. In this region the cyclic variation of the ensemble mean is in phase with the random unsteadiness which implies that there is momentum transfer due to the wake, although this is essentially a laminar region. The transitional region extends approximately from 45% to 67% surface length. In this region the relatively large increase in the shear stress signifies that the boundary layer flow starts to alternate between laminar and turbulent. As transition progresses the rms fluctuations no longer approach zero and the high frequency

fluctuations appear for longer periods of time. Finally the turbulent region extends from 67% surface length onwards. In this region the mean level of the rms traces are reduced and the random and the periodic components of the signal have similar magnitude.

An extensive experimental investigation of the transitional characteristics of the flow field through a five blade cascade has been reported by Deutsch and Zierke (1987, 1988a, 1988b). This experimental study has been undertaken using a relatively low inlet turbulence intensity level of 0.18% and a Reynolds number of 5 10^5. Laser Doppler Velocimeter has been employed in order to obtain detailed velocity and turbulence intensity data in a range of incidence angles (see also Zierke and Deutsch, 1990). A small leading edge separation bubble and a larger separated flow region at around 60% chord, have been found to be the dominant phenomena of the suction surface boundary layers. Measurement on the pressure surface indicated that the onset of transition occurred at around 63% chord. It has been also found that the transition process was not completed by the end of the blade. This behaviour has been attributed to the presence of a mild favourable pressure gradient near the trailing edge.

Summarising all the previous work, it can be concluded that transition in gas turbines is mainly dependent on the free stream turbulence, the various pressure gradients over the blade surfaces and the effect of the periodic and unsteady passing wakes. The effects of other sources of instability on transitional flows are minor compared to the effects of free stream turbulence. The onset and length of transition depends mainly on the free stream turbulence and pressure gradient. Additionally, the onset of transition might occur as a result of flow phenomena related to abrupt changes in the overall characteristics of the flow field such as periodic passing waves, shock waves, etc.

1.3 THE SCOPE OF THIS THESIS

The purpose of this thesis has been to study the effects of a more realistic flow environment on the transitional characteristics of the boundary layers developed on turbomachinery blading. Unfortunately, little of the available data is truly relevant to the complex flow within a turbomachine. Most of the previous work has been performed in an ideal environment involving flat plates with sharp leading edges in a very carefully kept "clean" flow. The present work has been undertaken in order to achieve a number of objectives:

1. To produce new more relevant data concerning the influence of turbomachinery flow effects on boundary layer development. This data added to that already existing, will help to develop a coherent view of the role of laminar to turbulent transition in gas turbine engines.

2. To investigate the effect of the leading edge shape on the characteristics of the boundary layer flow. The present study involved a number of test cases based on three flat plate configurations, in order to cover the range of transition modes involved in turbomachinery.

3. To study the effect of the free stream Reynolds number on the transitional characteristics of the boundary layer flow. The Reynolds numbers involved have been chosen to be in the relevant range for low speed gas turbine applications.

4. To examine the influence of the high free stream turbulence intensity on the characteristics of transition in the boundary layer. The free stream turbulence intensity levels considered were chosen to be in a range typical for turbomachinery applications.

5. To simulate the experimental test cases using a Navier-Stokes computer program equipped with suitable low Reynolds number turbulence models in order to develop more efficient computational schemes for the accurate prediction of turbomachinery flows. The evaluation and improvement of the ability of current turbulence models to predict transition under a variety of flow conditions has also been considered in the present study.

1.4 ORGANISATION OF THE THESIS

This thesis describes the experimental and computational studies performed in order to enhance the understanding of laminar to turbulent transition in gas turbines. Chapter 1 contains a general introduction to transition in turbomachinery flows, including a summary of the present state of knowledge. This section, in particular, describes the organisation of the remaining work presented in this thesis. In Chapter 2 the experimental arrangement used in this study is described. The main features of the test rig and the instrumentation used are discussed. The specifications and the manufacturing procedures used to construct the three sets of flat plates used in this project are being discussed. Chapter 3 addresses the experimental methods used in this investigation as well as their suitability for this work and their capacity to produce appropriate results in the framework of the objectives of this study. The flow visualisation experiments are described in Chapter 4. An overall survey for all the test cases at various free stream turbulence intensity and various Reynolds numbers has been conducted using the surface flow visualisation technique described in chapter 3. The data acquired in this way have been used to define the most relevant experimental investigation for more studies which involved a detailed investigation of the boundary layer on the C4 plate at high turbulence conditions. The results and discussion of this series of tests are presented in Chapter 5. The detailed measurements acquired with the hot wire technique using a high speed digital data acquisition system were used to determine the integral parameters of the boundary layer. Statistical analysis of these results is presented in the same chapter, including the method of statistical analysis and

information about intermittency and turbulence spectra. In Chapter 6 the computational approach is discussed. The procedure of numerical solution is addressed together with leading edge flow results as well as boundary layer transition results obtained using low Reynolds number turbulence modelling. The thesis is concluded in Chapter 7 where a short overall discussion of the results is presented. This chapter contains the conclusions of this study concerning the experimental and theoretical work as well as recommendations as to where further research should be focusing on.

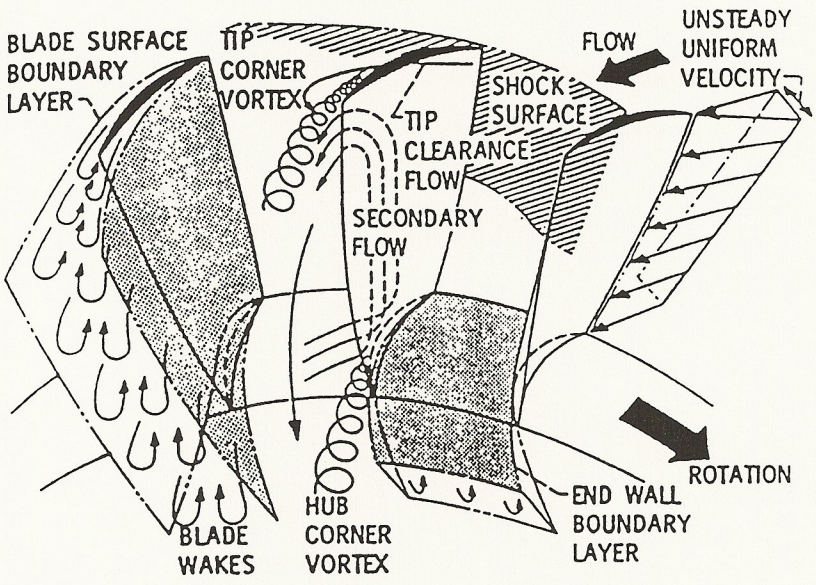


Figure 1.1	Fundamental Problems in Modern Compressor Flow Field (NASA-Lewis Research Center)

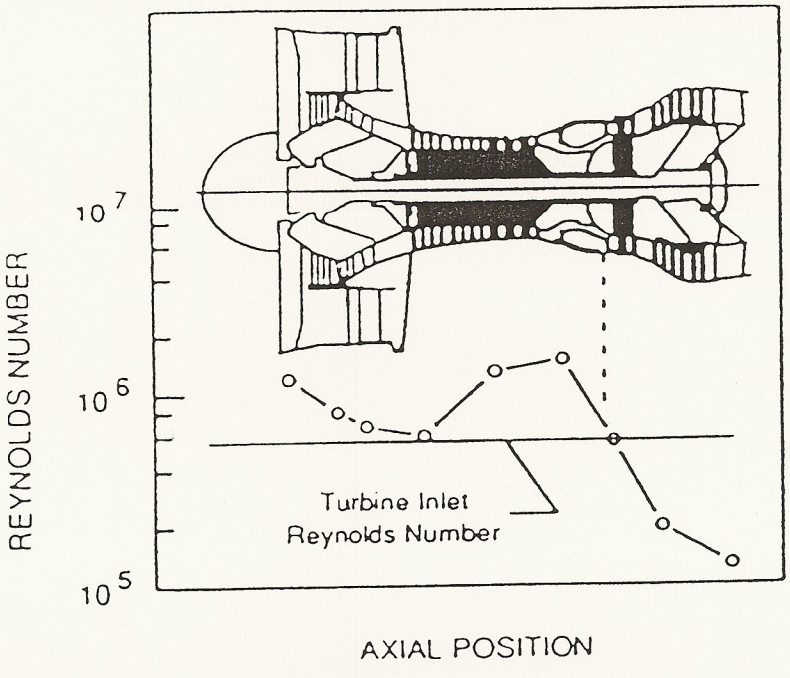
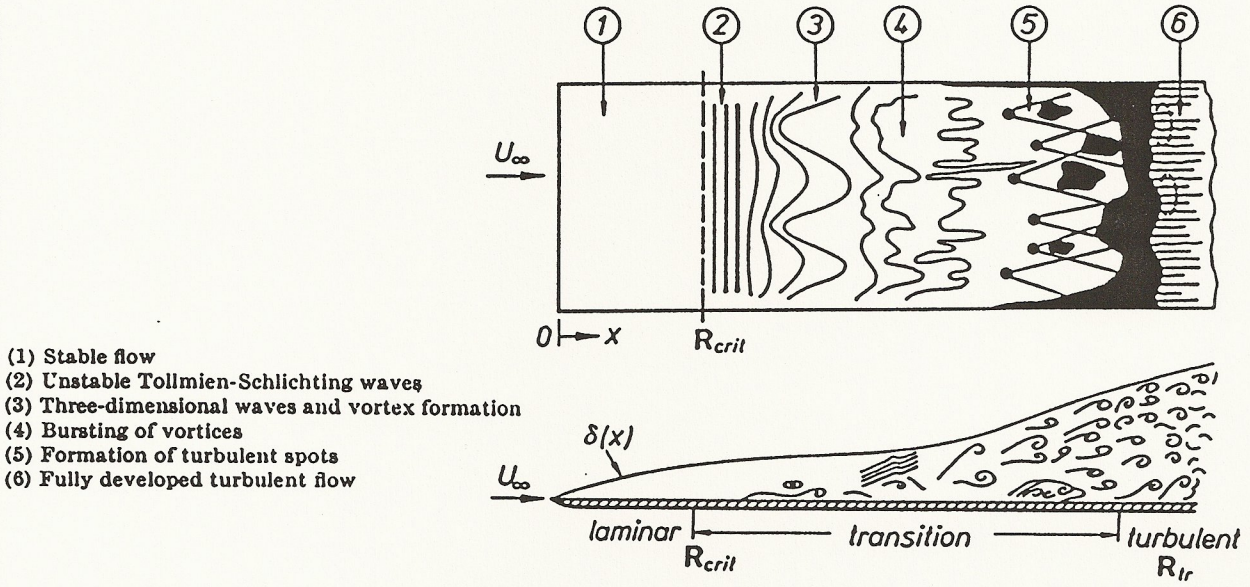


Figure 1.2	Reynolds Number Variation Through a Medium Size Gas Turbine (Hourmouziadis 1969)



(1) Stable flow
(2) Unstable Tollmien-Schlichting waves
(3) Three-dimensional waves and vortex formation
(4) Bursting of vortices
(5) Formation of turbulent spots
(6) Fully developed turbulent flow

Figure 1.3	Idealized Sketch of Transition Zone in the Boundary Layer on a Flat Plate at Zero Incidence {after White, (1974)}

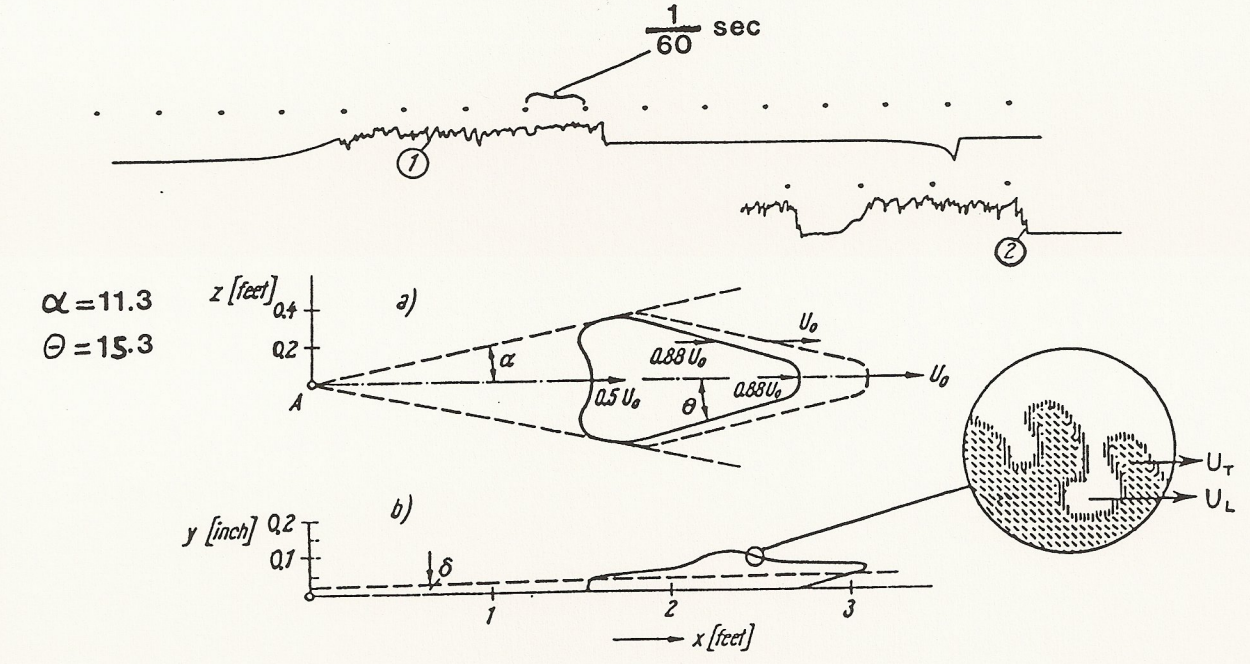


Figure 1.4	Growth of a Turbulent Spot in a Laminar Boundary Layer on a Flat Plate at Zero Incidence {after Schabauer-Klebanoff, (1955)}

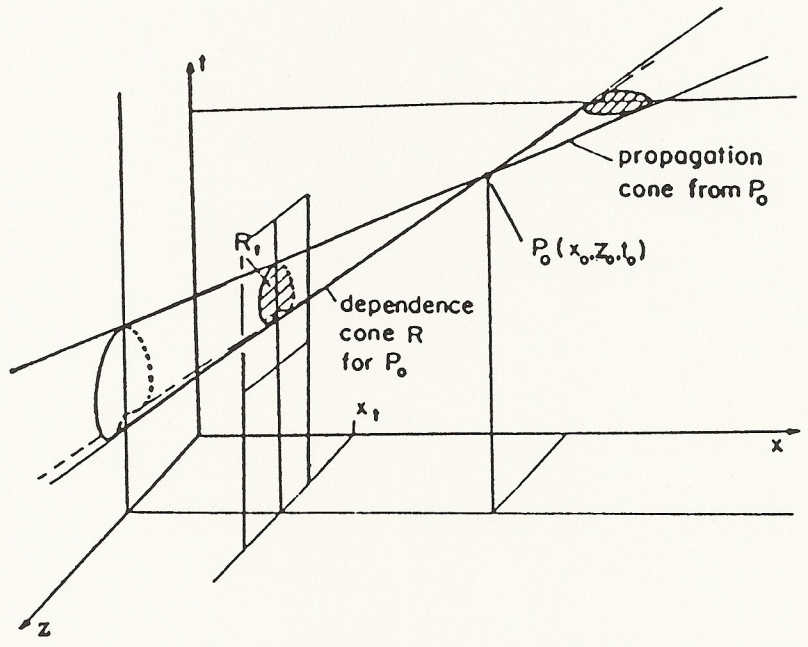


Figure 1.5	Propagation and Dependance Conelike Regions for any Point P_o (after Narasimha, 1985)

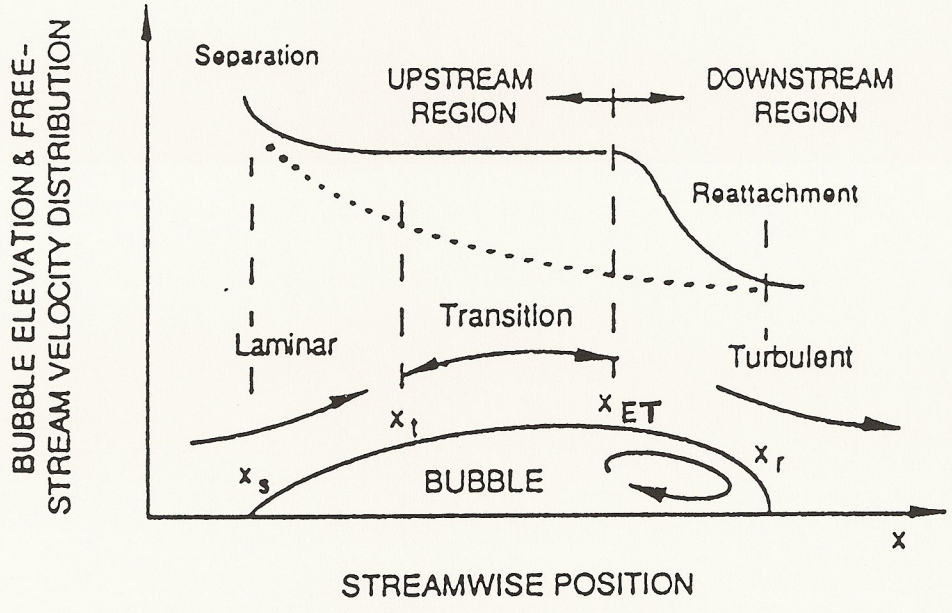
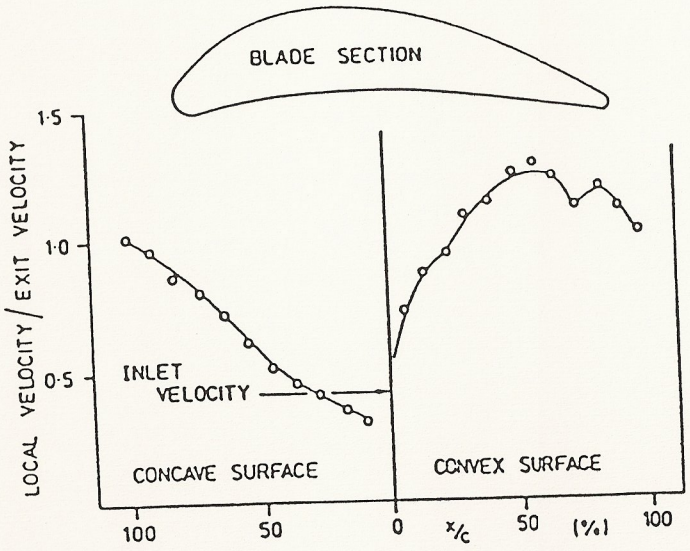


Figure 1.6	Flow Around a Separation Bubble Including the Corresponding Pressure Distribution (after Mayle, 1991)



TURBINE BLADE HEAT TRANSFER - TURNER

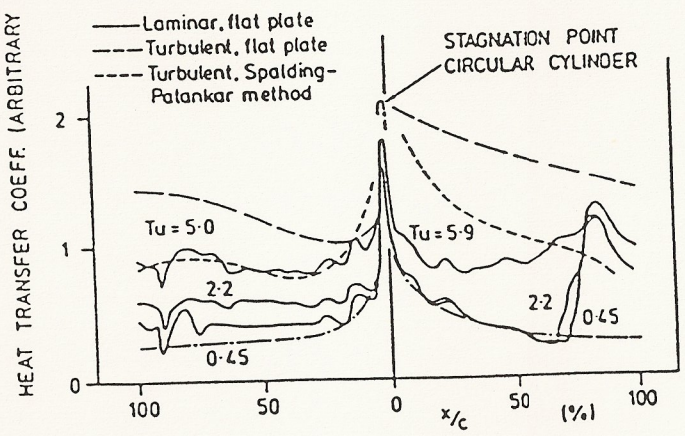


Figure 1.7	Surface Heat Transfer Measurements on Gas Turbine Blades (after Turner, 1971)

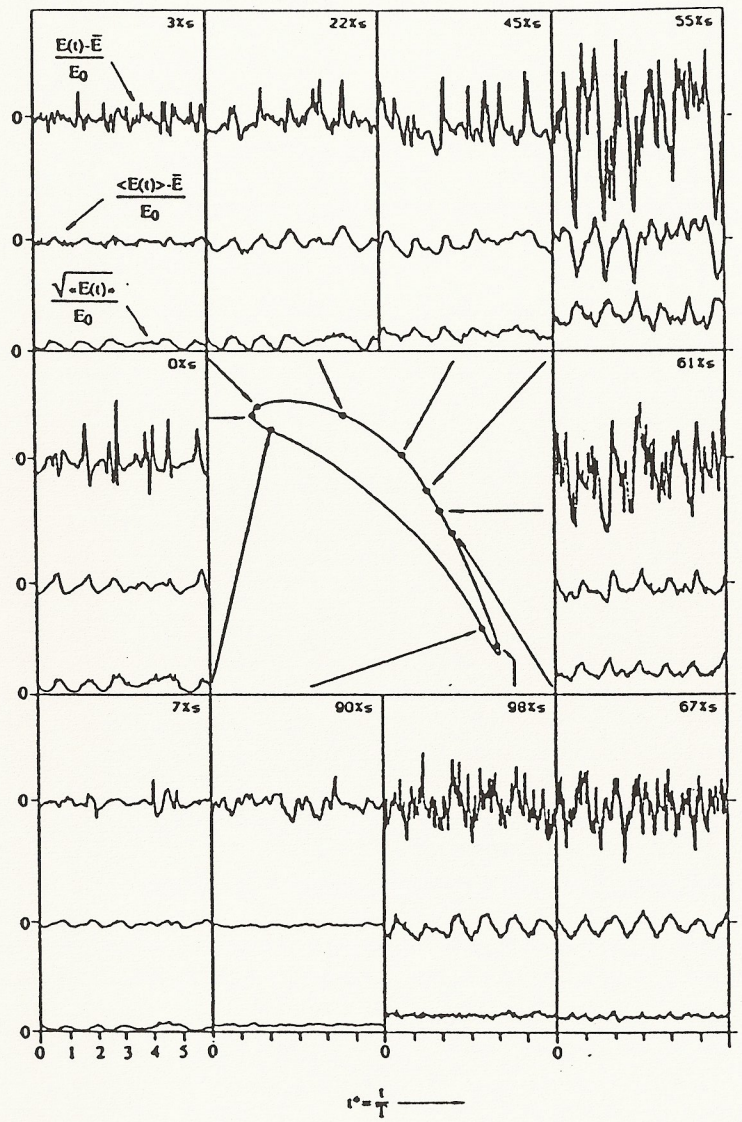


Figure 1.8	Rotor Mid-Span Hot-Film Results at Design Conditions(after Hodson and Addison, 1988)

CHAPTER 2

Experimental Arrangement

CHAPTER 2

Experimental Arrangement

2.1 INTRODUCTION

The experimental investigation involved in this project required a test rig capable of delivering the necessary flow conditions and providing the means for accurate measurements of the important flow parameters as described in the objectives of this thesis. The configuration of the test rig has been the subject of an extensive literature survey. A variety of similar test configurations have been used by previous investigators. The majority of these have been designed for boundary layer experiments under very low free stream turbulence intensity levels. The experimental facility used in this study has been designed and manufactured with certain objectives:

1. To be capable of generating constant, uniform and two-dimensional flow over the full length of the working section, in the range of main stream velocities of 0 m/s to 35 m/s under all free stream turbulence conditions.
2. To provide the necessary facilities for the generation of the appropriate turbulence intensity levels over the measuring surface, from very low levels (of fractions of one percent) to very high levels (of ten or even fifteen percent).
4. To accommodate the facilities for the simulation of the effect of the leading edge geometry of typical turbomachinery blading, on the characteristics of the boundary layer. Measuring surfaces with the required quality for measurements in the vicinity of the wall should be provided, in order to facilitate the recognition of the characteristics of the developing boundary layer.

5. To allow easy access to the measurement surfaces. Unrestricted optical access is required for the flow visualisation experiments as well as good access for the hot wire probes and traversing gears.
6. To have the ability of generating the necessary time record of the velocity field in the boundary layer using electronic equipment with adequate flexibility, in order to obtain the various statistical characteristics of turbulence.
7. To be simple from the design and manufacturing point of view.

The general arrangement comprises a small-scale low-speed wind tunnel equipped with the necessary electronic and other instrumentation. An overall schematic representation of the boundary layer wind tunnel developed in the course of this study, is shown in figure 2.1. The turbulence intensity level is increased artificially using various turbulence generating grids (fig. 2.12) located upstream of the working section of the tunnel. The general layout of the facility is shown in picture 2.2. In most wind tunnel configurations used for boundary layer investigation, special care is taken in order to keep the background turbulence level as low as possible. Although, the aim of this particular experimental investigation is to study the effects of high free stream turbulence intensities on transition to turbulence in the boundary layer, the background turbulence intensity of the tunnel has been controlled and reduced to very low levels using turbulence reduction screens and filtering material. A set of flat plates with appropriate leading edge shapes has been used in order to generate the appropriate surface for measurements. The flat plates were positioned at the mid-height of the test section in order to keep the flow around the plate as symmetric and two-dimensional as possible.

For the purposes of this work, a coordinate system had to be assigned to the tunnel in order to assure consistency in the references to the various measurement locations in the tunnel. This global coordinate system used appears in figure 2.4 attached to the wind tunnel. The streamwise coordinate (X) is measured from the leading edge of the plate. The crosswise coordinate (Y) is measured vertically to the flat plate (positive upwards) from the wind tunnel's central line. The coordinate (Z) is measured

normally to the other two (positive outwards) from the same point on the wind tunnel's central line. An auxiliary local coordinate system is used to describe distances measured from any point on the plate surface. The streamwise distance (x) is measured on the plate surface from the stagnation point, the crosswise distance (y) is measured normally to the wall (surface of the plate) having its zero value on the wall and the spanwise coordinate (z) is measured normally to the plane defined by x and y.

2.2 THE LOW SPEED WIND TUNNEL

A large variety of wind tunnel configurations have been used by previous investigators of transitional boundary layers under low speed conditions. Large close circuit tunnels have been used by Rolls Royce Plc (Roach and Brierley, 1989) and United Technologies Research Center (Blair et al., 1981). Gaster and coworkers (1975) at the University of Cambridge developed a closed circuit wind tunnel with particularly low background turbulence characteristics. An open circuit Clauser type wind tunnel has been used by Acharya (1985) at ABB. Abu-Ghannam and Shaw (1980) at the University of Liverpool carried out their work on natural transition using a moderate size open circuit tunnel. This experimental arrangement was used previously by Hall (1968) and in the recent years by Fasihfar and Johnson (1992). A similar wind tunnel configuration is being used by Gostelow and coworkers (1988) in Australia. The two other collaborators of Cranfield in the European Community funded research project used a large open circuit wind tunnel at the University of Brussels and a close circuit wind tunnel at the Aristotle University of Thessaloniki. A careful survey of the design principles used in all of the aforementioned experimental arrangements facilitated the development of the open circuit wind tunnel that was used in the course of this study.

2.2.1 General Layout of the Tunnel

The open circuit wind tunnel involved in this experimental investigation is a suction type tunnel. The design and assembly of the wind tunnel was carried out in such

a manner that any further modification could be easily performed. The tunnel is of open circuit design and consists of the inlet flare, a straight section of square ducting that contains the necessary facilities to accommodate the turbulence generating grids, the working section and the centrifugal fan that is driven by a powerful electric motor (fig. 2.1). The various tunnel components are discussed in the following sections.

The Inlet Flare: In an open circuit wind tunnel, the objective of the inlet flare is to accelerate the flow from ambient conditions to the flow conditions required in the working section. In this process special care should be taken in order to keep the flow smooth and attached all the way from the inlet to the throat. According to a general design concept, at the inlet of the flare where the air is moving slowly, steeper wall curvature can be used, since the flow can sustain strong acceleration without separating. As the acceleration progresses, the pressure gradient could change to adverse, reaching the limits of flow separation. In this case, the flare profile curvature is decreased (fig.2.3), in order to avoid the risk of recirculation. The shape of the inlet flare especially in the presence of adverse pressure gradients has been shown to have an important effect on the boundary layer thickness on the tunnel walls. The aerodynamic design of the inlet flare was based on an early work on flares for standard and annular air meters (McKenzie, 1966). Since the working section of the tunnel has a square cross-section, the original design which was based on circular ducts, has been transformed in order to match the overall dimensions of the tunnel. According to the general design principles the ratio (a^2/b^2) of the inlet highlight surface (a^2) to the throat of the flare (b^2) has been used as the main similarity parameter, where a and b signify the length of the inlet and throat cross-section sides respectively. Consequently, the flare shape has been approximated by a series of circular arcs to facilitate its construction. A schematic representation of the flare design procedure is given in figure 2.3. On the initial section of the parallel annulus a reference plane is prescribed for the static pressure measurement, that can be used in order to calculate the mass flow rate in the tunnel.

The contraction ratio obtained by the particular inlet flare design has to be calculated as the area ratio of an imaginary "imperceptible velocity" surface, upstream

of the inlet plane, to the surface of the throat. This imperceptible velocity surface has a hemi-spherical shape produced as a result of the intersection of four cylinders based on each of the four sides of the square inlet cross-section of the flare. The overall contraction ratio can then be calculated as:

$$R_f = \frac{S_a}{S_b} = \frac{\frac{\pi}{2}a^2}{b^2} \approx 4.867 \qquad (2.1)$$

The resultant contraction ratio, as calculated above, can be considered adequate for the purposes of this study. A higher contraction ratio would cause the background turbulence level of the wind tunnel to be reduced. Since this study is particularly concerned with flows involving high turbulence levels, further effort to decrease the background turbulence level would have minimal effect on the final results.

The Working Section: Ideally, the working section of a wind tunnel should have as large a cross-sectional area as possible. In this particular case the working section of the wind tunnel has been designed to be 1400 mm long and has a 400 mm by 400 mm square cross section. It has been constructed using high stability aluminium. The windows of the tunnel have been made of 10 mm thick high quality plexiglass that would be suitable for both flow visualisation and Laser anemometry experiments.

An appropriate suspension scheme for the flat plates has been utilised in the working section of the tunnel. A schematic of the flat plate suspension arrangement is given in figure 2.7. This arrangement provided three degrees of freedom in the adjustment of the position of the plate. The middle pair of screws could be fixed in such a way that they can serve as a pivot for the regulation of the angle of incidence. The other two pairs were used in order to suspend the plate from the tunnel walls using two pairs of "rose" joints. This arrangement permits the horizontal alignment of the flat plate in the tunnel as well as the regulation of the plate's location in the Y-direction.

The top wall of the working section has been manufactured to be completely detachable from the tunnel in order to facilitate the installation of all the necessary instrumentation. An alternative top wall has been made of plexiglass in order to improve the optical access to the flat plate during the flow visualisation experiments. Figure 2.4 shows a schematic view of the test section together with the position and overall dimensions of the flat plates.

The Driving Fan: The wind tunnel is driven by a powerful centrifugal fan with a flow rate of 9 m^3/s and 5 KPa pressure rise at 5500 rpm (maximum speed). A picture of the centrifugal impeller is presented in figure 2.5. The measured characteristics of the centrifugal fan, as derived from Dowly Rotol R.A.C. 4683(e) are presented in figure 2.6. The power output required from the fan is highly dependant on the aerodynamic load of the tunnel (i.e. the turbulence reduction screens, turbulence generating grids, and various other loss generating items located in the tunnel according to the needs of each particular test case). The flow rate and output of the fan are controlled by the impeller rotation speed. An aluminium disk of 46 mm diameter with 30 slots on its perimeter together with an optical switch was installed on the shaft of the fan in order to measure the rotational speed. Finally, a digital counter and a regulator were used to set and control the rotational speed of the fan. This configuration provided the flexibility of very fine regulation of the main stream velocity in the wind tunnel.

2.2.2 Wind Tunnel Characteristics

Investigations of the wind tunnel characteristics were carried out to identify the flow field quality over the range of Reynolds numbers used. Both pitot-static and single hot-wire probes (fig. 2.14) were used to take this series of measurements. A detailed analysis of these results has been presented in an earlier progress report (Kalfas & Elder, 1991).

A survey of the flow field has been performed without the test plate in position in order to establish that the flow field in the working section is free of major

distortions. A complete set of measurements including vertical and horizontal traverses at the working section's inlet plane, has been carried out using pressure probes. The development of the boundary layers on the walls of the tunnel covers approximately 15% of the cross section of the wind tunnel. It can, also, be considered that in the area surrounding the central line of the tunnel, where most of the measurements have been taken, the mean velocity of the main stream flow is constant and the lateral velocity gradients ($\partial U/\partial y$ and $\partial U/\partial z$) are not significant.

Using the single hot-wire probe shown in figure 2.14, the free stream turbulence was measured for the range of free stream velocities used. The flat plate was installed into the wind tunnel and the hot-wire sensor was positioned at X=0 mm, Y=100 mm and Z=0 mm with the probe support perpendicular to the test plate. This study was repeated for each plate and the results showed that the plate has no significant influence on the free stream turbulence intensity level. The total turbulence intensity was then approximated by the intensity of the streamwise normal stress, assuming the crosswise normal stress equal to the streamwise (isotropic turbulence), i.e. $u' = v' = w'$:

$$Tu = \frac{\sqrt{\frac{1}{3}\left(\overline{u'^2}+\overline{v'^2}+\overline{w'^2}\right)}}{U} \approx \frac{\sqrt{\overline{u'^2}}}{U} \qquad (2.2)$$

The overall residual turbulence intensity level in the working section of the tunnel was measured to be 0.3 percent when very fine turbulence reduction screens were installed upstream of the working section and special care was taken for noise and vibrations control. It can be considered, that in ordinary cases, where the mean level of turbulence intensity has been artificially augmented using turbulence generating grids, the impact of the residual turbulence intensity on the resultant turbulence intensity level was minimal. Under these circumstances, the background turbulence had a nominal value of 0.8 percent.

A series a measurements has been taken in order to quantify the integral length scale of the background turbulence, at a range of locations over the measuring surface.

In order to calculate the longitudinal integral length scale of turbulence L(X), a long high frequency sample has been taken at each measurement station.

Roughly speaking, a value for L(X) would indicate how far away from the measuring point in the X direction the streamwise velocity ceases to be correlated with itself. The physical meaning of the integral length scale could then be specified as the mean length of the vortices travelling with the velocity of the main stream.

$$L = \int_0^\infty R(r)\,dr \approx \int_0^\infty R_{11}(r)\,dr \tag{2.3}$$

where R(r) is the spatial correlation coefficient, defined as:

$$R(r) = \frac{\overline{u'(X)u'(X+r)}}{\sqrt{\overline{u'^2(X)}\;\overline{u'^2(X+r)}}} \tag{2.4}$$

The correlation coefficient in most turbulence work is approximated by the dimensionless quantity $R_{11}(r)$ defined as:

$$R_{11}(r) = \frac{\overline{u'(X)u'(X+r)}}{\overline{u'^2(X)}} \tag{2.5}$$

In practice, correlations with separation in the direction of the mean velocity U are difficult to measure because of the wake of any probe inserted in to the flow is liable to interfere with the flow field in the vicinity of the second probe. In this case, many experimentalists prefer to measure the autocorrelation coefficient $R(\tau)$ or the dimensionless quantity $R_{11}(\tau)$ defined as:

$$R_{11}(\tau) = \frac{\overline{u'(t)u'(t+\tau)}}{\overline{u'^2(t)}} \tag{2.6}$$

The autocorrelation coefficient could replace the spatial correlation coefficient quite efficiently, using "Taylor's hypothesis". Taylor (1938) argued that the changes in u with time at a fixed measuring point could be assumed to be due to the passage of a "frozen" pattern of turbulent motion past the point, provided that the mean (or free stream) velocity carrying the turbulent eddies was much larger than the turbulent velocity fluctuations. In other words, the velocity field at different instants could be related by the transformation:

$$u(x,t) = u(x - Ut,0) \tag{2.7}$$

and hence the local time derivative at the point of measurement could be replaced by the convective derivative:

$$\frac{\partial}{\partial t} \approx -U\frac{\partial}{\partial x} \qquad if \quad u' << U \tag{2.8}$$

The negative sign is necessary, because a positive value of ϑ/ϑX at a point in space corresponds to a negative value of ϑ/ϑt (Hinze, 1975).

Consequently, an accurate measurement of the autocorrelation with time separation τ can provide a good approximation of the spacial correlation with space separation $r = - U \tau$. The physical meaning of this relation is that the measurement, taken at $t_1 = t_0 + \tau$ (in the time domain), corresponds to the area of the "frozen" vorticity field which was situated at distance r behind the measurement point (in the space domain) at the time when the measurement was being undertaken at $t = t_0$ (in the time domain). The longitudinal length scale of turbulence can be approximated by:

$$L = \int_0^\infty R_{11}(r)dr \approx U \int_0^\infty R_{11}(\tau)d\tau \tag{2.9}$$

Considering that the background turbulence is homogenous and isotropic, the aforementioned velocity traces have been statistically analysed, in order to obtain the autocorrelation coefficient and length scale associated with the background turbulence of the mean flow in the working section of the tunnel. The overall value of the integral length scale was found to be approximately 15 mm, at the inlet of the working section.

2.3 The Experimental Model Plates

The experimental test plates used in this course of study have been designed and manufactured in order to provide measuring surfaces of high quality for the simulation of the effect of the leading edge shape on transition to turbulence. A series of three test plates with various leading edge shapes have been constructed to cover completely the

width of the working section (fig. 2.4). Apart from the leading edge shape, special care was taken to keep all the three plates identical in all other respects. The primary features of the three plates tested are compared in figure 2.8. An identical set of flat plates has been provided to the other two collaborating European Universities, in order to create a network of experimental facilities with similar geometrical configuration. This arrangement facilitated the exchange and inter-comparison of experimental results, between the three Universities.

2.3.1 Raw Material Specifications

Premachined aluminium alloy with hight dimensional stability was used for the construction of all plates. The material used, belongs to the 7000 series of Aluminium-Zinc-Magnesium-Cooper Alloys for aeronautical applications and is manufactured by CEGEDUR PECHINEY under the trade name FORTAL StS. The raw material specifications were as follows:

Tensile Strength	: 220 N/mm^2
Module of Elasticity	: 72000 N/mm^2
Density	: 2800 Kg/m^3
Thermal Conductivity at 20 °C	: 121 W/mK

The raw material came as a premachined flat plate, 10 mm thick with the following tolerances (maximum variation):

Surface Finish	: less than 0.6 μm CLA [1*]
Thickness	: ±0.1 mm
Flatness	: 0.15 mm/m (with the plate on a flat surface and concave side facing upwards)

[1*] CLA : Central Line Average

2.3.2 Leading Edge Design

The first plate has been manufactured with a cylindrical leading edge (fig. 2.8). In this case, the circular profile of the leading edge has a radius of 5 mm and covers the plate width. A laminar separation bubble has been formed in the area of the semi-circular leading edge for the whole range of free stream conditions tested. Under these circumstances, the separated shear layer over the recirculation bubble undergoes transition from laminar to turbulent. This geometrical formation was designed to study transition triggered by a laminar separation bubble (in the context of Mayle (1991) and Walker (1992)). A similar configuration has been used to study this mode of transition by Steward (1987). In this case the cylindrical leading edge has been combined with short converging tail, forming a quite blunt aerofoil shape.

The second flat plate configuration involves a sharp leading edge (fig. 2.8). This is the most conventional plate design and a great many boundary layer studies have been undertaken using similar configurations and therefore the data produced using this plate could be used for comparison with data appearing in the literature. Abu-Ghannam & Shaw (1980) used a similar aluminium plate with rounded leading edge that was introduced to the flow at a 0.5° angle of incidence so that the forward stagnation point was located at the upper side of the rounded leading edge. A similar plate configuration, made of plexiglass, has been utilised by Roach and Brierley (1989), set at an analogous angle of incidence in order to avoid leading edge separation (see also ERCOFTAC test cases T3A, T3B, T3C (Savill, 1992)). The underside of the leading edge area has been given an elliptical form. The main reason for this, was to avoid the formation of a separation bubble at the end of the inclined region which could effect the flow on the measuring surface of the plate (fig. 2.9). Gostelow & co-workers (1988, 1990) utilised the elliptical surface of a very similar polished wooden plate, as the measuring surface. The ellipse on the underside surface had a minor axis of 10 mm and a major to minor axis ratio of 7. To ensure the best performance of the flat plate the ellipse has been given a 10 degrees inclination with respect to the measuring surface. In this way, the

wedge angle of the leading edge is only slightly greater than 10 degrees and the end of the elliptical part is tangential to the underside surface.

The last plate of the series was designed with a leading edge shape based on a symmetric C4-aerofoil profile (fig. 2.8). Various previous investigators used symmetric leading edge shapes. Gaster and coworkers used a super-elliptic leading edge profile (see also ERCOFTAC test case T3D (Savill, 1992)). Hall and Hislop (1938) used two flat plate configurations including an elliptical profile. The following analytical expression of the C4 blade thickness distribution was used for the manufacturing of the flat plate with the C4 leading edge :

$$\begin{cases} 2(28.110p^3-25.281p^2-6.563p+15.492\sqrt{p})\dfrac{t_{max}}{10} & p<0.3 \\ 2\,(3.448p^3-14.632p^2+7.848p+3.869)\dfrac{t_{max}}{10} & p\geq 0.3 \end{cases} \quad (2.10)$$

where p is the fractional distance from the leading edge measured along the central line, and t_{max} is the designated maximum thickness of the blade (Calvert, 1987). The thickness distribution of the profile was used to the maximum thickness point, in a way that both sides meet tangentially with the flat plate surface. This configuration represents the most interesting test case from the turbomachinery applications point of view since the C4 profile is often used in the design of turbomachinery blading. This particular profile was selected in order to avoid laminar separation and to provide the means to study natural and bypass transition from laminar to turbulent on a realistic turbomachinery leading edge.

The circular leading edge was formed using a semi-circular form tool. The more complex geometries of the second and third plate required the use of more advanced Electro Discharge Machining (EDM) methods. In this process the desired thickness distribution was initially formed in a graphite electrode. The electrode was then used to take metal from the aluminium plate (fig. 2.9) and eventually provide the required shape.

The surface finish after the EDM operation was as low as 24 VDI [2*]. The leading edge area was then hand finished to a surface finish level equivalent to the rest of the plate, see section 2.3.1.

The leading edge shapes used in the course of this study were designed to cover a large range of test cases in order to produce some more relevant results for turbomachinery applications. In recent years, Double Circular Arc (DCA) airfoil design is often used in the development of new turbomachinery blading. The leading edge shape of a Double Circular Arc blade is cylindrical, where the included angle to the tangent points, measured on the circular arc, lies typically between 165° and 175° (see also AGARD-AR-275). Therefore, this configuration could be considered as being similar to the flat plate with a cylindrical leading edge where the equivalent included angle is 180°. However, on a C4 configuration the relevant included angle is of the order of 105°. Also there is a continuous curvature change in the geometrical formation of the C4 profile, as opposed to the constant radius of the DCA configuration. This arrangement provides gradual acceleration over the leading edge region which makes the C4 profile configuration more robust against laminar separation. On the other hand, the DCA profile configuration makes full use of the available length of the circular arc for accelerating the flow, since, as discussed later in this thesis, separation on the flat plate with cylindrical edge occurs in the range of 170° to 180° included angle on the circular arc.

There is actually a whole range of test cases between the circular arc and the C4 where the smoother flow acceleration takes place. The circular leading edge shape represents one extreme of the scale. The C4 profile configuration is sitting very near the other extreme of the scale. A full picture of the leading edge flow phenomena that affect laminar to turbulent transition could be obtained only by a careful investigation of transition process in conjunction with a number of leading edge configurations that cover the range between the two extremes.

[2*] According to VDI 3400 Standard (equivalent to 1.4 μm CLA)

2.3.3 Static Pressure Tappings

All the flat plates produced for this project are fitted with a large number of static pressure tappings. Nineteen gauge (1.016 mm OD and 0.508 mm ID)[3*] hypodermic tubes were embedded into the aluminium plates to carry the pressure levels to the trailing edge region and then to the manometer for measurement. The concentration of static pressure tappings is higher in the leading edge area because higher pressure gradients could be anticipated in this region. This arrangement of pressure tappings was used to measure the streamwise distribution of the pressure coefficient as well as to facilitate the setting of the zero incidence on the symmetrical plates. A more detailed description of the pressure tappings layout on all the flat plate configurations can be found in the progress report (Kalfas & Elder, 1991). Figure 2.10 shows the location of the pressure tappings on the three leading edge shapes. The location of the rest of the static pressure tappings on the working section coordinate system are given in table 2.1 for all three test plate configurations.

The cylindrical leading edge plate is equipped with 7 static holes distributed along the circular profile every 15 degrees starting from the central line (fig. 2.10). Another 9 pairs of static pressure tappings on either side of the plate are used to cover the flat surface. The latter are clustered towards the leading edge where larger variations in pressure are expected. Such static pressure tappings are used to measure the pressure distribution over the length of the plate and for adjusting the zero incidence.

The sharp leading edge plate has been fitted with one total pressure probe positioned just underneath the measuring surface at X=0 (fig. 2.10). The next pressure tapping is located 20 mm downstream of the leading edge because at closer stations the plate was insufficiently thick to accommodate static pressure tappings. A minimum length to diameter ration of 3 is required for a straight length of pipe, perpendicular to

---

[3*] OD : Outer Diameter

ID : Inner Diameter

No	Cylindrical		Sharp	C4	
	Top	Bottom	Top	Top	Bottom
1	0		0	0	
2	0.170		20	3.296	
3	0.670		25	10.846	
4	1.465		30	24.4	24.4
5	2.5		35	36.548	
6	3.706		40	41.406	
7			45	47.115	
8			50		
9					
10	5		55	50	50
11	7	7		52	52
12	13	13		56	56
13	21	21	64	64	64
14	37	37	80	80	80
15	69	69	92	92	92
16	133	133	176	176	176
17	261	261	304	304	304
18	517	517	560	560	560
19	1029	1029	1072	1072	1072

Table 2.1 : Location of Pressure Tappings in the X Direction, for the Three Plate Configurations (According to PB21200, PD21216/2-3)

the measuring surface, in order to achieve satisfactory accuracy on the static pressure measurements. The additional tappings are equally spaced up to 55 mm downstream of the leading edge and the rest arranged according to the clustering rule applied to the other plates. In this plate the underside was not fitted with static pressure tappings.

Finally, on the C4 leading edge plate, 8 static pressure tappings were distributed on the profiled plate in such a way that they were distributed from 0 to 90 degrees (fig.2.10). The fourth pressure tapping, located at 10 degrees, has a symmetrical tapping on the underside. These two tappings were used to provide a reference measurement point for arranging zero incidence. The rest of the pressure tappings are located using the same clustering rule used for the two other plates. All tappings on the flat surface have a corresponding tapping on the underside to help the zero incidence adjustment and ensure tunnel symmetry.

2.4 Turbulence Generating Grids

The flow in a turbomachine is known to experience a high degree of turbulence intensity. To simulate the effect of turbulence on the transitional characteristics of the flow and to create a range of representative environments in the wind tunnel, a number of sizes and types of turbulence generating grids have been prepared and tested. The grids involved are placed normally to the uniform upstream air flow which has relatively low background turbulence.

The preliminary design involved the development of three turbulence generating grids based on the suggestions of Roach (1986). The first grid was made using fine square mesh of stainless steel wire of 0.9 mm diameter (SMR). The second grid was formed using ¼ inch (6.35 mm) mild still parallel round bars (PR). The third grid was formed using mild steel 10 mm by 10 mm parallel square bars (PS). Two alternative locations in the wind tunnel were selected for the grid installation (X=-150 mm and X=-650 mm). The former was used for higher turbulence levels and the latter for lower

levels and more isotropic turbulence. Table 2.2 shows the principal characteristics of the turbulence generating grids used in this project. The table also contains information about the solidity of the grids, defined as the ratio of the area blocked by the bars to the total area of the tunnel's cross section.

When PR and PS grids were tested at X=-150 mm, signs of flow nonuniformity were detected. Flow visualisation over the cylindrical leading edge flat plate revealed that at this spacing, the vortices induced by the bars were still detectable. Much less distortion was noted at the plate leading edge position when these grids were installed at X= -650 mm although in some cases signs of nonuniformity were still detectable. The turbulence intensity was considerably diminished. This has led to the development of the PXR and PXS grids which are discussed later in this section.

The variation of turbulence in the streamwise direction, generated by the various grid configurations was measured for various representative mean free stream velocities, in the range of interest. After detailed investigation of the flow patterns induced by the various grids and using the suggestions existing in the literature (Blevins, 1986, Roach,1987, Uberoi & Wallis, 1967) it was decided that only the square mesh type of grids would be used during the hot-wire investigation of the flow field. Turbulence intensities of around 1.8% and 2% were observed when the SMR grid was positioned at X = -650 mm and X = -150 mm respectively. When PR and PS grids were positioned at the later streamwise location the turbulence intensity observed was approximately 10% and 15% respectively.

The location exactly above the leading edge, at mid-height between the tunnel wall and the plate (X=0, Y=100 mm, Z=0), was used as a reference point for these measurements. The rate of turbulence decay in this area is high. To reduce the long scale structure created by the grids and to improve the rate at which turbulence "equilibrium" is reached the PR and PS grids were modified to the PXR and PXS grids using crossed bars. In this way, a square mesh version of these grids was obtained, with the same mesh length and hydraulic diameter but increased solidity. The mean level of

turbulence generated by the PXR and PXS grids was approximately 1% - 2% less than the equivalent generated by PR and PS. Turbulence levels of 3.5% and 4% have been observed when the PXR and PXS grids were installed at X = -650 mm. The streamwise decay of turbulence intensity downstream of the PXR and PXS grids, shown in figure 2.13 is well calibrated with the -5/7 decay power law, as described by Frenkiel (1948a) in his early study on the decay of isotropic turbulence. The decay of turbulence generated by the aforementioned grids can be expressed as follows:

$$Tu = 0.8 \left(\frac{x}{d} \right)^{-\frac{5}{7}} \tag{2.11}$$

where d represents the characteristic diameter of the rods forming the grid, calculated as the equivalent hydraulic diameter. This correlation has been found to be consistent with the results obtained by previous investigators including Roach (1987) and Uberoi and Wallis (1967). The interested reader could also consult Frenkiel's early theoretical studies on the statistics of turbulence (1948b) and the kinematics of turbulence (1948c).

Additionally, table 2.2 contains some data concerning the dynamic behaviour of the turbulence generating grids. The introduction of the various grids in the uniform channel flow of the tunnel results in a total pressure loss which can be quantified using the total pressure loss coefficient ξ:

$$\xi = \frac{\Delta p_{Loss}}{\frac{1}{2}\rho U^2} \tag{2.12}$$

The total pressure loss coefficient expresses the percentage of the dynamic head that is dissipated due to the introduction of the grid. It depends only on the geometry of the grid and consequently has a constant value in turbulent flows.

An overall length scale of turbulence generated by the various grids has been determined according to the procedure discussed in section 2.2.2. A series of tests has been undertaken in order to cover the whole range of Reynolds numbers used in this

study. Finally, the overall length scale of turbulence generated by the grids has been found to have values between 14 mm and 32 mm in the free stream above the flat plate leading edge. The lowest value has been obtained using the SMR grid. PXR and PR turbulence generating grids provided overall length scales between 23 mm and 28 mm. The grids made out of square bars (PXS and PS) have been found to produce length scales in the range of 26 mm and 32 mm (see also appendix D). Although the above values represent a mean value of the length scale obtained using the various grids, they are considered as indicative of the strength of generated turbulence. The values of the intensity and length scale of turbulence generated by the grids have been found to be slightly dependent on the free stream velocity (see also figure 2.13).

Grid Type	d diameter or width of bar {mm}	M Mesh Length {mm}	S Solidity {%}	ξ Pressure Drop Coefficient
SMR	0.9 ○	4.23	38	0.09
PR	6.35 ○	25	23.8	-
PS	10 □	33.33	27.5	-
PXR	6.35 ○	25	42	-
PXS	10 □	33.33	47.4	0.25

Table 2.2 : Principal Characteristics of the Turbulence Generating Grids

It should be noted, that it is difficult to achieve a structure free and relatively constant (not decreasing) turbulence. Consequently, the experiments reported here were conducted in an environment of a decaying turbulence. This environment can be regarded as representative of the flow field in a real turbomachine, as the overall

turbulence level of the main flow is continuously decaying within a blade to blade passage.

2.5 Instrumentation

The various experimental tasks undertaken in this course of study have used a wide range of measurement techniques involving various instruments. Both time-averaged and instantaneous measurements have been made possible using the electronic equipment and data acquisition system of the wind tunnel. The operational function of all the instrumentation used in the experimental arrangement is discussed in brief. The following paragraphs contain a short description of the specifications of the main instruments in the experimental assembly.

2.5.1 Pneumatic Probes

The pitot-static tube shown in figure 2.14 was used for the pressure measurements reported here. With the plate not installed into the wind tunnel the reference static pressure was taken from a static pressure tapping made on the side wall of the wind tunnel located at X = -200 mm, Y = 100 mm and Z = 200 mm. The reference total pressure was taken from a pitot tube located at X = 0 mm, Y=100 mm and Z=0 mm. A differential Digital Pressure Indicator (Druck DPI 101) has been used to measure and automatically record the dynamic head during the investigation of the flow field with the hot wires. On the flat plate with the C4 leading edge, the central line total pressure tapping (No:1)[4*] together with the static pressure tapping at X = 92 mm on the underside (No:15B) were connected to the DPI in order to obtain an on line record of the dynamic head of the tunnel. A yaw meter probe with a 60° wedge angle was used in the initial test of wind tunnel flow uniformity as well as in the zero incidence adjustment of the flat plate with the sharp leading edge. The surface static

---

[4*] The notation refers to table (2.1). See also drawing PD21216 (Kalfas & Elder, 1991)

static pressure tappings of each flat plate have been connected to an inclined alcohol manometer bank in order to obtain the static pressure distribution.

2.5.2 Hot Wire Probes

Three different types of hot-wire sensors have been used to fulfil the requirements of this project (fig. 2.16). A DANTEC 55P11 straight general purpose single miniature wire probe, a DANTEC 55P01 straight general purpose single gold-plated wire probe and a DANTEC 55P05 boundary layer probe fitted with a single gold-plated wire. The sensing wire of all probes is made of Platinum-plated Tungsten wires of the same length (1.25 mm) and diameter (5 μm). The first type (DANTEC 55P11) was used for the free stream measurements. The other two probes are more suitable for boundary layer measurements. A longer wire length together with the gold coating was used in order to keep the supporting prongs sufficiently apart and reduce the effect of the prong wakes on the sensing length of the wire. The third probe was mounted on a special probe holder (fig. 2.14), designed and manufactured to cope with hot wire measurements on the flat surface of the plates. A strengthening plate has been used to support the horizontal stem of the probe support and an aerofoil has been used on the vertical stem in order to stabilise the probe aerodynamically and reduce the vibrations (Blevins, 1987). For measurements in the leading edge area the second probe (DANTEC 55P01) was used mounted on the same straight probe holder as the first probe.

The measuring element under any configuration was connected to a standard DANTEC Constant Temperature Anemometer system (comprising a 55M01 Main Unit, a 55M05 Power Supply and a 55M10 CTA Standard Bridge). The bridge output was connected to an oscilloscope and a three channel combined voltage level shifter and linear amplifier. Both conditioned and non-conditioned output were then connected to a 5½ digit display integrating voltmeters (proportional to $\overline{u}$) and DANTEC 55D35 RMS voltmeters (proportional to $\sqrt{\overline{u}^2}$). The conditioned output was then digitized using a 16 channel high speed (100 KHz maximum) KEITHLEY/METRABYTE DAS-20 A/D

converter. The digital signal was then decoded on a PC/286 using the transfer functions of the electronics and King's law. The data acquisition scheme used in this case is shown in figure 2.15.

2.5.3 Hot Film Multisensor Gauge

The location of the transition region at various Reynolds numbers and free stream turbulence intensities can be identified using hot-film anemometry. This technique involves the measurement of the wall shear stress assuming that the thermal boundary layer covariates with the momentum boundary layer. A hot-film multisensor was designed for this purpose and specially manufactured for the needs of this project by DANTEC of Denmark. An "array" of 31 hot-film gauges was arranged over an axial length of 110 mm on a 50 μm thick polyamide film. The purpose was to cover a considerable length of the plate around the transition region with fast response sensors in order to record the process. Ultimately, the transitional characteristics of the flow field can be measured and analysed in order to form an overall picture of the transition process.

The multisensor array was mounted on a 4500 mm long and 150 mm wide strip of 50 μm thick kapton film in such a manner that the sensor region could be relocated (traversed) to the region of interest. To achieve this a mechanism was arranged such that the kapton strip could be scrolled around the plate. To ensure that the kapton film adhered to the plate a light oil film was applied between the surfaces. The mechanism was not scrolled while the tunnel was operated but positioned prior to the test. The configuration is also transferable between the various flat plates allowing the use of the same equipment with all the flat plates.

The development of this measurement technique was found to be extremely difficult under the present circumstances. Two main reasons restricted the application of this method in the present study. In order to obtain an accurate record of the flow field using many sensing elements simultaneously, an appropriate data acquisition

scheme would be required. This could either be a multiple version of the data acquisition scheme used for the single hot-wire measurements or the development of a sophisticated electronic arrangement would be required, in order to achieve fast switch over between the consecutive measuring elements. Additionally, it was found that the transition lengths involved in the test cases considered presently, were larger than the length of the multigauge. Under these circumstances the application of this technique in the present study has been limited.

2.5.4. Other Instruments

The ambient atmospheric conditions under which this experimental study has been undertaken, were carefully recorded in order to ensure consistency between experiments undertaken on different days. The room temperature has been recorded manually using an analogue thermometer. The barometric pressure reference has been taken from the output of a Druck Digital Pressure Indicator (DPI 140) that was regularly read using a PC connected to the instrument. It should be noted that this instrument is using a pressure transducer that is well calibrated in the range of 800 to 1100 mbar.

In various circumstances when a continuous control reading of pressure was required an inclined alcohol manometer bank was used. The density of the methylated spirit with which the manometer was filled has been estimated by measuring the weight of a known volume of methylated spirit using a very accurate electronic balance. The value adopted in this study has been 810 Kg / m^3. The dependence of the value of the density of the methylated spirit on the atmospheric conditions has been taken into account using the suggestions of Hales and Ellender (1976) (see also ESDU, 1982).

2.6 CONCLUDING REMARKS

The experimental requirements and the final configuration of the experimental facility have been described. The initial tests undertaken to specify the experimental accuracy of the wind tunnel have been discussed. The specifications of the experimental test plates used in this study have been described. The geometrical formation and the dynamic performance of the turbulence generating grids have also been considered. Finally, the main functions of the instrumentation used in this study have been presented.

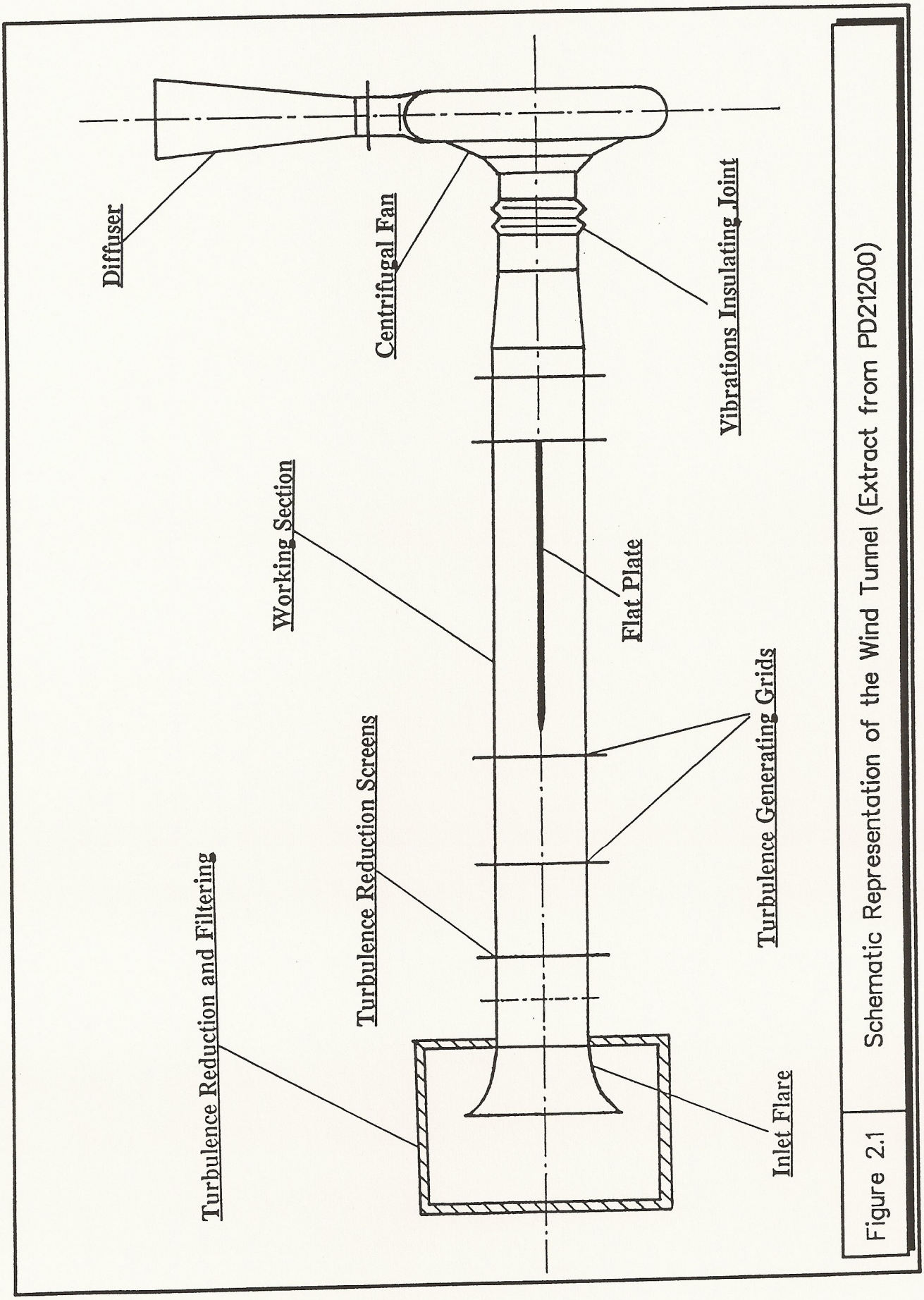


Figure 2.1 Schematic Representation of the Wind Tunnel (Extract from PD21200)



Figure 2.2 General Layout of Testing Facility

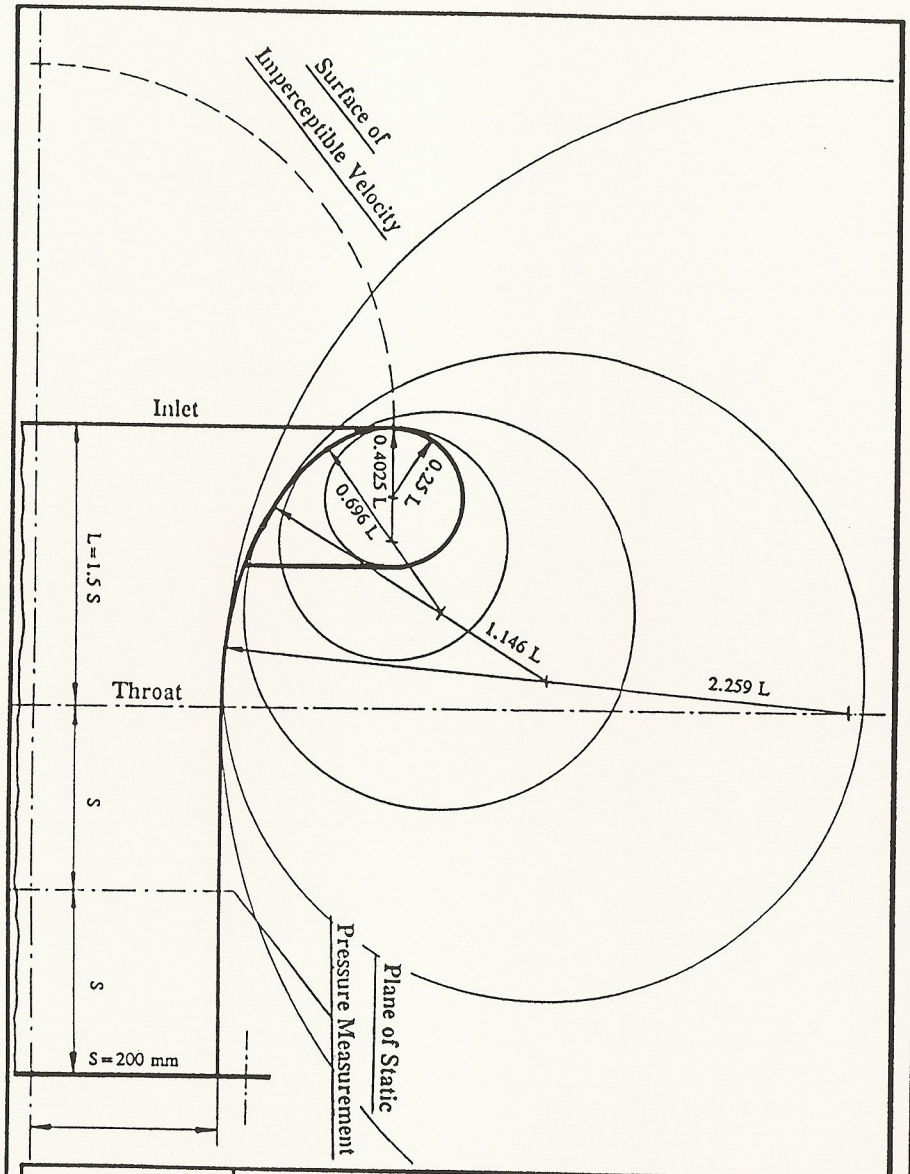


Figure 2.3 Inlet Flare Design

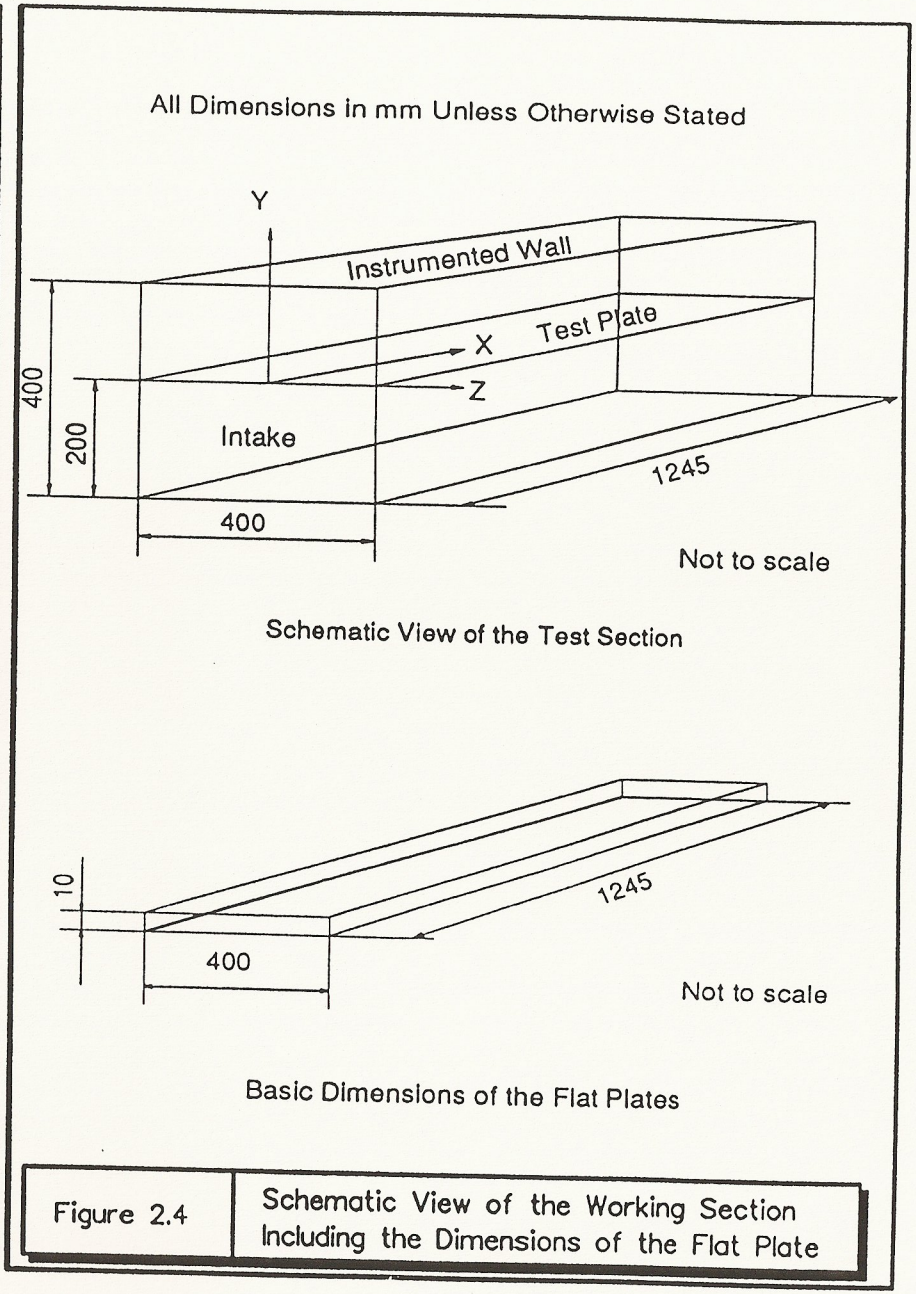


Figure 2.4 Schematic View of the Working Section Including the Dimensions of the Flat Plate

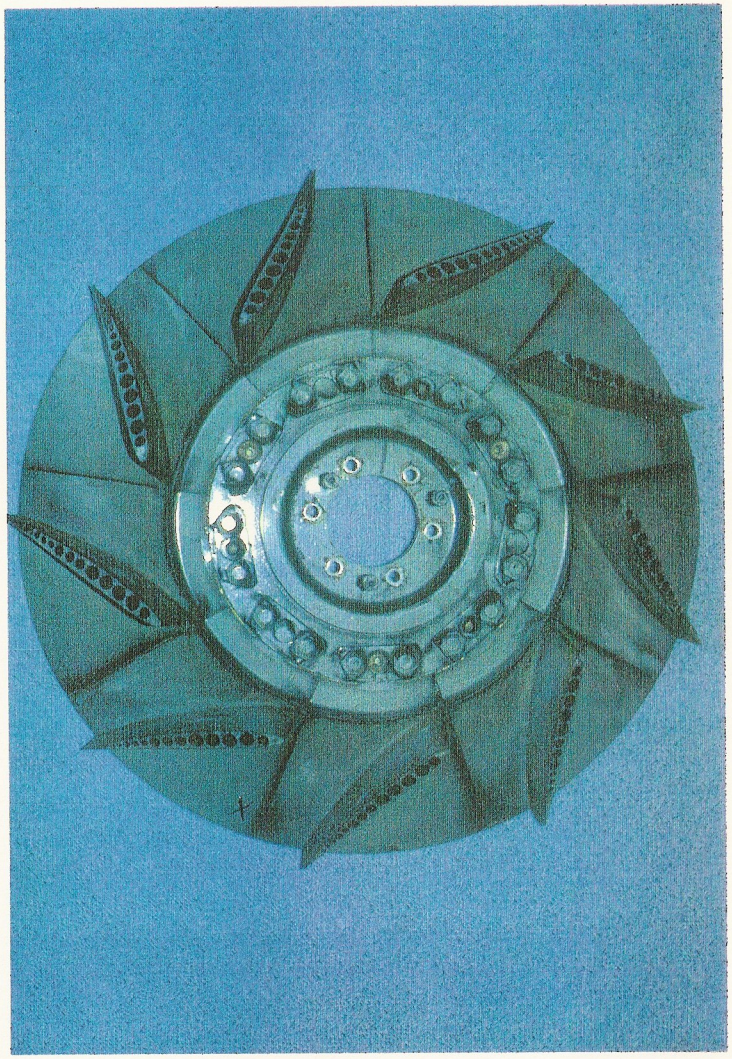


Figure 2.5	Picture of the Centifugal Impeller

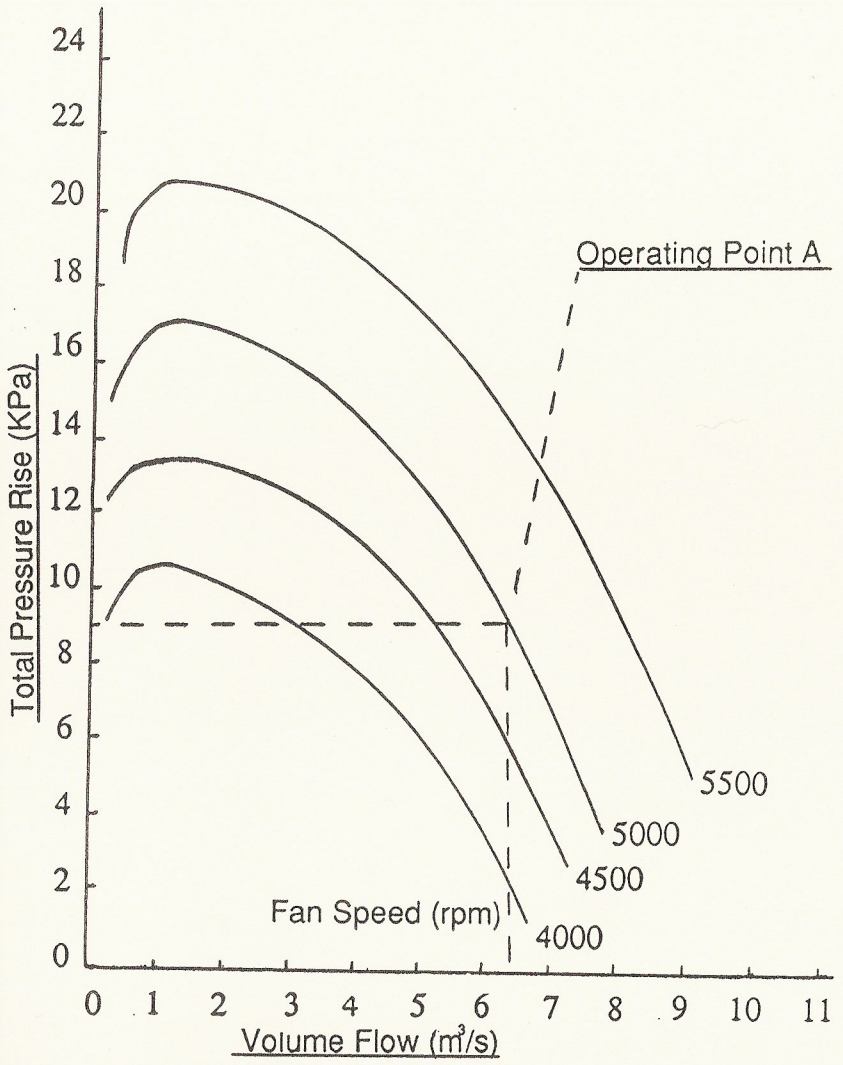


Figure 2.6	Measured Characteristic of Centrifugal Fan (Derived from Dowly Rotol R.A.C. 4683(e))

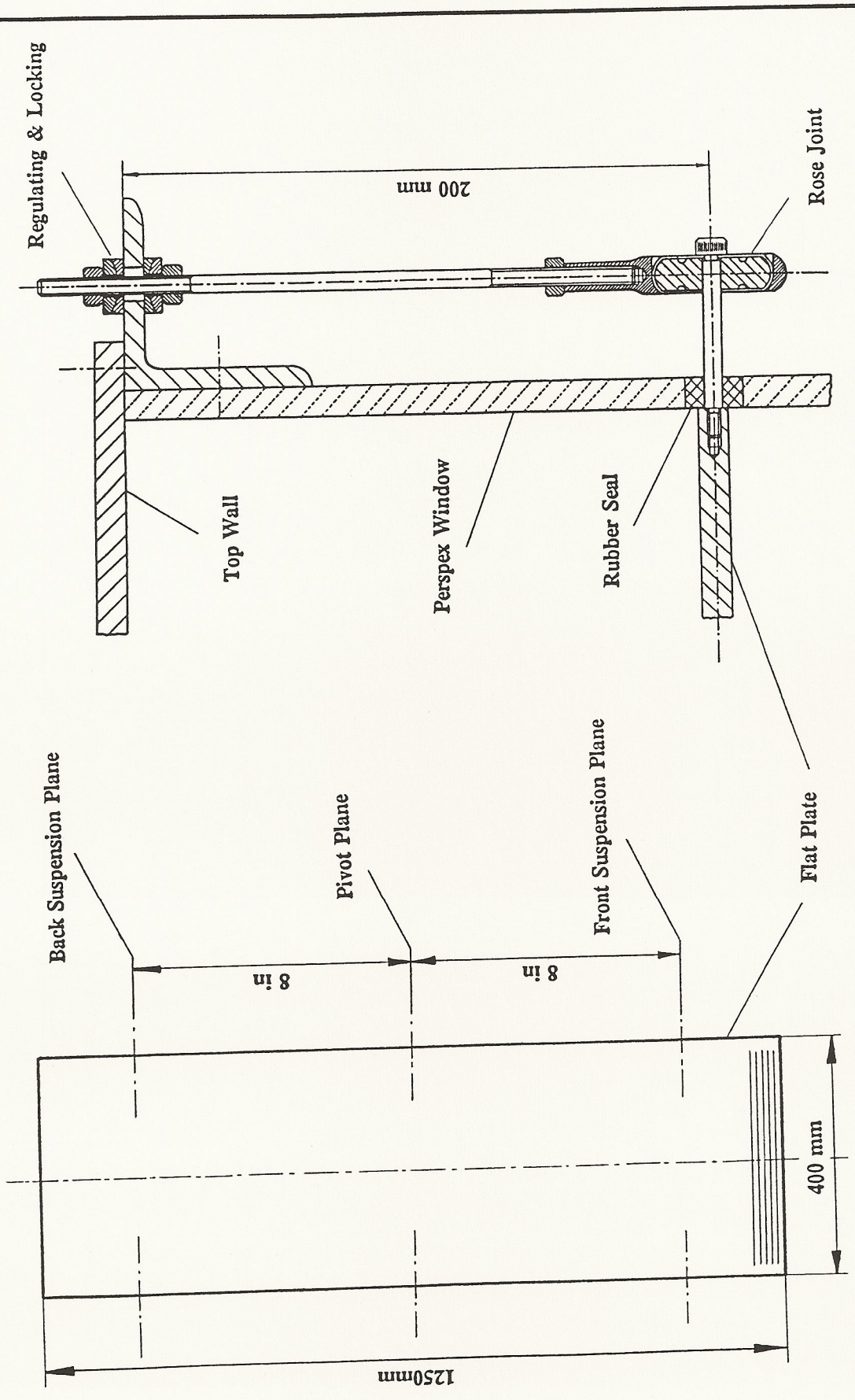


Figure 2.7 Flat Plate Suspension Scheme (Extract from PD21218)

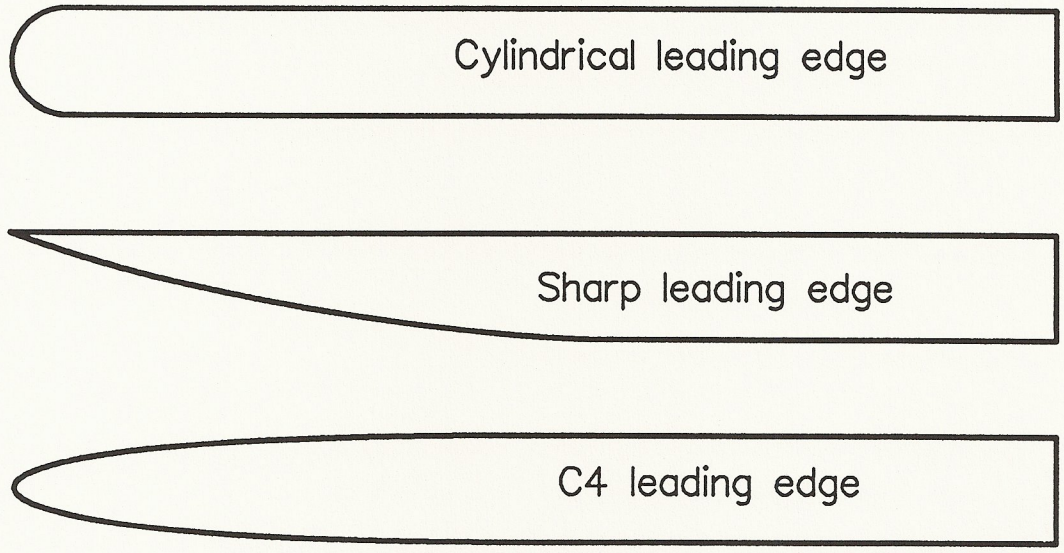
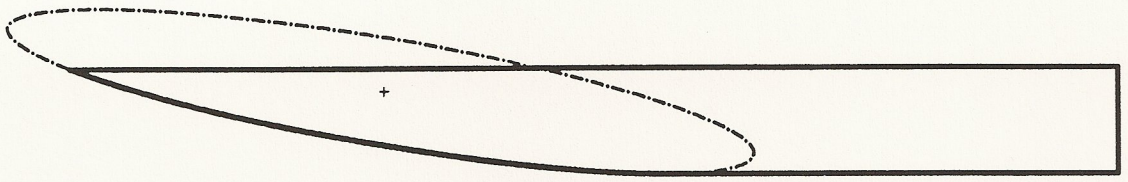


Figure 2.8	Comparison Between the Various Leading Edge Shapes



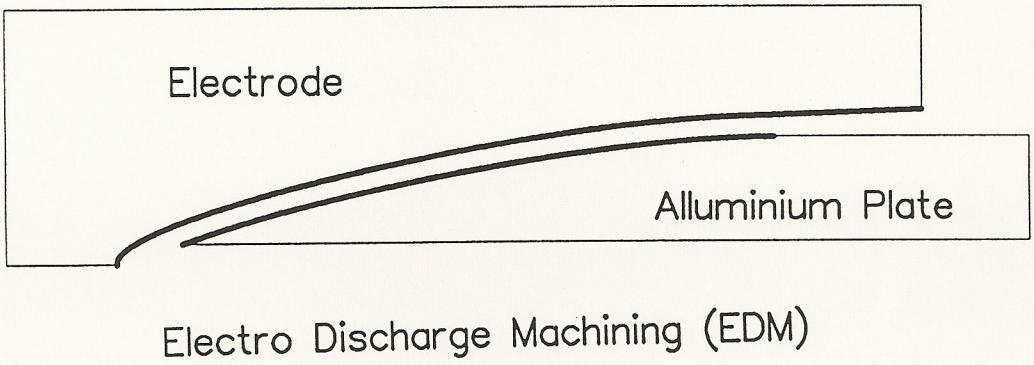


Figure 2.9	Schematic Representation of the Design and Manufacturing of the Sharp Leading Edge

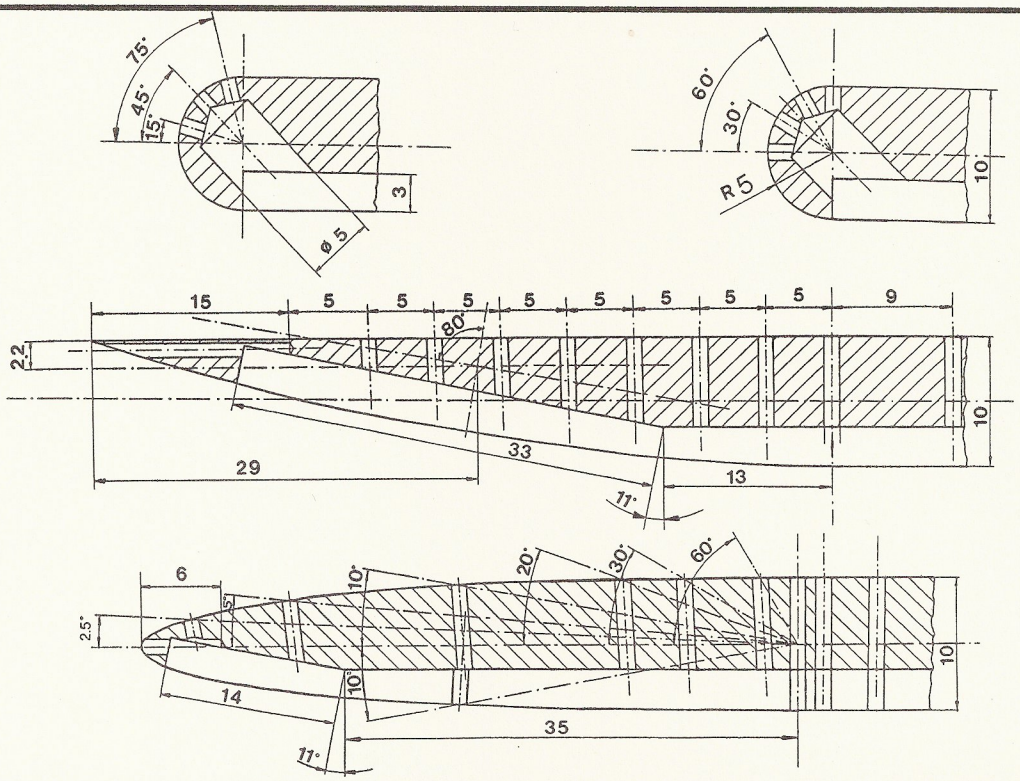


Figure 2.10	Static Pressure Tappings Distribution in the Leading Edge Area of the Various Flat Plates

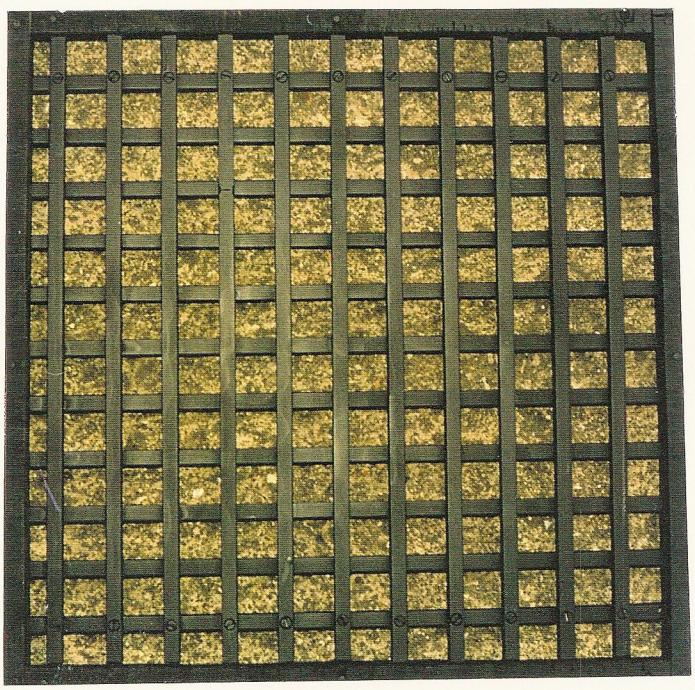


Figure 2.11	Picture of the PXS Turbulence Generating Grid

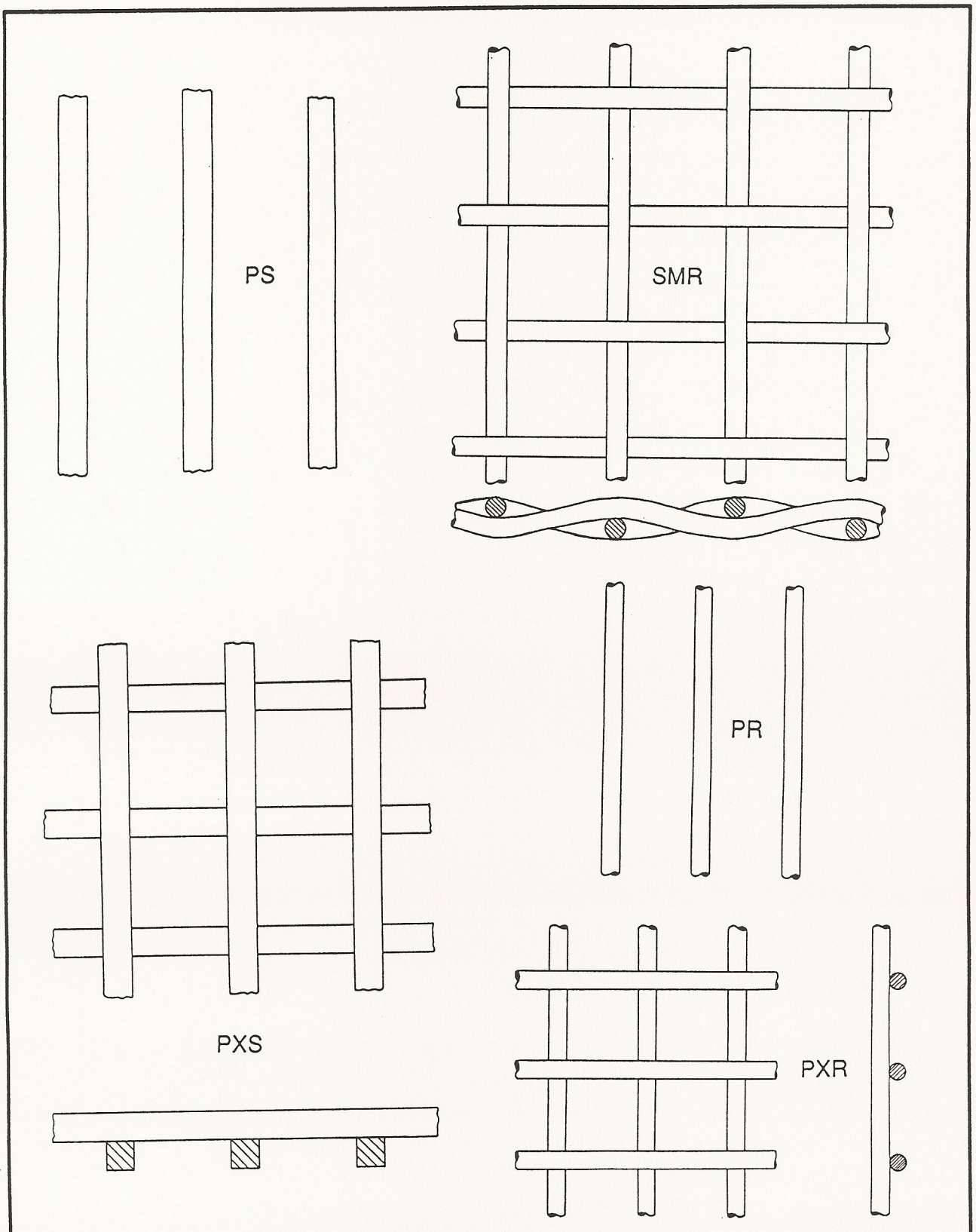


Figure 2.12	Schematic Representation of the Turbulence Generating Grids Scale SMR 4 : 1 and PR, PS, PXR, PXS 1 : 2

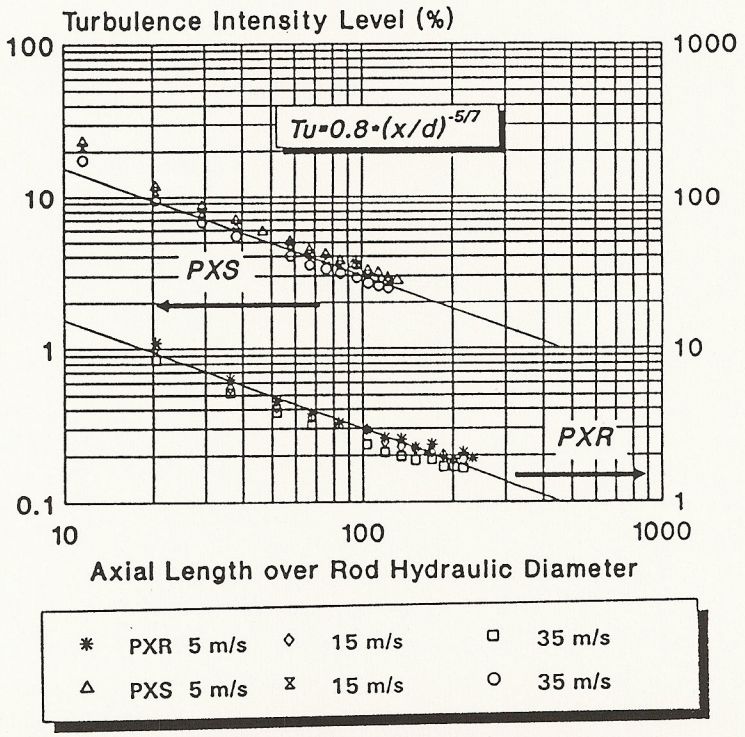


Figure 2.13	Streamwise Decay of Turbulence Downstream PXR and PXS Grids

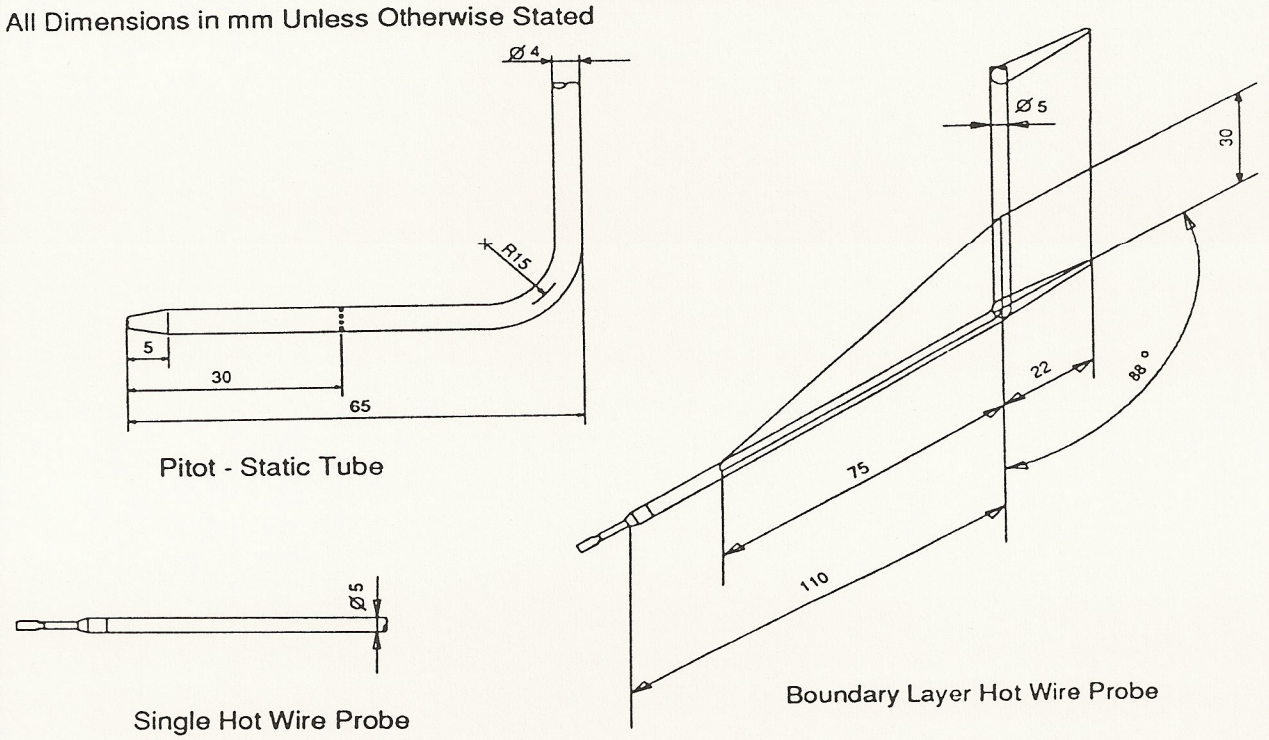


Figure 2.14	Pneumatic and Hot-Wire Probe Geometry



Figure 2.16	Picture of the Plug-In Hot-Wire Probes (DANTEC 55P01, 55P05 and 55P11)

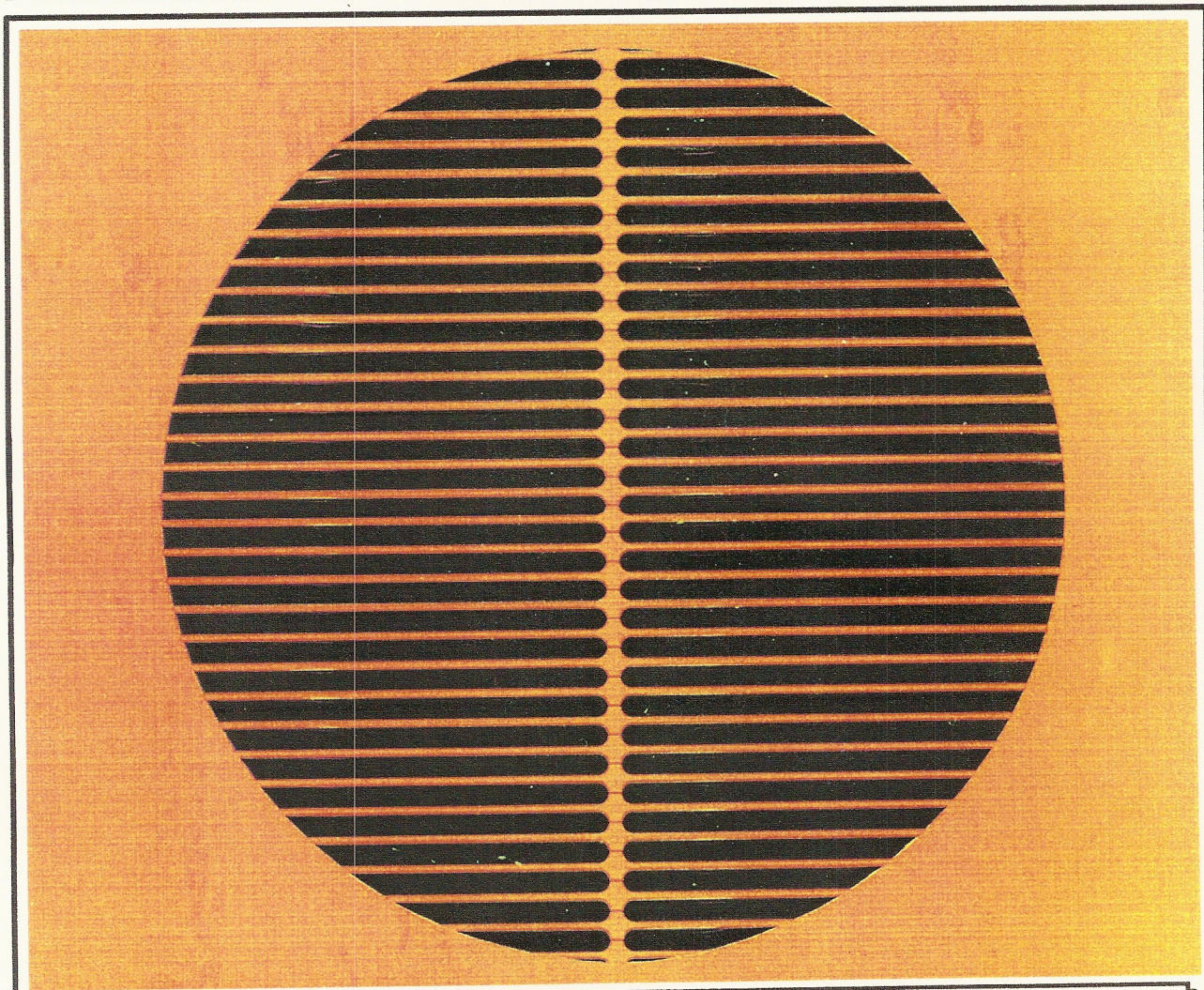


Figure 2.17	Picture of the Hot-Film Multigauge

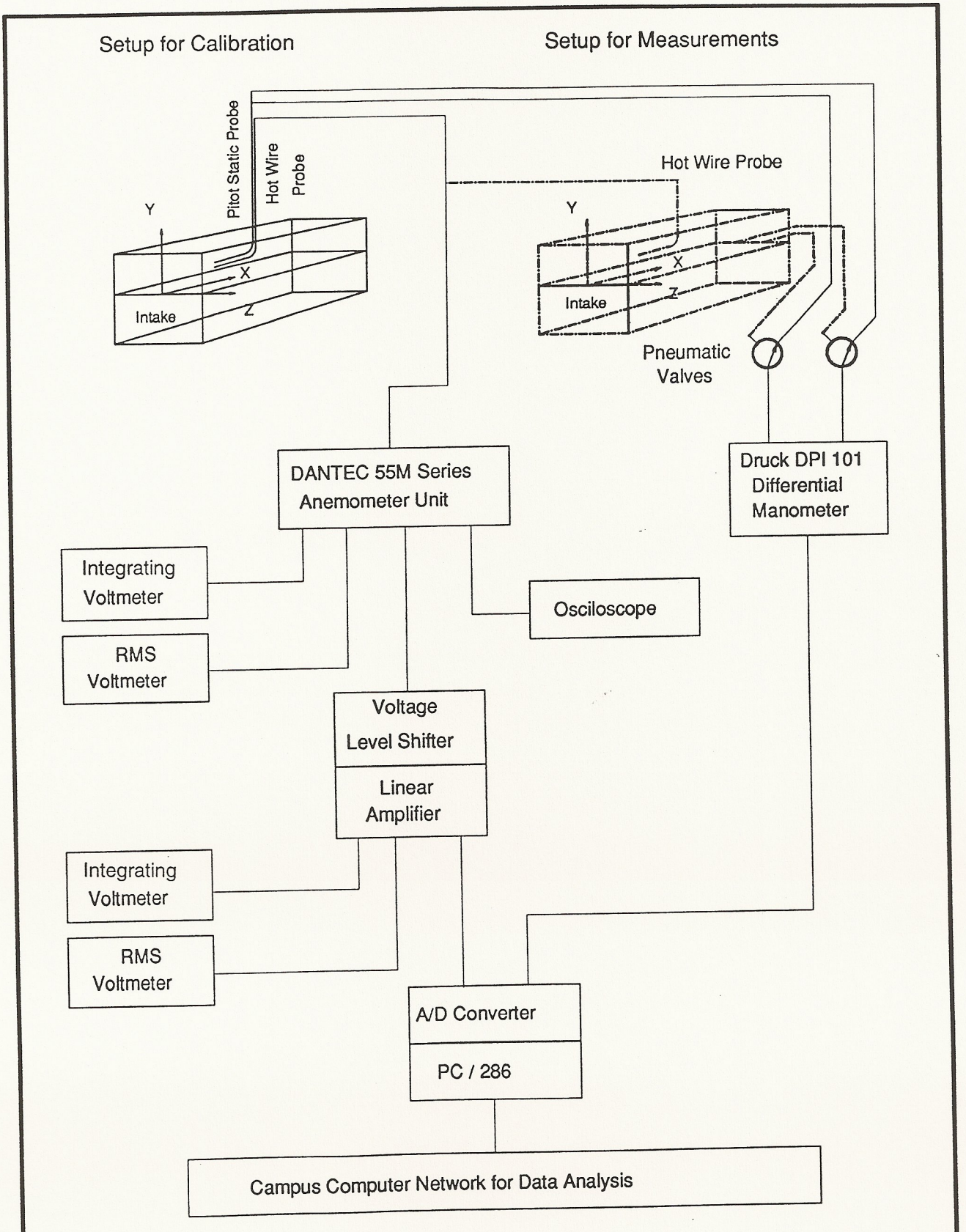


Figure 2.15 Data Acquisition Scheme for Calibration and Measurements

CHAPTER 3

Experimental Methods

CHAPTER 3

Experimental Methods

3.1 INTRODUCTION

This chapter deals with the presentation of the various experimental methods used in this study. In general, the aim of the experimental methods is to extract information about the physics of the phenomena under consideration. Experimental methods can be classified as direct and indirect, depending on whether the studied quantities are the direct outcome of a measurement. Unfortunately, the information produced from the majority of the experimental methods used in fluid dynamics is indirect. Ultimately, the required information is obtained from the measured quantities using a "calibration" procedure.

A common method of extracting information about the characteristics of the fluid flow is to introduce a rigid probe carrying an appropriate sensor and to position this sensor at a particular point in the flow. An obvious consequence of the insertion of such a probe in the flow is to generate some unwanted side-effects through its interaction with the flow field. These kinds of experimental methods are intrusive and extra care has to be taken in order to minimise their unwanted side effects or compensate for them whenever it is necessary.

Another distinction between experimental techniques can be made with respect to their ability of producing point or field measurements. The ability of modern data acquisition systems to record and store enormously large quantities of experimental data gave rise to the development of new techniques that can produce significant amounts of detailed experimental information. Using suitable supporting equipment, the full potential

of fast response sensors that traditionally have only been used to measure time- averaged mean values, can be used. Additionally, field measurements which require a lot of data storage capacity have become more common in the recent years.

This experimental investigation largely involved point measurements using pressure and hot wire probes that have been proven to be very reliable in the flow environments considered. The only field measurement technique employed has been surface flow visualisation (two dimensional method). Experimental techniques involving lasers have not been applied in this study. The application of lasers in experimental fluid mechanics has provided considerable potential for the investigations of fluid flow phenomena. Being an optical technique, laser anemometry is generally thought to be less intrusive than the traditional methods involving the insertion of probes into the flow. However, the extra need for seeding has been proven to be a major drawback of the former method, especially in boundary layer measurements where low velocities are involved. In these circumstances more seeding in required which might affect quite significantly the entire flow field. An additional limit to boundary layer measurements is set by the size of the measurement volume of the laser beam that could be quite inflexible in the near wall area. The fact that turbulence measurements are not very efficient with experimental techniques involving laser beams has restricted their application in this project.

3.2 FLOW VISUALISATION TECHNIQUES

Flow visualisation techniques have been used from the early stages of fluid mechanics research. Simple flow visualisation experiments can be easy to implement and relatively inexpensive. These methods usually produce a quick picture of the flow field. They are very powerful in identifying a broad range of flow phenomena. An interesting characteristic of flow visualisation experiments is that the interpretation of the obtained results is usually the most challenging part of the whole procedure. In the following paragraphs the basic principals of flow visualisation techniques have been generally

outlined. Additionally, a short account of the flow visualisation methods employed in this study is presented.

3.2.1 A General Discussion of the Flow Visualisation Techniques

The basic idea involved in any flow visualisation method is that a small quantity of an additive substance that can be distinguished from the main fluid is introduced into the flow in order to make the various flow patterns visible. There are a number of parameters related to the physical and chemical characteristics of the additive substance which define how close the additive substance (visible) follows the patterns formed by the studied fluid (invisible). Large differences in density between the additive substance and the studied fluid can generate some gravitational effects. Also, the attractive forces between the same and different kinds of molecules (viscosity effects), are largely responsible for the way the particles of the additive material are swept away along with the studied fluid. In general, differences between the properties of the additive substance and the studied fluid are critical to the successful visual representation of the flow. A recent review of the flow visualisation techniques has been presented by Merzkirch (1987).

Smoke or dye flow visualisation are the most commonly used methods in aerodynamic and hydraulic research, respectively. They belong to the larger category of "direct injection methods". The particles of the injected material are required to be small so that they can follow the flow. The injected particles are so many that the motion of the individual particles cannot be identified in the observation. Instead, the observation concentrates on a continuous ensemble of marked fluid. In steady flow the smoke patterns can be considered to follow the streamlines. However, in unsteady flow, the marked fluid follows a quite erratic path forming the so called streaklines. These lines consist of the locus of the fluid elements that passed the specific position in the flow domain where the tracer material is injected.

Another large category of flow visualisation methods are those dealing with surface flow patterns. These methods of flow visualisation make use of a coating of the surface with a material that interacts with the flow and produces visual information. This interaction could be mechanical, chemical or thermal and can produce information about a number of quantities including wall pressure, skin friction or simply flow direction, as well as heat transfer rate and wall temperature. The physical processes involved in surface flow visualisation methods are strongly influenced by conditions of the flow near the solid surface such as whether the flow is laminar or turbulent, attached or separated. A particular surface flow visualisation method involving mixtures including china clay is often used in order to identify the laminar from the turbulent regions of the boundary layer (Moir, 1986). The shiny aluminium finish of the experimental surfaces used in this investigation was not appropriate for this method because it requires a dark or preferably black background in order to achieve a satisfactory visual result.

In all flow visualisation techniques, the lighting method involved plays a very important role in the quality of the visual result obtained. A few flow visualisation techniques in particular make use of laser beams in order to illuminate appropriately the specific regions of the flow field under investigation. Other related methods are based on laser induced fluorescence of the tracer material. These methods combined with advanced video recording technology have been proven to be very powerful in producing field measurements in a time space domain.

3.2.2 Flow Visualisation Methods Employed in this Study

A surface flow visualisation technique was used in order to study the transitional characteristics of the flow over the test plates. Natural and bypass transition was visualised using various combinations of a paint mixture. The mixture of paint was prepared using a highly volatile fluid, such as a light oil (kerosine, paraffin etc) or a spirit (methanol, ethanol) together with a solid agent, in the form of very fine pigments, which was introduced into the mixture, in small quantities, together with some additional substances that would help the visualisation process. A homogenous thin film of the

suspension was then applied onto the plate surface by either spraying or painting with a soft brush. The air stream flowing over the plates modifies the concentration and the homogeneity of the oil film according to the flow conditions very close to the wall. The film was dried by the airflow and photographed for analysis. The time taken for drying depended on the mixture and test being undertaken.

The combined action of the following two mechanisms, constitutes the principal method involved in the production of the final visual result obtained with the foregoing flow visualisation technique. Firstly, the higher skin friction involved in a turbulent boundary layer will help the evaporation of the volatile fluid. Secondly, the higher velocities near the wall involved in the turbulent boundary layer, will activate more energetically the physical movement of the mixture towards the trailing edge of the flat plate. In a laminar flow region which involves lower near wall velocities, the former effect dominates the visualisation process, unlike transitional regions where the latter effect is dominant.

For a successful experiment, the physical and chemical properties of the mixture applied onto the plate should be chosen in a way that the complete painted area is covered after the test with fine structures or ligaments (i.e. surface flow patterns of pigments formed by the residue of the mixture on the surface). The most appropriate flow visualisation recipe has always been chosen by trial and error.

In this series of boundary layer investigations, three different mixtures were used. The majority of experiments reported here were conducted using a simple mixture of Titanium Dioxide (TiO_2) and kerosine. A small quantity of TiO_2 was mixed with approximately the same amount of kerosine until it forms a uniform, lump free paste. The rest of the kerosine was then added to the mixture in small quantities up to the point that the required concentration was reached. In the majority of the cases considered, the concentration of solid pigments of TiO_2 in the final mixture was typically 0.1 gr/cm^3. This value was increased up to 0.3 gr/cm^3 in extreme cases in order to obtain a more dense mixture for measurements in the upper range of free stream

velocities and turbulence levels. An alternative flow visualisation recipe was used to prepare a mixture with improved fluidity and surface tension (Garry, 1990). In this case, the TiO_2 was initially mixed with Talpa Oil 30 to form the uniform lump free paste. Small quantities of boiled linseed oil and oleic acid were then added to the mixture before any paraffin or kerosine was used to form the final mixture. These extra substances improved the fluidity of the mixture in low concentrations (e.g. when the mixture is nearly dried). Both recipes have produced a light, very white and viscous mixture.

A slightly different mixture was used for the visualisation of flow around the plate with the C4 leading edge. The visualisation mechanism introduced here involved a mixture of flurescein sodium diluted with methylated spirit which is the common name used for a mixture of methanol and ethanol, rich in ethanol. Both elements of the solution have properties that improved the performance of the mixture under the test conditions used. Firstly, flurescein sodium fluoresces when illuminated by ultra violet light. This property allows much thinner liquid films to be used with an improved homogeneity. Secondly, the methylated spirit has a higher volatility than kerosine or paraffin, so the film drys quicker.

The flow visualisation patterns developed under the full range of the flow conditions used, have been recorded using 35 mm ASA 200 still photographic film. For the TiO_2 mixture, normal daylight conditions and flash light were used to illuminate the visualised surface. The dried flurescein mixture was exposed in ultra violet light. Low speed and high aperture photography was used to record the surface patterns developed on the plate. Ultra violet scatter was removed using light filters. A number of pictures were taken in order to record the flow patterns over the full length of the flat plates. Special attention was given to regions of interest. At the same time, the overall characteristics of the surface patterns were measured. The obtained data were compiled in order to derive information about the transitional characteristics of the flow field. Transition lengths were then plotted against the free stream Reynolds number for various free stream turbulence intensity levels.

3.3 HOT-WIRE ANEMOMETRY

This section deals with the presentation of the fundamental characteristics of hot wire anemometry. The majority of the experimental data obtained in the course of this study have been acquired using this experimental technique. Hot wire anemometry has been proven to be a very robust method to obtain data concerning the random motion involved in turbulent flows because it employs a fast response sensor with miniature physical size.

3.3.1 Fundamentals of Hot Wire Anemometry

The theoretical background of hot wire anemometry has been investigated since the beginning of the century. In the sixties this technique became wide spread with a large range of applications, as the required electronic equipment became more accessible to the ordinary user. The fundamentals of hot wire anemometry have been recently reviewed by Perry (1982) and Lomas (1986). The important features of hot wire anemometry in connection with the turbulence measurements have been discussed in detail by Hinze (1975) and Bradshaw (1971).

The fundamentals of hot wire anemometry can be summarised as follows. The hot wire sensor can be described as a thermal transducer. The operation principal of the technique is based on the measurement of the resistance of a fine filament which is exposed to a cross flow. A suitable electrical current is passed through the filament and as a result the wire is heated up to a temperature higher than the working fluid. The cooling effect of the cross stream is measured as a temperature driven resistance change using the supporting electronic equipment. Accordingly, the fluid velocity can be deduced from the measured heat transfer rate from the heated wire. There are two variations of the method. The first variation of the method involves an electronic arrangement that actively keeps the filament in constant temperature in which case the changes in the stream velocity are measured through the variations in the current supplied to the filament. The second variation of the method involves an arrangement

that supplies constant current to the filament in which case the measured quantity is the resistance of the wire. This method can supply information about the temperature or the velocity of the working fluid.

When a hot wire sensor experiences a sudden change in velocity, a finite time is required for the sensor temperature to reach its new value. This is due to a number of effects, the most important being the heat storage capacity of the sensor itself. Hinze (1975) suggested that the frequency response of a typical hot wire sensor is of the order of a few hundred Hz. This value is considered far too low to allow the probe to be used for turbulence measurements in constant current mode without temperature compensation. In the constant temperature mode the frequency response of the arrangement depends only on the supporting electronics and it has been proved to be sufficient for turbulence measurements.

Hot wire anemometry is a typical example of an indirect measurement method, because the quantity under investigation is calculated using data concerning a related quantity that can be directly measured. Hot wire anemometry has been developed as a point measurement technique. In this case, extensive information about the flow at a specific point in the flow field can be obtained although it is quite difficult to obtain simultaneous measurements at various points throughout the flow field. Finally, it should be noted that hot wire anemometry is an intrusive measurement technique. The introduction of the probe support and the required electrical wires into the flow can alter the general characteristics of the flow field.

3.3.2 Hot Wire Calibration

There is enough variation in the physical characteristics of seemingly identical probes to require a separate calibration curve for each probe and temperature range used. The calibration procedure involves the production of a correlation between the required quantity (velocity) and the measured data (output voltage), in the form of a function that

involves the measured quantity as the only independent variable. All secondary effects are taken into account using appropriate calibration constants.

The calibration of the hot wires used in this investigation was performed using the Digital Pressure Indicator (Druck DPI 101) described in section 2.5.1. In the low turbulence test case the calibration was performed in situ. The pitot static tube shown in figure 2.14 was clamped onto the hot wire traversing gear in a way that the two probes stood only 20 mm apart. In the test cases with a higher turbulence intensity level the calibration has been performed utilising the DANTEC 55D90 calibration equipment. Sixty four calibration points (pairs of dynamic head - anemometer output voltage) were automatically acquired each time using the data acquisition scheme shown in figure 2.14. Multivariate linear regression analysis was then applied in order to find the constants involved in King's law formulation $E^2 = A + B * U^n$ (Lomas, 1986). The theoretical formulation of this relation can be found in King's early publication on the convection of heat from hot wires (King, 1914). A typical calibration curve obtained for a DANTEC 55P05 hot wire probe is presented in figure 3.1.

An interactive computer program in BASIC computer language (HWCLB.BAS) has been prepared in order to guide, control and help the operator to perform the calibration procedure. The program generates and stores the values of the calibration constants used in King's law formulation, in a universally accessible file. As a result, all the related computer programs (including data acquisition and post processing programs) obtain immediate access to the same set of values for the calibration constants, in order to assure consistency.

3.3.3 Digital Data Acquisition and Data Reduction

For each of the free stream conditions tested the reference value of the free stream velocity U_∞ turbulence intensity Tu_∞ is taken at 25 mm above the leading edge on the central line. Twenty one profiles per free stream condition have been acquired in order to cover the region where transition occurs. At each station the local reference

values have been acquired at a point 25 mm away from the wall before and after the experiment to ensure consistency of the hot-wire readings. Seventy two points in the normal to the wall direction, have been acquired at each streamwise station.

A data acquisition program has been prepared on the PC in BASIC computer language (TURBO.BAS). The principal goal of this program has been to automate and standardise the data acquisition procedure. In order to assist the operator with the whole procedure, this program has been prepared in an interactive format that helps to minimise operational errors. Finally, it should be noted that all the related computer programs on the PC have been prepared in a modular format in order to obtain good compatibility and reduce the probability of human errors. The BASIC computer language has been employed as a common platform for development because of its simplicity and its increased ability to produce a good interactive working environment as well as to drive the data acquisition boards at a lower programming level.

Using the data acquisition scheme shown in figure 2.15 and the aforementioned computer programs, the hot-wire signal at each point, has been recorded for ten seconds (T_S = 10 sec) with a sampling frequency of f_S = 1 KHz (resulting in a total of N_S = 10000 samples per point). Using the relationship $T_S = N_S * \Delta t$ (where Δt = 1 msec) the following formulations were used to calculate the mean velocity, the turbulence intensity and the skewness and the flatness factor of the fluctuating signal (see also Hinze, 1975 and Bradshaw, 1971):

Mean Velocity

$$\bar{u} = \frac{1}{T_S}\int_0^{T_S} u\,dt = \frac{1}{N_S}\sum_0^{N_S} u \qquad (3.1)$$

Turbulence Intensity

$$Tu = \frac{\sqrt{\frac{1}{T_S}\int_0^{T_S}\frac{1}{3}(u'^2+v'^2+w'^2)dt}}{U_\infty} \approx \frac{\sqrt{\frac{1}{T_S}\int_0^{T_S}(u-\bar{u})^2 dt}}{U_\infty} \approx \frac{\sqrt{\frac{1}{N_S}\sum_0^{N_S}(u-\bar{u})^2}}{U_\infty} \qquad (3.2)$$

Skewness Factor

$$S = \frac{\overline{u'^3}}{\left(\overline{u'^2}\right)^{\frac{3}{2}}} \approx \frac{\frac{1}{T_S}\int_0^{T_S}(u-\bar{u})^3\,dt}{\left[\frac{1}{T_S}\int_0^{T_S}(u-\bar{u})^2\,dt\right]^{\frac{3}{2}}} \approx \frac{\frac{1}{N_S}\sum_0^{N_S}(u-\bar{u})^3}{\left[\frac{1}{N_S}\sum_0^{N_S}(u-\bar{u})^2\right]^{\frac{3}{2}}} \tag{3.3}$$

Flatness Factor

$$T = \frac{\overline{u'^4}}{\left(\overline{u'^2}\right)^2} \approx \frac{\frac{1}{T_S}\int_0^{T_S}(u-\bar{u})^4\,dt}{\left[\frac{1}{T_S}\int_0^{T_S}(u-\bar{u})^2\,dt\right]^2} \approx \frac{\frac{1}{N_S}\sum_0^{N_S}(u-\bar{u})^4}{\left[\frac{1}{N_S}\sum_0^{N_S}(u-\bar{u})^2\right]^2} \tag{3.4}$$

In statistical terms, the mean value of the velocity u can be considered as the first order moment of the probability distribution with respect to zero. It should also be noted that the first moment of the probability distribution with respect to the mean value is zero. The turbulence intensity, the skewness factor and the flatness factor express a dimensionless form of the second, third and forth central moments of the probability distribution of the fluctuating signal, respectively. The term central moment of order n refers to the ensemble average of the n-th power of the deviations of the instantaneous value from the mean. The turbulence intensity as formulated above, gives an expression of the standard deviation of the velocity signal. This non-dimensional form is obtained using the mean velocity of the free stream. By the same token, the skewness and flatness factors represent the dimensionless third and forth central moments. In this case, the non-dimensional form is obtained using the standard deviation raised to the power of 3 and 4, respectively.

The physical meaning of the skewness and flatness factors is presented in a schematic form in figures 3.5 and 3.6, respectively (see also Psoinos, 1985). The skewness and flatness factors are often used in order to compare the studied distribution

to the normal. When a stochastic variable u is normally distributed then the probability density distribution of u is given by:

$$P(u) = \frac{1}{\sqrt{\overline{u'^2}}\sqrt{2\pi}} \; e^{-\frac{1}{2}\frac{u'^2}{\overline{u'^2}}} \tag{3.5}$$

Using the normalised form of the stochastic variable, i.e.

$$u_N = \frac{u'}{\sqrt{\overline{u'^2}}} \tag{3.6}$$

the above formulation can be transformed to:

$$P(u_N) = \frac{1}{\sqrt{2\pi}} \; e^{-\frac{1}{2}u_N^2} \tag{3.7}$$

The latter formulation is more widely used because of its non-dimensional character. Most of the discussion presented in the following chapters has been based on the above formulation.

In case that the probability distribution of a fluctuating quantity u is skewed to the left (fig. 3.5a), the corresponding skewness factor (S) obtains negative values and vice versa for probability distributions skewed to the right. Symmetric probability distributions, like the normal distribution, have zero skewness factors. This factor also characterises the relative position of the most probable value of the distribution with respect to the mean. In negatively skewed distributions ($S < 0$), the value with the highest probability is greater than the mean ($\bar{u} < \hat{u}$) and vice versa ($\bar{u} > \hat{u}$) for positively skewed distributions ($S > 0$). Furthermore, if the probability distribution is platykurt (fig. 3.6a), then the corresponding flatness factor obtains values less than 3 ($T < 3$) and vice versa for a leptokurt distribution ($T > 3$). In the former case, the distribution is more flat around its mean and in the latter case, the distribution is more peaked around the mean with respect to the normal distribution. The normal distribution is described as mesokurt with a flatness factor of 3 ($T = 3$).

The same data acquisition scheme has been also used in order to measure the turbulence spectra. Turbulence spectra were acquired at each streamwise station at two locations of constant height (i.e. y = 0.2 mm and y = 1. mm). The sampling frequency used for these tests was f_s = 10 KHz (dt = 100 μsec) in order to be at least twice as much as the maximum expected significant frequency (around 3 KHz) in the signal, according to the Nyquist sampling theorem. The sampling period employed in this case has been T_s = 18 sec resulting in a sample size of N_s = 180,000 samples. Finally, it should be noted that a total of 0.5 GBytes of data have been acquired for the three test cases considered.

The digitised signal was then, analysed on a workstation, in order to obtain the power spectral density (psd) in the frequency domain. Taylor's hypothesis was used in order to approximate the spacial derivatives with their equivalent derivatives with respect to time:

$$\frac{\partial}{\partial x} = - \frac{1}{\overline{u}} \frac{\partial}{\partial t} \tag{3.8}$$

According to the Taylor's hypothesis the frequency spectra can be considered as very nearly the same as the spectra in the wave number domain.

At every station the integral parameters of the boundary layer were also calculated. The velocity at the edge of the boundary layer u_e has been considered to be the maximum velocity measured at each station. The boundary layer thickness δ is then defined as the distance normal to the wall at which the boundary layer value of the velocity equals to 99.5 % of the velocity at the edge of the boundary layer ($u(\delta) = 0.995 * u_e$). The following formulations are used for the displacement, momentum and energy dissipation thickness as well as the shape factors of the boundary layer:

Displacement Thickness

$$\delta^* = \int_0^{\infty} \left(1 - \frac{u}{u_e}\right) dy \approx \int_0^{\delta} \left(1 - \frac{u}{u_e}\right) dy \tag{3.9}$$

Momentum Thickness

$$\theta = \int_0^{\infty} \frac{u}{u_e}\left(1-\frac{u}{u_e}\right) dy \approx \int_0^{\delta} \frac{u}{u_e}\left(1-\frac{u}{u_e}\right) dy \qquad (3.10)$$

Energy Dissipation Thickness

$$\delta_3 = \int_0^{\infty} \frac{u}{u_e}\left[1-\left(\frac{u}{u_e}\right)^2\right] dy \approx \int_0^{\delta} \frac{u}{u_e}\left[1-\left(\frac{u}{u_e}\right)^2\right] dy \qquad (3.11)$$

Shape Factors

$$H_{12} = \frac{\delta^*}{\theta} \qquad H_{23} = \frac{\theta}{\delta_3} \qquad (3.12)$$

The momentum thickness Reynolds number Re_θ as well as the shear stress τ_w and the skin friction coefficient c_f have been used in order to evaluate the transitional characteristics of the boundary layer. The following formulation has been employed:

$$Re_\theta = \frac{U_\infty\, \theta}{\nu} \qquad c_f = \frac{\tau_w}{\frac{1}{2}\rho U_\infty^2} \qquad (3.13)$$

Finally, it should also be noted here, that during the hot-wire investigation of the boundary layer, a regular record of the dynamic head Δp of the wind tunnel was taken by digitising the instantaneous output of the Digital Pressure Indicator. The following expression has been used to calculate the reference velocity U_0 of the wind tunnel:

$$\frac{P}{p} = \left(1 + \frac{\gamma-1}{2} M^2\right)^{\frac{\gamma}{\gamma-1}} \Rightarrow U_0 = \sqrt{2\frac{\gamma}{\gamma-1} RT_a \left[\left(\frac{P}{p}\right)^{\frac{\gamma-1}{\gamma}} - 1\right]} \qquad (3.14)$$

where T_a is the ambient Temperature in K, $P = P_B - \Delta P_{Loss}$, $p = P_B - \Delta P_{Loss} - \Delta p$ in Pa and R is the gas constant (273 Joule/Kg/K).

3.4 INSTALLATION METHOD AND APPARATUS SET UP

All the flat plates were positioned in the wind tunnel using the three point suspension scheme presented in figure 2.7. The symmetrical flat plates (with the cylindrical and the C4 leading edge) have been installed in the wind tunnel in such a way that the surface static pressure distribution on both sides of the plate were nearly the same. Under these circumstances, the aerodynamic incidence was taken as zero. In both cases the initial setting was with the test plate parallel to the walls of the tunnel and only minor further adjustment was required. The test plate with sharp leading edge was arranged at a slight incidence angle to avoid separation at the leading edge. In order to ensure consistency in measurements, the distribution of the static pressure coefficient has been recorded manually several times during each test using the inclined alcohol manometer bank. Typical static pressure coefficient distribution obtained for the cylindrical and the C4 flat plates are presented in figures 3.3 and 3.4 respectively.

The plates were adjusted so that the pressure coefficients on the upper and lower surfaces of the flat surface near the leading edge were equal. The high pressure gradient occurring near the leading edge combined with a degree of uncertainty in the exact positioning of the pressure tappings, is believed to be responsible for any small discrepancies between the top and bottom surface pressure readings. Near the trailing edge of the plate it was observed that the static pressure decreases (corresponding to an increase in the local mean flow velocity) as a result of the development of tunnel blockage.

Since the geometry of the flat plate with the sharp leading edge is not symmetric the pressure distribution on the underside of the plate was not measured. The installation was performed using mainly the flow visualisation technique which showed that if the aerodynamic angle of attack on the sharp plate was greater than zero, a small laminar separation bubble would occur immediately after the leading edge. The criterion set for adjustment in this case was to rotate the flat plate to the condition at which the laminar

separation bubble disappears. Using this criterion, the flat plate was set to avoid separation. Separate measurements showed that in order to achieve these conditions the plate had to be given an inclination of around -0.5° with respect to the tunnel walls.

3.5 ACCURACY IN MEASUREMENTS

A very important aspect of every experimental investigation is the accuracy of the obtained measurements. The purpose of this section is to specify the accuracy of the experimental methods used in this study. Most of the uncertainties in the present measurements are generated due to the limited accuracy of the instrumentation.

The positioning of the pneumatic and hot-wire probes in the wind tunnel has been performed using manual traversing gears with two degrees of freedom (one crosswise along the y-direction and one angular on the x-Z plane). Consequently, the uncertainty in the y direction was defined by the least counts of the traversing gears and amounted to 0.0127 mm. The closest measurement location to the plate has been 0.050 mm from the wall. This minimum distance from the wall has been dictated by the physical dimensions of the 55P05 hot-wire probe. In order to measure the radius of the tip of the hot wire probe, it has been inspected under a microscope. Figure 3.2 presents a picture of this probe attached to a microscopic scale which suggests that the probe radius at the tip is 0.050 mm. In order to locate the boundary layer probe very accurately near the wall, a travelling microscope with long local length (250 mm) has been employed. The location of the probe for all the subsequent measurements through the boundary layer has been cross checked using the travelling microscope. Since all the measurements have taken place on a specific spanwise location, the setting up of the probe location in the Z-direction has been performed once for every data set under a microscope resulting in an uncertainty of 0.05 mm. The longitudinal positioning has been performed manually involving an accuracy of 0.5 mm along the X-direction.

Most of the pressure measurements have been performed very carefully using a digital pressure indicator which involved an uncertainty of 0.5 Pa. The rest of the pressure measurements have been taken with an alcohol manometer bank inclined at 20^0 with respect to the horizontal plane, that resulted to a similar uncertainty. The latter case should be considered as less accurate since it involves the extra uncertainty of the manual reading by the operator. The measurement of the reference velocity has been performed using the pitot static tube shown in figure (2.14), connected to the digital pressure indicator described above. This configuration resulted in an uncertainty of 0.2%. In general, velocity measurements performed using pneumatic probes can be considered to be subjected to an uncertainty level of 0.5%.

Hot wire measurements have been made using the digital data acquisition system described before as well as digital voltmeters. The accuracy of the data acquisition card is 12 bits (or 2^{12} = 4096 increments) over the range of zero to ten volts. In order to improve the accuracy of the hot-wire output voltage measurements a voltage level shifter and a linear amplifier have been used, resulting in a total uncertainty of 0.4 mV. In general, the accuracy of velocity measurements using the hot wire probes can be considered to be 0.5%. Finally, it should be noted that all the electronic equipment has been calibrated regularly.

The data acquisition scheme developed for the hot wire measurements reported here, permitted measurements under a maximum frequency of 100 KHz. When only averaged quantities were needed, the frequency range of the data acquisition system was set to 1 KHz and the velocity signal was recorded for 10 seconds. For the measurement of frequency spectra and other quantities requiring a high speed signal record the data acquisition speed has been set to 10 KHz and a 18 seconds record has been acquired.

The flow visualisation experiments should not be considered as particularly accurate as the whole procedure involved various sources of uncertainty. In order to increase the accuracy of these measurements, the various lengths on the plates have been recorded using two complementary methods. As described in previous paragraphs, still

photography has been used to record the two-dimensional arrangement of pigments in the surface of the flat plates. More accurate length measurements have been obtained manually involving an uncertainty of 0.5 mm in every direction.

3.6 CONCLUDING REMARKS

The main experimental techniques available to the fluid dynamics investigator have been presented. The experimental methods applied in the course of this study have been described and the purpose served by each methods used has also been outlined. Flow visualisation experiments were used to obtain a general overview of the flow field. Alternatively, the detailed measurements obtained using hot-wire anemometry were used to form a more elaborate description of the mean and other statistical characteristics of the boundary layer flow. A short note on the calibration procedures involved in this study has been given in this chapter. Finally, the experimental accuracy of the measuring devices used has been outlined.

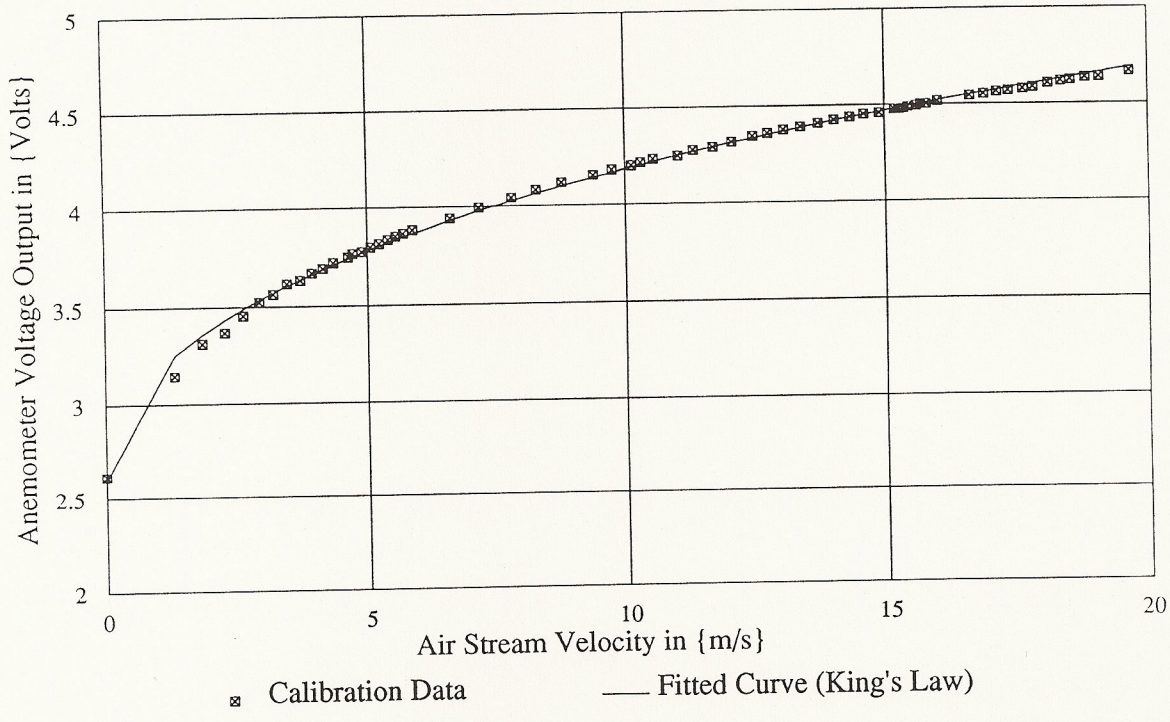


Figure 3.1	Typical Hot Wire Calibration Curve

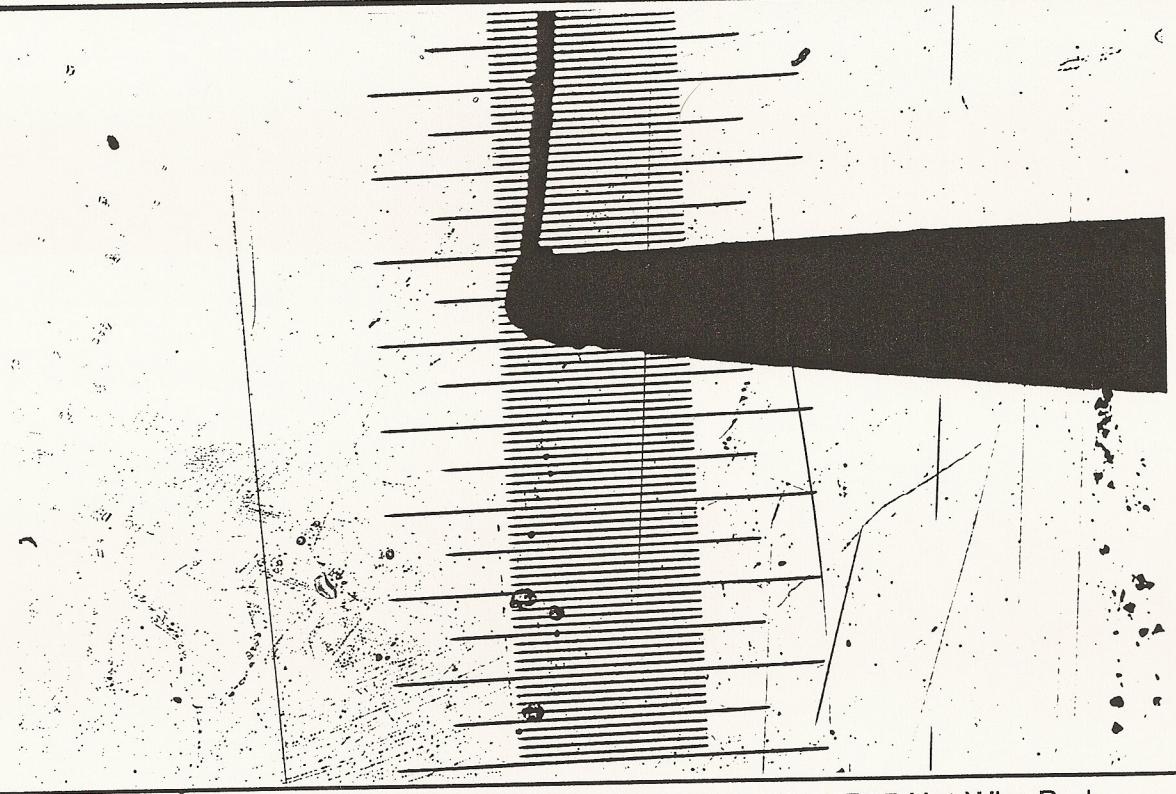


Figure 3.2	Picture of the Prong Tip of a DANTEC 55P05 Hot Wire Probe Attached to a Microscopic Scale (10 μm Increments)

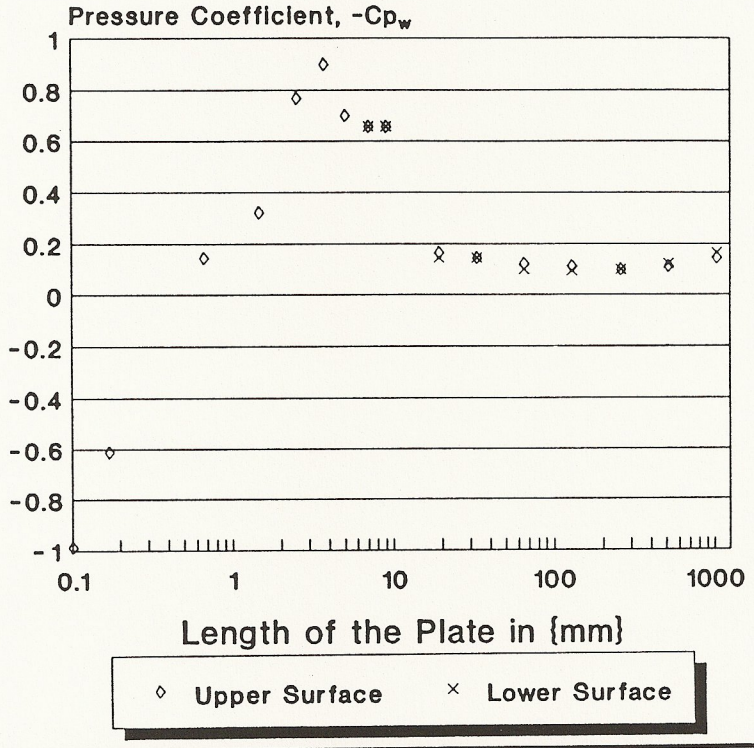


Figure 3.3 Static Pressure Coefficient Distibution for the Flat Plate with the Cylindrical Leading Edge

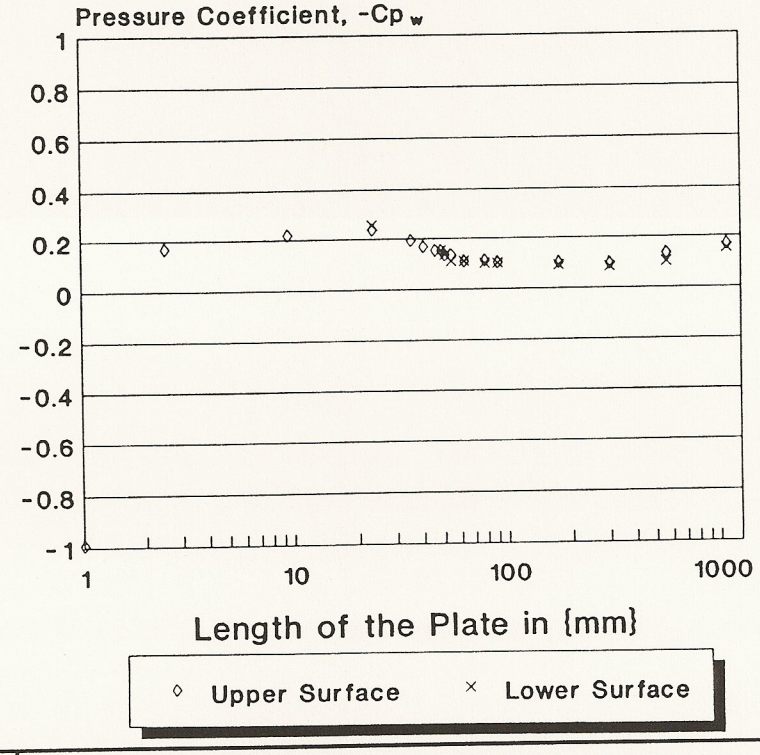
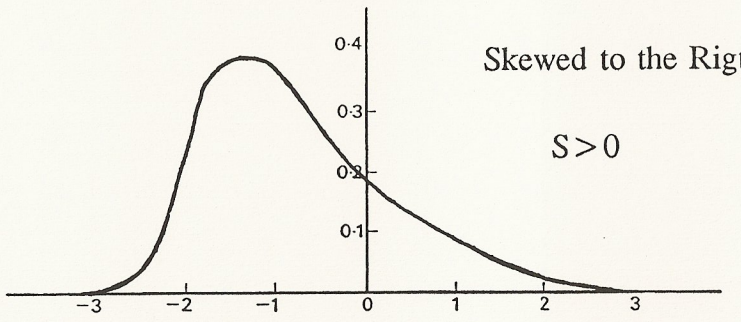
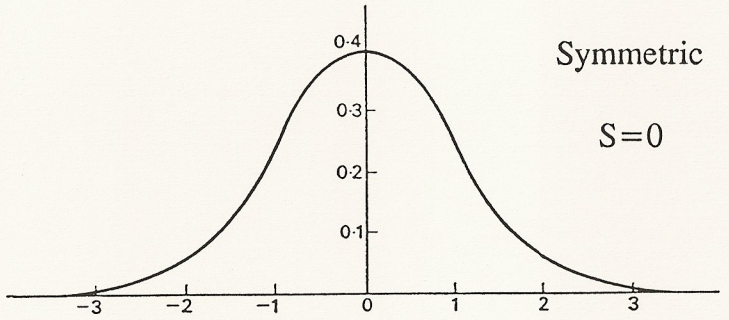


Figure 3.4 Static Pressure Coefficient Distibution for the Flat Plate with the C4 Leading Edge





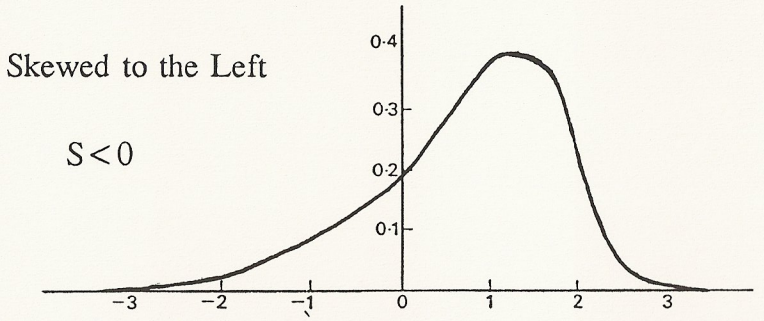
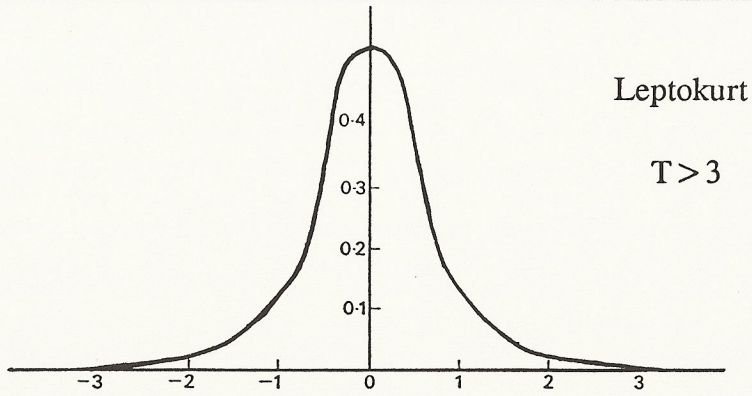
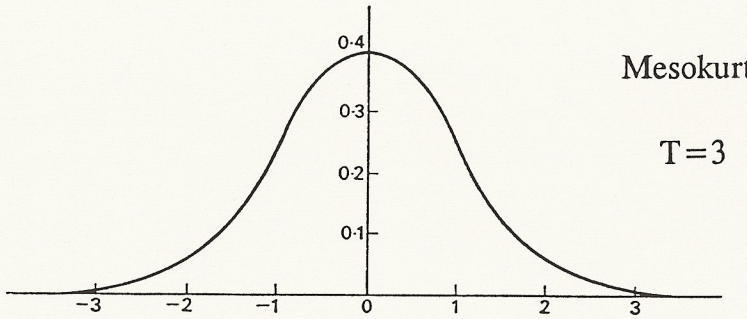


Figure 3.5	Schematic Representation of the Physical Meaning of the Skewness Factor S





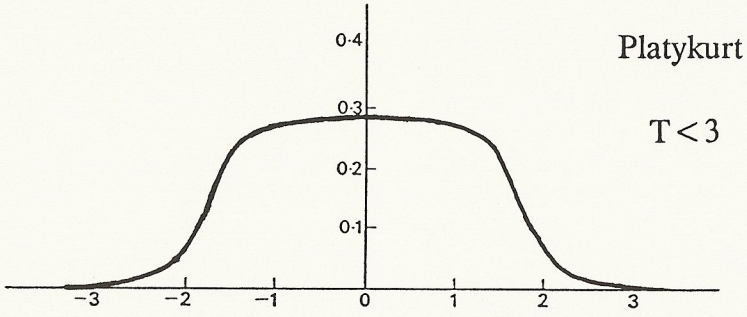


Figure 3.6	Schematic Representation of the Physical Meaning of the Flatness Factor T

CHAPTER 4

The Flow Visualisation Experiments

CHAPTER 4

The Flow Visualisation Experiments

4.1 INTRODUCTION

This chapter deals with the flow visualisation results obtained using all the flat plates in a number of free stream flow conditions. Analysis of the results obtained here is presented with respect to the modes of transition studied. A global approach to the wide range of flow phenomena involved in laminar to turbulent transition has been attempted. Other flow phenomena encountered in this study as a result of the flow visualisation process, are also discussed here. The ultimate goal of this experimental investigation is to obtain a global picture of the effects of various flow parameters on the boundary layer flow, using a relatively quick and easy to implement experimental technique.

A set of twelve different free stream conditions has been applied to each of the three flat plate configurations. Three free stream velocities have been used, namely, 5 m / s, 15 m / s and 35 m / s, corresponding to Reynolds numbers (based on one meter length) of $3.3\ 10^5$, $9.9\ 10^5$ and $2.3\ 10^6$, respectively. The set of flow visualisation experiments presented here has been undertaken using four different turbulence intensity levels. These included the residual turbulence intensity of the wind tunnel which amounted to 0.8%. Additionally, three turbulence generating grids have been employed in order to achieve turbulence intensity levels of 2.5%, 10% and 15%. SMR, PR and PS grids respectively have been installed 150 mm upstream of the leading edge of the flat plates in order to achieve the foregoing turbulence intensity levels. The intensity of turbulence generated using the aforementioned grids has been found to be slightly dependent on the free stream Reynolds Number. This effect has been demonstrated in

figure 2.13, for the intensity of turbulence generated by PXR and PXS grids. It should be noted that the analysis of the results obtained using this flow visualisation technique, initiated the reformation of PR and PS grids into PXR and PXS grids as described later in this chapter. These flow visualisation results have been used to orientate the more detailed investigation of the flow field undertaken afterwards using hot wires.

Another important feature of this section of the experimental investigation is that the results presented here have been undertaken before any hot wire investigation of the boundary layer had taken place, which permitted a relatively independent interpretation of the obtained results. The limitation of the flow visualisation method lies largely in the interpretation of the pictured data which can be imprecise. The results shown here, therefore, are based on a personal interpretation and some human error is possible. To reduce this to a minimum the results have been compared to the hot wire data where available. This procedure served as a calibration for the flow visualisation results since the point measurements with hot wires are considered as more accurate but much more time consuming.

4.2 SEPARATED FLOW TRANSITION

In this section of chapter 4 the flow visualisation results obtained using the flat plate with semi-circular leading edge are summarised. The present experimental investigation has been undertaken with the flat plate exposed to a uniform air stream at zero incidence. Under these circumstances and in all free stream conditions tested, a leading edge separation bubble has been detected. The formation of this separation bubble has been dictated by the strong adverse pressure gradient in the leading edge area (see also figure 3.2).

In order to obtain these results, a suitable mixture of Titanium dioxide and kerosine has been prepared. The concentration of TiO_2 in the mixture was kept in relatively low levels in order to minimise the undesirable effects of the multiphase fluid

flow. The fluidity of the mixture played an important role in the visualisation process as some of the painted mixture was trapped in the recirculation region and some of the rest was swept away by the airstream. Additionally, it should be noted that the size of TiO_2 particles used in the aforementioned mixtures has been between 0.5μm and 2μm.

4.2.1 Separated Flow Transition Results

The main objective of this section is to present a collection of representative pictured data concerning the recirculation bubble detected in the leading edge area. The measurement process involved the generation of a photographic record of the surface flow patterns generated by the interaction of the boundary layer flow and the film of the TiO_2 and kerosine solution. These pictures illustrate the pigment formations generated on the flat plate surface. In order to obtain these formations the upper surface of the flat plate was painted with an appropriate mixture of TiO_2 and kerosine and the wind tunnel was operated at constant speed for an appropriate length of time. Finally, in order to generate an accurate and properly scaled record of the surface flow patterns the photographic camera was positioned perpendicular to the plate.

The documentation of all the test cases considered, involved several pictures of the flow patterns formed on the plate surface. Additionally, manual measurements of the relevant lengths on the recirculation bubble have been taken. In order to form a global idea of the obtained results, a selection of the acquired pictures is presented in figures 4.1 to 4.10. These figures are presented in increasing order of free stream turbulence intensity and mean velocity. Picture 4.1 demonstrates the results obtained under background turbulence intensity level (Tu = 0.8%) and 15 m/s free stream velocity. Figures 4.2 to 4.4 summarise the results obtained using the SMR turbulence generating grid (Tu = 2.5%) for 5 m/s, 15 m/s and 35 m/s respectively.

Figures 4.5 to 4.7 and 4.8 to 4.10 illustrate the surface flow patterns obtained using PR (Tu = 10 %) and PS (Tu = 15%) turbulence generating grids respectively. The

representative sample of the results presented in this section have been generated with the turbulence generating grids located 150 mm upstream of the leading edge.

The characteristic length of the rods forming the turbulence generating grids has been used to non-dimensionalise the streamwise distance downstream of the grids. The relative location of the turbulence generating grids with respect to the leading edge of the flat plates can be calculated using the geometrical characteristics of the grids. The relative location of the three grids located at 150 mm upstream of the leading edge can be calculated as 167, 24 and 15 characteristic lengths for the SMR, PR and PS grids, respectively. The experimental arrangement involving the two latter grids resulted in a non-dimensional distance that was too low and affected the final results as it will be discussed in the following section of the thesis.

4.2.2 Data Analysis and Discussion

In this section, a discussion of the separated flow transition results including some global observations and theoretical considerations is presented. The identification of the laminar, transitional and turbulent boundary layer regions for the flat plate with cylindrical leading edge was aided by the presence of a recirculation bubble. Some of the liquid mixture was "framed" between the separation and reattachment lines locally improving the definition of the process and clearly illustrating the regions of interest. The raw data were compiled in order to derive integral parameters that will help us to study the transitional characteristics of the flow.

As already noted, a leading edge separation bubble was detected, under all free stream conditions tested. Having undergone a strong acceleration over the initial part of the circular arc of the leading edge, the laminar boundary layer separates under strong deceleration near the end of the curved section (fig. 2.16). The separated shear layer undergoes transition from laminar to turbulent and reattaches to the flat plate as a turbulent boundary layer. The results obtained for the range of free stream Reynolds numbers and turbulence intensities are reviewed in figures 4.11 to 4.14. At this point

attention should be drawn to the analogy between the regions indicated in the aforementioned figures with the regions illustrated in figure 1.6. In figure 4.11 a comparison of the present results with the hot-wire data obtained at VUB (Hazarika and Hirsch 1991a&b) for very low free stream turbulence intensity, is also presented. It should be noted that the compared data were obtained in a different (0.1% instead of 0.8%) turbulence intensity environment. However, the overall agreement appears very good. In this graphical representation of the flow field around the semi-circular leading edge, the recirculation region has been divided into three regions corresponding to the laminar, transitional and turbulent areas using the data acquired for the three Reynolds numbers used. The lines separating these regions have been set approximately after close inspection of the raw data. In order to assist the interested reader in the interpretation of the pictured data the above described regions have been marked in figure 4.2.

The forgoing results show that the position of the initial separation was influenced by the turbulence intensity much less than by the Reynolds number. The reason for this appears to be that the thin laminar boundary layer (formed in the accelerating region of the flow), is robust enough to sustain the external interference from the free stream velocity fluctuations. By the same token, the separated shear layer was very susceptible to the free stream velocity fluctuations, and the turbulent reattachment point was therefore strongly influenced by the free stream turbulence level. As a result, the total length of the recirculation bubble was quite significantly diminished at higher turbulence levels.

The overall length of the recirculation bubble L_{sr}, defined as the distance between the separation and the reattachment point, was observed to be dependant on both the free stream Reynolds number Re_∞ (based on 1 m length) and the free stream turbulence intensity level Tu_∞ (fig. 4.15). The turbulence intensity level seems to have quite a strong effect on the recirculation length. The Reynolds number has a similar effect and in combination with the turbulence effect this results in the minimisation of the recirculation length.

Under most of the investigated flow conditions, the laminar zone of the shear layer covered the larger section of the recirculation region. Effectively, the separated shear layer continued to be laminar for a significant section of the area over the recirculating flow region. In the laminar region of the recirculation bubble, the TiO_2 particles formed a quite uniform white layer on the bubble surface. The disturbances that existed into the overflowing fluid were developed and propagated faster and easier in flow conditions dominated by the separated shear layer. Eventually, when transition occurred in the separated shear layer, the structure of the pigments was altered and the patterns formed involved less TiO_2 particles with increasing non-uniformity in structure. Transition to turbulence aided the shear layer to reattach to the surface of the plate as a turbulent boundary layer. In this way, the turbulent region of the recirculation bubble was found to be shorter than the laminar region.

At the reattachment point the flow conditions are similar to the flow around a stagnation point where the fluid divides into the fluid that follows the development of the attached boundary layer and the fluid that is incorporated in the recirculation area (see also figure 1.6). The surface flow patterns in this area were generated at very small mean velocities in conjunction with high pressures and velocity gradients that dominate the development of the flow field. As a result very fine TiO_2 pigments were accumulated in this area to form a finite zone where turbulent reattachment occurs.

The free stream turbulence intensity was observed to have a more significant effect on the laminar region. Thus, transition to turbulence occurred earlier as a result of the free stream fluctuations. The turbulent area was also shortened due to the turbulence intensity increase. The turbulent shear layer, by becoming more stable, forced a quicker reattachment. In more general terms though, the proportions of laminar, turbulent and transitional flow over the recirculation bubble were not observed to change dramatically as a result of the increase in the free stream velocity although the extent of these regions was modified.

Within the limits of this particular investigation the time-mean turbulence intensity in the free stream can be considered as constant over the limited region of the recirculation bubble. However, its local turbulence intensity varies considerably as the local velocity changes and care should be taken as to how such parameters are used.

The two dimensional formation of the separation bubble detected in the leading edge of the flat plate with circular leading edge has been illustrated in picture 4.20. It can be clearly seen that the recirculation length near the side walls of the tunnel is diminished (see also fig. 4.1 and 4.3). This behaviour could be explained assuming that the three dimensional vortex structure generated by the interaction of the boundary layers on the two perpendicular solid surfaces of the tunnel wall and the flat plate, influences the formation of the separation bubble in a way that reduces its length.

Another interesting phenomenon can be observed in the series of pictures presented in figures 4.1 to 4.10. The use of the PR and PS grids located 150 mm upstream of the leading edge results in a non-uniform distribution of the recirculation length across the span of the flat plate (fig. 4.5 to 4.7 and 4.8 to 4.10 respectively). By the same token, when either no turbulence generated grid or SMR grid is used there is no evidence of the above phenomenon (fig. 4.1 to 4.4). In order to explain this behaviour, it can be considered that the turbulence generated by the above grids only 150 mm upstream of the leading edge is not completely homogenised by the time that it hits the leading edge. This approach is supported by the fact that the number of peaks and troughs in the waviness observed in the leading edge separation bubble, corresponds to the number of steel bars forming the turbulence generating grids.

The high blockage ratio of these grids is thought to assist this process because the flow behind the grids requires a considerable recovery length. Another flow phenomenon that can possibly influence the formation of the above described flow structures, is the occurrence of mushroom shaped stall cells in separated flow. A number of publications concerning this process suggest that a long two dimensional separation bubble can become unstable and begin to break down in recirculation cells of finite

length in the lateral direction forming mushroom shaped flow patterns similar to the ones observed in this study (see for example Winkelmann, 1983).

The above described phenomena initiated the replacement of the PR and PS turbulence generating grids by the PXR and PXS grids, respectively. In the beginning, a few trial tests have been undertaken in order to establish the best way of transforming the grids. Various combinations of turbulence grids located at 150 mm as well as 650 mm upstream of the leading edge have been tried. Figure 4.21 illustrates the laminar separation bubble which occurred when the PS grid was located at 650 mm upstream of the leading edge. In this picture, signs of the previously described waviness in the recirculation region, including a series of couples of little white spots of TiO_2 pigment can be observed. This sort of behaviour has been reduced to a minimum by the introduction of PXR and PXS grids. Accordingly, it was decided to use only square mesh grids in the course of the hot-wire investigation of the flow field.

4.3 NATURAL AND BYPASS TRANSITION

In this section, the flow fields around the flat plates with the sharp and the C4 leading edges are considered. The flow patterns obtained with the flow visualisation technique used, indicated that the boundary layer development on both plates is very similar. Slight differences in the measured lengths of transition occurred due to the different static pressure distribution in the leading edge area of the two plates.

4.3.1 Results and Discussion

These results are summarised in figures 4.16, 4.17 and 4.18 for the three turbulence intensity levels considered. The layout of these figures is similar to the one presented in figure 4.11. In these graphs, two lines are formed by plotting the profile distance from the leading edge where the structure of the pigment patterns starts changing and where this structure is eventually stabilised to a new shape. The area from

the leading edge to the first line relates to the region where the flow is laminar and the area from the second line to the end of the plate relates to the region where the flow is turbulent. Consequently, the transitional region is lying within the two lines. Lengths measured between these two lines should be considered as greater than the transition length. This area should be treated carefully because there is an increased degree of uncertainty involved in the measurement technique used. The fluidity of the mixture involved in these tests has been critical for the quality of the output visual result. It should be noted here that the series of experiments involved in this investigation has been repeated a number of times to ensure good repeatability of the obtained results because both the effectiveness of the measurement process and the accuracy of the photographic record were not particularly good.

The results obtained using plates with the sharp and the C4 leading edge were plotted together in order to be easily compared. It can be considered that the transition lengths measured in both cases are very similar. It can also be noted that the transitional area is moved slightly towards the end of the C4 plate due to the small acceleration that the flow is undergoing in the leading edge area. The transition start and length is diminished rapidly with increasing free stream Reynolds number and turbulence intensity. The uncertainty in measurements was also decreased significantly with increasing free stream Reynolds number.

The flat plate with the sharp leading edge had been set at a small negative incidence in order to avoid laminar separation near the leading edge. When the plate was set parallel to the tunnel walls, a small separation bubble had been always detected. The inclination of the plate with respect to the tunnel walls was then gradually increased until any sign of laminar separation had disappeared.

The accurate regulation of the incidence of the flat plate is quite important in the experimental investigation of transition because the pressure distribution around the leading edge is strongly dependent on the incidence, especially when the non-symmetrical sharp leading edge is involved. In order to assure that the full span of the

flat plate has been adjusted at the same incidence, the surface flow visualisation technique employed in this chapter has been used. Figure 4.19 presents surface flow visualisation results obtained for high free stream Reynolds number on the flat plate with sharp leading edge, that illustrates the lateral misalignment of the flat plate.

4.4 CONCLUSIONS

The flow visualisation results obtained for the full range of free stream conditions and leading edge geometries have been presented. The flow visualisation method employed here, was found to be appropriate for the identification of the global characteristics of the transitional region. The application of this experimental technique to test cases involving separated flow transition has been particularly successful.

The flow visualisation study undertaken, provided the means to take measurements in the extended range of test conditions used. Since the results obtained are quite well calibrated to the hot wire data, this technique appears to provide a good way in which to review a large number of configurations and to facilitate the experimental planing. More accurate experimental techniques can then be applied in the regions which present special interest. Accordingly, the flow visualisation results presented here, served as preliminary tests for the more detailed investigation of the flow field with hot-wires.

The flow visualisation technique employed here, facilitated the recognition of flow irregularities that appear in the flow field around the flat plates. Also, the visualisation process assisted the development of turbulence generating grids that are capable of delivering high turbulence intensity levels without introducing a great deal of distortion in the mean flow.

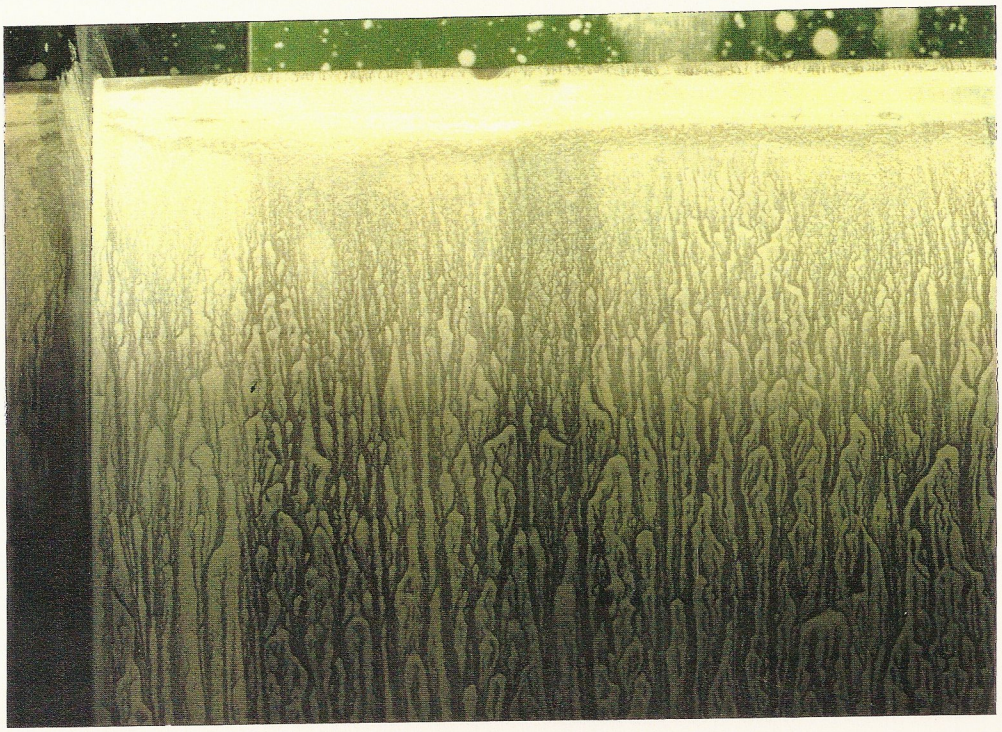


Figure 4.1 Picture of the Surface Flow Patterns Generated Under Background Turbulence (Tu=0.8%) and 15 m/s Free Stream Velocity

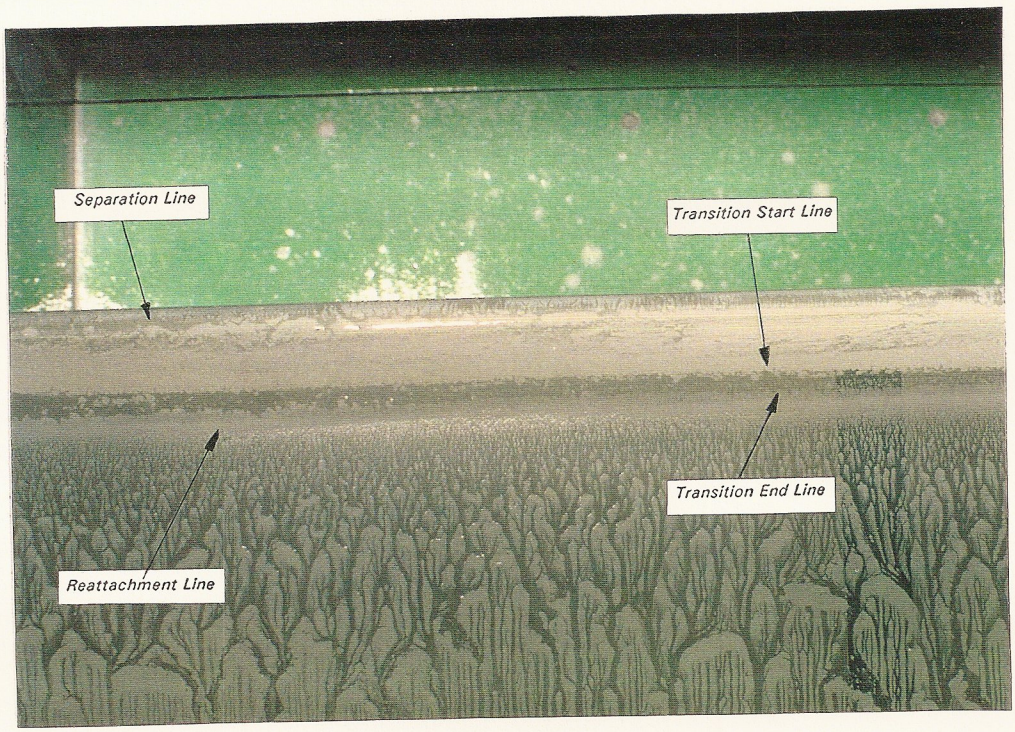


Figure 4.2 Picture of the Surface Flow Patterns Generated Under 2.5% Free Stream Turbulence Intensity and 5 m/s Free Stream Velocity

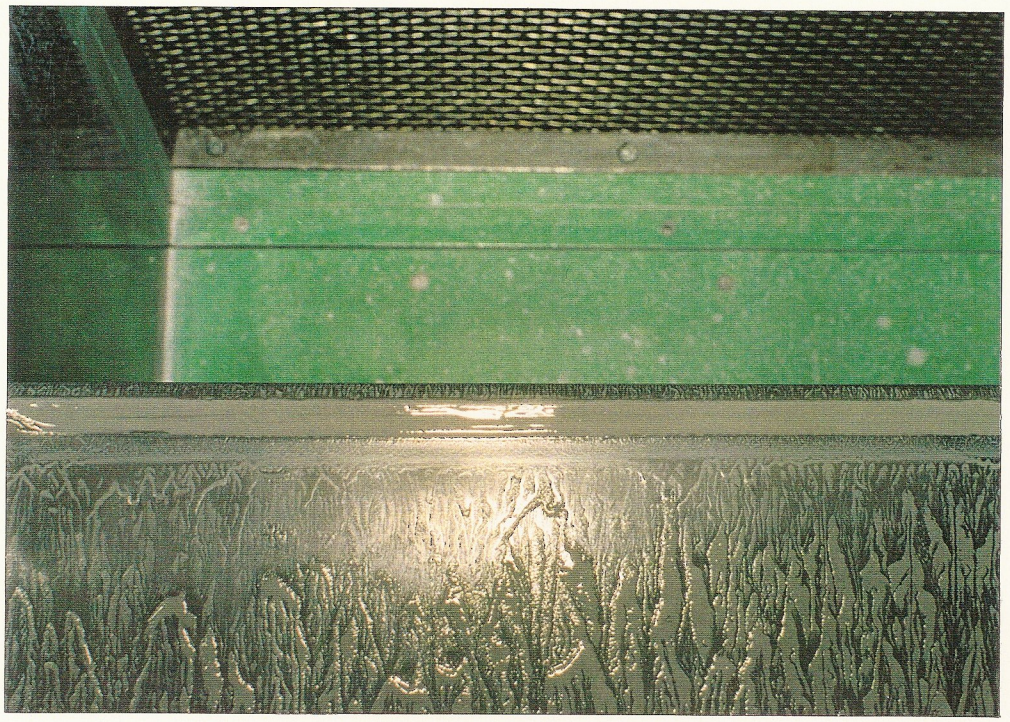


Figure 4.3	Picture of the Surface Flow Patterns Generated Under 2.5 % Free Stream Turbulence Intensity and 15 m/s Free Stream Velocity

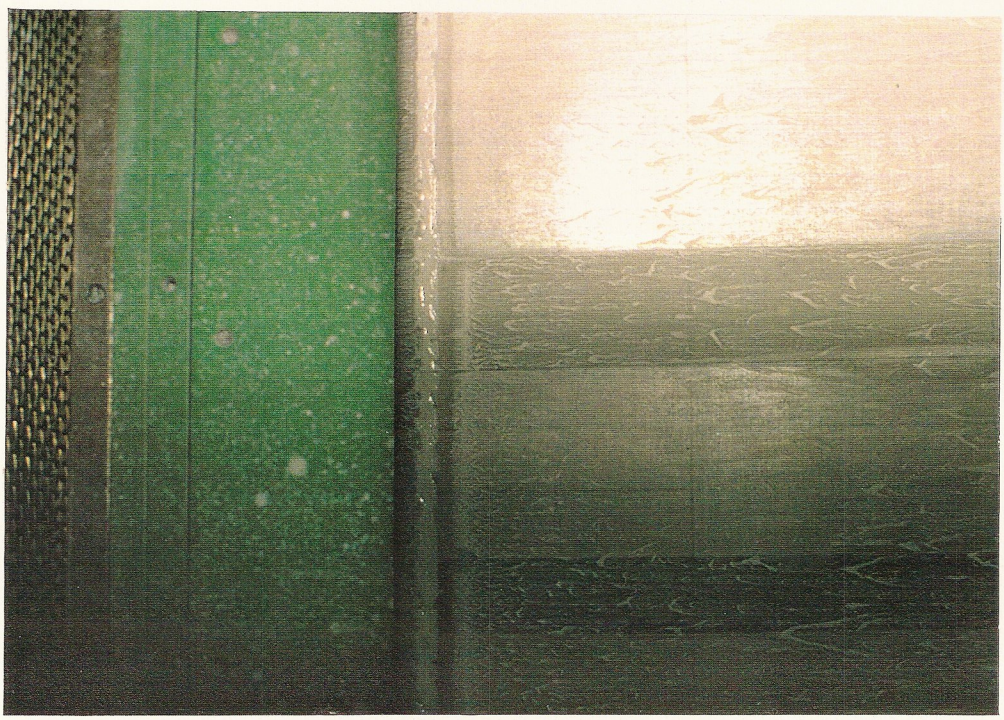


Figure 4.4	Picture of the Surface Flow Patterns Generated Under 2.5 % Free Stream Turbulence Intensity and 35 m/s Free Stream Velocity

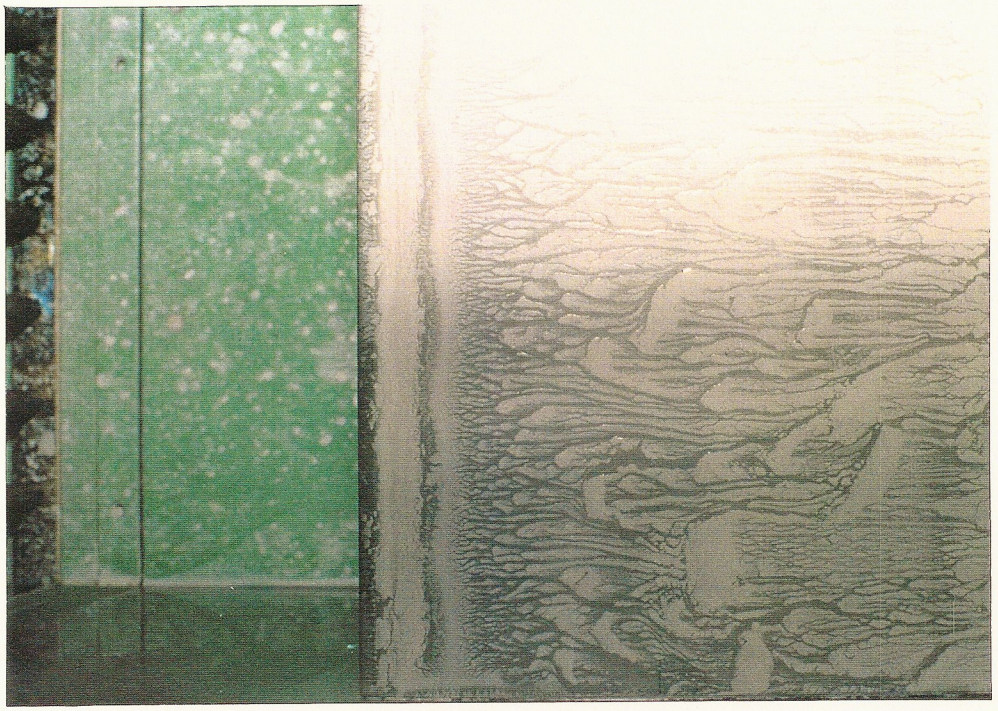


Figure 4.5	Picture of the Surface Flow Patterns Generated Under 10 % Free Stream Turbulence Intensity and 5 m/s Free Stream Velocity



Figure 4.6	Picture of the Surface Flow Patterns Generated Under 10 % Free Stream Turbulence Intensity and 15 m/s Free Stream Velocity

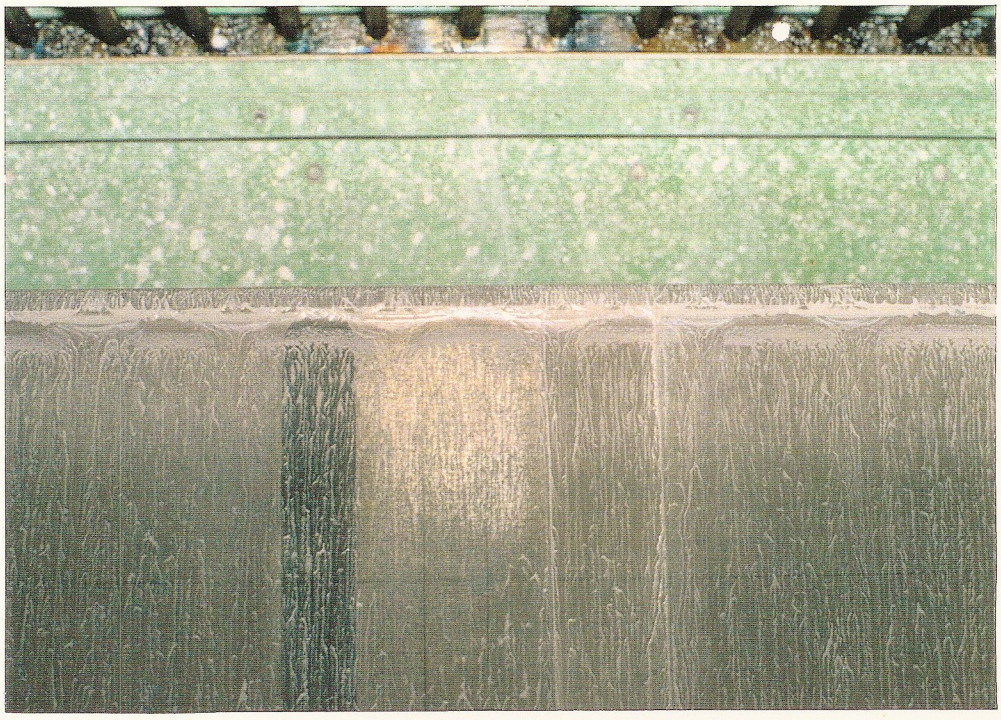


Figure 4.7	Picture of the Surface Flow Patterns Generated Under 10 % Free Stream Turbulence Intensity and 35 m/s Free Stream Velocity

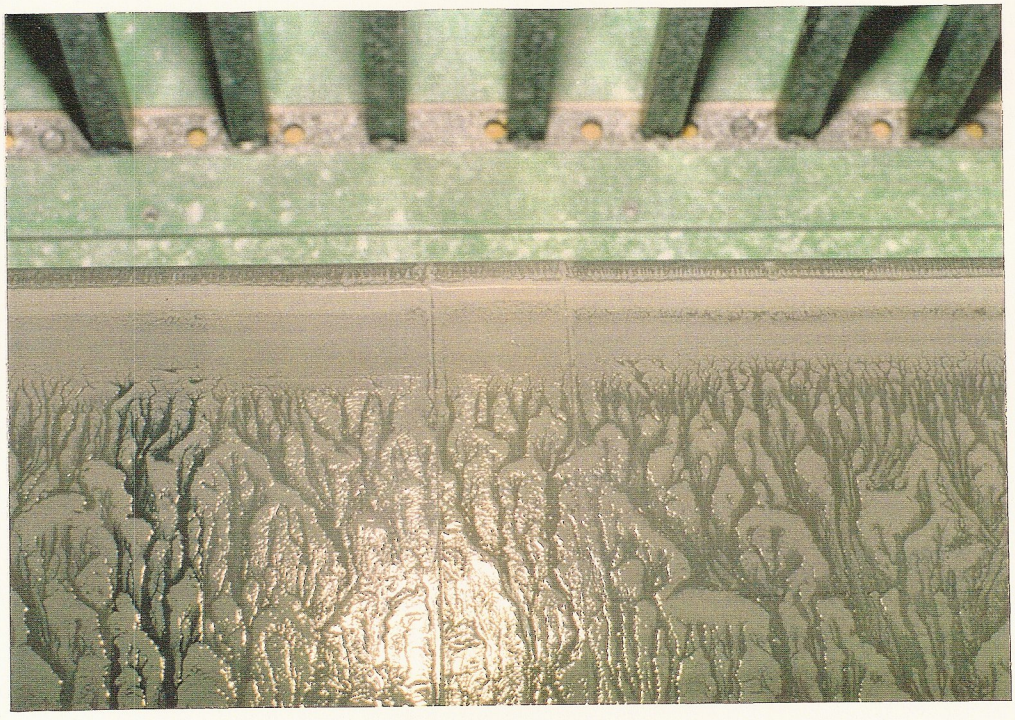


Figure 4.8	Picture of the Surface Flow Patterns Generated Under 15 % Free Stream Turbulence Intensity and 5 m/s Free Stream Velocity

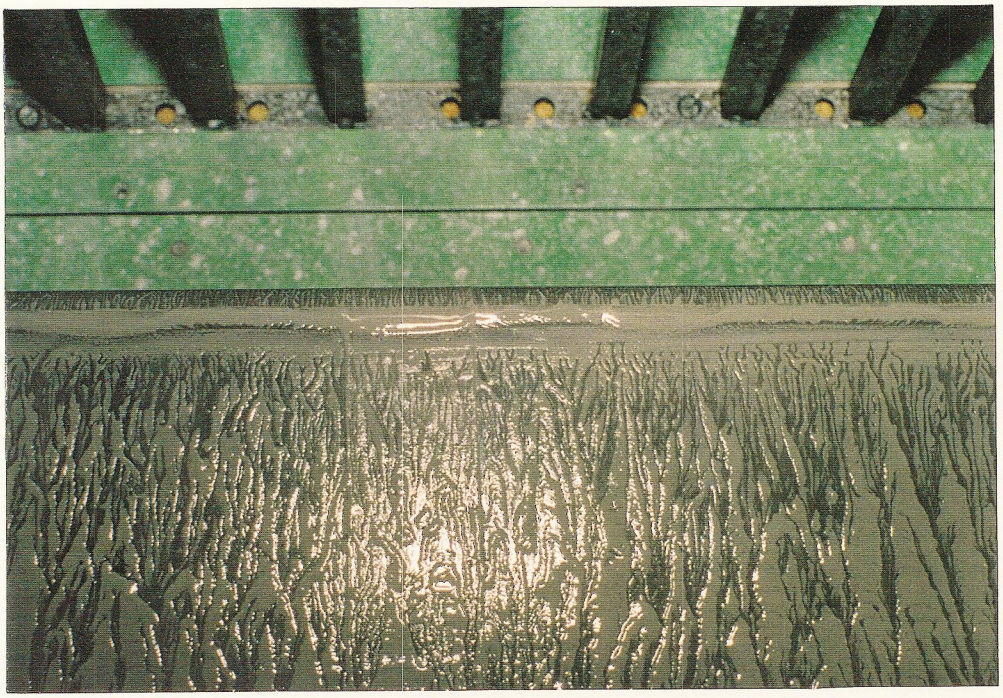


Figure 4.9	Picture of the Surface Flow Patterns Generated Under 15 % Free Stream Turbulence Intensity and 15 m/s Free Stream Velocity

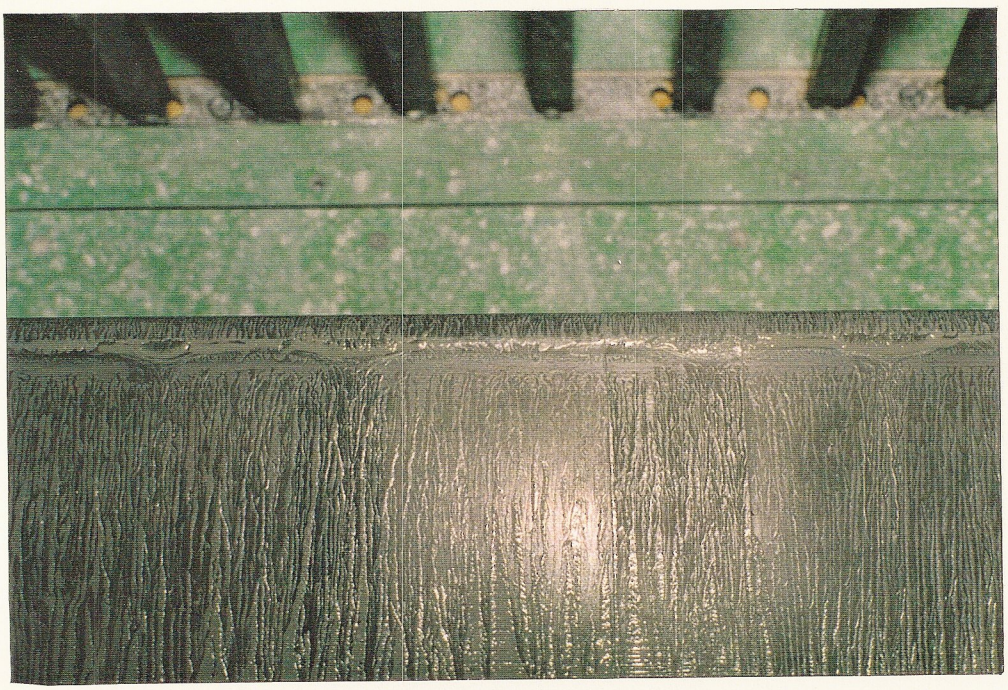


Figure 4.10	Picture of the Surface Flow Patterns Generated Under 15 % Free Stream Turbulence Intensity and 35 m/s Free Stream Velocity

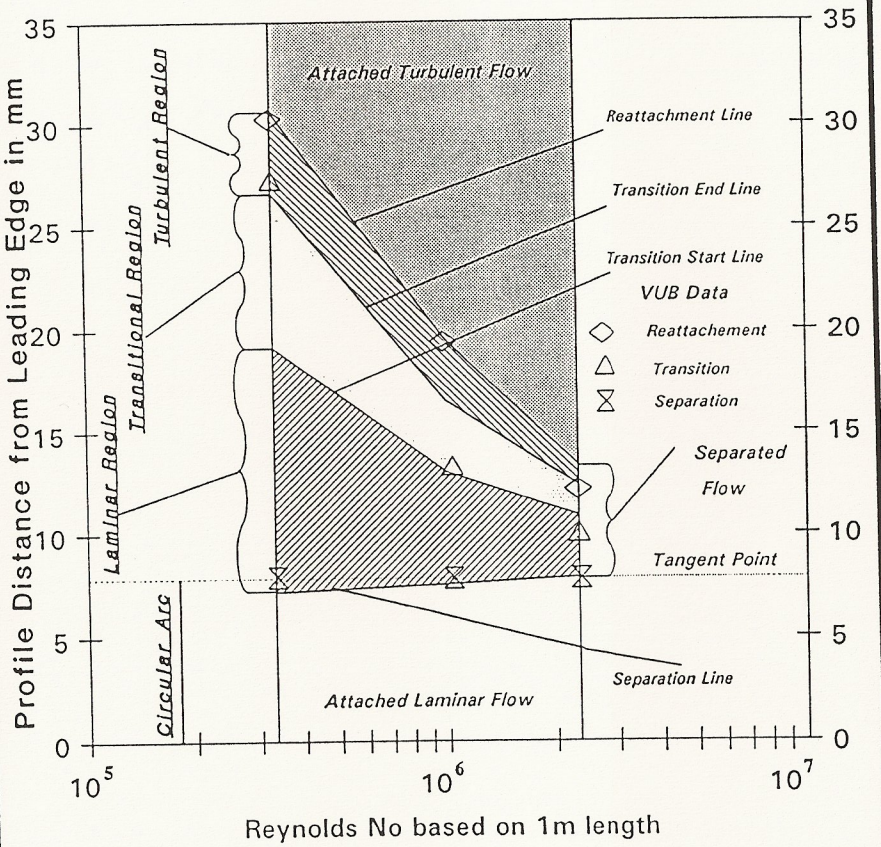


Figure 4.11 The Present Results Compared with VUB Hot Wire Data at Background Turbulence

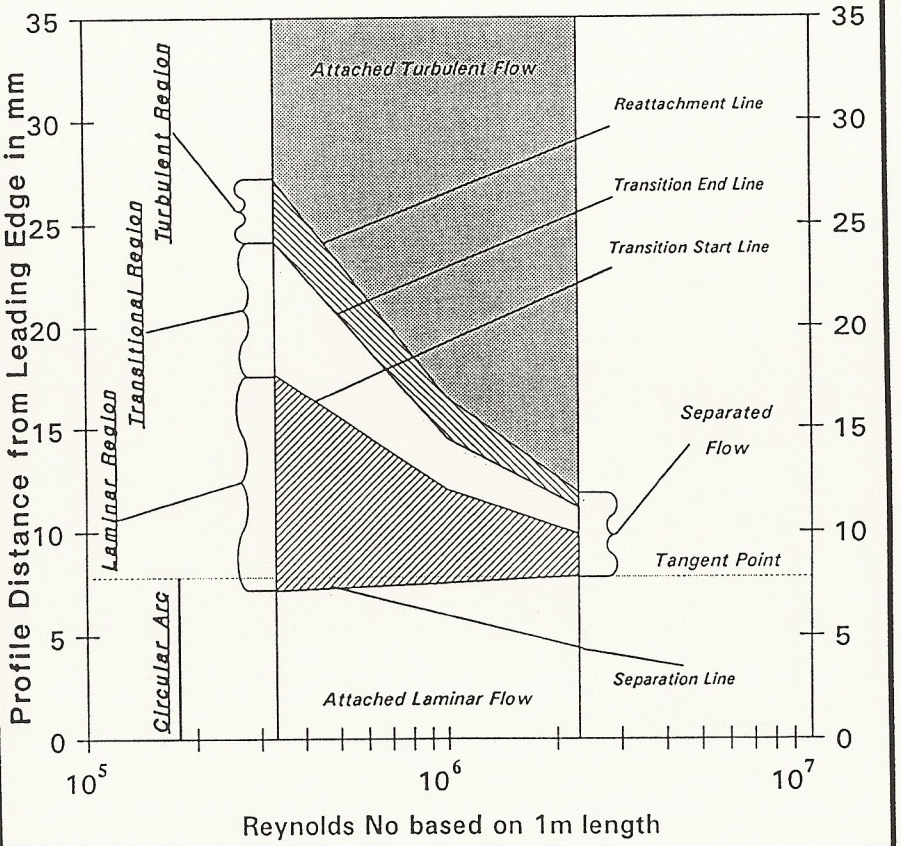


Figure 4.12 Separated Flow Transition Measurements Using SMR Grid Located at X=−150 mm

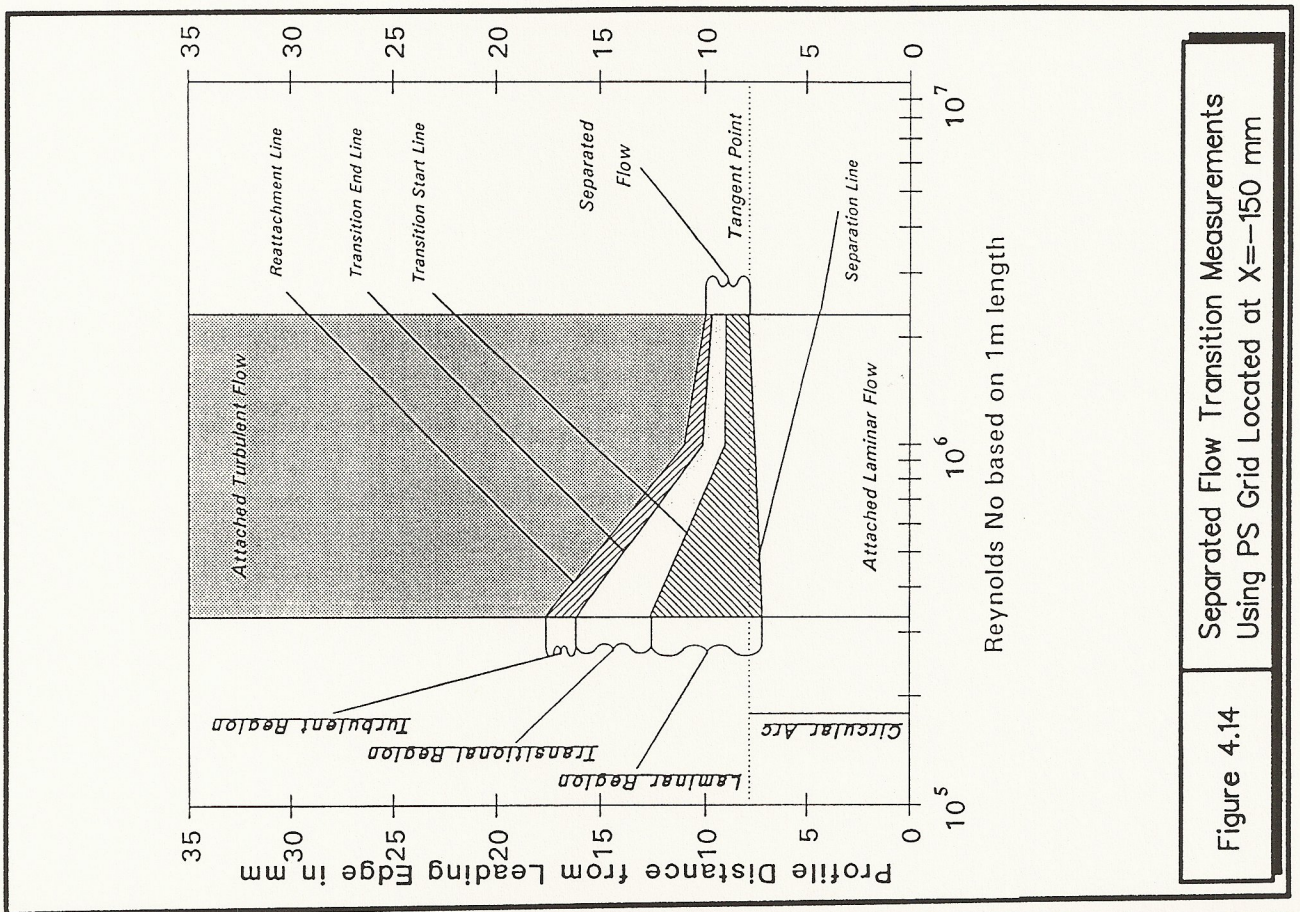


Figure 4.13 Separated Flow Transition Measurements Using PR Grid Located at X=−150 mm

Figure 4.14 Separated Flow Transition Measurements Using PS Grid Located at X=−150 mm

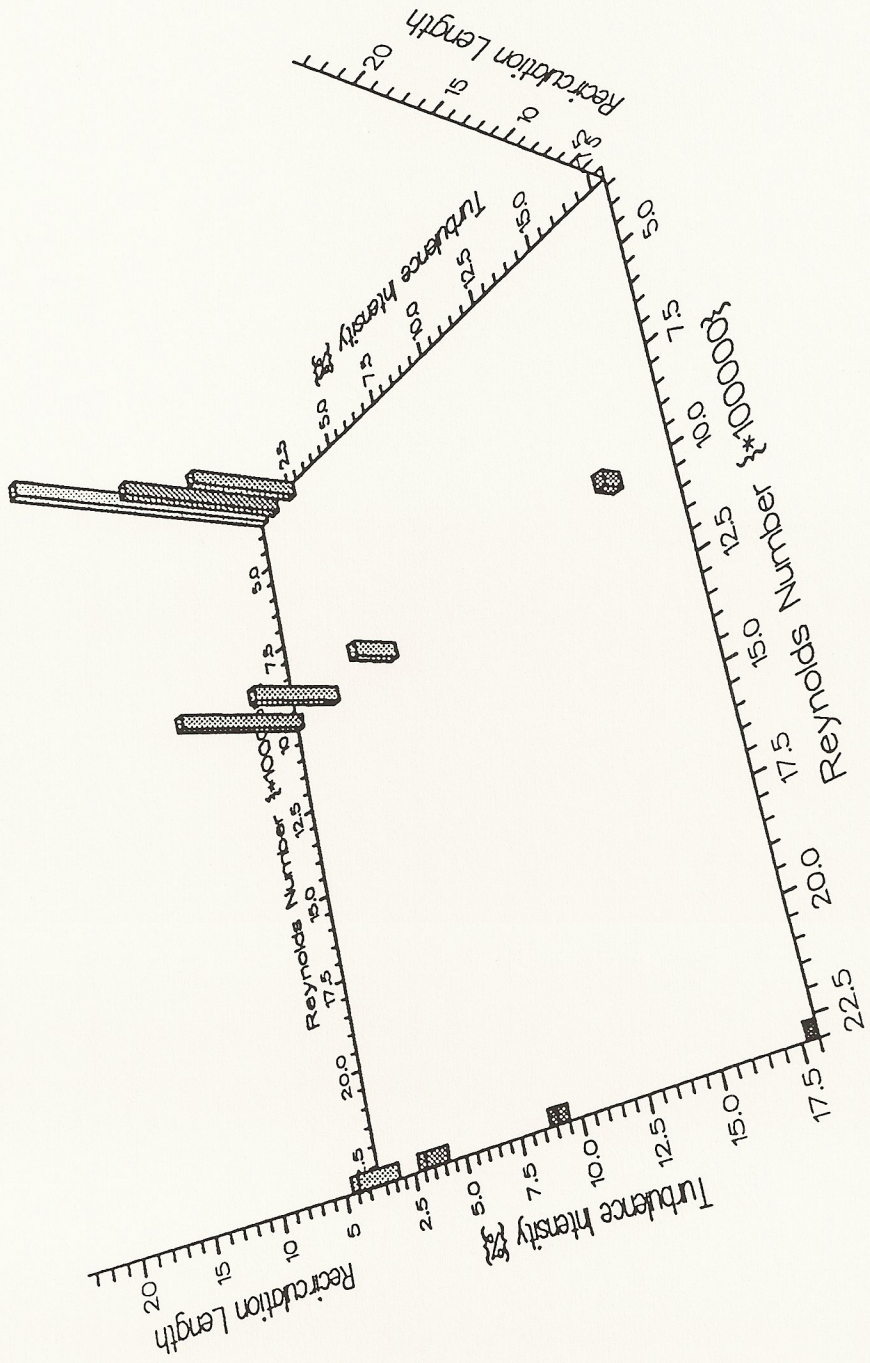


Figure 4.15 Variation of the Recirculation Length with Free Stream Reynolds Number and Turbulence Intensity

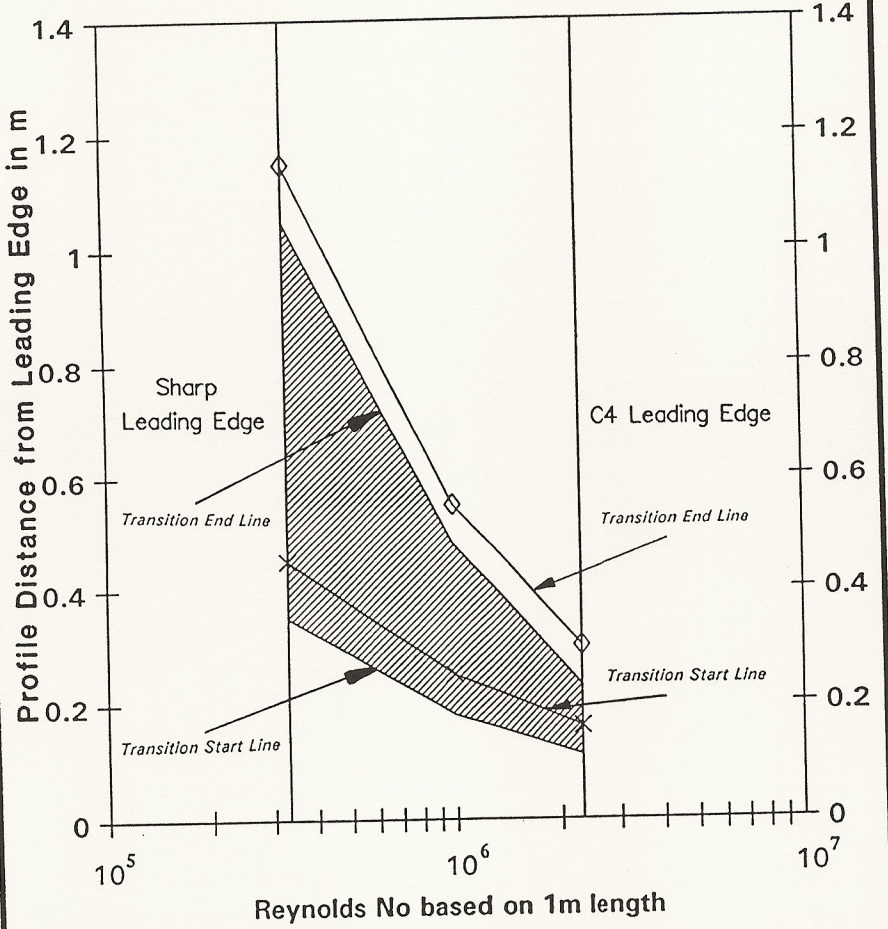


Figure 4.16 Comparison Between Transition Results for the Sharp and C4 Leading Edge at Tu=2.5%

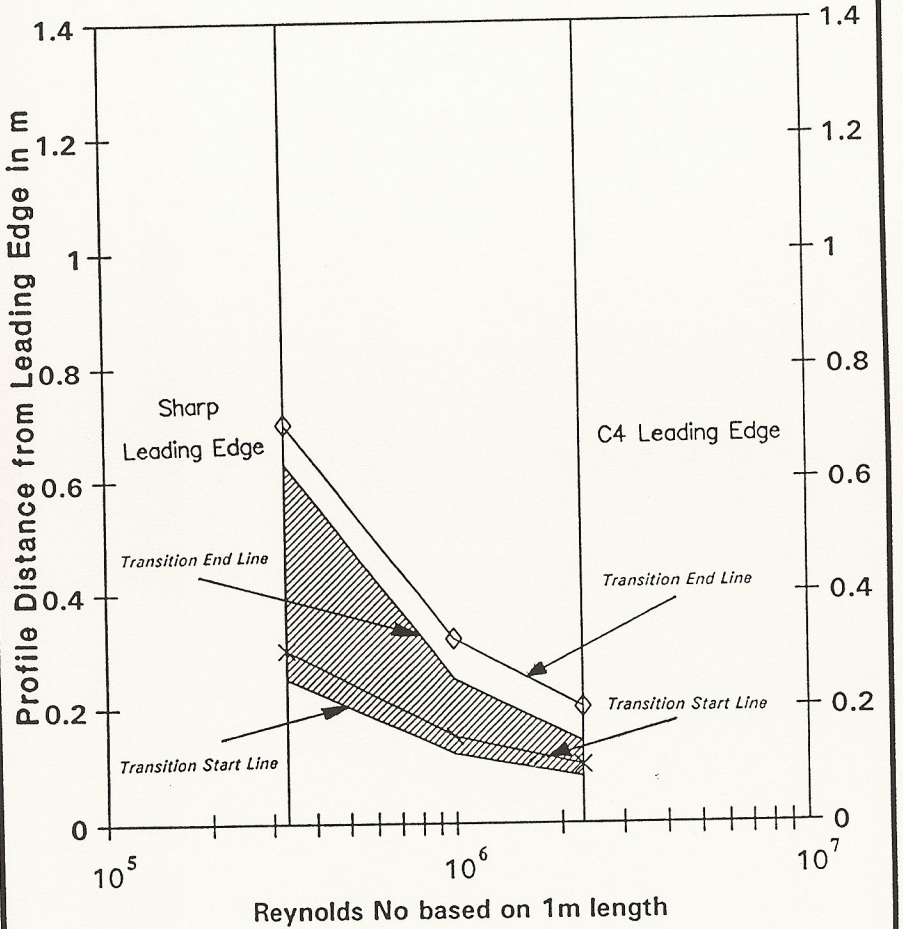


Figure 4.17 Comparison Between Transition Results for the Sharp and C4 Leading Edge at Tu=10%

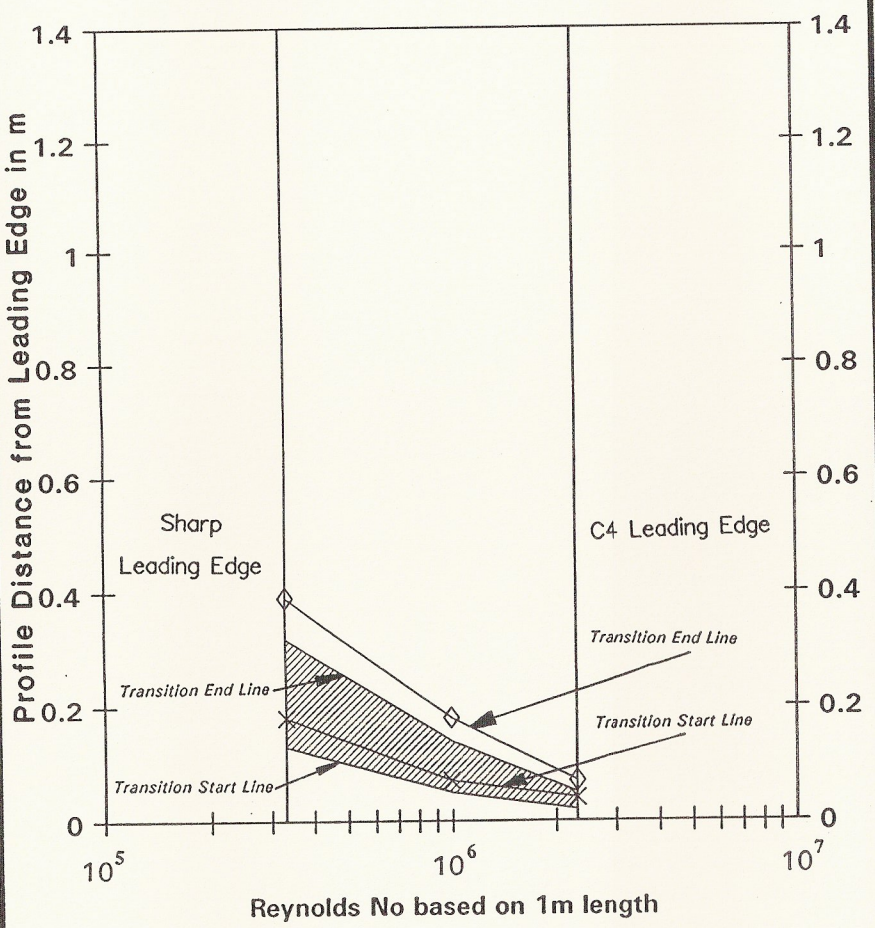


Figure 4.18	Comparison Between Transition Results for the Sharp and C4 Leading Edge at Tu=15%

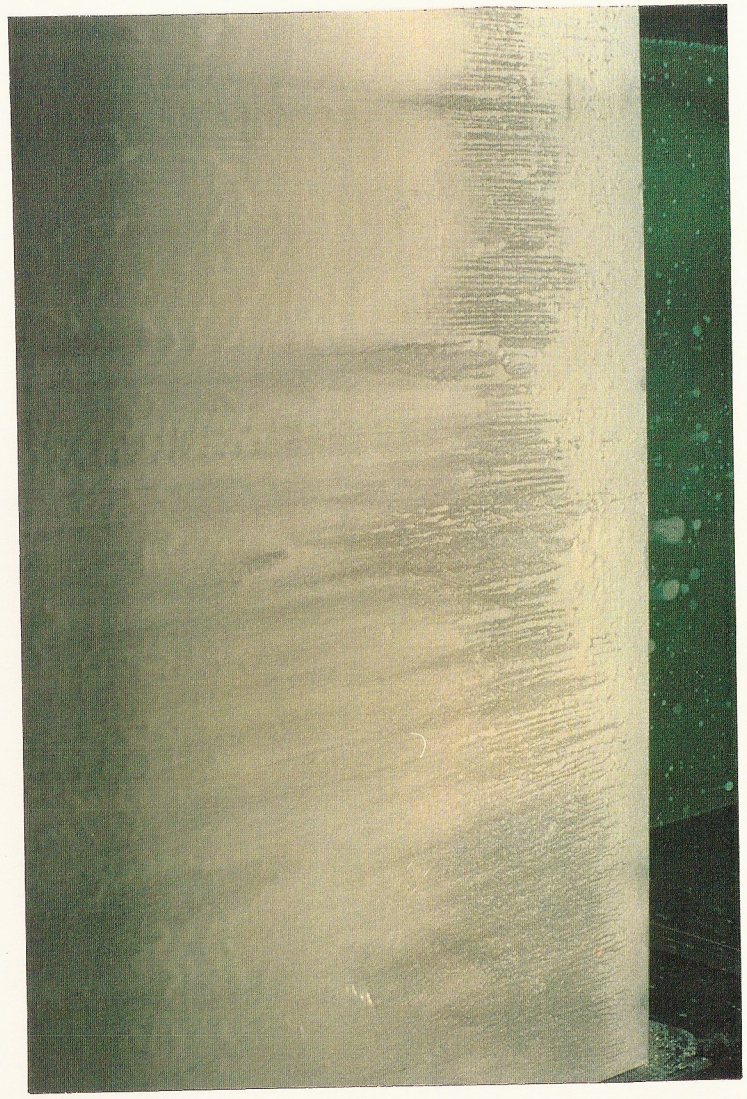


Figure 4.19	Visualisation of the Lateral Misalignment of the Plate Using the Present Technique

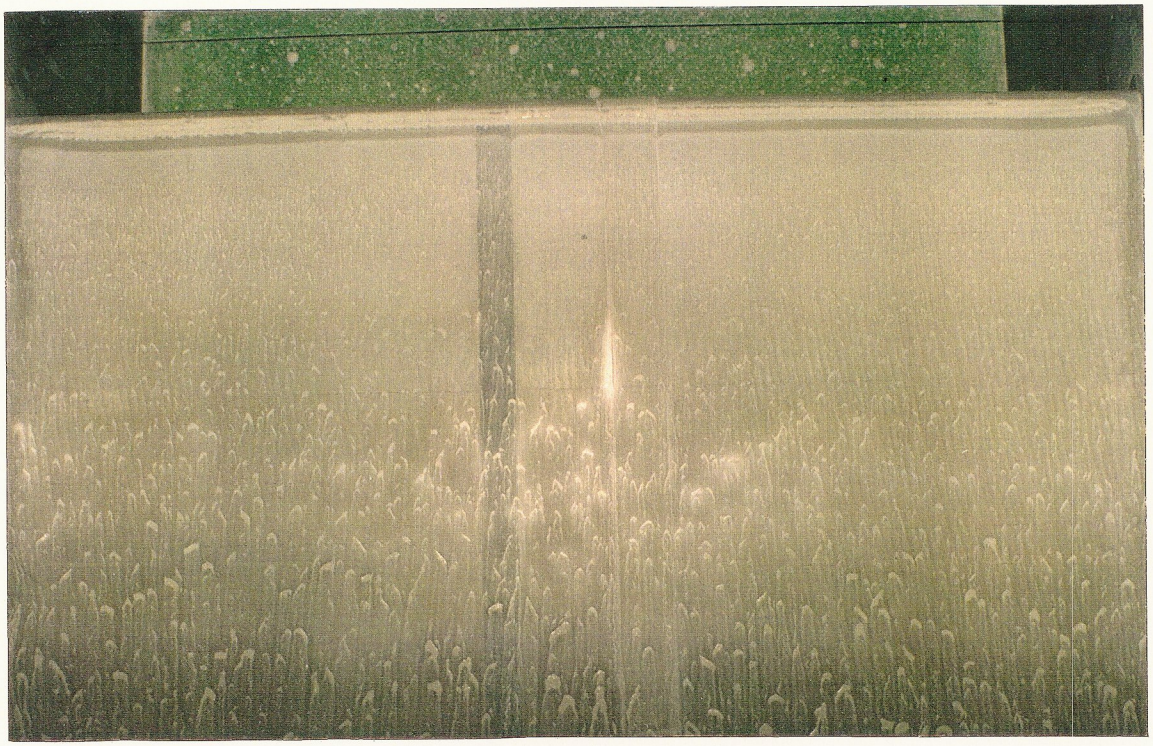


Figure 4.20 Visualisation of the Two-Dimensional Structure of the Recirculation Bubble

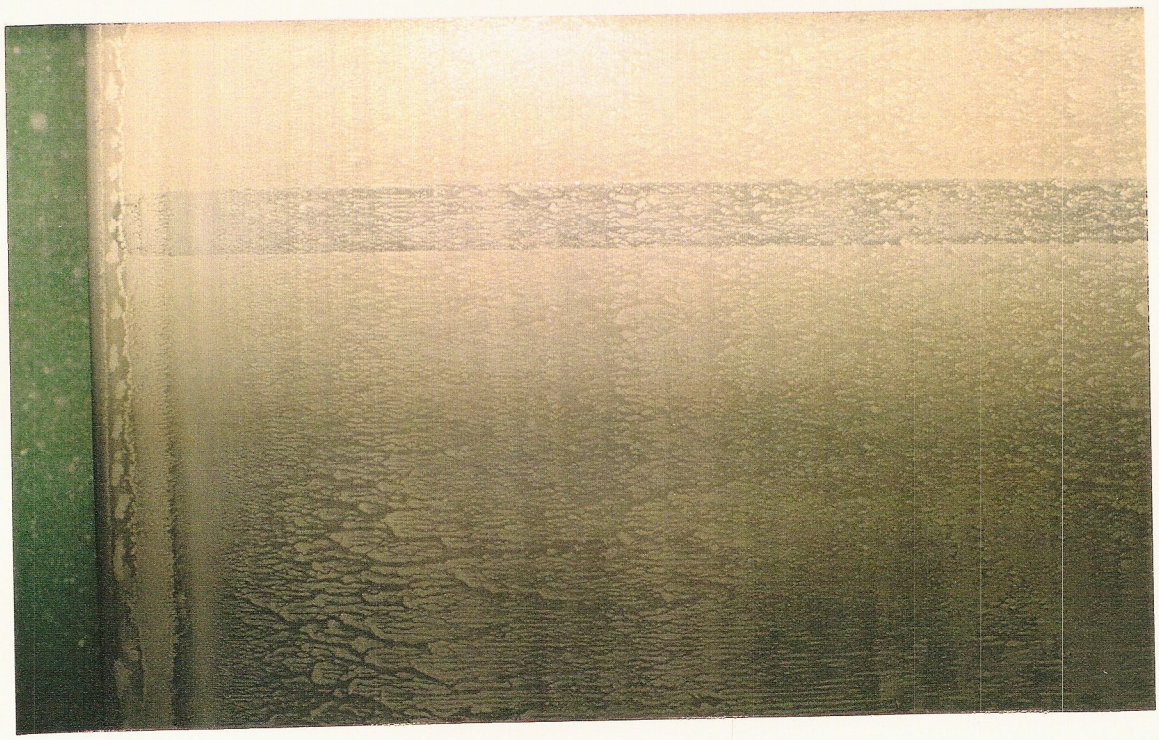


Figure 4.21 Visualisation of the Recirculation Structure Generated with PS Grid Located at X=-650 mm

CHAPTER 5

Investigation of the Boundary Layer of the C4 Plate

CHAPTER 5

Investigation of the Boundary Layer of the C4 Plate

5.1 INTRODUCTION

In this chapter of the thesis, the hot-wire investigation of the flow field around the flat plate with the C4 profile leading edge is presented. This experimental configuration provided the means to study the effect of a more realistic leading edge shape for turbomachinery purposes. The objective of this design of the C4 profile leading edge was to create an adequate pressure distribution in the leading edge area. In the first section of the profiled leading edge, the flow undergoes a quite strong acceleration which results initially in a thin boundary layer. In the following section of the profiled leading edge the pressure gradient is not very steep and serves as a recovery zone in order to avoid separation. The pressure distribution along the rest of the plate is dictated only by the geometry of the wind tunnel. Hence, the results described in this section are considered to be influenced by the pressure distribution along the plate (fig.3.4) and should be examined from this point of view.

This particular experimental investigation of the boundary layer of the flat plate with the C4 leading edge has been performed using hot wire anemometry. This experimental technique supported by an appropriate data acquisition system, provided the opportunity to collect a lot of useful data. In order to make full use of the collected data, both the integral quantities of the acquired samples have been calculated and further statistical analysis of the samples has been performed. The main constraint of this experimental technique is that it provides data for only one particular point of the

flow field at a time. As a result, in order to obtain a global picture of the flow field, a sequence of measurements at various points is necessary. The obvious assumption involved in this process is that the flow field is statistically stationary. In other words, the overall characteristics of the free stream flow remain unaffected between the individual point measurements.

Three test cases have been considered in order to cover the range of free stream velocities and turbulence intensities used in this study. The first test case considered the lower free stream Reynolds number ($Re_\infty = 3.3\ 10^5$) in a moderate to high free stream turbulence environment ($Tu_\infty = 4\%$). In the second test case the free stream turbulence intensity was kept the same but the free stream Reynolds number was increased to $Re_\infty = 9.9\ 10^5$. Finally, in the third test case the free stream Reynolds number was kept the same as in the second test case and the free stream turbulence intensity used was in the lower range of values ($Tu_\infty = 1.8\%$). A minimum of twenty profiles of detailed data has been acquired for each test case studied.

In the following sections of chapter 5, the analysis of the hot wire results is presented. Firstly, the description of the boundary layer flow using the time mean quantities is discussed. Further statistical analysis of the hot wire signals, including turbulence spectra and intermittency information is also presented. Finally, an attempt to reconstruct the global picture of the boundary layer flow using these detailed hot wire data, is made. This experimental investigation is concluded with the discussion of the results obtained for some integral parameters of the boundary layer.

5.2 PRESENTATION AND STATISTICAL ANALYSIS OF THE OBTAINED RESULTS

5.2.1 Introduction

This section of chapter five is devoted to the description of the boundary layer flow around the flat plate with the C4 leading edge, using profiles of time averaged quantities. The term time averaged quantities is used to describe quantities such as the mean velocity and turbulence intensity that can be calculated as the time average of the relevant quantity. The skewness and flatness factors of the probability density distribution that express the higher order central moments in a dimensionless form, can also be considered to belong in the same category. Careful examination of the variation of these quantities throughout the boundary layer could reveal interesting information about the distribution of turbulently moving fluid in the transitional boundary layer.

For all the free stream conditions involved and every point considered, profiles of the mean velocity $\overline{u}$, the turbulence intensity Tu, the skewness factor S and flatness factor T have been acquired. These quantities have been obtained from the velocity signals acquired using hot wire anemometry in conjunction with the data acquisition system. The theoretical considerations presented in chapter three have been used for the calculation of the foregoing parameters.

Analytical plots of the acquired profiles are presented in appendix A (sections i, ii and iii for the first, second and third set of free stream conditions, respectively). Each of the presented figures contains information about all four parameters plotted in the same scale in order to facilitate the comparison between the various stations and test cases involved. The crosswise distance y has been non-dimensionalised using the boundary layer thickness in order to increase the clarity of the presented results. Figures

A1.1-A1.40, A2.1-A2.42 and A3.1-A3.20 contain the complete set of results concerning the foregoing time averaged quantities.

In the following paragraphs, a discussion of the results concerning the profiles of the time averaged quantities, is presented. In order to facilitate and enhance the analysis of the present results, some representative profiles of the time averaged quantities for each test case are discussed here. The gradual evolution of the boundary layer parameters from a totally laminar to a totally turbulent character is demonstrated using representative profiles for the laminar, transitional and turbulent regions in the boundary layer.

In order to explain this procedure in more detail, data acquired under the free stream conditions involved in the following test cases, have been used. In the first test case (U_∞ = 5 m/s, Tu_∞ = 4%) five streamwise locations throughout the transitional zone have been considered, namely, X = 100 mm, 200 mm, 300 mm, 350 mm and 600 mm, respectively. The equivalent Reynolds number based on the streamwise distance from the leading edge obtained values of 3.45 10^4, 6.9 10^4, 1.04 10^5, 1.21 10^5 and 1.9 10^5, respectively. The second test case (U_∞ = 15 m/s, Tu_∞ = 4%) involved four streamwise locations, namely, X = 45 mm, 75 mm, 118 mm and 175 mm. In this case, the equivalent Reynolds numbers based on the streamwise distance obtain values of 4.65 10^4, 7.76 10^4, 1.22 10^5 and 1.81 10^5 ,respectively. The results from the above test cases are presented in figures 5.2, 5.4, 5.6, 5.8 and 5.10 for the first test case and 5.12, 5.14, 5.16 and 5.18 for the second test case. The last test case (U_∞ = 15 m/s, Tu_∞ = 1.8%) also involved four streamwise locations, namely, X = 150 mm, 350 mm, 425 mm and 650 mm. The equivalent Reynolds numbers amounted to 1.55 10^5, 3.62 10^5, 4.4 10^5 and 6.72 10^5. Results from the last test case are presented in figures 5.19 to 5.22.

The first and last streamwise locations have been selected in order to be in the area of transition start and end respectively. The second location coincides with the overall maximum observed deviations of the skewness and flatness factors from the values corresponding to the normal distribution. Finally, the penultimate streamwise

location coincides with the observed overall maximum of the turbulence intensity. This location can be considered to be the centre of the transitional zone. The importance of those measurement stations will be discussed in more detail in the following sections of this chapter.

5.2.2 The concept of intermittency

The means by which a turbulent flow regime propagates and evolves into a non-turbulent fluid constitutes a particularly interesting and challenging problem. The lack of detailed knowledge of the physics of the turbulent/non-turbulent interface prevented for many years the successful theoretical explanation of the intermittent character of transitional flow regimes. Even though, the physical properties of the boundary layer are easily outlined using the time averaged quantities as described in the previous sections of the thesis, the statistical properties of the velocity fluctuations could provide useful tools for understanding the time dependencies involved in the transition process.

In this section of chapter five, further analysis of the obtained results is presented. An attempt is made to use the statistics of boundary layer turbulence, in order to improve the understanding of the boundary layer evolution from laminar to turbulent. The concept of intermittency is employed in order to describe the alternating character of the transitional area of the boundary layer. Finally, it should be noted that the term "laminar" is often used here to describe the characteristics of the non-turbulent fluid.

Using the concept of intermittency, which has been defined in chapter one as the percentage of time that the flow is turbulent, the mean velocity can be expressed as the average of the mean velocities of the laminar and turbulent portion of the signal, weighted by the intermittency factor:

$$\overline{u} = (1-\gamma)\,\overline{u_L} + \gamma\,\overline{u_T} \qquad (5.1)$$

Consider a transitional velocity signal that consists of N samples taken at equal time intervals Δt. Letting N_L be the number of samples in the non-turbulent (laminar)

portion of the signal and N_T be the number of samples in the turbulent portion of the signal, then the intermittency factor, γ, can be described as the ratio N_T/N and by definition $(1-\gamma)$ equals N_L/N. In the following discussion the velocity samples that belong to the turbulent and non-turbulent population of the signal are symbolised as u_T and u_L, respectively. Similarly, the deviations from the mean value $\overline{u_T}$ of the turbulent and $\overline{u_L}$ of the non-turbulent populations in the combined velocity signal can be described as $u'_T = u_T - \overline{u_T}$ and $u'_L = u_L - \overline{u_L}$, respectively. In the general case of a transitional boundary layer signal, the mean value of the non-turbulent portion of the signal is different to the mean value of the turbulent portion of the signal. The mean velocity difference is defined as: $\Delta\bar{u} = \overline{u_T} - \overline{u_L}$.

Assuming that the two distinctively different velocity populations of the turbulent and non-turbulent portion of the signal follow the normal probability distribution, it can be argued that the moments of odd order of the two distributions equal to zero, i.e.:

$$\overline{u_L'^n} = \overline{u_T'^n} = 0 \qquad n = 1,3,5,7,\ldots \tag{5.2}$$

The variance, $\overline{u'^2}$, of the signal as a whole can be expressed as a function of the variance, $\overline{u_L'^2}$, of the non-turbulent portion of the signal and the variance $\overline{u_T'^2}$ of turbulent portion of the signal by the following equation:

$$\overline{u'^2} = (1-\gamma)\,\overline{u_L'^2} + \gamma\,\overline{u_T'^2} + \gamma\,(1-\gamma)\,\Delta\bar{u}^2 \tag{5.3}$$

Similar relationships can be derived for the higher order central moments of the probability distribution. The third central moment of probability distribution can be expressed as:

$$\overline{u'^3} = \gamma\,(1-\gamma)\,\Delta\bar{u}\left(3\left(\overline{u_T'^2} - \overline{u_L'^2}\right) - (2\gamma-1)\,\Delta\bar{u}^2\right) \tag{5.4}$$

and the fourth central moment of the probability distribution can be given by the

following equation:

$$\overline{u'^4} = (1-\gamma)\,\overline{u_L'^4} + \gamma\,\overline{u_T'^4} + \\ + \gamma\,(1-\gamma)\,\Delta\bar{u}^2\left(6\left((1-\gamma)\,\overline{u_T'^2} + \gamma\,\overline{u_L'^2}\right) + (3\gamma^2-3\gamma+1)\,\Delta\bar{u}^2\right) \tag{5.5}$$

Although the mean velocity of the overall signal can be expressed as an average of the turbulent and the non turbulent values weighted by the intermittency factor (eq.5.1), the impulsive changes from one behaviour to the other generate a "switching" effect which becomes apparent in the expression of the higher order central moments as an extra term dependent on the mean value difference, $\Delta\bar{u}$, as well as the intermittency factor (eqs. 5.2-5.4).

The influence of the intermittency factor, γ, on the "switching" effect is given as a parabola of the form $\gamma\,(1 - \gamma)$ which obtains its maximum value for $\gamma = ½$ and becomes zero at the two extremes ($\gamma = 0$ and $\gamma = 1$). The physical consequence of the previous discussion is that the "switching" between the turbulent and non-turbulent motion in the transitional boundary layer has its maximum effect for $\gamma = ½$. The intermittency factor, $\gamma = \gamma(x,y)$, is understood to have a streamwise as well as a crosswise "switching" effect, although the streamwise effect has a very important physical significance. The variation of the mean velocity difference, $\Delta\bar{u}$, plays a significant role in the crosswise direction, as it changes from positive to negative in the near wall area and finally tends to zero in the region near to the free stream.

As a concluding remark, it can be stated that the expressions of the higher moments of the probability distribution present a strong similarity between each other. More specifically, it can be considered that the "switching" effect on the variance of the signal as a whole, is always positive. The central moment of third order (as well as all the central moments of odd order) is expressing the switching effect because the equivalent moments of the separated turbulent and non-turbulent portions of the signal have the value of zero. Accordingly, the distribution of the skewness factor throughout

the boundary layer could be considered as an indication of the variation of the mean velocity difference, $\Delta\bar{u}$.

5.2.3 Probability Density Distribution

Before proceeding with the discussion of the profiles of the mean velocity, the turbulence intensity and the skewness and flatness factors individually, it would be useful to examine the characteristics of the probability density distribution of the velocity signals throughout the boundary layer in a number of selected locations across the length of the plate. The purpose of this section is to assist the discussion of the behaviour of the profiles of the above parameters in the transitional area.

In the following paragraphs, the various characteristics of the probability density distribution of the velocity signals are discussed. In order to enhance the understanding of the physical meaning of the skewness and flatness factors of the probability density distribution, the measured profiles have been examined with respect to their conformance to the equivalent values of the normal distribution. At each particular measurement point, the acquired velocity signal is used to generate the probability density distribution. The integral quantities of the distribution are subsequently calculated. In this process, normalised stochastic variables have been used (eq. 3.6) in order to have a common platform for comparisons with the Gaussian probability distribution (eq. 3.7). This procedure can be used in order to produce information relevant to the transitional characteristics of the flow at the measurement point under consideration. First of all, the physical implications of a normally distributed signal as well as the effect of the deviations from the Gaussian distribution will be considered.

A velocity signal acquired in a totally laminar flow regime is likely to be distributed normally. The reason behind this behaviour is that in practical laminar flows, the deviations of the instantaneous velocity from the mean occur as a result of a large number of independent sources of small irregularities in the free stream conditions (residual turbulence). As a result, the standard deviation of the laminar velocity signal

is very small compared to the turbulent. Velocity fluctuations in a totally turbulent flow regime, can be considered as the sum of a large number of small velocity fields of elementary vortex lines. In isotropic turbulence, the velocity distribution can be also considered as normal. Accordingly, the skewness and the flatness factors of the velocity distribution in an either totally laminar or totally turbulent flow regime should have the values of 0 and 3, respectively. Accordingly, the free stream velocity fluctuations of a flow field with homogenous background turbulence should be normally distributed, unlike the transitional regions of the boundary layer.

In the opposite case, where the observed probability distribution is not similar to the normal, some estimations of the characteristics of the transitional velocity field can be made. It can be assumed that the transitional velocity signal incorporates the effect of two different populations of turbulent and non turbulent flow regimes. The mean value of the two portions of the signal is different in the general case, and the standard deviation of the turbulent portion of the signal is several times higher that the standard deviation of the non-turbulent portion of the signal. A sharp peak in the probability distribution ($T > 3$) could be interpreted as a sign of concentration of deviations from the mean velocity in a particular range with standard deviation relatively smaller than the signal as a whole. Apparently, this behaviour could be attributed to the non-turbulent portion of the signal. By the same token, a skewed probability distribution could be understood as an indication of significant difference between the mean values of the turbulent and non-turbulent portions of the signal.

It is usually the case that when the flatness factor is different to 3, the probability density distribution is skewed as well. In this case, a probability density distribution skewed to the right, could be interpreted as the result of a transitional signal in which the non-turbulent portion of the signal has a mean value greater than the common mean, and visa versa when the probability density distribution is skewed to the left.

In order to enhance the understanding of the significance of the shape of the probability distribution, the profiles of the time averaged quantities of the boundary layer

are presented in parallel to the probability distributions at each measurement station. The probability density distribution at six selected crosswise locations throughout the boundary layer has been plotted at each of the above described streamwise stations. These locations have been selected in such a way that they coincide with points of special interest throughout the boundary layer.

The first point has always been selected to be in the outer boundary layer, in the area where the boundary layer parameters obtain free stream values. In this area the probability distribution appears very similar to the Gaussian distribution (eq. 3.7). Another point has been selected in the area of the outer boundary layer where the flatness factor, T, obtains a local maximum and the inclination of the skewness factor (dS/dy) and the turbulence intensity (dTu/dy) changes to its outer boundary layer behaviour. The probability distribution in this area is usually very steep ($T > 3$) and skewed to the left ($S < 0$), indicating that the non-turbulent portion of the signal is distributed around a mean value that is greater than the common mean. This behaviour is usually associated with the effect of the "switching" between the turbulent and non-turbulent motion of the boundary layer fluid. In the outer boundary layer, the initially smooth non-turbulent signal gets distorted by the aperiodic passing of the turbulent spots which appear to have lower mean value in this area.

The following points have been chosen to be in the area of the inner boundary layer where the turbulence intensity, Tu, obtains its maximum value. In this region, the skewness factor, S, obtains the value of zero and the flatness factor, T, obtains its minimum value (often less than 3 in the transitional region). In this case the points selected for presentation are the ones where the flatness factor, T, obtains the value of 3 as well as the point at which the skewness factor, S, becomes zero. At the latter point the flatness factor, T, becomes minimum and the turbulence intensity, Tu, obtains its maximum value. This point is quite important because all the central moments of the probability distribution examined here (Tu, S, and T) reach a point of significant change in their behaviour through the boundary layer. This behaviour could be associated with the end of the viscous sublayer. It is important to note at this point that the most

probable explanation of a zero value of the skewness factor, S, is that both turbulent and non-turbulent portions of the signal are distributed around the same mean value ($\Delta\bar{u}=0$). The overall characteristics of this region will be discussed in greater extent later in this chapter.

Finally, a point has been always selected in the near wall area. The probability distribution in this area has similar characteristics to the probability distribution of the outer boundary layer. A very steep peak around the most probable value of the velocity, $\hat{u}$, is usually observed. The overall probability distribution is skewed to the right, in this area, indicating that the portion of the non-turbulent portion of the signal (smaller variance) is distributed around a mean value lower that the common mean and as a result, lower than the turbulent portion of the signal (larger variance).

5.2.4 Mean Velocity Profiles

Discussion on the forgoing results is presented separately for the mean velocity profiles, the turbulence intensity profiles and finally the profiles of the skewness and flatness factors of the probability distribution of the velocity signal. The results from the first test case (U_∞ = 5 m/s, Tu_∞ = 4%) are presented in figures 5.1, 5.3, 5.5, 5.7 and 5.9, for the second test case (U_∞ = 15 m/s, Tu_∞ = 4%) in figures 5.11, 5.13, 5.15 and 5.17 and for the last test case (U_∞ = 15 m/s, Tu_∞ = 1.8%) in figures 5.19, 5.20, 5.21 and 5.22.

In order to assist the discussion of the velocity profiles and to facilitate comparisons, the mean velocity profiles have been plotted in a non-dimensional form. The distance, y, from the wall has been non-dimensionalised with the boundary layer thickness, δ. The mean velocity at the edge of the boundary layer, U_e, has been used in order to non-dimensionalise the mean velocity, $\bar{u}$, throughout the boundary layer. Laminar and turbulent correlations have been also plotted in parallel to the measured data, in order to provide a common platform for comparisons. It should be noted that both laminar and turbulent correlations plotted here, have been calculated as if a purely

laminar or purely turbulent boundary layer had started from the leading edge of the flat plate. The Blasius analytical solution of the Navier Stokes equations has been employed as the laminar correlation (Schlichting, 1979). There is a widespread belief that turbulent profiles are represented well by the $1/7^{th}$ power velocity distribution law. Experimental evidence from previous investigators show that actually the exponent varies from one-third to one-tenth (see also Clauser, 1956). In the present investigation, the following formulation is used as the turbulent correlation:

$$\frac{\bar{u}}{U_\infty} = \left(\frac{y}{\delta}\right)^{\frac{1}{7}} \tag{5.6}$$

Figures 5.1, 5.11 and 5.19 present velocity profiles from the initial stages of transition for the three test cases considered. The value of the intermittency at this stage is very low. The mean velocity profiles in these early stations follow the Blasius analytical solution of the Navier-Stokes equations for laminar boundary layers. As the intermittency factor increases, moving downstream of the transition onset, the turbulent portion of the signal develops fast. Due to the presence of the turbulent spots in the transitional region, the laminar portion of the boundary layer flow becomes more and more contaminated by turbulently moving fluid. Initially, only small changes in the mean velocity profiles are observed (see also fig. 5.3, 5.13 and 5.20 with respect to the three test cases considered). This behaviour can be explained considering the fact that the origin of the turbulent portion of the boundary layer is at the onset of transition. Consequently, the contribution of the turbulent portion of the signal to the overall mean velocity is small due to its very small boundary layer thickness. This effect can be also demonstrated by the shape of the laminar and turbulent correlations presented in the relevant figures. The development of the boundary layer leads to profiles with increasingly turbulent characteristics (fig. 5.5, 5.7, 5.15 and 5.21). The outer section of the boundary layer seems to be affected first and more drastically than the near wall section. Finally, at the later stages of transition (fig. 5.9, 5.17 and 5.22), where the turbulent portion of the signal becomes dominant, the mean velocity profiles obtain shapes that are similar to the turbulent correlation.

5.2.5 Profiles of the Turbulence Intensity

The process of boundary layer transition from laminar to turbulent can be followed using the turbulence intensity profiles. In general terms, it can be considered that the variance (second central moment of the probability distribution) of the velocity signal, $\overline{u'^2}$, expresses the Reynolds normal stress in the streamwise direction. This term is particularly important in turbulence studies. In isotropic turbulence $\left(\overline{u'^2} = \overline{v'^2} = \overline{w'^2}\right)$, the turbulent kinetic energy per unit mass is directly proportional to the Reynolds normal stress in the streamwise direction and it can be expressed as follows:

$$k = \frac{1}{2}\left(\overline{u'^2} + \overline{v'^2} + \overline{w'^2}\right) \approx \frac{3}{2}\ \overline{u'^2} \qquad (5.7)$$

The profiles of the turbulence intensity demonstrate that even at the early stages of transition, turbulence kinetic energy reaches high values in the boundary layer. This is mainly due to the development of the shear layer in the boundary layer and the free stream turbulence that is fed into the outer boundary layer. Figures 5.1, 5.11 and 5.19 demonstrate this effect for the three test cases considered here.

As transition progresses, this smooth peak in the profiles of turbulence intensity develops into a sharper peak closer to the wall (fig. 5.3, 5.5, 5.15 and 5.20). This behaviour is observed constantly throughout the transition region. In particular, at the mid transition stages, where turbulence activity is very strong, the overall turbulence intensity reaches values as large as 15%. In this region, the near wall peak is followed by a sharp drop in the turbulence intensity values. At the outer boundary layer, the rate of decrease in the values of the turbulence intensity becomes more smooth. The change in behaviour is quite pronounced especially in the third test case (see also fig. 5.20 to 5.22). The variation in the characteristics of the turbulence intensity distribution across the boundary layer can be attributed to the contribution of the "switching" between the

laminar and the turbulent portions of the intermittent signal (eq. 5.3) (see also Arnal and Juillen, 1979).

At the later stages of transition the turbulence intensity retains high values near the wall (fig. 5.9, 5.17 and 5.22). Across the outer boundary layer the turbulence intensity diminishes gradually until reaching its free stream value at the edge of the boundary layer. This outer region of the boundary layer seems to be constantly affected by the turbulent activity in the free stream as it holds its basic characteristics throughout the transition region. Finally, in the totally turbulent boundary layer, the slope of the gradual descent in the turbulence intensity profile is uniform until the inner boundary layer.

5.2.6 Profiles of the Skewness and Flatness Factors

Some relevant information about the mechanism that triggers the transition process can be extracted from the profiles of the non-dimensional higher order central moments of the probability density distribution of the fluctuating velocity signal. Most turbulence studies attempt to evaluate the statistical quantities related to the spatial distribution of turbulence. The present analysis is based on the theoretical considerations presented in chapter 3 and should be regarded as an initial approach to the problem of identifying the particularities of the spatial distribution of turbulent energy within the boundary layer. The skewness and flatness factor of the velocity fluctuations have been plotted against the crosswise distance y non-dimensionalised with the boundary layer thickness (appendix A).

In general terms, profiles of the skewness and flatness factor can indicate departures from the normal distribution and to a certain extent, quantify the magnitude and identify the causes behind these departures. In the case of transition, this can be used as a detector of intermittent flow regimes because an intermittent signal always consists of both laminar and turbulent sections that upset the normal distribution. As discussed earlier in this chapter, this behaviour can be attributed to the fact that the

mean value and standard deviation of velocity of the two regimes are very different to each other. An interesting feature of these profiles is that they vary similarly throughout the boundary layer.

The instantaneous time traces of the velocity (oscilloscope patterns and digitized velocity traces), suggested that within the transitional region, the initially undisturbed laminar signal gets skewed by turbulence bursts which have the form of high amplitude velocity fluctuations. Very near to the wall the probability distribution is positively skewed ($S>0$) as a result of the wall proximity, unlike the outer boundary layer where it is negatively skewed ($S<0$) due to the influence of the free stream. The mean value of the turbulent flow regime is higher than the laminar near to the wall and visa versa at the outer boundary layer. The behaviour of the flatness factor can be explained along the same lines as the skewness factor. The flatness factor of the fluctuating signal obtains values higher than 3 for the majority of the crosswise stations in the transitional profiles. It can be considered that this is mainly the result of the superposition of the probability distributions of the turbulent and non-turbulent portions of the signal.

The evolution of the skewness and flatness in the streamwise direction follows a regular pattern for all the test cases examined here. It involves the development of the profiles from the uniformity in the values of the normal distribution for the totally laminar flow to the maximum deviations from the normal distribution. Finally, the profiles tend to obtain values equivalent to the normal distribution again as the intermittency factor tends to unity, in the fully turbulent flow regime.

In the case where $S = 0$, the laminar and turbulent regimes of the intermittent signal can be considered to have the same mean value ($\overline{\Delta u}= 0$). The distribution of both the laminar and the turbulent portions of the intermittent velocity signal is normal with the same mean but quite different standard deviations. As a result, the observed probabilities around the common mean value in the total distribution of the intermittent signal can be considered as the result of the superposition of the probabilities of the laminar and the turbulent distributions. Naturally, the variance of the turbulent portion

of the signal has a larger contribution to the overall variance and becomes more dominant as the intermittency factor increases. In this region, the estimation of the higher order integral quantities does not depend on the "switching" between the turbulent and non-turbulent behaviour. Since the combined probability distribution of the intermittent signal becomes symmetrical around the common mean value, the observed skewness factor obtains the value of zero.

It is interesting to note that there is a region in the boundary layer where the skewness and flatness factors of the probability distribution of the velocity signal obtain values close to the representative values for the normal distribution (S=0, T=3). As transition progresses, the flatness factor obtains values less than 3 in the area where the skewness factor equals 0. Naturally, at either side of this point, there are two other neighbouring points at which the flatness factor obtains the value of 3 and the skewness factor is positive or negative, respectively. The above described area defines the boundaries between two regions with distinctively different characteristics: the near wall region in which $S > 0$ and $T > 3$ and the outer boundary layer region in which $S<0$ and $T > 3$.

5.3 REPRESENTATION OF THE MEASURED QUANTITIES IN A DIMENSIONLESS SPACE DOMAIN

5.3.1 Introduction

In the light of the various points raised in the previous discussion, the full set of data obtained for the three test cases involved could be examined in a Re_x-y^+ plane The results obtained for the three test cases considered are presented in figures 5.23, 5.24 and 5.25, respectively. Before attempting the forgoing examination, the significance of the Re_x-y^+ plane will be discussed in brief.

The description of the laminar boundary layer has been achieved with remarkable success using the Blasius parameter $y / Re_x^{½}$ or simple non-dimensional parameters of the form u/U and y/δ. In 1956, Clauser discussed possible ways of representing the turbulent boundary layer in a non-dimensional form. It became apparent, that profiles of turbulent boundary layers, having different values of Reynolds numbers and other dynamic characteristics but the same skin friction coefficient, c_f, will have identical non-dimensional velocity profiles. The effect of the skin friction coefficient (non-dimensional shear stress) $c_f = \tau_w / ½\rho U_\infty^2$, is usually taken into account using the, so called, friction velocity $u^* = (\tau_w/\rho)^{½}$. Consequently, the dimensionless form of the important parameters of the boundary layer is obtained using the friction velocity. The dimensionless crosswise distance in wall units, obtains the form: $y^+ = y\, u^* / \nu$. By the same token, the boundary layer velocity (instantaneous or mean) obtains the following non-dimensional form: $u^+ = \overline{u} / u^*$ (see also Appendix C).

In the laminar sublayer where the shear stress can be assumed to be constant across its width, the linear relationship $u^+ = y^+$ holds true. Clauser suggested that apart from the viscous sublayer, the profiles of the turbulent boundary layer can be approximated by the following equation: $u^+ = 5.6 \log y^+ + 4.9$. This logarithmic law has

been widely used in the past as a reference for the necessary comparisons with experimentally obtained profiles in the transitional region.

In figure 5.26, the universal velocity distribution for turbulent layers near smooth walls has been reproduced after Clauser (1954). The above described figures summarise the Clauser type of plots for each test case considered in this study. In these plots, the streamwise variation of the studied parameters have been taken in to account using the Reynolds number based on the streamwise distance, Re_x. Accordingly, a two dimensional representation of the flow field has been used on a Re_x - y^+ plane, in order to improve the understanding of the distribution of the turbulently moving fluid in the boundary layer throughout the transitional region. The two dimensional contour plots presented here, contain a lot of concentrated information which should be looked at very carefully.

5.3.2 Distribution of the Dimensionless Velocity u^+

Very interesting information about the transition process can be extracted from the contour plots of the non-dimensional velocity u^+ in this frame of reference. The present discussion concerns the results obtained for all three test cases considered here. In the laminar regime (low Re_x), the non-dimensional velocity profiles of constant Re_x are similar to each other. These profiles are dominated by parallel contour lines corresponding to the linear behaviour ($u^+ = y^+$) of the laminar boundary layer (see also fig. 5.26). This behaviour changes gradually in the region of the outer boundary layer where the profile tends to its free stream value. In the transitional region, drastic changes in the profiles of constant Re_x can be observed. The rapid changes that take place in the transitional regime, are followed by a restabilisation in the profiles of u^+. In this area, the profiles of constant Re_x become similar to each other again. In this case, the profiles represent the turbulent regime, obtaining a shape similar to the one presented in figure 5.26.

As the laminar boundary layer develops, the free stream value of the non-dimensional velocity u^+ is gradually increased. Taking into account the fact that the mean velocity in the free stream remains practically constant, this behaviour can be attributed to the gradual decrease in the wall shear stress which is reflected to the value of the friction velocity u^*. Immediately after the peak in the free stream values of u^+, dramatic changes happen to the distribution of u^+ in the outer boundary layer. The non-dimensional velocity, u^+, decreases drastically, as the boundary layer undergoes transition. Finally, the decrease in the free stream values comes to an end at the end of transition when the dimensionless free stream velocity reaches its turbulent values. The inner boundary layer, though, retains its laminar characteristics throughout the transitional and turbulent regimes. For values of y^+ less than about 11 which correspond roughly to the region of the viscous sublayer and some of the buffer layer, the contour lines remain parallel to each other.

5.3.3 Distribution of the Turbulence Intensity

Equally interesting phenomena can be observed in the contour plots of the turbulence intensity in the Re_x-y^+ plane. The distribution of the turbulence intensity could be used to monitor the principal characteristics of the transition process. The turbulence intensity is showing a peak, in the near wall area, throughout the measurement region. In the region that precedes the transitional zone, the peak level of turbulence intensity (for constant Re_x profiles) occurs for increasing y^+, as the laminar boundary develops. This behaviour could be partially attributed to the drastic changes in the values of the wall shear stress in this area.

The highest peak is found to occur in the middle of the transitional regime (intermittent signals) where turbulence intensity reaches values as high as 13% to 15%. This value does not seem to be very sensitive to the level of the free stream turbulence. It is interesting to observe that after the dramatic changes in the transition region, the turbulence intensity peak occurs for gradually diminishing values of y^+. The location of this peak in the turbulence intensity values seems to be quite consistently between y^+ =

17.5 (for the early stations) and y^+ =10 (for the later stations) for all the test cases considered (see also figures 5.23, 5.24 and 5.25). A core of increased turbulence activity that appears in the foregoing plots, signifies the mid-transition area. Another interesting observation is that the turbulence intensity obtains its maximum values in the area where the contribution of the "switching" effect vanishes, as discussed in the following section of this chapter.

In the turbulent regime (higher values of Re_x), the turbulence intensity profiles (for constant Re_x) are similar to each other. Up to about y^+=10, the turbulence intensity values rise to the peak value. From the region of the peak onwards, the value of the turbulence intensity is falling at a large rate. Finally, there is a marked change in the rate of decrease at around y^+=100. In the outer region, the turbulent boundary layer continues developing under the influence of the free stream turbulence. It should be noticed that the rate of falling in the outer boundary layer is similar throughout the zone of transition.

5.3.4 Distribution of the Skewness and Flatness Factors

The skewness and flatness factors of the probability density distribution of the velocity signal behave very similarly when plotted on the Re_x-y^+ plane. In general, it could be said that values of the skewness and flatness factor different from the values corresponding to a normally distributed signal, can be interpreted a sign of the occurrence of turbulent spikes. These results, treated carefully, can also provide a measure of the number and the intensity of the turbulent spots crossing the measurement point. Figures 5.23 and 5.24 illustrate in a more pictorial way the skewness and flatness factor distribution on a Re_x - y^+ plane.

Using this representation of the flow field, it can be observed that there are two core regions of increased switching activity. The above plots show that there are two areas where the skewness and flatness factor obtain local maxima (peak) or local minima, in the case of skewness factor (trough), one at the inner and the other at the

outer boundary layer. Both inner and outer regions of interest are considered to be under the intense influence of the switching between the turbulent and the non-turbulent portions of the intermittent signal. The first core appears to be adjacent to the wall ($0 < y^+ < 10$) corresponding to the near wall behaviour of the skewness and flatness factors. The second core corresponds to the outer boundary layer characteristics and it is located at around $30 < y^+ < 100$.

These areas signify strong departures of the probability distribution of the velocity signal from the normal distribution that occurs due to the gradual development of turbulent spots. The outer zone is associated with the turbulence energy that is fed to the boundary layer from the free stream resulting in negative values of the skewness factor. On the contrary, the inner zone is more concentrated and can be associated with near wall turbulence. These two zones are strongly correlated. In contrast to the turbulence intensity, the peaks in the skewness and flatness factors occur closer to the start of transition. This is expected because at the start of transition, the mean velocity and the standard deviation of the velocity fluctuations in the laminar part of the intermittent signal are significantly different to the equivalent quantities of the turbulent portion.

It should also be noted that in the region between the two cores, the turbulence intensity obtains its peak values. This behaviour could be attributed to the fact that in this region both laminar and turbulent sections of the intermittent signal have the same mean value, and accordingly, the estimate of the mean value and standard deviation of the overall signal is free from the additional effect of the switching between the turbulent and the non-turbulent portions of the intermittent signal. Careful observation of the two distributions reveals that there is a point in the initial stages of transition at around $y^+=12.5$, where both skewness and flatness factors obtain values corresponding to the normal distribution. This point coincides with the beginning of the two core regions in the streamwise direction. Finally, it is interesting to note that the locus of the maxima in the turbulence intensity profiles, coincides with the zero skewness factor contour line.

5.4 INTEGRAL QUANTITIES OF THE FLOW FIELD

5.4.1 Introduction

In the previous sections of this chapter, the detailed profiles of the various parameters have been closely examined. This section, on the other hand, discusses the streamwise distribution of the integral quantities of the flow field. The term integral quantities of the flow field is used here to describe quantities such as boundary layer thicknesses as well as non-dimensional parameters of the flow field including the shape factors, the skin friction coefficient and the momentum thickness Reynolds number. Most of the above quantities have been obtained by applying an integration procedure on the detailed velocity profiles, following the theoretical considerations presented in chapter 3. The significance of the streamwise distribution of the above described quantities lies in their remarkably different behaviour in laminar and turbulent boundary layers. Accordingly, an investigation of their streamwise distribution can help the assessment of the transition start, end and length.

5.4.2 Integral quantities of the flow field

A short discussion of the obtained results in both a dimensional and a non-dimensional domain is presented here. The development of the boundary layer from laminar to turbulent on a dimensional frame, can be followed using the distribution of the thickness of the boundary layer. Apart from the boundary layer thickness, δ, that has been obtained using the detailed velocity profiles presented in the previous sections of this chapter, the displacement thickness, δ^*, the momentum thickness, θ, and the energy dissipation thickness, δ_3, have been considered. These results have been plotted in figures 5.27 to 5.30 for the first test case (U_∞ = 5 m/s, Tu_∞ = 4%), in figures 5.35 to 5.38 for the second test case (U_∞ = 15 m/s, Tu_∞ = 4%) and in figures 5.43 to 5.46 for the last test case (U_∞ = 15 m/s, Tu_∞ = 1.8%). Similarly, the boundary development can be studied using the shape factors, H_{12} and H_{23}, of the boundary layer as well as the skin

friction coefficient, c_f, and the momentum thickness Reynolds number Re_θ plotted against the dimensionless streamwise distance in the form of Re_x. The obtained results in this framework, for the three test cases considered in the course of this study are presented in figures 5.31 to 5.34, 5.39 to 5.42 and 5.47 to 5.50, respectively.

	Laminar Boundary Layer	Turbulent Boundary Layer
Boundary Layer Thickness	$\delta = 5\ x\ Re_x^{-\frac{1}{2}}$	$\delta = 0.37\ x\ Re_x^{-\frac{1}{5}}$
Boundary Layer Displacement Thickness	$\delta^* = 1.721\ x\ Re_x^{-\frac{1}{2}}$	$\delta^* = 0.046\ x\ Re_x^{-\frac{1}{5}}$
Boundary Layer Momentum Thickness	$\theta = 0.664\ x\ Re_x^{-\frac{1}{2}}$	$\theta = 0.036\ x\ Re_x^{-\frac{1}{5}}$
Boundary Layer Energy Thickness	$\delta_3 = 1.043\ x\ Re_x^{-\frac{1}{2}}$	$\delta_3 = 0.065\ x\ Re_x^{-\frac{1}{5}}$
Boundary Layer Shape Factor H_{12}	$H_{12} = 2.59$	$H_{12} = 1.286$
Boundary Layer Shape Factor H_{23}	$H_{23} = 0.6365$	$H_{23} = \frac{5}{9}$
Skin Friction Coefficient	$c_f = 0.664\ Re_x^{-\frac{1}{2}}$	$c_f = 0.0592\ Re_x^{-\frac{1}{5}}$
Momentum Thickness Reynolds Number	$Re_\theta = 0.664\ Re_x^{\frac{1}{2}}$	$Re_\theta = 0.036\ Re_x^{\frac{4}{5}}$

Table 5.1 : Theoretically Derived Correlations for the Behaviour of the Integral Quantities in Laminar and Turbulent Boundary Layers

In order to assist the examination of the present results in the above framework, laminar and turbulent correlations have been plotted together with the experimental results. The forgoing correlations have been primarily derived from the theoretical considerations presented by Schlichting (1979). The correlations used in this study concerning all the quantities considered, for both laminar and turbulent boundary layers, are summarised in table 5.1. It should be noted that the turbulent correlations have been calculated as if a turbulent boundary layer had started from the leading edge of the flat plate. This leads to an over-prediction of the values corresponding to the turbulent boundary layer. Accordingly, the plotted turbulent correlations are used to indicate the trends more than the absolute values expected in the turbulent flow regime.

The distribution of the boundary layer thicknesses in all of the test cases under consideration followed the laminar correlations in the beginning. Once the transition process is started the measured boundary layer thicknesses start to divert slightly from the laminar correlations and after a finite transition length they start following the theoretical predictions concerning the turbulent boundary layer. This form of presentation of the results helps to obtain a better understanding of the physical lengths involved in the transition process. Alternatively, the dimensionless representation of the streamwise distribution of the obtained results, can facilitate inter-comparisons with existing transition data. In this format they could also be used for comparisons with existing transition correlations as well as for the development of new correlations that would incorporate the present findings.

For the test cases that involved a reference turbulence intensity of 4% the momentum thickness Reynolds number at the start of transition $Re_{\theta\,ST}$ is lying between 150 and 200, depending on the free stream conditions at the start of transition. The Reynolds number at the end of transition $Re_{\theta\,ET}$ is lying between 375 and 400. Similarly, for the test case with 1.8% reference turbulence intensity the corresponding values are $Re_{\theta\,ST} = 360$ and $Re_{\theta\,ET} = 600$. Finally, an overall assessment of the results including the present findings will be presented later in this chapter.

5.5 BOUNDARY LAYER SPECTRA

5.5.1 Introduction

In the previous sections of this chapter, the distribution of the mean square of the velocity fluctuations in the streamwise and crosswise directions has been examined in detail. This section, on the contrary, deals with the analysis of the obtained results in the frequency and wave number domain. As discussed previously in this chapter, the square of the velocity fluctuations has dimensions of energy per unit mass { m^2 / s^2 } and can be regarded as a measure of the kinetic energy of turbulence contained in the range of vortices that appear in a viscous flow field. The distribution of those fluctuations over different frequencies is usually referred to as the power (energy) spectrum of turbulence (see also Bradshaw, 1971 and Hinze, 1975). Since only the streamwise velocity component has been recorded in the present study, the turbulence kinetic energy estimation is based on the streamwise velocity fluctuations, resulting in an one dimensional power spectrum. It is useful to recall at this point, that both natural transition occurs as a result of the amplification of the unstable Tollmien-Schlichting waves and bypass transition occurs through the perturbation of the laminar boundary layer generated by large finite non-linear disturbances. Therefore, close examination of the boundary layer spectra could assist the determination of the way that free stream disturbances are transmitted into the boundary layer.

The contribution of the square of the velocity fluctuations within each frequency bandwidth to the overall variance of the fluctuating signal is defined as the power spectral density $\phi(\omega)$. Accordingly, the frequency spectrum has the following property:

$$\overline{u'^2} = \int_0^\infty \phi(\omega)\, d\omega \qquad (5.8)$$

Using the Fourier transformation it can be shown that there is a simple connection between the power spectral density $\phi(\omega)$ and the autocorrelation coefficient $R(\tau)$:

$$R(\tau) = \int_0^\infty \phi(\omega) \cos(\omega\tau)\, d\omega \tag{5.9}$$

and

$$\phi(\omega) = \frac{2}{\pi} \int_0^\infty R(\tau) \cos(\omega\tau)\, d\tau \tag{5.10}$$

Additionally, the normalised power spectral density, E(f), can be expressed as follows:

$$E(f) = \phi(\omega)\, 2\pi\, \overline{u'^2} \tag{5.11}$$

Using Taylor's hypothesis (eqs. 2.7 and 2.8) we can define the wave number as follows:

$$k = \frac{\omega}{U} = \frac{2\pi f}{U} \tag{5.12}$$

and correspondingly, the power spectral density in the wave number domain can be expressed as:

$$\phi(k) = U\, \phi(\omega) \tag{5.13}$$

Finally, it should be noted that the longitudinal integral length scale can be obtained by evaluating the value of the power spectral density as frequency approaches zero:

$$L = \frac{U}{4\, \overline{u'^2}} E_0 \tag{5.14}$$

5.5.2 Results and Discussion

The forgoing formulation has been used in order to obtain turbulence spectra of the boundary layer in the frequency and wave number domain from the high speed record of the velocity fluctuations. The obtained turbulence spectra, have been plotted in a non-dimensional form both in the frequency and wave number domain. The frequency spectra have been made dimensionless using the overall average of the power spectral density and have been plotted against frequency, f, in Hz. On the wave number

domain, the power spectral density bas been non-dimensionalised using the value of the power spectral density at zero, E_0. By the same token, the wave number k has been non-dimensionalised using the boundary layer thickness, δ.

Frequency spectra have been acquired at each station for the full range of test cases involved. Two crosswise locations have been selected for turbulence spectra acquisition. A near wall location at y = 0.2 mm that corresponds to the inner boundary layer and another one at y = 1 mm which corresponds to the outer boundary layer. Accordingly, the power spectra for each individual test case, are presented for decreasing values of y/δ. In figures 5.51 to 5.56 the frequency spectra at all the measurement stations have been plotted together on a 'carpet plot'. In order to increase the clarity of the presented results the values of the power spectral density have been shifted by a power of ten between the consecutive measurement locations. Accordingly, the value on the axis of the power spectral density refers only to the spectrum for the first streamwise location. The distributions of the power spectral density for the first test case (U_∞ = 5 m/s, Tu_∞ = 4%) are presented in figures 5.51 and 5.52 for the two crosswise locations, respectively. Results for the second test case (U_∞ = 15 m/s, Tu_∞ = 4%) are presented in figures 5.53 and 5.54 and for the last test case (U_∞ = 15 m/s, Tu_∞ = 1.8%) in figures 5.55, 5.56. Two lines with -5/3 slope between power spectral density and the wave number have been plotted at the top and bottom corners of each 'carpet' plot. This slope corresponds to the decaying range of eddies and it is used here as a reference in order to facilitate comparisons.

In the frequency domain, it can be observed that in the initial stages of transition, the power spectral density is increased across the spectrum. This increase is more marked in the low frequency range. As transition progresses, the power spectral density reaches a maximum and then it decreases again when the boundary layer becomes fully turbulent. A similar development pattern has been described in an earlier section of this chapter with respect to the behaviour of the turbulence intensity. Therefore, it can be concluded that the increase in the overall turbulence intensity is reflected more at the

lower frequency range which seems to be more sensitive to the changes that occur during transition.

At this point, it is interesting to investigate how various disturbances inherent to the wind tunnel configuration have been reflected on the frequency spectrum. As discussed in chapter two in more detail, it has been observed that the hot-wire probe support has a resonant frequency at around 140 Hz. Additionally, the Strouhal frequencies corresponding to the turbulence generating grid geometry and the free stream velocity range, are 100 Hz, 300 Hz and 3333 Hz for the three test cases considered here, respectively (see also Blevins, 1977). From the power spectra obtained in the boundary layer of the flat plate, there is no evidence that any of the aforementioned frequencies plays an important role in the development of the boundary layer.

The work of previous investigators such as Elder (1960) and Suder et al. (1988), suggests that there is a critical value of the peak in turbulence intensity in the boundary layer above which the turbulence bursting begins. It has been found that this level ranges between 2% and 3.5% in boundary layer studies that involved a lower free stream turbulence value than the present investigation. The first and second test cases involved a quite high free stream turbulence intensity level (Tu = 4%) and as a result the turbulence bursting is initiated from the quite early measurement stations.

The power spectra at the initial measurement stations for the first test case show an increased turbulent activity at certain frequencies in the range of 600 Hz to 1200 Hz. The forgoing peaks in the power spectral density are covered by the increase in the turbulence kinetic energy as the boundary layer develops. The highest peak, though, that is observed at around 900 Hz appears consistently throughout the transition region, but it does not seem to be amplified. In general, it appears that in the process of transition there is a turbulence kinetic energy transfer from the low to the high frequency range. The turbulence spectra acquired for the third test case, indicate a more obvious distinction between the low and high frequency range, that smooths out as the boundary layer becomes more turbulent. At the latter stages of transition, a larger proportion of

the boundary layer spectra seems to follow the -5/3 slope that is representative of vortices in the decaying range of frequencies.

5.6 THE INTERMITTENCY DISTRIBUTION

5.6.1 Introduction

The time averaged quantities of the flow field discussed in the previous sections of this chapter, have been obtained using the intermittent signal as a whole. The values of these quantities can be considered to represent the mean level of turbulent activity at any particular measurement point. In general, it would be very interesting to quantify the contributions of the turbulent and non-turbulent portions of the intermittent signal to the above described time averaged quantities. Furthermore, this procedure could facilitate the conditional analysis of the obtained results. The implementation of the concept of intermittency, as discussed earlier in this chapter, is instrumental to the achievement of this goal.

In recent years, the introduction of fast electronic data acquisition systems brought about the demand for the development of determination procedures for the turbulent intermittency based on long high speed records of the velocity field. A variety of intermittency determination procedures has been applied by previous investigators. A great deal of these procedures have been based on the idea that both turbulent and non-turbulent velocity fluctuations in the intermittent signal are distributed normally with similar mean values and standard deviations that differ significantly between each other. The effect of this property of the intermittent signal on the cumulative probability distribution of the velocity fluctuations has often been employed in order to assist the turbulent/non-turbulent decisions.

Hedley and Keffer (1974) attempted to generalise the experimental method for turbulent/non-turbulent decisions in intermittent flows. They also summarised the existing methods of sensitising the intermittent velocity signal in order to achieve the separation of the turbulent from the non-turbulent portions. Arnal, Juillen and coworkers presented their intermittency study of transitional boundary layers in a series of

publications in the late 70s (e.g. Arnal and Juillen, 1977c), using a similar method to the one presented by Hedley and Keffer. More recently, Fasihfar and Johnson (1992) presented a boundary layer transition study using another intermittency measurement technique. Their intermittency algorithm attempted to use more of the physics and some spectral characteristics of the intermittent motion in order to achieve an effective discrimination between the turbulent and non-turbulent flow regimes. Finally, Hazarika and Hirsch (1993) presented a study of boundary layer transition on a flat plate with sharp leading edge using a similar digital technique for the determination of the intermittency factor.

At this point, it is interesting to recall that the intermittency factor varies significantly in the crosswise direction as well as in the streamwise direction. The streamwise intermittency distribution follows the exponential law represented by equation 1.5. In the crosswise direction, the turbulent intermittency retains a nearly constant value in the region between the wall and approximately 20% of the boundary layer thickness (near wall intermittency, γ_o). From that point onwards, the dimensionless factor γ/γ_o has been found to decrease in a way similar to the normal distribution, tending asymptotically to zero in the free stream area (see also Mayle, 1991). Accordingly, the intermittency factor is always regarded as a function of both x and y, although the main objective of this study is to determine the streamwise distribution of the near wall intermittency.

5.6.2 Determination of the Intermittency Function

In this section of the thesis, the theoretical considerations involved in the process of separation of the turbulent from the non-turbulent portion of the signal, are discussed. Furthermore, the numerical treatment applied to the velocity signal obtained from the hot-wire arrangement is presented. The data acquisition system employed in this study, permitted the generation of long and high speed records of the velocity in the boundary layer flow. At each particular measurement point, the intermittency factor has been obtained as a result of a discrimination procedure between the turbulent and non-

turbulent portions of the signal. A detailed account of the above procedure including a step by step description of the signal processing, is given in the following paragraphs.

First of all, the velocity signal, u(t), has been obtained by applying the transfer functions of the signal conditioner and King's law onto the digital signal record of the data acquisition system output voltage, E(t). The next step has been to obtain a detector function, D(t), suitable for deciding whether the signal is turbulent or not. Finally, using a selection procedure based on the choice of a suitable threshold, C, the temporal variation of the intermittency function, I(t), has been obtained. In simple terms, the intermittency function, I(t), is obtained by applying the following principal on the detector function D(t):

$$I(t) = 1 \quad for \quad D(t) \geq C \quad and \quad I(t) = 0 \quad for \quad D(t) < C \qquad (5.15)$$

Various formulations for the detector function have been used by previous investigators. The choice of the most appropriate detector function D(t) has been discussed in detail by Hedley and Keffer (1974). Since the primary signal u(t) is quite often difficult to exploit, the detector function D(t) is usually based on the temporal derivatives of the velocity signal. The effect of the differentiation of the signal in the time domain is to emphasise the differences between the turbulent and the non-turbulent portions of the signal. Likewise, the detector function incorporates the effect of the large differences between the turbulent and non-turbulent velocity fluctuations, in the frequency domain. In this particular study, the detector function has been based on the second time derivative of the velocity signal. Practically, the second time derivative has been calculated using the following discretised formulation:

$$\frac{\partial^2 u}{\partial t^2}\Big|_i = \frac{u_{i-1} - 2\,u_i + u_{i+1}}{\Delta t^2} \qquad (5.16)$$

where Δt is constant with a value of 0.1 ms (sampling frequency 10 KHz) and i obtains values from 1 to 180000 (sampling time t = 18 s).

It is expected that similarly to the velocity signal itself, the second derivative of the signal follows the normal distribution in totally turbulent or non-turbulent flow

regimes. Furthermore, it can be proved that if a stochastic variable u follows the normal distribution, the normalised variable $\frac{1}{2}\left(\frac{u-\bar{u}}{\sqrt{\overline{(u-\bar{u})^2}}}\right)^2$ follows the Gamma probability distribution with parameter $\kappa = 1/2$ (see also Meyer, 1970 and Psoinos, 1985). It should be noted here, that the probability density function of the Gamma distribution with parameter κ is given by the following expression:

$$\phi(u) = \frac{e^{-u}\, u^{\kappa-1}}{\Gamma(\kappa)} \qquad for \qquad u>0 \qquad (5.17)$$

$$\phi(u) = 0 \qquad for \qquad u\leq 0$$

where the function $\Gamma(\kappa)$ of the parameter is given by the following expression:

$$\Gamma(\kappa) = \int_0^\infty e^{-u}\, u^{\kappa-1}\, du \qquad (5.18)$$

The value of the mean and the standard deviation of Gamma distribution equals the value of the parameter κ.

In order to obtain an appropriate frame of reference, the detector function used in this study has been expressed in the following manner:

$$D(t) = \frac{1}{2}\left(\frac{\ddot{u} - \bar{\ddot{u}}}{\sqrt{\overline{(\ddot{u}-\bar{\ddot{u}})^2}}}\right)^2 \qquad (5.18)$$

where, ü, represents the second time derivative of the velocity signal with respect to time. The detector function in the above form is obviously a positive quantity. The effect of the squaring is mainly to accentuate the high frequency range of velocity fluctuations and hence, to emphasise the differences in the detector function amplitude between the turbulent and non-turbulent portions of the signal.

A rather simplistic but quite illustrative explanation of the latter can be given by considering that the elementary velocity fluctuations in both turbulent and non-turbulent flow regimes can be described as follows:

$$u_{i_T} = \overline{u_{i_T}} + A_{i_T} \sin(\omega_{i_T} t) \quad and \quad u_{i_L} = \overline{u_{i_L}} + A_{i_L} \sin(\omega_{i_L} t) \qquad (5.19)$$

where, u_i, is used to describe the velocity of an elementary flow regime which fluctuates sinusoidally with amplitude A_i and circular frequency ω_i. The squared second

derivative of the above expressions obtains the following form:

$$\ddot{u}_{i}^{2}{}_{T} = \left(-A_{i_T}\,\omega_{i}^{2}{}_{T}\,\sin(\omega_{i_T} t)\right)^2 \quad \textit{and} \quad \ddot{u}_{i}^{2}{}_{L} = \left(-A_{i_L}\,\omega_{i}^{2}{}_{L}\,\sin(\omega_{i_L} t)\right)^2 \quad (5.20)$$

The amplitude ratio of the squared second derivatives, $\left(\frac{A_{i_T}}{A_{i_L}}\right)^2 \left(\frac{\omega_{i_T}}{\omega_{i_L}}\right)^4$, is a function of the square of the amplitude ratio and the forth power of the circular frequency ratio. Although, the difference in amplitude between the turbulent and the non-turbulent portions of the signal is not very large, the difference in frequencies encountered in the two portions of the signal are in general quite considerable. Accordingly, the detector function in the above form, can facilitate the distinction between the turbulent and the non-turbulent portions of the fluctuating signal.

Unfortunately, it is possible that the detector function expressed in the forgoing form, obtains in the turbulent regions, values smaller than the values encountered in the non-turbulent regions. In order to overcome this difficulty, the detector function signal has been smoothed over a period of 0.5 ms. The physical implication of the smoothing is that any portion of the signal obtaining values in the non-turbulent range, is classified as turbulent in case that the residence time within this range is quite small.

As mentioned earlier, a final step towards the separation of the turbulent from the non-turbulent portions of the intermittent signal is taken by applying a threshold, C, on the detector function D(t). The value of the appropriate threshold level at each measurement station has been obtained by cross examination of the development of the original velocity signal, u(t), the second derivative signal, ü(t) and the detector function, D(t) along with the normalised probability distribution of the second derivative and the cumulative probability distributions of the second derivative and the detector function.

5.6.3 Results and Discussion

The above described procedure has been applied to the full range of data obtained for the three test cases considered in this study. Four measurement stations

from the third test case (U_∞ = 15 m/s, Tu_∞ = 1.8%), have been selected for the analytical presentation of the separation procedure. They correspond to early, middle and late stages of transition. It should be noted that the normalised form of the stochastic variables is always used in the graphical representation of the signal processing, in order to increase the clarity and facilitate inter-comparisons between the data at various measurement stations and under different free stream conditions. The subscript 'n' is used to notify that the parameter in consideration has been normalised. Also, the subscript 's' is used to indicated that the signal has been smoothed.

Figures 5.57 to 5.64 present in a graphical form, a detailed account of the results obtained at X = 250 mm, 300 mm, 400 mm and 550 mm. Figures 5.57, 5.59, 5.61 and 5.63 contain a 60 msec record of the velocity traces, u(t), as well as the smoothed signals of the second time derivative, ü(t), and the detector function, D(t). The parallel presentation of the traces obtained by the signal processing is used to demonstrate the various stages of the determination procedure of the intermittency function I(t).

It is interesting to observe, that the graphical representation of the signal processing could reveal important information about the duration and the morphology of the turbulent spots. The initial appearance of a turbulent spot (fig. 5.57) is accompanied by some low frequency oscillations in the vicinity of the spot. Also, the duration of the non-turbulent intervals could be judged and ultimately be used to estimate the spot production rates. Another interesting feature of the initial stages of transition (fig. 5.57, 5.59) is that within the portions of the signal which are classified as turbulent there is a finite number of smaller regions where the detector function obtains ultra-high values. This behaviour is gradually smoothed out as transition progresses with the merging of the various turbulent spots.

The probability density distributions of the sensitised velocity signals and the detector functions are presented in figures 5.58, 5.60, 5.62 and 5.64. These figures include the probability density distribution, $g(\ddot{u}_{sn})$ (top left) and the cumulative probability density distribution, $G(\ddot{u}_{sn})$, (top right) of the normalised second time

derivative, as well as the cumulative probability density distribution of the detector function, D(t), in a logarithmic (bottom left) and linear (bottom right) form. The dotted lines represent the values corresponding to a normally distributed signal. The function G(u) of a stochastic parameter, u, that is used here to describe the cumulative probability density distribution, is defined as: $\int_{C}^{\infty} g(u)\,du$. It should be noted though, that in strict statistical terms, the cumulative probability density distribution of a stochastic parameter, u, should be defined as 1-G(u).

The graphical representation of the probability density distributions has been used mainly to judge the appropriate level of the threshold, C. The criterion used for the selection of the appropriate threshold level, has been to minimise the erroneous selections due to the overlap of the turbulent and non-turbulent probability distributions. Also, in all of the above graphs, the range defined by the selected threshold has been marked with dashed lines.

A number of observations with respect to the probability density distributions, has been used in order to determine the appropriate level of the threshold, C. First of all, it can be observed that as soon as the transition process gets under way, the probability density distribution g(ü) shows a very intense concentration in a narrow band around the mean. The change in the behaviour of the velocity fluctuations is marked on the cumulative probability distribution G(ü), by the sudden drop that occurs around the mean value. Similarly, the cumulative probability density distribution of the normalised detector function shows a distinctive change in this region.

Finally, the distribution of the near wall intermittency across the length of the flat plate has been determined. The results obtained for the three test cases considered, are presented in figures 5.65 to 5.68, 5.69 to 5.72 and 5.73 to 5.76, respectively. The determination of the transition inception and completion which leads to the definition of the extent of the transition region is a quite complicated procedure. The most consistent technique has been proposed by Narasimha (1985) that ultimately leads to the

universal intermittency distribution (see also Gostelow et al., 1992). This technique involves plotting a logarithmic function of the intermittency, namely:

$$F(\gamma) = \sqrt{-\ln(1-\gamma)} \tag{5.21}$$

against the non-dimensional streamwise parameter in the transitional region defined as:

$$\eta = \frac{x - x_{ST}}{x_{ET} - x_{ST}} \tag{5.22}$$

It has been found that the function F(γ) varies linearly with η in the range of intermittency levels between 25% and 75%. The obtained results are used to calculate the best line fit in this area. The determination of the effective transition start according to the Narasimha procedure, is obtained by finding the value η_t of the dimensionless streamwise parameter at which the forgoing straight line intersects with the horizontal axis. Accordingly, the location of the transition onset, x_t, as well as the characteristic length scale of transition, $\lambda = x_{(\gamma=0.75)} - x_{(\gamma=0.25)}$, according to the Narasimha procedure, can be evaluated. The above described procedure has been presented in a graphical form in figures 5.65 and 5.66 for the first test case (U_∞ = 5 m/s, Tu_∞ = 4%), in figures 5.69 and 5.70 for the second test case (U_∞ = 15 m/s, Tu_∞ = 4%) and in figures 5.73 and 5.74 for the third test case (U_∞ = 15 m/s, Tu_∞ = 1.8%).

Using the characteristic length scale of transition, λ, a new dimensionless streamwise coordinate, ξ, can be defined as follows:

$$\xi = \frac{x - x_t}{\lambda} \tag{5.23}$$

The obtained results are presented in the physical plane as well as in a non-dimensional plane as a function of ξ for the three test cases in figures 5.67-5.68, 5.71-5.72 and 5.73-5.74, respectively. Narasimha proposed that the streamwise distribution of the intermittency factor can be expressed universally in the following form:

$$\gamma = 1 - e^{-0.412\,\xi^2} \tag{5.24}$$

A curve corresponding to the universal intermittency distribution has been plotted in dashed line, together with the experimental results in order to provide an appropriate frame of reference. It should be noted that the results obtained for the various test cases,

have been found to be in good agrement with Narasimha's universal intermittency distribution.

A cross inspection of the results obtained for the various test cases could reveal some interesting information about the effect of the free stream velocity and turbulence intensity on the transitional characteristics of the boundary layer. Before proceeding any further, it is useful to recall that the second test case has common free stream velocity with the first test case and common free stream turbulence intensity level with the third. Hence, the second test case is used as a reference for all comparisons made here. The obtained results suggest that an increase in either the free stream velocity or turbulence intensity result in an earlier start of transition and smaller transition lengths. Furthermore, it is interesting to observe that the end of transition in the first and third test cases, occurs at around the same streamwise location. The start of transition on the other hand, occurs earlier for the third test case. Although this result is rather coincidental, it should be noticed that a decrease in the free stream velocity from 15 m/s to 5 m/s resulted in a later start of transition, compared to the effect of the decrease in free stream turbulence intensity for 4% to 1.8%. In fact the relative change in the latter case is of the order of 50 mm. Since the start of transition in the second and third test cases occurs in the vicinity of the leading edge, the start of transition in this case should be considered to be under the influence of the pressure gradient. On the contrary, the start of transition in the first test case occurs more than 250 mm downstream of the leading edge where the influence of pressure gradient is minimal.

5.7 OVERALL ASSESSMENT OF THE RESULTS AND CONCLUSIONS

Experimental investigation of boundary layer transition has been carried out on a flat plate with C4 leading edge. Hot-wire anemometry has been used in order to obtain information about the transitional characteristics of the boundary layer. The effect that the free stream Reynolds number and turbulence intensity have on the process of transition has been studied. The free stream Reynolds number has been found to have a rather small effect on the non-dimensional characteristics of transition, probably by slightly altering the pressure distribution in the leading edge area of the flat plate. Increase in the free stream turbulence intensity results in an earlier onset of transition.

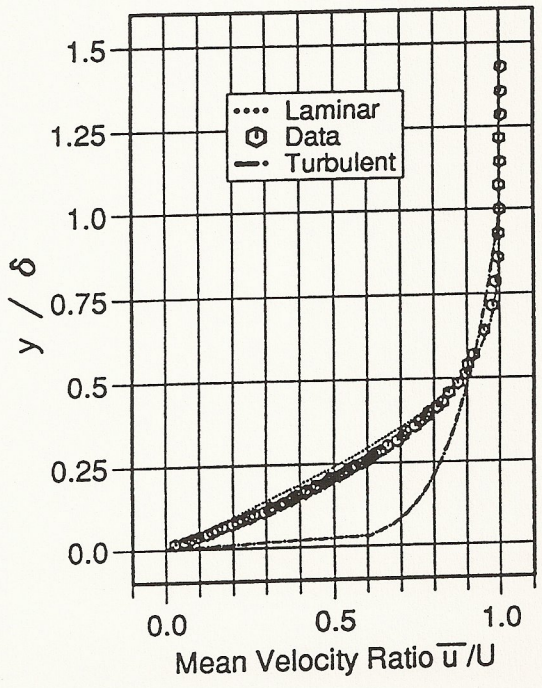
A global picture of the transitional characteristics of the boundary layer has been obtained by analysing the hot-wire results. The necessary tools for the analysis and graphical representation of the hot-wire signals have been developed. The data analysis involved several levels of refinement. Initially, the time averaged quantities of the flow field such as the mean velocity, turbulence intensity, the skewness factor and the flatness factor, have been examined in both physical and dimensionless space domains. Two dimensional contour plots of the non-dimensional parameters of the boundary layer on a Re_x-y^+ plane, provided better access to transitional data sets and improved the understanding of the flow patterns that precede and follow transition in the boundary layer. The integral measures of the boundary layer have been obtained for all of the three test cases considered. The obtained results have been Fourier analysed in order to examine the spectral characteristics of the boundary layer flow. Finally, a study of the intermittency distribution across the length of the flat plate has been presented.

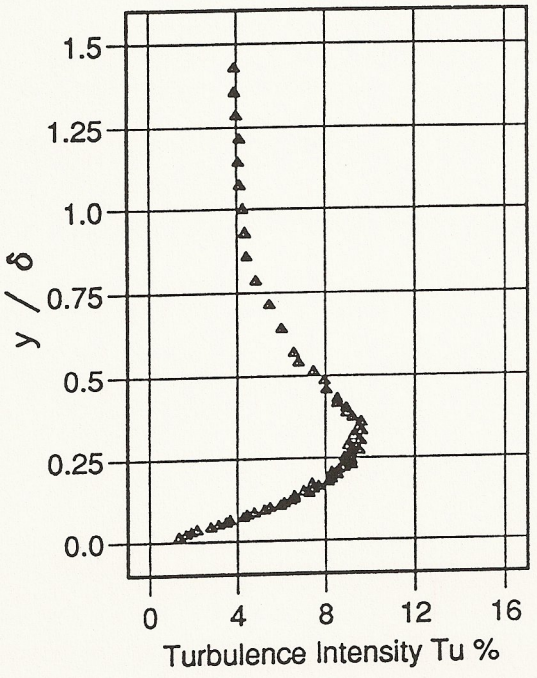
The present results have been examined in parallel with results existing in the literature, concerning transition over flat plates that in most cases have a sharp leading edge. A few attempts have been made by previous investigators to develop correlations between the critical Reynolds numbers for the start, end and length of transition (Re_θ

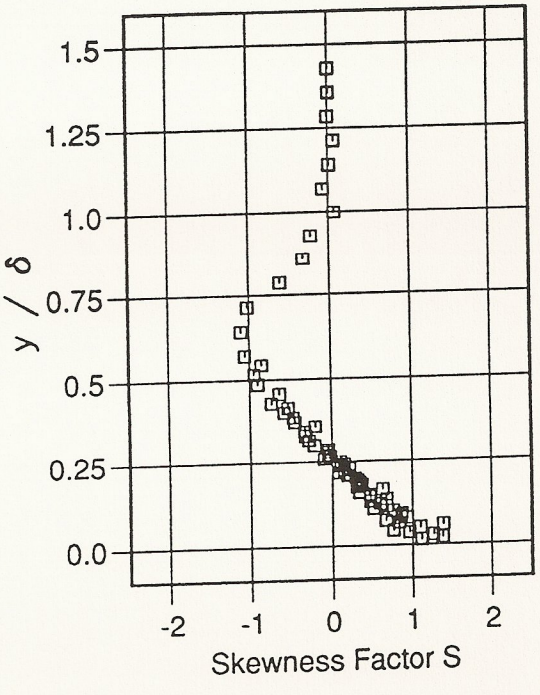
$_{ST}$, $Re_{\theta ET}$ and $Re_{x LT}$) and the overall turbulence intensity level and the pressure gradient parameter. Other flow parameters that have also been found to have a less important effect on the transition process. Mayle (1991) and Hourmouziadis (1969) proposed similar correlations between $Re_{\theta ST}$ and Tu_∞ for zero pressure gradient derived from a series of data produced by previous investigators, including Suder et al. (1988), Blair (1982) and Gostelow et al. (1988). Mayle's correlation predicts $Re_{\theta ST}$ (1.8%) = 277 and $Re_{\theta ST}$ (4%) = 168, although Hourmouziadis' correlation provides $Re_{\theta ST}$ (1.8%) = 312 and $Re_{\theta ST}$ (4%) = 186. Using the same original data sets Mayle [6] produced a correlation between $Re_{\theta ET}$ and $Re_{x LT}$. The effect of the pressure gradient parameter has been found by these authors to be more complicated especially when combined with the effect of free stream turbulence. The present data also suggest that the momentum thickness Reynolds numbers at the onset of transition obtain values in the range of 160 and 200 for large values of the free stream turbulence (Tu_∞ = 4%). The momentum thickness Reynolds number in the third test case (Tu_∞ = 1.8%) was found to be significantly higher obtaining a value around 330.

Considerable agreement of the present intermittency results to the predictions of the Narasimha method has been found. The estimation of transition start and length using the Narasimha procedure has been more accurate than the streamwise distribution of the integral parameters of the boundary layer. The main reason for this relates to the fact that the Narasimha method is based on well defined criteria for the inception of transition.

The present results have been found to be in good agreement with the work of previous investigators as well as the existing correlations for the boundary layer over a flat plate. The slight differences in the characteristics of the process of transition, with respect to the flat plate with other leading edge shapes, can be attributed to the gradual acceleration of the flow around the C4 leading edge (see also Kalfas and Elder, 1992). Finally, calculations with an inviscid-viscous method performed by Calvert (19y94), predicted that the location of transition on the plate with the C4 leading edge was expected to occur downstream of the leading edge area.







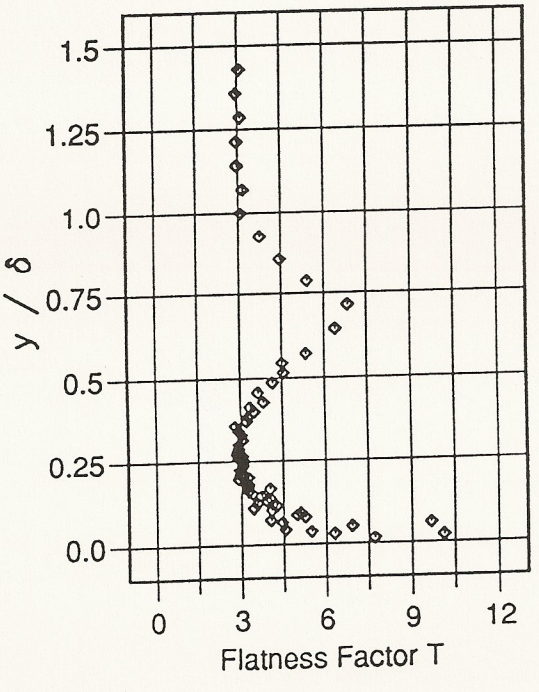


Figure 5.1	Profiles of the Integral Boundary Layer Quantities C4 Plate U_∞ = 5 m/s Tu_∞ = 4 % X = 100 mm

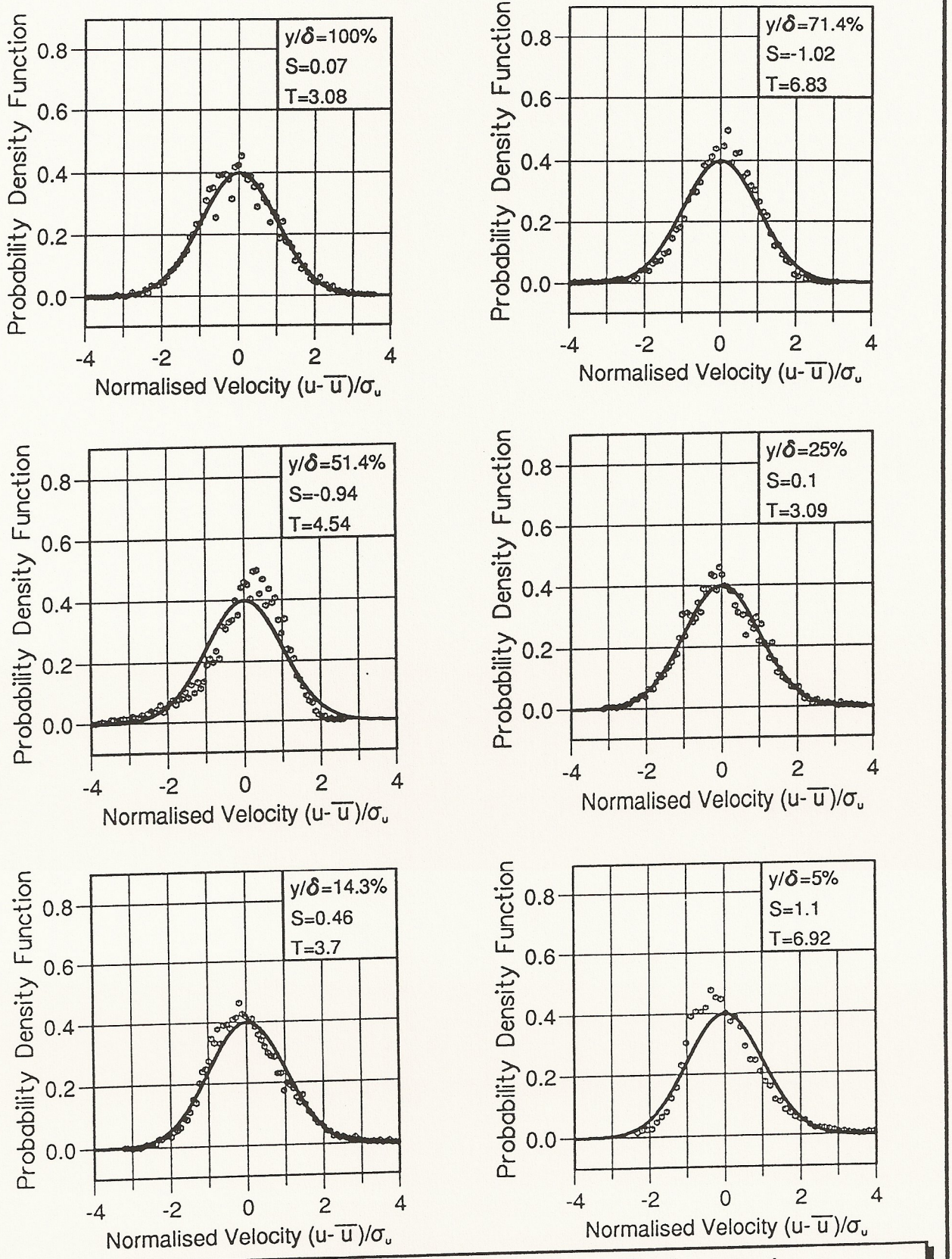
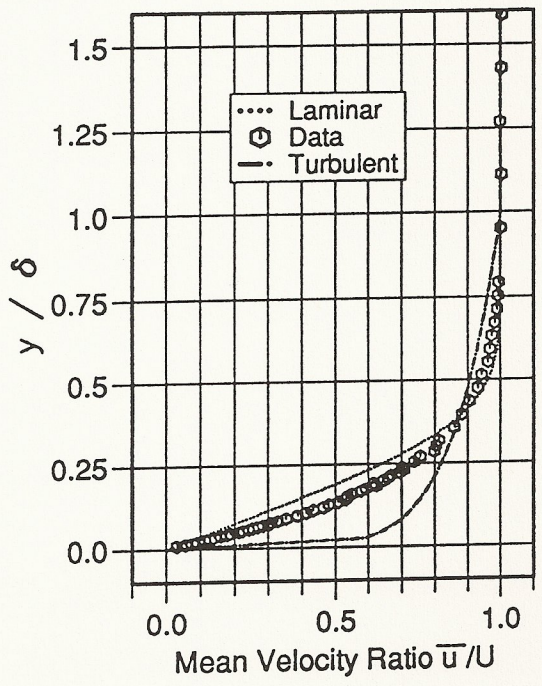
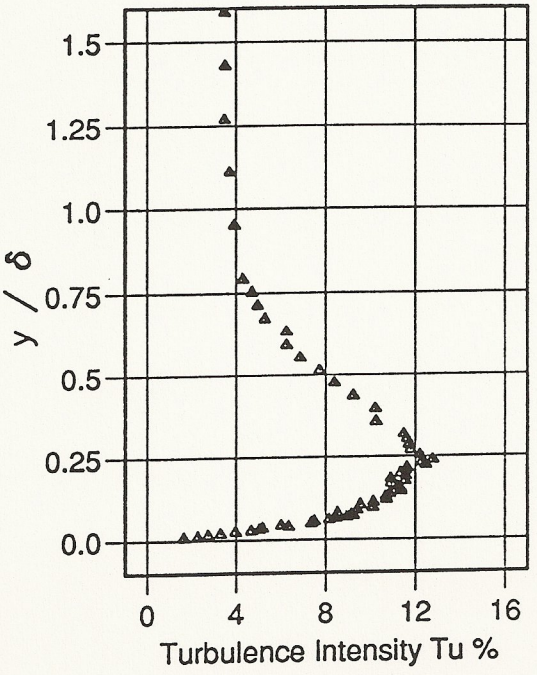
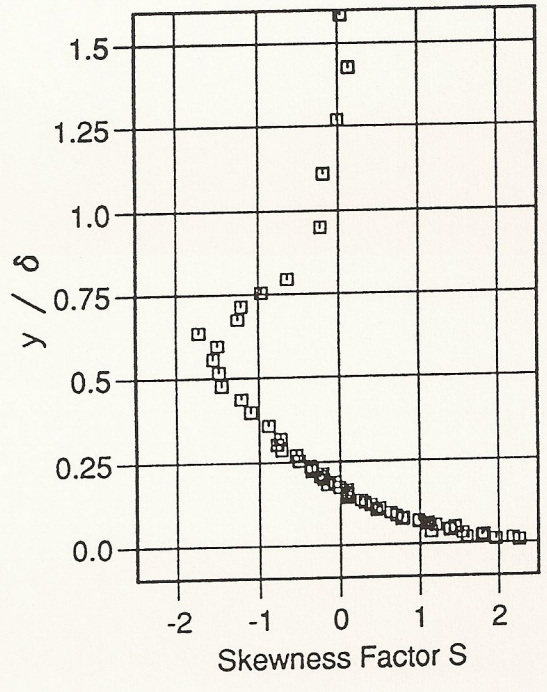


Figure 5.2 Probability Distributions of the Velocity in the Boundary Layer
C4 Plate $U_\infty = 5$ m/s $Tu_\infty = 4\%$ $X = 100$ mm







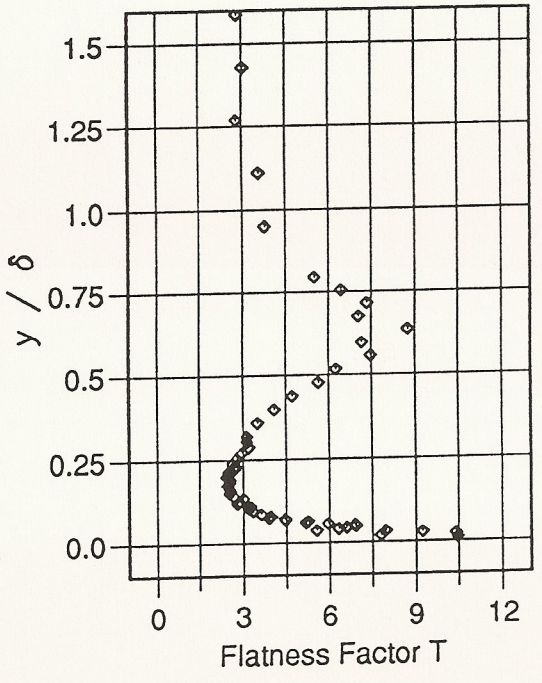


Figure 5.3	Profiles of the Integral Boundary Layer Quantities C4 Plate U_∞ = 5 m/s Tu_∞ = 4 % X = 200 mm

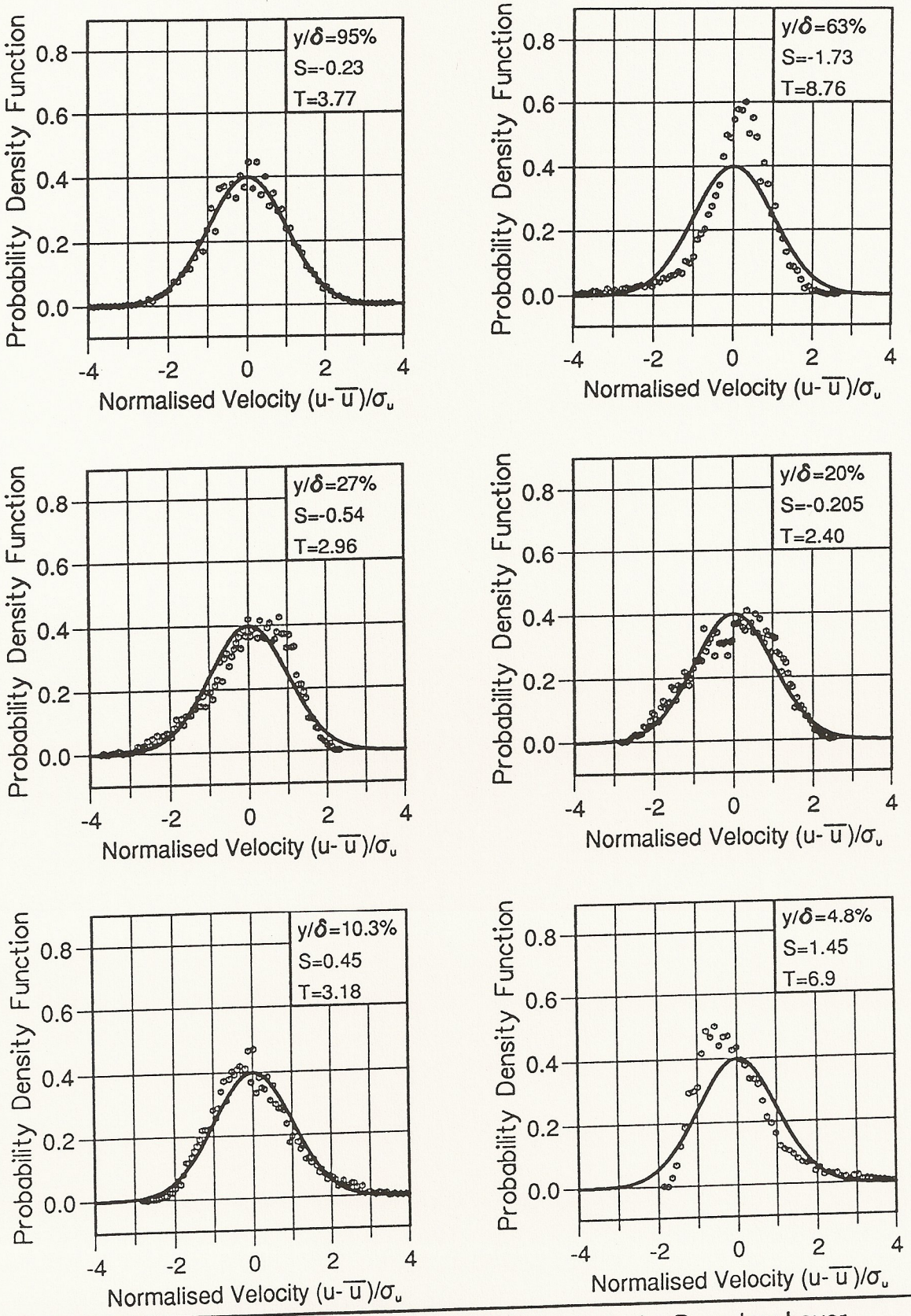
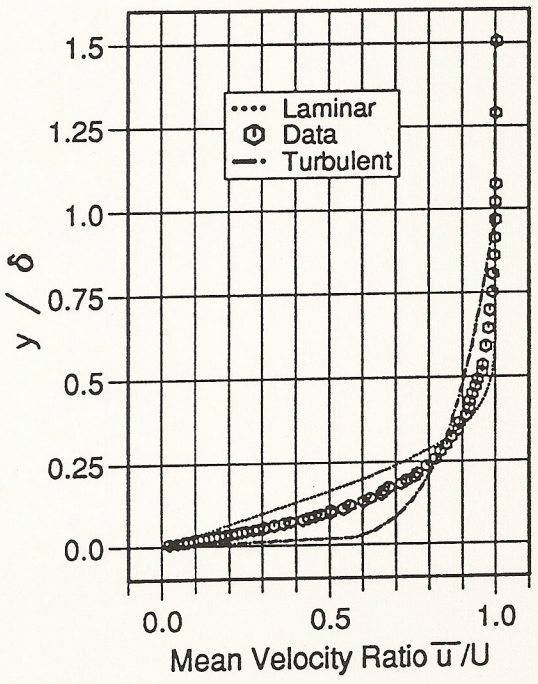
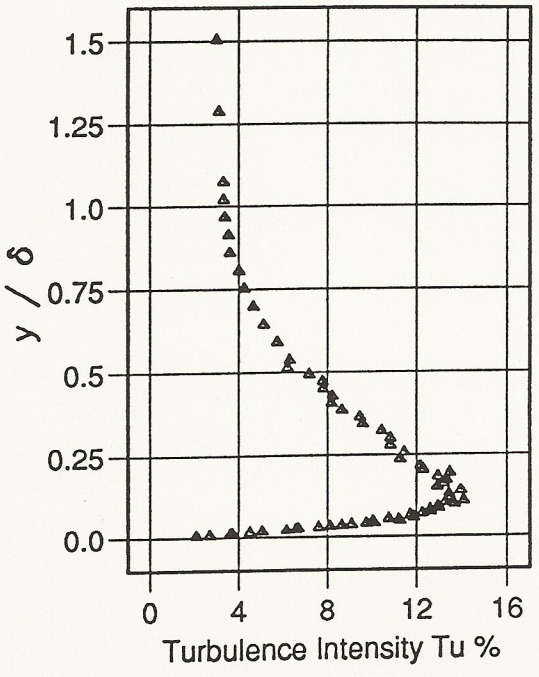
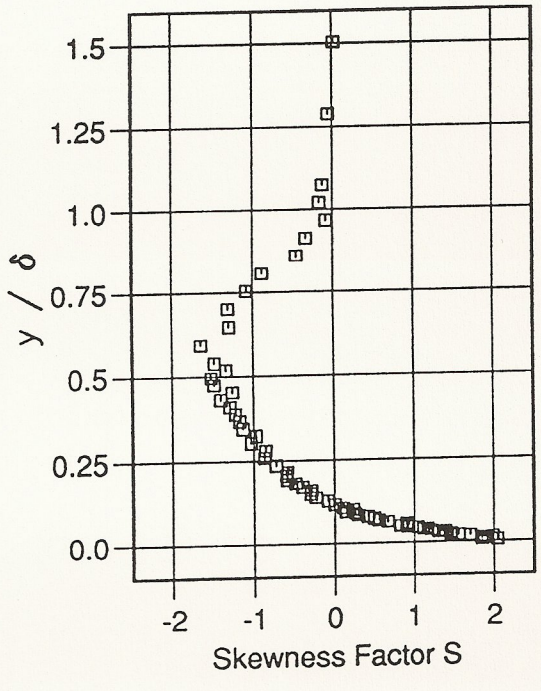


Figure 5.4 Probability Distributions of the Velocity in the Boundary Layer
C4 Plate $U_\infty = 5$ m/s $Tu_\infty = 4$ % X = 200 mm







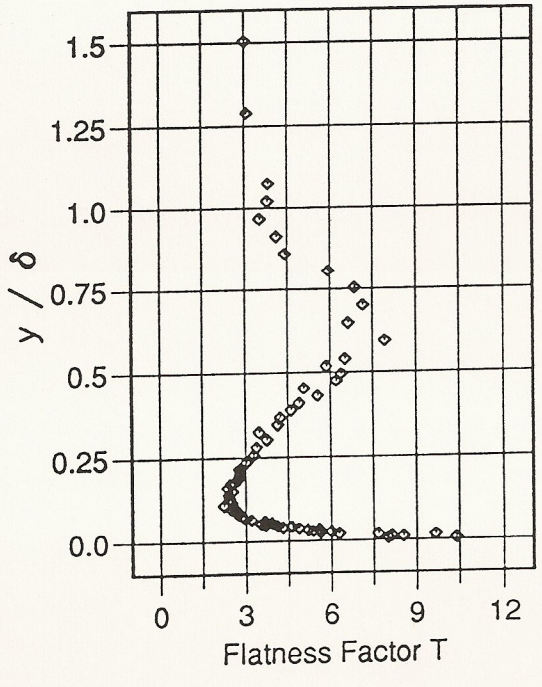


Figure 5.5	Profiles of the Integral Boundary Layer Quantities C4 Plate U_∞ = 5 m/s Tu_∞ = 4 % X = 300 mm

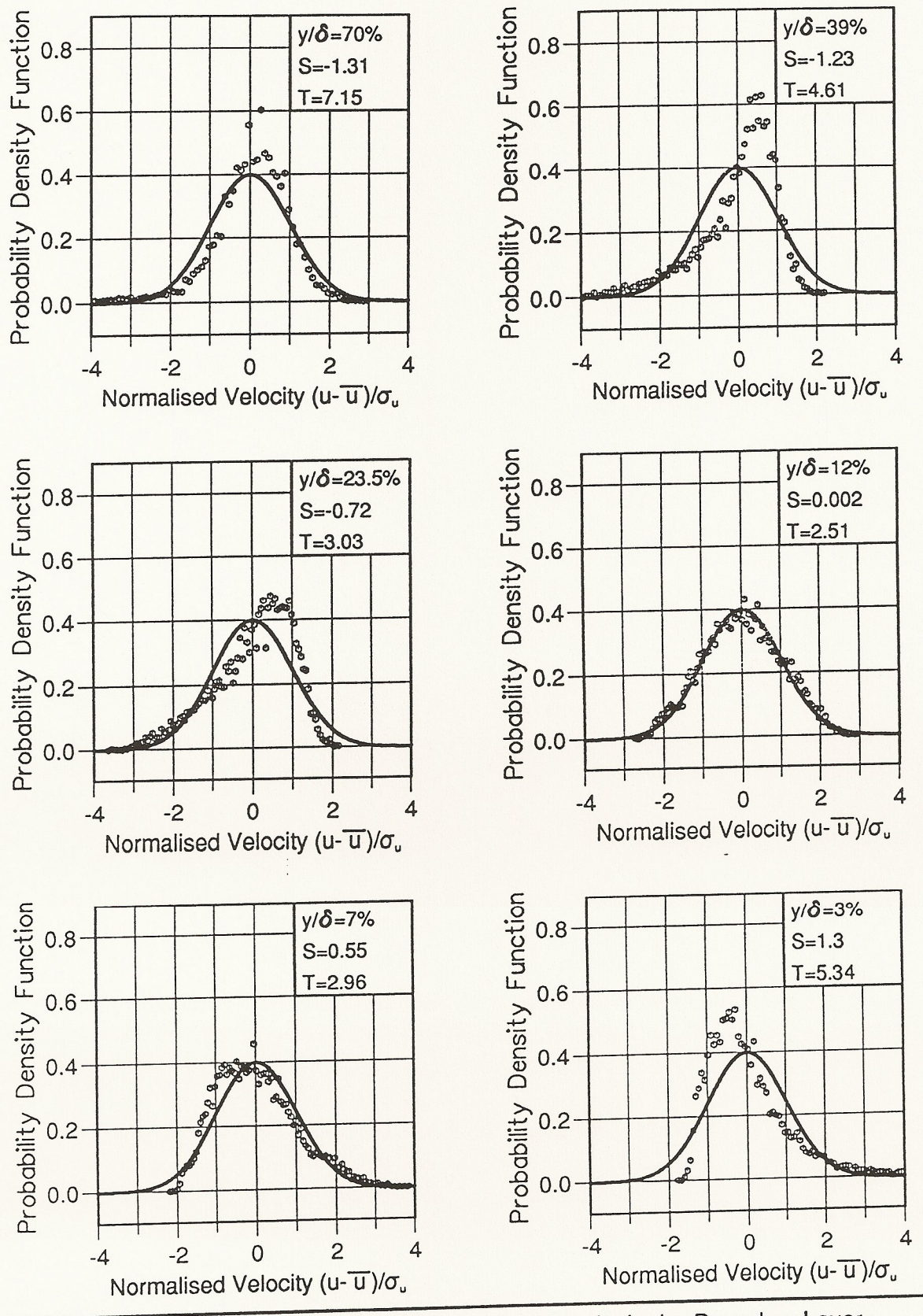
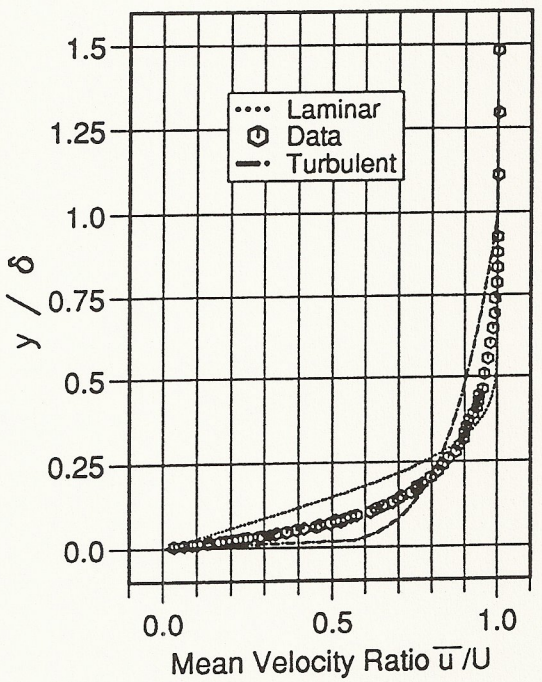
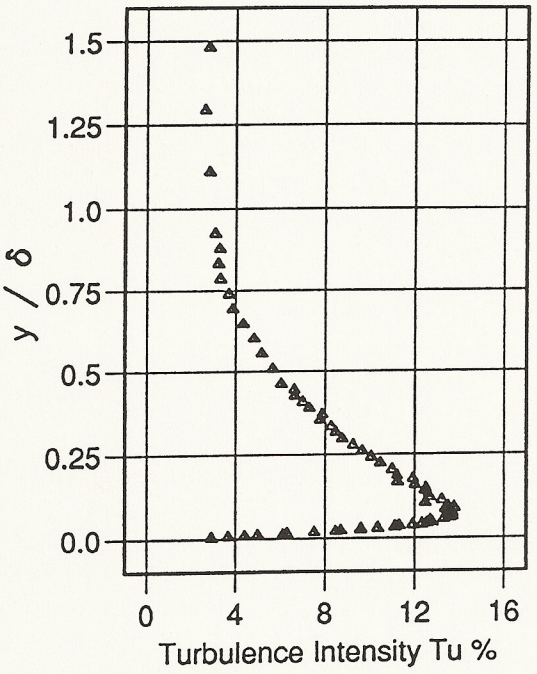
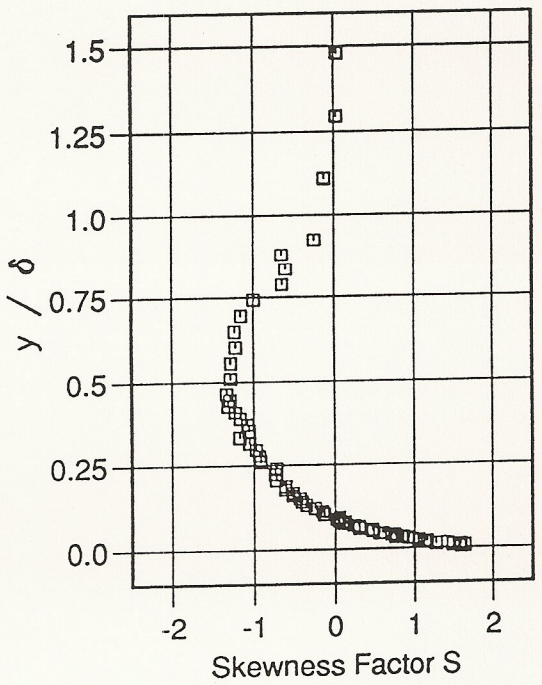


Figure 5.6 Probability Distributions of the Velocity in the Boundary Layer
C4 Plate $U_\infty = 5$ m/s $Tu_\infty = 4\%$ X = 300 mm







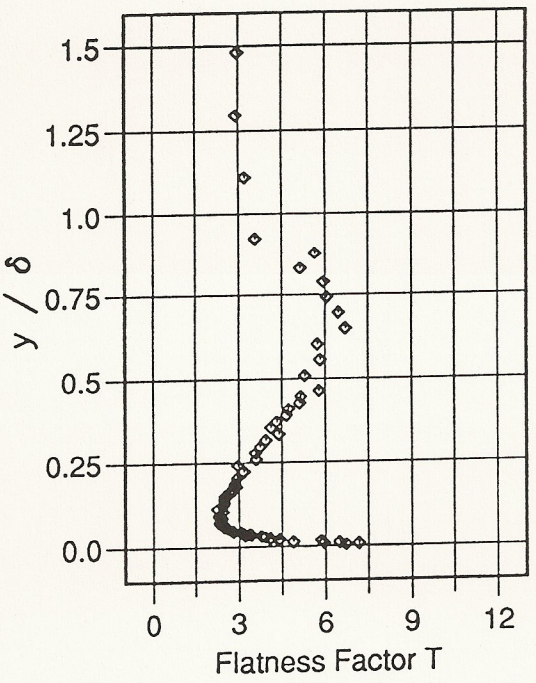


Figure 5.7	Profiles of the Integral Boundary Layer Quantities C4 Plate U_∞ = 5 m/s Tu_∞ = 4 % X = 350 mm

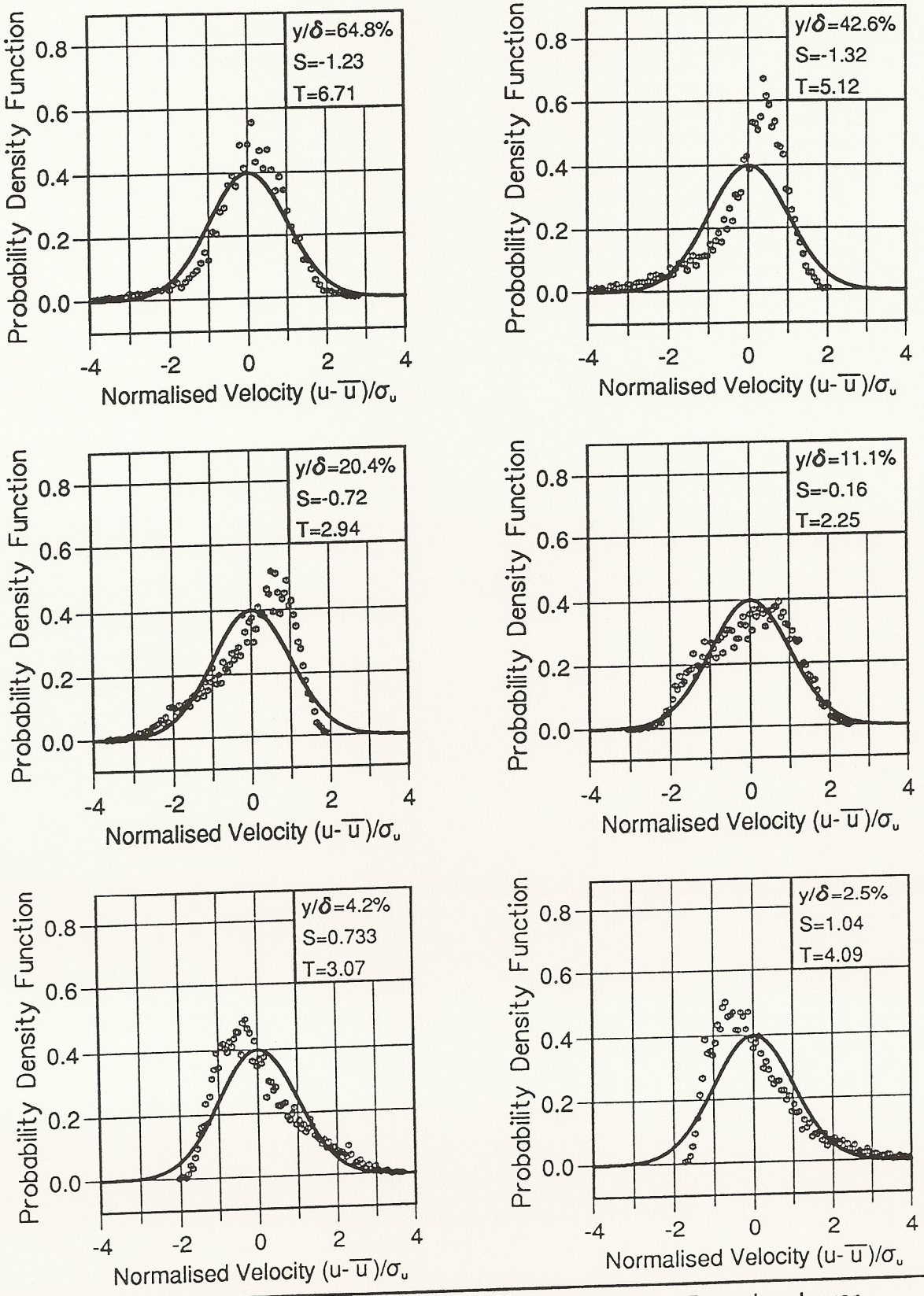
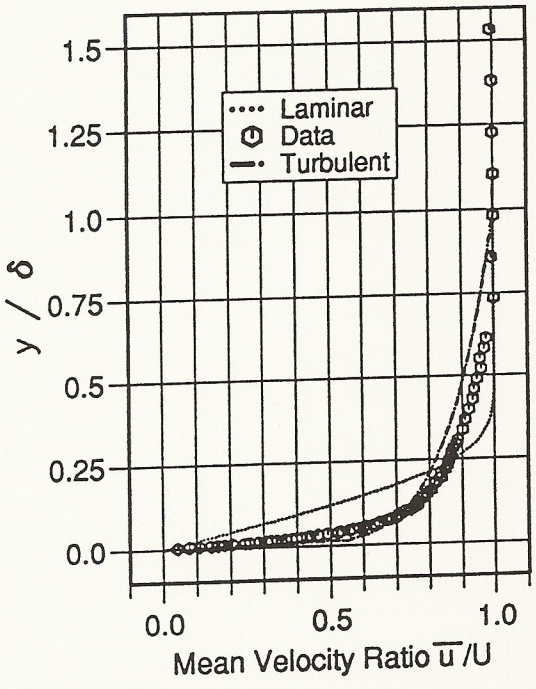
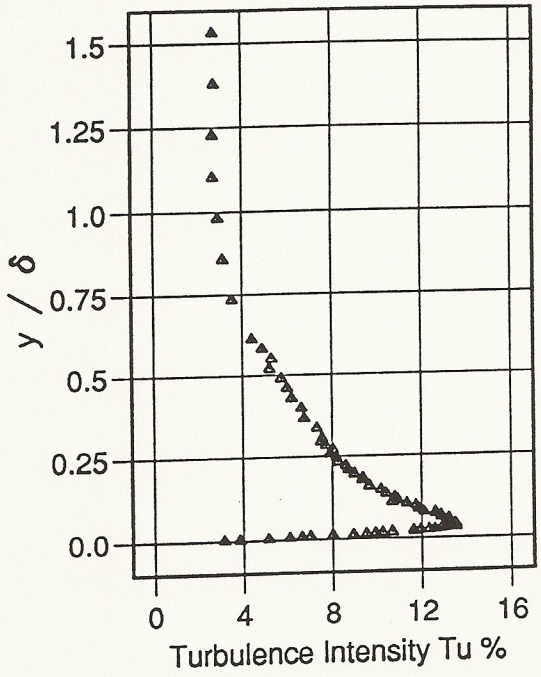
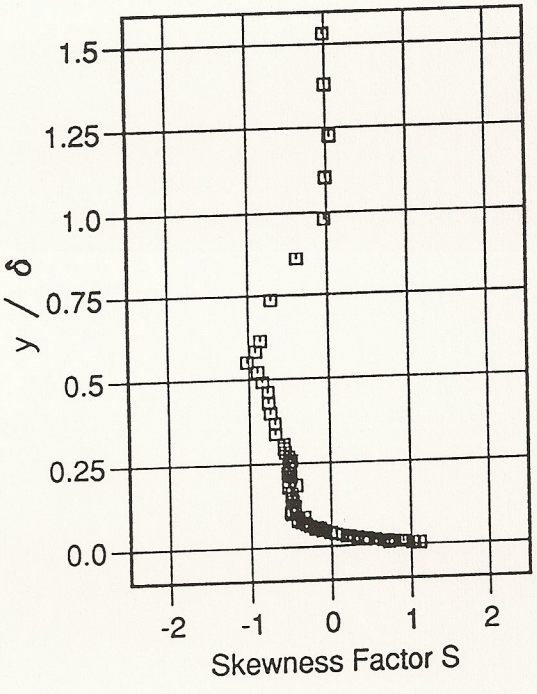


Figure 5.8 Probability Distributions of the Velocity in the Boundary Layer
C4 Plate $U_\infty = 5$ m/s $Tu_\infty = 4$ % X = 350 mm







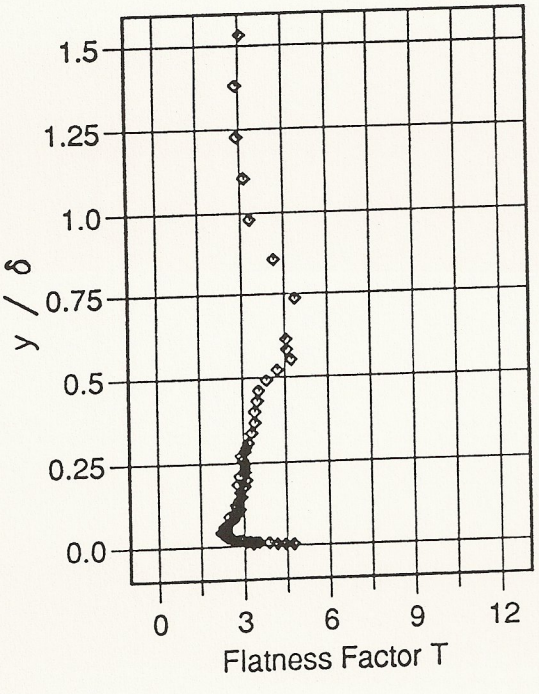


Figure 5.9	Profiles of the Integral Boundary Layer Quantities C4 Plate U_∞ = 5 m/s Tu_∞ = 4 % X = 550 mm

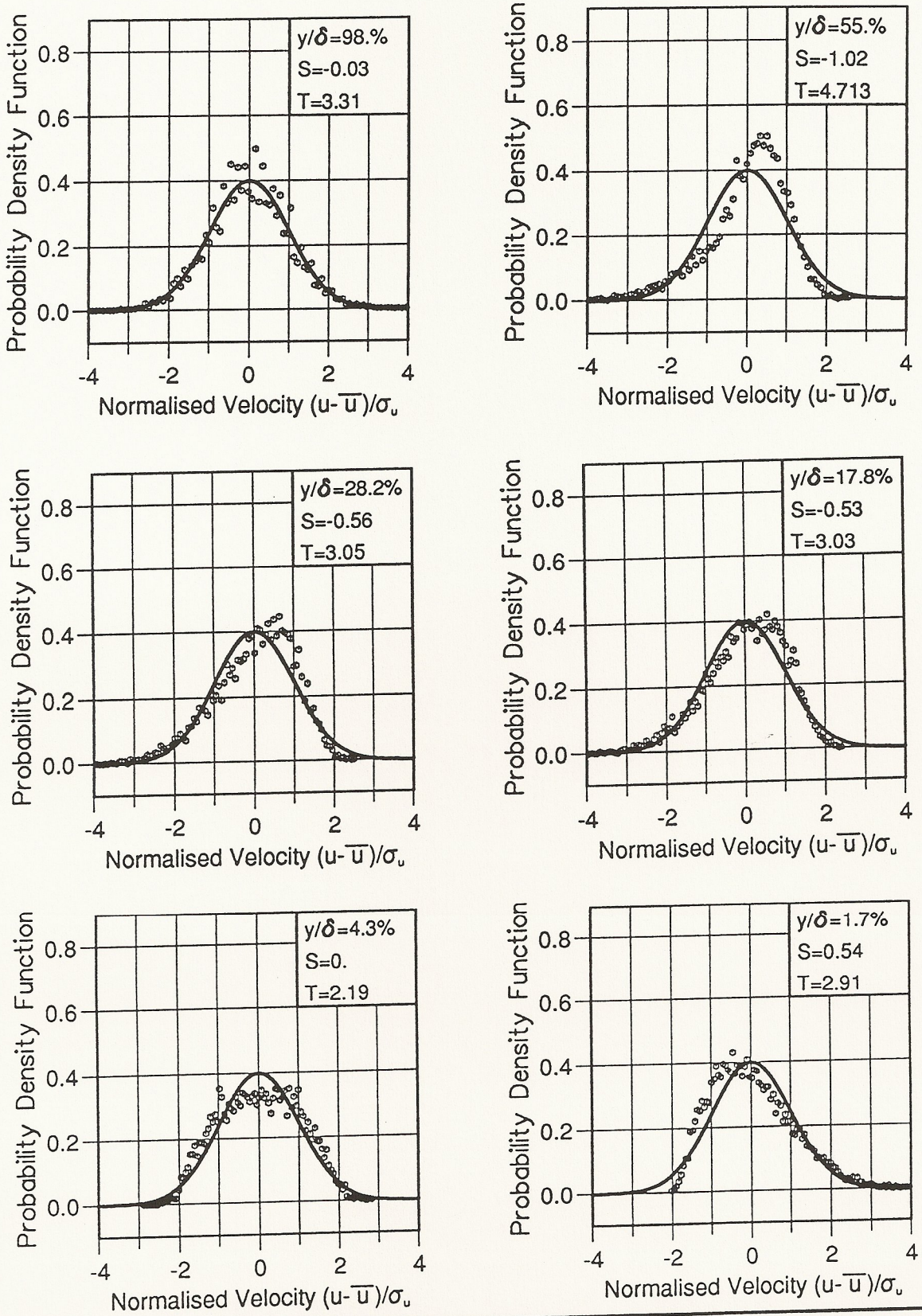


Figure 5.10 Probability Distributions of the Velocity in the Boundary Layer
C4 Plate U_∞ = 5 m/s Tu_∞ = 4 % X = 550 mm

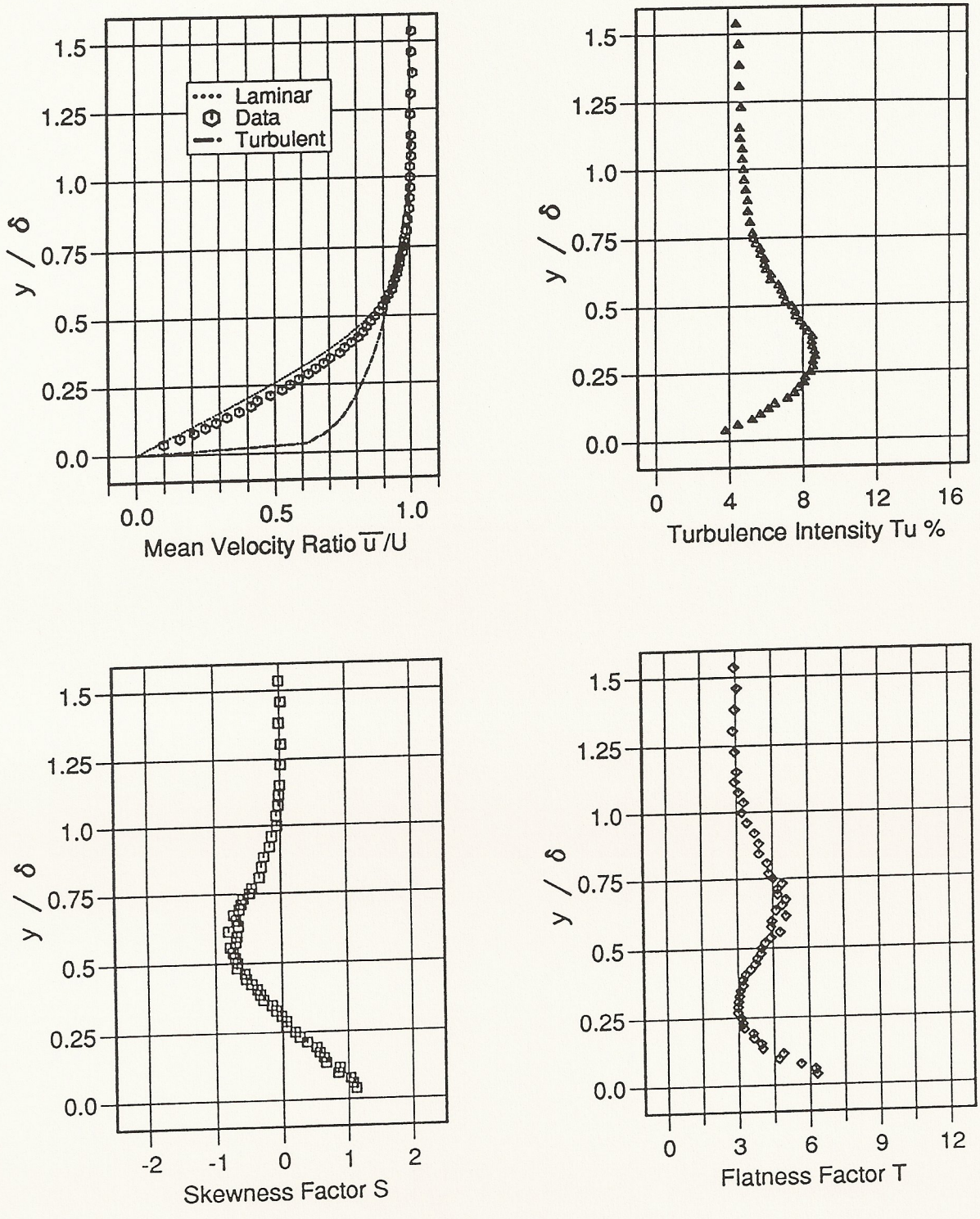


Figure 5.11	Profiles of the Integral Boundary Layer Quantities C4 Plate U_∞ = 15 m/s Tu_∞ = 4 % X = 45 mm

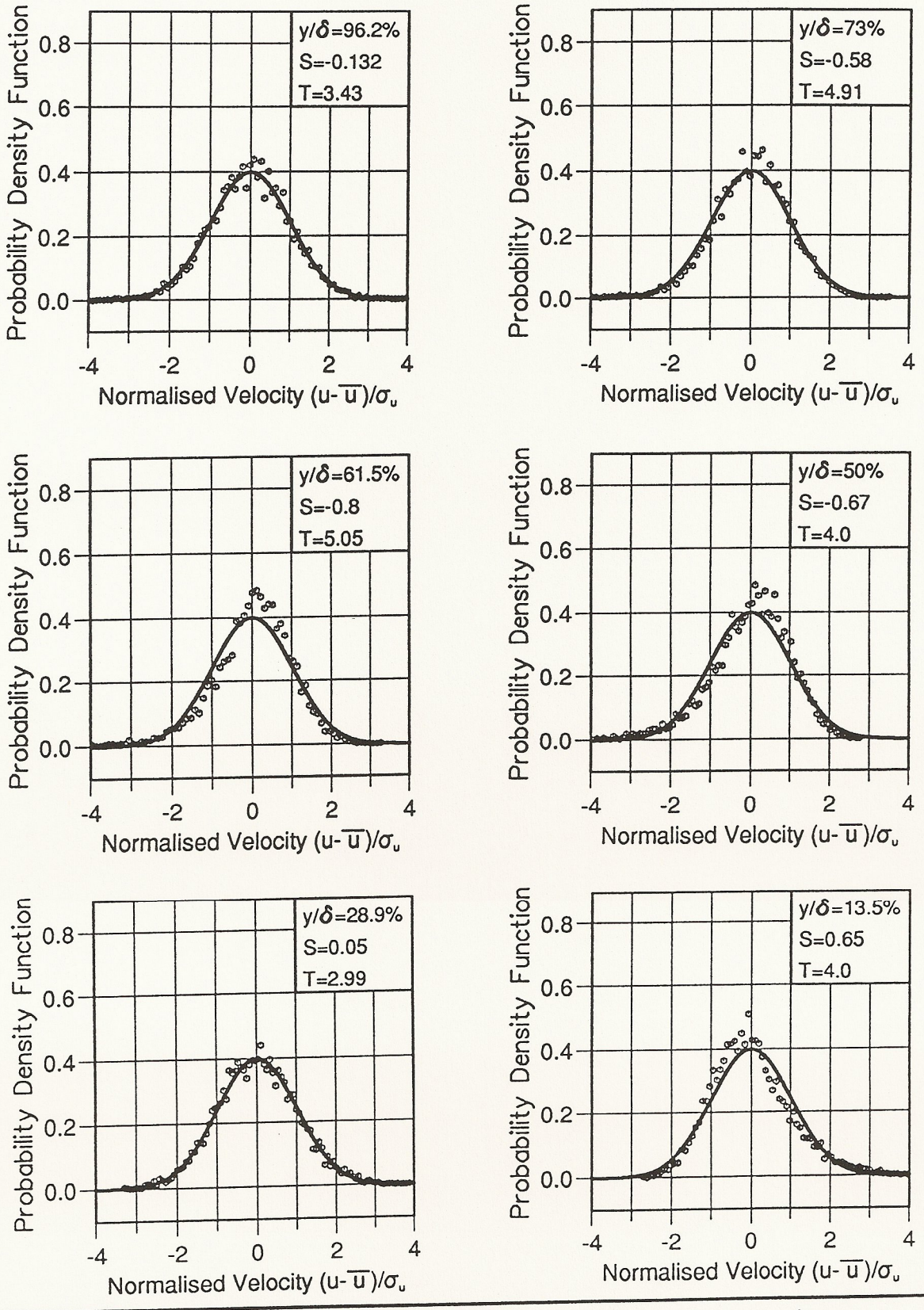
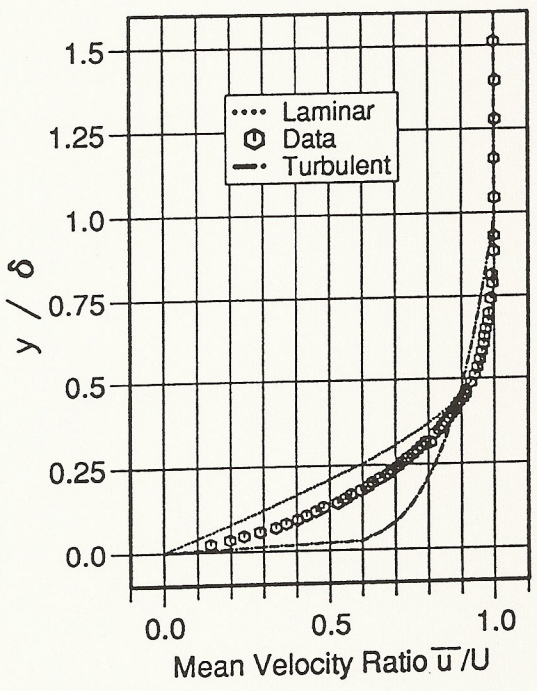
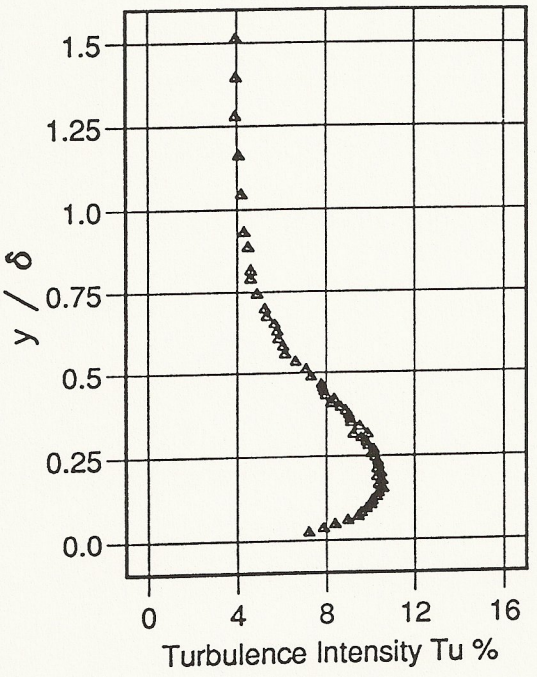
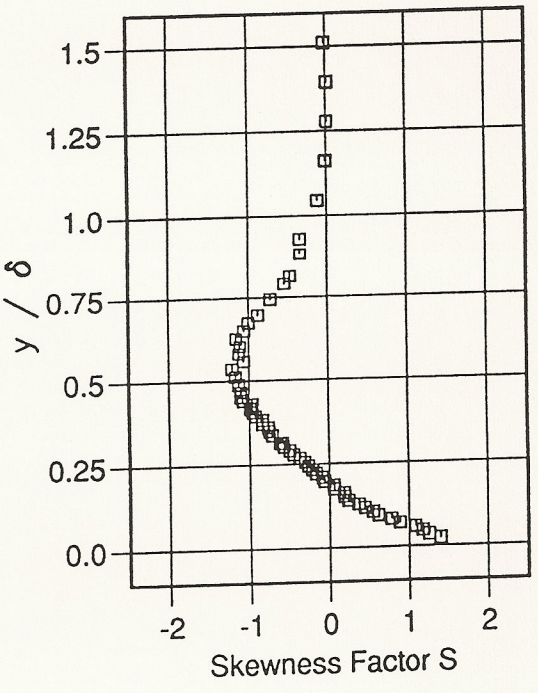


Figure 5.12 Probability Distributions of the Velocity in the Boundary Layer
C4 Plate U_∞ = 15 m/s Tu_∞ = 4 % X = 45 mm







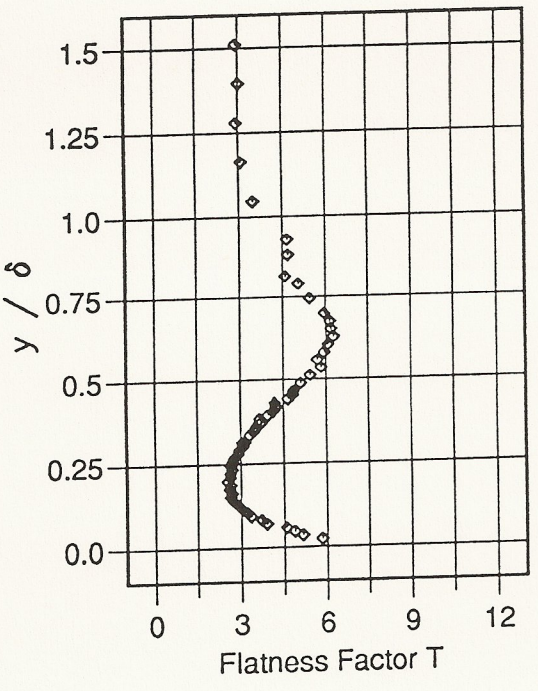


Figure 5.13	Profiles of the Integral Boundary Layer Quantities C4 Plate U_∞ = 15 m/s Tu_∞ = 4 % X = 75 mm

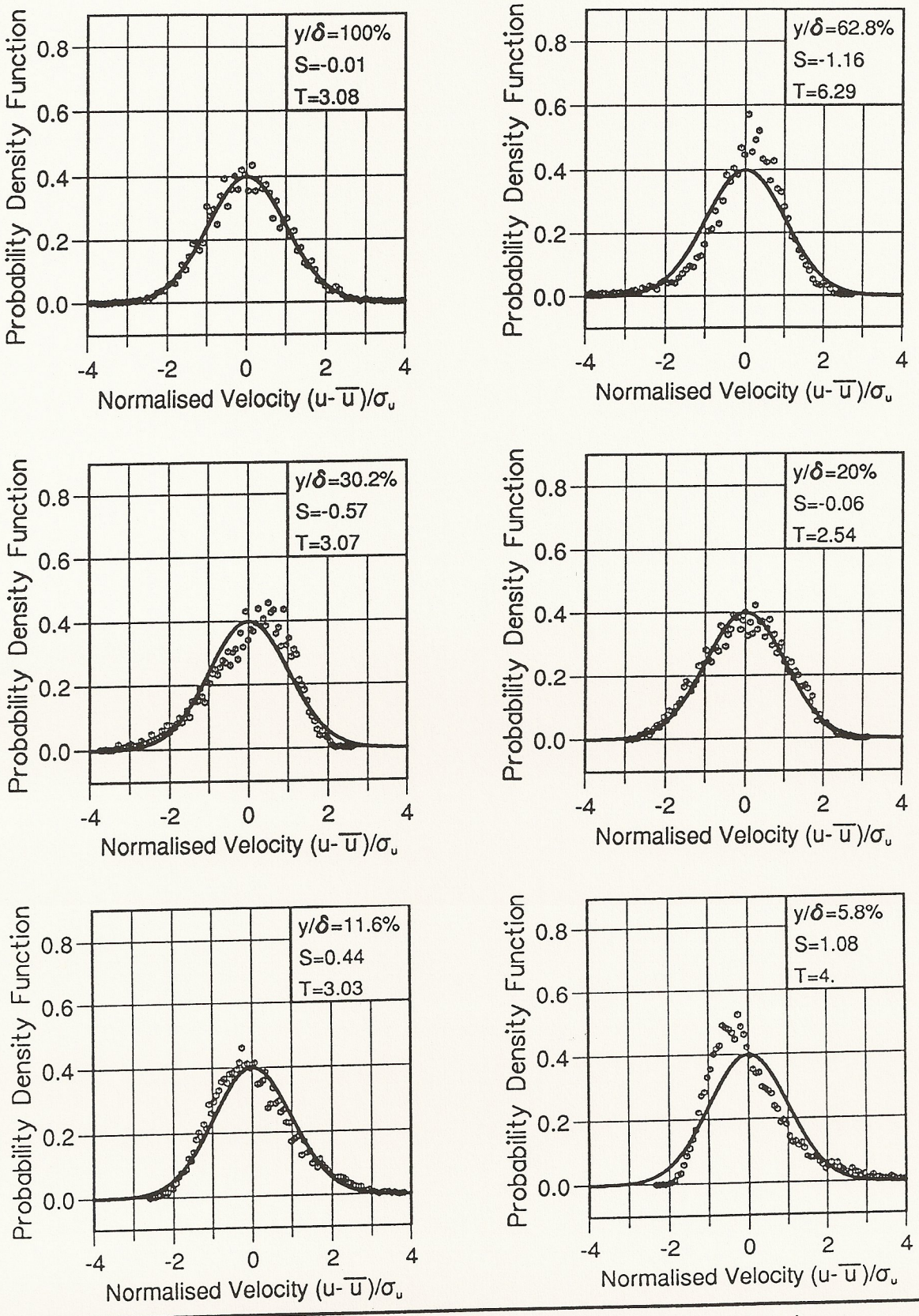
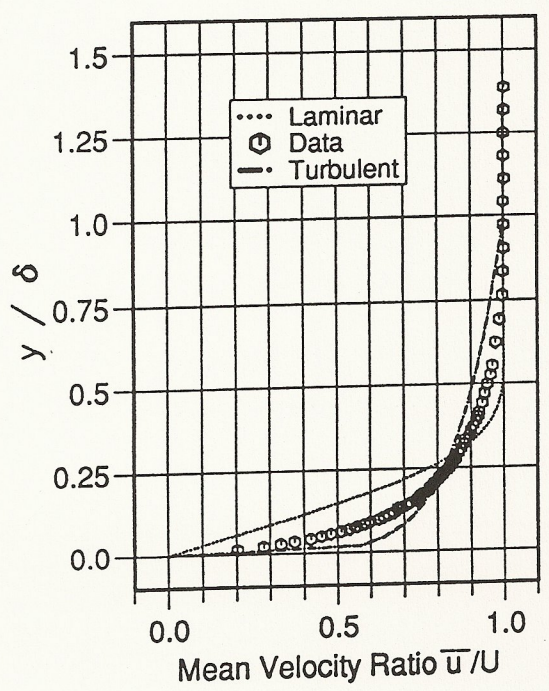
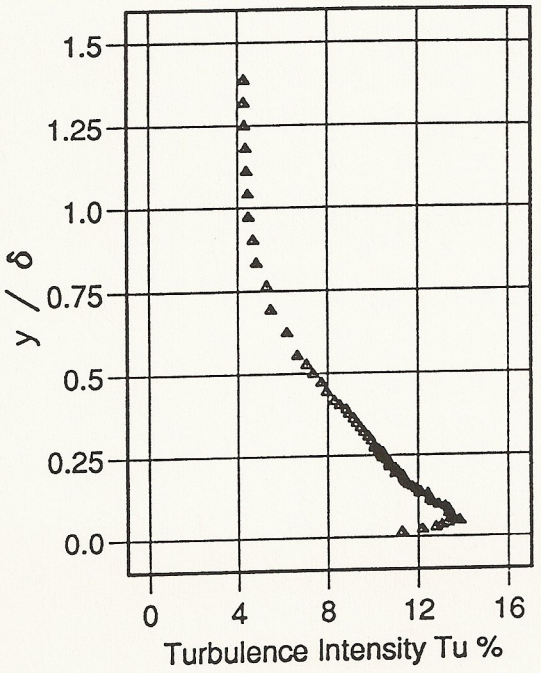
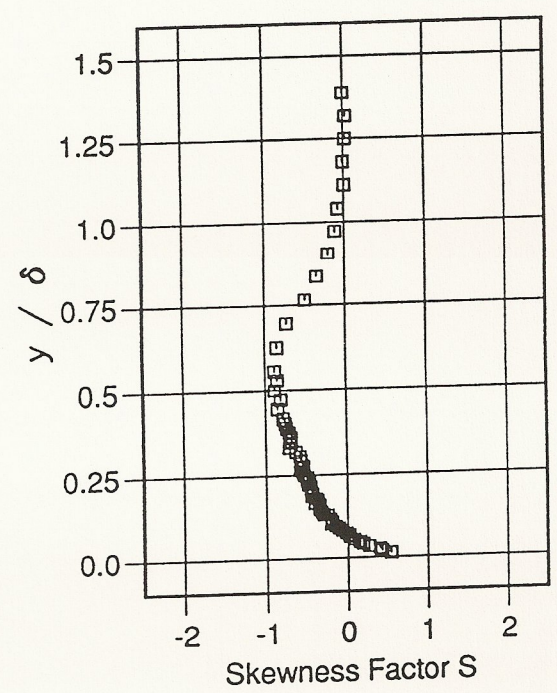


Figure 5.14 Probability Distributions of the Velocity in the Boundary Layer
C4 Plate U_∞ = 15 m/s Tu_∞ = 4 % X = 75 mm







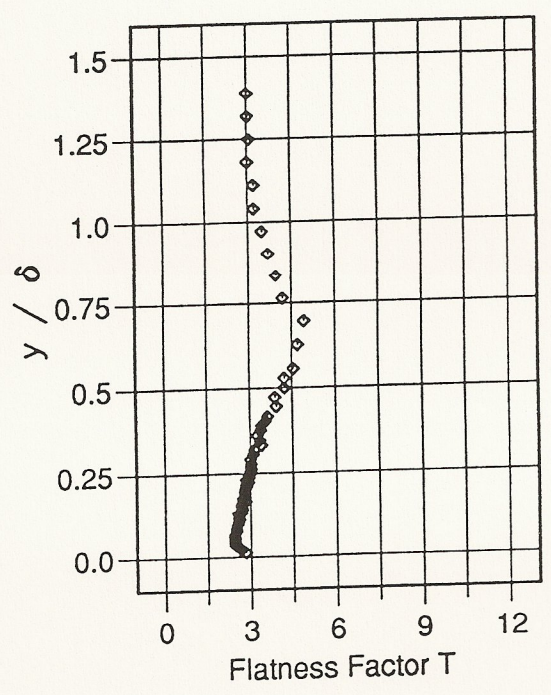


Figure 5.15	Profiles of the Integral Boundary Layer Quantities C4 Plate U_∞ = 15 m/s Tu_∞ = 4 % X = 118 mm

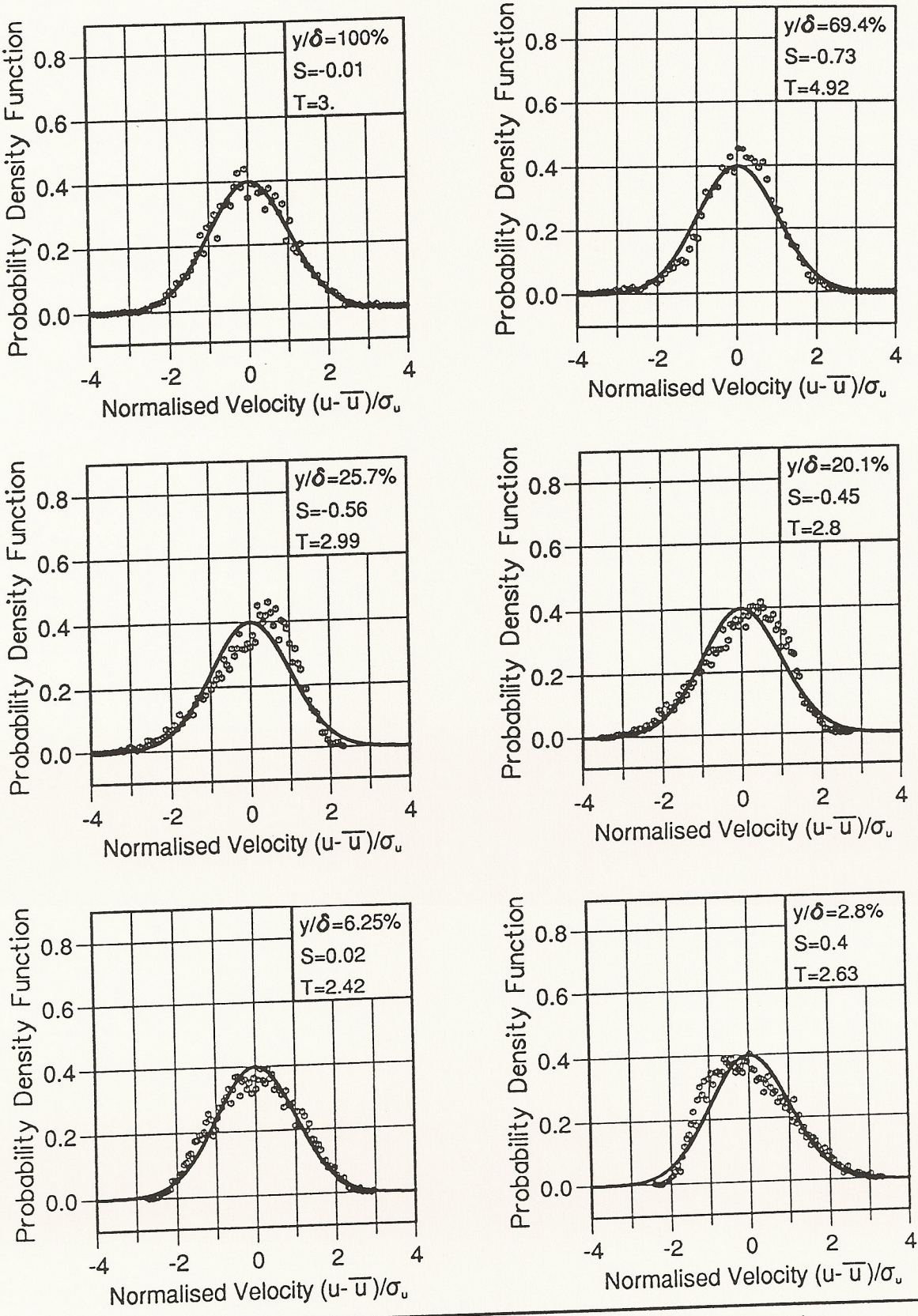


Figure 5.16 Probability Distributions of the Velocity in the Boundary Layer
C4 Plate U_∞ = 15 m/s Tu_∞ = 4 % X = 118 mm

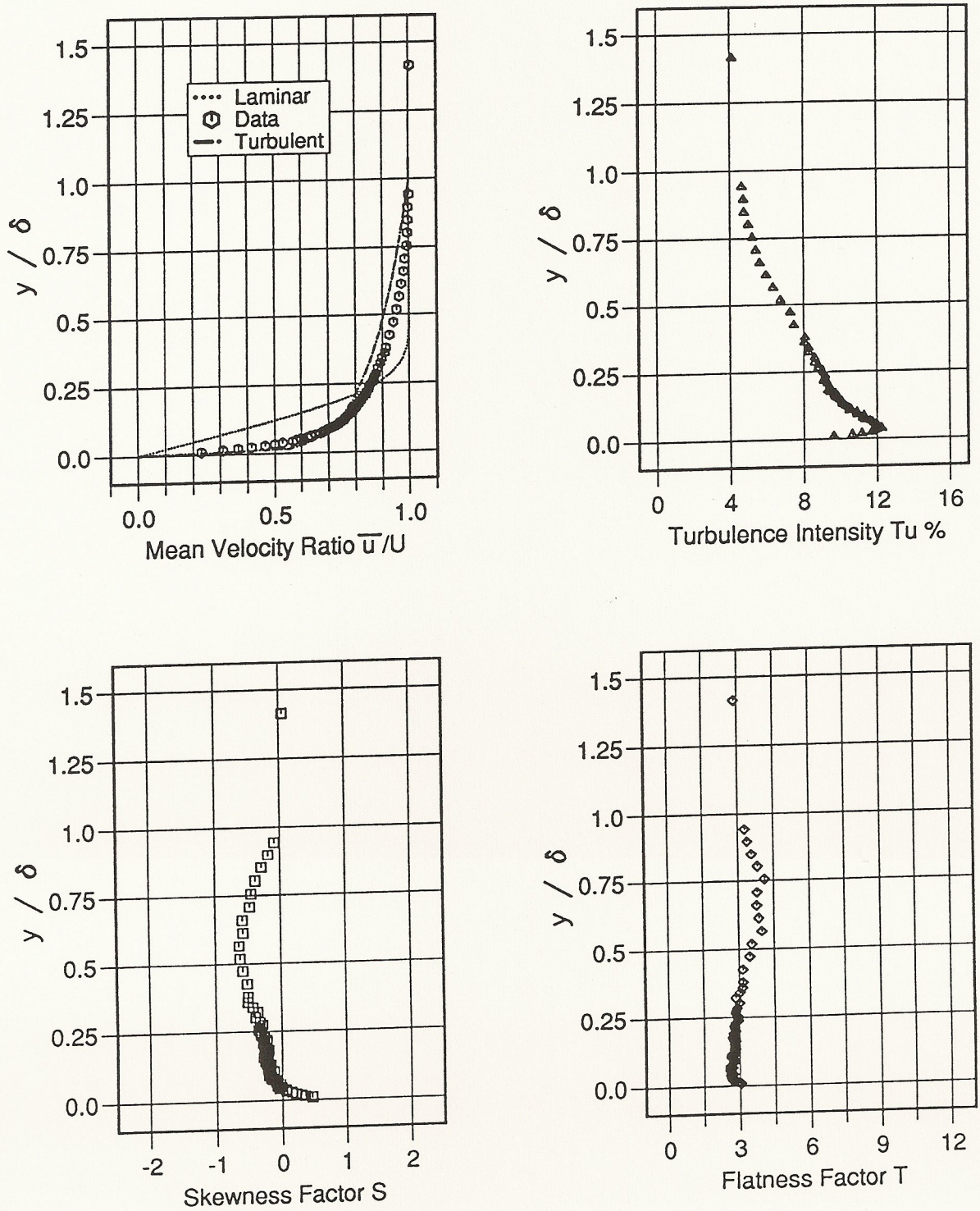


Figure 5.17	Profiles of the Integral Boundary Layer Quantities C4 Plate U_∞ = 15 m/s Tu_∞ = 4 % X = 175 mm

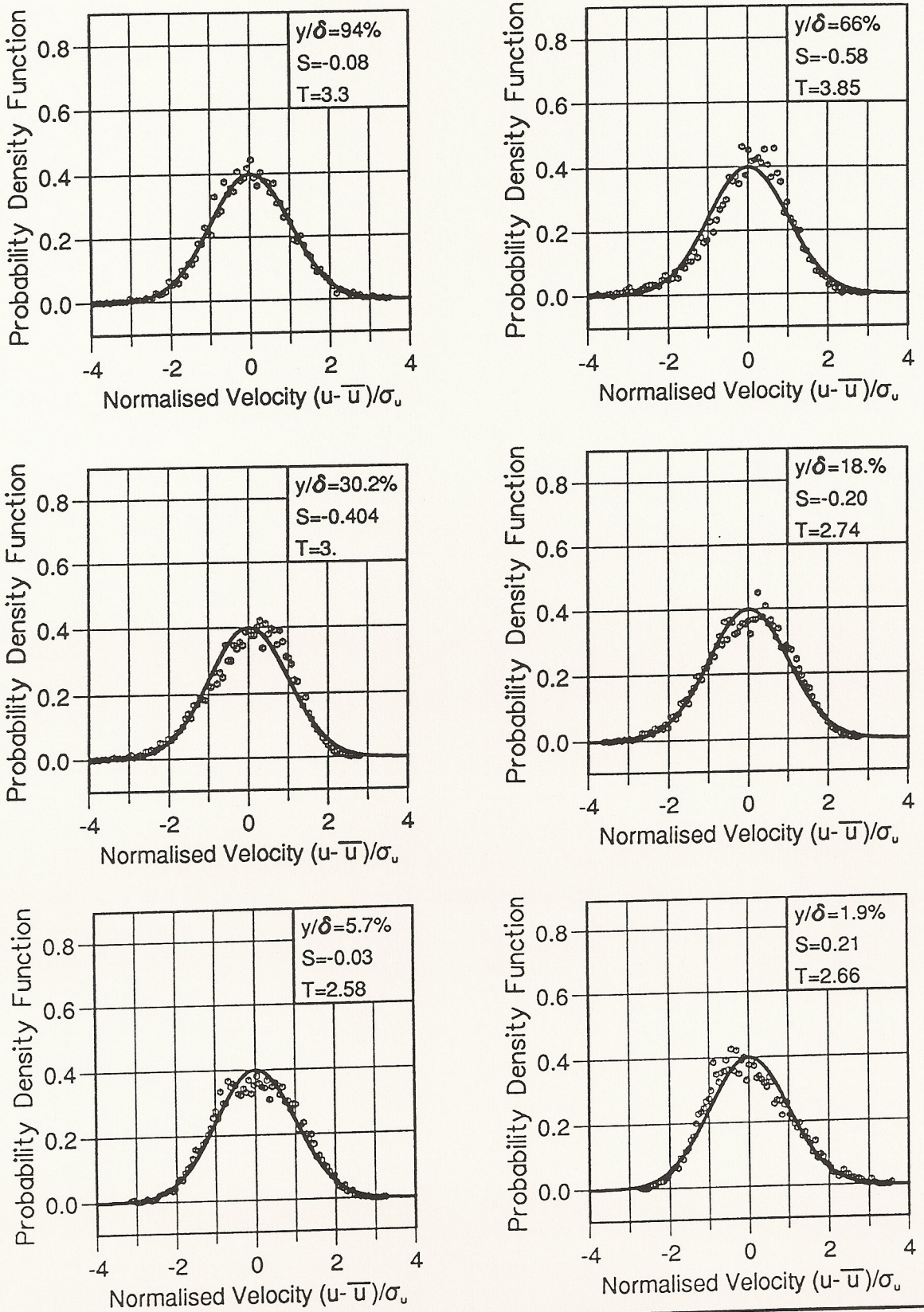


Figure 5.18 Probability Distributions of the Velocity in the Boundary Layer
C4 Plate U_∞ = 15 m/s Tu_∞ = 4 % X = 175 mm

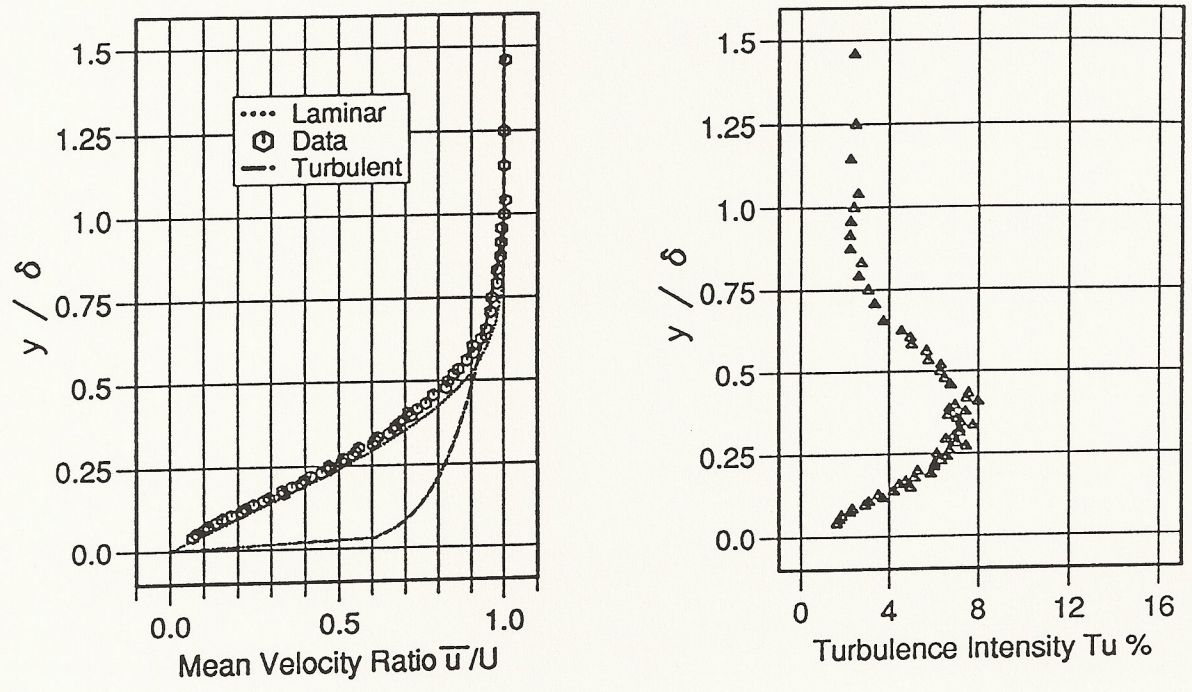


Figure 5.19	Profiles of the Integral Boundary Layer Quantities C4 Plate U_∞ = 15 m/s Tu_∞ = 1.8 % X = 150 mm

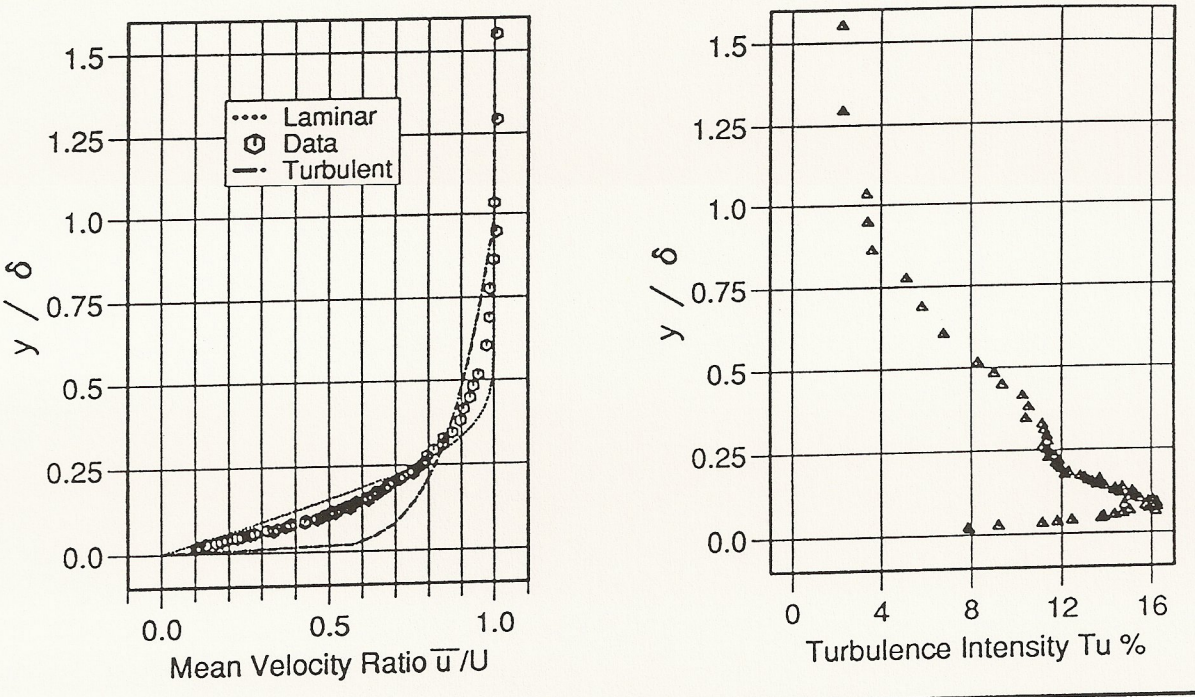
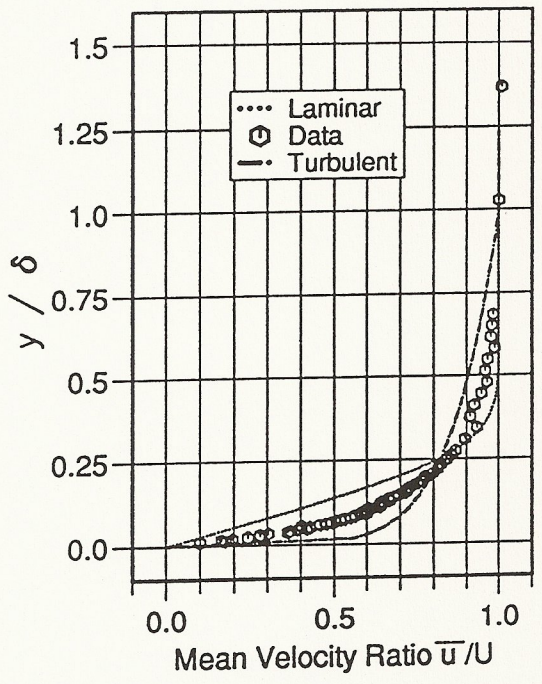


Figure 5.20	Profiles of the Integral Boundary Layer Quantities C4 Plate U_∞ = 15 m/s Tu_∞ = 1.8 % X = 350 mm



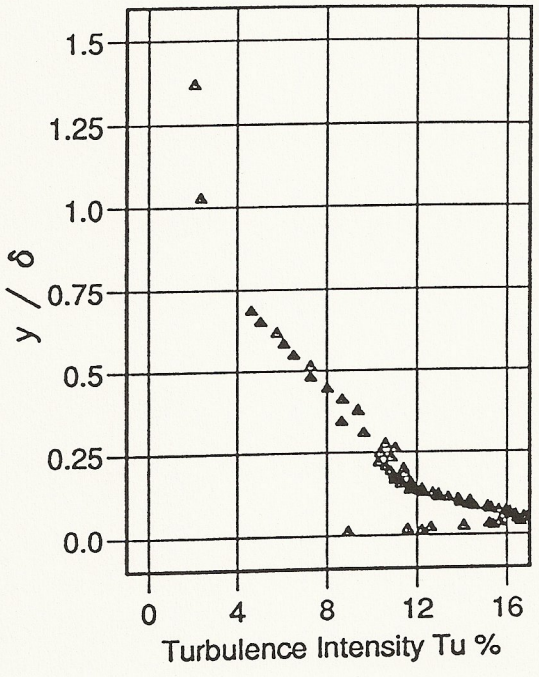
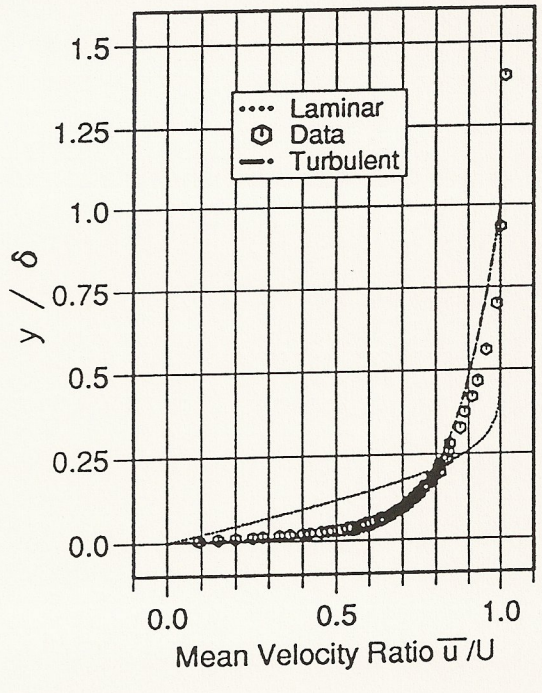


Figure 5.21	Profiles of the Integral Boundary Layer Quantities C4 Plate U_∞ = 15 m/s Tu_∞ = 1.8 % X = 425 mm



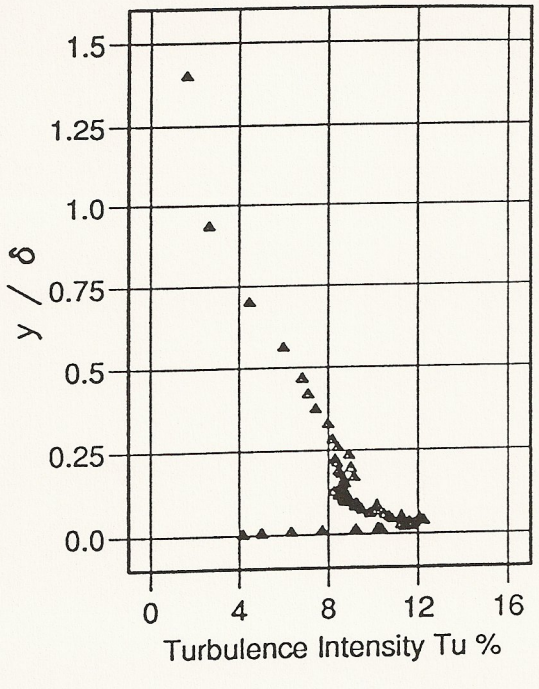


Figure 5.22	Profiles of the Integral Boundary Layer Quantities C4 Plate U_∞ = 15 m/s Tu_∞ = 1.8 % X = 650 mm

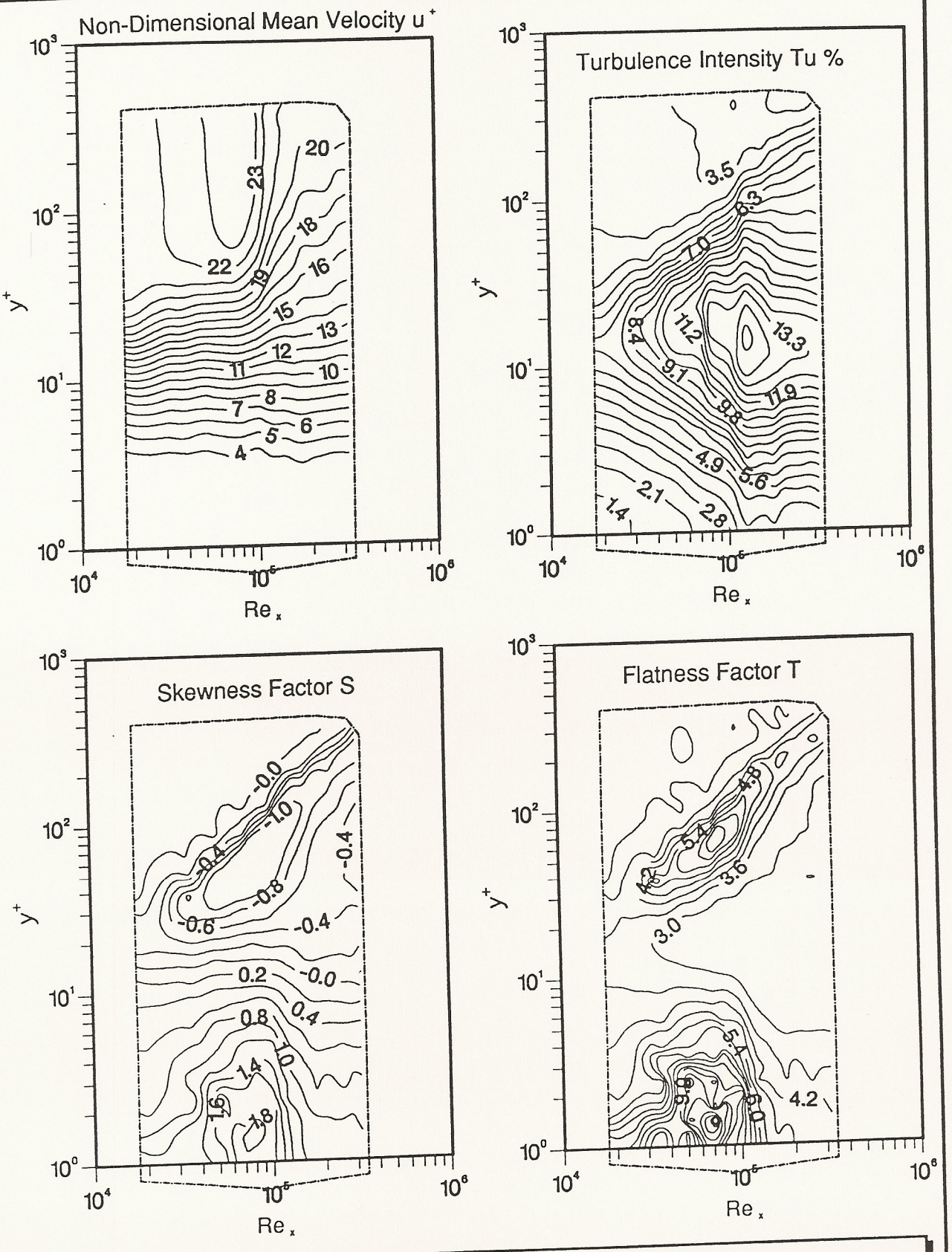


Figure 5.23 Boundary Layer Parameter Distribution on a Re_x - y^+ PLane
C4 Plate U_∞ = 5 m/s Tu_∞ = 4 %

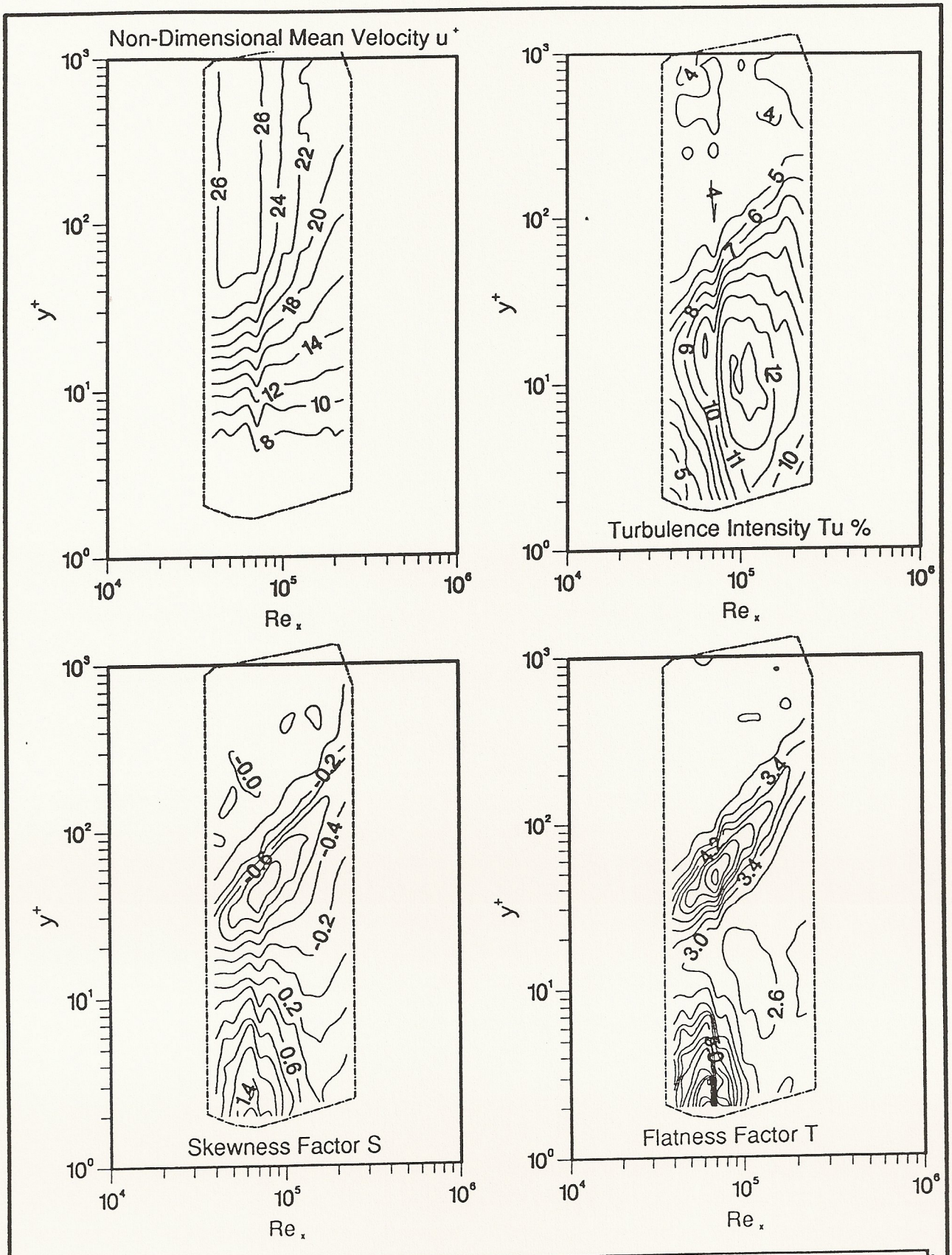


Figure 5.24 Boundary Layer Parameter Distribution on a Re_x - y^+ PLane
C4 Plate U_∞ = 15 m/s Tu_∞ = 4 %

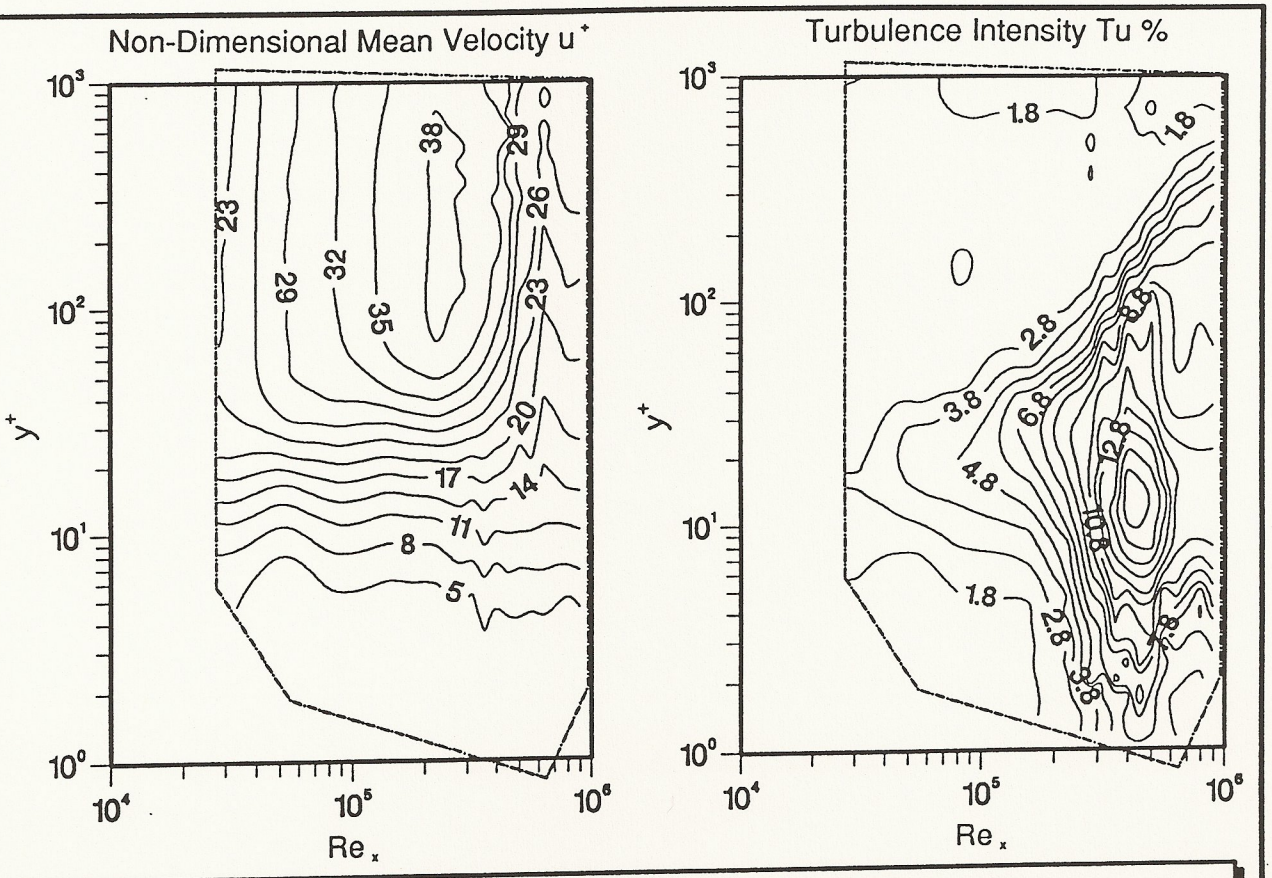


Figure 5.25	Boundary Layer Parameter Distribution on a Re_x - y^+ Plane C4 Plate U_∞ = 15 m/s Tu_∞ = 1.8 %

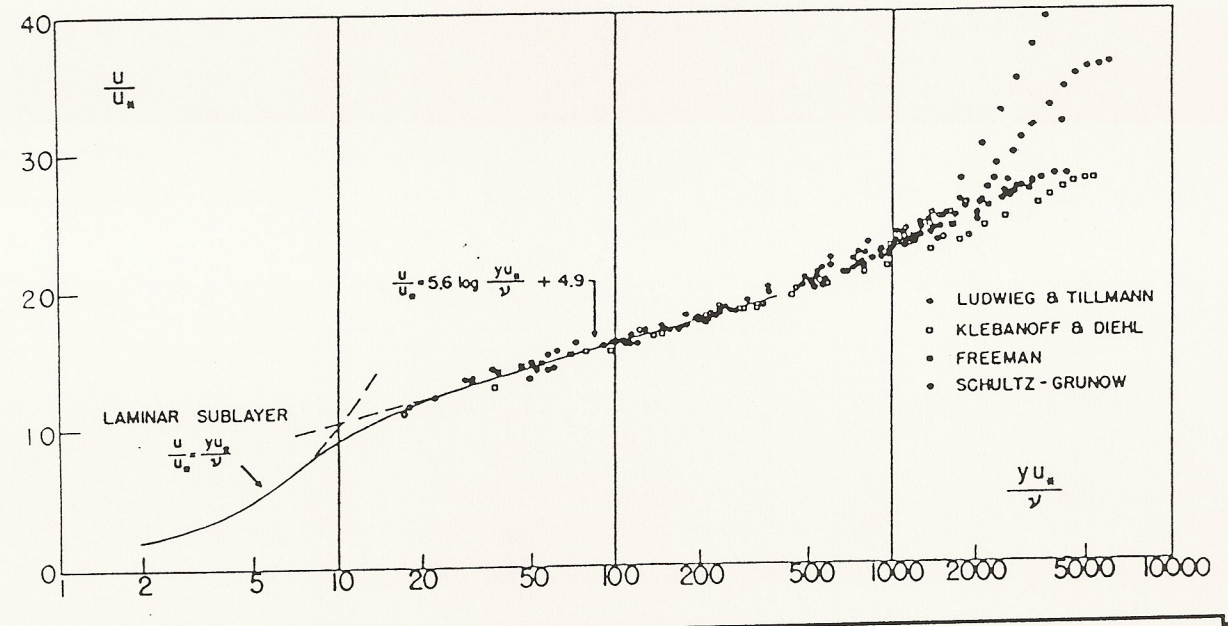


Figure 5.26	Universal Velocity Distribution for Turbulent Velocity Profiles Near Smooth Wall (after Clauser, 1954)

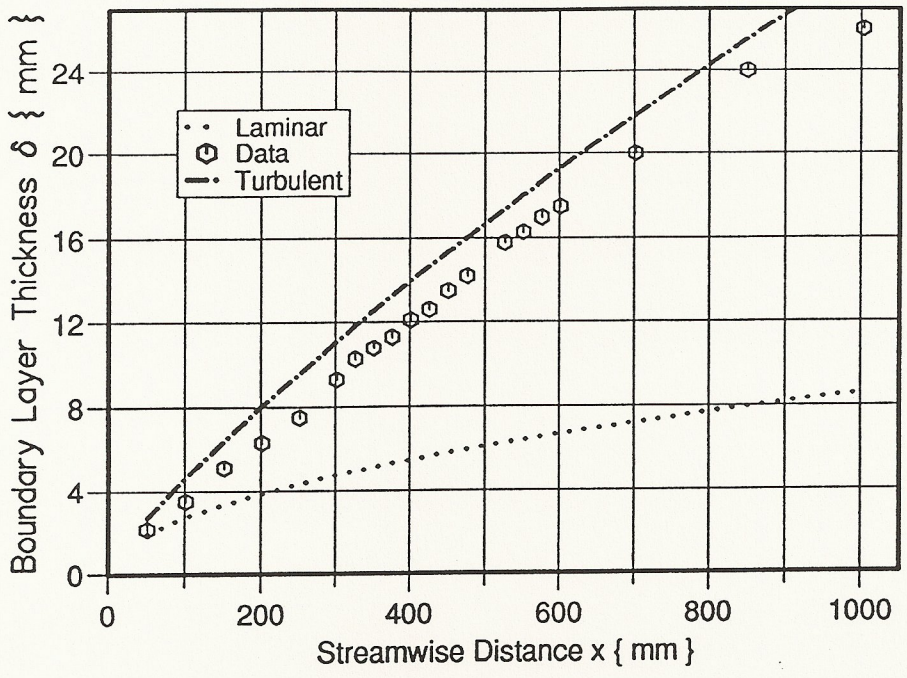


Figure 5.27	Distribution of the Boundary Layer Thickness C4 Plate U_∞ = 5 m/s Tu_∞ = 4 %

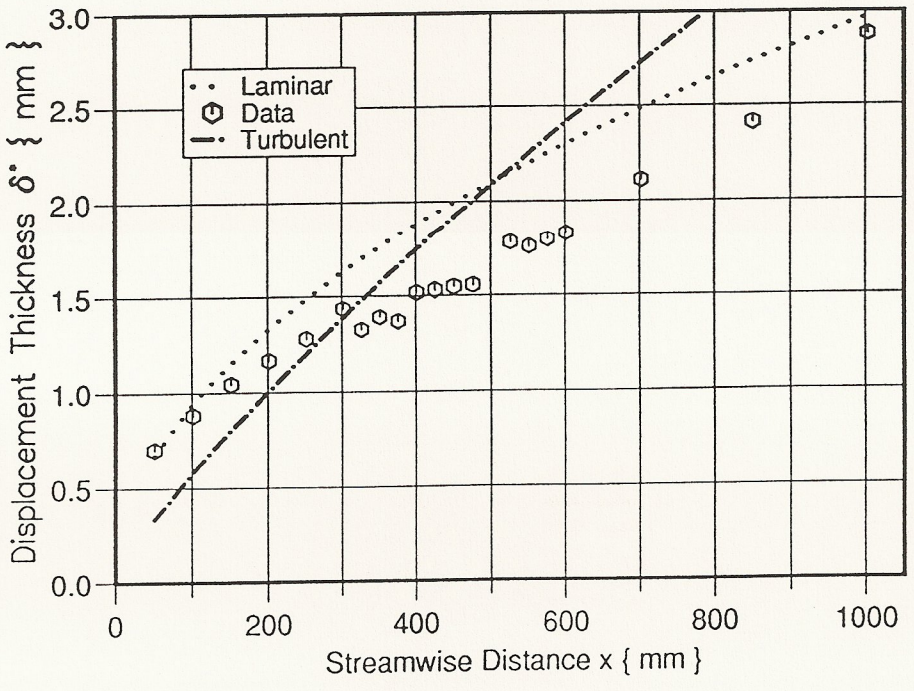


Figure 5.28	Distribution of the Boundary Layer Displacement Thickness C4 Plate U_∞ = 5 m/s Tu_∞ = 4 %

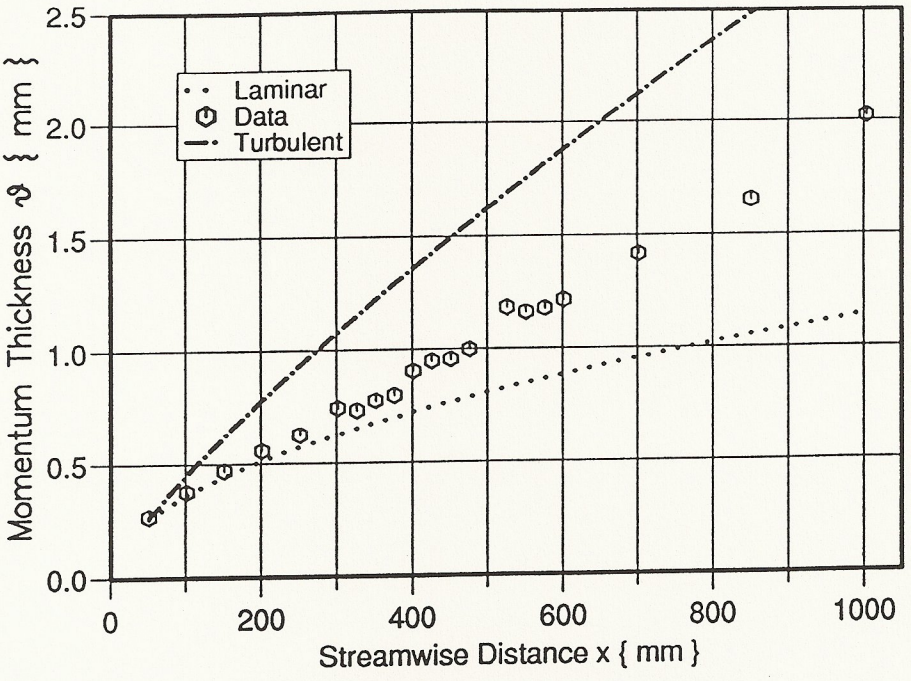


Figure 5.29	Distribution of the Boundary Layer Momentum Thickness C4 Plate U_∞ = 5 m/s Tu_∞ = 4 %

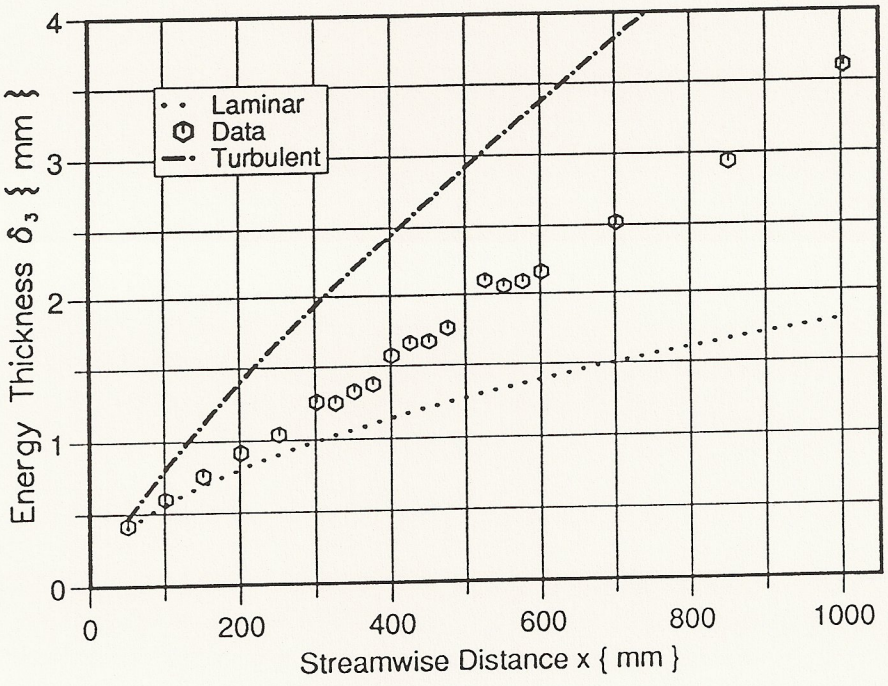


Figure 5.30	Distribution of the Boundary Layer Energy Thickness C4 Plate U_∞ = 5 m/s Tu_∞ = 4 %

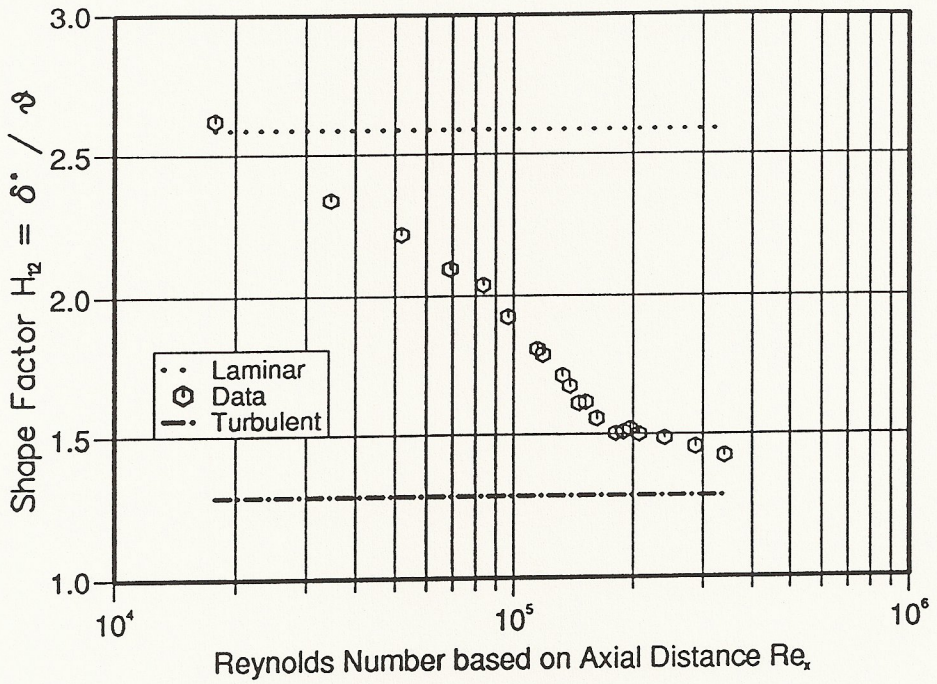


Figure 5.31	Shape Factor H_{12} Distribution C4 Plate U_∞ = 5 m/s Tu_∞ = 4 %

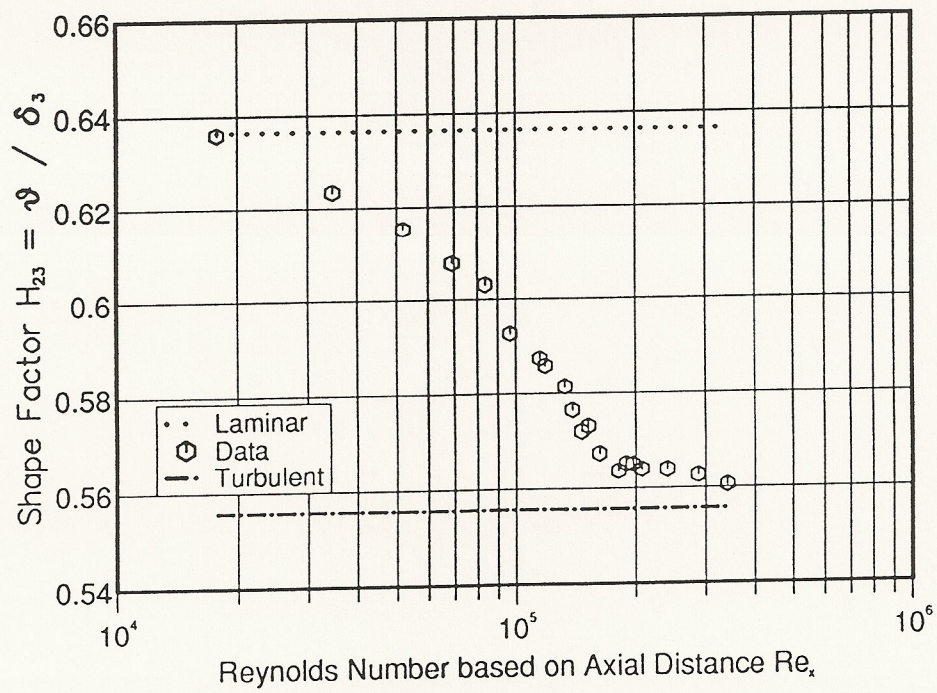


Figure 5.32	Shape Factor H_{23} Distribution C4 Plate U_∞ = 5 m/s Tu_∞ = 4 %

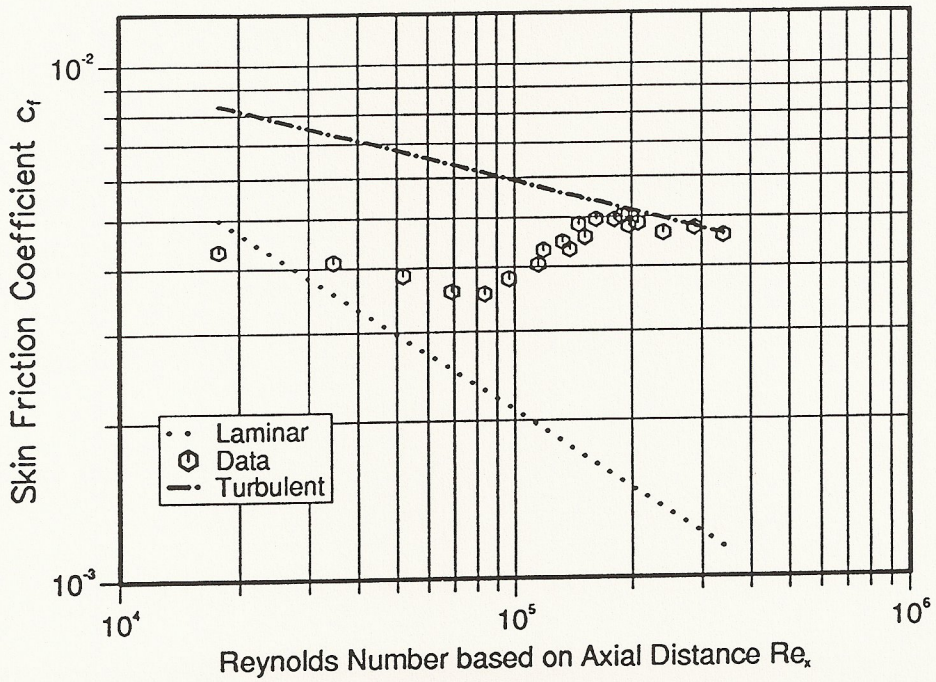


Figure 5.33	Skin Friction Coefficient Distribution C4 Plate U_∞ = 5 m/s Tu_∞ = 4 %

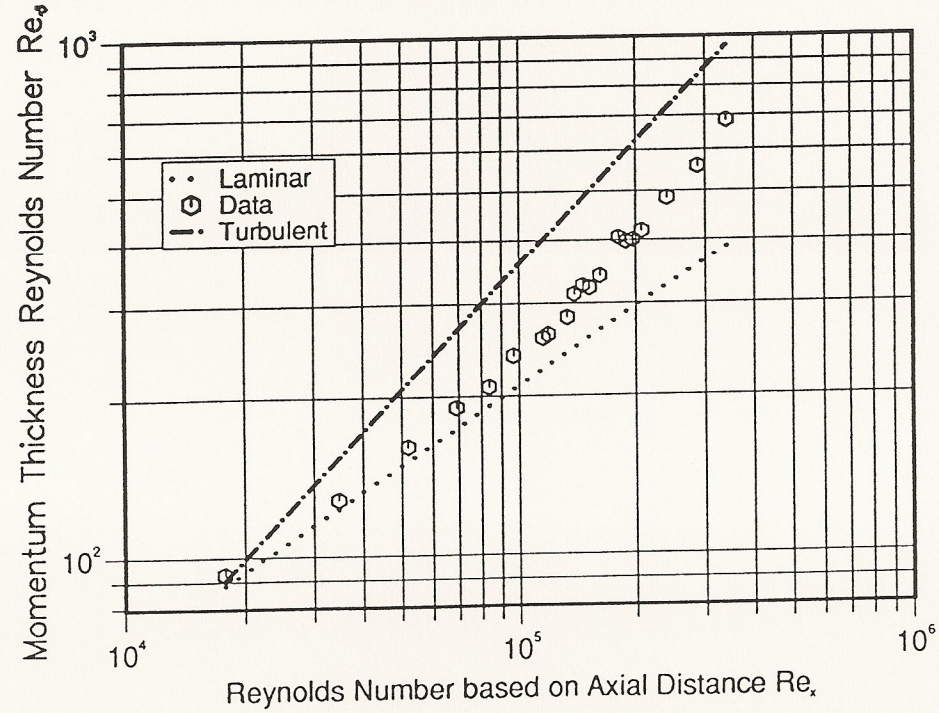


Figure 5.34	Momentum Thickness Reynolds Number Distribution C4 Plate U_∞ = 5 m/s Tu_∞ = 4 %

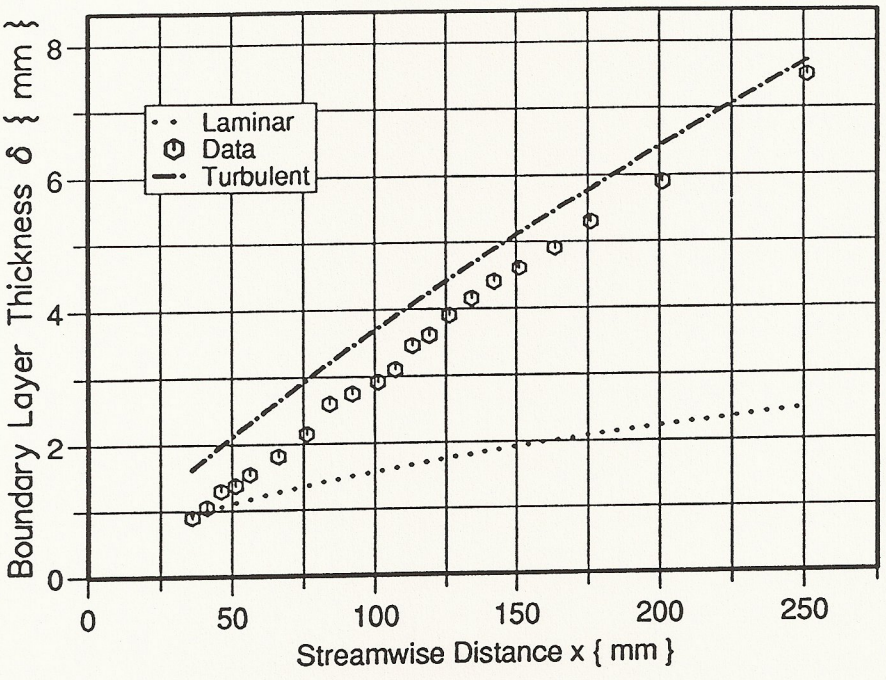


Figure 5.35	Distribution of the Boundary Layer Thickness C4 Plate U_∞ = 15 m/s Tu_∞ = 4 %

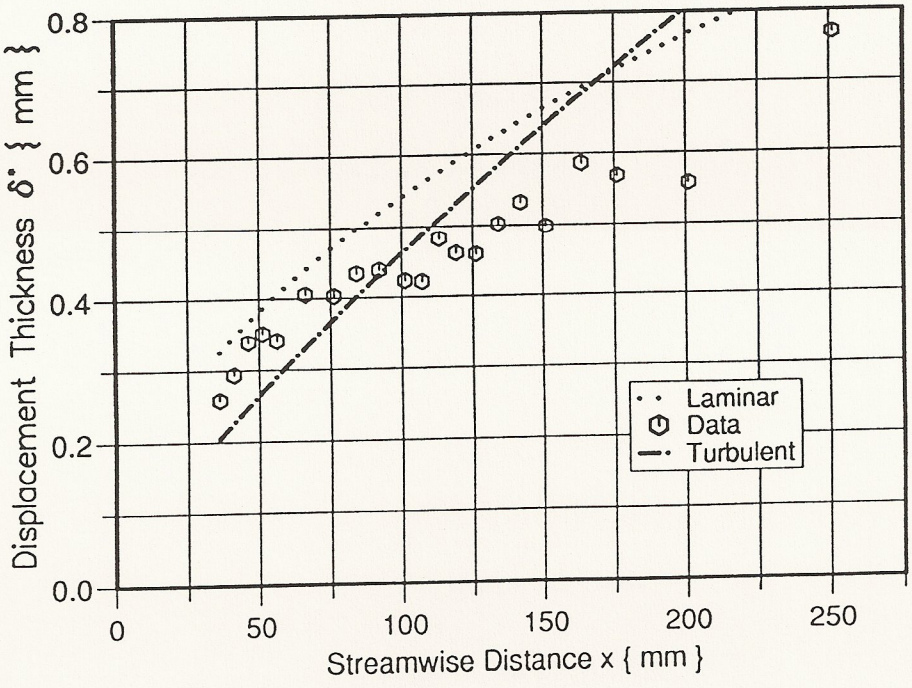


Figure 5.36	Distribution of the Boundary Layer Displacement Thickness C4 Plate U_∞ = 15 m/s Tu_∞ = 4 %

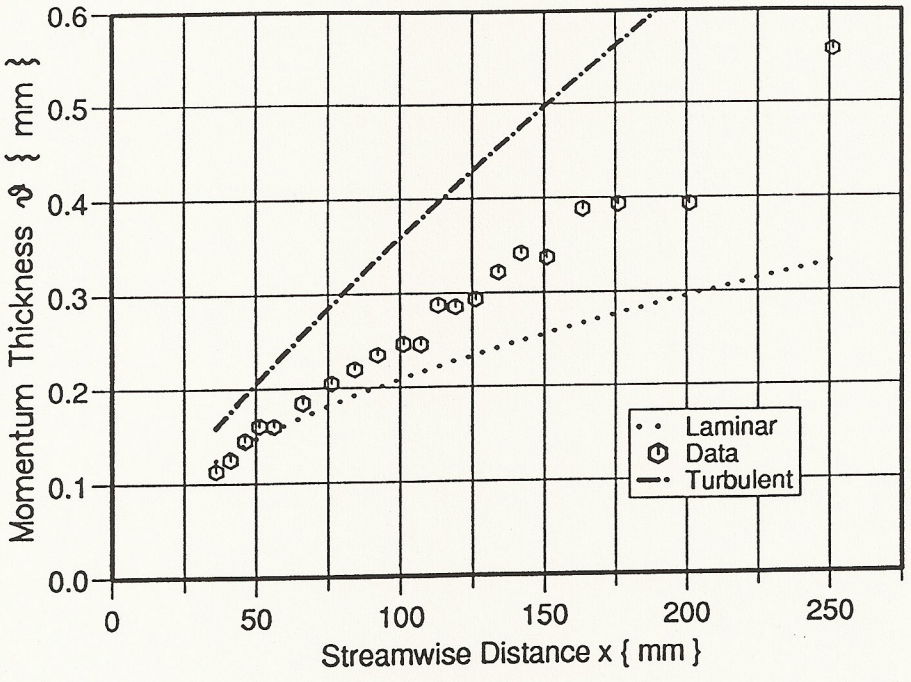


Figure 5.37 Distribution of the Boundary Layer Momentum Thickness
C4 Plate U_∞ = 15 m/s Tu_∞ = 4 %

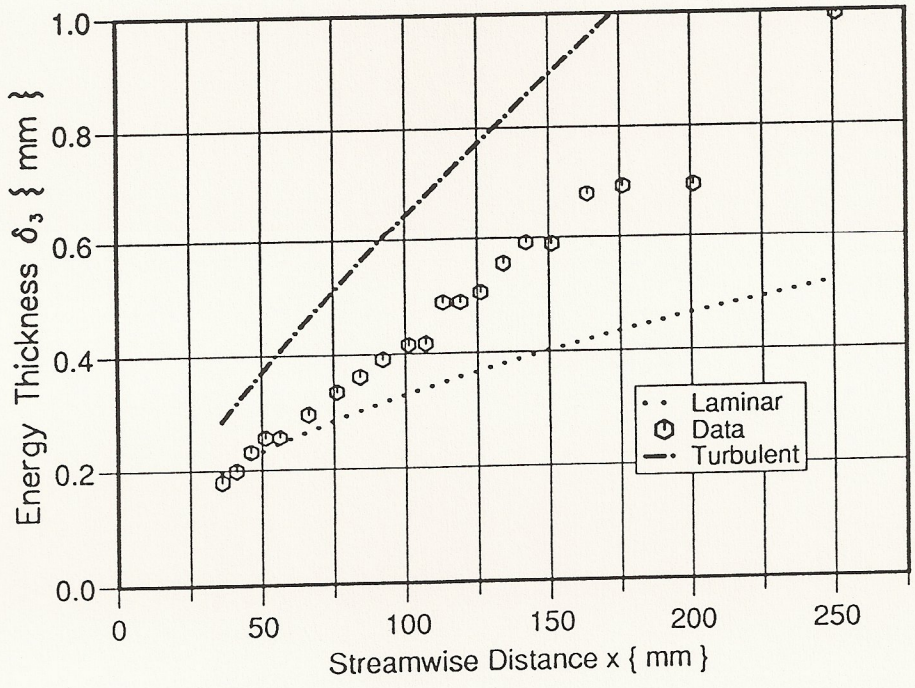


Figure 5.38 Distribution of the Boundary Layer Energy Thickness
C4 Plate U_∞ = 15 m/s Tu_∞ = 4 %

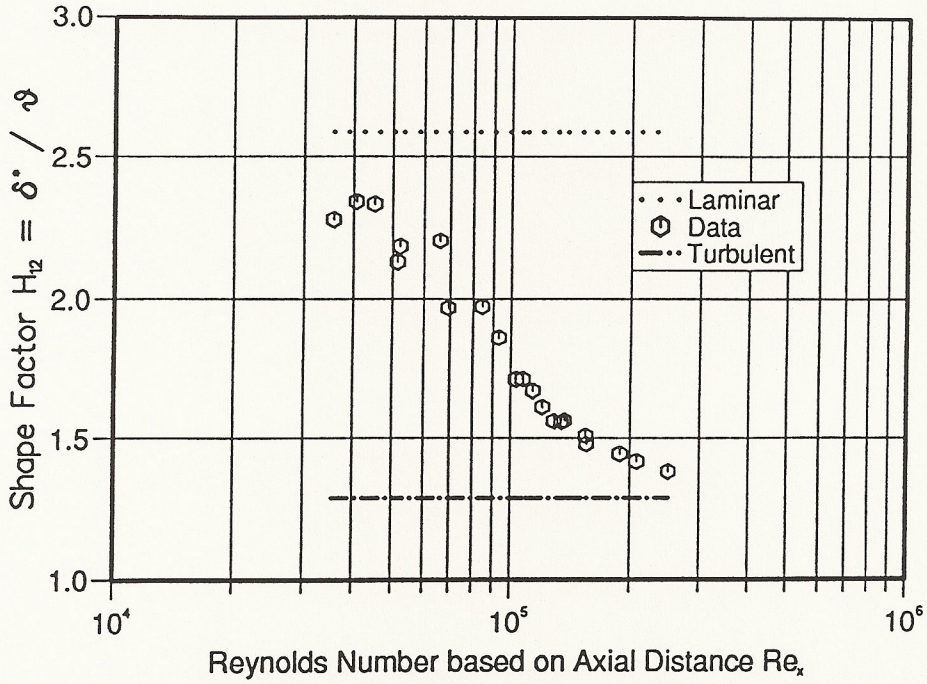


Figure 5.39	Shape Factor H_{12} Distribution C4 Plate U_∞ = 15 m/s Tu_∞ = 4 %

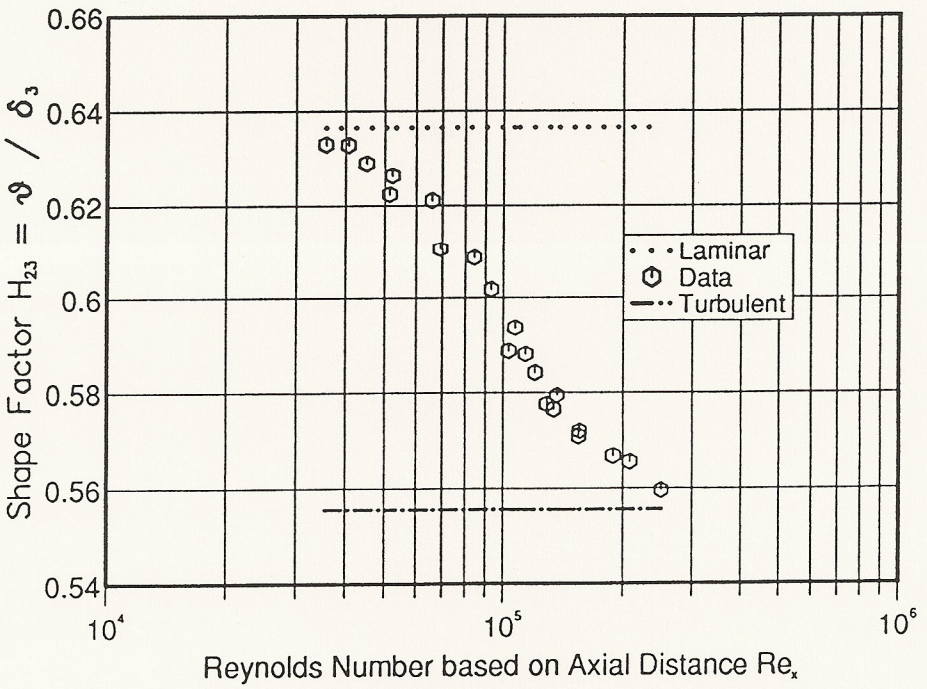


Figure 5.40	Shape Factor H_{23} Distribution C4 Plate U_∞ = 15 m/s Tu_∞ = 4 %

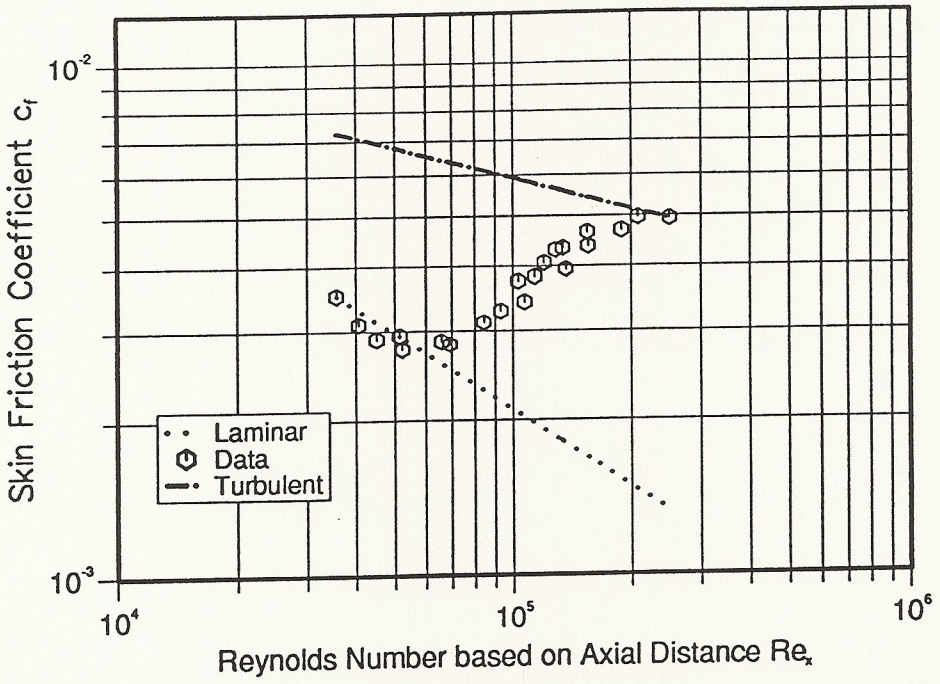


Figure 5.41	Skin Friction Coefficient Distribution C4 Plate U_∞ = 15 m/s Tu_∞ = 4 %

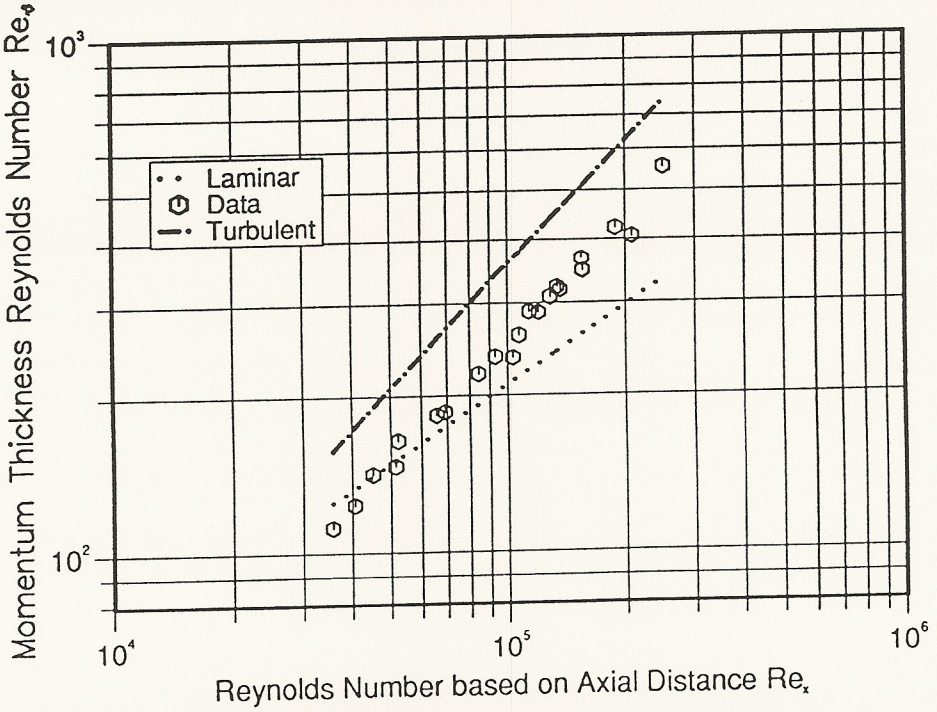


Figure 5.42	Momentum Thickness Reynolds Number Distribution C4 Plate U_∞ = 15 m/s Tu_∞ = 4 %

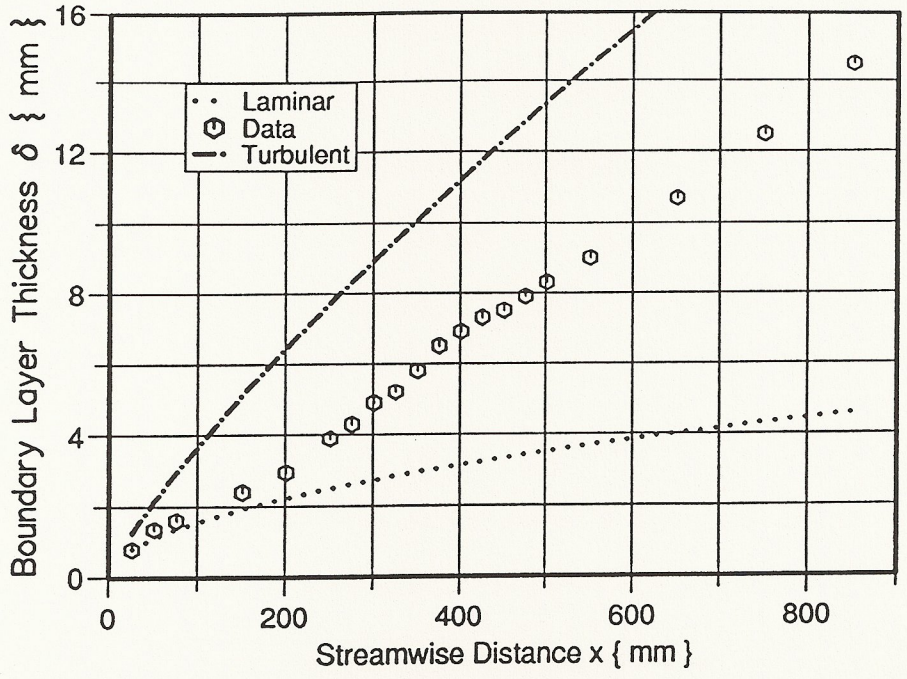


Figure 5.43	Distribution of the Boundary Layer Thickness C4 Plate U_∞ = 15 m/s Tu_∞ = 1.8 %

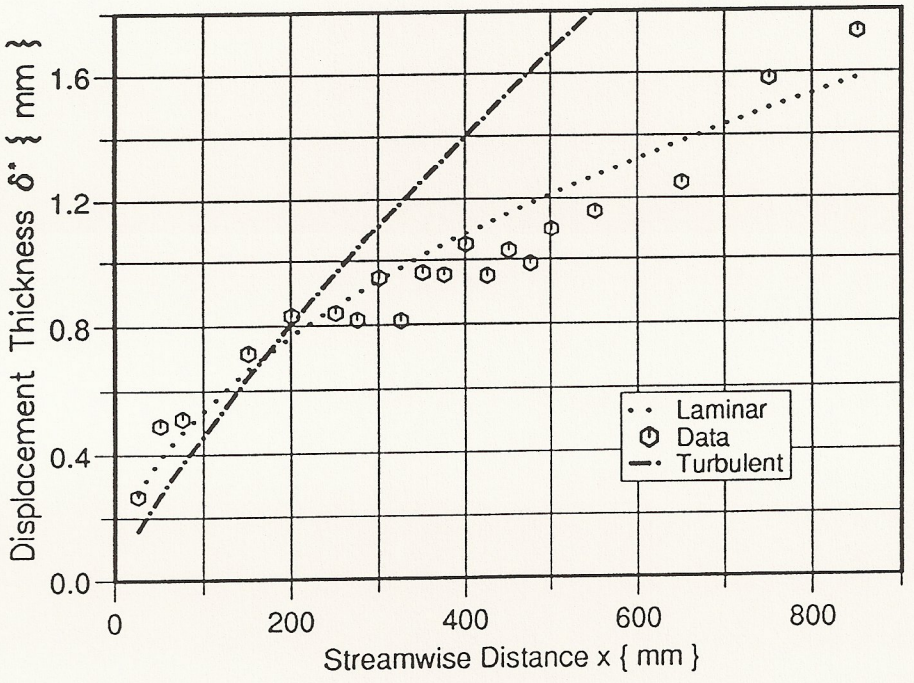


Figure 5.44	Distribution of the Boundary Layer Displacement Thickness C4 Plate U_∞ = 15 m/s Tu_∞ = 1.8 %

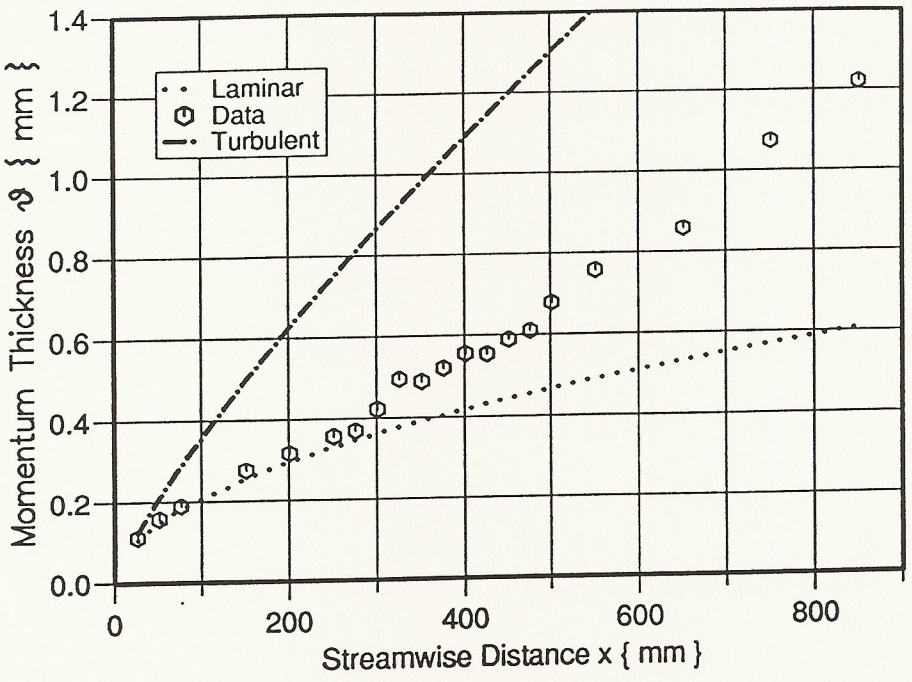


Figure 5.45	Distribution of the Boundary Layer Momentum Thickness C4 Plate U_∞ = 15 m/s Tu_∞ = 1.8 %

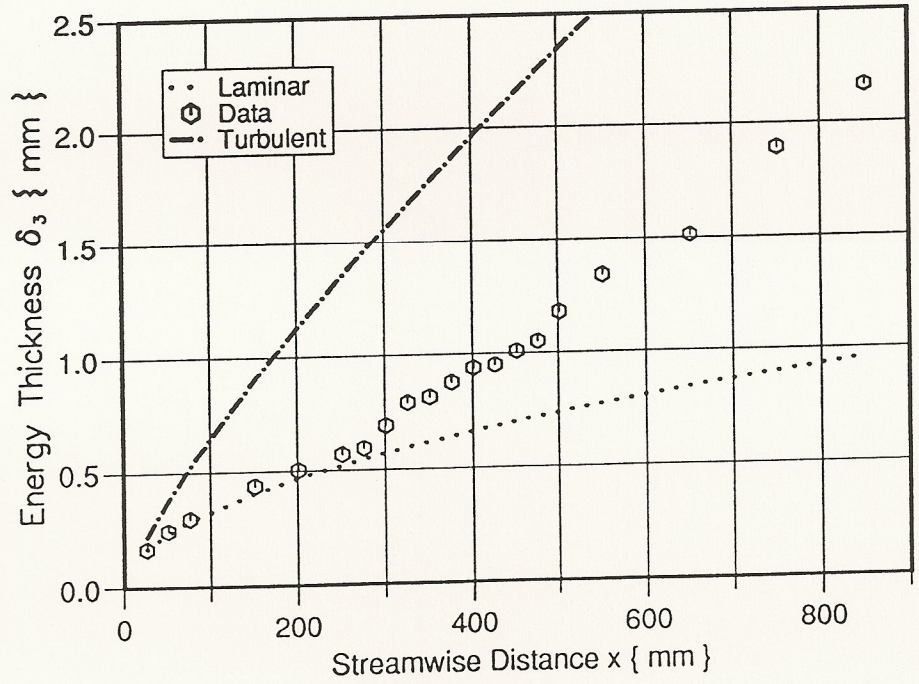


Figure 5.46	Distribution of the Boundary Layer Energy Thickness C4 Plate U_∞ = 15 m/s Tu_∞ = 1.8 %

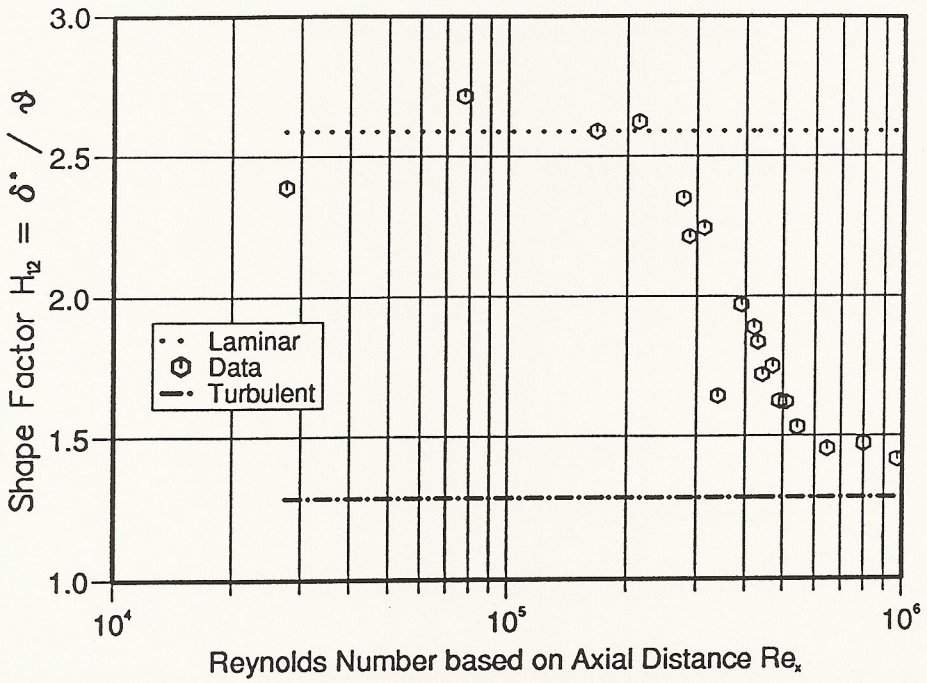


Figure 5.47	Shape Factor H_{12} Distribution C4 Plate U_∞ = 15 m/s Tu_∞ = 1.8 %

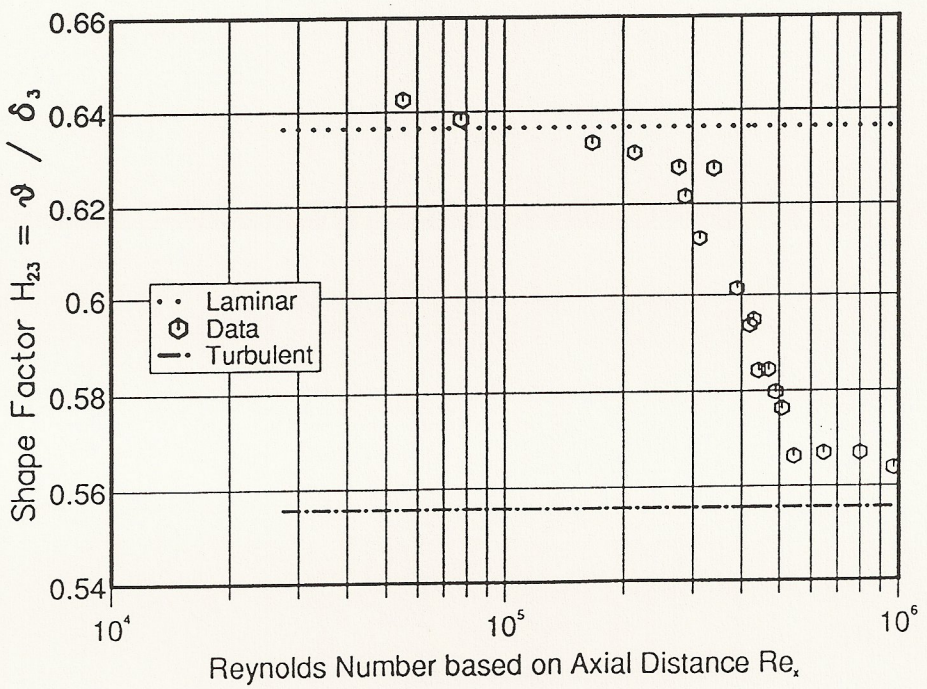


Figure 5.48	Shape Factor H_{23} Distribution C4 Plate U_∞ = 15 m/s Tu_∞ = 1.8 %

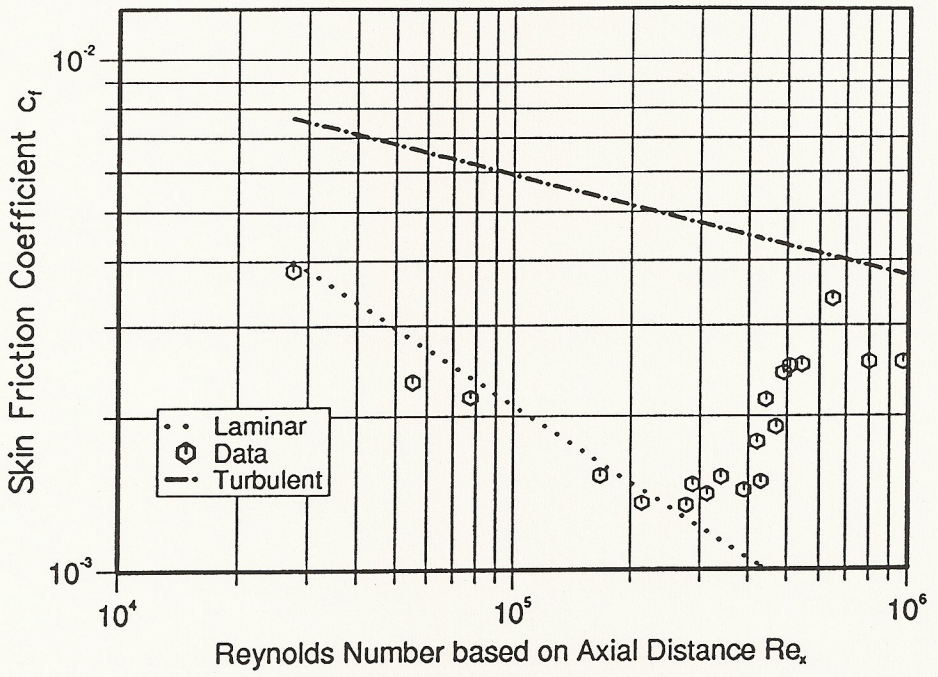


Figure 5.49	Skin Friction Coefficient Distribution C4 Plate U_∞ = 15 m/s Tu_∞ = 1.8 %

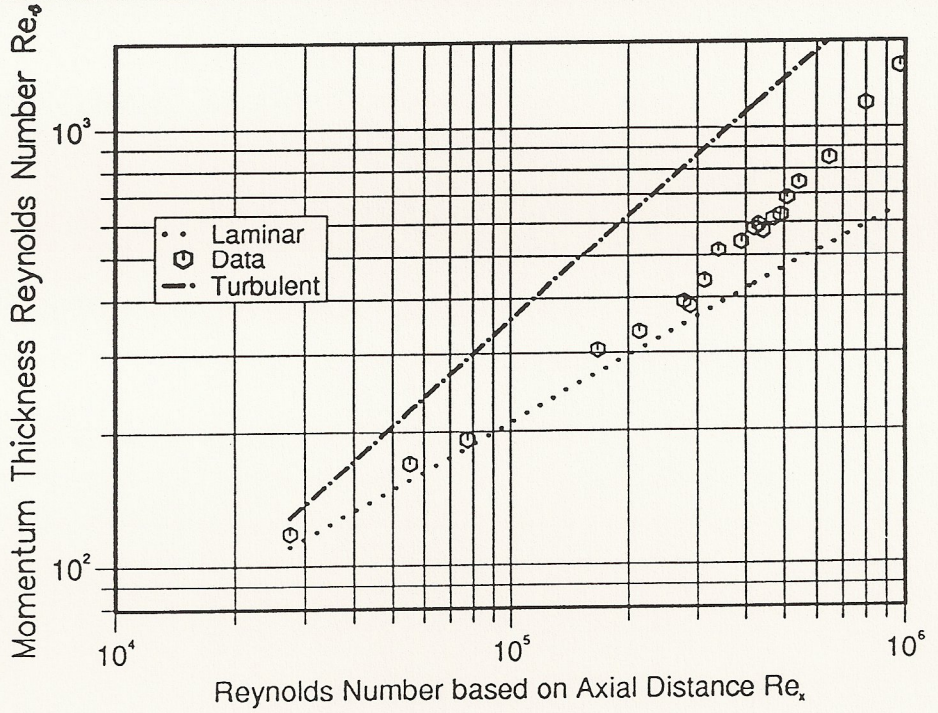


Figure 5.50	Momentum Thickness Reynolds Number Distibution C4 Plate U_∞ = 15 m/s Tu_∞ = 1.8 %

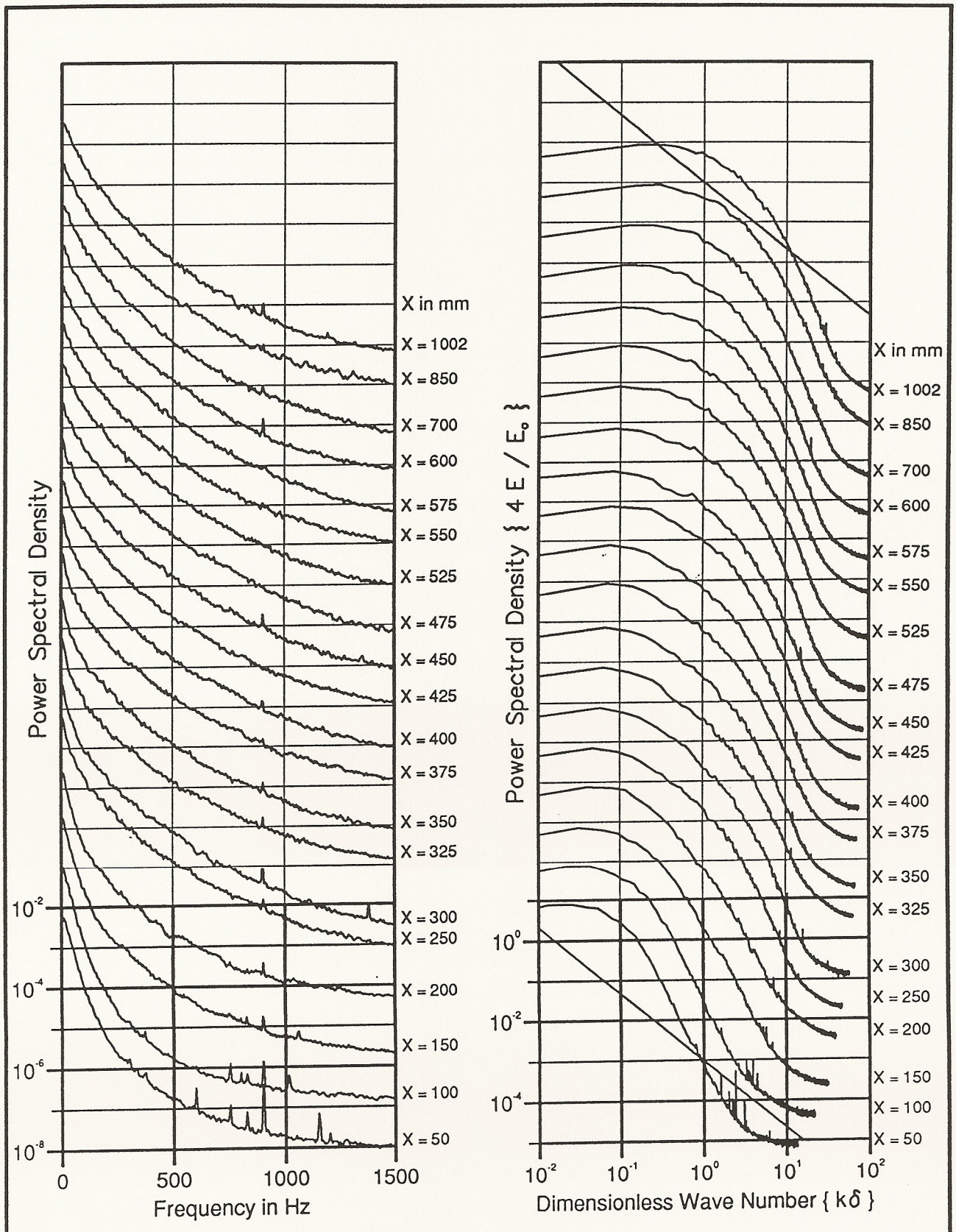


Figure 5.51	Power Spectral Density on the Frequency and Wave Number Domain C4 Plate U_∞ = 5 m/s Tu_∞ = 4 % Y = 0.2 mm

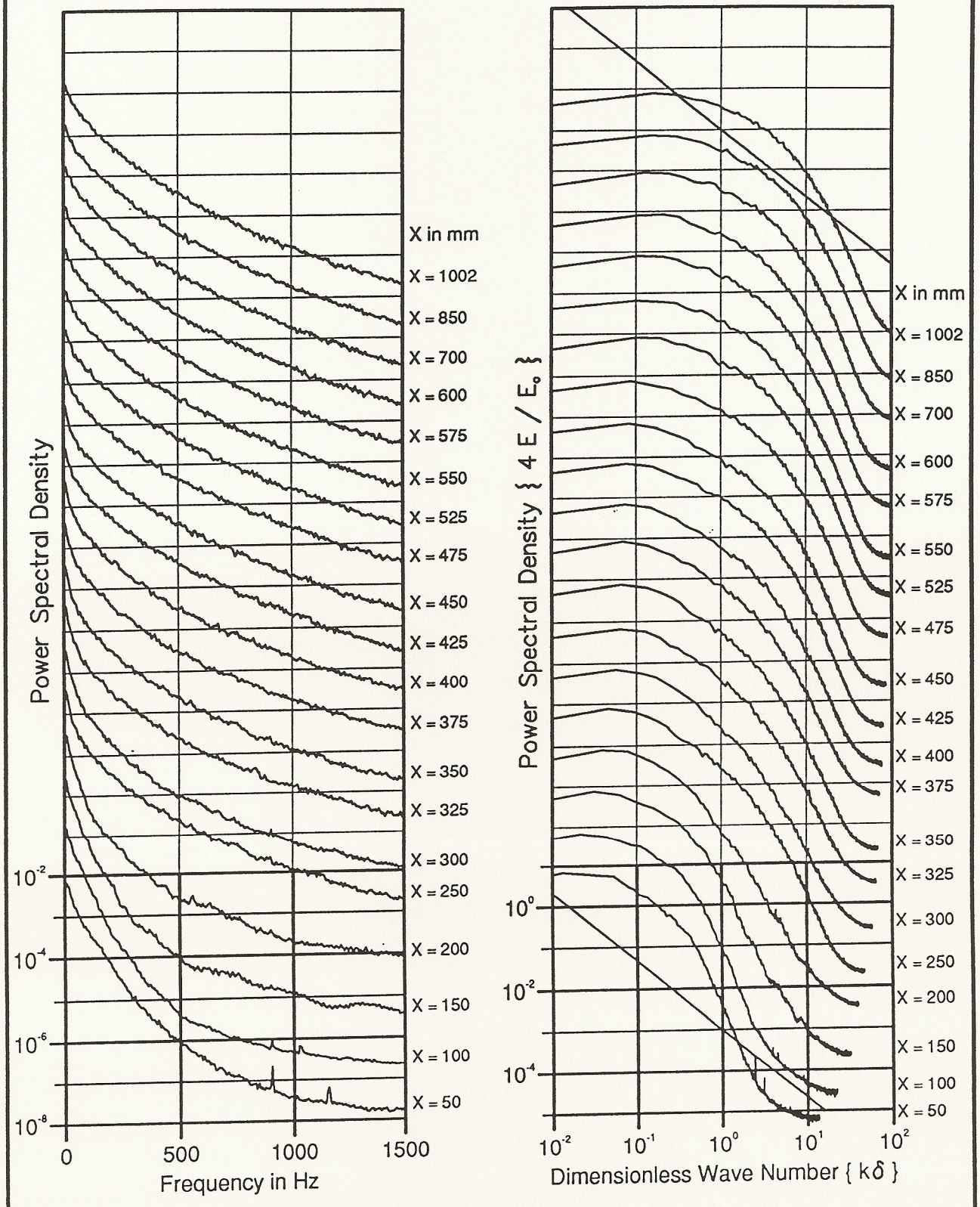


Figure 5.52	Power Spectral Density on the Frequency and Wave Number Domain C4 Plate U_∞ = 5 m/s Tu_∞ = 4 % Y = 1.0 mm

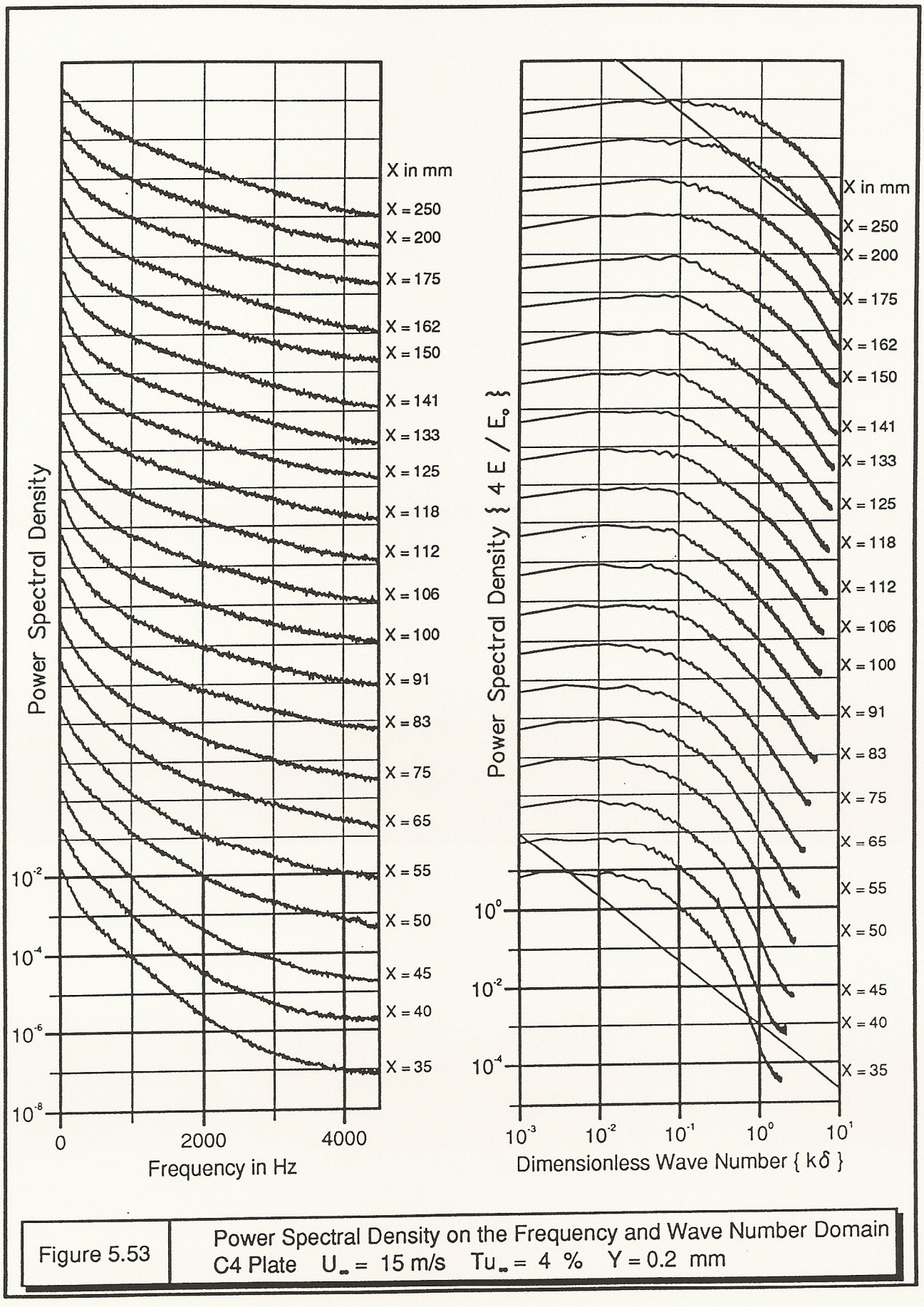


Figure 5.53	Power Spectral Density on the Frequency and Wave Number Domain C4 Plate U_∞ = 15 m/s Tu_∞ = 4 % Y = 0.2 mm

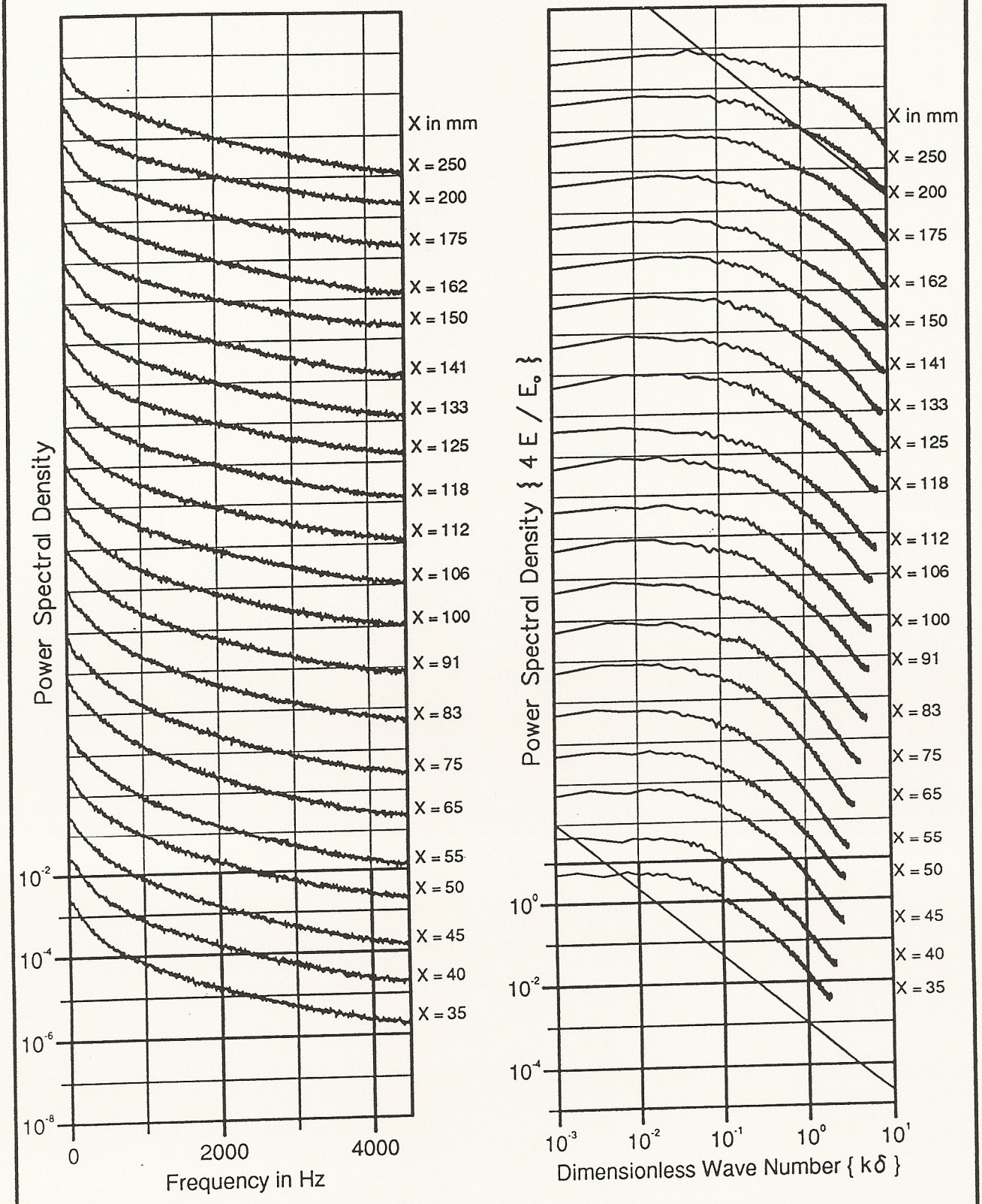


Figure 5.54	Power Spectral Density on the Frequency and Wave Number Domain C4 Plate U_∞ = 15 m/s Tu_∞ = 4 % Y = 1.0 mm

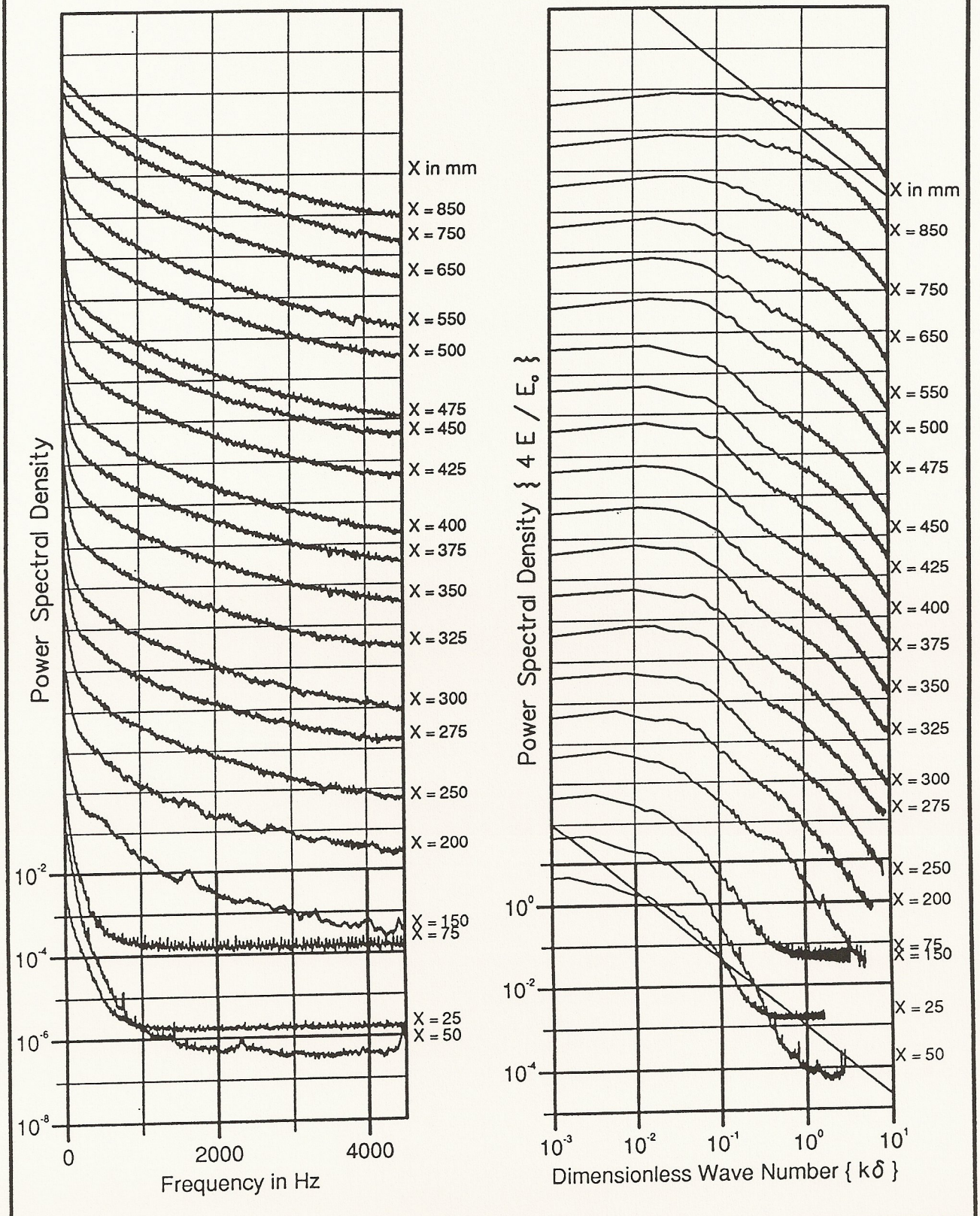


Figure 5.55	Power Spectral Density on the Frequency and Wave Number Domain C4 Plate U_∞ = 15 m/s Tu_∞ = 1.8 % Y = 0.2 mm

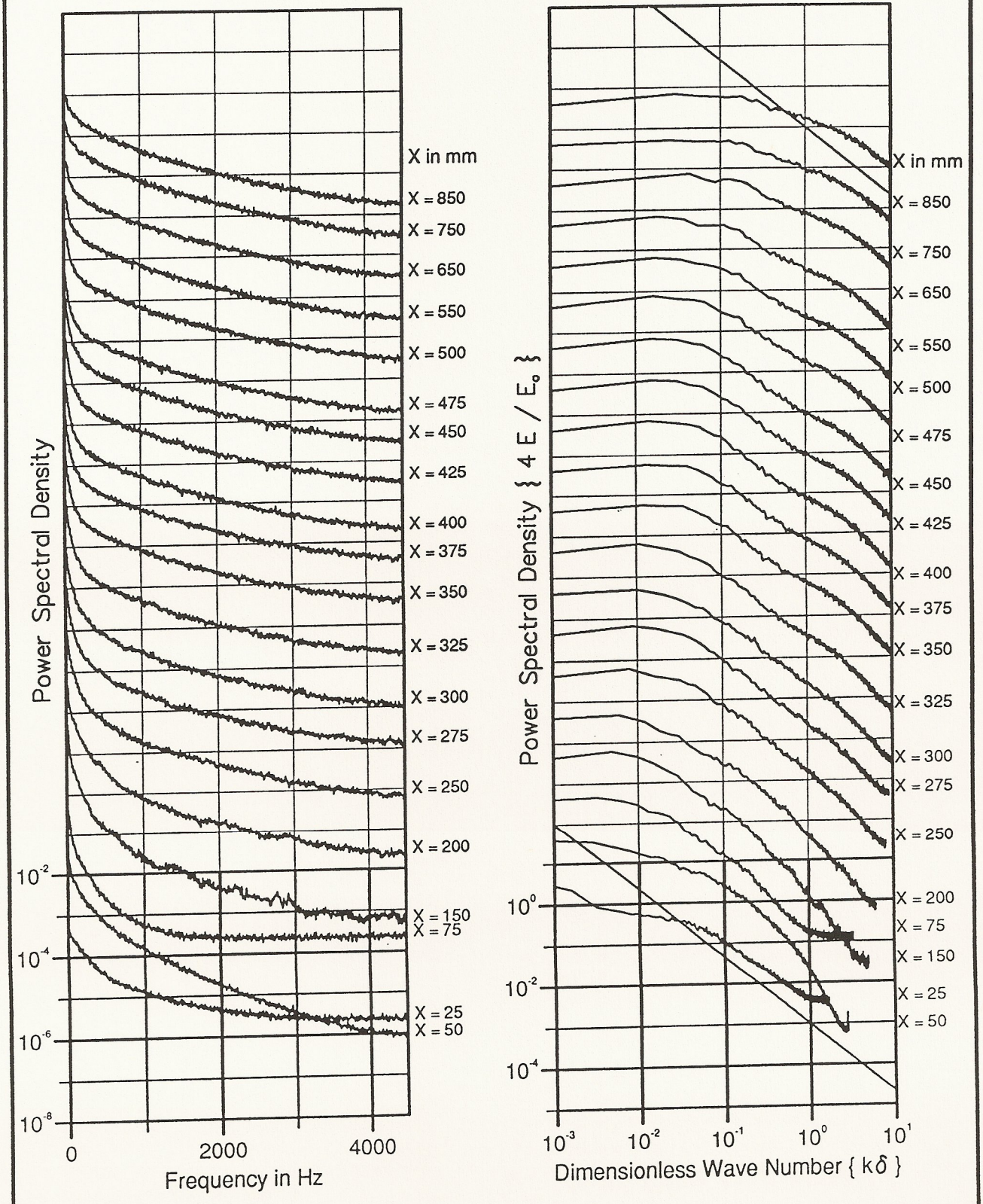


Figure 5.56	Power Spectral Density on the Frequency and Wave Number Domain C4 Plate U_∞ = 15 m/s Tu_∞ = 1.8 % Y = 1.0 mm

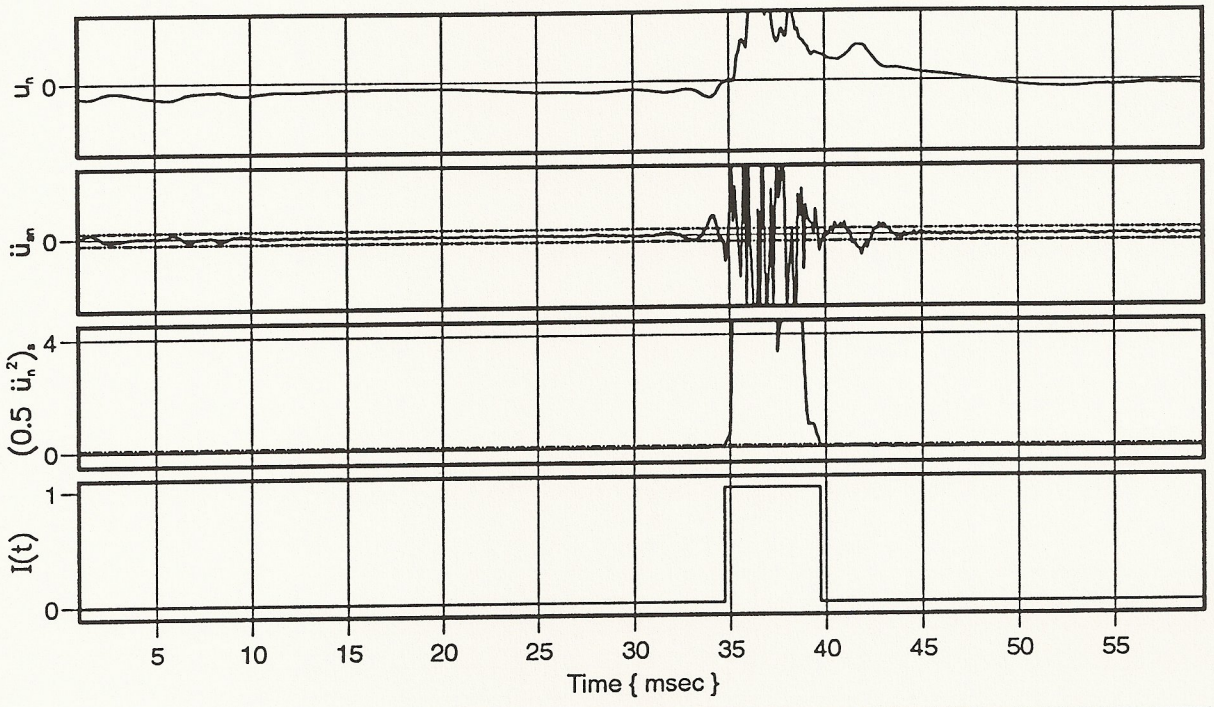


Figure 5.57	Velocity Signal Processing for Intermittency Determination C4 Plate U_∞ = 15 m/s Tu_∞ = 1.8 % X = 250 mm Y = 0.2 mm

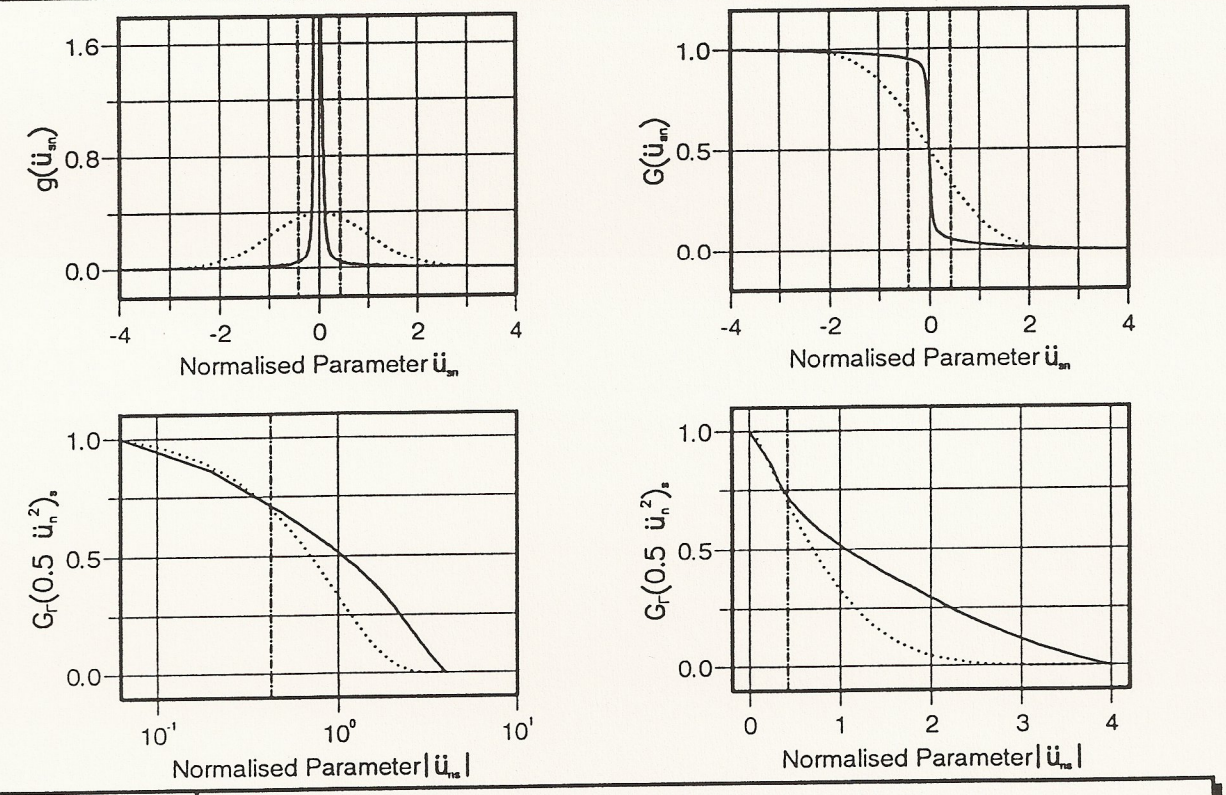


Figure 5.58	Probability Density Distributions of the Velocity Signals C4 Plate U_∞ = 15 m/s Tu_∞ = 1.8 % X = 250 mm Y = 0.2 mm

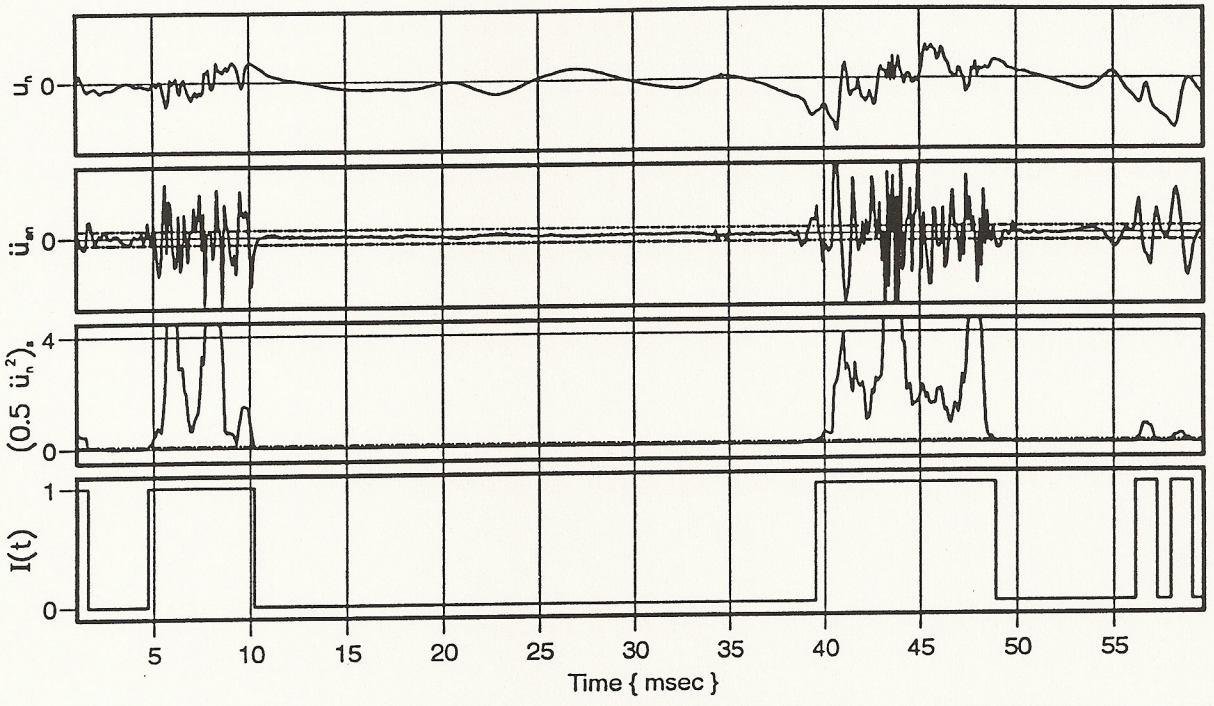


Figure 5.59	Velocity Signal Processing for Intermittency Determination C4 Plate U_∞ = 15 m/s Tu_∞ = 1.8 % X = 300 mm Y = 1.0 mm

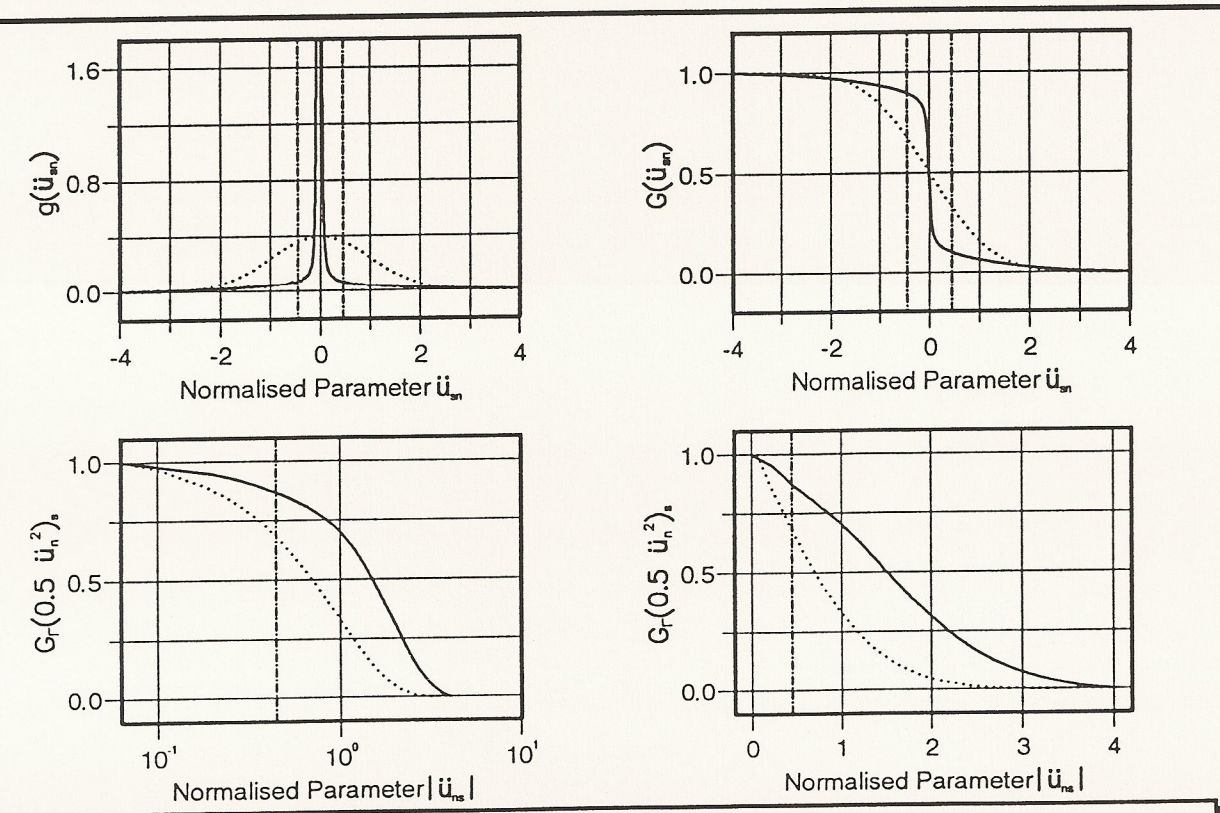


Figure 5.60	Probability Density Distributions of the Velocity Signals C4 Plate U_∞ = 15 m/s Tu_∞ = 1.8 % X = 300 mm Y = 1.0 mm

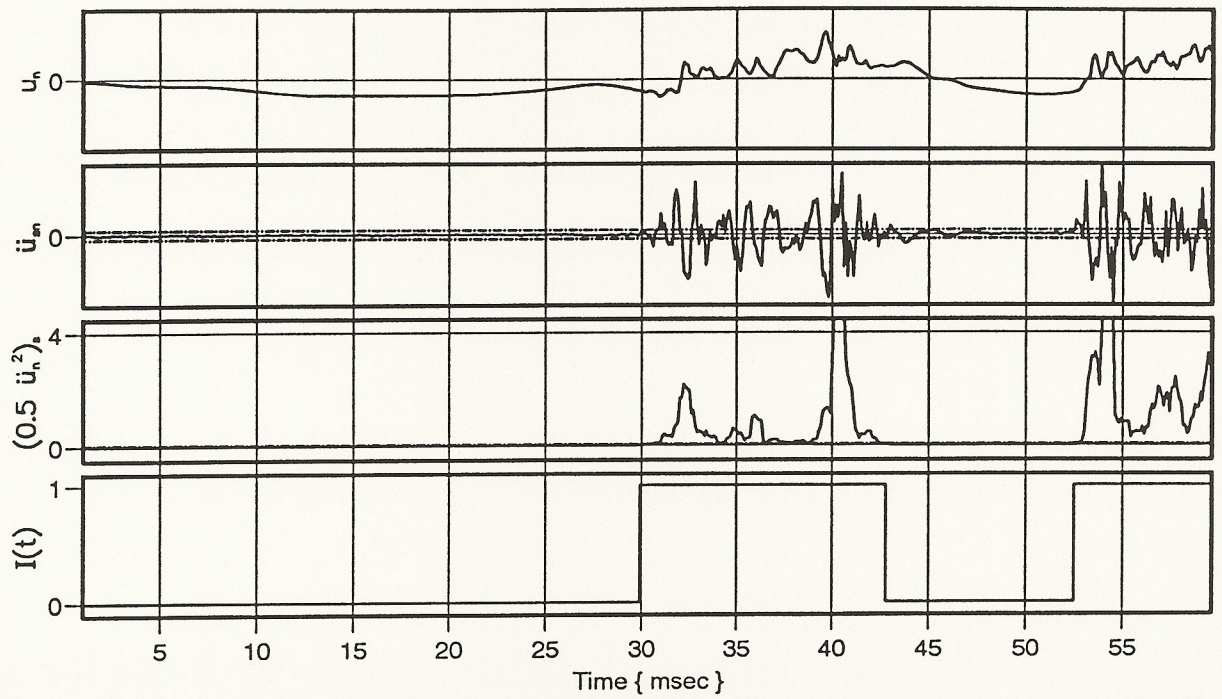


Figure 5.61	Velocity Signal Processing for Intermittency Determination C4 Plate U_∞ = 15 m/s Tu_∞ = 1.8 % X = 400 mm Y = 0.2 mm

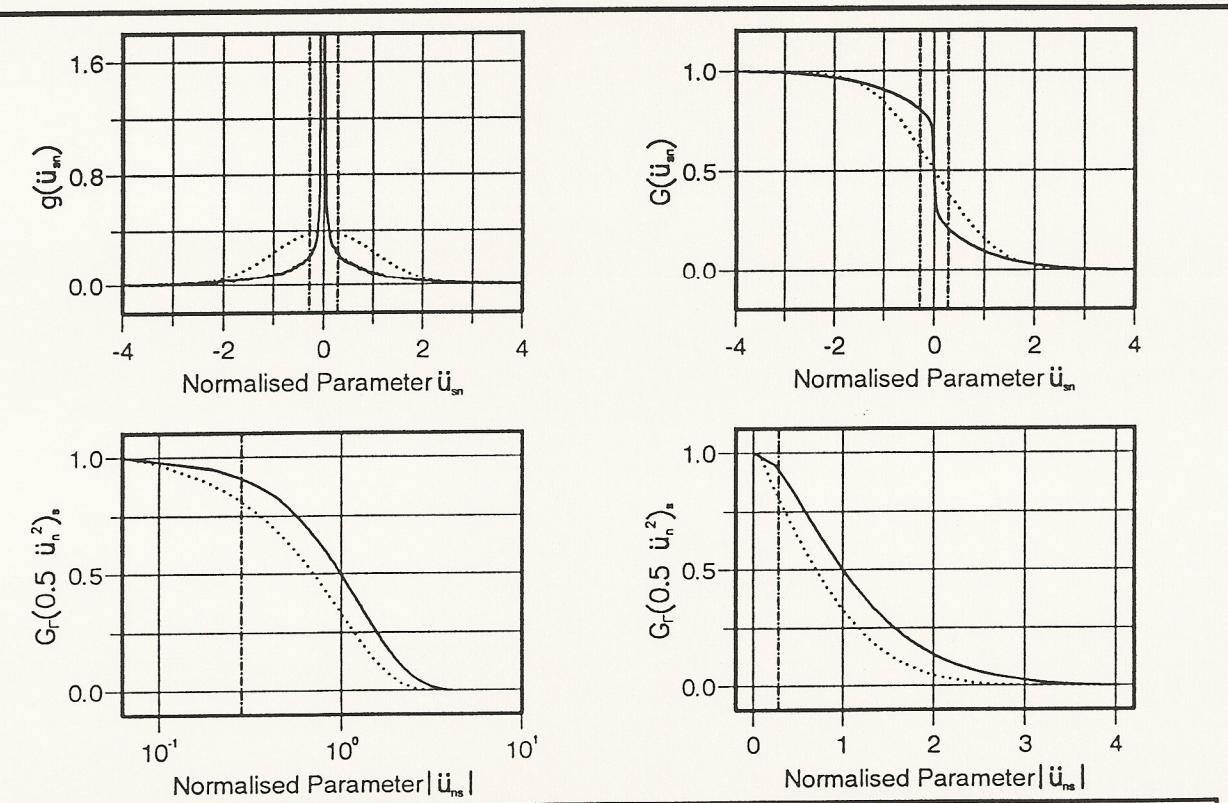


Figure 5.62	Probability Density Distributions of the Velocity Signals C4 Plate U_∞ = 15 m/s Tu_∞ = 1.8 % X = 400 mm Y = 0.2 mm

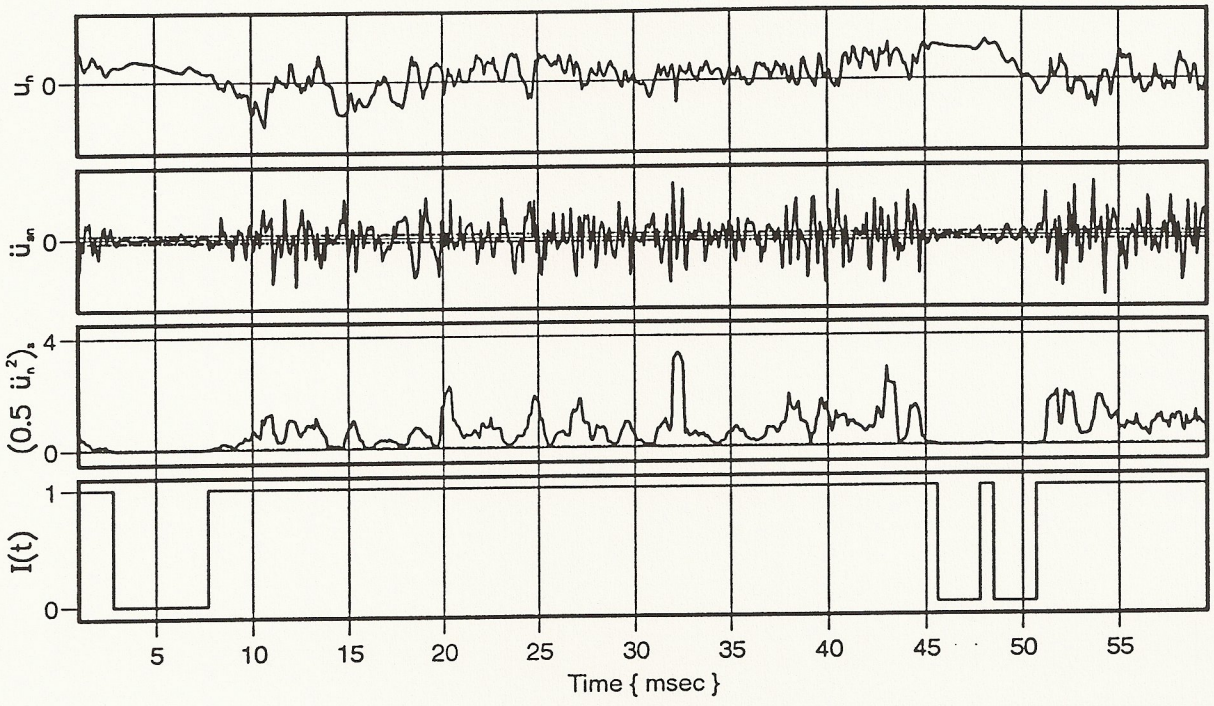


Figure 5.63	Velocity Signal Processing for Intermittency Determination C4 Plate U_∞ = 15 m/s Tu_∞ = 1.8 % X = 550 mm Y = 1.0 mm

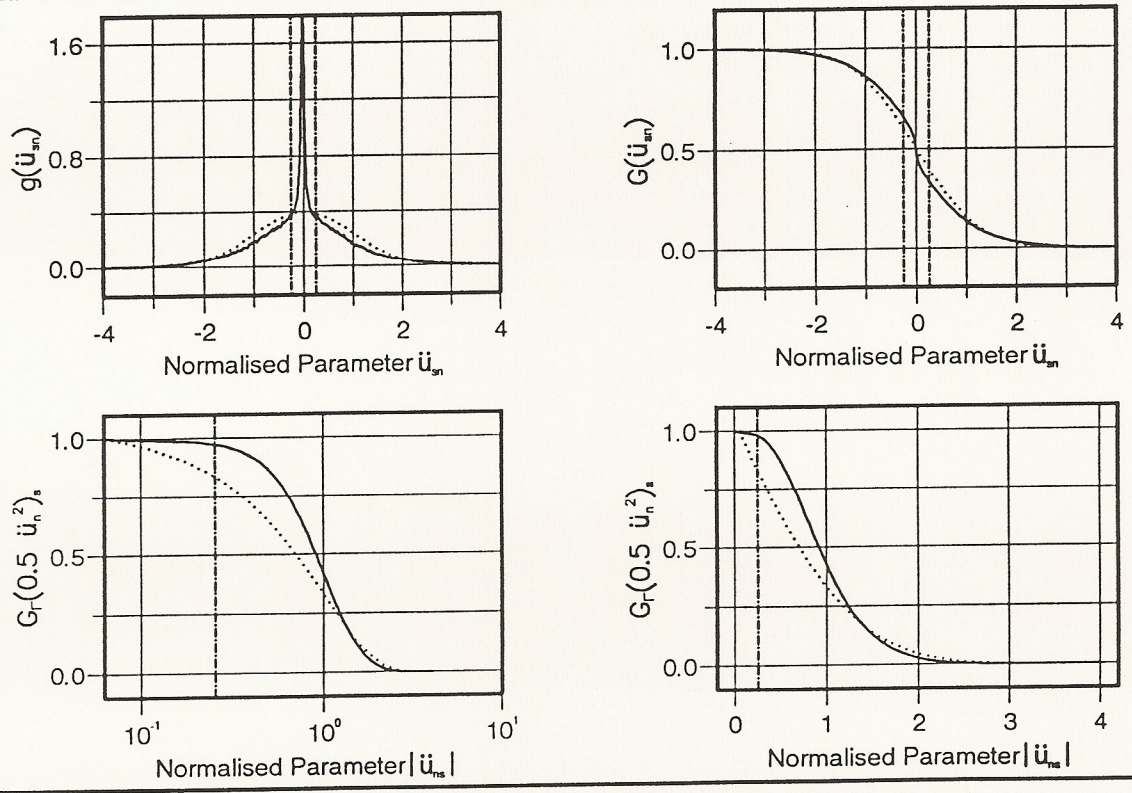


Figure 5.64	Probability Density Distributions of the Velocity Signals C4 Plate U_∞ = 15 m/s Tu_∞ = 1.8 % X = 550 mm Y = 1.0 mm

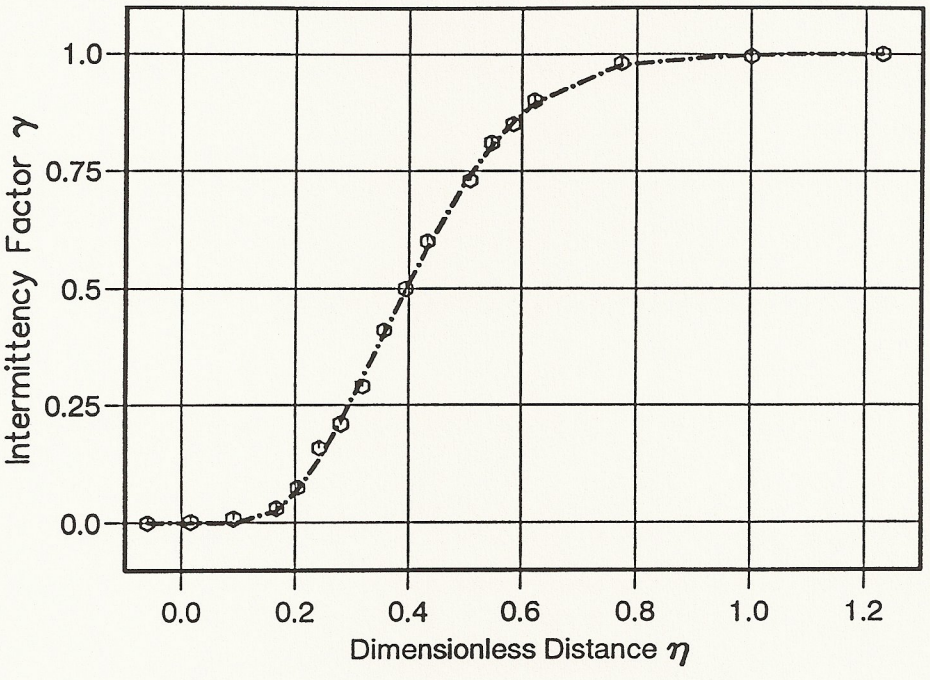


Figure 5.65	Intermittency Factor Distribution as a Function of η C4 Plate U_∞ = 5 m/s Tu_∞ = 4 %

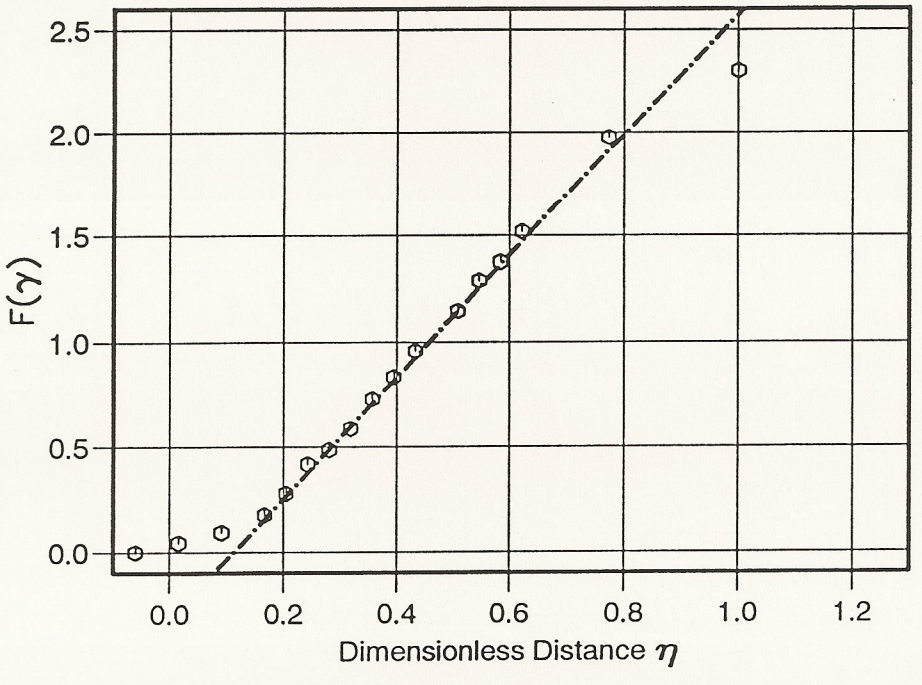


Figure 5.66	Determination of Transition Inception Using Narasimha Procedure C4 Plate U_∞ = 5 m/s Tu_∞ = 4 %

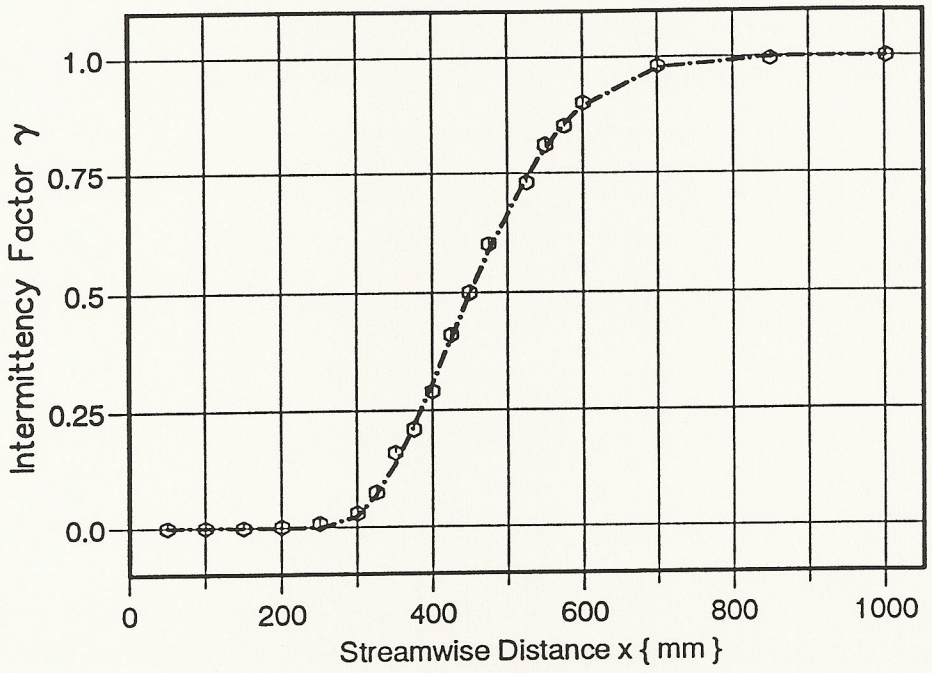


Figure 5.67	Intermittency Factor Distribution in the Physical Plane C4 Plate U_∞ = 5 m/s Tu_∞ = 4 %

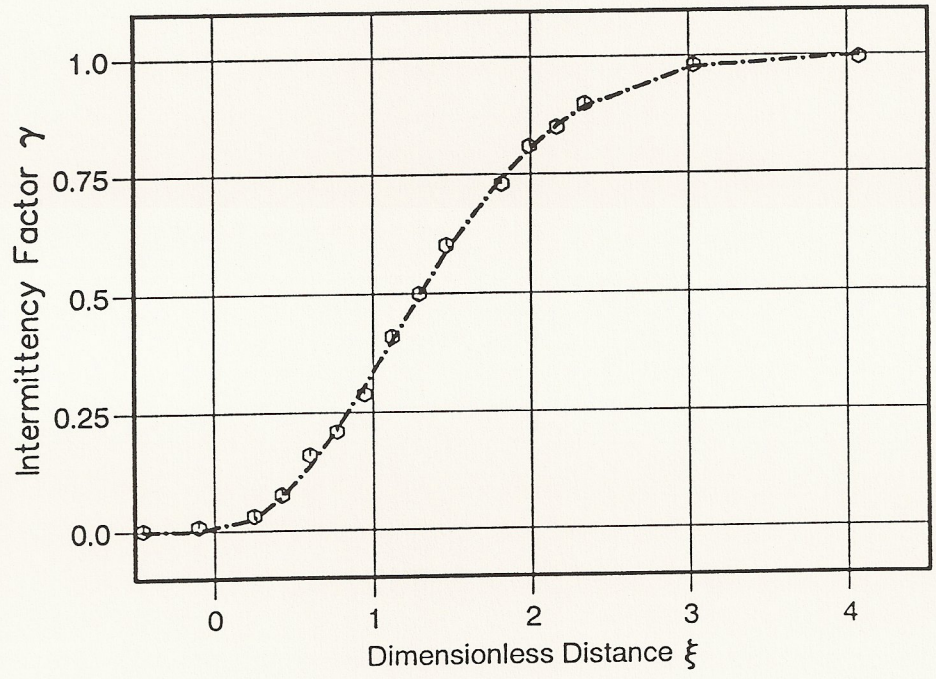


Figure 5.68	Intermittency Factor Distribution as a Function of ξ C4 Plate U_∞ = 5 m/s Tu_∞ = 4 %

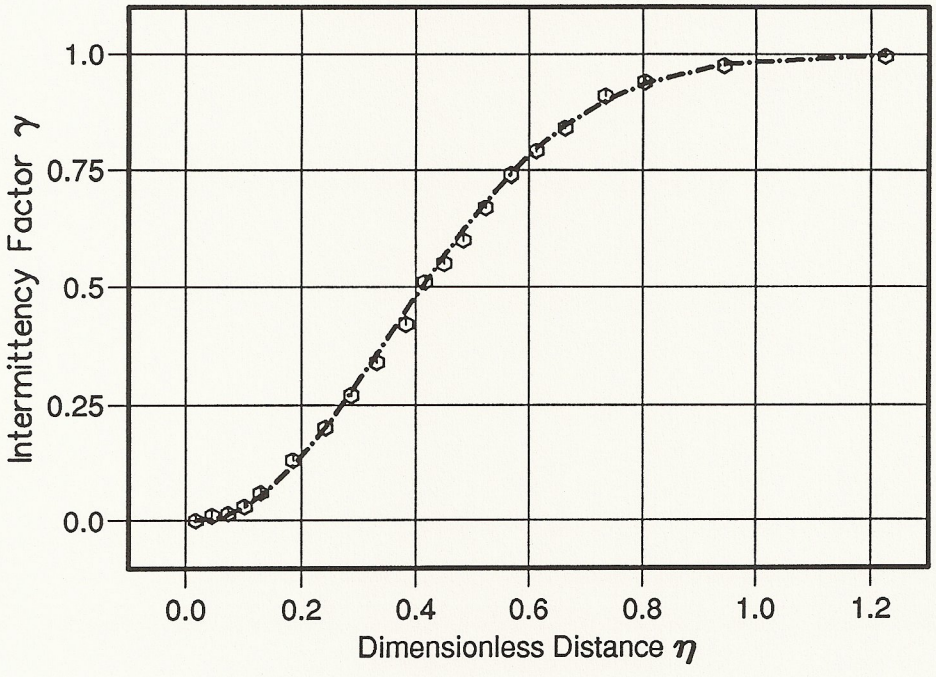


Figure 5.69	Intermittency Factor Distribution as a Function of η C4 Plate U_∞ = 15 m/s Tu_∞ = 4 %

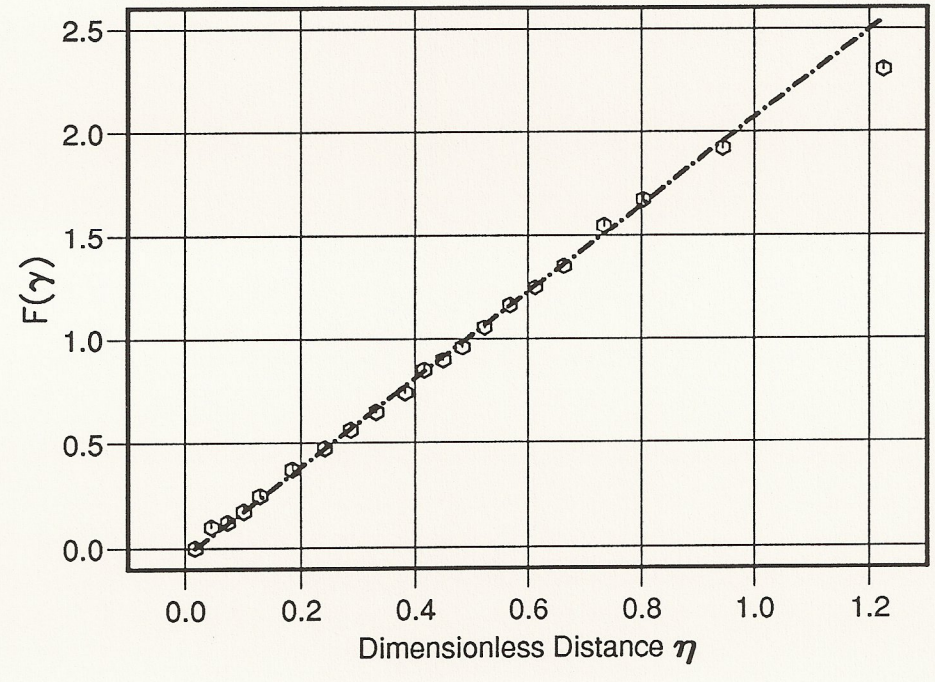


Figure 5.70	Determination of Transition Inception Using Narasimha Procedure C4 Plate U_∞ = 15 m/s Tu_∞ = 4 %

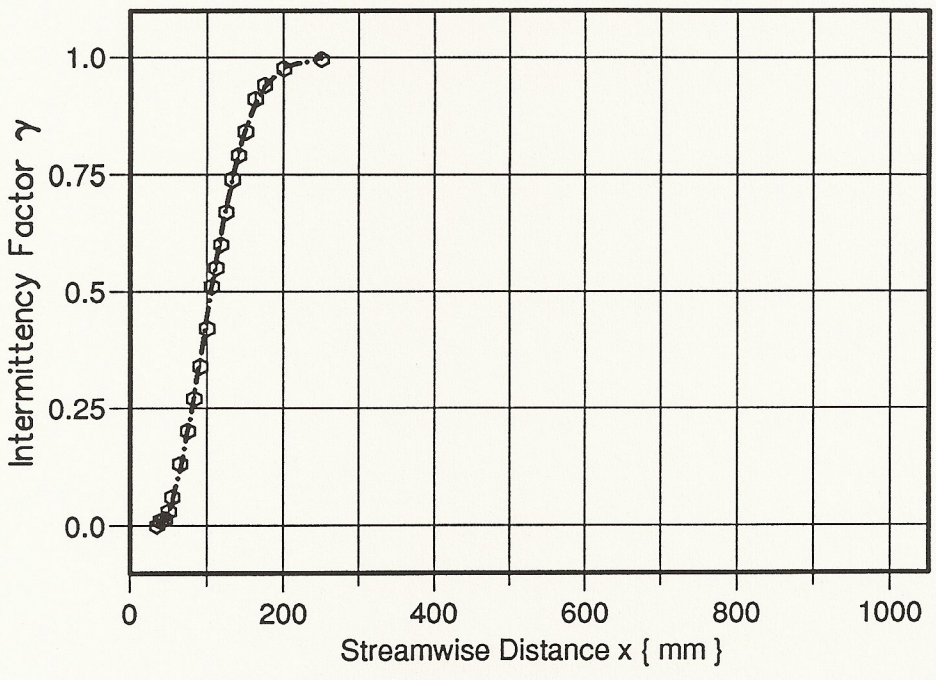


Figure 5.71 Intermittency Factor Distribution in the Physical Plane
C4 Plate U_∞ = 15 m/s Tu_∞ = 4 %

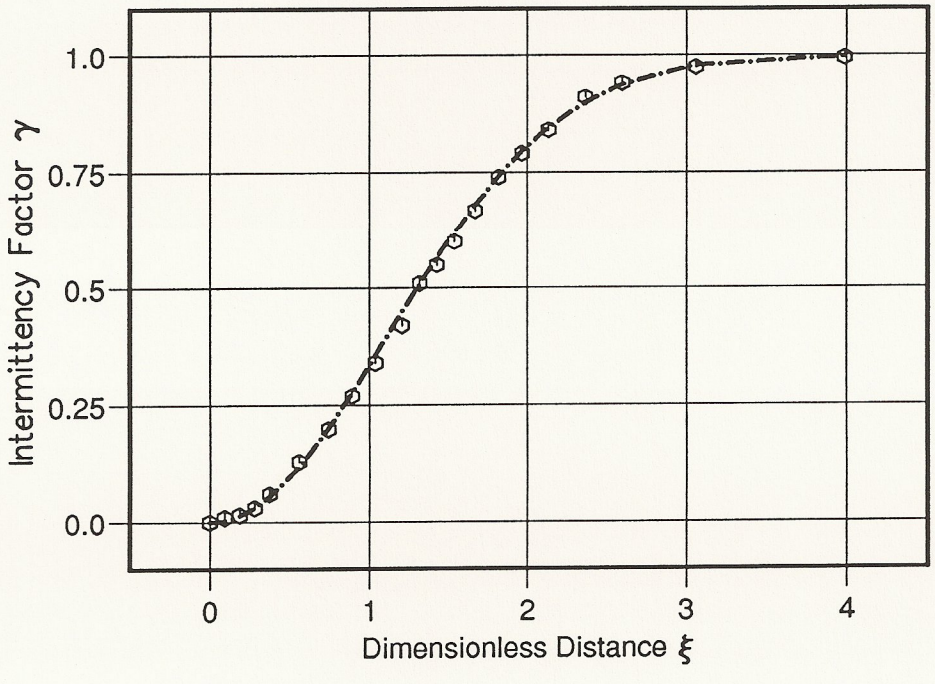


Figure 5.72 Intermittency Factor Distribution as a Function of ξ
C4 Plate U_∞ = 15 m/s Tu_∞ = 4 %

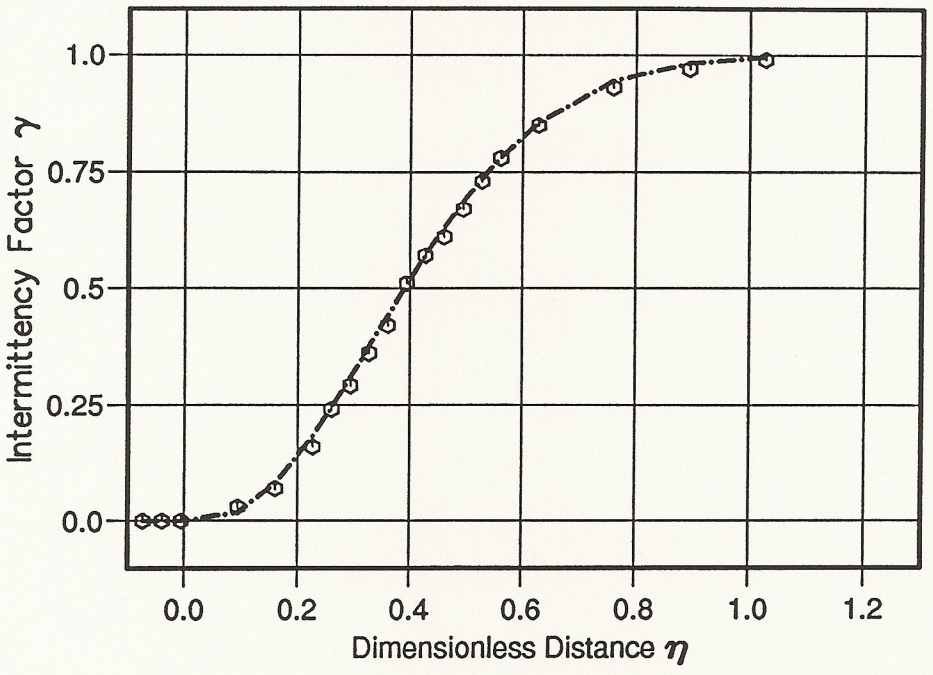


Figure 5.73	Intermittency Factor Distribution as a Function of η C4 Plate U_∞ = 15 m/s Tu_∞ = 1.8 %

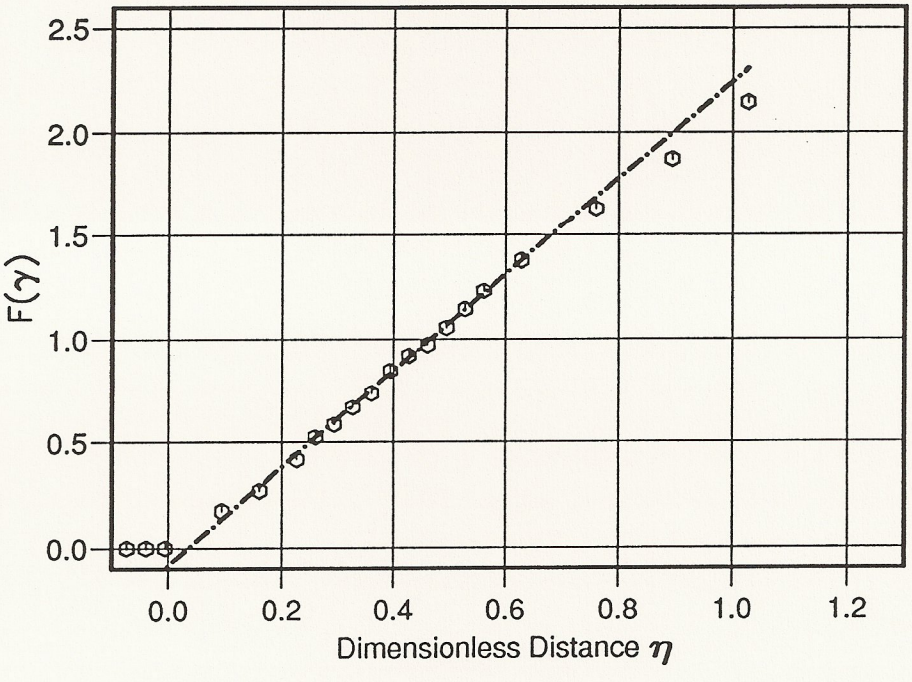


Figure 5.74	Determination of Transition Inception Using Narasimha Procedure C4 Plate U_∞ = 15 m/s Tu_∞ = 1.8 %

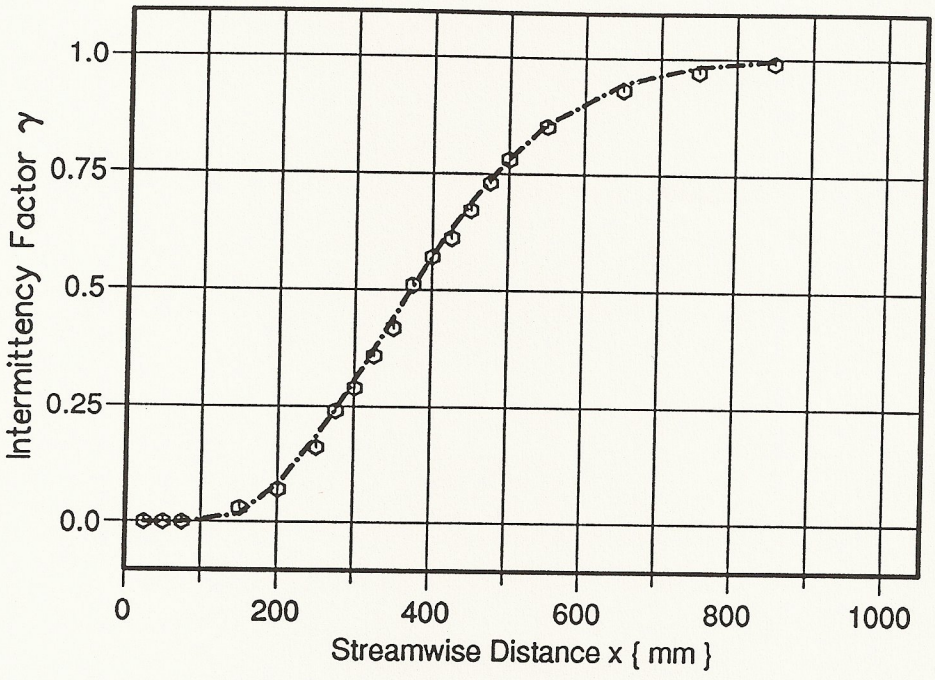


Figure 5.75 Intermittency Factor Distribution in the Physical Plane
C4 Plate U_∞ = 15 m/s Tu_∞ = 1.8 %

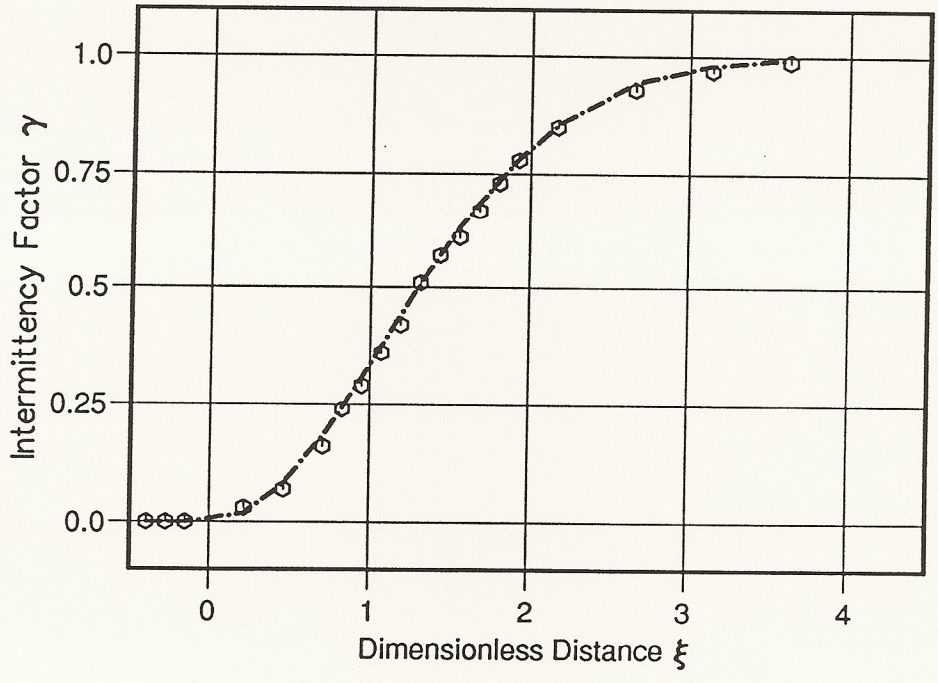


Figure 5.76 Intermittency Factor Distribution as a Function of ξ
C4 Plate U_∞ = 15 m/s Tu_∞ = 1.8 %

CHAPTER 6

Computational Approach

CHAPTER 6

Computational Approach

6.1 INTRODUCTION

During the last two decades, computational fluid dynamics has become more and more successful in predicting efficiently a wide range of flow phenomena. This process has been assisted by the significant advances in computer technology that have been taking place in parallel to the development of the computational methods. Computational fluid dynamics is currently gaining more confidence within the industrial world. This is mainly due to the successful application of CFD in a wide variety of complicated engineering problems.

In the previous chapters, a detailed account of the experimental investigation undertaken has been given. This chapter on the other hand, describes a computational investigation of a range of flow phenomena related to the boundary layer transition as well as to the flow around the leading edge of turbomachinery blading. The present computational approach is complementary to the experimental investigation of the transitional boundary layer of the flat plates and should be regarded as an attempt to develop a global picture of the laminar to turbulent transition phenomena in turbomachinery flows.

Similarly to the experimental arrangement, the turbomachinery flow environment has been simulated with the flow field around flat plates with various leading edge shapes. The efficiency of the computational methods employed in the numerical simulation of the above phenomena has been considered. The ability of the current turbulence models to predict the onset and extent of transition under a variety of free

stream conditions has been evaluated. In order to achieve these objectives, a series of three computational test cases has been prepared. The initial approach to this issue involved the modelling of the laminar to turbulent transition effect independently from the additional complexity of the leading edge flow.

The first test case involved a flat plate with cylindrical leading edge in accordance with the experimental test case described in the previous chapters. The second test case has been prepared in order to model the flow over a flat plate with elliptical leading edge which does not involve boundary layer separation similarly to the experimental test case involving the C4 leading edge. In the first two test cases, no turbulence modelling has been employed in an attempt to isolate the leading edge flow effects from the boundary layer transition. Finally, the last computational test case has been prepared in order to simulate the experimental results obtained on the flat plate with the sharp leading edge. However, the obtained results can be regarded as relevant for the previous test case in which the boundary layer starts to develop on a flat surface following an unseparated leading edge flow.

The following sections of this chapter present a short review of the literature that is closely related to the computational methods employed in the present study. Subsequently, the present computational approach is discussed in detail. The numerical scheme employed in these computations is presented and finally the obtained results are analysed.

6.2 COMPUTATIONAL METHODS

For many years, the wider application of computational fluid dynamics has been restricted by the very high cost and the limited power of the available computing machines. However, computers are becoming more and more powerful and cost-effective. The successful application of CFD in a wide range of engineering problems has been assisted by the technological advances and the development of more powerful numerical methods that can deal with the various physical problems involved in fluid dynamics. The main objective of this section of the thesis is to summarise the various numerical methods and solution techniques that are closely connected to the computational methods employed in this study.

The mathematical description of many important physical phenomena can be accomplished using a set of partial differential equations that described the fundamental conservation laws. A wide variety of numerical methods have been developed in order to model fluid flow. In most cases, fluid flow phenomena with significant engineering importance can be described using the time averaged form of the Navier-Stokes equations. Accordingly, the solution of the governing equations of the flow can be given in terms of time averaged quantities with practical importance (e.g. mean velocity, pressure, etc.).

Consider now, a two dimensional, steady and incompressible fluid flow on an x-y plane. The governing equations for the mean flow quantities can be written as follows:

Continuity Equation:

$$\frac{\partial \bar{u}}{\partial x} + \frac{\partial \bar{v}}{\partial y} = 0 \tag{6.1}$$

Momentum Equation in the x-direction:

$$\bar{u}\frac{\partial \bar{u}}{\partial x} + \bar{v}\frac{\partial \bar{u}}{\partial y} = -\frac{1}{\rho}\frac{\partial \bar{p}}{\partial x} + \nu\left(\frac{\partial^2 \bar{u}}{\partial x^2} + \frac{\partial^2 \bar{u}}{\partial y^2}\right) - \frac{\partial \overline{u'u'}}{\partial x} - \frac{\partial \overline{u'v'}}{\partial y} \tag{6.2}$$

Momentum Equation in the y-direction:

$$\bar{u}\frac{\partial \bar{v}}{\partial x} + \bar{v}\frac{\partial \bar{v}}{\partial y} = -\frac{1}{\rho}\frac{\partial \bar{p}}{\partial y} + \nu\left(\frac{\partial^2 \bar{v}}{\partial x^2} + \frac{\partial^2 \bar{v}}{\partial y^2}\right) - \frac{\partial \overline{v'u'}}{\partial x} - \frac{\partial \overline{v'v'}}{\partial y} \qquad (6.3)$$

In summary, there is one mean-flow conservation law and two mean-flow equations of motion. However, apart from the pressure, $\bar{p}$, and the mean velocity components, $\bar{u}$ and $\bar{v}$, the above set of differential equations includes the Reynolds stresses as independent variables. In the foregoing formulation, the Reynolds stresses account for the contribution of the turbulent motion into the mean momentum transfer. In general the Reynolds stresses can be expressed as follows:

Normal stresses:

$$\tau_{xx} = -\rho\,\overline{u'u'} = -\rho\,\overline{u'^2} \quad \textit{and} \quad \tau_{yy} = -\rho\,\overline{v'v'} = -\rho\,\overline{v'^2} \qquad (6.4)$$

Shear stresses:

$$\tau_{xy} = \tau_{yx} = -\rho\,\overline{u'v'} \qquad (6.5)$$

Accordingly, the time averaged Navier-Stokes equations, as presented above, result in a "closure problem" due to the existence of more unknown variables than the available equations. In order to overcome this problem, several attempts have been made to relate the Reynolds stresses to the mean flow quantities (e.g. u, v, p, etc.) and their gradients, in some physical and plausible manner. This constitutes a fundamental problem in turbulence modelling.

Among the various turbulence models that have been proposed, three kinds of models have received particular attention by a number of investigators, namely, the algebraic models, the two equation models and the Reynolds stress models. The first two are based on Boussinesq's assumption (see also Schlichting, 1979) that in time averaged turbulent flows the strain-stress law can be expressed in a similar way to the equivalent law for viscous laminar flows. In more simple terms, this assumption implies that the turbulent stresses can be expressed as a function of the velocity gradient using a proportionality parameter μ_t, as follows:

$$\tau_{xy} = -\rho\,\overline{u'v'} = \mu_t \frac{\partial \bar{u}}{\partial y} \qquad (6.6)$$

The turbulent viscosity, μ_t, is often referred to as eddy viscosity and unlike the fluid's viscosity, μ, should not be regarded as a property of the fluid. The value of the eddy viscosity varies a lot throughout the flow field and largely expresses the structure of turbulence at each particular location.

Prandtl's mixing length model, the Cebeci-Smith model and the Baldwin-Lomax model are merely a few of the several algebraic models that have been proposed in order to evaluate the shear stress using Boussinesq's assumption (for a more analytical description of the above models see also Abbott and Basco (1989), Anderson et al. (1984) and Bradshaw et al. (1981)). The main assumption involved in these models is that the production and dissipation of turbulence are the same and as a result turbulence is in equilibrium. Accordingly, the eddy viscosity can be estimated by giving an empirical value to a single scalar variable (e.g. a length scale in Prandtl's mixing length model). The main advantage of these models is that they are simple, easy to implement and they do not require the solution of any more additional differential equations (zero equation models). On the other hand, the principal disadvantage of these models is that they are not capable of describing turbulent flows containing more than one velocity and one length scale (Tennekes and Lumley, 1972).

The concept of eddy viscosity has been adopted as a fundamental assumption into the two-equation type of models including the k-ε turbulence model. These models are based on turbulence kinetic energy budgets and to a certain extent provide the means of studying the dynamics of turbulence. In more mathematical terms, the k-ε model involves the use of a transport equation for the turbulence kinetic energy per unit mass:

$$k = \frac{1}{2}\left(\overline{u'^2} + \overline{v'^2}\right) \tag{6.7}$$

and its dissipation rate:

$$\varepsilon = \left(\frac{\partial \bar{u}}{\partial y} + \frac{\partial \bar{v}}{\partial x}\right)^2 + \left(\frac{\partial \bar{u}}{\partial x}\right)^2 + \left(\frac{\partial \bar{v}}{\partial y}\right)^2 \tag{6.8}$$

These transport equations can be derived in exact form from the momentum equations. However, in the following formulation the higher order terms have been empirically quantified using a set of constants.

Turbulence Kinetic Energy Equation:

$$\bar{u}\frac{\partial k}{\partial x} + \bar{v}\frac{\partial k}{\partial y} = \frac{\nu_t}{\sigma_k}\left(\frac{\partial^2 k}{\partial x^2}+\frac{\partial^2 k}{\partial y^2}\right) + \nu_t G_s - C_D\varepsilon \tag{6.9}$$

Equation for the Dissipation Rate of Turbulence:

$$\bar{u}\frac{\partial \varepsilon}{\partial x} + \bar{v}\frac{\partial \varepsilon}{\partial y} = \frac{\nu_t}{\sigma_\varepsilon}\left(\frac{\partial^2 \varepsilon}{\partial x^2}+\frac{\partial^2 \varepsilon}{\partial y^2}\right) + C_1\nu_t\frac{\varepsilon}{k}G_s - C_2\frac{\varepsilon^2}{k} \tag{6.10}$$

where G_s represents the generation term that can be expressed as follows:

$$G_s = 2\left[\left(\frac{\partial \bar{u}}{\partial x}\right)^2 + \left(\frac{\partial \bar{v}}{\partial y}\right)^2\right] + \left(\frac{\partial \bar{u}}{\partial y} + \frac{\partial \bar{v}}{\partial x}\right)^2 \tag{6.11}$$

The above transport equations can enable the turbulent viscosity to be expressed in terms of the turbulent kinetic energy and its dissipation rate in the following form:

$$\mu_t = C_\mu \rho \frac{k^2}{\varepsilon} \tag{6.12}$$

As shown above, the formulation of the transport equations for the kinetic energy and the dissipation rate of turbulence includes a set of five empirical constants. The values assigned to the five constants in the initial publication by Launder and Spalding (1974) are:

$$C_\mu=0.09 \quad C_1=1.44 \quad C_2=1.92 \quad \sigma_k=1.0 \quad \sigma_\varepsilon=1.3 \tag{6.13}$$

The foregoing values of the five constants have been found by the above authors to be appropriate to plane jets and mixing layers. Several publications on the implementation of the k-ε models on a number of different flow conditions have proposed a variety of values for those constants. The k-ε turbulence model has been applied to high Reynolds number flows. For wall flows, the foregoing set of equations had to be used in conjunction with empirical formulas, the so-called "wall-functions". These formulae bypass the problem of modelling the effect of viscosity by empirically relating wall boundary conditions with points in the fluid.

Jones and Launder (1972) were the first to extend the prediction domain of the k-ε model to low-Reynolds number flows. Numerous investigators have proposed a

number of similar formulations for the low-Reynolds number k-ε model. A critical review of these formulations has been presented by Patel et al. (1984). This extension was based on the introduction of additional terms into the equations k and ε which depend on local Reynolds numbers of the form:

$$R_t = \frac{k^2}{\nu\varepsilon} \qquad and \qquad R_y = \frac{\sqrt{k}\,y}{\nu} \tag{6.14}$$

The equations of the k-ε model are slightly modified and for two-dimensional boundary layers can be expressed in the following form:

Turbulence Kinetic Energy Equation:

$$\bar{u}\frac{\partial k}{\partial x} + \bar{v}\frac{\partial k}{\partial y} = \frac{\partial}{\partial y}\left[\left(\nu + \frac{\nu_t}{\sigma_k}\right)\frac{\partial k}{\partial y}\right] + \nu_t\left(\frac{\partial \bar{u}}{\partial y}\right)^2 - (\tilde{\varepsilon} + D) \tag{6.15}$$

Equation for the Dissipation Rate of Turbulence:

$$\bar{u}\frac{\partial \tilde{\varepsilon}}{\partial x} + \bar{v}\frac{\partial \tilde{\varepsilon}}{\partial y} = \frac{\partial}{\partial y}\left[\left(\nu + \frac{\nu_t}{\sigma_\varepsilon}\right)\frac{\partial \tilde{\varepsilon}}{\partial y}\right] + C_1 f_1 \frac{\tilde{\varepsilon}}{k}\nu_t\left(\frac{\partial \bar{u}}{\partial y}\right)^2 - C_2 f_2 \frac{\tilde{\varepsilon}^2}{k} + E \tag{6.16}$$

where $\tilde{\varepsilon}$ is the energy dissipation parameter that can be defined as ε-D. Similarly to the high Reynolds number models the time-averaged flow field can be determined using the concept of eddy viscosity that is given by:

$$\mu_t = C_\mu f_\mu \rho \frac{k^2}{\tilde{\varepsilon}} \tag{6.17}$$

Accordingly, the low-Reynolds number version of the k-ε turbulence model accounts directly for the viscous effects and hence, resolves the flow field across the boundary layer down to the near-wall region. This goal is achieved by multiplication of the empirical constants C_μ, C_1 and C_2 with functions f_μ, f_1 and f_2 respectively, which involve molecular viscosity. A number of slightly different low-Reynolds number turbulence models have been proposed. The basic differences between those models lies in the analytical expression of the above functions. The physical phenomena taken into account with these functions are quite complex and hence the proposed formulations do not have universal applicability.

In recent years, two-equation turbulence models received far more attention than the algebraic or one-equation models. It was only lately that the Reynolds stress models began to be employed by an increasing number of researchers. The reason behind that

is that the Reynolds stress models employ a more complex set of differential equations and hence require extensive computer power. These models apply transport equations to solve directly the Reynolds stresses and turbulent heat fluxes and therefore avoid the assumption of isotropic turbulence. The transport equations for the Reynolds stresses can also be derived exactly from the momentum equations. Unfortunately, the introduction of the extra equations for the Reynolds stresses does not resolve the closure problem. In order to avoid closure problems, empirical constants have to be introduced in order to replace terms of higher order than the Reynolds stresses.

6.3 THE PRESENT COMPUTATIONAL APPROACH

6.3.1 Introduction

This section of the thesis describes the numerical formulation employed in this study. The objectives of the present computational effort include the investigation of the flow characteristics around flat plates with leading edge shapes related to turbomachinery blading. Furthermore, the present study incorporates an attempt to model the process of laminar to turbulent transition in the boundary layer. Both of the above described phenomena are quite important from the engineering point of view.

An accurate prediction of the flow field would require that the employed numerical model takes into account the particular characteristics of the flow phenomena involved in turbomachinery flows. Leading edge flows often include recirculation bubbles. The numerical prediction of the recirculation zones in a steady state, requires the use of information from both upstream and downstream of the recirculation area. On the other hand, it is usually possible to predict the boundary layer development using only upstream information. The fact that the boundary layer undergoes transition from laminar to turbulent complicates the existing configuration further. The following discussion considers the numerical treatment of all the foregoing flow phenomena.

The test cases considered in the present study involved the investigations of the flow field around two leading edge shapes with particular importance for the turbomachinery blading design. Specifically, a semicircular leading edge and an elliptical leading edge with a major to minor axis ratio of three have been considered. In both cases, the profiled leading edges extended to the full width of the flat plate. This arrangement has been adopted in order to obtain test cases with an increased degree of similarity with the experimental arrangement. Finally, a test case involving flow over a flat plate under specified free stream conditions has been employed in order to study transition related phenomena in a case where significant published work already exists.

6.3.2 The Numerical Model

The numerical model used here, involved the solution of the governing Navier-Stokes equations on a computational plane that simulates the experimental test plane (i.e. a plane vertical to the flat plate including its central line). It should be noted that from the mathematical point of view, the Navier-Stokes equations for compressible fluid flow can be classified as a combination of hyperbolic and parabolic equations. On the contrary, for incompressible fluid flow, the Navier-Stokes equations are a combination of elliptic and parabolic equations. In the present study, the elliptic formulation of the mass averaged Navier-Stokes equations for incompressible fluid has been used. The reason behind that is that a parabolic formulation would not be adequate for the simulation of the flow field around the leading edge, especially in those cases involving laminar separation and recirculation bubbles. By the same token, the elliptic formulation has the ability of predicting the boundary layer flow which is, in principal, a parabolic phenomenon. Furthermore, the flow field in the mid section of the wind tunnel where most of the experimental results have been acquired, can be considered as two dimensional. Accordingly, a two-dimensional computer code has been employed in order to deal with these computational tasks.

An iterative pressure correction scheme has been used to predict the flow field. The numerical solution of the Navier-Stokes equations in the form presented in the

previous section of this chapter, has been based on the SIMPLE algorithm, which stands for Semi-Implicit Method for Pressure Linked Equations. This procedure has been described by Patankar and Spalding (1972). This method is based on a series of guesses and corrections of the velocity and pressure fields. The velocity fields are calculated first using the initial guess for the pressure field and thereafter the pressure field is corrected in order to satisfy the continuity equation (see also Patankar, 1981).

The computer code involved in the present study, was required to have the ability to predict a wide range of flow phenomena. Since the ultimate stage of transition is turbulence, the numerical method involved should have a turbulence model incorporated in order to predict successfully the turbulent boundary layer. In fact, the prediction of transition requires special treatment in the vicinity of the wall where the viscous forces play a principal role. Accordingly, a low Reynolds number formulation of the k-ε turbulence model has been employed in order to simulate the boundary layer flow very close to the wall.

Patel et al. (1984) summarised the various assumptions and functions introduced by eight different models to account for the low Reynolds number and wall proximity effects, including the Launder Sharma (1974) version of the k-ε model. Additionally, Schmidt and Patankar (1988) presented a study on the performance of the Jones-Launder (1972) and Lam-Bremhorst (1981) low-Reynolds number k-ε models. Their ability to predict boundary layer transition under prescribed free stream conditions has been evaluated. Furthermore, the present study involved the application of the low-Reynolds number k-ε model formulation presented by Nagano and Hishida (1987). Table 6.1 summarises the low-Reynolds functions used in the foregoing versions of the k-ε turbulence model.

The main differences between the first three models and the Lam-Bremhorst formulation reside in the selection of the dissipation variable (ε or $\tilde{\varepsilon}$) and the description of the functional dependence of C_μ from the "turbulent Reynolds numbers", R_t and R_y, through the definition of f_μ. The value of the turbulent kinetic energy on a

	Nagano Hishida	Launder Sharma	Jones Launder	Lam Bremhorst
f_μ	$\left(1-e^{-\frac{y^+}{26.5}}\right)^2$	$e^{\frac{-3.4}{1+0.02R_t}}$	$e^{\frac{-2.5}{1+0.02R_t}}$	$\left(1-e^{-0.0165R_y}\right)^2\left(1+\frac{20.5}{R_t}\right)$
f_1	1.0	1.0	1.0	$1.+\left(\frac{0.05}{f_\mu}\right)^3$
f_2	$1-0.3e^{-R_t^2}$	$1-0.3e^{-R_t^2}$	$1-0.3e^{-R_t^2}$	$1-e^{-R_t^2}$
E	$\nu\nu_t(1-f_\mu)\left(\frac{\partial^2\bar{u}}{\partial y^2}\right)^2$	$2\nu\nu_t\left(\frac{\partial^2\bar{u}}{\partial y^2}\right)^2$	$2\nu\nu_t\left(\frac{\partial^2\bar{u}}{\partial y^2}\right)^2$	0.
D	$2\nu\left(\frac{\partial\sqrt{k}}{\partial y}\right)^2$	$2\nu\left(\frac{\partial\sqrt{k}}{\partial y}\right)^2$	$2\nu\left(\frac{\partial\sqrt{k}}{\partial y}\right)^2$	0.

Table 6.1 : The Low-Reynolds Functions Used in Various k-ε Turbulence Models

solid surface is zero. However the value of the dissipation rate as defined in equation (6.8) is not zero. For computational reasons, some turbulence models choose to avoid this boundary condition by introducing a simple transformation ($\varepsilon=\tilde{\varepsilon}+D$) in such a way that the dissipation parameter $\tilde{\varepsilon}$ obtains the value of zero on the wall. Alternatively, the boundary condition used for the dissipation rate ε on the wall is that the derivative $\partial\varepsilon/\partial y$ obtains the value of zero.

6.3.3 The Computational Mesh

The present computational formulation involved the solution of the Navier-Stokes equations using a finite volume discretisation scheme on a staggered grid, according to the original suggestions of Patankar (1981). Since a cartesian coordinate system with rectangular grid lines is usually insufficient for the proper treatment of test cases

involving arbitrary shaped configurations, a boundary fitted computational mesh has been employed. In this case, the physical boundaries of the flow domain constitute the only restriction applied to the grid generation. The angle of intersection between the grid lines and the geometrical boundaries can affect the accurate expression of the boundary conditions. Hence, effort has been made to keep the grid lines perpendicular to the boundaries.

The prediction of laminar to turbulent transition in the boundary layer required a substantial refinement of the computational grid, especially in the region of the viscous sublayer, which tends to be very thin in turbulent boundary layers. In order to obtain sufficient points in the laminar sublayer an exponential law of clustering the computational mesh, has been employed. Various types of mesh arrangements including c-type grids have been employed for the simulation of the flow field around the leading edge of the flat plate. The particular significance of the type of grid used will be discussed in the following sections together with the analysis of the obtained results.

6.3.4 Leading Edge Flow Results

A solution of the velocity and pressure fields around both the semi-circular and the elliptical leading edge configurations has been obtained. In this case, the numerical solution of the governing equations has been performed without the use of k-ε turbulence model. As a result, a laminar solution of the flow field around the leading edge of the two flat plate configurations has been obtained.

The study of the flow around the two leading edge shapes involved the formation of appropriate c-type computational meshes. A significant advantage of c-grids is that the computational mesh engulfs the blade geometry in such a way that the singularity associated with the physical location of the leading edge (stagnation point) can be modelled independently of the form and density of the mesh. It should be noted that the c-type of grids could result in significant simplification in the numerical treatment of the

boundary conditions. On the other hand, the use of c-type grids could increase the complexity in the description of the blade geometry.

Figure 6.1 presents a general view of the computational mesh employed in the test case involving the flat plate with cylindrical leading edge. The computational domain has been split into several sections in the streamwise direction where the density of the mesh points has been intensified. However, a uniform exponential clustering law has been applied to the crosswise direction. This mesh arrangement has provided a quite high concentration of grid points in the wall vicinity and in particular in the leading edge area (fig. 6.2). The same principles have been applied to the formation of the computational mesh for the test case involving the elliptical leading edge. Figures 6.3 and 6.4 illustrate a general view and a leading edge detail of the above mesh arrangement. In both cases, the computational mesh has been arranged to follow the geometrical formation of the flat plate. The grid arrangement has been extended to 150 mm downstream of the leading edge. Finally, it should be noted that in order to generate these grids a total of 21,080 grid points has been arranged in an array of 248 mesh points in the streamwise direction (124 points on either side of the plate) and 85 points in the crosswise direction.

Similar sets of boundary conditions have been imposed on both circular and elliptical leading edge configurations. The use of c-type grids permitted the imposition of the boundary conditions in a simplified form. At the inlet region (upstream of the leading edge) uniform velocity has been imposed. At the free stream (both upper and lower surfaces of the flat plate) the gradients of all the variables with respect to the crosswise direction have been set equal to zero apart from the crosswise velocity v that has been given a zero value. At the exit of the computational domain (both sides of the plate) the derivatives of the flow quantities with respect to the streamwise direction have been set to zero. On the surface of the plate the non-slip condition has been imposed by setting both velocity components equal to zero. Finally, the streamwise velocity component is adjusted in order to obtain overall mass balance on the flow domain. In the solution procedure, particular attention has been given to the region upstream of the

leading edge, where the mass flow has been monitored at several cross sections (line by line mass balance).

The obtained results for both semi-circular and elliptical leading edge test cases are presented in the form of vector plots. Figures 6.5 and 6.6 illustrate the obtained results for the flow field around the flat plate with the cylindrical leading edge. Specifically, figure 6.5 presents an overall view of the complete computational domain. Figure 6.6 illustrates the prediction of the flow field around the stagnation point and over the profiled leading edge. Similarly, figures 6.9 and 6.10 present an overall velocity vector plot of the complete computational domain and a detail of the vector plot around the elliptical leading edge.

The prediction of the flow field in the vicinity of the stagnation point on the leading edge of the flat plate involved very interesting flow phenomena, including the start of the boundary layer development and flow characteristics associated with the stagnation point. At the stagnation point, the flow is locally forced to turn at right angles to the main stream flow resulting to large velocity and pressure gradients. The computational method employed here, has been found to give reasonable predictions of the flow field around the leading edge (fig. 6.6 and 6.10). It can be observed that intense acceleration follows the minute magnitude of the velocity vectors near the stagnation point. In this area the flow follows the shape of the solid boundary, in both test cases considered.

The initiation and the subsequent development of the boundary layer flow is another very interesting phenomenon in the leading edge region. It can be observed that initially, the boundary layer is restricted to very few points near the wall in the acceleration zone. Depending on the geometrical configuration, the accelerating boundary layer tends to separate at the later sections of the profiled leading edge. The foregoing behaviour has been captured by the computational model. The numerical prediction of the later stages of the leading edge flow seemed to indicate successfully the approximate location of the recirculation zone. However, no recirculation has been

predicted in either cases. This behaviour can be attributed to the fact that the present solution did not take into account the turbulent effects.

Additionally, the present numerical method has been found to give a quite good description of the boundary layer development downstream of the profiled leading edge, for both semi-circular and elliptical leading edge configurations. Figures 6.7 and 6.8 illustrate the boundary layer flow development immediately after and further downstream of the semi-circular leading edge. The same information about the flow downstream of the elliptical leading edge is presented in figures 6.11 and 6.12. In both cases, the boundary layer seems to recover quickly from the acceleration zone under the influence of the free stream boundary conditions and forms a developed laminar boundary layer further downstream of the leading edge. In these areas, the obtained results for the two test cases considered have been found to be very similar to each other.

Furthermore, the present numerical results for the flow over the flat plate with an elliptical leading edge have been compared against the experimental results obtained for the flat plate with C4 leading edge. The two test cases have been regarded as similar because the start of the boundary layer development follows an unseparated leading edge flow. Figure 6.13 presents a comparison between the computational and the experimental results for three stations (X = 50 mm, X = 100 mm and X = 150 mm) along the length of the plate where experimental results have been available. It can be observed that the predictions are in good agreement with the experimental results in the inner boundary layer where the viscous forces prevail for all three stations. However, the experimental results in the outer boundary layer show a gradual tendency to produce a fuller velocity profile under the influence of the free stream turbulence intensity. At a first stage, the above behaviour has not been taken in to account by the computational model because no turbulence modelling has been used.

6.3.5 Numerical Prediction of Transition

The two test cases presented in the previous section of this chapter involved a laminar solution of the flow field around the leading edge of the flat plate. This section, on the other hand, deals with the prediction of the transitional characteristics of the flow downstream of the leading edge of a flat plate. The numerical method employed in this case involved the use of the low-Reynolds k-ε turbulence model, as described previously in this chapter. The present test case has been formulated following the suggestions of the ERCOFTAC test case T3A (see also Savill, 1991). In this case, the numerical prediction of the flow field over a flat plate under prescribed inlet and free stream conditions has been attempted.

The European Research Community On Flow Turbulence And Combustion (ERCOFTAC) constitutes an international organisation involving a large number of European as well as American, Japanese and other Universities and Research Centres that is aiming to assist and coordinate research in many areas. At this initial stage of development of the present numerical method, it was thought that the ERCOFTAC test case series on transition in turbomachinery would be the most appropriate framework for the evaluation and intercomparison of the obtained results. Furthermore, the forgoing series of test cases are prepared in order to assess the obtained results and to gradually lead to the successful application of the developed methods in more complex test cases. Finally, it should be noted that the present research project contributed some experimental results for the preparation of the recently proposed ERCOFTAC test case T3B+ (Savill, 1993). In the course of the present study, the suggestions of the ERCOFTAC test case T3A have been used for the numerical prediction of transition because it provided a quite standard test case and the Rolls Royce experimental results (Roach and Brierley, 1989) have been already available at the beginning of this project.

The computational mesh employed in this test case involved a simpler orthogonal structure (see also illustration in figure 6.14). In order to obtain a suitable resolution in the wall vicinity a uniform exponential clustering law has been applied, as discussed

earlier in this chapter. The clustering of grid points has been used in both x and y directions resulting in a very dense computational mesh in the leading edge area. In order to generate this grid, a total of 15,251 grid points has been arranged in an array of 101 point in the streamwise direction and 151 in the crosswise direction. The present computational mesh has significant similarities with the grid arrangement employed over the flat surface in the previous test cases. The reason behind that is that the present test case has been regarded as an extension of the previous test cases. At a further stage, the two test cases could be combined in order to model globally the flow field around the flat plate and obtain a solution that accounts both for the effect of the profiled leading edge and the transitional characteristics of the boundary layer.

The Blasius analytical solution of the Navier-Stokes equations has been used to generate the inlet boundary conditions for the velocity components (fig. 6.15). The start of the computations has been set at x = 10 mm downstream of the leading edge (fig.6.14). The length of the computational domain has been 1700 mm in accordance with the experimental set up used by Roach and Brierley (1989). At the outlet the streamwise gradient of all the flow quantities has been set to zero. On the solid wall all velocity components have been set to zero. The turbulent kinetic energy and the dissipation parameter on the wall boundary has also been set to zero. At the free stream, the gradient of pressure and velocity components with respect to the crosswise direction have been set to zero. At the inlet, the free stream velocity has been set to 5.2 m/s. The inlet profiles and the free stream distribution of the turbulent kinetic energy and the dissipation rate have been generated using the suggestions of Rodi and Scheuerer (1985) combined with the conditions proposed by the ERCOFTAC test case T3A (Savill, 1991). The following empirical relations have been used in order to generated the initial profiles for the turbulent kinetic energy and its dissipation rate:

$$k = k_e \left(\frac{\bar{u}}{\bar{u}_e} \right)^2 \qquad \varepsilon = \alpha_1 \, k \, \frac{\partial \bar{u}}{\partial y} \tag{6.18}$$

where the parameter α_1 accounts for the effect of the free stream turbulence level (see also Rodi and Scheuerer, 1985). In the present study a value of 0.48 has been assumed for the parameter α_1 using the suggestions of ERCOFTAC test case T3A.

The computational results generally indicated an early start of transition and longer transition lengths than the experimental results. The predicted skin friction coefficient distribution over the length of the plate has been plotted in figure 6.16 together with the experimental results obtained by Roach and Brierley (1989) of the Rolls Royce Applied Science Laboratory. The same experimental results have been used by ERCOFTAC test case T3A for comparisons (Savill, 1991).

The present numerical method which involves the Nagano-Hishida (1987) low-Reynolds number turbulence model, has been found to be very sensitive to the initial dissipation profiles. A parametric study of the effect of the initial dissipation profiles on the prediction of the start and length of transition has been presented at the ERCOFTAC Special Interest Group on Transition (Savill, 1991) by the proposers of the Nagano-Hishida model. This study showed that the Nagano-Hishida model is very sensitive to the initial dissipation profiles and predicts quite early transition (see also figure 6.17). This is despite the fact that this model has been designed to ensure compliance with the correct wall-limiting behaviour of the turbulent quantities, as pointed out by Savill (1991). Furthermore, the prediction of transitional characteristics of the boundary layer obtained during the course of the present study has been to be found in good agreement with the results obtained by the proposers of the model (fig. 6.16 and fig. 6.17).

In general terms, the present computational results have not been particularly satisfactory as far as boundary layer transition prediction is concerned. The findings of the present study along with the results obtained by other researchers within the ERCOFTAC Special Interest Group on Transition suggest that the Nagano-Hishida low-Reynolds number turbulence model predicts very early transition. This is despite the fact the Nagano-Hishida and related models produce good results for low-Reynolds near wall flows. The aforementioned ERCOFTAC research initiative seems to have reached the conclusion that the Launder-Sharma (1974) near wall treatment is the optimum choice amongst current k-ε turbulence models. The present computational effort has been restricted to the first ERCOFTAC test case because it became apparent that in order to improve the obtained results an alternative low-Reynolds formulation of the k-ε

turbulence model should be employed. The apparent way forward is to implement the Launder-Sharma (1974) and Lam-Bremhorst (1981) turbulence models and test their ability to predict the transitional characteristics of the boundary layer.

6.4 CONCLUDING REMARKS

Computations of the flow field around flat plate configurations simulating the experimental set up have been undertaken. In particular, two flat plate configurations have been used including a flat plate with a semi-circular and a flat plate with an elliptical leading edge. A laminar flow prediction has been obtained for the above test cases. The two-dimensional Navier-Stokes solver used in this study, has been found to give reasonably successful predictions of the flow in the vicinity of the stagnation point, as well as the start and the development of the laminar boundary layer.

Furthermore, the flow downstream of the leading edge of a flat plate has been modelled using the foregoing computer code equipped with a low-Reynolds number k-ε turbulence model. The obtained results predicted earlier start of transition and longer transition lengths than the experimental data. Alternative formulations of the turbulence model could be used in order to improve the numerical prediction of transition. Ultimately, the prediction of the leading edge flow can be combined with the transition prediction in order to obtain a more global approach with respect to transition predictions in turbomachinery flows. Finally, it can be argued that despite the limited success in the transition predictions the present computational approach can provide the framework for the development and assessment of numerical methods suitable for the prediction of transition in the boundary layer of turbomachinery blading.

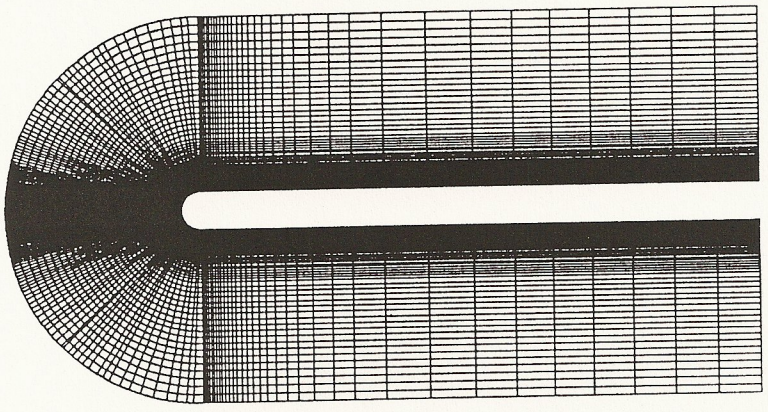


Figure 6.1 General View of the Computational Mesh Employed in the Study of the Flow Around the Cylindrical Leading Edge

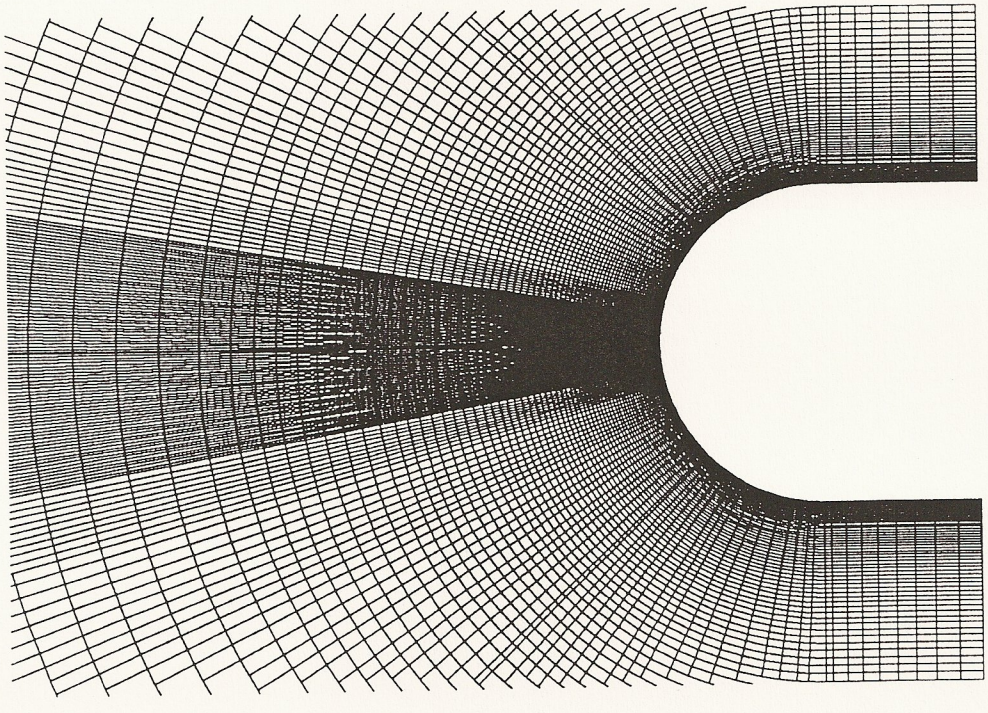


Figure 6.2 Leading Edge Detail of the Computational Mesh Employed in the Study of the Flow Around the Cylindrical Leading Edge

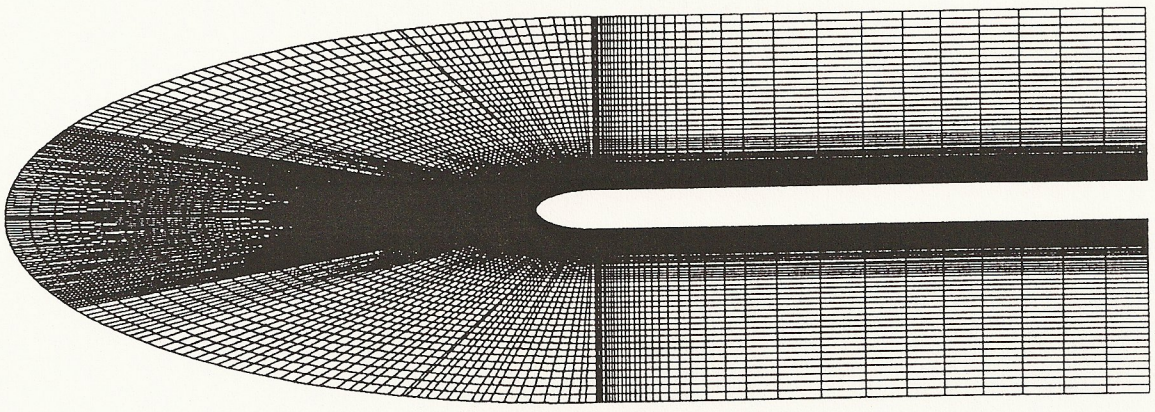


Figure 6.3 General View of the Computational Mesh Employed in the Study of the Flow Around the Elliptical Leading Edge

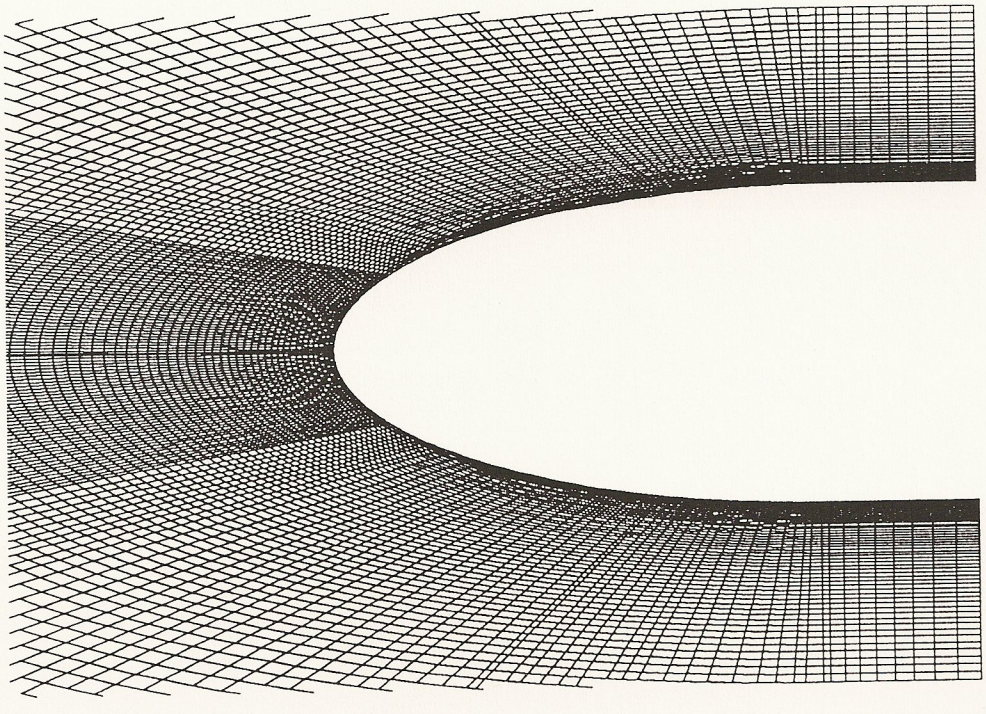


Figure 6.4 Leading Edge Detail of the Computational Mesh Employed in the Study of the Flow Around the Elliptical Leading Edge

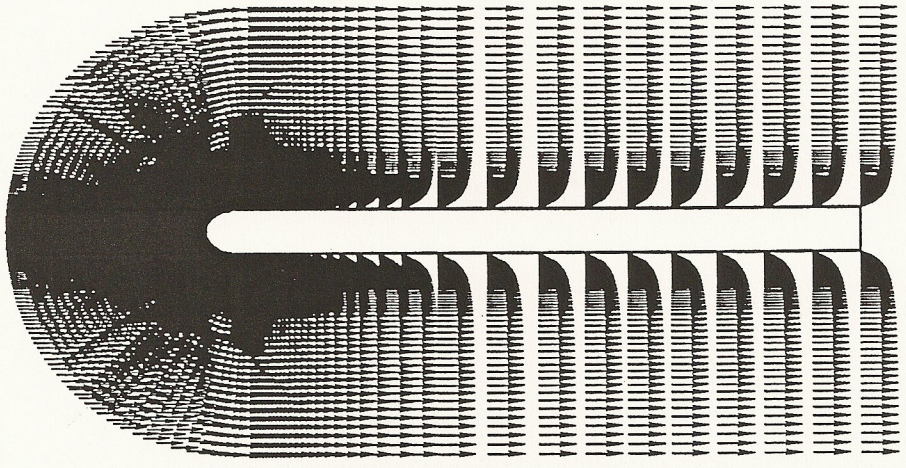


Figure 6.5	Velocity Vector Plot of the Complete Computational Domain Around the Cylindrical Leading Edge

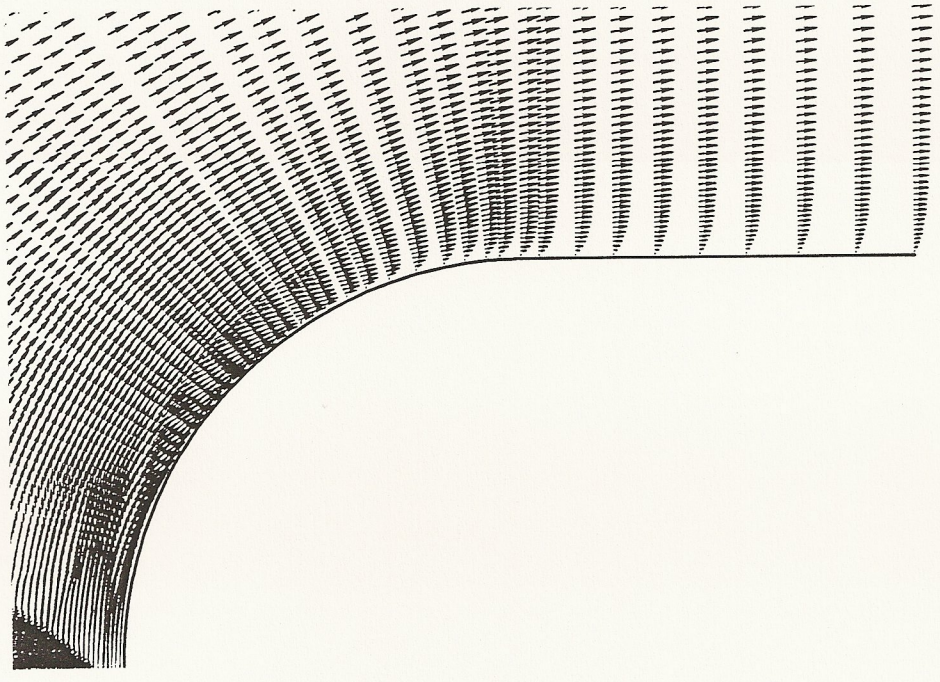


Figure 6.6	Leading Edge Detail of the Vector Plot Illustrating the Flow Around the Stagnation Point of the Cylindrical Leading Edge

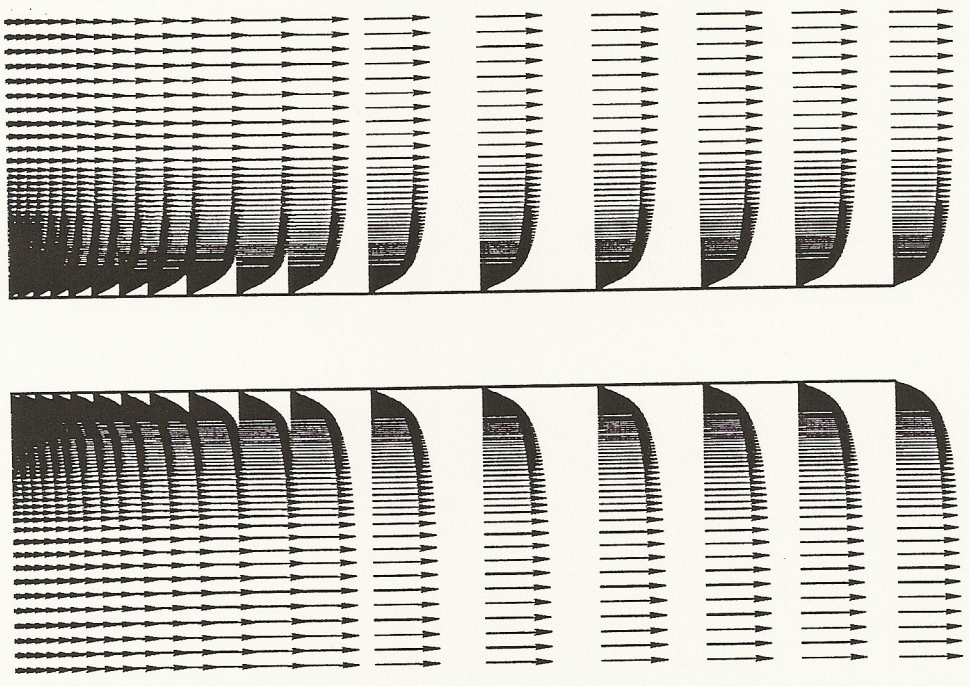


Figure 6.7 Detail of the Vector Plot Illustrating the Boundary Layer Flow Immediately After the Cylindrical Leading Edge

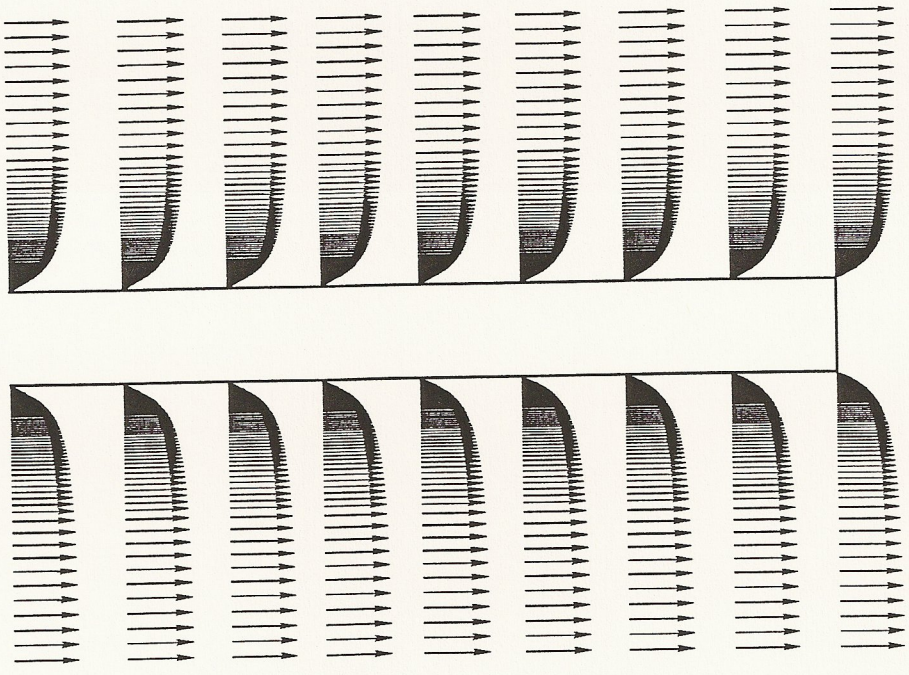


Figure 6.8 Detail of the Vector Plot Illustrating the Boundary Layer Flow Further Downstream of the Cylindrical Leading Edge

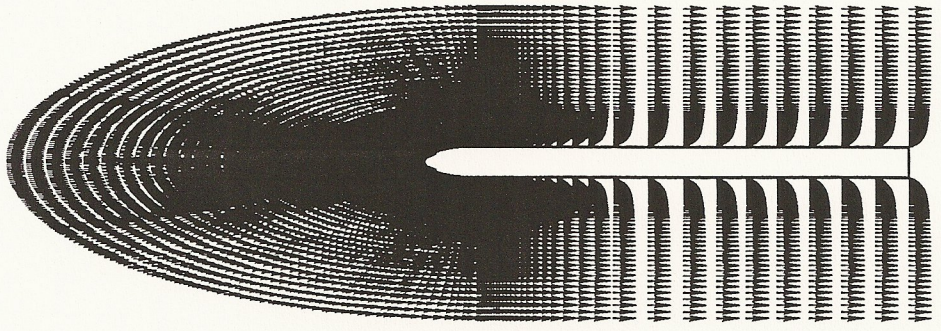


Figure 6.9	Velocity Vector Plot of the Complete Computational Domain Around the Elliptical Leading Edge

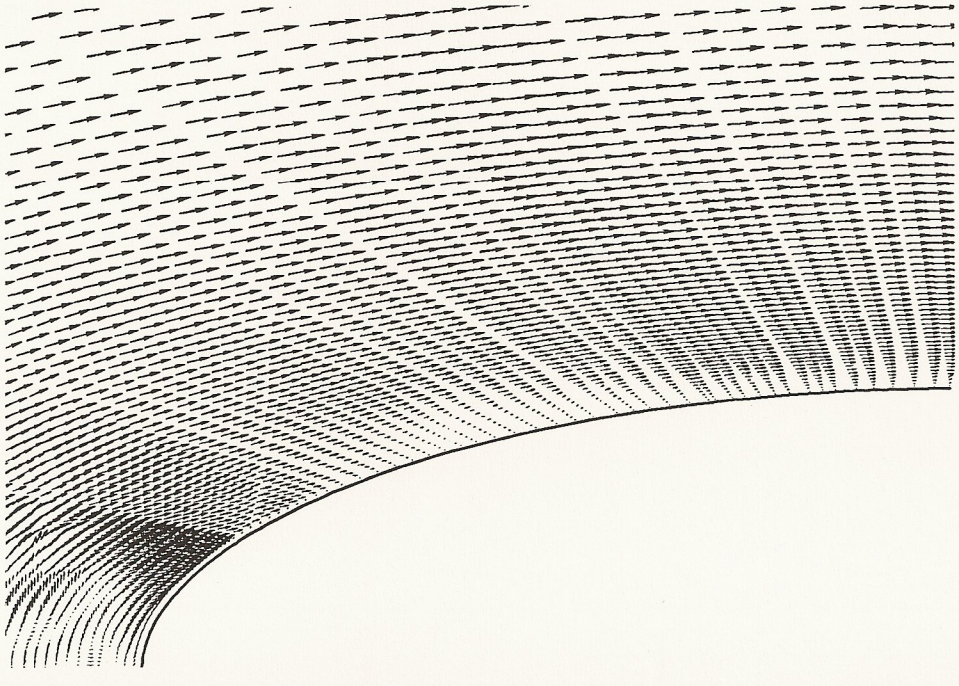


Figure 6.10	Leading Edge Detail of the Vector Plot Illustrating the Flow Around the Stagnation Point of the Elliptical Leading Edge

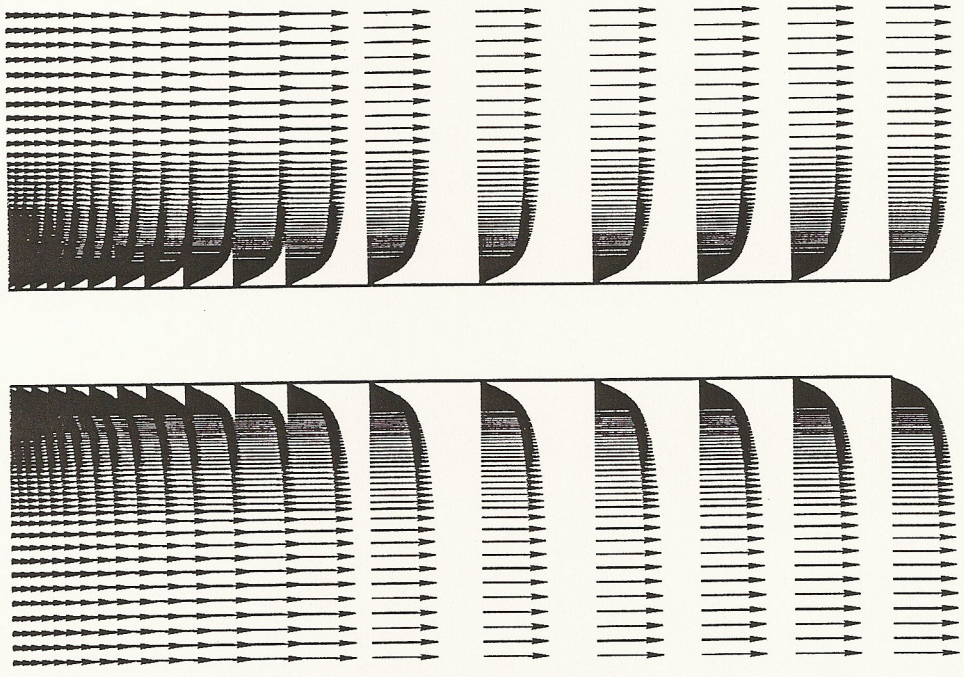


Figure 6.11 Detail of the Vector Plot Illustrating the Boundary Layer Flow Immediately After the Elliptical Leading Edge

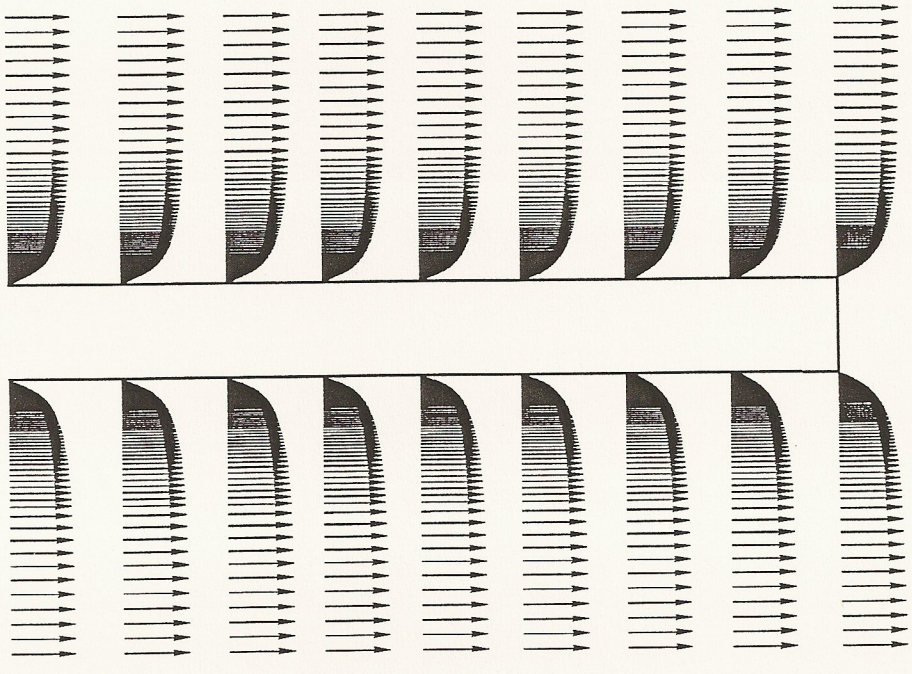


Figure 6.12 Detail of the Vector Plot Illustrating the Boundary Layer Flow Further Downstream of the Elliptical Leading Edge

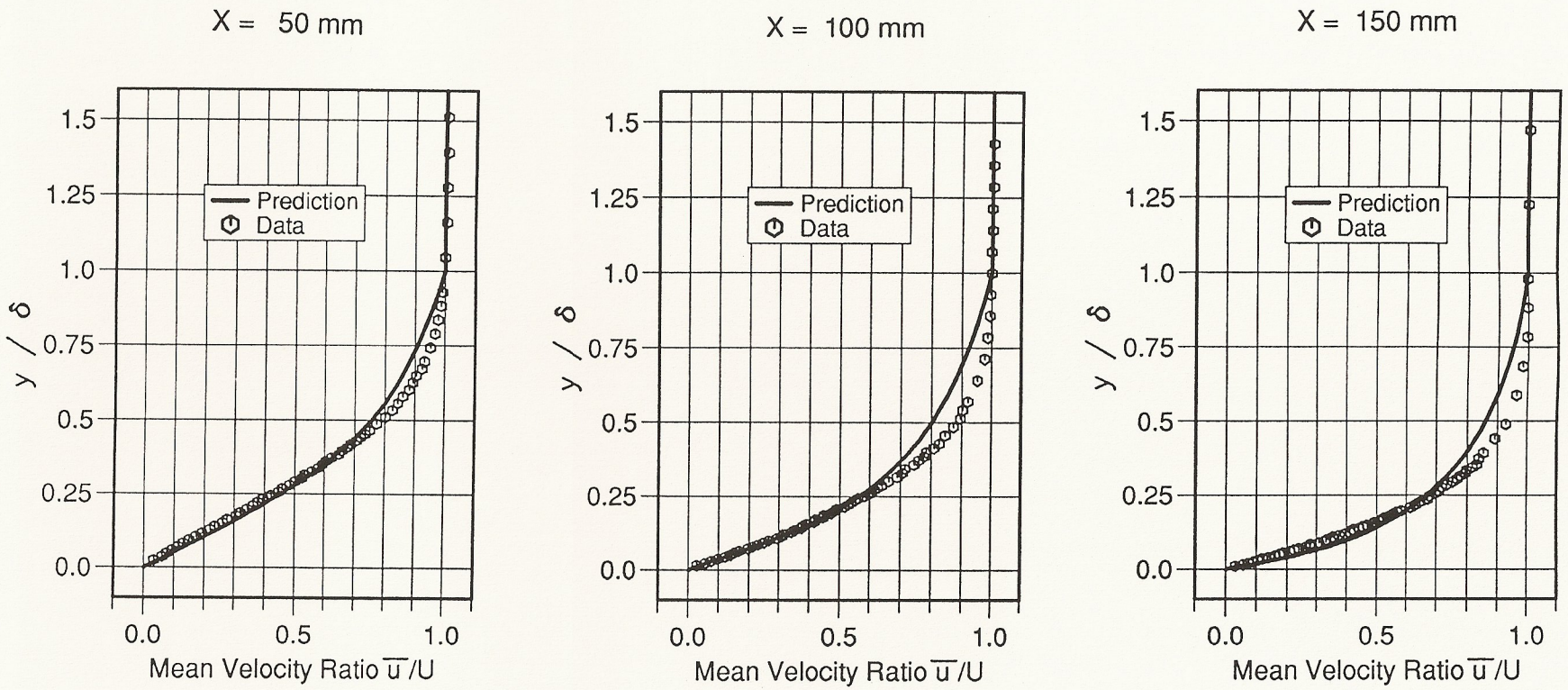


Figure 6.13 Comparison of the Predicted Velocity Profiles Downstream of the Elliptical Leading Edge Against the Present Experimental Results for the C4 Test Case

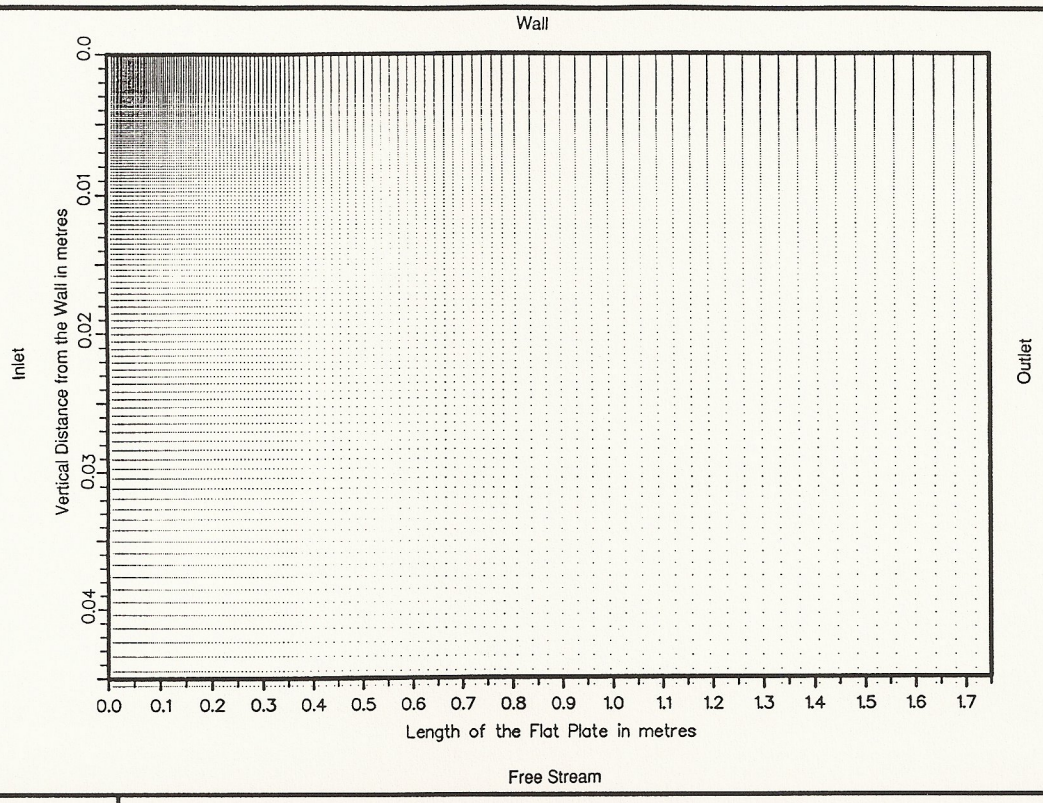


Figure 6.14 General View of the Computational Mesh Employed in the Numerical Prediction of Transition

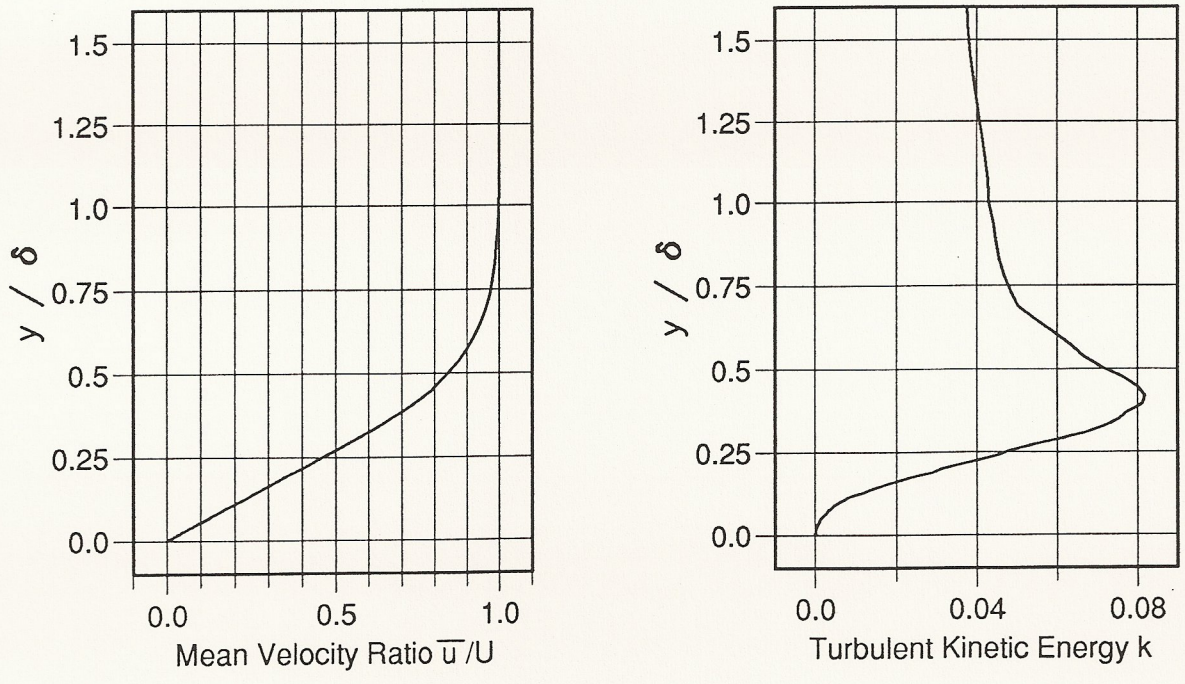


Figure 6.15 Inlet Profiles for Mean Velocity and Turbulent Kinetic Energy

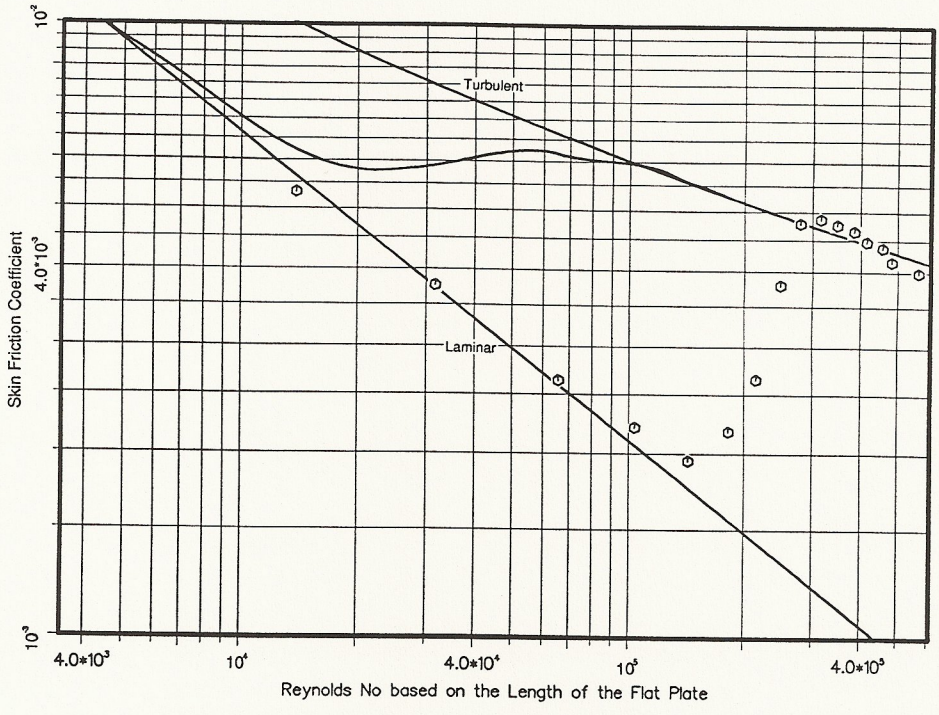


Figure 6.16	Comparison of the Predicted Skin Friction Coefficient Distribution Against Experimental Results

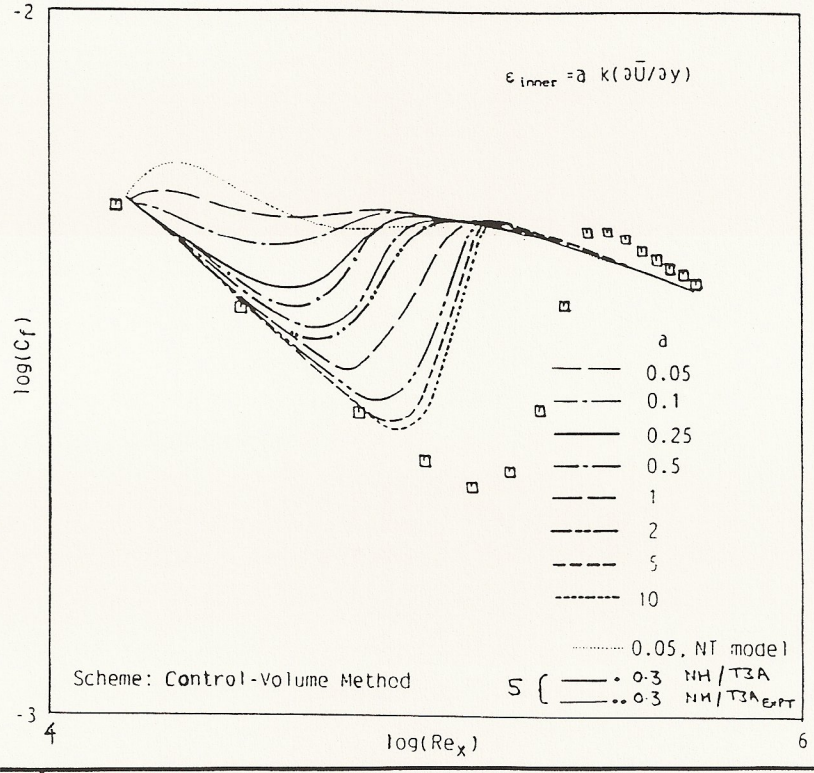


Figure 6.17	Nagano-Hishida Model Predictions for Various Initial Dissipation Profiles in ERCOFTAC Case T3A (after Savill, 1991)

CHAPTER 7

Conclusions and Suggestions for Future Work

CHAPTER 7

Conclusions and Suggestions for Future Work

7.1 CONCLUSIONS

The boundary layer that develops over turbomachinery blading undergoes transition under the influence of quite turbulent and unsteady free stream flow conditions. A great deal of the existing transition work has been preformed in an ideal environment involving very low disturbances in the free stream flow. The present investigation has been undertaken in order to study the effect of a more realistic turbomachinery flow environment on the transitional characteristics of the boundary layer. The simulation of the turbomachinery flow environment on both experimental and theoretical studies has been performed using flat plate configurations with more appropriate leading edge shapes for turbomachinery applications. Additionally, the present investigation involved the generation of a free stream environment with moderate to high turbulence intensity levels. This section of the thesis is intended to summarise the findings of the present study.

This project has been the first phase of the development of an experimental facility and a theoretical model for the study of transition phenomena related to turbomachinery flows. The experimental facility developed during the present study included a small scale wind tunnel, three flat plates with a cylindrical, a sharp and a C4 leading edge and a series of turbulence generating grids able to deliver quasi homogenous and isotropic turbulence levels according to predefined requirements and constraints.

A variety of experimental techniques including surface flow visualisation and hot-wire anemometry have been employed in order to investigate the transitional characteristics of the boundary layer. The flow visualisation method has been used to obtain a general overview of the flow field and to cover a large number of test cases. In addition, hot-wire anemometry has been used to generate a more detailed description of the mean and statistical characteristics of the boundary layer flow.

The surface flow visualisation method employed in this study has been found to be appropriate for the identification of the global characteristics of the transitional region. This method has been more successful for the test cases involving separated flow transition. Additionally, the present flow visualisation technique facilitated the recognition of flow irregularities in the boundary layer flow over the flat plates and thereby assisted the development of the turbulence generating grids.

A laminar separation bubble has been detected in the area around the cylindrical leading edge, under all of the free stream conditions tested. The laminar separation point moved from approximately 80 degrees to 90 degrees on the circular arc of the leading edge as the free stream velocity and turbulence intensity were increased. The starting point of turbulent transition moved towards the leading edge and the transition length as well as the overall length of the separated region were shortened, with increasing free stream velocity and turbulence intensity.

The transitional characteristics on the flow over the flat plates with the sharp and the C4 leading edge were found to be largely similar. Nevertheless, on the flat plate with C4 leading edge, the laminar to turbulent transition occurred at a slightly higher Reynolds number based on the longitudinal distance from the leading edge. This behaviour can be attributed to the acceleration that the flow undergoes in the leading edge area.

Experimental investigation of boundary layer transition has been carried out on the flat plate with C4 leading edge using hot-wire anemometry. The effect of free stream

Reynolds number and turbulence intensity on the process of transition has been studied. Increase in the free stream turbulence intensity results in an earlier onset of transition. The free stream Reynolds number has been found to have a rather small effect on the non-dimensional characteristics of transition, probably by slightly altering the pressure distribution in the leading edge area of the flat plate.

The necessary computational tools for the analysis and graphical representation of the hot-wire signals have been developed. A global picture of the transitional characteristics of the boundary layer has been obtained by plotting the non-dimensional parameters of the boundary layer on a Re_x-y^+ plane. The above method provided better access to transitional data sets and improved the understanding of the flow patterns that precede and follow transition in the boundary layer. This process has been assisted by the acquisition of boundary layer spectra which show the distribution of turbulent energy over a range of frequencies. The boundary layer spectra obtained during the experimental investigation have shown that the overall turbulence intensity increases in the core of the transition region particularly the lower frequency components.

The present results have been found to be in good agreement with existing results concerning transition over flat plates. The experimental data obtained in the course of this study suggest that the momentum thickness Reynolds numbers at the onset of transition obtain values in the range of 160 and 200 for large values of the free stream turbulence (Tu_∞ = 4%). The momentum thickness Reynolds number in the test case involving lower turbulence intensity level (Tu_∞ = 1.8%) was found to be significantly higher obtaining a value around 330.

There was considerable agreement between the present intermittency results and the predictions of the Narasimha method. The estimation of transition start and length using the Narasimha procedure has been more accurate than the streamwise distribution of the integral parameters of the boundary layer. The main reason for this relates to the fact that the Narasimha method is based on well defined criteria for the inception of transition.

The present results have been found to be in good agreement with the work of previous investigators as well as the existing correlations for the boundary layer over a flat plate. Slight differences in the characteristics of the transition process have been observed between the flat plate with C4 leading edge and the flat plate with other leading edge shapes. This behaviour can be attributed to the gradual acceleration of the flow around the C4 leading edge.

Computations of the flow field around flat plate configurations simulating the experimental arrangement have been undertaken. A laminar flow prediction has been obtained for two flat plate configurations including a flat plate with a semi-circular and a flat plate with an elliptical leading edge. The two-dimensional Navier-Stokes solver used in this study, has been found to give reasonably successful predictions of the flow in the vicinity of the stagnation point, as well as the start and the development of the laminar boundary layer. The flow downstream of the leading edge of a flat plate has been modelled using the foregoing computer code equipped with a low-Reynolds number k-ε turbulence model. The obtained results predicted earlier start and end of transition. It can be argued that despite the limited success in the transition predictions the present computational approach can provide the framework for the development and assessment of numerical methods suitable for the prediction of transition in the boundary layer of turbomachinery blading.

7.2 SUGGESTIONS FOR FUTURE WORK

Investigations of boundary layer transition phenomena have shown that the two most important parameters that affect the process of transition are the free stream turbulence and the longitudinal pressure distribution (pressure gradient). The present study has been focused on the leading edge and free stream turbulence effects under zero pressure gradient. At a further stage the transitional characteristics of the boundary layer could be studied under pressure gradients encountered in turbomachinery blade passages. Additionally, the understanding of the mechanics in which free stream

turbulence affects boundary layer transition should be enhanced by studying the effect of more turbulence intensity levels. The concept of using more realistic leading edge shapes for turbomachinery should be retained and other leading edge designs could be tested such as the Double Circular Arc blade design. This process can ultimately lead to a global approach in the modelling of the effect of free stream turbulence and pressure gradient on boundary layer transition.

The present computational study involved the investigation of the flow around the leading edge of the flat plates without the use of turbulence modelling. Also, the transitional boundary layer downstream of the leading edge has been studied using a low-Reynolds number k-ε turbulence model. At a further stage, the forgoing test cases can be combined in order to achieve a global prediction of the flow field including both leading edge and boundary layer transition effects. Additionally, alternative versions of the low-Reynolds number k-ε turbulence model could be implemented in the present numerical scheme in order to assess their ability to predict the transitional characteristics of the boundary layer. This process could ultimately lead to the development of a turbulence model dedicated to transitional boundary layer flows in order to substitute the concept of simulating the transitional flow as a semi-turbulent state of the boundary layer.

In the present study, a statistical method of analysing hot-wire data in order to obtain intermittency information has been presented. At a further step forward, this method can be easily used in order to conditionally average the intermittent signals. This method can facilitate the analysis of high frequency velocity samples in order to quantify more accurately the contributions of the turbulent and non-turbulent motion to the process of transition.

Future experimental and theoretical research activities should be directed towards the enhancement of understanding of the flow phenomena involved in the initiation of the transition process as well as the mechanisms with which the free stream environment interacts with the boundary layer flow. Also, more review work needs to be undertaken

in order to assess globally the existing data and facilitate the development of new transition correlations for turbomachinery design purposes as well as more appropriate turbulence models for the simulation of transitional flows in turbomachinery.

Finally, it should be noted that the present study has been incorporated in the initial stage of transition research within the framework of the EURAM-BRITE project on transition in turbomachinery flows involving three European Universities namely, the Aristotle University of Thessaloniki, the Vrije Universiteit of Brussels and Cranfield University. At the second stage of this project, the working group has been expanded by the introduction of two new partners including the Rolls Royce Applied Science Laboratory (RRASL) and the Design Sciences Group of Rolls Royce Plc. as well as the ERCOFTAC Special Interest Group on Transition involving twenty European and a number of non-European associated research groups led by Cambridge University. This follow-up EURAM-BRITE project has been set up in order to investigate further the various phenomena related to transition in turbomachinery flows. The aim of the forgoing research project is to provide new experimental data, more relevant for turbomachinery applications which could be used immediately by the ERCOFTAC group in order to set up more accurately the transition prediction techniques which are under development.

BIBLIOGRAPHY

BIBLIOGRAPHY

Abbot, M.B. and Basco, D.R. (1989)

"Computational Fluid Dynamics: An Introduction for Engineers",

Longman Scientific & Technical, London, U.K.

Abu-Ghannam, B.J. and Shaw, R. (1980)

"Natural Transition of Boundary Layers - The Effects of Turbulence, Pressure Gradient, and Flow History", *Journal of Mechanical Engineering Science, vol. 22, no. 5.*

Acharya, M. (1985)

"Pressure-Gradient and Free-Stream Turbulence Effects on Boundary-Layer Transition",

ABB Research Centre, Report No. KLR 85-127C, Baden, Switzerland.

Acharya, M., Bornstein, J. and Escudier, M.P. (1986)

"Turbulent Boundary Layers on Rough Surfaces",

Experiments in Fluids, vol.4, pp.33-47.

Acharya, M. and Escudier, M.P. (1983)

"Measurements of the Wall Shear Stress in Boundary Layer Flows", *Proceedings of the Fourth Symposium on Turbulent Shear Flow, Karlsruhe, Germany, pp.277-286.*

Addison, J.S. and Hodson, H.P. (1990a)

"Unsteady Transition in an Axial-Flow Turbine: Part 1 - Measurements on the Turbine Rotor", *Transactions of ASME, Journal of Turbomachinery, vol.112, pp. 206-214.*

Addison, J.S. and Hodson, H.P. (1990b)

"Unsteady Transition in an Axial-Flow Turbine: Part 2 - Cascade Measurements and Modelling", *Transactions of ASME, Journal of Turbomachinery, vol.112, pp. 215-221.*

Addison, J.S. and Hodson, H.P. (1991)

"Modelling of Unsteady Transitional Boundary Layers"

ASME IGTACE Orlando 1991, ASME Paper No 91-GT-282.

Anderson, D.A., Tannehill, J.C. and Pletcher R.H. (1984)

"Computational Fluid Mechanics and Heat Transfer",

Hemisphere Publishing Co., New York, U.S.A.

Arnal, D., Juillen, J.C. and Michel, R. (1979)

"Analyse Experimentale de la Transition de la Couche Limite avec Gradient de Pression Nul ou Positif", *ONERA TP 1979-8.*

Arnal, D. and Juillen, J.C. (1979a)

"Techniques d' Analyse Conditionnelle d' un Signal Fil Chaud pour l' Etude de l' Intermittence de Transition", *ONERA TP 1979-34.*

Baines, W. and Peterson, E. G. (1951)

"An Investigation of the Flow Through Screens",

Transactions of ASME, vol. 73, No.5, pp. 467-480.

Batchelor, G. K. (1953)

"The Theory of Homogenous Turbulence",

Cambridge University Press, Cambridge, U.K.

Bhatia, J.C., Durst, F. and Jovanovic, J. (1982)

"Corrections of Hot-Wire Anemometer Measurements Near Walls",

Journal of Fluid Mechanics, vol. 122, pp. 411-431.

Birch, N.T. (1987)

"Turbulence and Transition Modelling in Turbomachinery", *PhD Thesis, Cranfield Institute of Technology, Cranfield, U.K.*

Blair, M.F. (1982)

"Influence of Free-Stream Turbulence on Boundary Layer transition in Favourable Pressure Gradients",

Transactions of ASME, Journal of Engineering for Power, vol. 104, pp. 743-750.

Blair, M.F. (1983a)

"Influence of the Free-Stream Turbulence on Turbulent Boundary Layer Heat Transfer and Mean Profile Development, Part I-Experimental Data",

Transactions of ASME, Journal of Heat Transfer, vol.105, pp. 33-40.

Blair, M.F. (1983b)

"Influence of the Free-Stream Turbulence on Turbulent Boundary Layer Heat Transfer and Mean Profile Development, Part II-Analysis of Results",

Transactions of ASME, Journal of Heat Transfer, vol.105, pp. 41-47.

Blair, M.F. (1989)

"Bypass-Mode Boundary Layer Transition in Accelerating Flows",

United Technologies Research Centre Report, East Hartford, Conn., U.S.A.

Blair, M.F. (1992a)

"Boundary-Layer Transition in Accelerating Flows with Intense Freestream Turbulence: Part 1-Disturbances Upstream of Transition Onset",

Transactions of ASME, Journal of Fluid Engineering, vol. 114, pp.313-321.

Blair, M.F. (1992b)

"Boundary-Layer Transition in Accelerating Flows with Intense Freestream Turbulence: Part 2-The Zone of Intermittent Turbulence",

Transactions of ASME, Journal of Fluid Engineering, vol. 114, pp.322-332.

Blair, M.F., Bailey, D.A. and Schlinker, R.H. (1981)

"Development of Large-Scale Wind Tunnel for the Simulation of Turbomachinery Airfoil Boundary Layers",

Transactions of ASME, Journal of Engineering for Power, vol. 103, pp. 678-687.

Blair, M.F., Dring, R.P. and Joslyn, H.D. (1989a)

"The Effects of Turbulence and Stator/Rotor Interaction on Turbine Heat Transfer: Part I-Design Operating Conditions",

Transactions of ASME, Journal of Turbomachinery, vol.111, pp.87-96.

Blair, M.F., Dring, R.P. and Joslyn, H.D. (1989b)

"The Effects of Turbulence and Stator/Rotor Interaction on Turbine Heat Transfer: Part II-Effects of Reynolds Number and Incidence",

Transactions of ASME, Journal of Turbomachinery, vol.111, pp. 97-103.

Blasius, H. (1908)

"Grenzschichten in Flüssigkeiten mit Kleiner Reibung",

Z. Math. Phys. 56, pp. 1-37; English Translation in NACA TM 1256.

Blevins, R.D. (1977)

"Flow Induced Vibrations", *Van Nostrand Reinhold Company.*

Bradshaw, P. (1971)

"An introduction to turbulence and its measurement",

1st edition, Pergamon Press, Oxford, U.K.

Bradshaw, P., Cebeci, T. and Whitelaw, J.H. (1981)

"Engineering Calculation Methods for Turbulent Flows",

Academic Press, London,U.K.

Calvert, W.J. (1985)

"Private Communication", *RAE[1] Pyestock, U.K.*

Calvert, W.J. (1994)

"An Inviscid-Viscous Method to Model Leading Edge Separation Bubbles",

To Be Presented at ASME IGTACE, The Hague 1994

CEGEDUR-PECHINEY (1988)

"FORTAL StS Premachined Aluminium Alloy with Hight Dimensional Stability",

Manufacturers Data Sheet.

Charters, A.C. Jr (1943)

"Transition between Laminar and Turbulent Flow dy Transverse Contamination",

NACA TN 891.

Clauser, F.H. (1956)

"The Turbulent Boundary Layer", *Advances in Applied Mechanics, vol. IV, pp. 1-51.*

Clauser, F.H. (1954)

"Turbulent Boundary Layers in Adverse Pressure Gradients",

Journal of the Aeronautical Sciences, February 1954, vol. 21, pp. 91-108.

Costa, J. and Arts, T. (1992)

"Influence of freestream turbulence spectrum on boundary layer transition",

ISABE Paper No ISABE-91-7086.

Crabtee, L.F. (1959)

"The Formation of Regions of Separated Flow on Wing Surfaces", *ARC CP 220.*

Cumsty, N.A. (1989)

"Compressor Aerodynamics",

Longman Scientific & Technical, New York, U.S.A.

---

[1] DRA : Defence Research Agency, formerly
RAE : Royal Aerospace Establishment

Dong, Y. and Cumsty, N.A. (1990a)

"Compressor Blade Boundary Layers: Part 1-Test Facility and Measurements with No Incident Wakes",

Transactions of ASME, Journal of Turbomachinery, vol. 112, pp. 222-230.

Dong, Y. and Cumsty, N.A. (1990b)

"Compressor Blade Boundary Layers: Part 2-Measurements with Incident Wakes",

Transactions of ASME, Journal of Turbomachinery, vol. 112, pp. 231-240.

Deutsch, S. and Zierke, W.C. (1987)

"The measurement of Boundary Layers on a Compressor Blade in Cascade Part 1-A Unique Experimental Facility",

Transactions of ASME, Journal of Turbomachinery, vol. 109, pp. 520-526.

Deutsch, S. and Zierke, W.C. (1988a)

"The measurement of Boundary Layers on a Compressor Blade in Cascade: Part 2-Suction Surface Boundary Layers",

Transactions of ASME, Journal of Turbomachinery, vol. 110, pp. 138-145.

Deutsch, S. and Zierke, W.C. (1988b)

"The measurement of Boundary Layers on a Compressor Blade in Cascade: Part 3-Pressure Surface Boundary Layers and the Near Wake",

Transactions of ASME, Journal of Turbomachinery, vol. 110, pp. 146-152.

Deutsch, S. and Zierke, W.C. (1990)

"The measurement of Boundary Layers on a Compressor Blade in Cascade: Part 4-Flow Fields for Incidence Angles of -1.5 and -8.5 Degrees",

Transactions of ASME, Journal of Turbomachinery, vol. 112, pp. 241-255.

Dhawan, S. and Narasimha, R. (1958)

"Some Properties of Boundary Layer Flow During the Transition from Laminar to Turbulent Motion", *Journal of Fluid Mechanics, vol. 3, pp. 418-438.*

Dryden, H.L. (1936)

"Airflow in the Boundary Layer Near a Plate", *NACA Report 562.*

Dryden, H.L. (1943)

"A Review of the Statistical Theory of Turbulence",

Quarterly of Applied Mathematics, vol. 1, pp. 7-42.

Emmons, H.W. (1951)

"The Laminar-Turbulent Transition in a Boundary Layer - Part 1",

Journal of the Aeronautical Sciences, July 1951, pp. 490-498.

Elder, J.W. (1960)

"An experimental Investigation of Turbulent Spots and Breakdown to Turbulence"

Journal of Fluid Mechanics, vol. 9, pp.235-246.

ESDU (1982)

"Thermophysical Properties of Heat Pipe Working Fluids: Operating Range Between -60 °C and 300 °C", *Data Item 80017, Engineering Sciences Data Unit, London, U.K.*

Fasihfar, A. and Johnson, M.W. (1992)

"An Improved Boundary Layer Transition Correlation",

ASME IGTACE Cologne, June 1992, ASME Paper No 92-GT-245.

Frenkiel, F.N. (1948)

"On the Kinematics of Turbulence", *Journal of the Aeronautical Sciences, pp. 57-64.*

Frenkiel, F.N. (1948)

"Statistical Study of Turbulence - Spectral Functions and Correlation Coefficients",

NACA TM 1436.

Frenkiel, F.N. (1948)

"The Decay of Isotropic Turbulence", *Journal of Applied Mechanics,vol.15,pp.311-321.*

Garry, K.P. (1990)

"Private Communication", *Cranfield University, Cranfield, U.K.*

Gaster, M. (1969)

"The Formation of Regions of Separated Flow on Wing Surfaces",

Part I and Part II, ARC R&M No 3122.

Gaster, M. (1974)

"On the Effect of Boundary Layer Growth on Flow Stability",

Journal of Fluid Mechanics, vol. 66, pp. 465-480.

Gaster, M. and Jordinson, R. (1975)

"On the Eigenvalues of the Orr-Sommerfeld Equation",

Journal of Fluid Mechanics, vol. 66, pp. 121-133.

Gibbings, J.C., Goksel, O.T. and Hall, D.J. (1986)

"The Influence of Roughness Trips upon Boundary Layer Transition Part 1^{+} Characteristics of Wire Trips", *Aeronautical Journal, October 1986, pp. 289, 301.*

Gostelow, J.P. and Blunden, A.R. (1988)

"Investigations of Boundary Layer Transition in an Adverse Pressure Gradient", *ASME Journal of Turbomachinery, Vol. 111, pp.366-375 (ASME 88-GT-298).*

Gostelow, J.P., Blunden, A.R. and Walker G.J. (1992)

"Effects of Free-Stream Turbulence and Adverse Pressure Gradients on Boundary Layer Transition", *ASME IGTACE Cologne, June 1992, ASME Paper No 92-GT-380.*

Gostelow, J.P. and Walker, G.J. (1990)

"Similarity Behaviour in Transitional Boundary Layers over a Range of Adverse Pressure Gradients and Turbulence Levels", *ASME IGTACE Brussels 1990,* ASME Paper No 90-GT-130.

Goulas, A., Nychas, S., Kastrinakis, E., Fotea, K. and Kyriakides, N. (1992a)

"Transition in Turbomachinery Flows: Effect of Turbulence Level", *Report on BRITE/EURAM Project Contract AERO-002-C(TT), Aristotle University of Thessaloniki, Thessaloniki, Greece.*

Goulas, A., Nychas, S., Kastrinakis, E., Fotea, K. and Kyriakides, N. (1992b)

"Transition in Turbomachinery Flows: Coherent Structures", *Report on BRITE/EURAM Project Contract AERO-002-C(TT), Aristotle University of Thessaloniki, Thessaloniki, Greece.*

Hales, J.L. and Ellender, J.H. (1976)

"Liquid Densities from 293 to 490 K of nine aliphatic alcohols", *Journal of Chemical Thermodynamics, vol. 8, pp. 1177-1184.*

Hall, D.J. (1968)

"Boundary Layer Transition", *PhD Thesis, University of Liverpool, Liverpool, U.K.*

Hall, D.J. and Gibbings, J.C. (1972)

"Influence of Steam Turbulence and Pressure Gradient upon Boundary Layer Transition", *Journal of Mechanical Engineering Science, vol. 14, No 2, pp. 134-146.*

Hazarika, B.K. and Hirsch, Ch. (1991a)

"Transition in Turbomachinery Flows",*Report on BRITE-EURAM Project Contract AERO-0002-C(TT), Report No TR/1/91, Vrije Universiteit Brussel.*

Hazarika, B.K. and Hirsch, Ch. (1991b)

"Transition in Turbomachinery Flows", *Progress Report on BRITE-EURAM Project Contract AERO-0002-C(TT), Report No VUB-STR-17, Vrije Universiteit Brussel.*

Hazarika, B.K. and Hirsch, Ch. (1991c)

"Transition in Turbomachinery Flows: Effect of Shear Flow", *Report on BRITE-EURAM Project Contract AERO-0002-C(TT), Report No VUB-STR-18, Vrije Universiteit Brussel.*

Hazarika, B.K. and Hirsch, Ch. (1992)

"Transition in Turbomachinery Flows", *Final Report on BRITE-EURAM Project Contract AERO-0002-C(TT), Report No VUB-STR-19, Vrije Universiteit Brussel.*

Hebbar, K.S. (1980)

"Wall Proximity Corrections for Hot-Wire Readings in Turbulent Flows",
DISA Information No. 25, pp. 15-16.

Hendley, T.B. and Keffer, J.F. (1974)

"Turbulent / Non-Turbulent Decisions in an intermittent flow",
Journal of Fluid Mechanics, vol. 64, part 4, pp. 625-644.

Hinze, J.O. (1975)

"Turbulence", *2nd edition, McGraw-Hill, New York.*

Hirsch,, Ch. (1988)

"Numerical Computation of Internal and External Flows",
J. Wiley & Sons Publishing, vol. 1 and 2, New York, U.S.A.

Hodson, H.P. (1984)

"Boundary Layer Transition and Separation Near the Leading Edge of a High-Speed Turbine Blade", *IGTACE Amsterdam, June 1984, ASME paper No 84-GT-179.*

Hourmouziadis, J. (1989)

"Aerodynamic Design of Low Pressure Turbines", *Lecture 8, AGARD LS-167.*

Jones, W.P. and Launder, B.E. (1973)

"The calculation of Low-Reynolds-Number Phenomena with a Two-Equation Model of Turbulence", *International Journal of Heat and Mass Transfer, vol.16, pp.1119-1129.*

Jonson, J.R. (1989)

"Introduction to Digital Signal Processing",

Prentice-Hall International Inc., New Jersey, U.S.A.

Kalfas, A.I. (1989)

"A Study of the Flow Around Blading. Interactive Calculation of the Core Flow and the Viscous Boundary Layers",

Diploma Thesis, Aristotle University of Thessaloniki, Thessaloniki, Greece.

Kalfas, A.I. and Elder, R.L. (1991)

"Transition in Turbomachinery Flows",

Progress report on the BRITE - EURAM project contract AERO-0002-C(TT), Report No TR/91/1, Cranfield Institute of Technology, Cranfield, U.K.

Kalfas, A.I. and Elder, R.L. (1992)

"Transition in Turbomachinery Flows",

Final Report on BRITE-EURAM project contract AERO-0002-C(TT), Report No TR/92/1, Cranfield Institute of Technology, Cranfield, U.K.

Kalfas, A.I. and Elder, R.L. (1993)

"Experimental Investigation of Boundary Layer Transition on a Flat Plate with C4 Leading Edge", *Paper No ISABE-93-7123, XI ISABE, Tokyo, Japan.*

Kármán, Th. von (1948)

"Progress in the Statistical Theory of Turbulence",

Journal of Marine Research, vol 7, pp. 252-264.

King, L.V. (1914)

"On the Convection of Heat from Small Cylinders in a Stream of Fluid: Determination of the Convection Constants of Small Platinum Wires with Applications to Hot-Wire Anemometry", *Philosophical Transactions of the Royal Society of London: Series A, vol. 214, pp. 373 - 432.*

Krishnamoorthy, I.V., Wood, D.H., Antonia, R.A. and Chambers, A.J. (1985)
"Effect of Wire Diameter and Overheat Ratio Near a Conducting Wall",
Experiments in Fluids, vol. 3, pp. 121-127.

Lam, C.K.G. and Bremhorst, K. (1981)
"A Modified Form of the k-ε Model for Predicting Wall Turbulence",
Transaction of ASME, Journal of Fluids Engineering, vol. 103, pp. 456-460.

Launder, B.E. and Sharma, B.I. (1974)
"Application of the Energy-Dissipation Model of Turbulence to the Calculation of Flow Near a Spinning Disc", *Letters in Heat and Mass Transfer, vol. 1, pp. 131-138.*

Launder, B.E. and Spalding, D.B. (1974)
"The Numerical Computation of Turbulent Flows",
Computational Methods in Applied Mechanical Engineering, vol. 3, pp. 269-289.

Lee, D.A. and Tan, H.S. (1967)
"Study of Inhomogeneous Turbulence",
The Physics of Fluids, vol. 10, no. 6, pp.1224-1230.

Lomas, C. G. (1986)
"Fundamentals of Hot-Wire Anemometry",
Cambridge University Press, Cambridge, U.K.

Masker, A.J. (1979)
"Explicit Expression for the Smooth Wall Velocity Distribution in a Turbulent Boundary Layer", *AIAA Journal, vol. 17, no.6, pp. 655-657.*

Mayle, R.E. (1991)
"The Role of Laminar-Turbulent Transition in Gas Turbine Engines",
IGTACE Orlando, June 1991, ASME paper No 91-GT-261.

Mayle, R.E. and Dullenkopf, K. (1990)
"A Theory for Wake-Induced Transition",
Transactions of ASME, Journal of Turbomachinery, vol.112, pp. 188-195.

McCroskey, W.J. (1971)
"Measurements of Boundary Layer Transition, Separation and Streamline Direction on Rotating Blades", *NASA TN D-6321.*

Merzkirch, W. (1987)

"Techniques of Flow Visualization", *AGARD-AG-302.*

Meyer, P. L. (1970)

"Introductory Probability and Statistical Applications",

Addison-Wesley Publishing Co., Reading, Massachusetts, U.S.A.

Moir, I.R.M. (1986)

"Recent Experience in the RAE 5 Metre Wind Tunnel of a China Clay Method for Indicating Boundary Layer Transition", *Aeronautical Journal, Paper No 1391.*

Morkovin, M.V. (1978)

"Instability, Transition to Turbulence and Predictability", *AGARD-AG-236.*

Nagano, Y. and Hishida, M. (1987)

"Improved Form of the k-ε Model for Wall Turbulent Shear Flows",

Transactions of ASME, Journal of Fluids Engineering, vol. 109, pp. 156-160.

Narasimha, R. (1957)

"On the Distribution of Intermittency in the Transition Region of a Boundary Layer",

Journal of the Aeronautical Sciences, September 1957, pp. 711-712.

Narasimha, R. (1985)

"The Laminar-Turbulent Transition Zone in the Boundary Layer",

Progress in the Aerospace Science, vol. 22, pp. 29-80.

Oka, S. and Kostič, Ž. (1972)

"Influence of wall Proximity on Hot Wire Velocity Measurements",

DISA Information No. 13, pp.29-33.

Owen, P.R. and Klanfer, L. (1955)

"On the Laminar Boundary Layer Separation from the Leading Edge of a Thin Aerofoil", *ARC C.P. 220.*

Owen, D.B. (1962)

"Handbook of Statistical Tables", *Pergamon Press, London.*

Patankar, S.V. and Spalding, D.B. (1972)

"A Calculation Procedure for Heat Mass and Momentum Transfer in Three-Dimensional Parabolic Flows",

International Journal of Heat and Mass Transfer, vol. 15, pp. 1787-1806.

Patankar, S.V. (1981)

"A Calculation Procedure for Two-Dimensional Elliptic Situations",

Numerical Heat Transfer, vol.4, no. 4, pp. 409-426.

Patel, V.C., Rodi, W. and Scheuerer, G. (1985)

"Turbulence Models for Near-Wall and Low Reynolds Number Flows: A Review", *AIAA Journal, vol. 23, pp.1308-1319.*

Paxson, D.E. and Mayle, R.E. (1991)

"Laminar Boundary Layer Interaction with an Unsteady Passing Wake",

Transactions of ASME, Journal of Turbomachinery, vol.113, pp. 419-427.

Perry, A.E. (1982)

"Hot-Wire Anemometry", *Oxford University Press, Oxford, U.K.*

Psoinos, D.P. (1985)

"Applied Statistics", *Ziti Publications, Thessaloniki, Greece.*

Rai, M.M and Moin, P. (1991)

"Direct Numerical Simulation of Transition and Turbulence in a Spatially Evolving Boundary Layer", *AIAA-91-1607-CP, pp. 890-914.*

Ramirez, R. (1985)

"The FFT, Fundamentals and Concepts", *Prentice- Hall, New Jersey.*

Reichardt, H. (1940)

"Die Wärmeübertrangung in Turbulenten Reibungsschichten",

Z. Angew. Math. Mech. 20, 297-328.

Reynolds, O. (1883)

"On the Experimental Investigation of the Circumstances which Determine whether the Motion of Water shall be Direct or Sinuous, and the Law of Resistance in Parallel Channels",

Philosophical Transactions of the Royal Society of London A 174, pp. 935-982.

Roach, P.E. (1989)

"The Generation of Nearly Isotropic Turbulence by Means of Grids",

Heat and Fluid Flow, Vol.8, No 2, pp 82-91.

Roach, P.E., and Brierley, D.H. (1989)

"The Influence of Turbulent Free Stream on Zero Pressure Gradient Transitional Boundary Layer Development". *Rolls-Royce Plc, Derby, U.K.*

"Part I : Summary of the Present Work", *Interim Report, RR(OH)1003.*

"Part II : Start and of Transition", *Interim Report, RR(OH)1029.*

"Part III: Laminar Boundary Layers", *Interim Report, RR(OH)1030.*

"Part IV : Turbulent Boundary Layers", *Interim Report, RR(OH)1031.*

"Part V : Transitional Boundary Layers", *Interim Report, RR(OH)1032.*

Rodi, W. and Scheuerer, G. (1985)

"Calculation of the Heat Transfer to Convection-Cooled Gas Turbine Blades", *Transactions of ASME, Journal of Engineering for Gas Turbines and Power, vol.107, pp. 620-627.*

Royal Aeronautical Society (1991)

"Proceedings of the Boundary Layer Transition and Control Conference", *Cambridge, U.K.*

Savill, A.M. (1991)

"Turbulence Model Predictions for Transition under Free-Stream Turbulence", *Poster Paper for RAeS Transition and Boundary Layer Conference, Cambridge, U.K.*

Savill, A.M. (1993)

"Transition Modelling for Turbomachinery; A Summary of ERCOFTAC Transition SIG Progress", *1st Workshop of the BRITE-EURAM Aero-CT92-0052 Project Transition in Turbomachinery, UMIST, Manchester, December 14-15, 1993.*

Schlichting, H. (1933)

"Zur Entstehung der Turbulenz bei der Plattenströmung", *Math. Phys. Klasse 182-208.*

Schlichting, H. (1979)

"Boundary layer theory", *7th edition, McGraw Hill, New York.*

Schubauer, G.B. and Klebanoff, P.S. (1955)

"Contributions on the Mechanics of Boundary-Layer Transition", *NACA TN 3489.*

Schubauer, G.B. and Skramstad, H.K. (1948)

"Laminar-Boundary-Layer Oscillations and Transition on a Flat Plate", *NACA Report 909.*

Singh, U.K. and Shaw, R. (1972)

"Hot-Wire Anemometer Measurements in Turbulent Flow Close to a Wall", *Proceedings of DISA Conference, pp. 35-38.*

Sohn, K.H., O'Brien, J.E., and Reshotko, E. (1989)

"Some Characteristics of Bypass Transition in a Heated Boundary Layer",

NASA TM 102126.

Suder, L.S., O'Brien, J.E., and Reshotko, E. (1988)

"Experimental Study of Bypass Transition in a Boundary Layer", *NASA TM 100913.*

Stewart, I.R. (1987)

"A Model for Transition by Attachment Line Contamination and an Examination of Cross Flow Instability in Three-Dimensional Boundary Layers",

PhD Thesis, Cranfield Institute of Technology, Cranfield, U.K.

Tan, C.N. and Auld, D.J. (1991)

"Experimental Investigation of Laminar to Turbulent Boundary Layer Transition with Separation Bubbles at Low Reynolds Number", *RAeS Boundary Layer Transition & Control Conference, Cambridge, UK.*

Taylor, G.I. (1938a)

"Statistical Theory of Turbulence, Parts I-IV",

Proceedings of the Royal Society of London A164, pp.192-215.

Taylor, G.I. (1938b)

"The Spectrum of Turbulence",

Proceedings of the Royal Society of London A164, pp.476-490.

Tennekes, H. and Lumley, J.L. (1972)

"A First Course in Turbulence", *MIT Press, Cambridge, Massachusetts, U.S.A.*

Thinh, N. van (1969)

"On Some Measurements Made by Means of a Hot Wire in a Turbulent Flow Near a Wall", *DISA Information No 7, pp. 13-18.*

Thwaites, B. (1949)

"Approximate Calculation of the Laminar Boundary Layer",

Aeronautical Quarterly, vol. 1.

Toupin, T. (1989)

"Computational Modelling of Turbine Blade Boundary Layers",

MSc Thesis, Cranfield Institute of Technology, Cranfield, U.K.

Tollmien, W. (1929)

"Über die Entstehung der Turbulenz",

Math. Phys. Klasse 21-44; English Translation in NACA TM 609 (1931).

Turner, A.B. (1971)

"Local Heat Transfer Measurements on a Gas Turbine Blade",

Journal of Mechanical Engineering Sciences, vol. 13, pp. 1-12.

Uberoi, M.S. and Wallis, S. (1967)

"Effect of Grid Geometry on Turbulence Decay",

Physics of Fluids, Vol. 10, No 6, pp 1216-1224.

Walker, G.J. (1974)

"The Unsteady Nature of Boundary Layer Transition on an Axial Compressor Blade",

ASME Paper 74-GT-135.

Walker, G.J. (1975)

"Observations of Separated Laminar Flow on Axial Compressor Blading",

ASME Paper 75-GT-63.

Walker, G.J. (1987)

"Transitional Flow on Axial Turbomachine Blading", *AIAA 25th Aerospace Sciences Meeting, January 1987, Reno, Nevada, Paper No. AIAA-87-0010.*

Walker, G.J. (1992)

"The Role of Laminar-Turbulent Transition in Gas Turbine Engines: A Discussion",

ASME IGTACE Cologne, June 1992, ASME Paper 92-GT-301.

Walker G.J. and Gostelow, J.P. (1990)

"Effects of Adverse Pressure Gradients on the Nature and Length of Boundary Layer Transition", *Transactions of ASME, Journal of Turbomachinery, vol.112, pp.196-205.*

Walker, G.J., Subroto, P.H. and Platzer (1988)

"Transition Modelling Effects on Viscous/Inviscid Analysis of Low Reynolds Number Airfoil Flows Involving Laminar Separation Bubbles",

ASME IGTACE Amsterdam, June 1988, ASME Paper 88-GT-32.

White, F.M. (1974)

"Viscous Fluid Flow", *McGraw Hill, New York, U.S.A.*

Wills, J.A.B. (1962)

"The Correction of Hot-Wire Readings for proximity to a solid boundary", *Journal of Fluid Mechanics, vol. 12, pp. 388-396.*

Woodward, D.S. (1967)

"An Investigation of the Parameters Controlling the Behaviour of Laminar Separation Bubbles", *RAE TM 1003.*

Young, A.D. (1989)

"Boundary Layers", *BSP Professional Books, Oxford, U.K.*

Zarić, Z. (1975)

"Wall Turbulence Studies", *Advances in Heat Transfer, vol 8, pp. 285-350.*

APPENDIX A

Analytical Plots of the Profiles of the Time Averaged Quantities Obtained with Hot Wire Anemometry

APPENDIX A

Analytical Plots of the Profiles of the Time Averaged Quantities Obtained with Hot Wire Anemometry

This appendix contains the detailed profiles of the time averaged quantities of the boundary layer that have been obtained using hot wires over a flat plate with C4 leading edge. At each measurement station, the profile of the mean velocity $\bar{u}$ is plotted non-dimensionalised with the local free stream velocity U as well as the profile of the turbulence intensity across the boundary layer. Also, profiles of the skewness factor S and flatness factor T, as defined in chapter 3, are presented in a common scale in order to facilitate comparisons. In all cases, the crosswise coordinate y in non-dimensionalised using the thickness of the boundary layer δ.

Appendix A is organised in three sections. Each section contains the results from the investigation of the boundary layer for the three test cases considered.

Section i> C4 plate U_∞ = 5 m/s Tu_∞ = 4. %

Section ii> C4 plate U_∞ = 15 m/s Tu_∞ = 4. %

Section iii> C4 plate U_∞ = 15 m/s Tu_∞ = 1.8 %

Analytical Plots of the Profiles of the Time Averaged Quantities Obtained with Hot Wire Anemometry

Section i

Boundary layer Investigation of the C4 plate

U_∞ = 5 m/s

Tu_∞ = 4. %

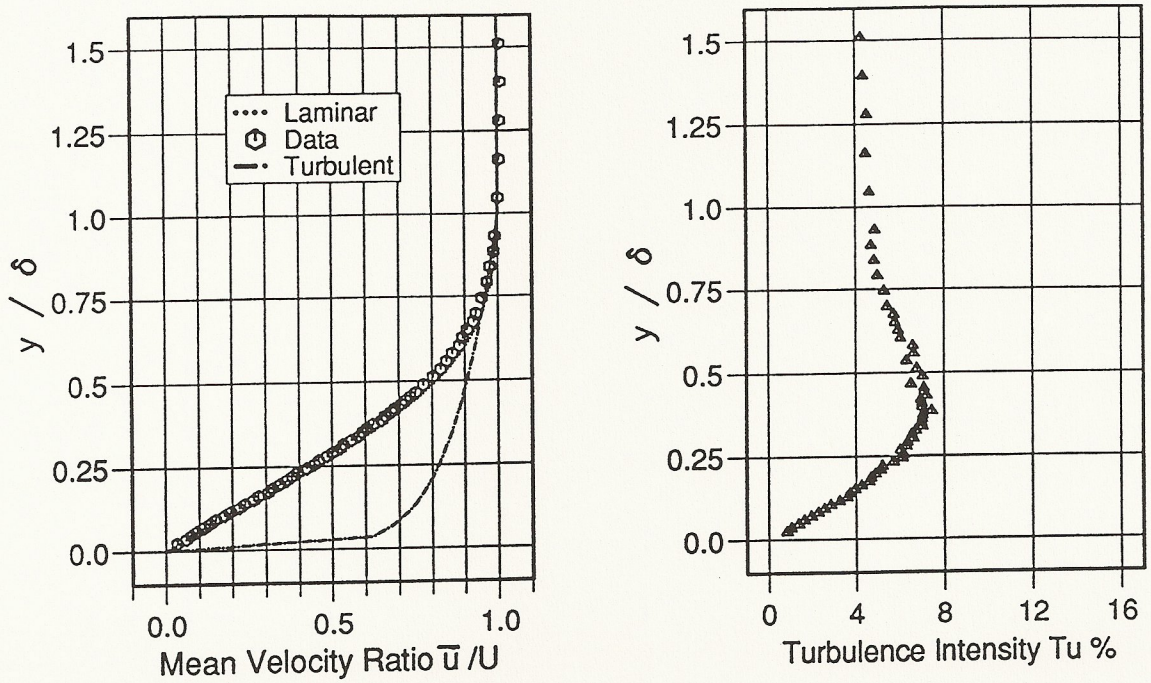


Figure A1.1 — Profiles of the Mean Velocity and Turbulence Intensity
C4 Plate $U_\infty = 5$ m/s $Tu_\infty = 4$ % X = 50 mm

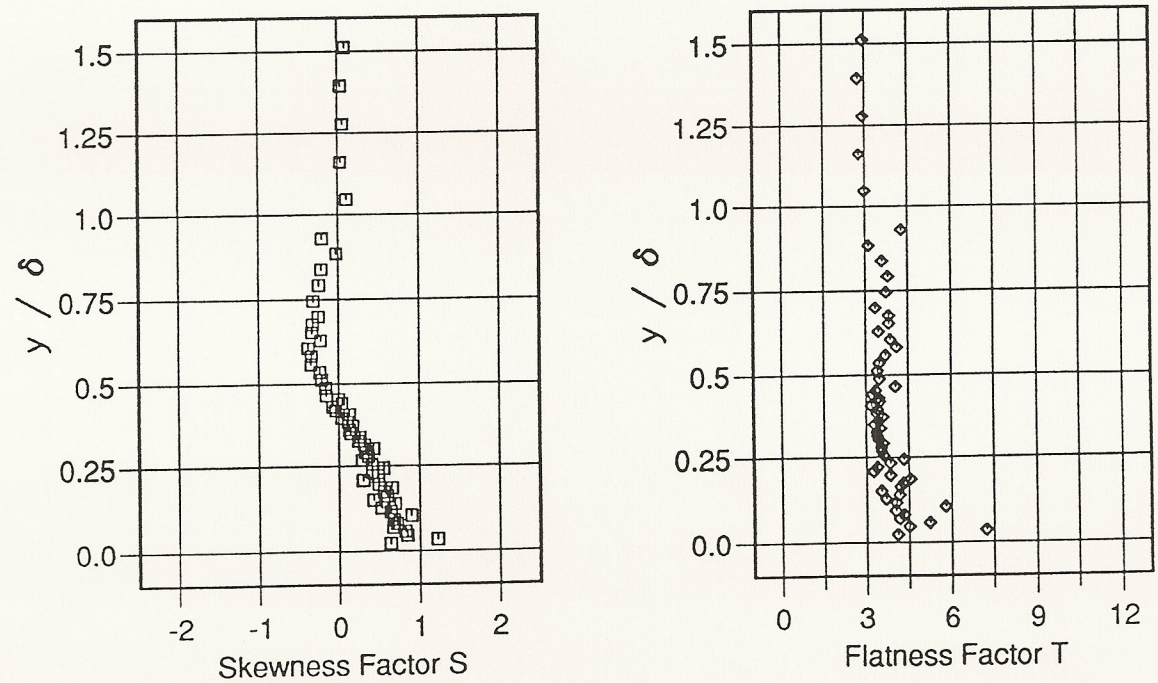
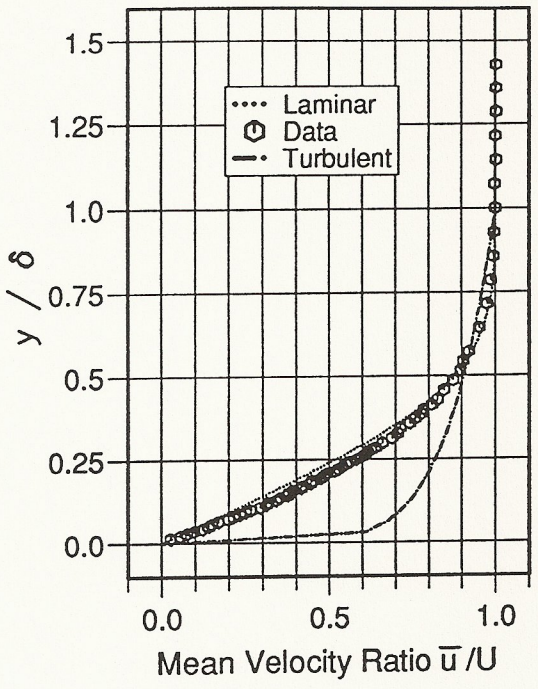


Figure A1.2 — Profiles of the Skewness and Flatness Factors
C4 Plate $U_\infty = 5$ m/s $Tu_\infty = 4$ % X = 50 mm



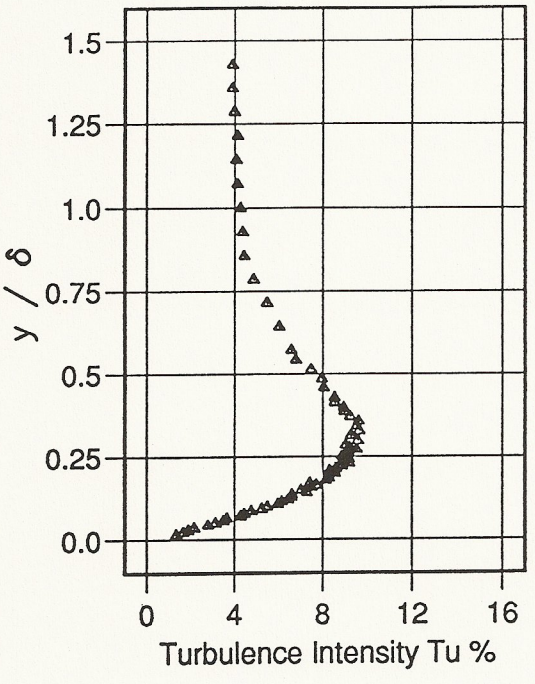
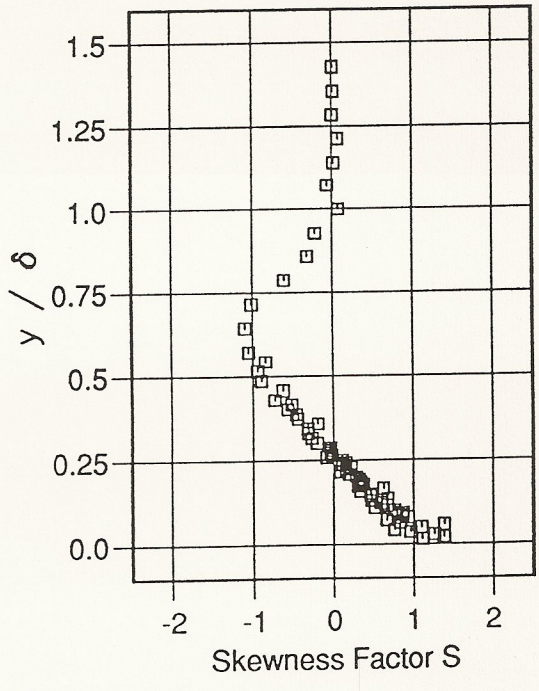


Figure A1.3	Profiles of the Mean Velocity and Turbulence Intensity C4 Plate $U_\infty = 5$ m/s $Tu_\infty = 4$ % X = 100 mm



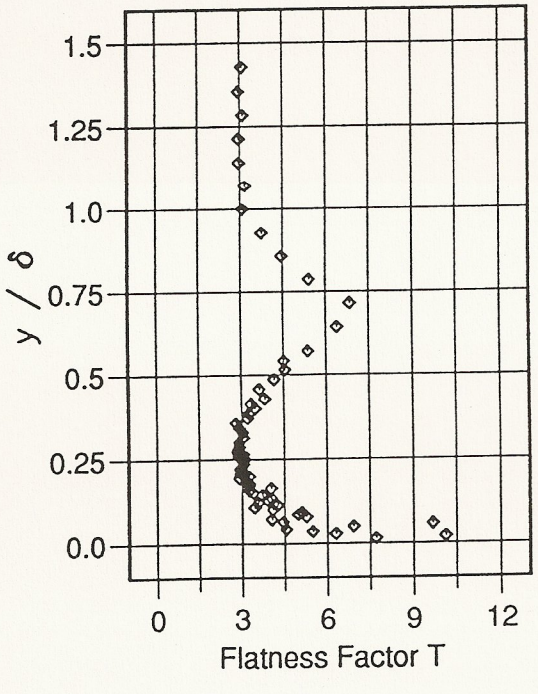
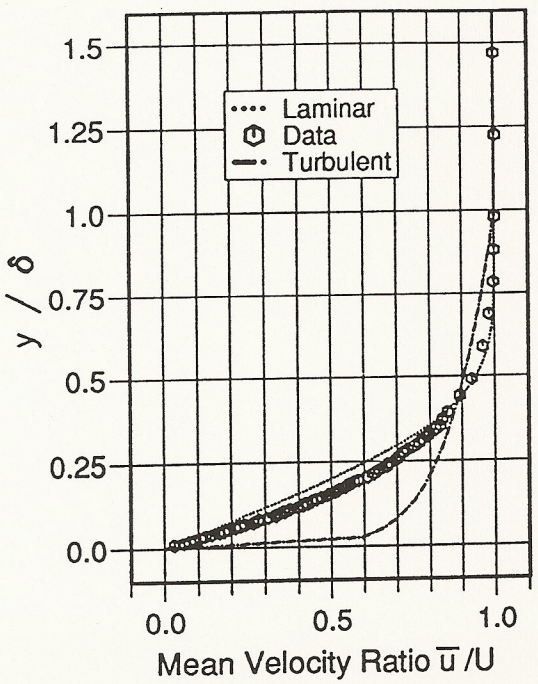


Figure A1.4	Profiles of the Skewness and Flatness Factors C4 Plate $U_\infty = 5$ m/s $Tu_\infty = 4$ % X = 100 mm



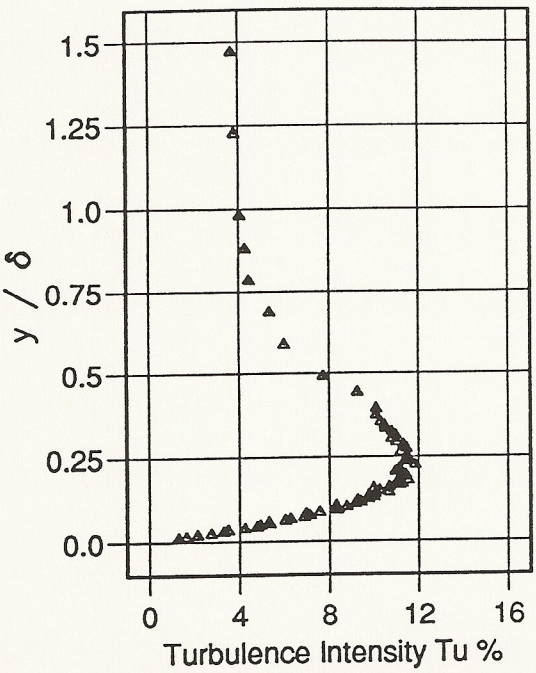
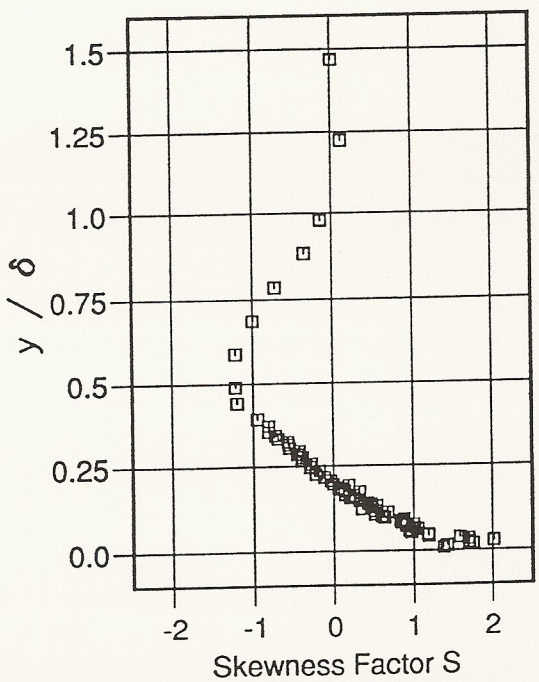


Figure A1.5	Profiles of the Mean Velocity and Turbulence Intensity C4 Plate U_∞ = 5 m/s Tu_∞ = 4 % X = 150 mm



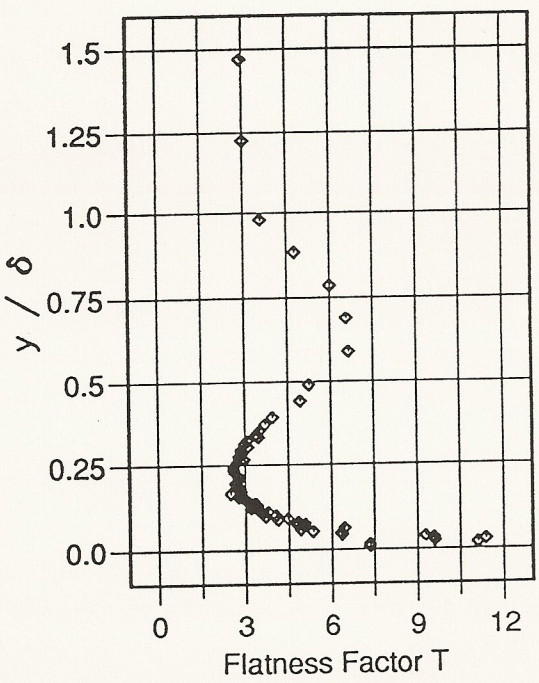


Figure A1.6	Profiles of the Skewness and Flatness Factors C4 Plate U_∞ = 5 m/s Tu_∞ = 4 % X = 150 mm

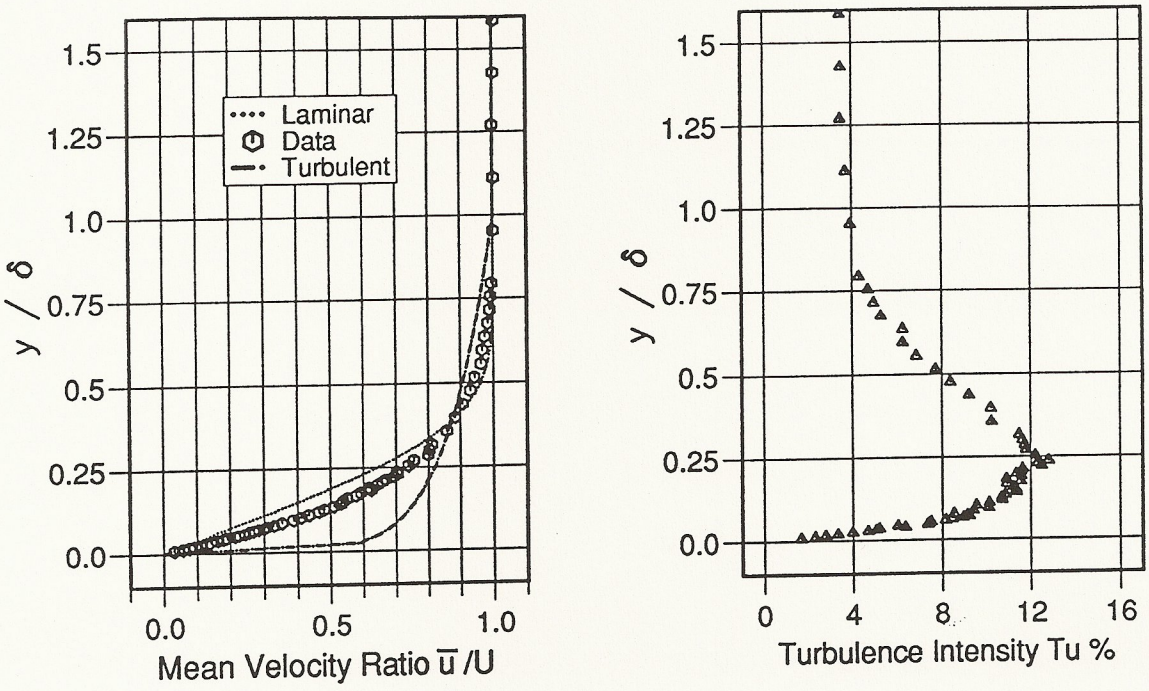


Figure A1.7 — Profiles of the Mean Velocity and Turbulence Intensity
C4 Plate $U_\infty = 5$ m/s $Tu_\infty = 4$ % X = 200 mm

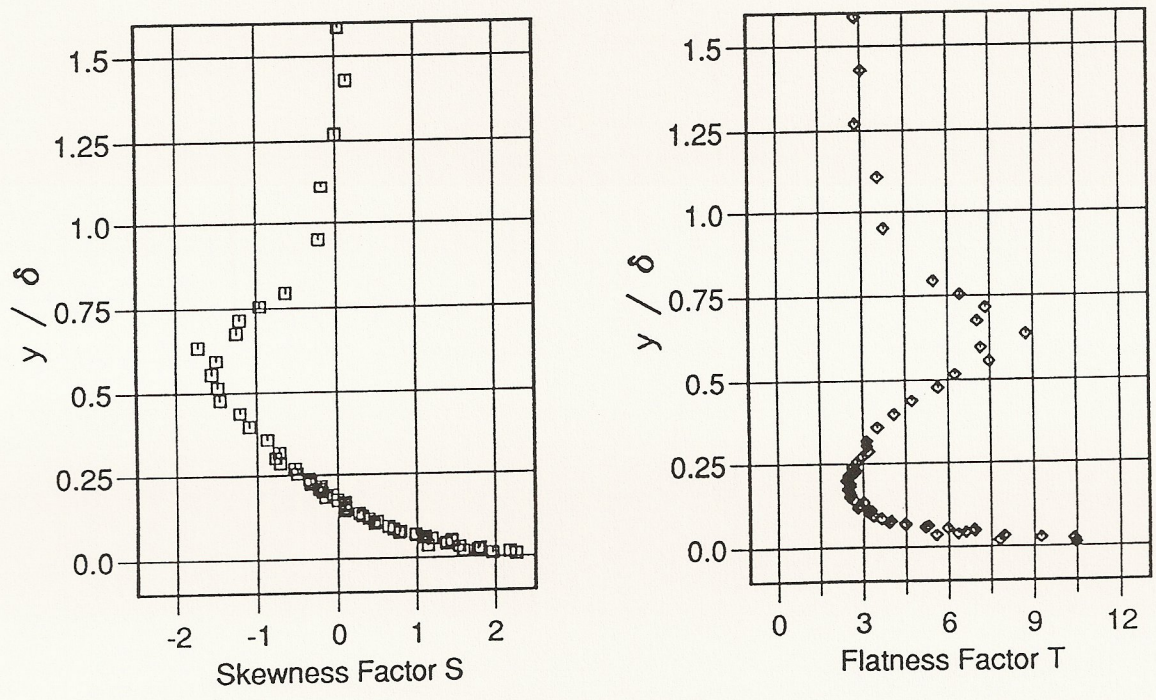
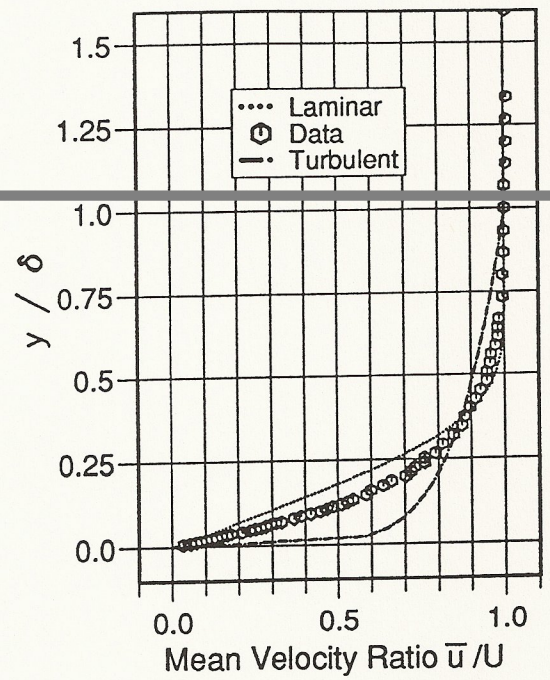


Figure A1.8 — Profiles of the Skewness and Flatness Factors
C4 Plate $U_\infty = 5$ m/s $Tu_\infty = 4$ % X = 200 mm



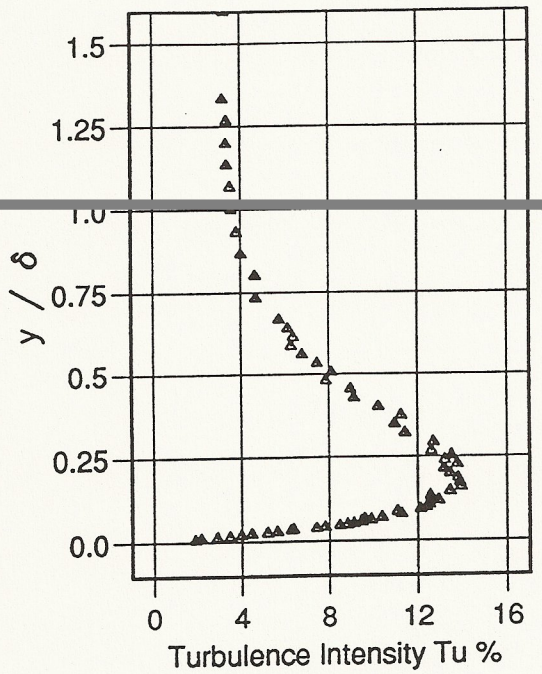
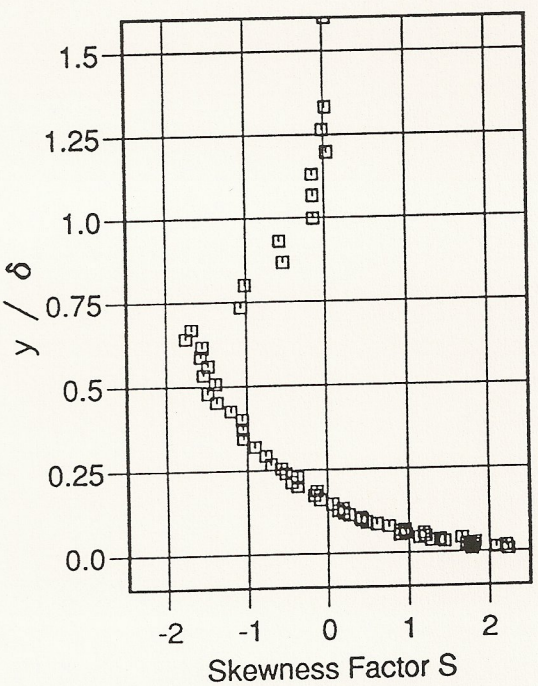


Figure A1.9 — Profiles of the Mean Velocity and Turbulence Intensity
C4 Plate $U_\infty = 5$ m/s $Tu_\infty = 4$ % X = 250 mm



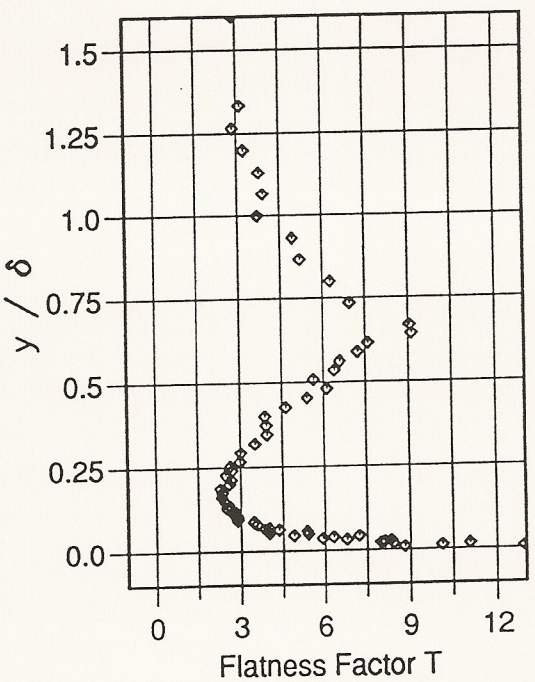
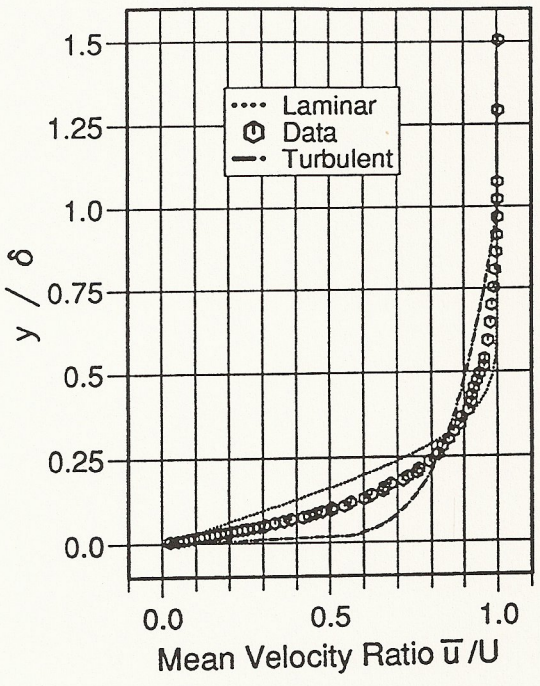


Figure A1.10 — Profiles of the Skewness and Flatness Factors
C4 Plate $U_\infty = 5$ m/s $Tu_\infty = 4$ % X = 250 mm



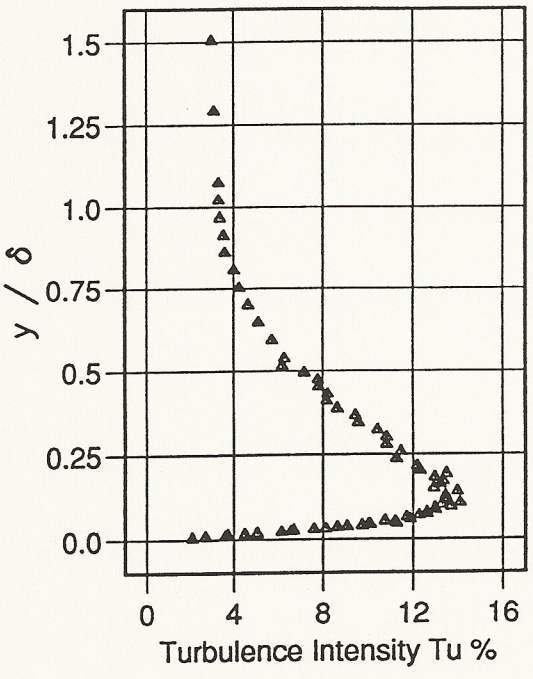
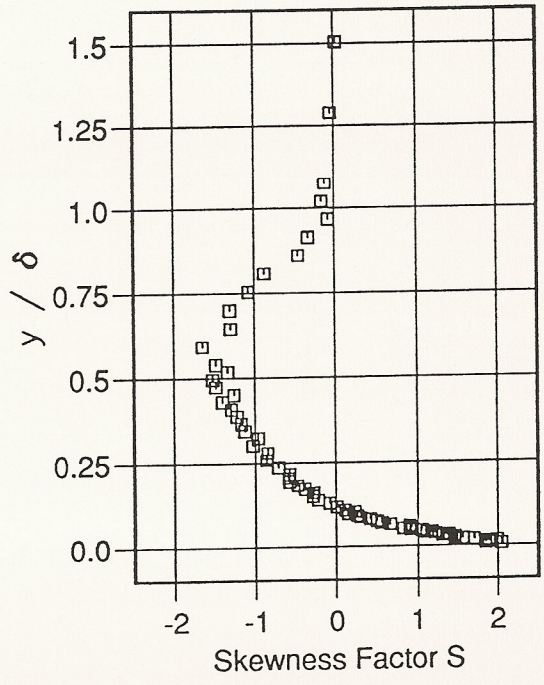


Figure A1.11	Profiles of the Mean Velocity and Turbulence Intensity C4 Plate $U_\infty = 5$ m/s $Tu_\infty = 4$ % X = 300 mm



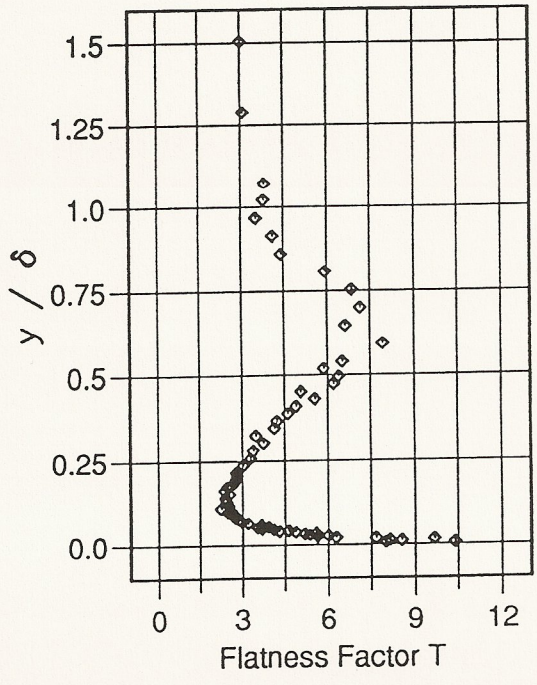


Figure A1.12	Profiles of the Skewness and Flatness Factors C4 Plate $U_\infty = 5$ m/s $Tu_\infty = 4$ % X = 300 mm

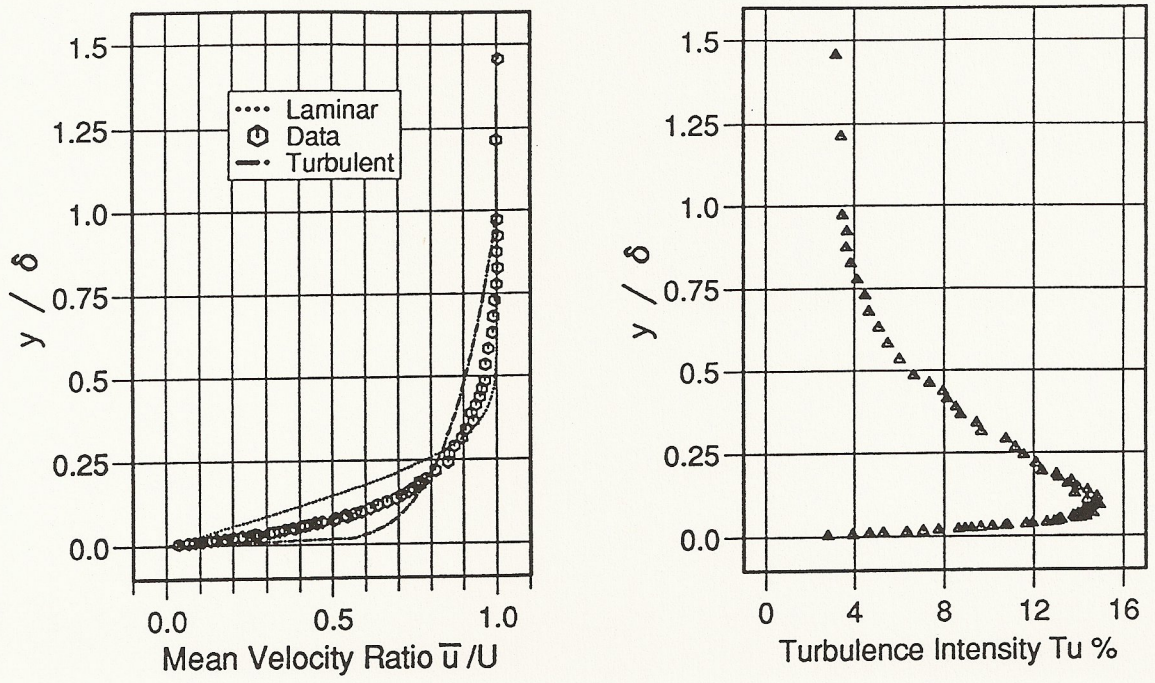


Figure A1.13	Profiles of the Mean Velocity and Turbulence Intensity C4 Plate $U_\infty = 5$ m/s $Tu_\infty = 4$ % X = 325 mm

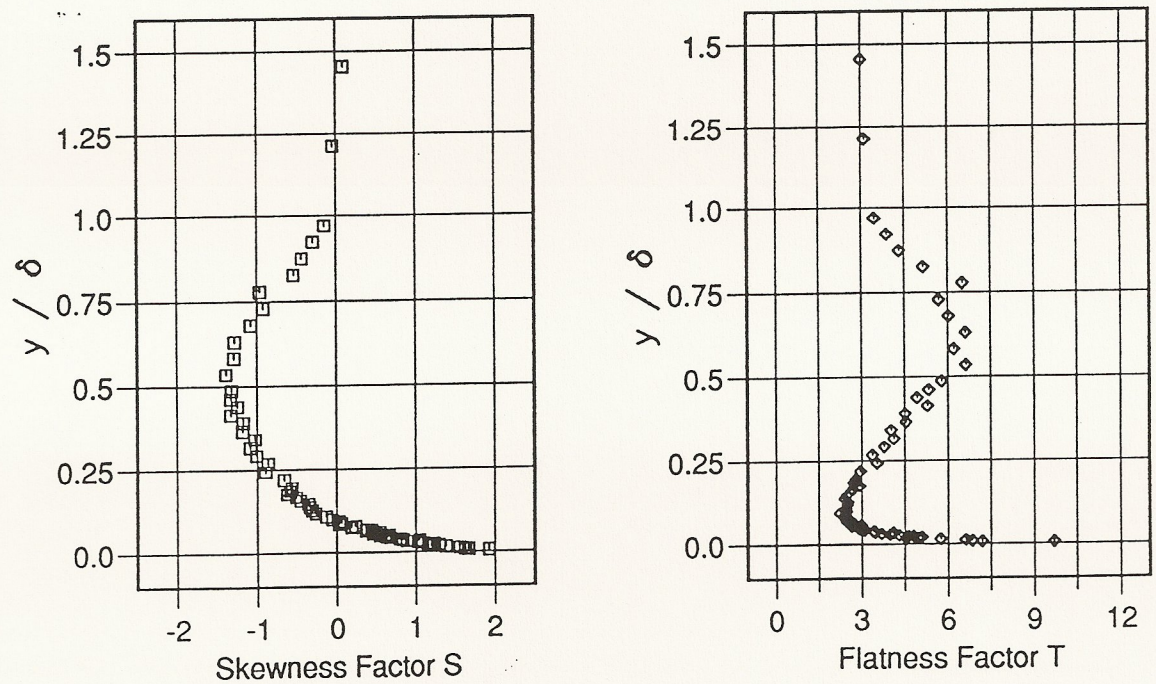
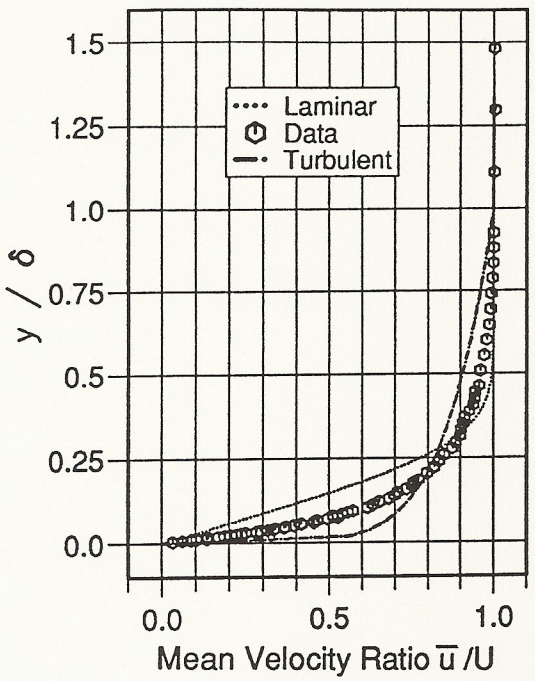


Figure A1.14	Profiles of the Skewness and Flatness Factors C4 Plate $U_\infty = 5$ m/s $Tu_\infty = 4$ % X = 325 mm



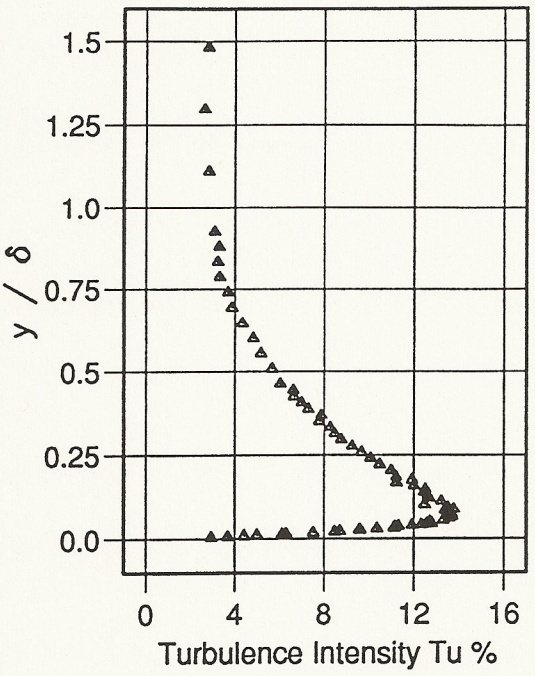
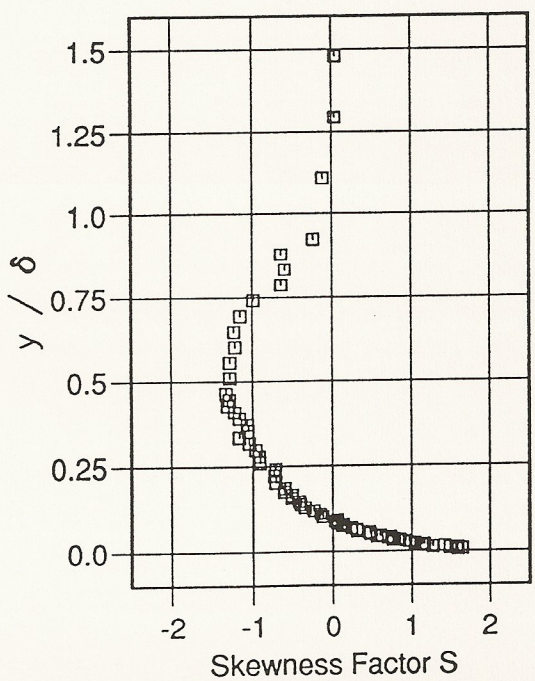


Figure A1.15	Profiles of the Mean Velocity and Turbulence Intensity C4 Plate $U_\infty = 5$ m/s $Tu_\infty = 4$ % X = 350 mm



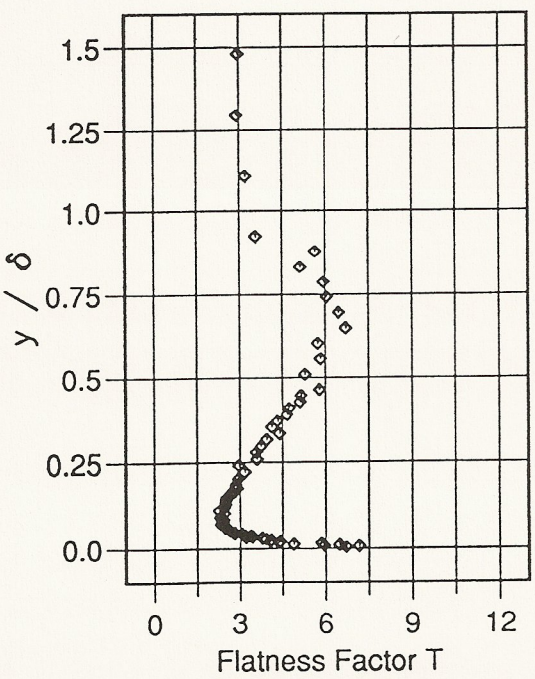
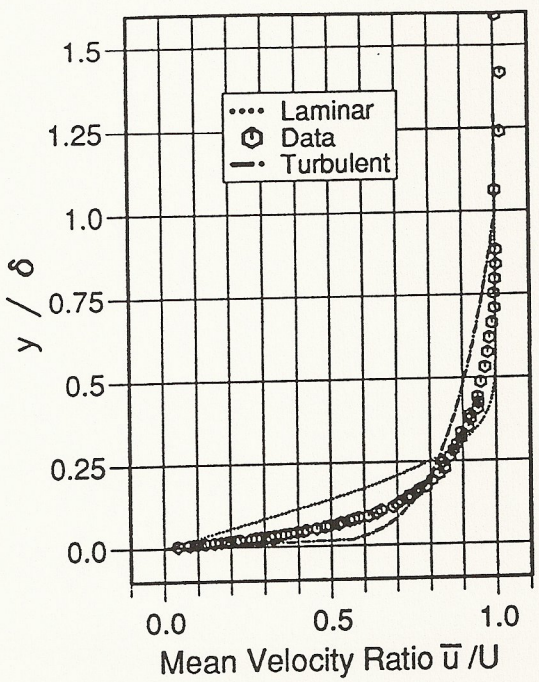


Figure A1.16	Profiles of the Skewness and Flatness Factors C4 Plate $U_\infty = 5$ m/s $Tu_\infty = 4$ % X = 350 mm



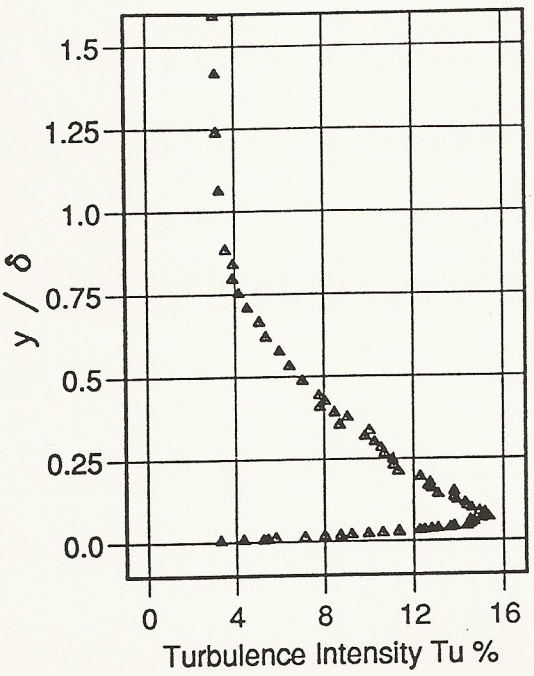
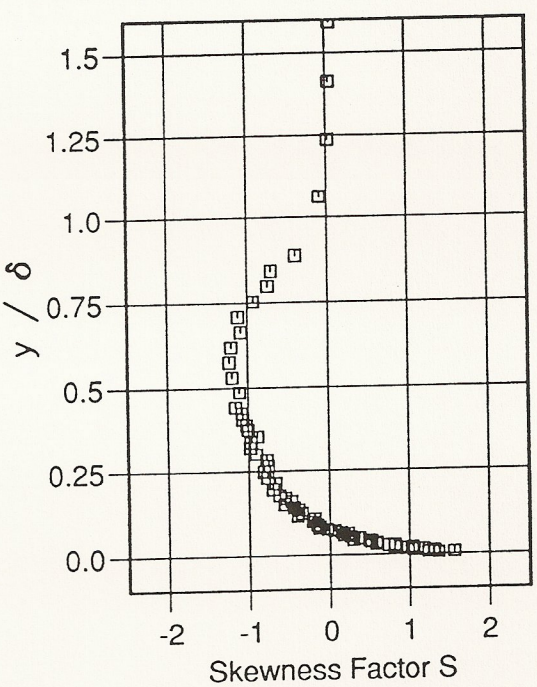


Figure A1.17	Profiles of the Mean Velocity and Turbulence Intensity C4 Plate $U_\infty = 5$ m/s $Tu_\infty = 4$ % X = 375 mm



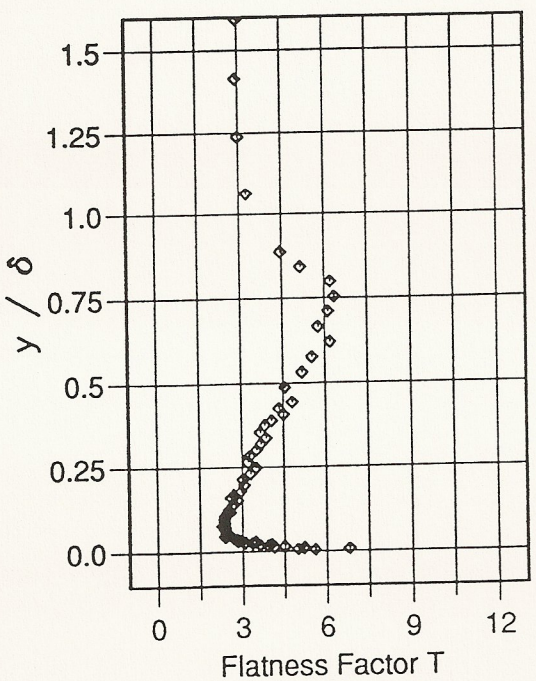
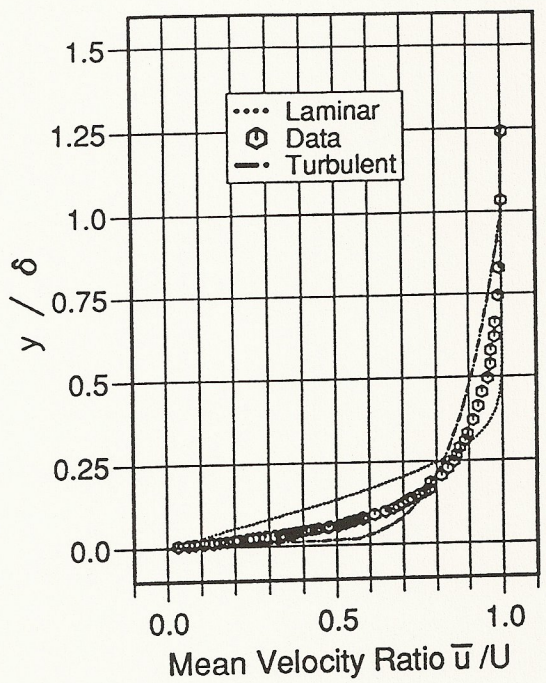


Figure A1.18	Profiles of the Skewness and Flatness Factors C4 Plate $U_\infty = 5$ m/s $Tu_\infty = 4$ % X = 375 mm



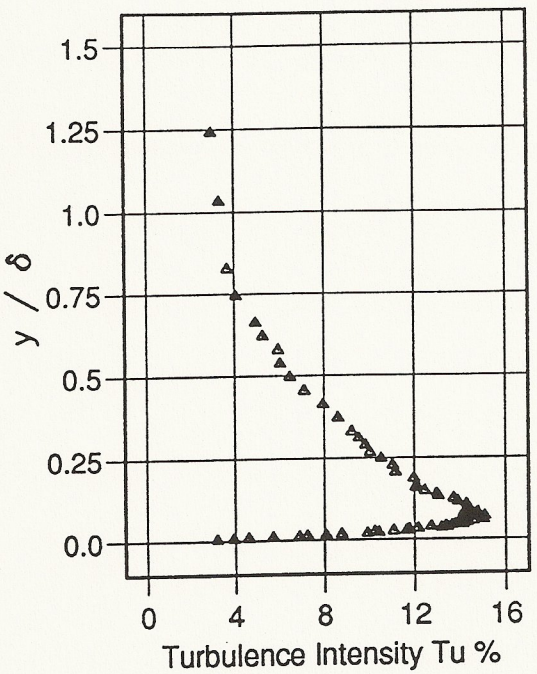
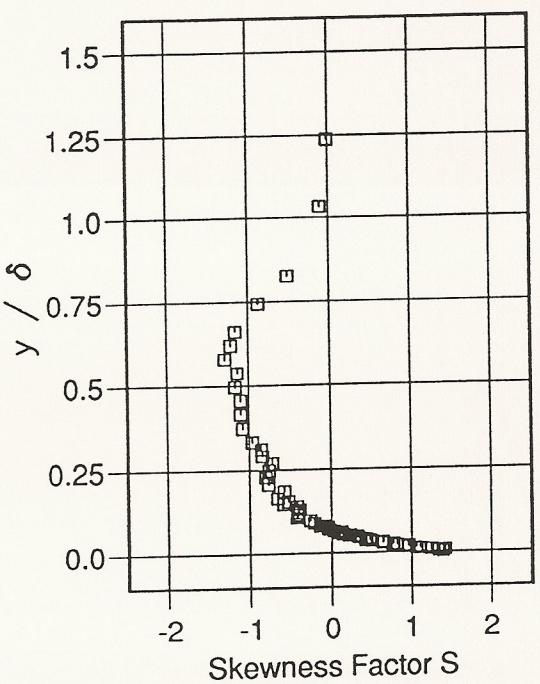


Figure A1.19	Profiles of the Mean Velocity and Turbulence Intensity C4 Plate $U_\infty = 5$ m/s $Tu_\infty = 4$ % X = 400 mm



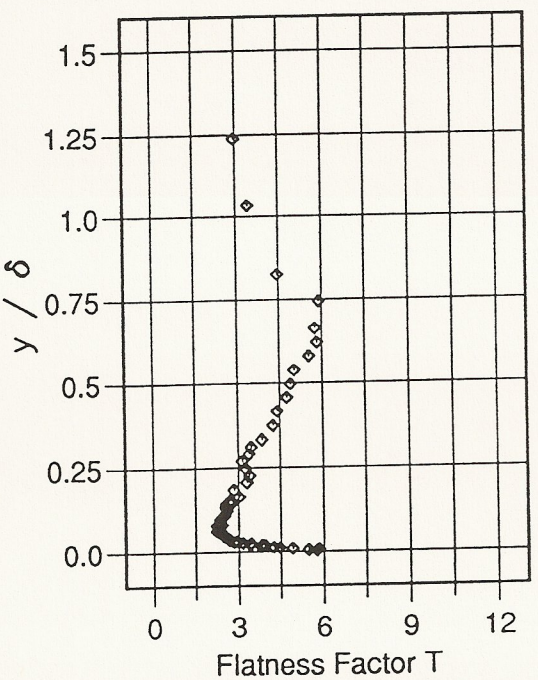
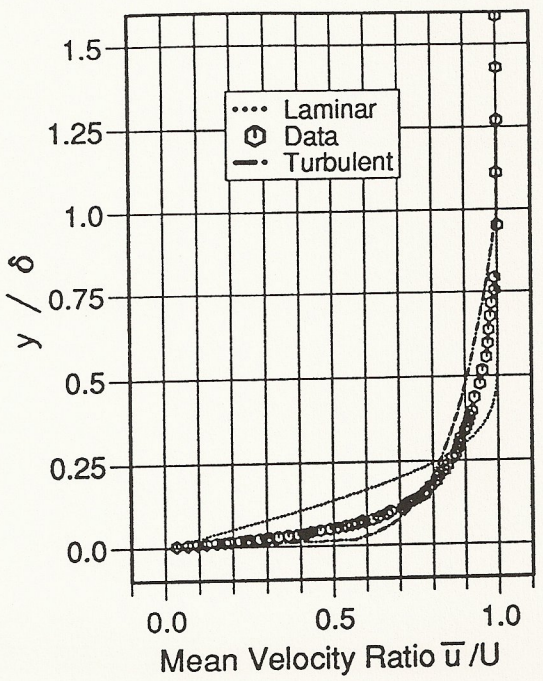


Figure A1.20	Profiles of the Skewness and Flatness Factors C4 Plate $U_\infty = 5$ m/s $Tu_\infty = 4$ % X = 400 mm



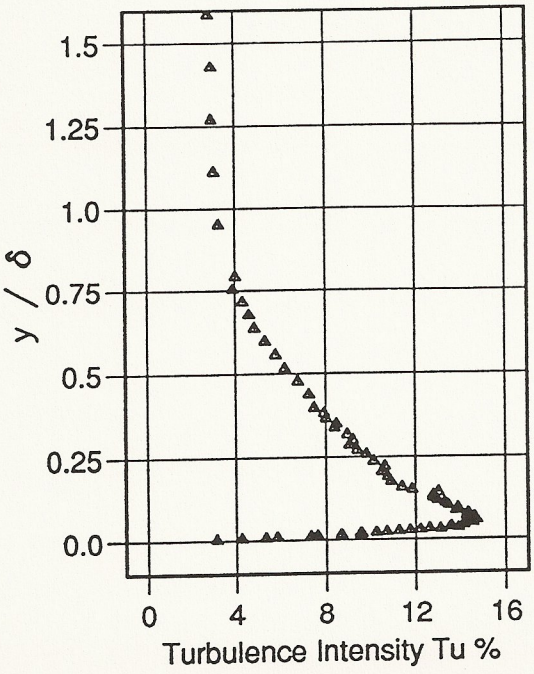
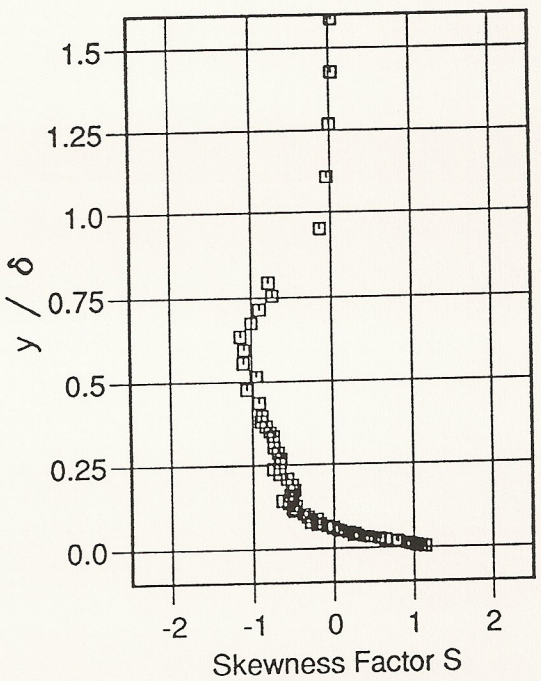


Figure A1.21	Profiles of the Mean Velocity and Turbulence Intensity C4 Plate $U_\infty = 5$ m/s $Tu_\infty = 4$ % X = 425 mm



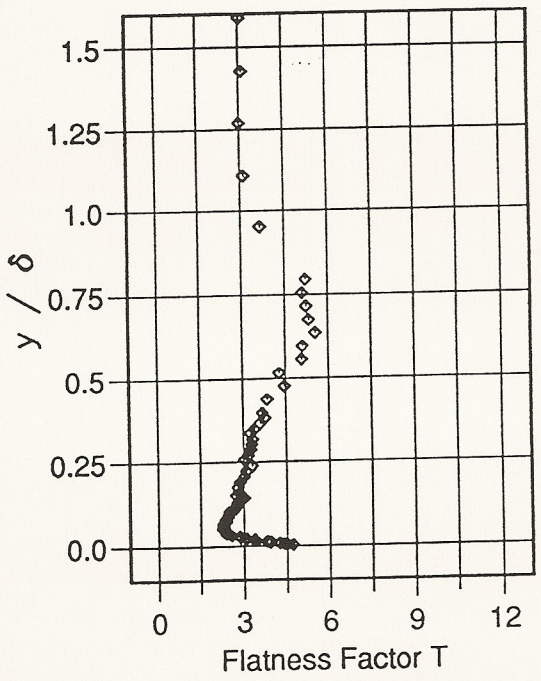
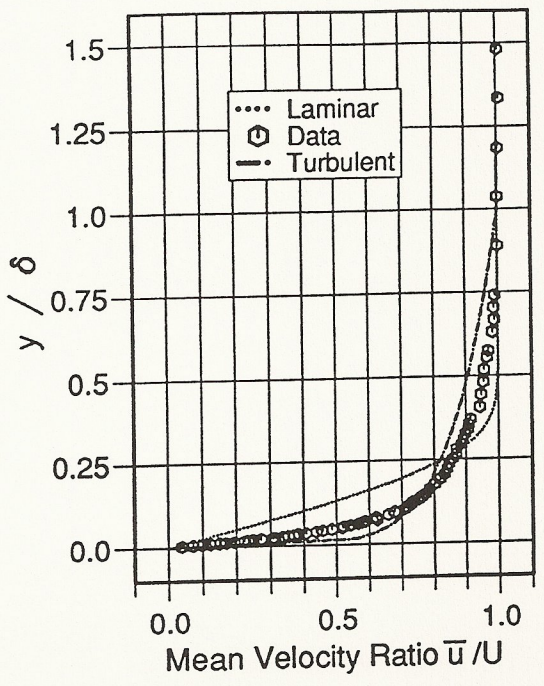


Figure A1.22	Profiles of the Skewness and Flatness Factors C4 Plate $U_\infty = 5$ m/s $Tu_\infty = 4$ % X = 425 mm



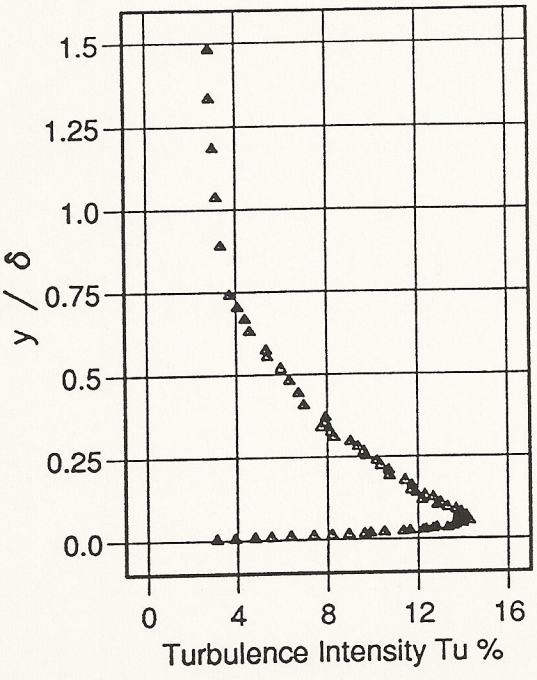
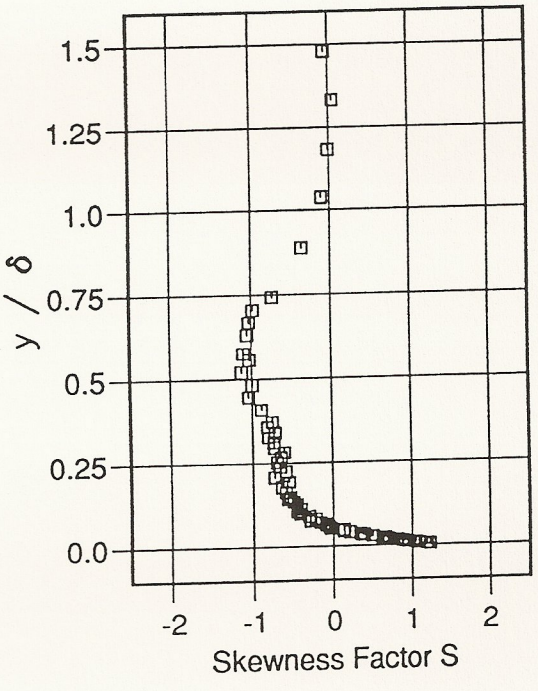


Figure A1.23	Profiles of the Mean Velocity and Turbulence Intensity C4 Plate $U_\infty = 5$ m/s $Tu_\infty = 4$ % X = 450 mm



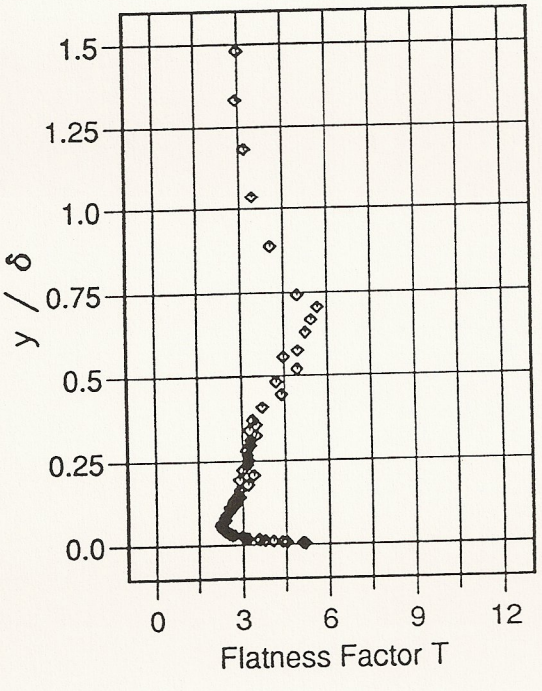
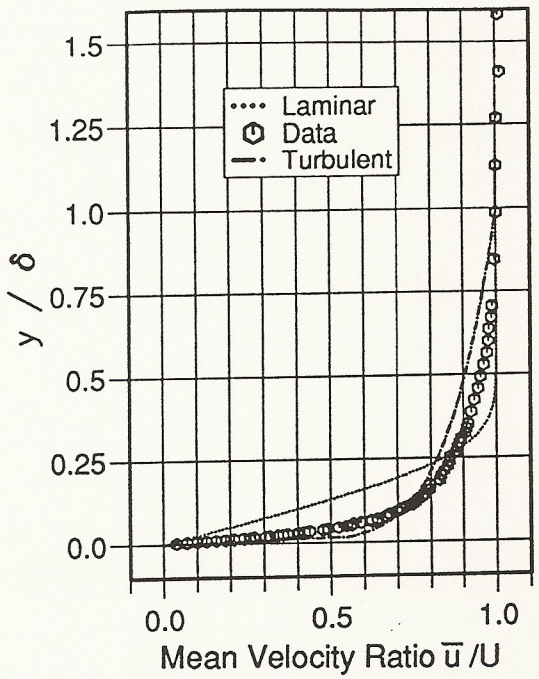


Figure A1.24	Profiles of the Skewness and Flatness Factors C4 Plate $U_\infty = 5$ m/s $Tu_\infty = 4$ % X = 450 mm



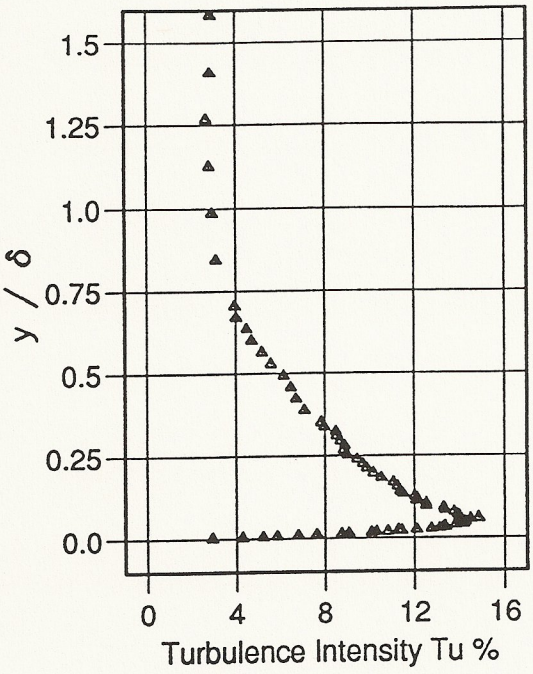
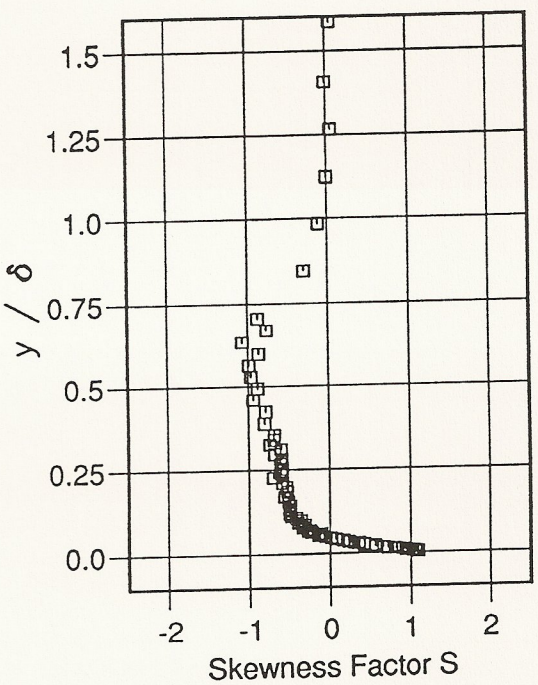


Figure A1.25	Profiles of the Mean Velocity and Turbulence Intensity C4 Plate $U_\infty = 5$ m/s $Tu_\infty = 4$ % X = 475 mm



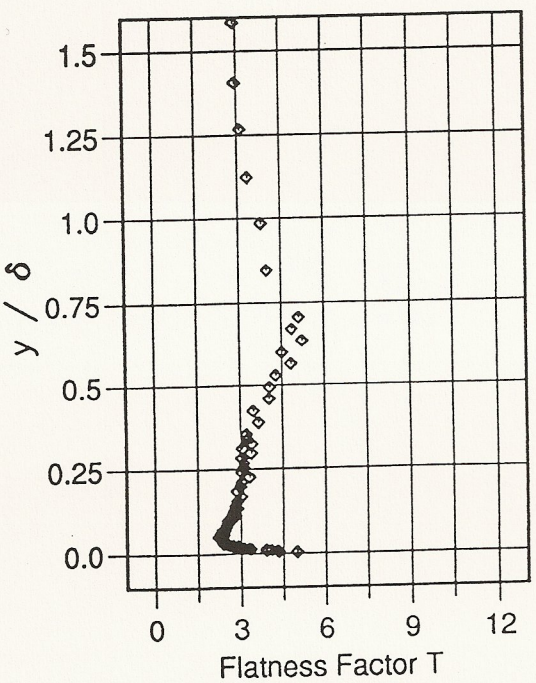


Figure A1.26	Profiles of the Skewness and Flatness Factors C4 Plate $U_\infty = 5$ m/s $Tu_\infty = 4$ % X = 475 mm

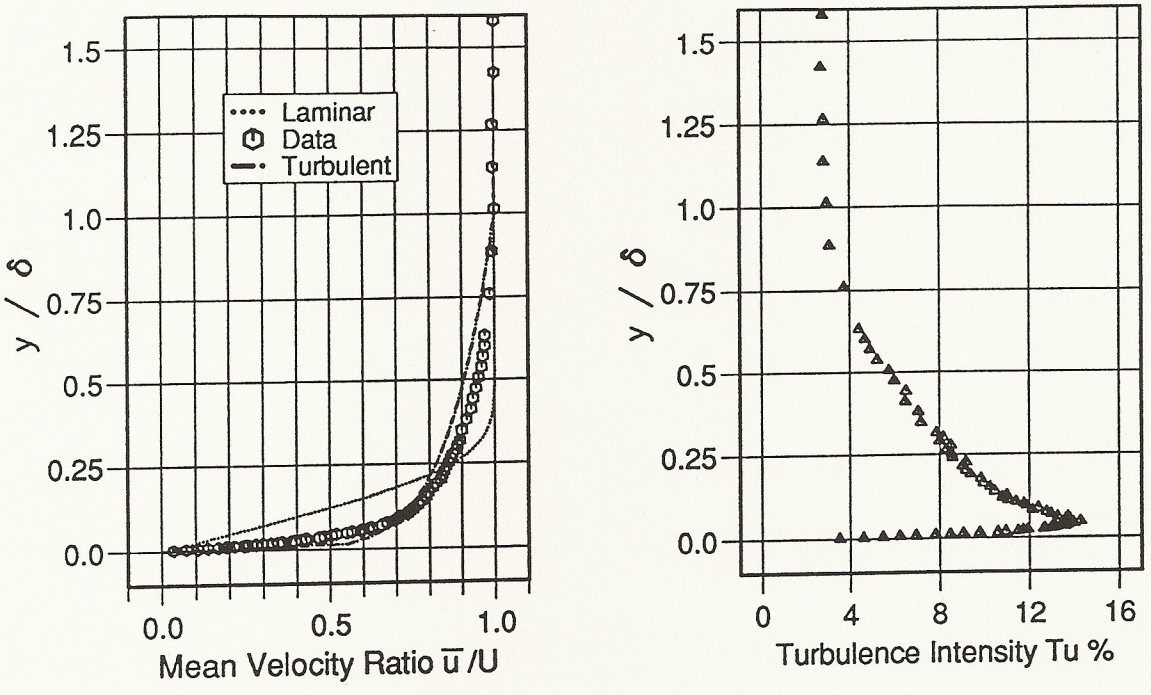


Figure A1.27 Profiles of the Mean Velocity and Turbulence Intensity
C4 Plate $U_\infty = 5$ m/s $Tu_\infty = 4$ % X = 525 mm

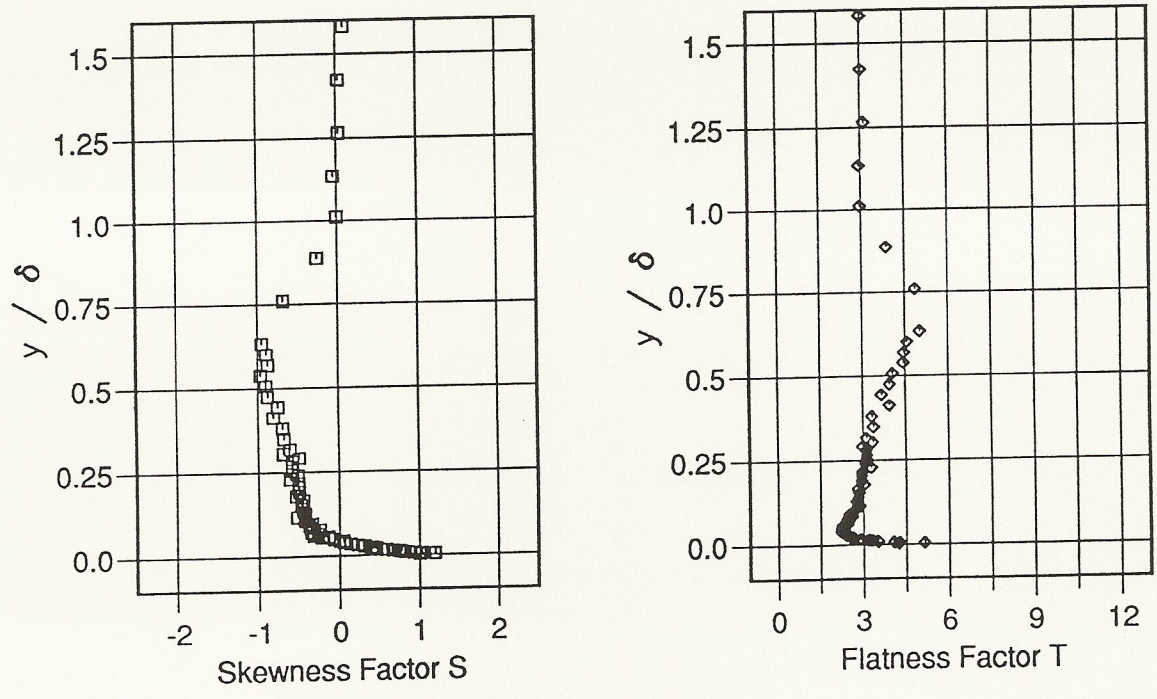
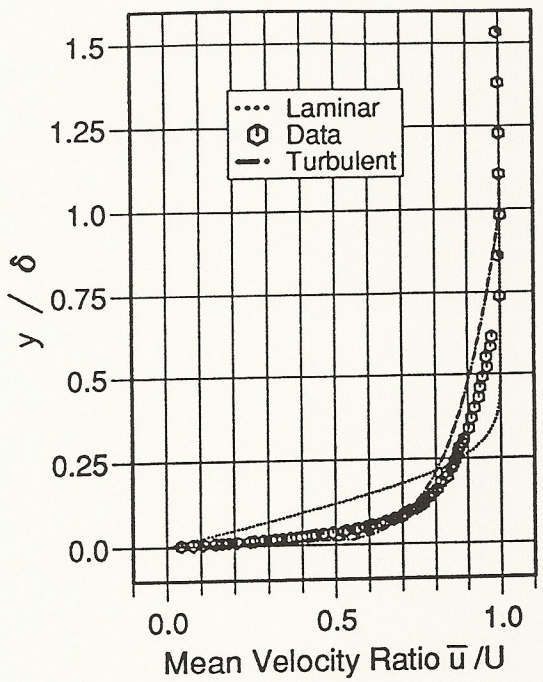


Figure A1.28 Profiles of the Skewness and Flatness Factors
C4 Plate $U_\infty = 5$ m/s $Tu_\infty = 4$ % X = 525 mm



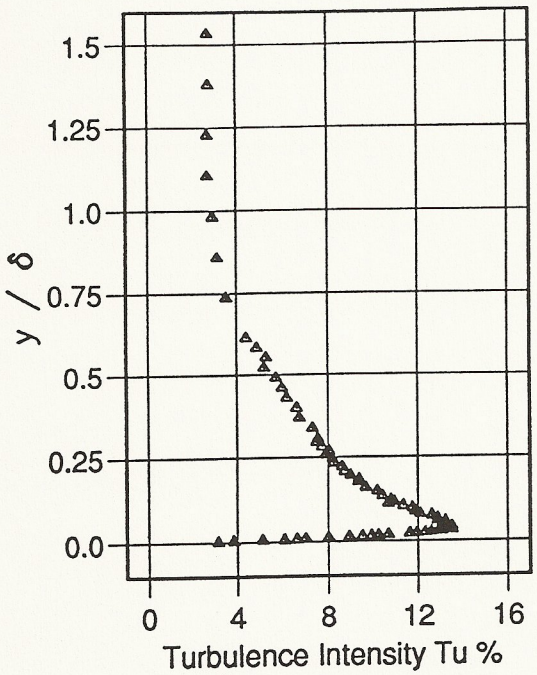
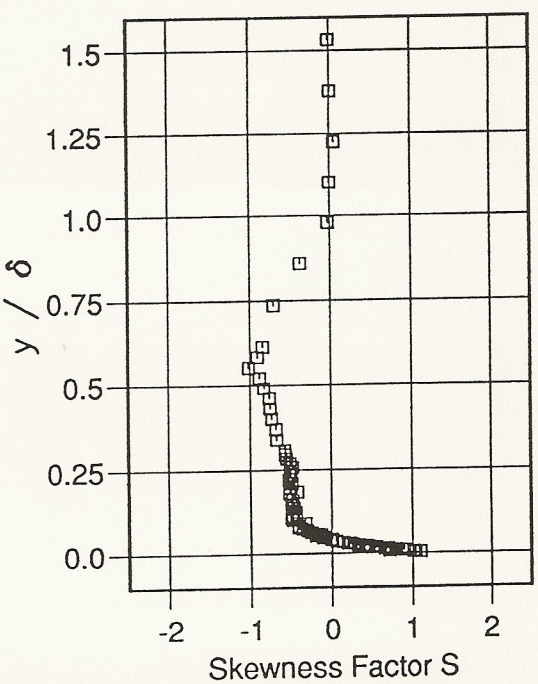


Figure A1.29	Profiles of the Mean Velocity and Turbulence Intensity C4 Plate $U_\infty = 5$ m/s $Tu_\infty = 4$ % X = 550 mm



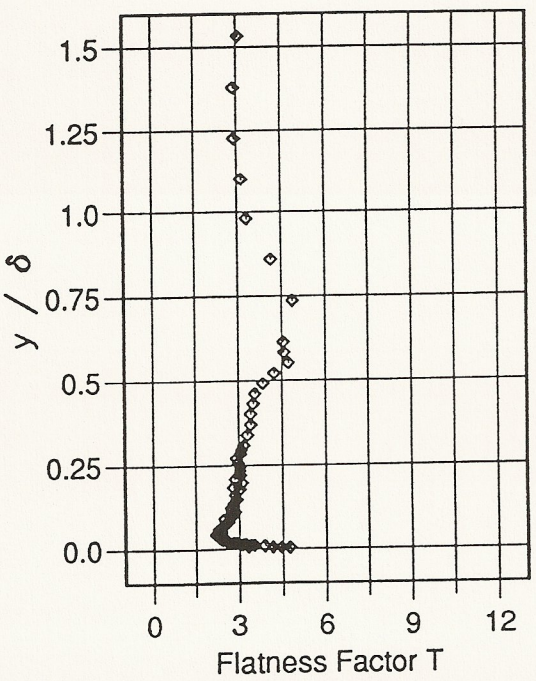


Figure A1.30	Profiles of the Skewness and Flatness Factors C4 Plate $U_\infty = 5$ m/s $Tu_\infty = 4$ % X = 550 mm

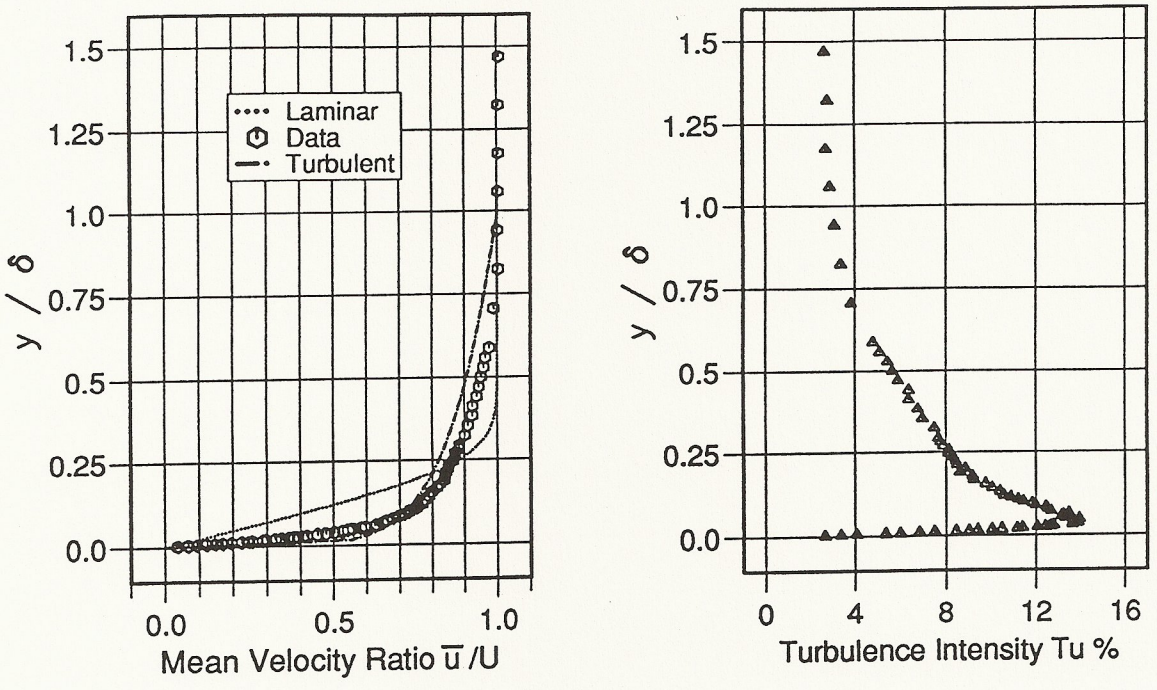


Figure A1.31	Profiles of the Mean Velocity and Turbulence Intensity C4 Plate $U_\infty = 5$ m/s $Tu_\infty = 4$ % X = 575 mm

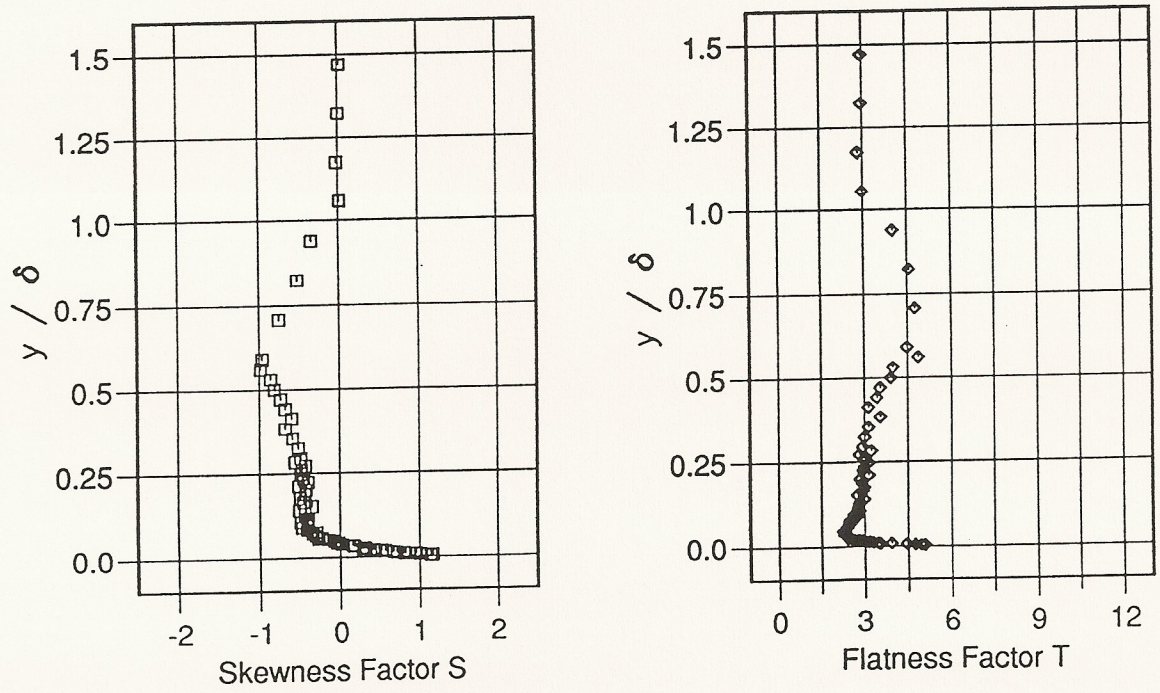
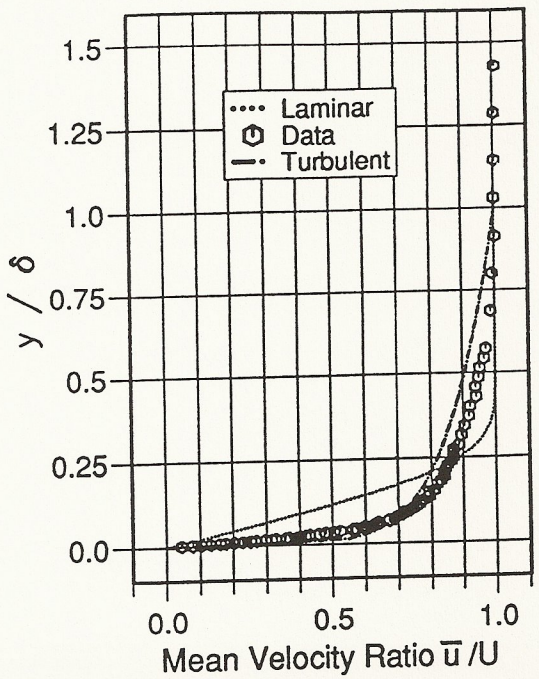


Figure A1.32	Profiles of the Skewness and Flatness Factors C4 Plate $U_\infty = 5$ m/s $Tu_\infty = 4$ % X = 575 mm



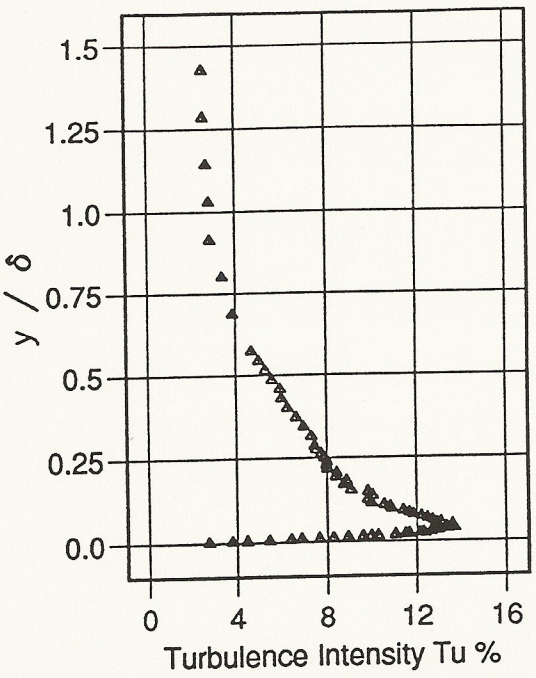
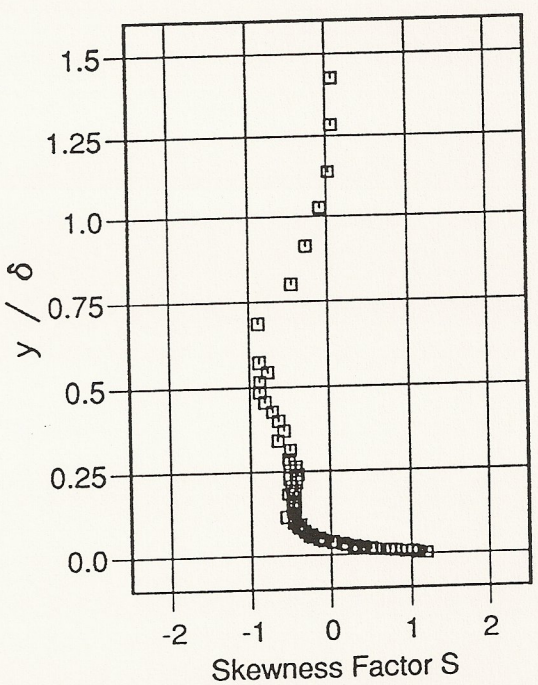


Figure A1.33	Profiles of the Mean Velocity and Turbulence Intensity C4 Plate U_∞ = 5 m/s Tu_∞ = 4 % X = 600 mm



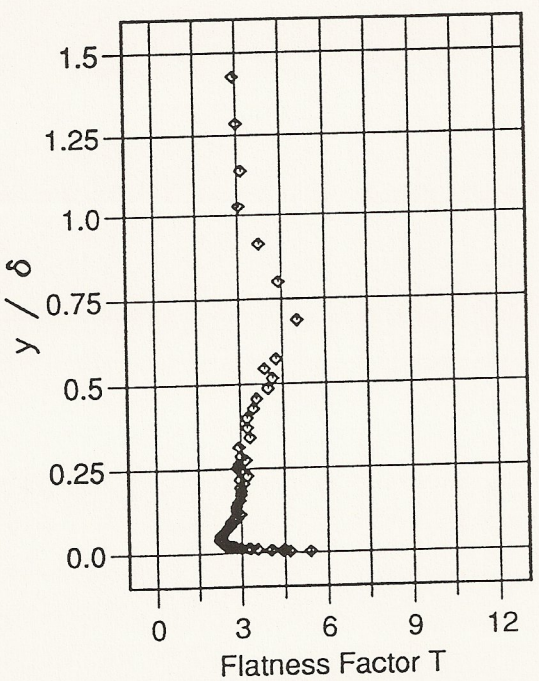
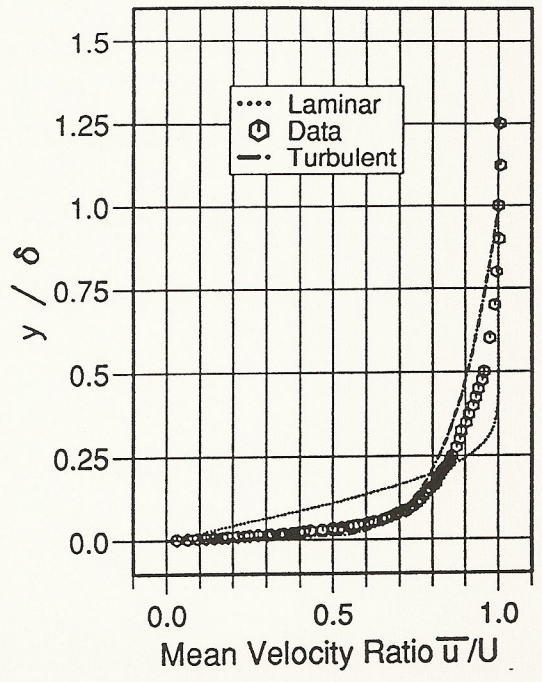


Figure A1.34	Profiles of the Skewness and Flatness Factors C4 Plate U_∞ = 5 m/s Tu_∞ = 4 % X = 600 mm



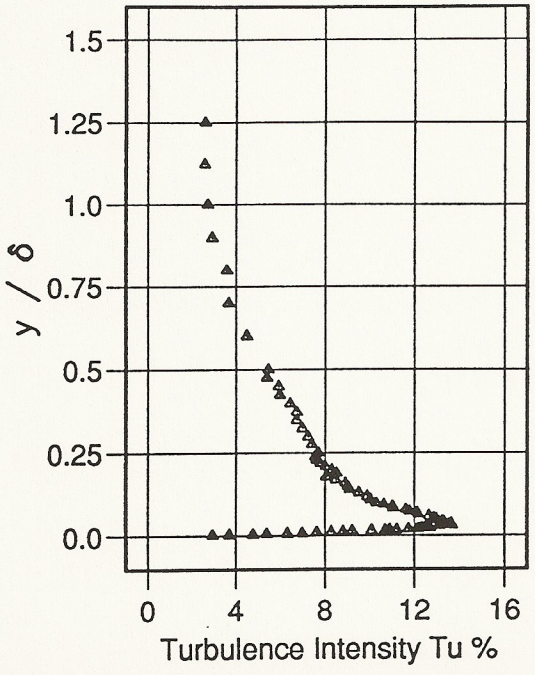
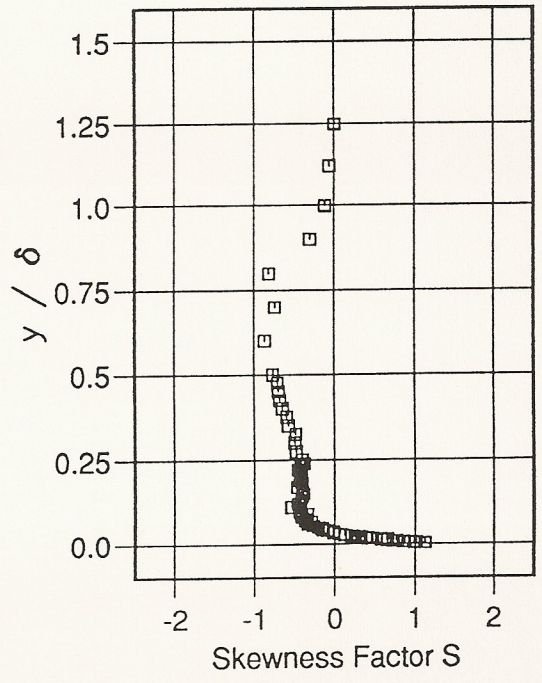


Figure A1.35	Profiles of the Mean Velocity and Turbulence Intensity C4 Plate U_∞ = 5 m/s Tu_∞ = 4 % X = 700 mm



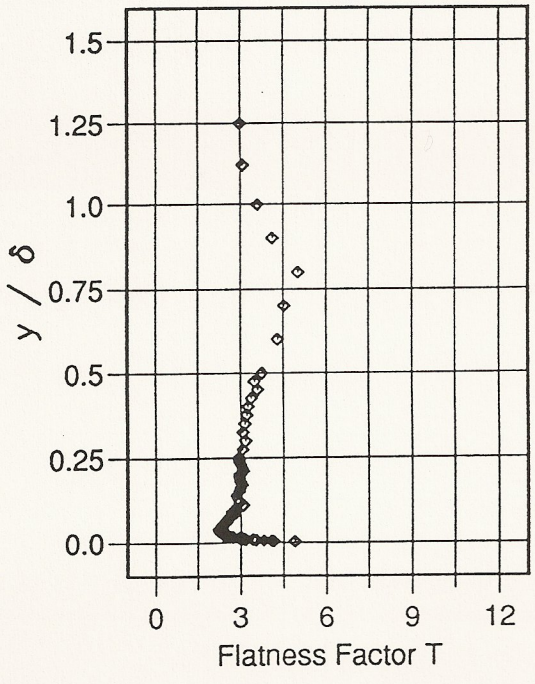
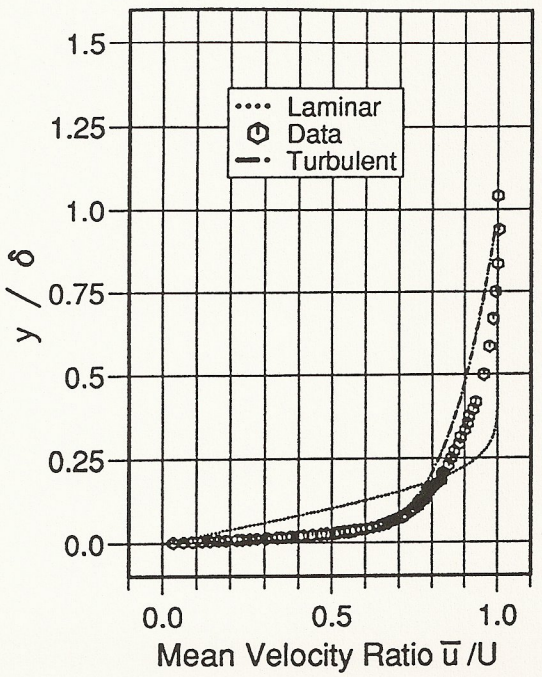


Figure A1.36	Profiles of the Skewness and Flatness Factors C4 Plate U_∞ = 5 m/s Tu_∞ = 4 % X = 700 mm



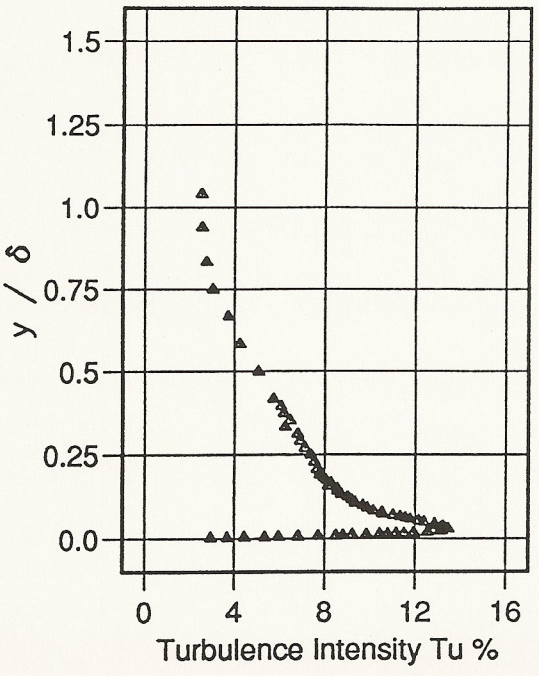
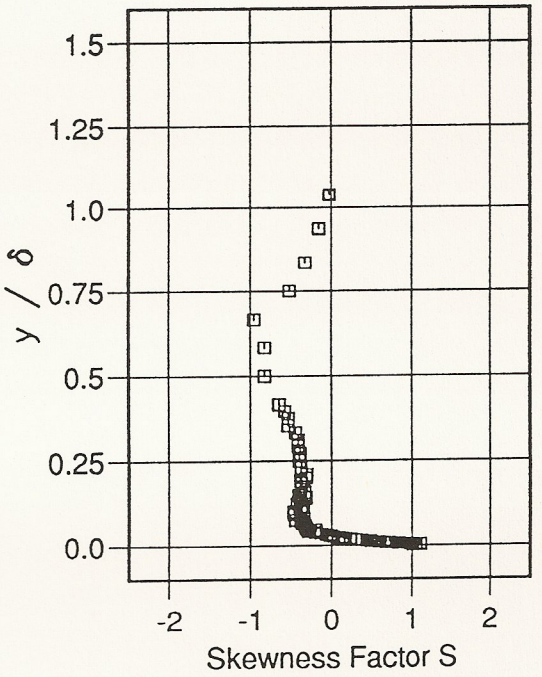


Figure A1.37	Profiles of the Mean Velocity and Turbulence Intensity C4 Plate $U_\infty = 5$ m/s $Tu_\infty = 4$ % X = 850 mm



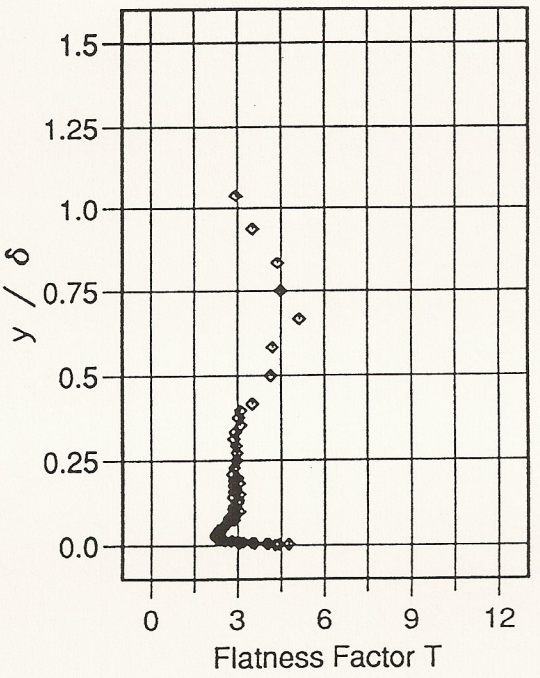
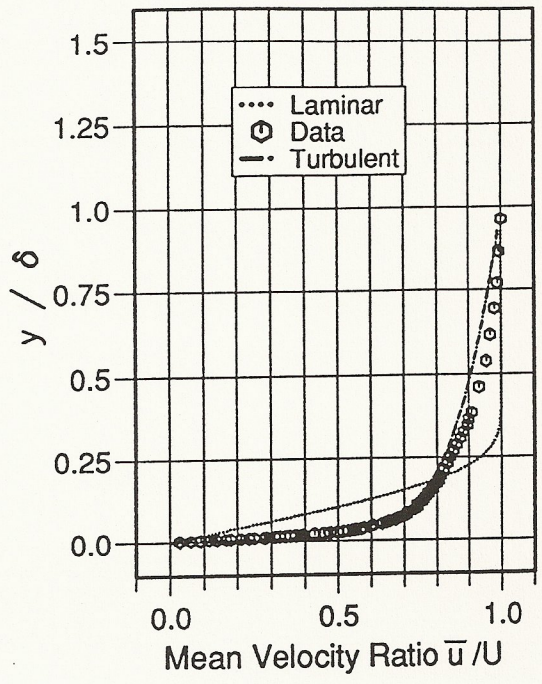


Figure A1.38	Profiles of the Skewness and Flatness Factors C4 Plate $U_\infty = 5$ m/s $Tu_\infty = 4$ % X = 850 mm



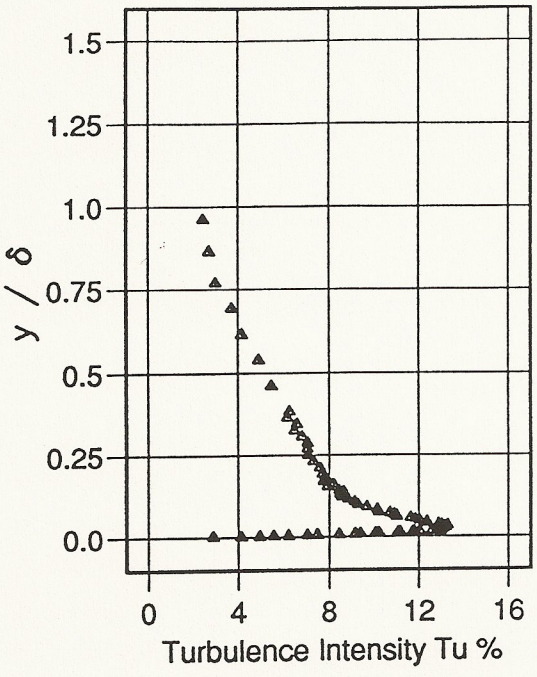
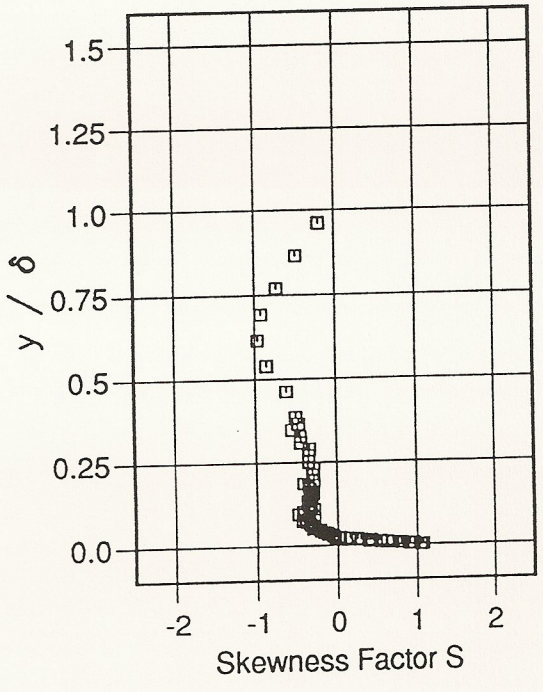


Figure A1.39	Profiles of the Mean Velocity and Turbulence Intensity C4 Plate $U_\infty = 5$ m/s $Tu_\infty = 4$ % X = 1002 mm



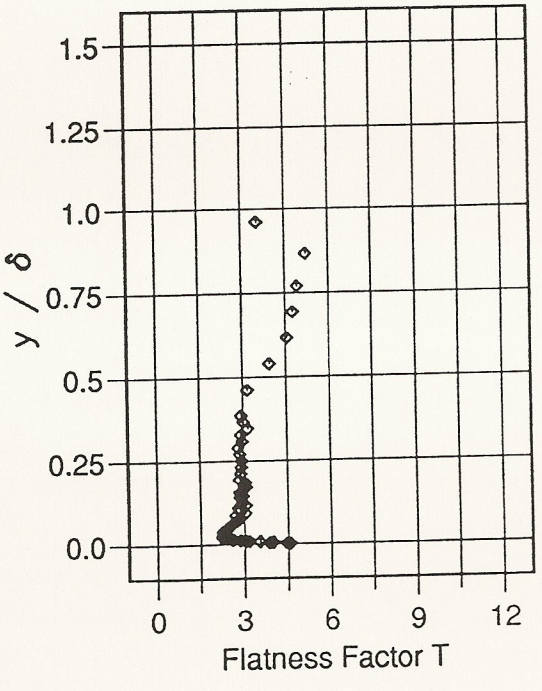


Figure A1.40	Profiles of the Skewness and Flatness Factors C4 Plate $U_\infty = 5$ m/s $Tu_\infty = 4$ % X = 1002 mm

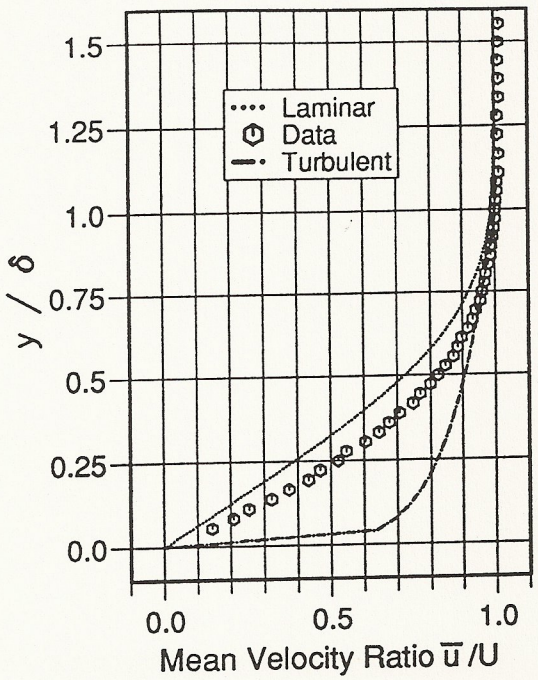
Analytical Plots of the Profiles of the Time Averaged Quantities Obtained with Hot Wire Anemometry

Section ii

Boundary layer Investigation of the C4 plate

U_∞ = 15 m/s

Tu_∞ = 4. %



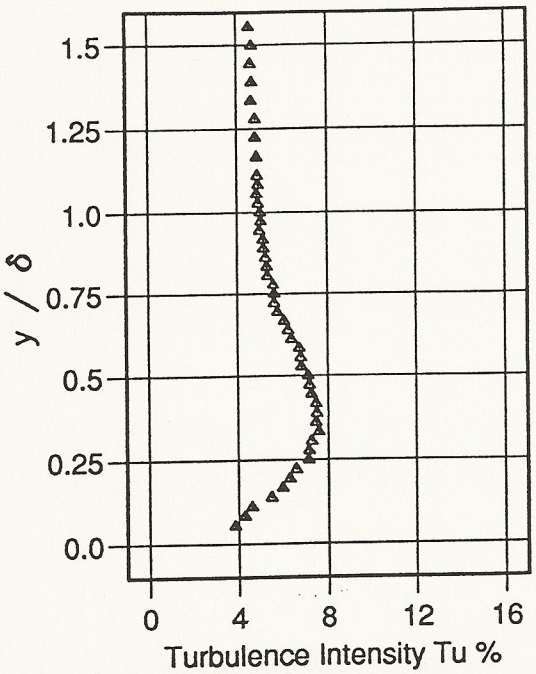
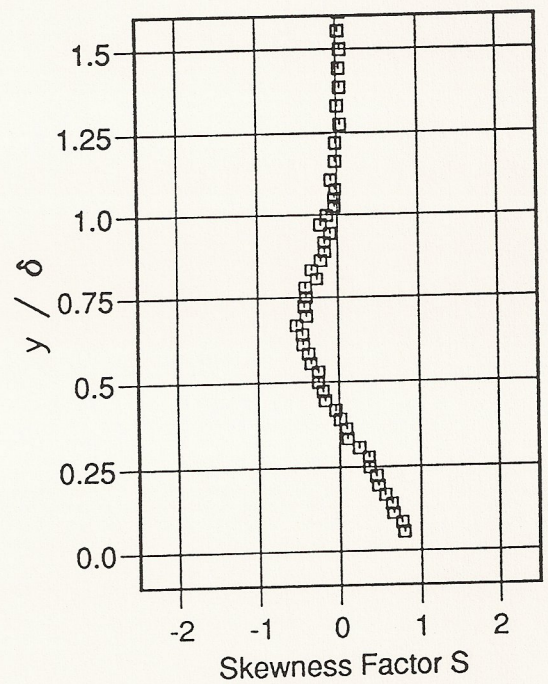


Figure A2.1	Profiles of the Mean Velocity and Turbulence Intensity C4 Plate U_∞ = 15 m/s Tu_∞ = 4 % X = 35 mm



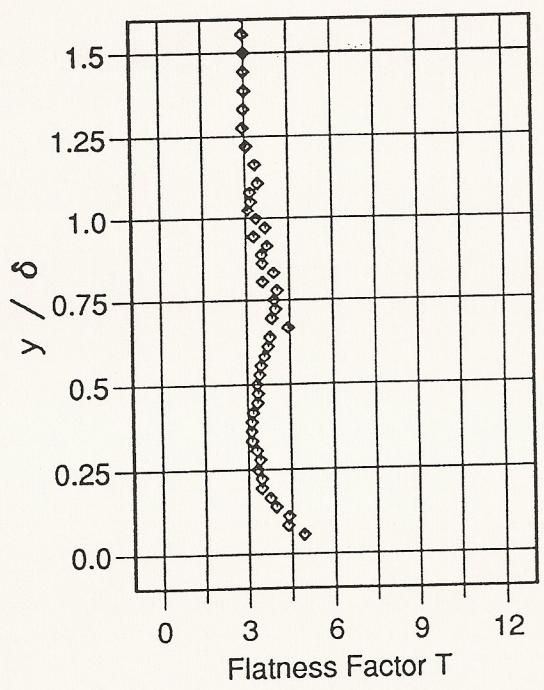
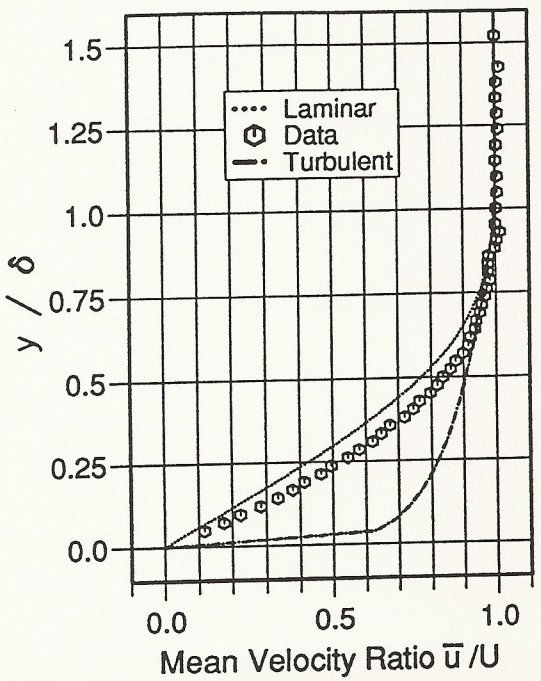


Figure A2.2	Profiles of the Skewness and Flatness Factors C4 Plate U_∞ = 15 m/s Tu_∞ = 4 % X = 35 mm



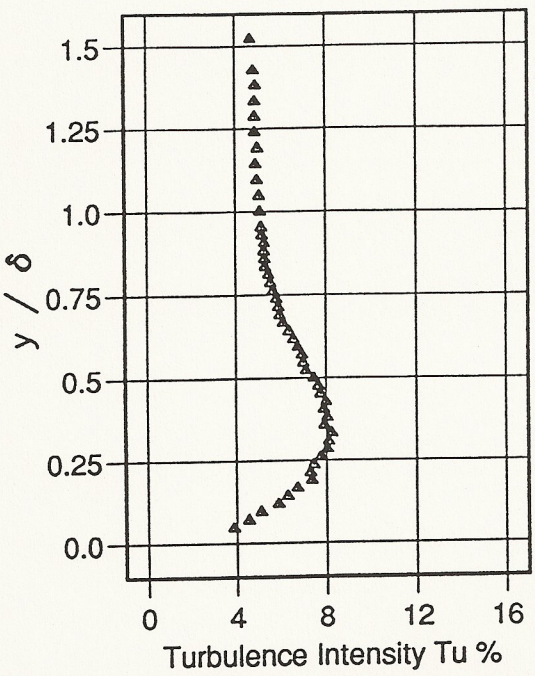
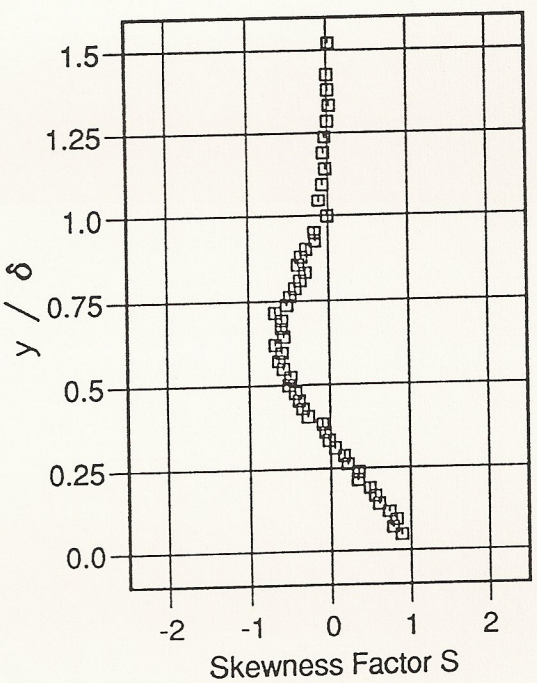


Figure A2.3	Profiles of the Mean Velocity and Turbulence Intensity C4 Plate U_∞ = 15 m/s Tu_∞ = 4 % X = 40 mm



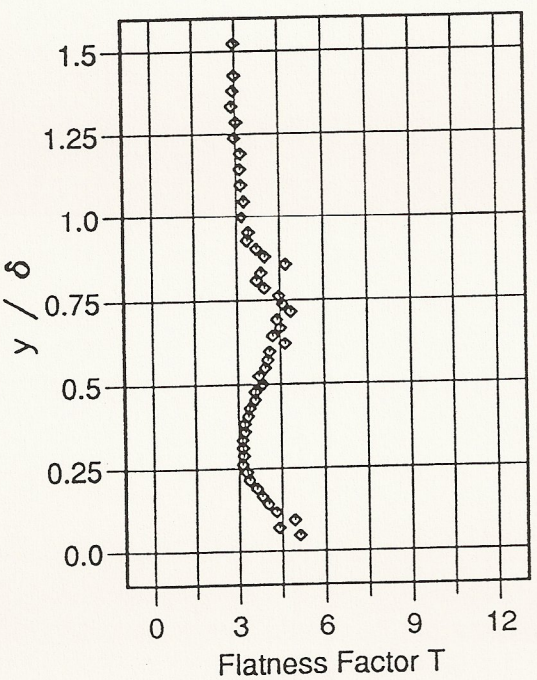


Figure A2.4	Profiles of the Skewness and Flatness Factors C4 Plate U_∞ = 15 m/s Tu_∞ = 4 % X = 40 mm

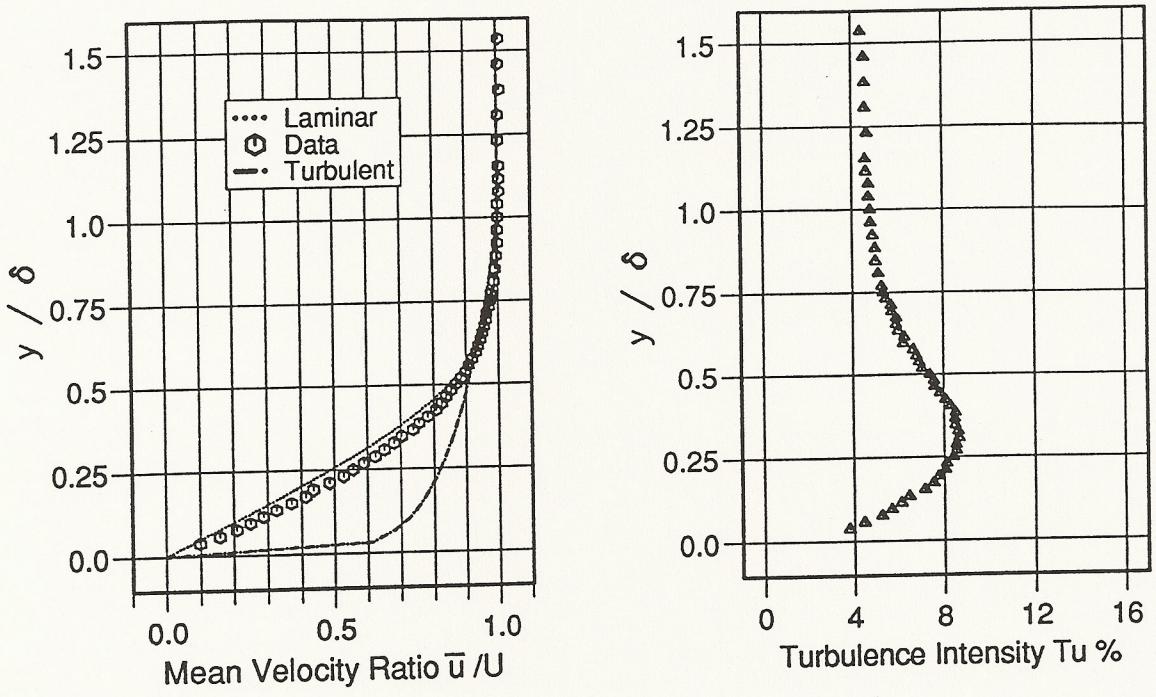


Figure A2.5	Profiles of the Mean Velocity and Turbulence Intensity C4 Plate U_∞ = 15 m/s Tu_∞ = 4 % X = 45 mm

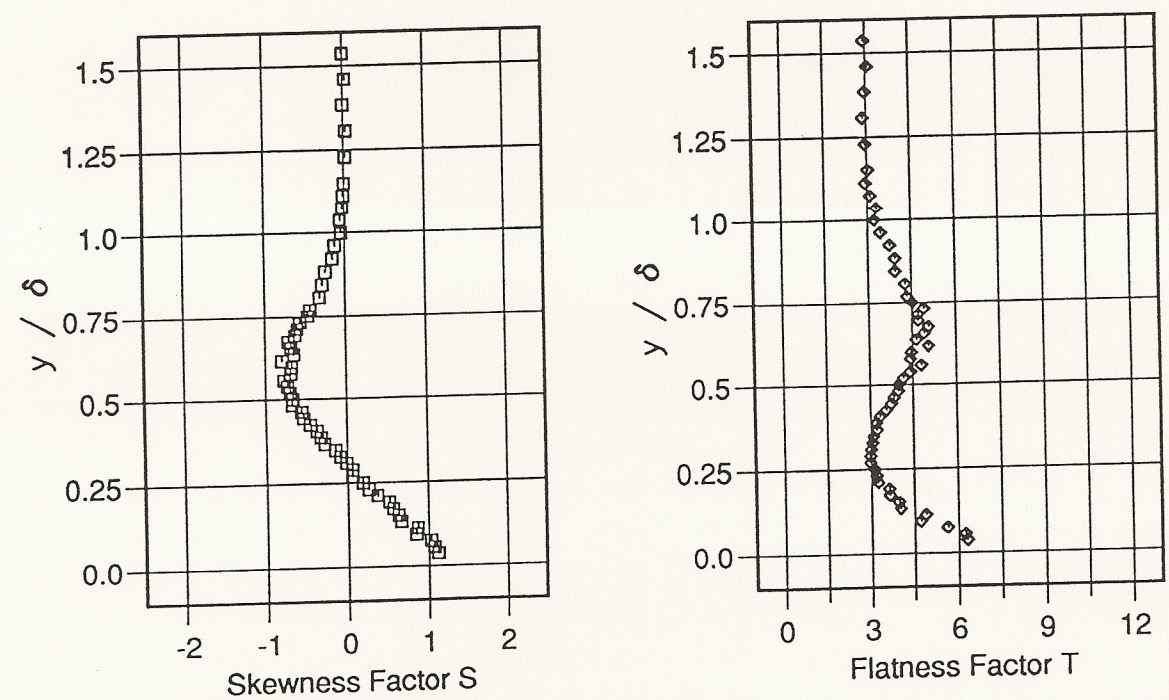
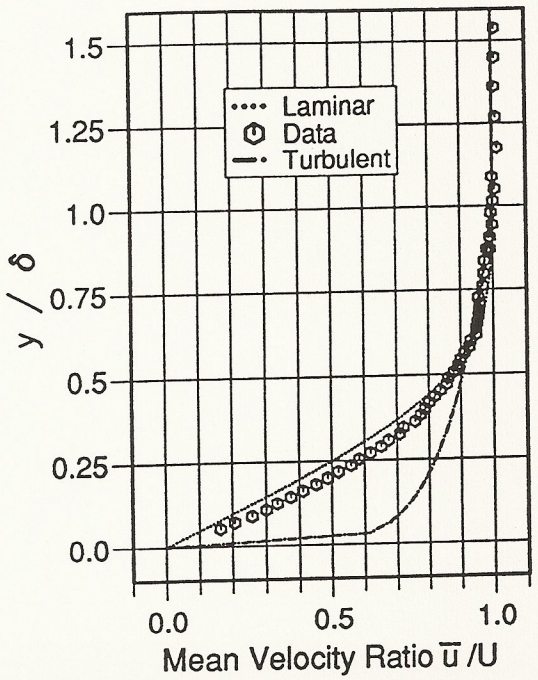


Figure A2.6	Profiles of the Skewness and Flatness Factors C4 Plate U_∞ = 15 m/s Tu_∞ = 4 % X = 45 mm



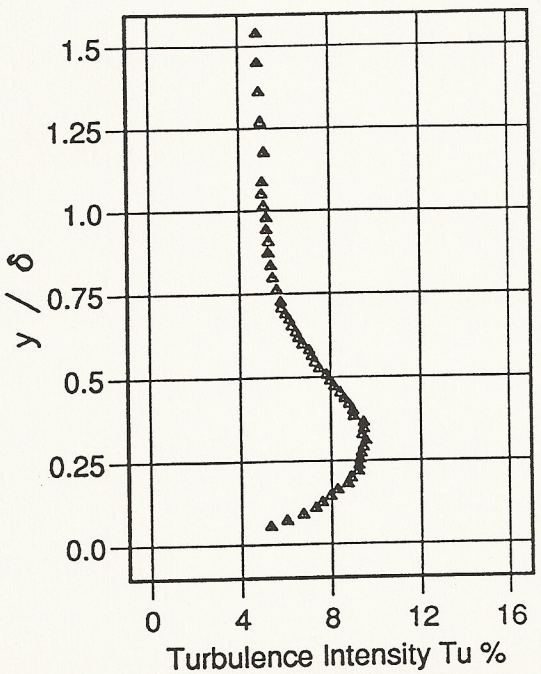
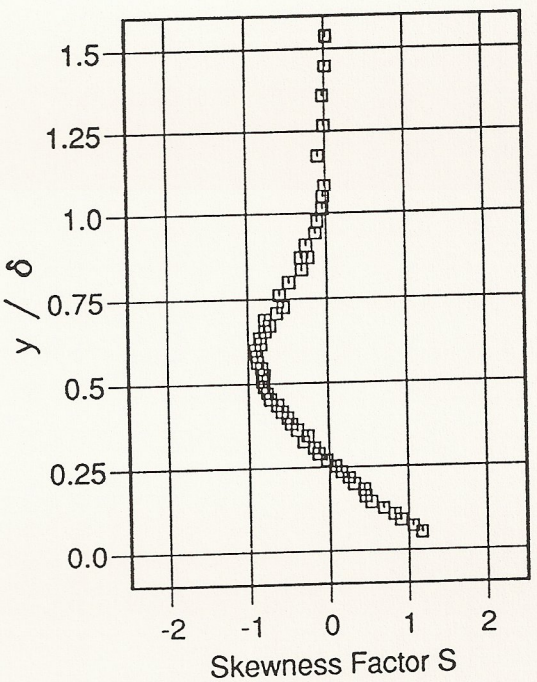


Figure A2.7	Profiles of the Mean Velocity and Turbulence Intensity C4 Plate U_∞ = 15 m/s Tu_∞ = 4 % X = 50 mm



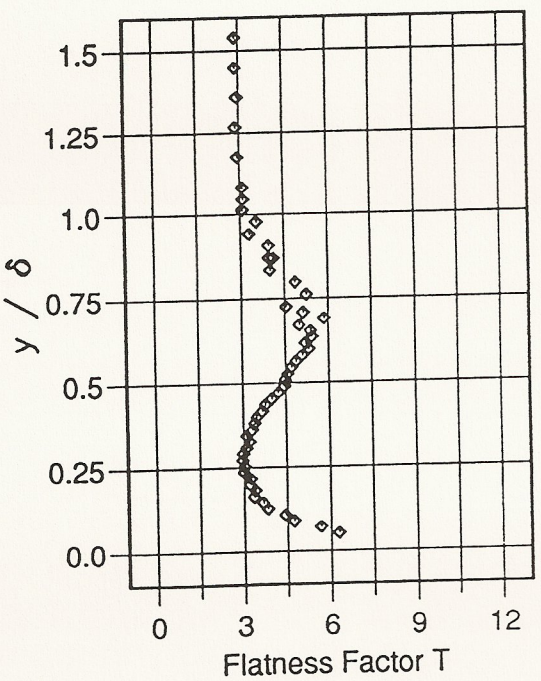
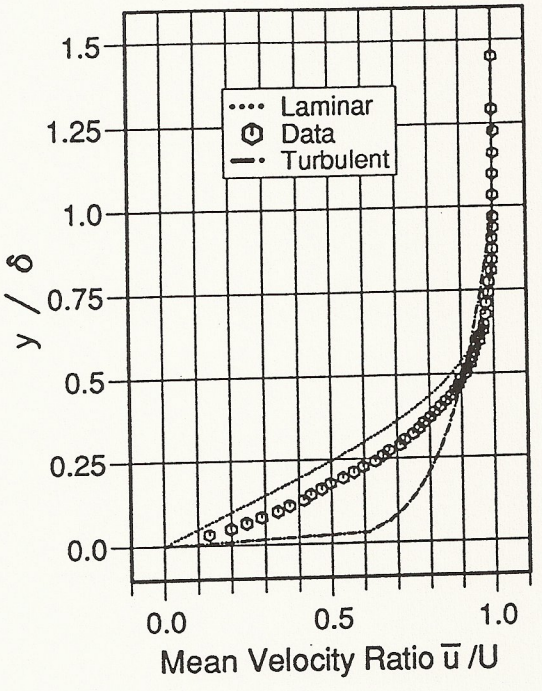


Figure A2.8	Profiles of the Skewness and Flatness Factors C4 Plate U_∞ = 15 m/s Tu_∞ = 4 % X = 50 mm



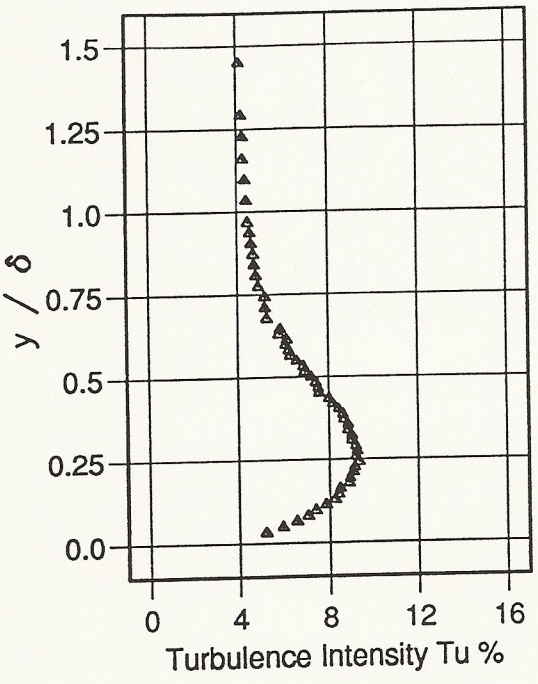
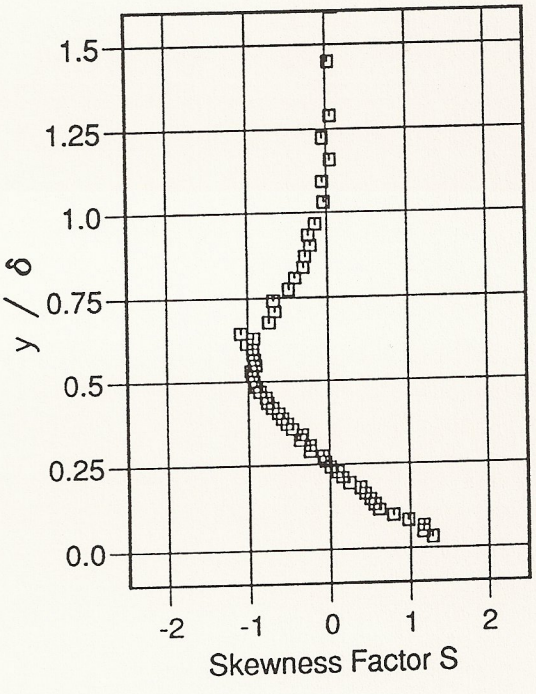


Figure A2.9	Profiles of the Mean Velocity and Turbulence Intensity C4 Plate U_∞ = 15 m/s Tu_∞ = 4 % X = 55 mm



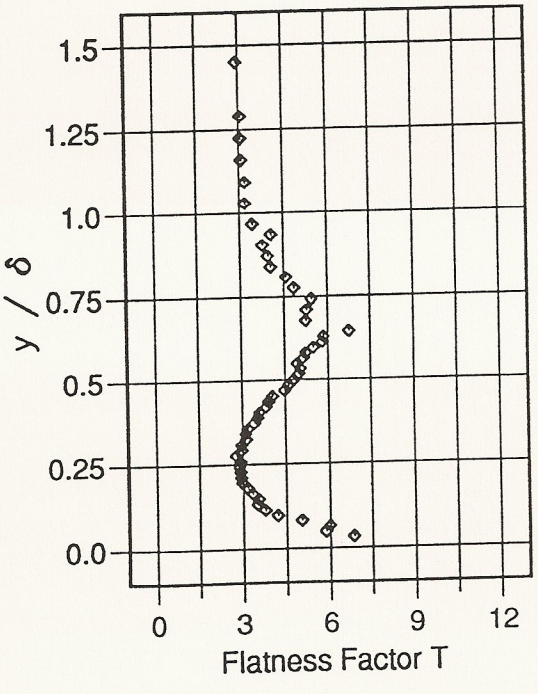


Figure A2.10	Profiles of the Skewness and Flatness Factors C4 Plate U_∞ = 15 m/s Tu_∞ = 4 % X = 55 mm

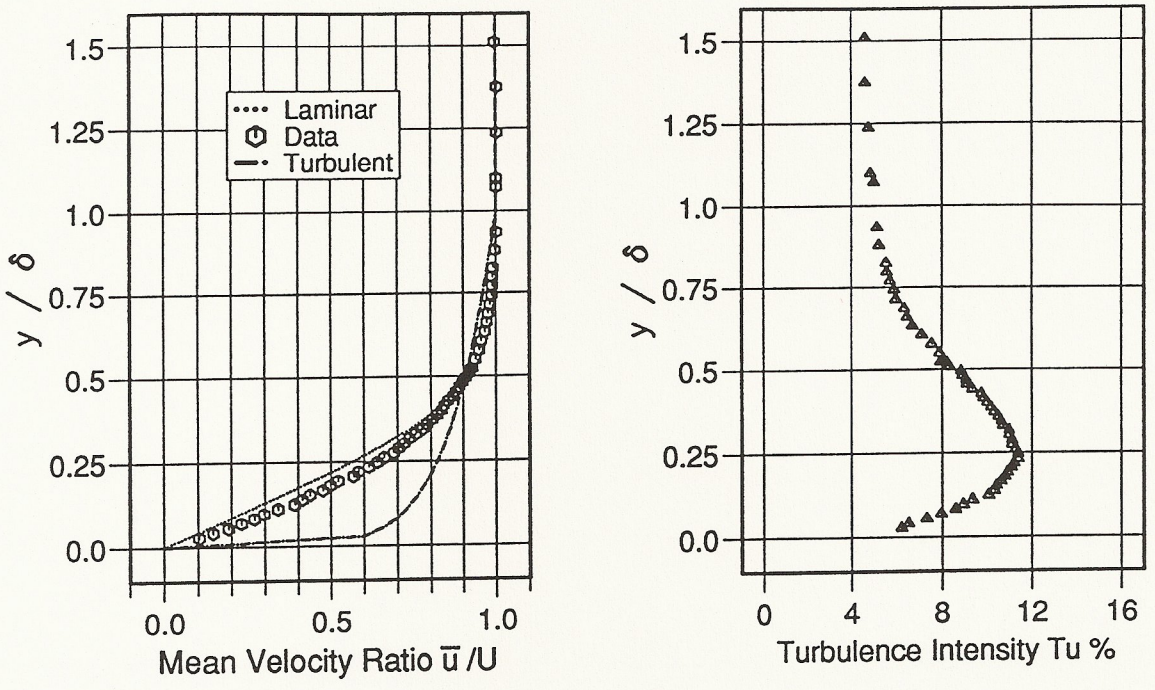


Figure A2.11	Profiles of the Mean Velocity and Turbulence Intensity C4 Plate U_∞ = 15 m/s Tu_∞ = 4 % X = 65 mm

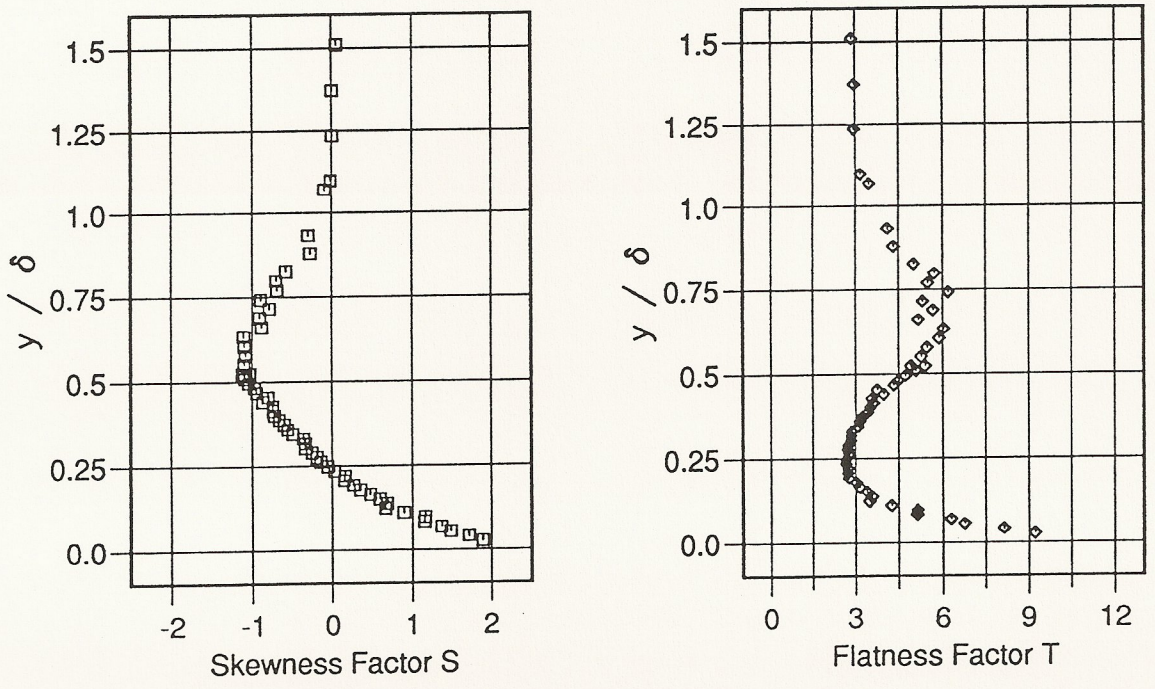


Figure A2.12	Profiles of the Skewness and Flatness Factors C4 Plate U_∞ = 15 m/s Tu_∞ = 4 % X = 65 mm

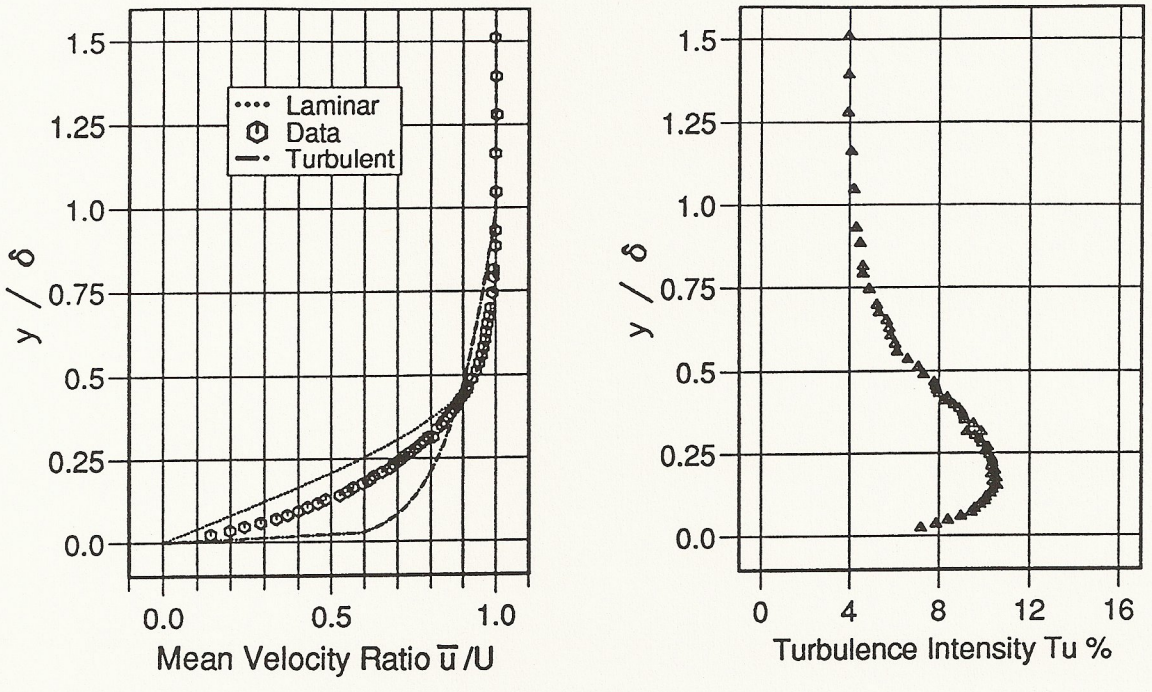


Figure A2.13	Profiles of the Mean Velocity and Turbulence Intensity C4 Plate U_∞ = 15 m/s Tu_∞ = 4 % X = 75 mm

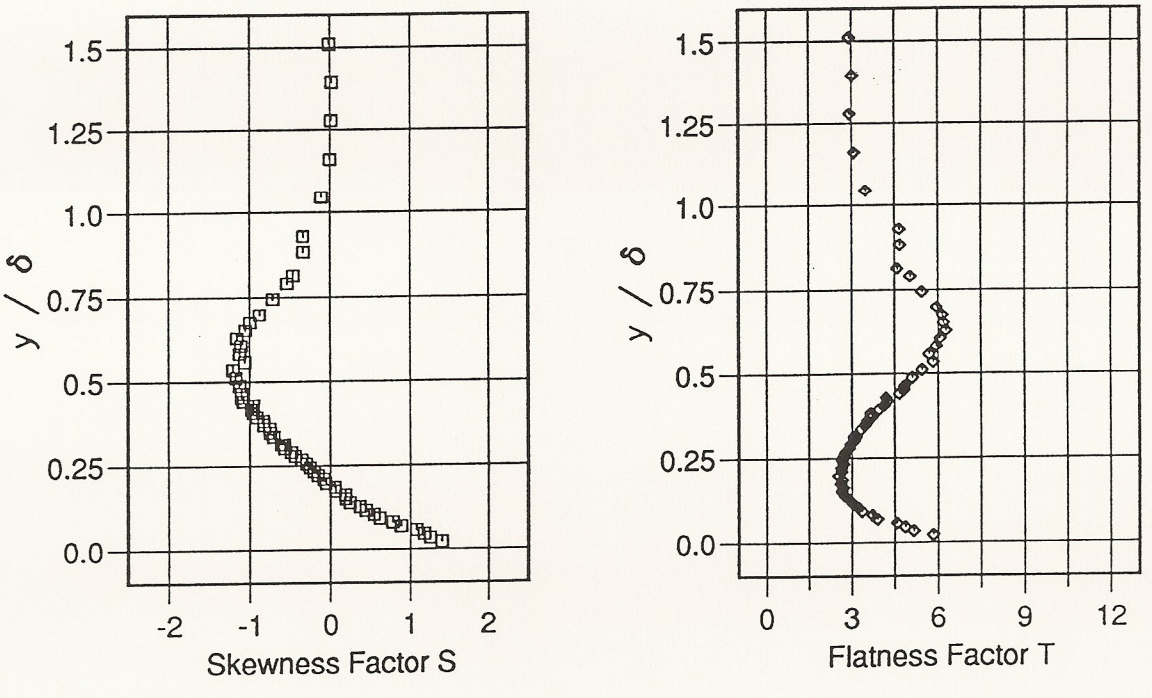
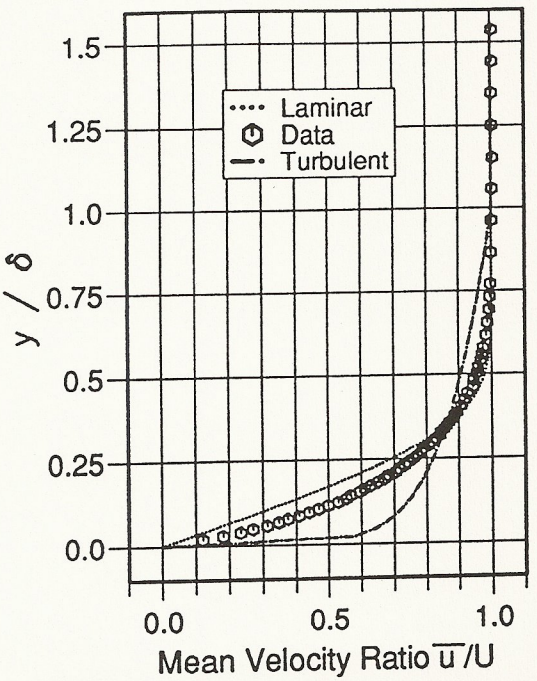


Figure A2.14	Profiles of the Skewness and Flatness Factors C4 Plate U_∞ = 15 m/s Tu_∞ = 4 % X = 75 mm



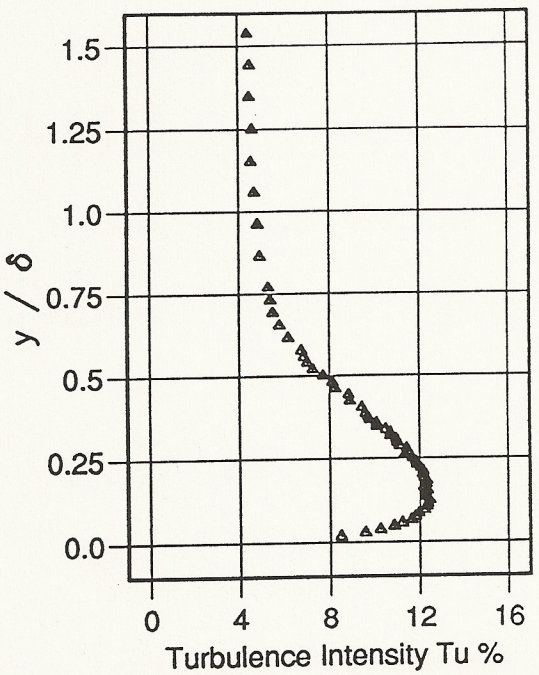
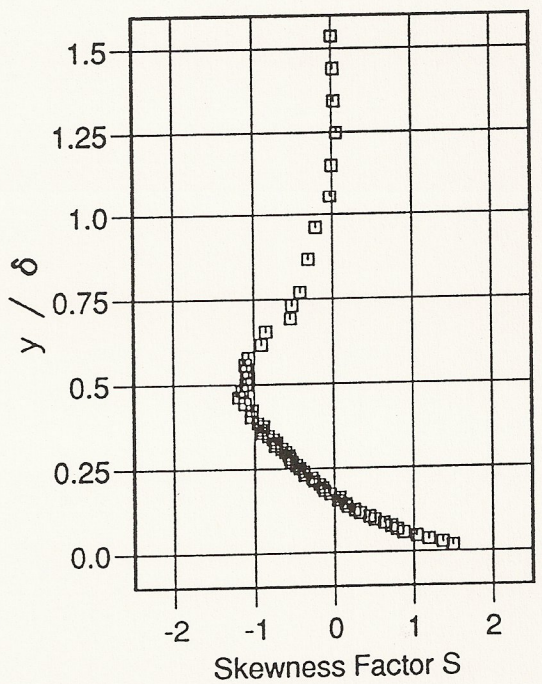


Figure A2.15	Profiles of the Mean Velocity and Turbulence Intensity C4 Plate U_∞ = 15 m/s Tu_∞ = 4 % X = 83 mm



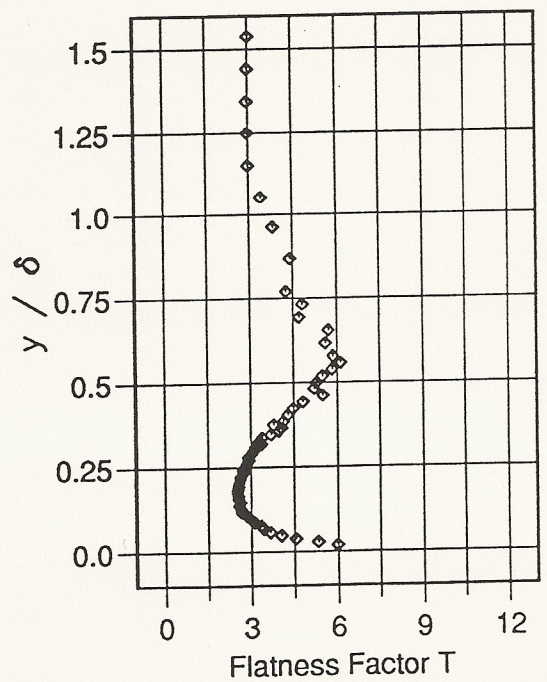
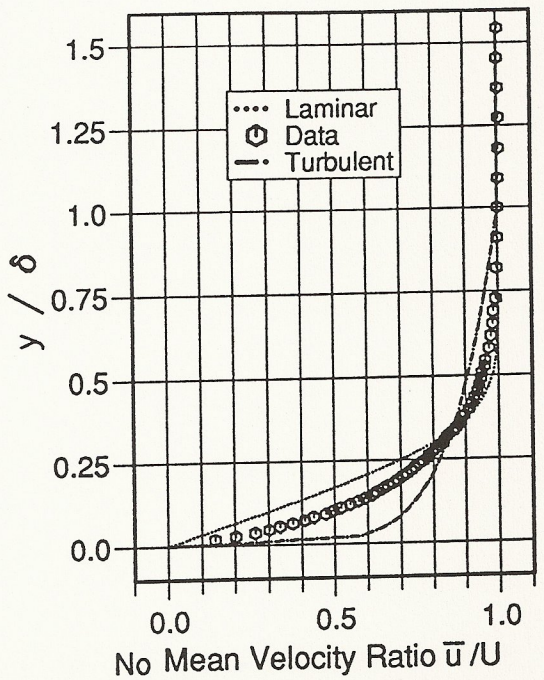


Figure A2.16	Profiles of the Skewness and Flatness Factors C4 Plate U_∞ = 15 m/s Tu_∞ = 4 % X = 83 mm



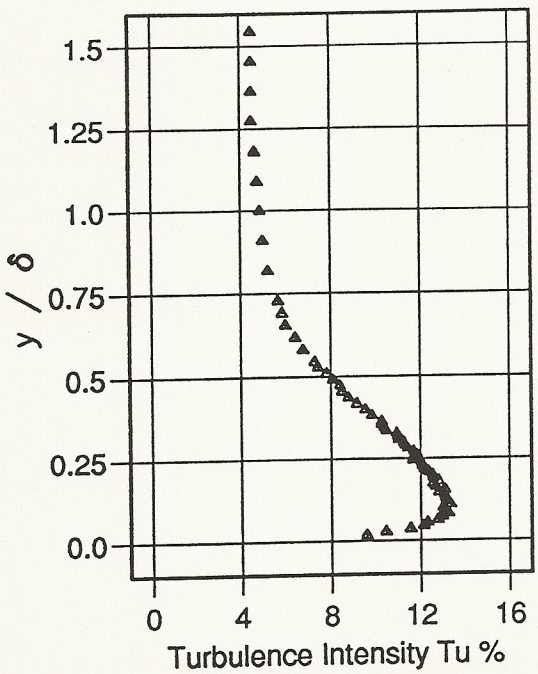
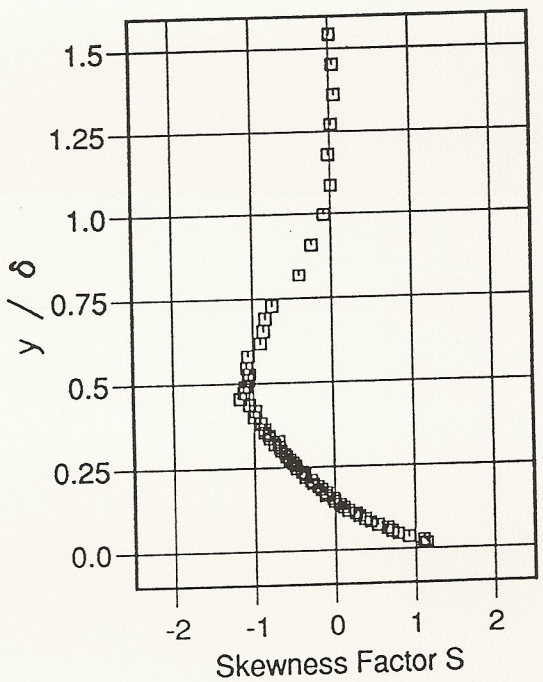


Figure A2.17	Profiles of the Mean Velocity and Turbulence Intensity C4 Plate $U_\infty = 15$ m/s $Tu_\infty = 4$ % X = 91 mm



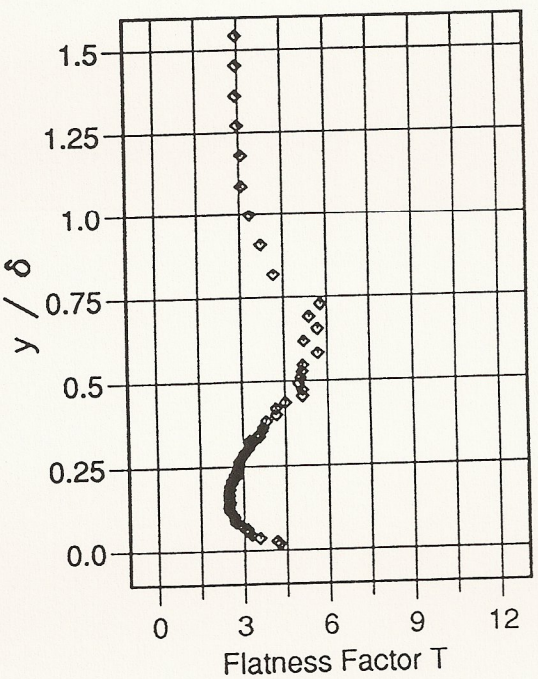
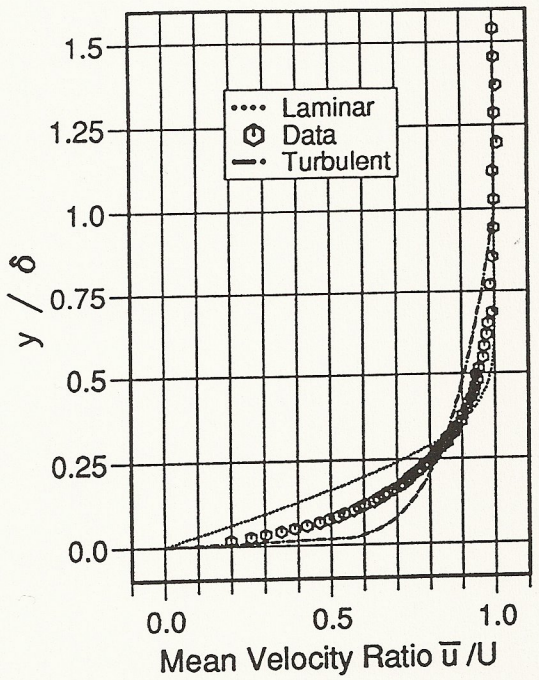


Figure A2.18	Profiles of the Skewness and Flatness Factors C4 Plate $U_\infty = 15$ m/s $Tu_\infty = 4$ % X = 91 mm



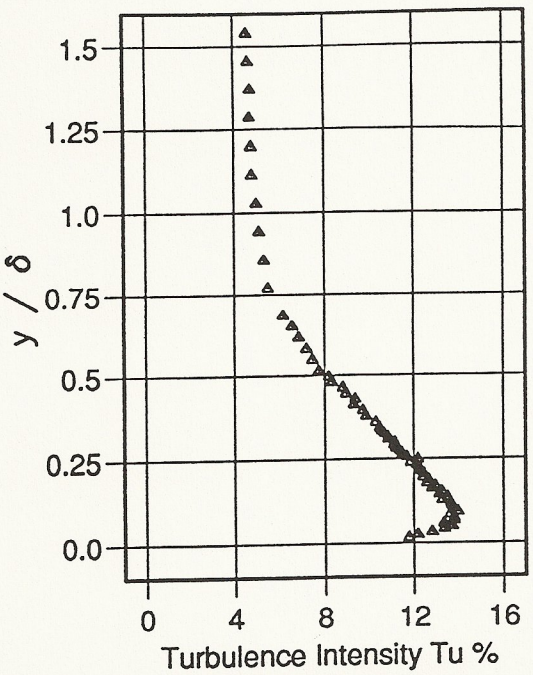
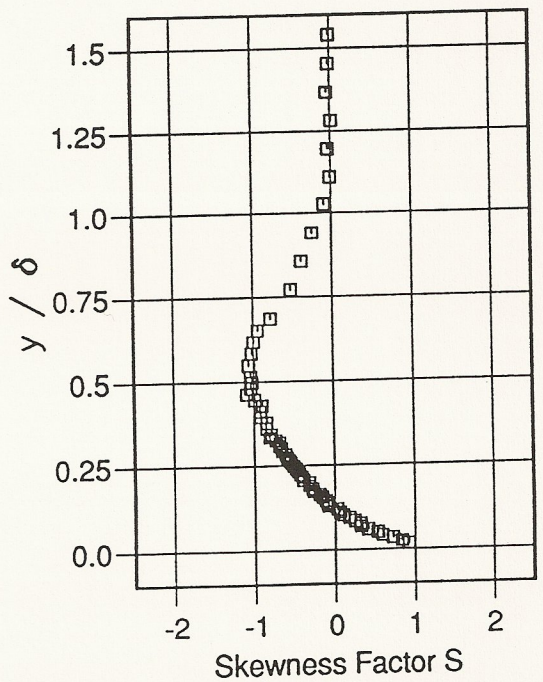


Figure A2.19	Profiles of the Mean Velocity and Turbulence Intensity C4 Plate $U_\infty = 15$ m/s $Tu_\infty = 4$ % X = 100 mm



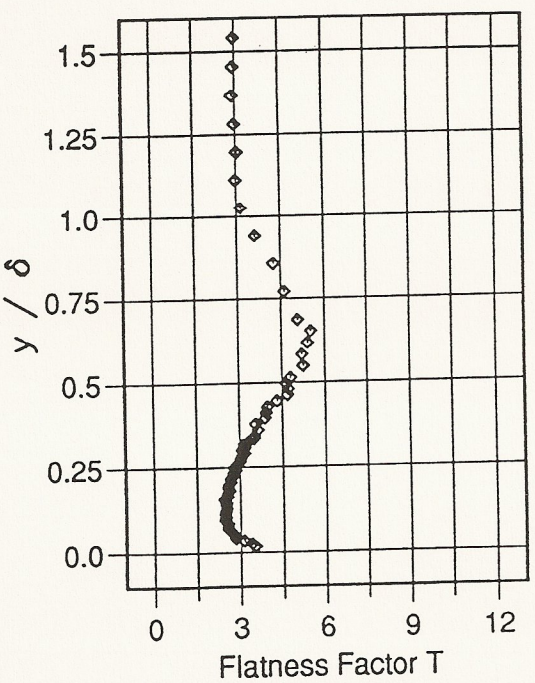
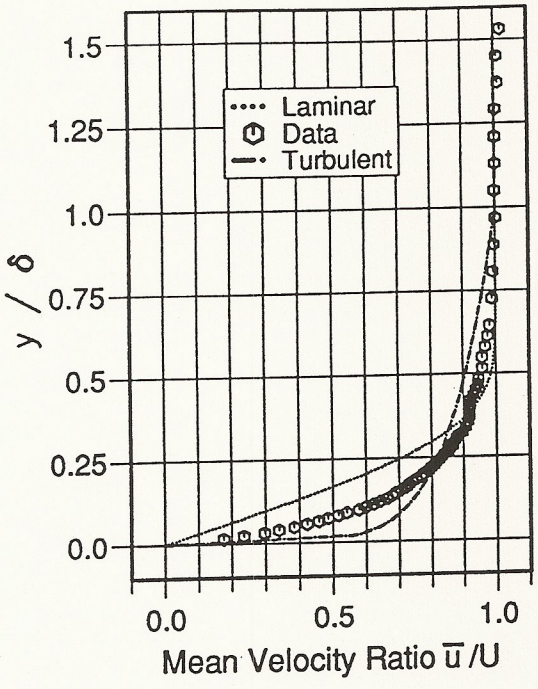


Figure A2.20	Profiles of the Skewness and Flatness Factors C4 Plate $U_\infty = 15$ m/s $Tu_\infty = 4$ % X = 100 mm



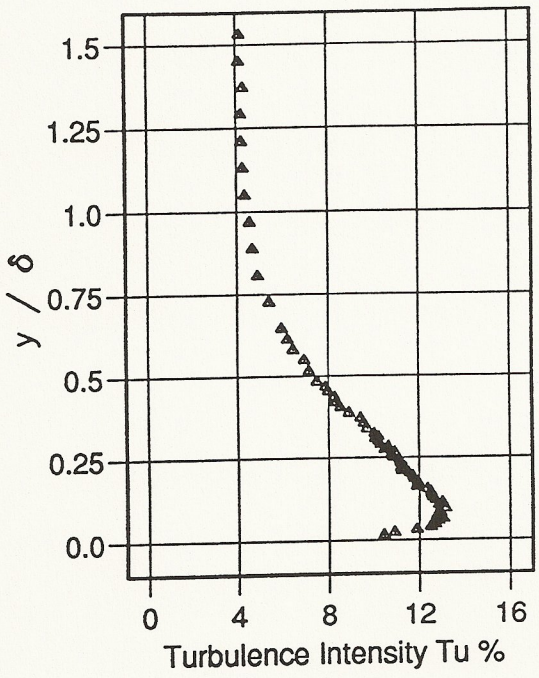
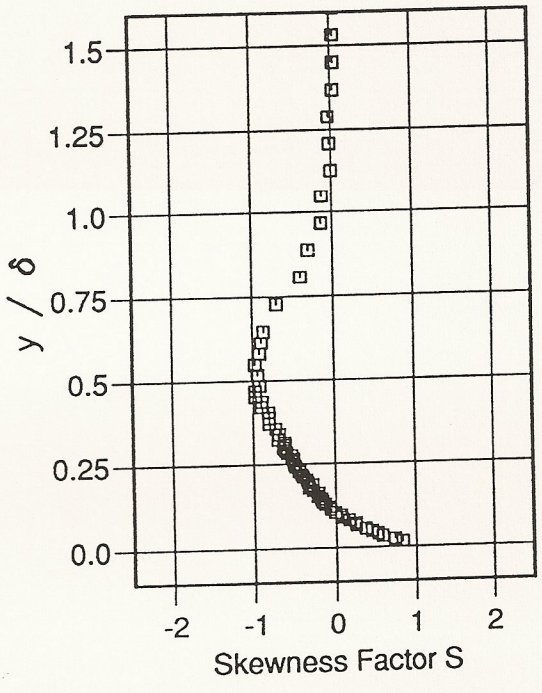


Figure A2.21	Profiles of the Mean Velocity and Turbulence Intensity C4 Plate U_∞ = 15 m/s Tu_∞ = 4 % X = 106 mm



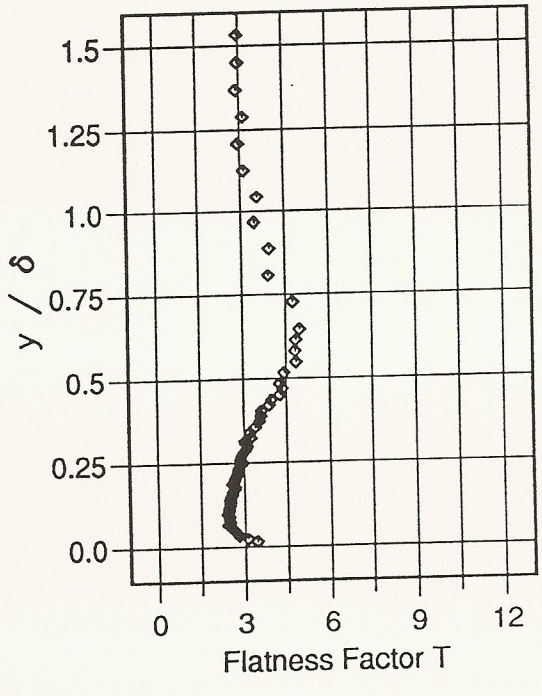
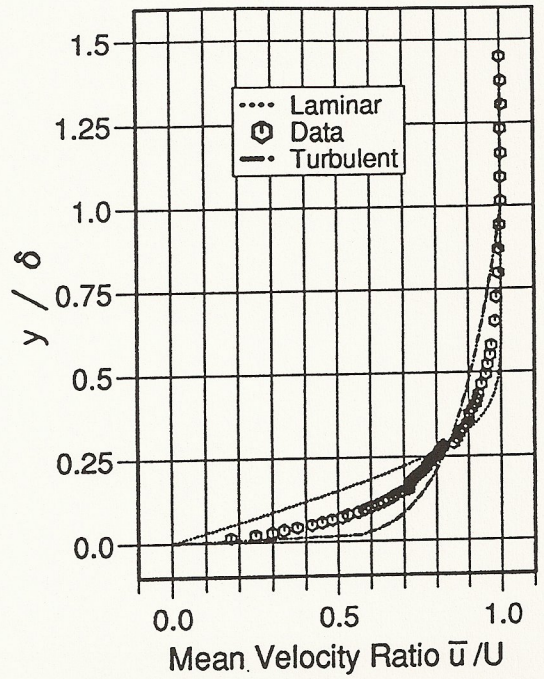


Figure A2.22	Profiles of the Skewness and Flatness Factors C4 Plate U_∞ = 15 m/s Tu_∞ = 4 % X = 106 mm



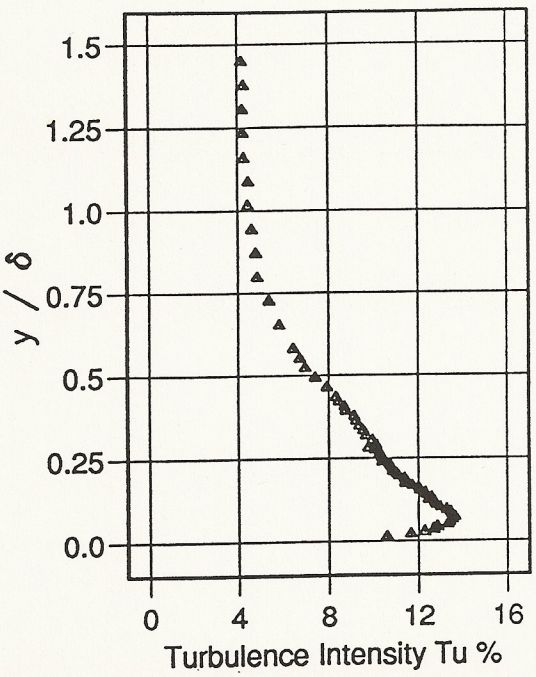
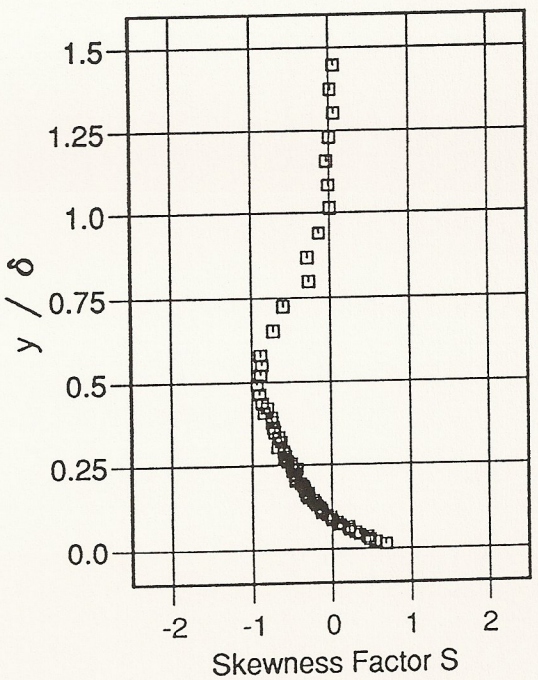


Figure A2.23	Profiles of the Mean Velocity and Turbulence Intensity C4 Plate U_∞ = 15 m/s Tu_∞ = 4 % X = 112 mm



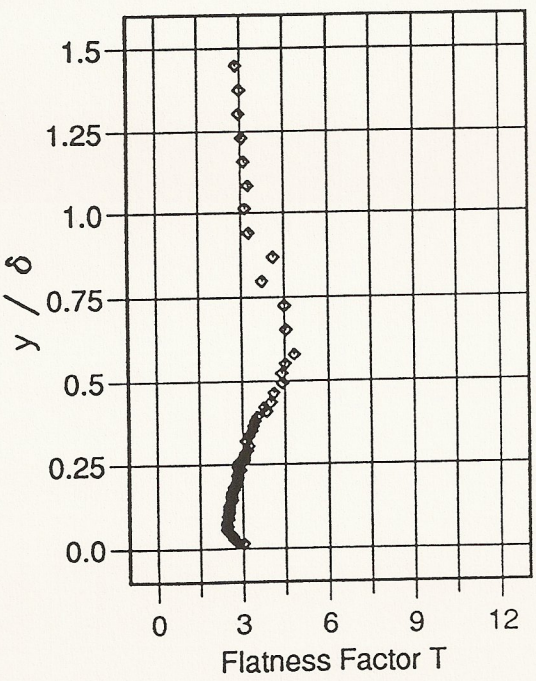
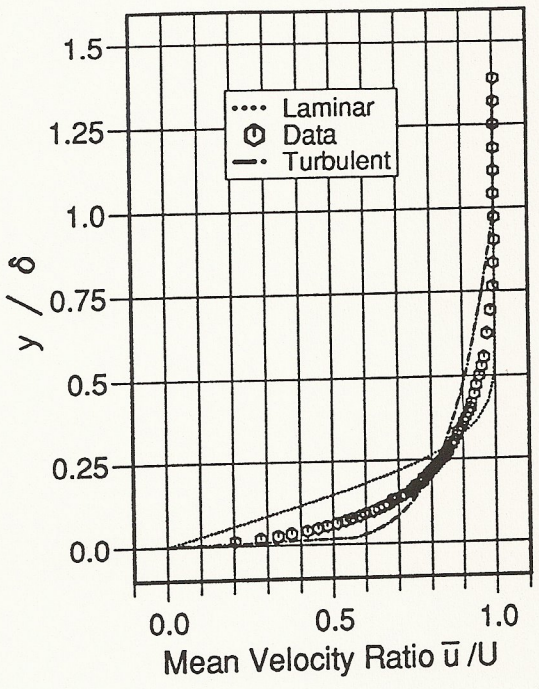


Figure A2.24	Profiles of the Skewness and Flatness Factors C4 Plate U_∞ = 15 m/s Tu_∞ = 4 % X = 112 mm



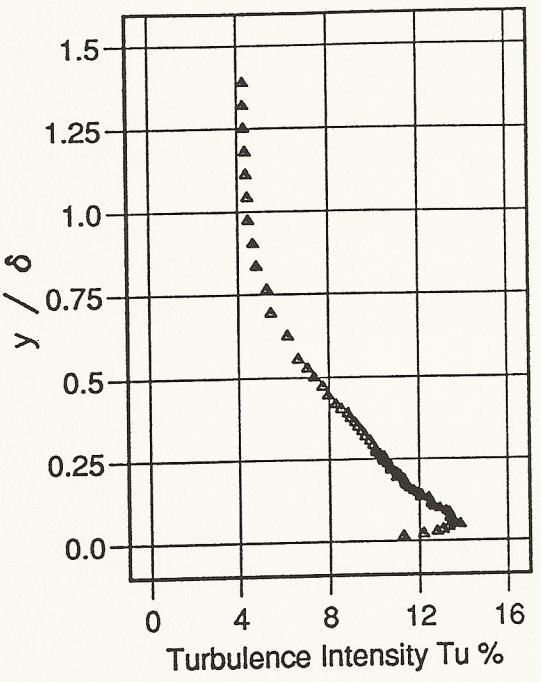
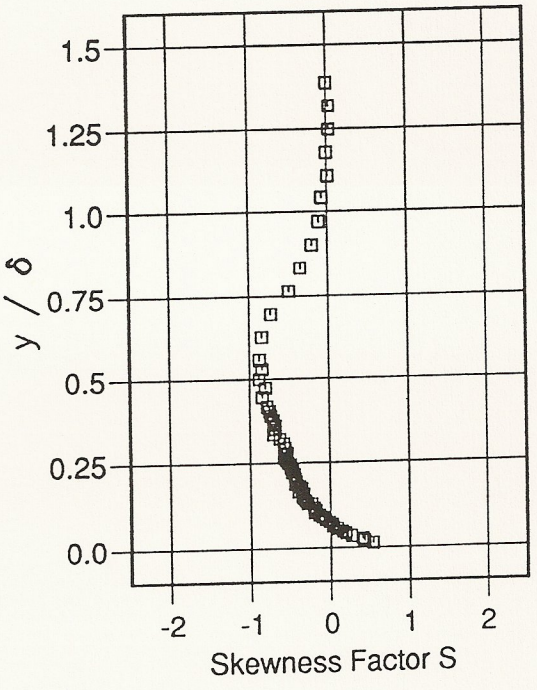


Figure A2.25	Profiles of the Mean Velocity and Turbulence Intensity C4 Plate U_∞ = 15 m/s Tu_∞ = 4 % X = 118 mm



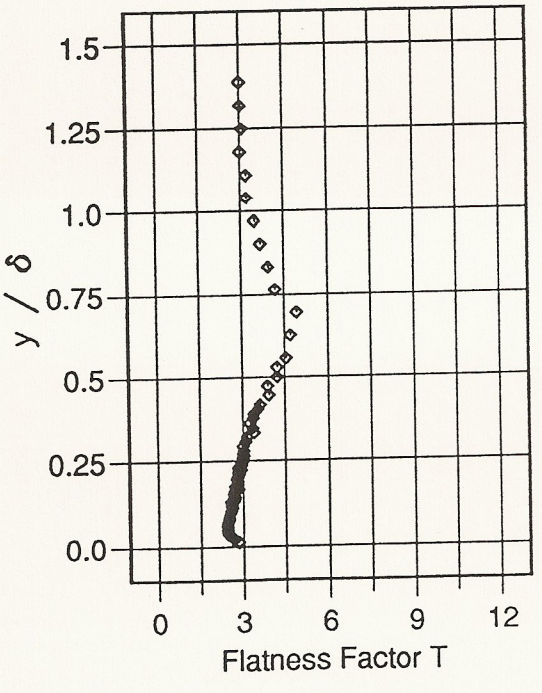
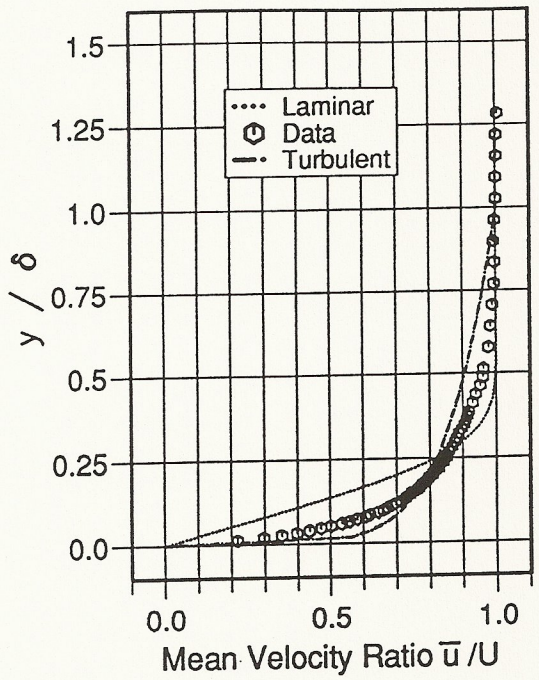


Figure A2.26	Profiles of the Skewness and Flatness Factors C4 Plate U_∞ = 15 m/s Tu_∞ = 4 % X = 118 mm



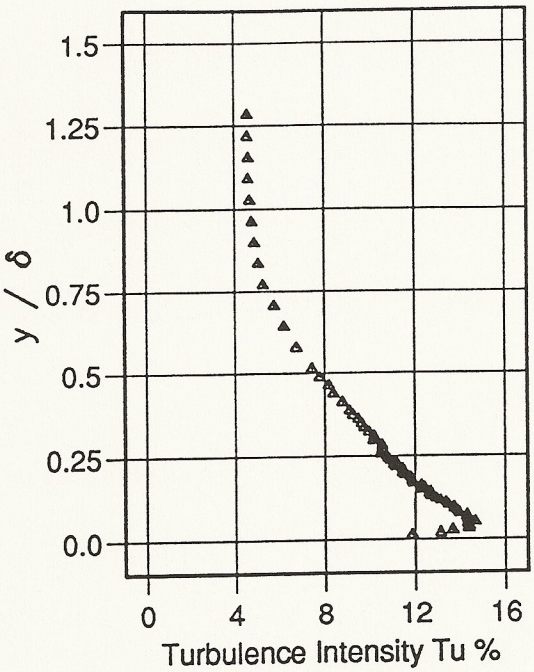
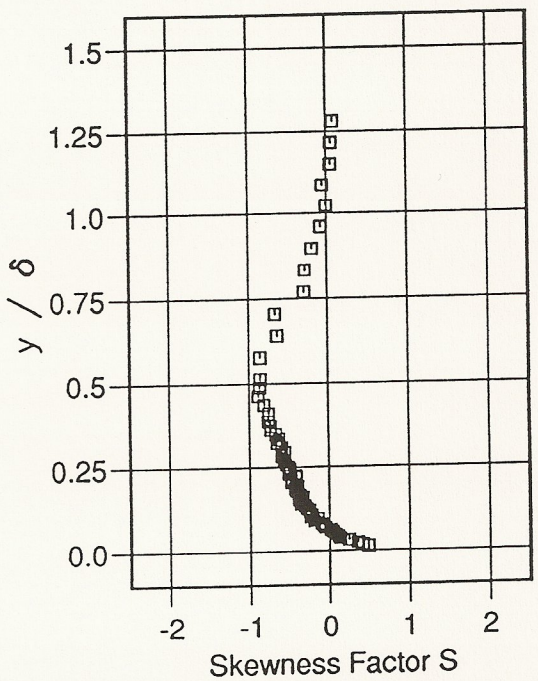


Figure A2.27	Profiles of the Mean Velocity and Turbulence Intensity C4 Plate U_∞ = 15 m/s Tu_∞ = 4 % X = 125 mm



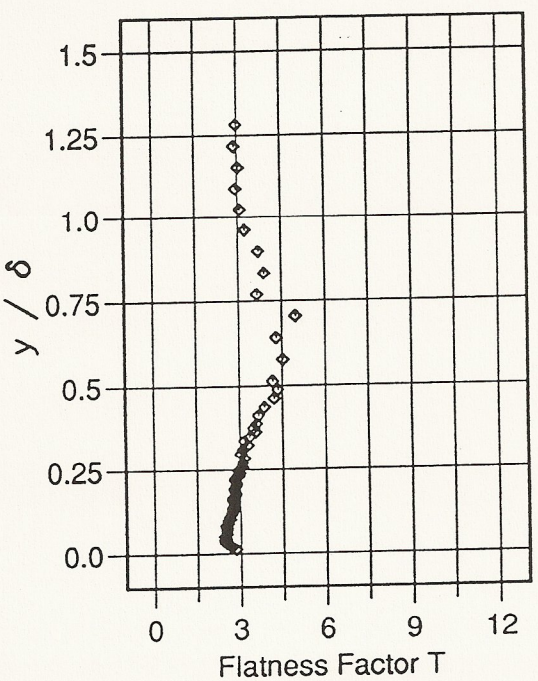
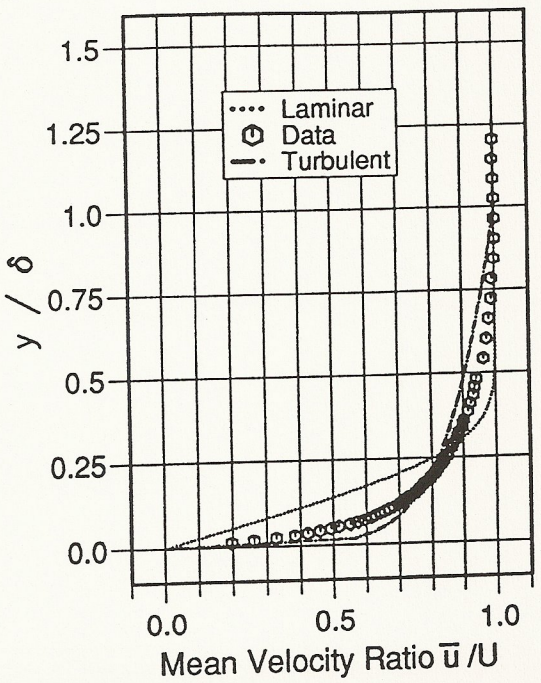


Figure A2.28	Profiles of the Skewness and Flatness Factors C4 Plate U_∞ = 15 m/s Tu_∞ = 4 % X = 125 mm



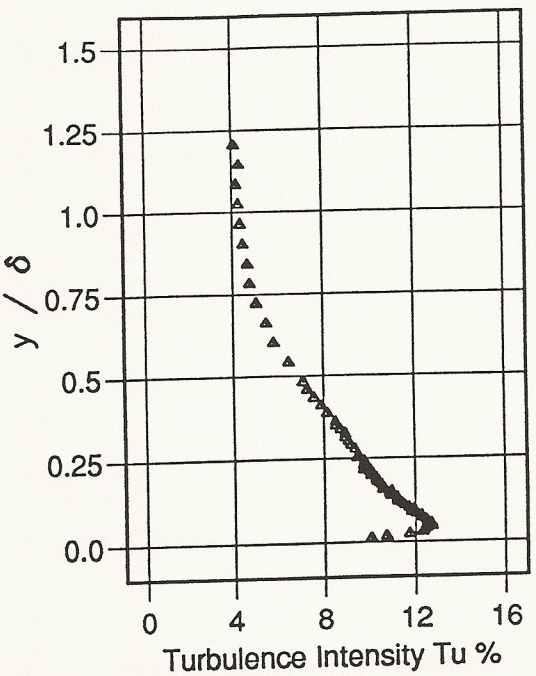
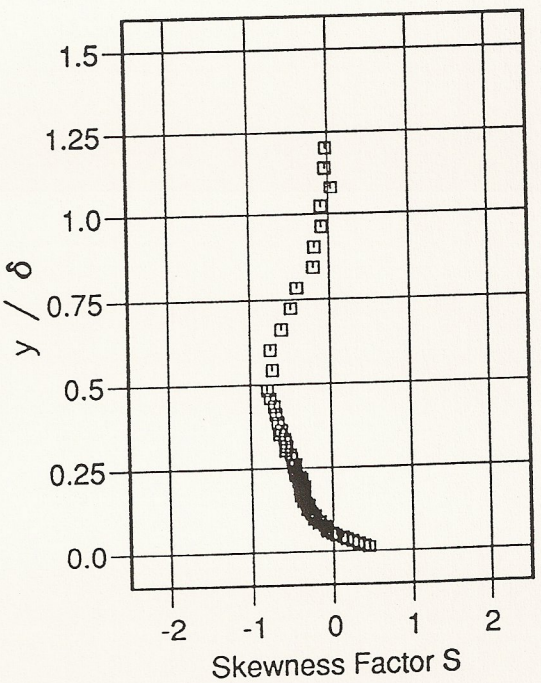


Figure A2.29	Profiles of the Mean Velocity and Turbulence Intensity C4 Plate U_∞ = 15 m/s Tu_∞ = 4 % X = 133 mm



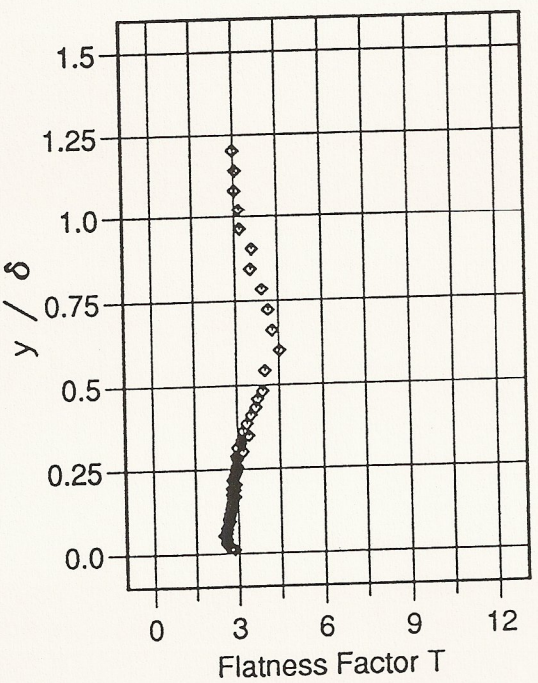
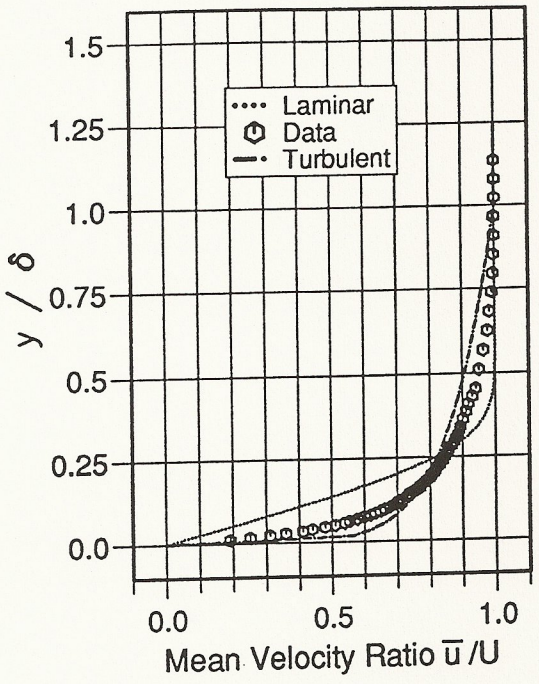


Figure A2.30	Profiles of the Skewness and Flatness Factors C4 Plate U_∞ = 15 m/s Tu_∞ = 4 % X = 133 mm



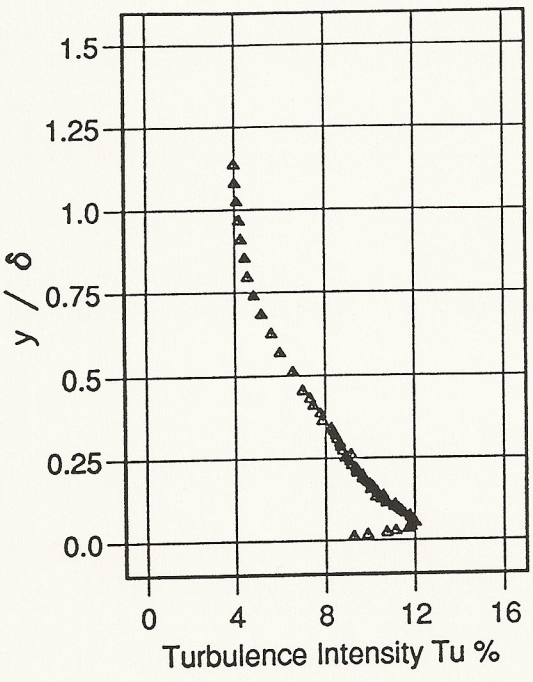
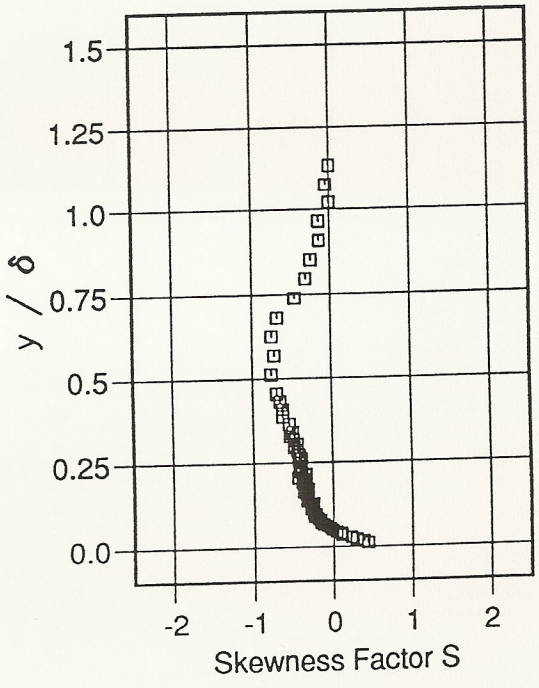


Figure A2.31	Profiles of the Mean Velocity and Turbulence Intensity C4 Plate U_∞ = 15 m/s Tu_∞ = 4 % X = 141 mm



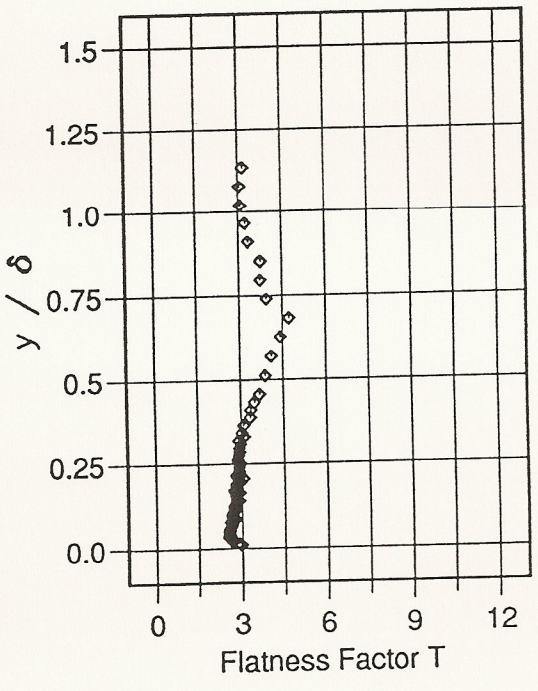
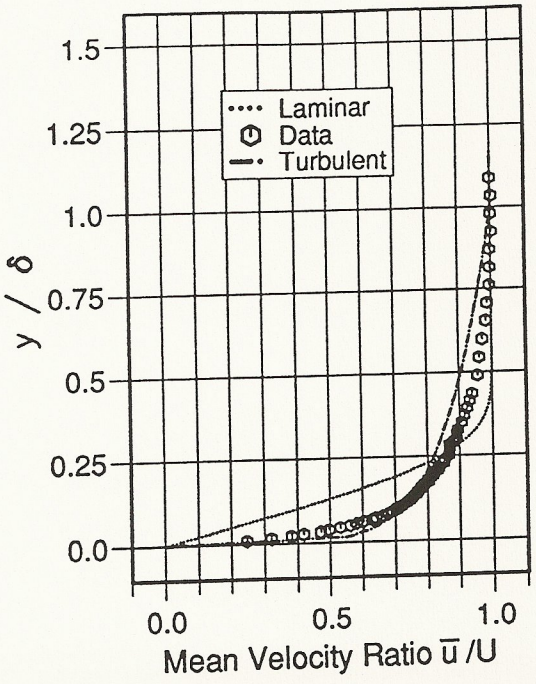


Figure A2.32	Profiles of the Skewness and Flatness Factors C4 Plate U_∞ = 15 m/s Tu_∞ = 4 % X = 141 mm



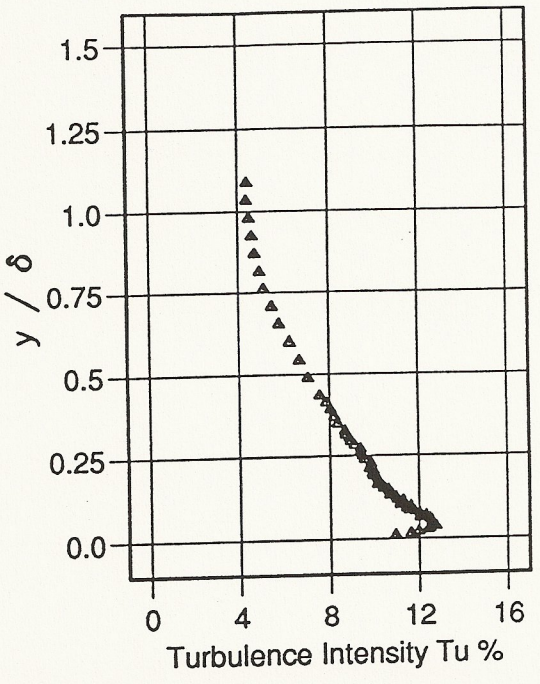
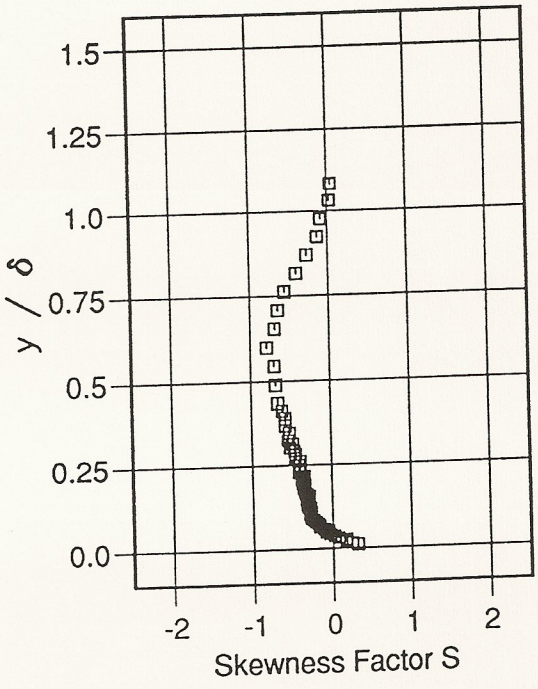


Figure A2.33	Profiles of the Mean Velocity and Turbulence Intensity C4 Plate U_∞ = 15 m/s Tu_∞ = 4 % X = 150 mm



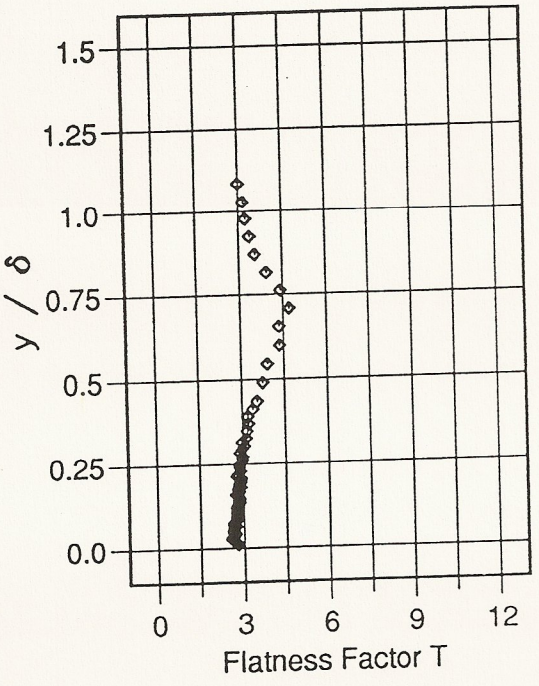


Figure A2.34	Profiles of the Skewness and Flatness Factors C4 Plate U_∞ = 15 m/s Tu_∞ = 4 % X = 150 mm

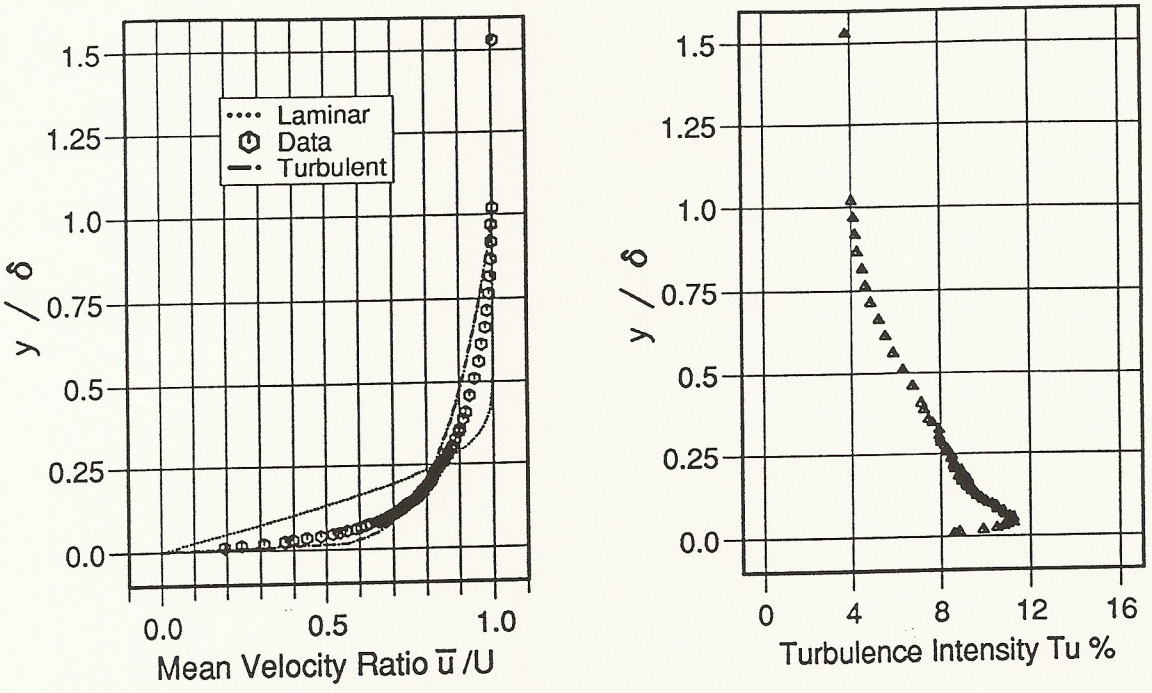


Figure A2.35	Profiles of the Mean Velocity and Turbulence Intensity C4 Plate U_∞ = 15 m/s Tu_∞ = 4 % X = 162.5 mm

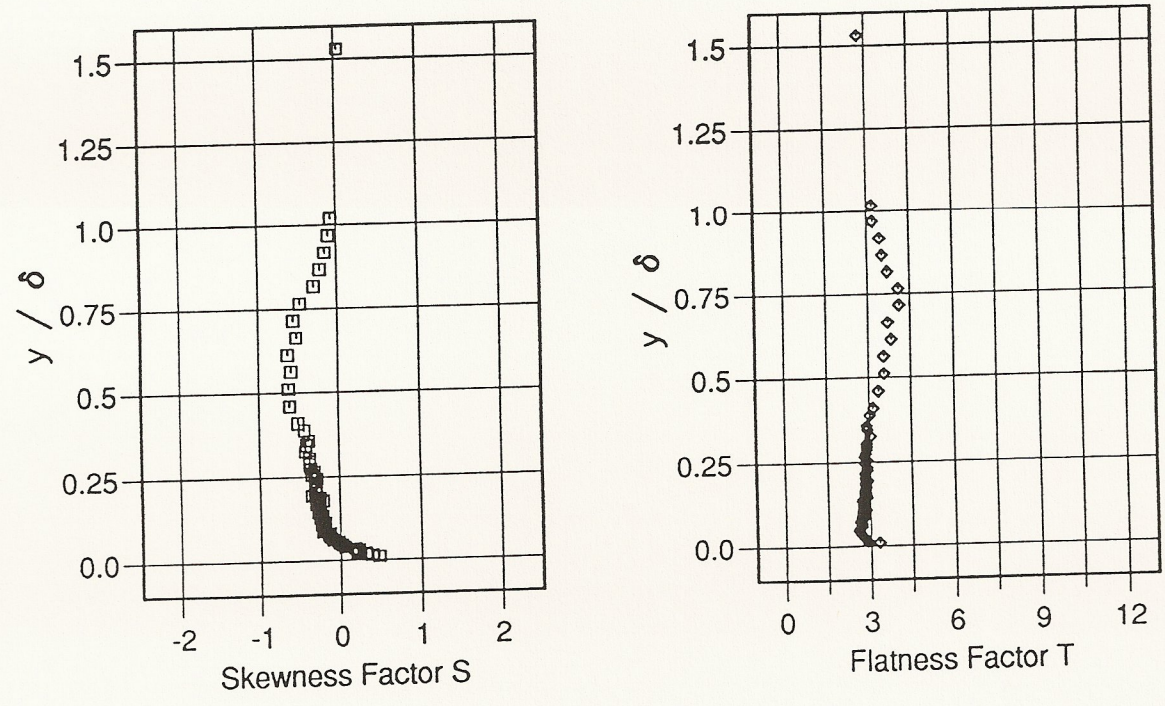
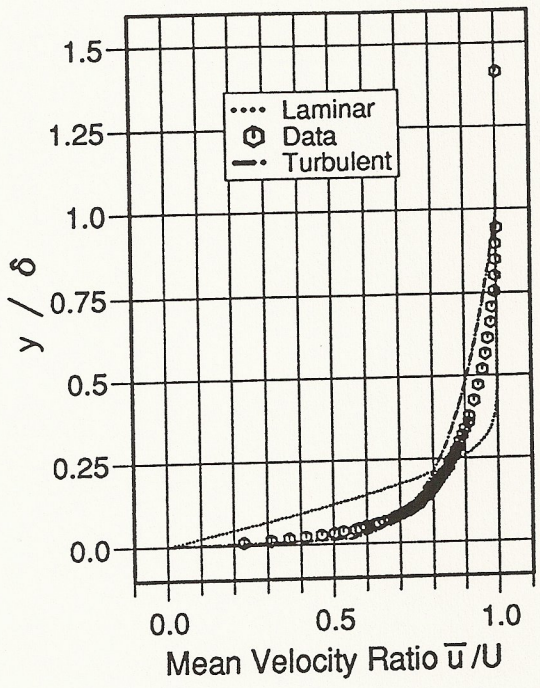


Figure A2.36	Profiles of the Skewness and Flatness Factors C4 Plate U_∞ = 15 m/s Tu_∞ = 4 % X = 162.5 mm



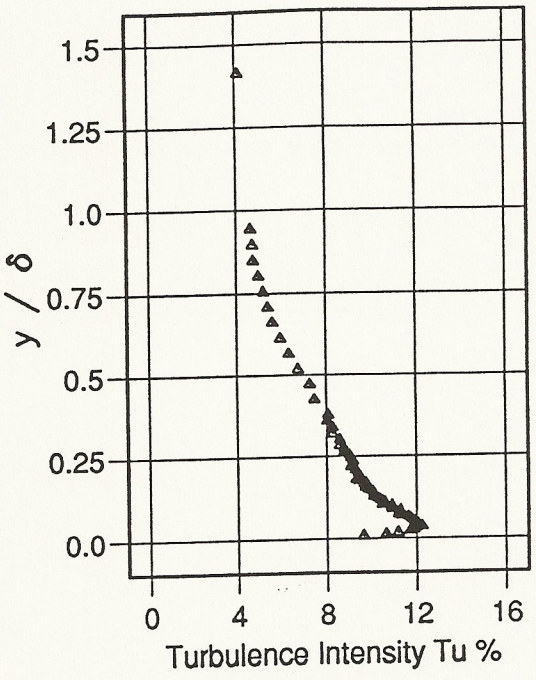
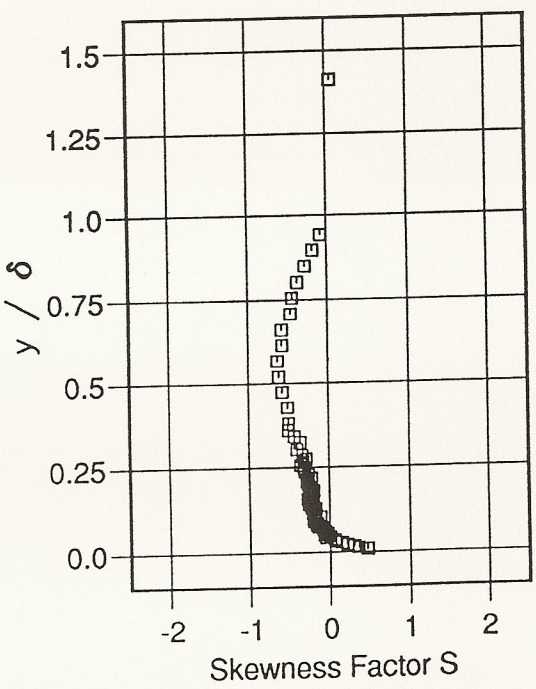


Figure A2.37	Profiles of the Mean Velocity and Turbulence Intensity C4 Plate U_∞ = 15 m/s Tu_∞ = 4 % X = 175 mm



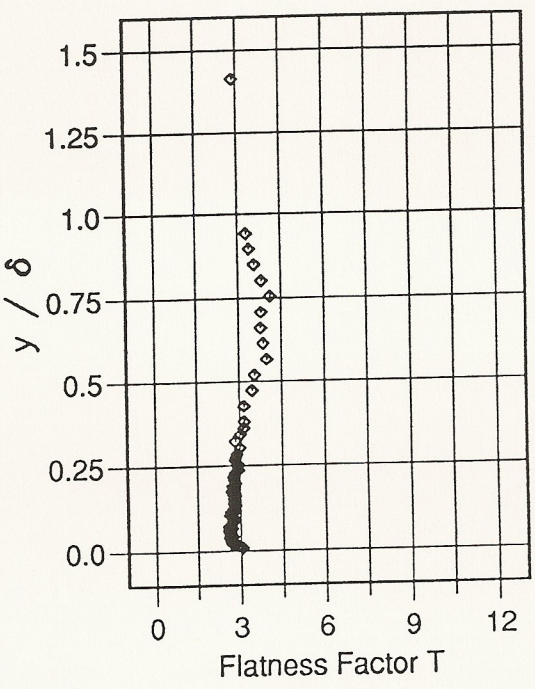
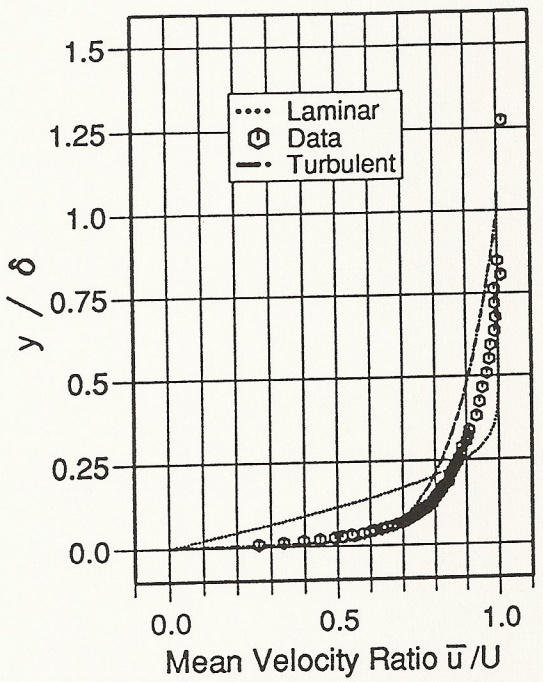


Figure A2.38	Profiles of the Skewness and Flatness Factors C4 Plate U_∞ = 15 m/s Tu_∞ = 4 % X = 175 mm



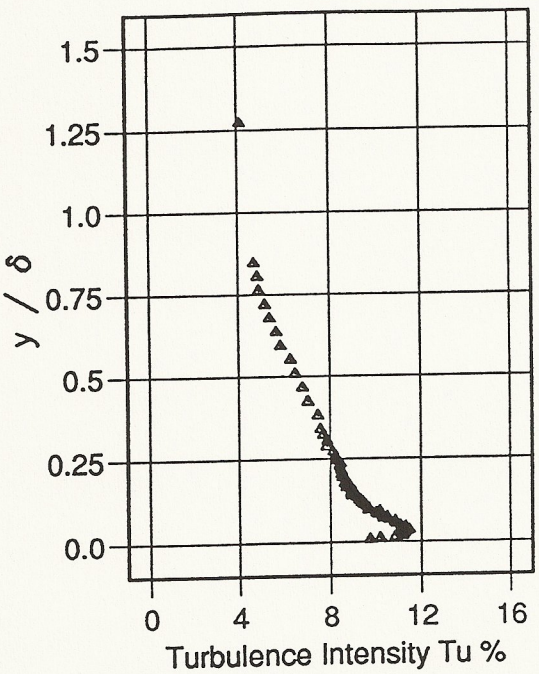
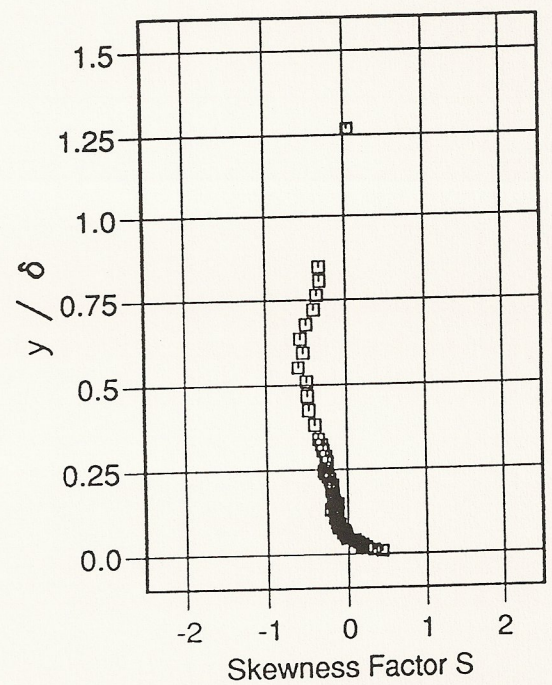


Figure A2.39	Profiles of the Mean Velocity and Turbulence Intensity C4 Plate U_∞ = 15 m/s Tu_∞ = 4 % X = 200 mm



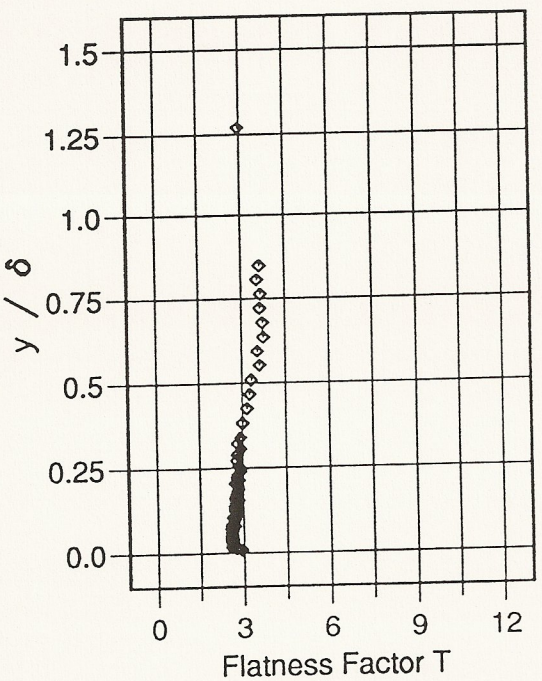


Figure A2.40	Profiles of the Skewness and Flatness Factors C4 Plate U_∞ = 15 m/s Tu_∞ = 4 % X = 200 mm

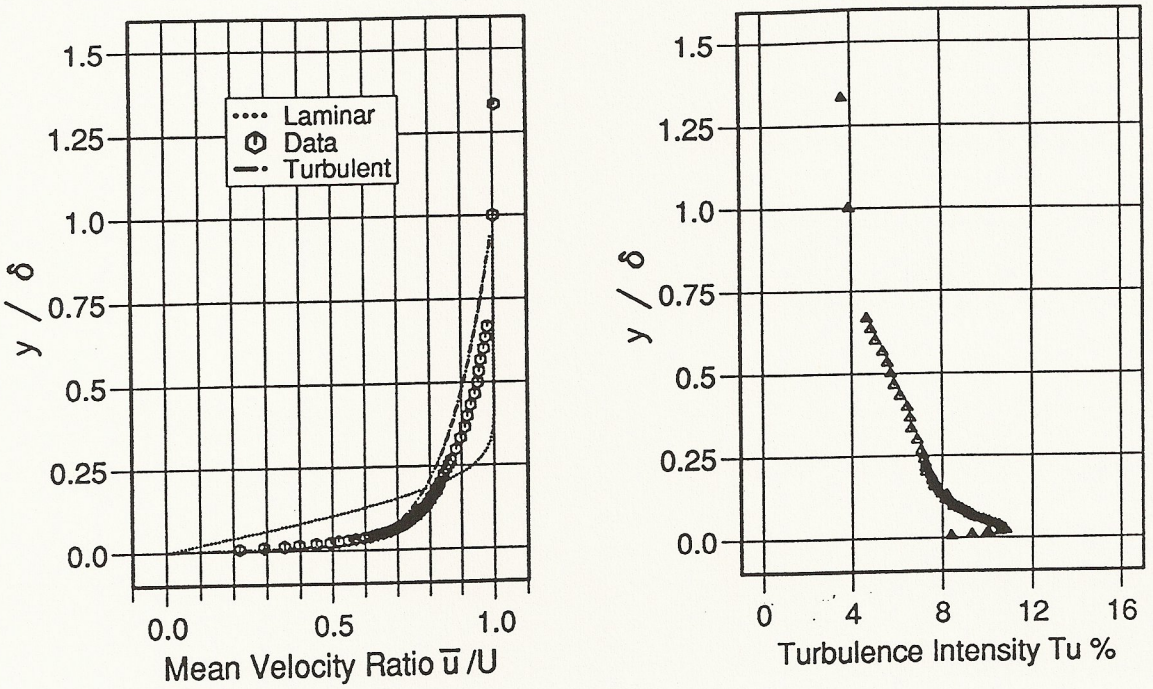


Figure A2.41	Profiles of the Mean Velocity and Turbulence Intensity C4 Plate U_∞ = 15 m/s Tu_∞ = 4 % X = 250 mm

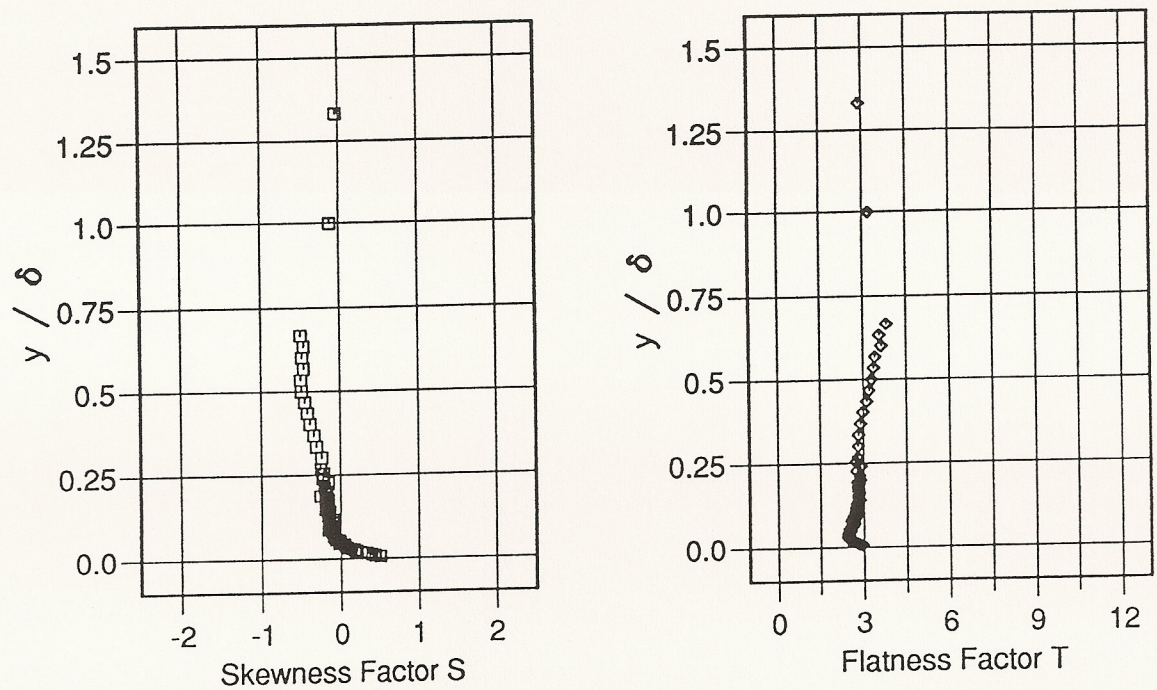


Figure A2.42	Profiles of the Skewness and Flatness Factors C4 Plate U_∞ = 15 m/s Tu_∞ = 4 % X = 250 mm

Analytical Plots of the Profiles of the Time Averaged Quantities Obtained with Hot Wire Anemometry

Section iii

Boundary layer Investigation of the C4 plate

U_∞ = 15 m/s

Tu_∞ = 1.8 %

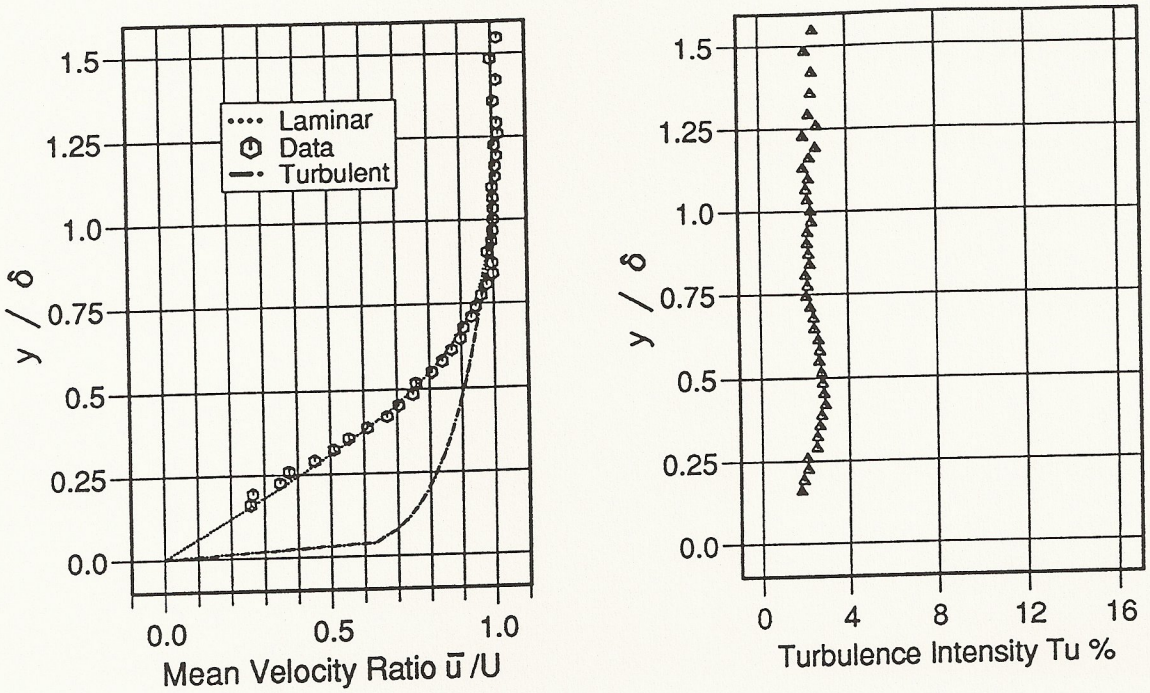


Figure A3.1	Profiles of the Mean Velocity and Turbulence Intensity C4 Plate U_∞ = 15 m/s Tu_∞ = 1.8 % X = 25 mm

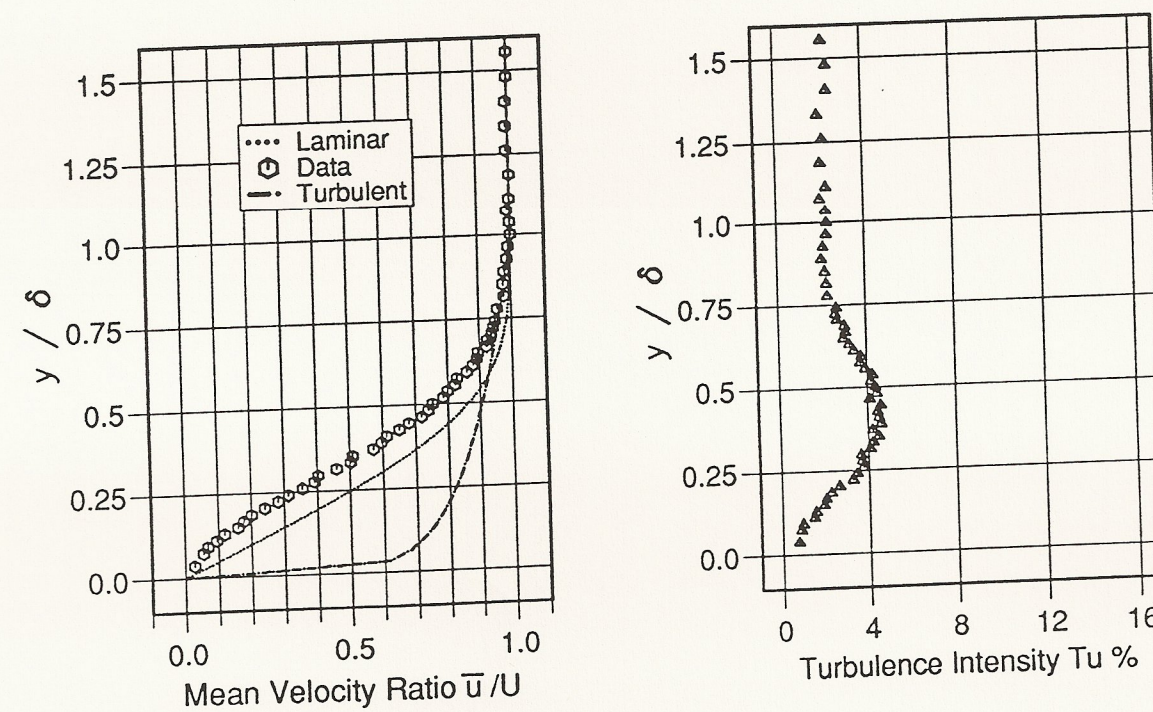


Figure A3.2	Profiles of the Mean Velocity and Turbulence Intensity C4 Plate U_∞ = 15 m/s Tu_∞ = 1.8 % X = 50 mm

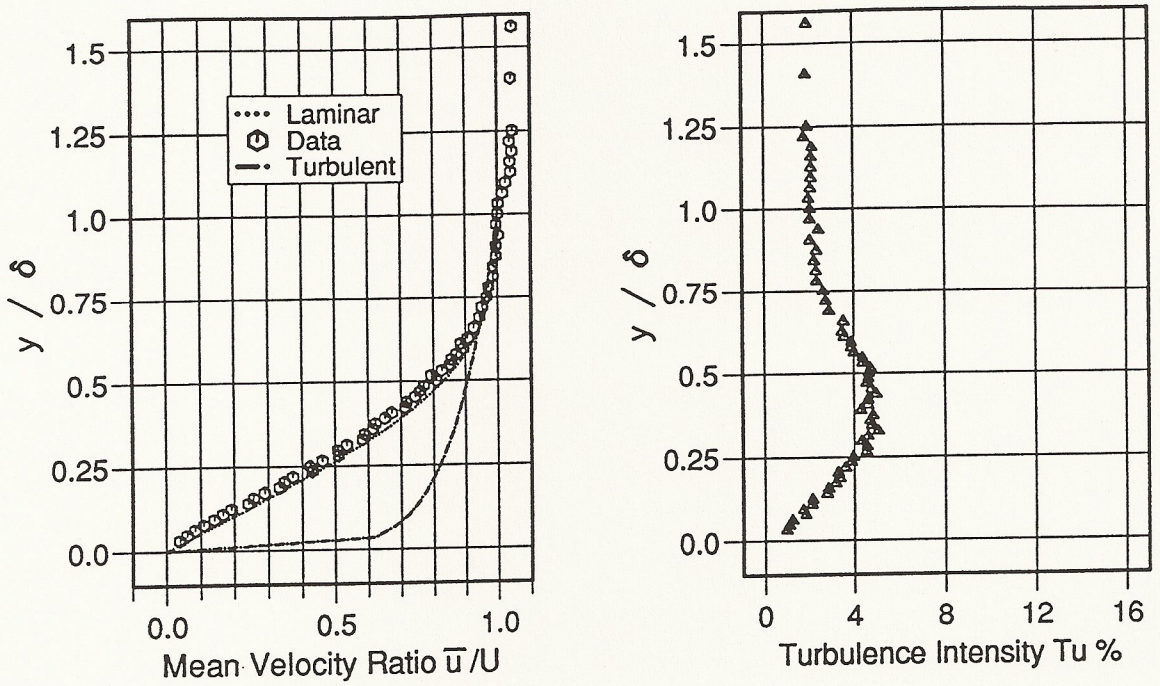


Figure A3.3	Profiles of the Mean Velocity and Turbulence Intensity C4 Plate U_∞ = 15 m/s Tu_∞ = 1.8 % X = 75 mm

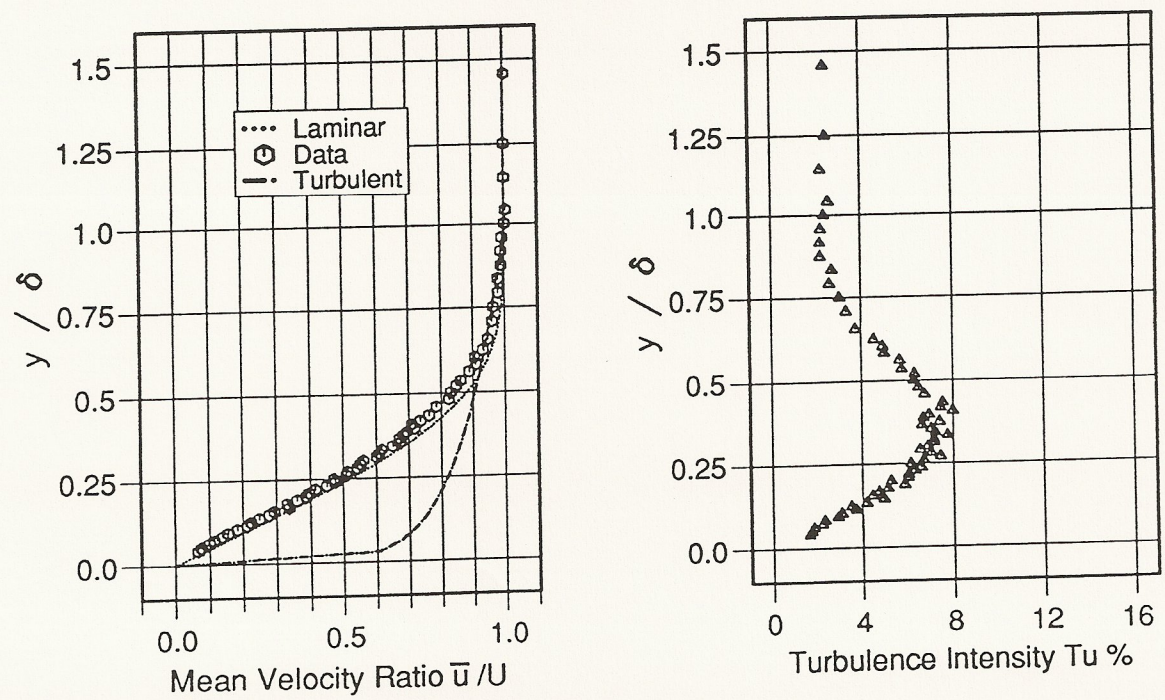


Figure A3.4	Profiles of the Mean Velocity and Turbulence Intensity C4 Plate U_∞ = 15 m/s Tu_∞ = 1.8 % X = 150 mm

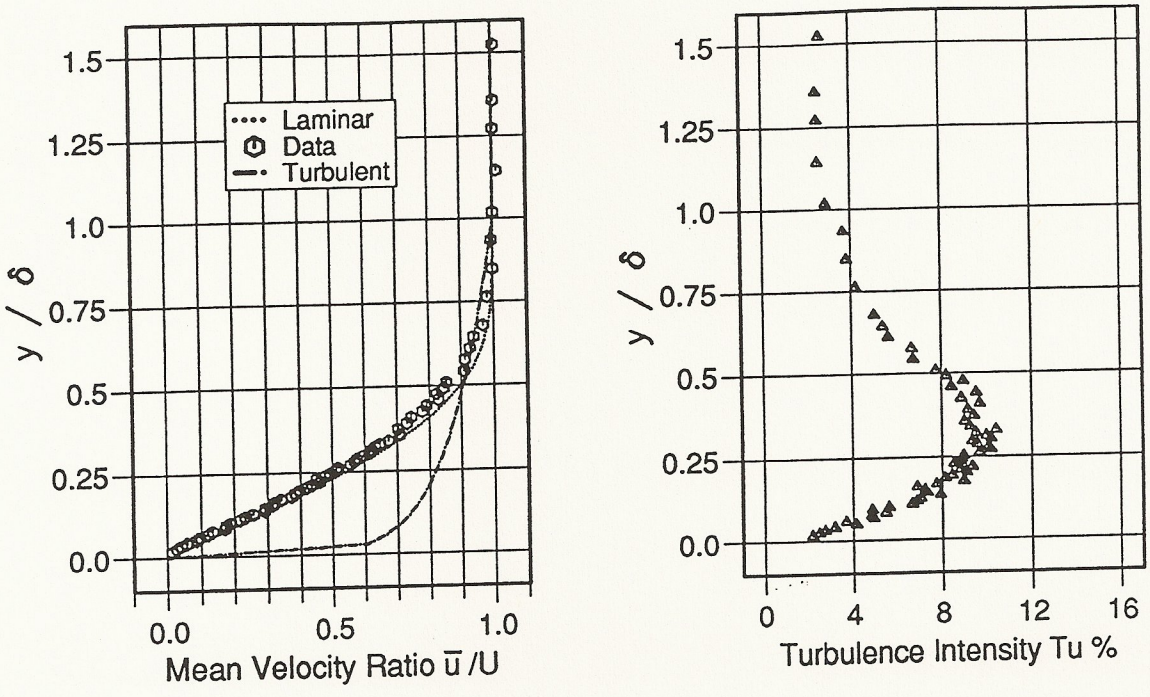


Figure A3.5	Profiles of the Mean Velocity and Turbulence Intensity C4 Plate U_∞ = 15 m/s Tu_∞ = 1.8 % X = 200 mm

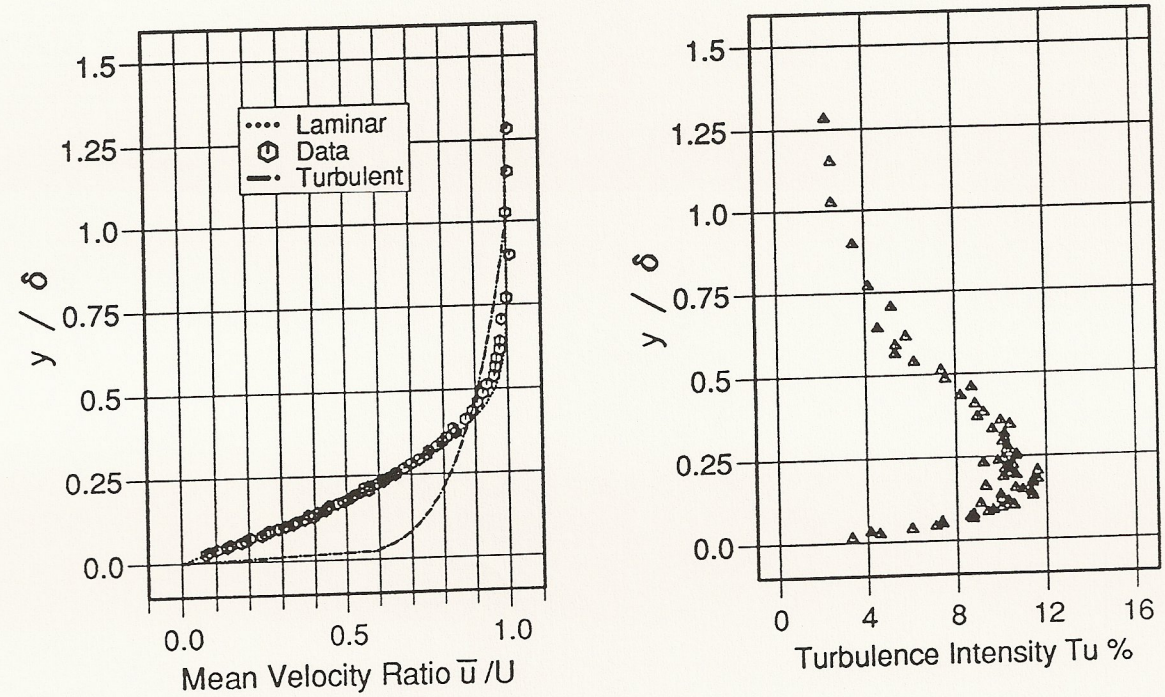


Figure A3.6	Profiles of the Mean Velocity and Turbulence Intensity C4 Plate U_∞ = 15 m/s Tu_∞ = 1.8 % X = 250 mm

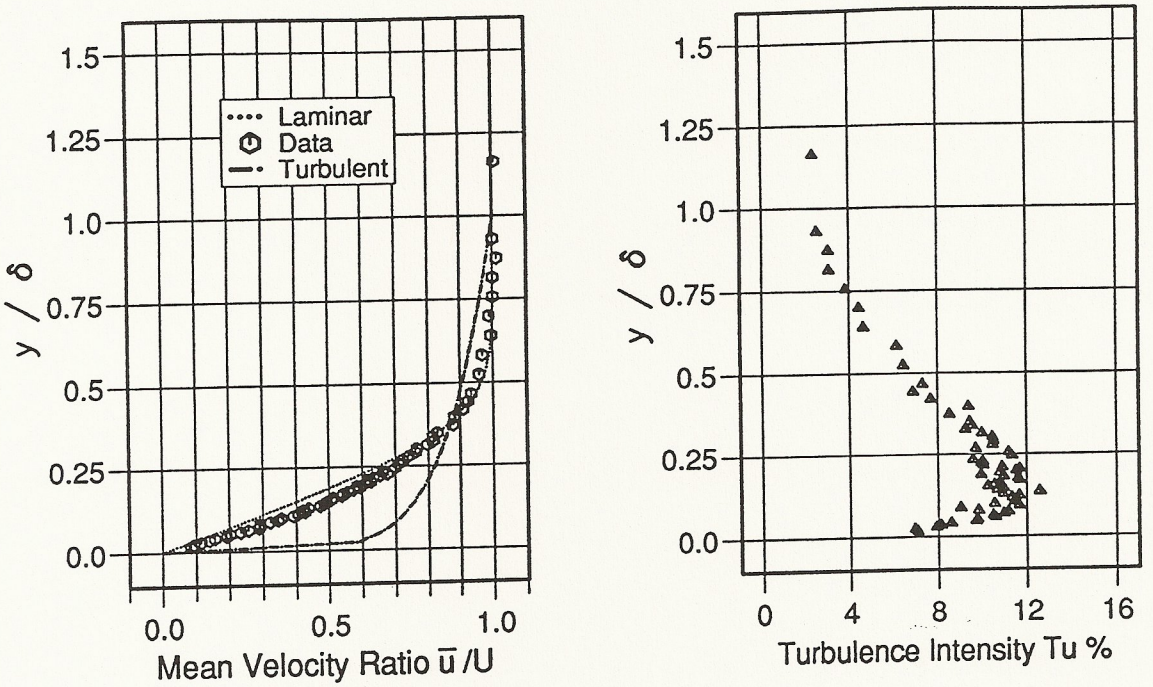


Figure A3.7	Profiles of the Mean Velocity and Turbulence Intensity C4 Plate U_∞ = 15 m/s Tu_∞ = 1.8 % X = 275 mm

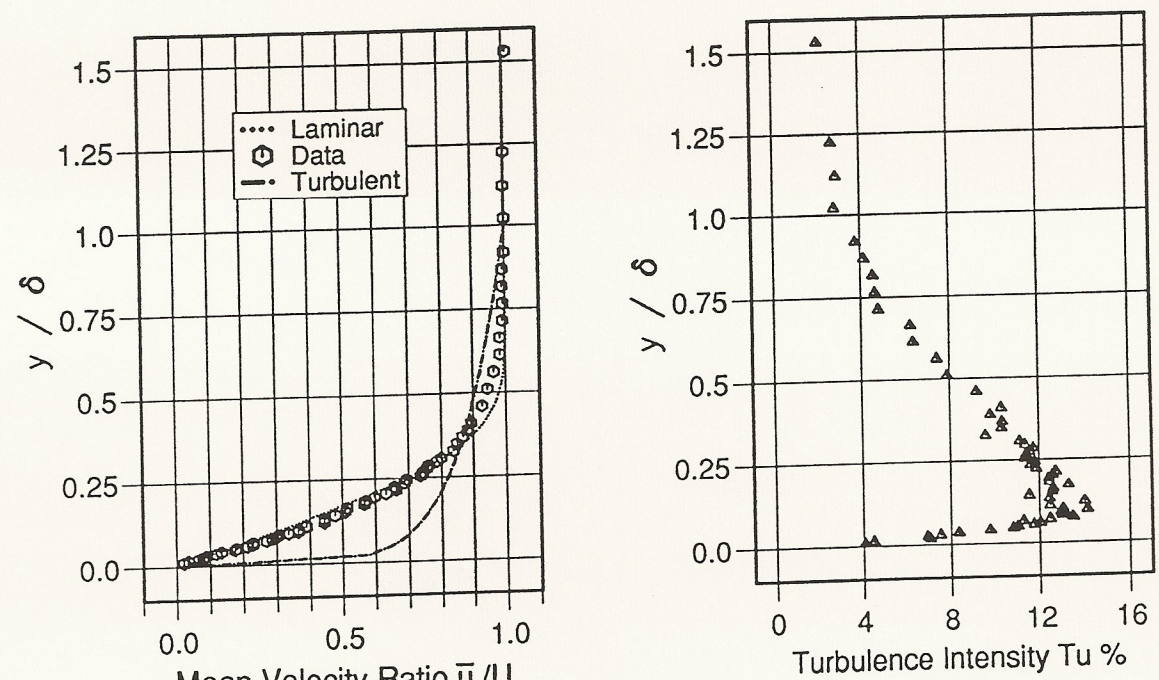


Figure A3.8	Profiles of the Mean Velocity and Turbulence Intensity C4 Plate U_∞ = 15 m/s Tu_∞ = 1.8 % X = 300 mm

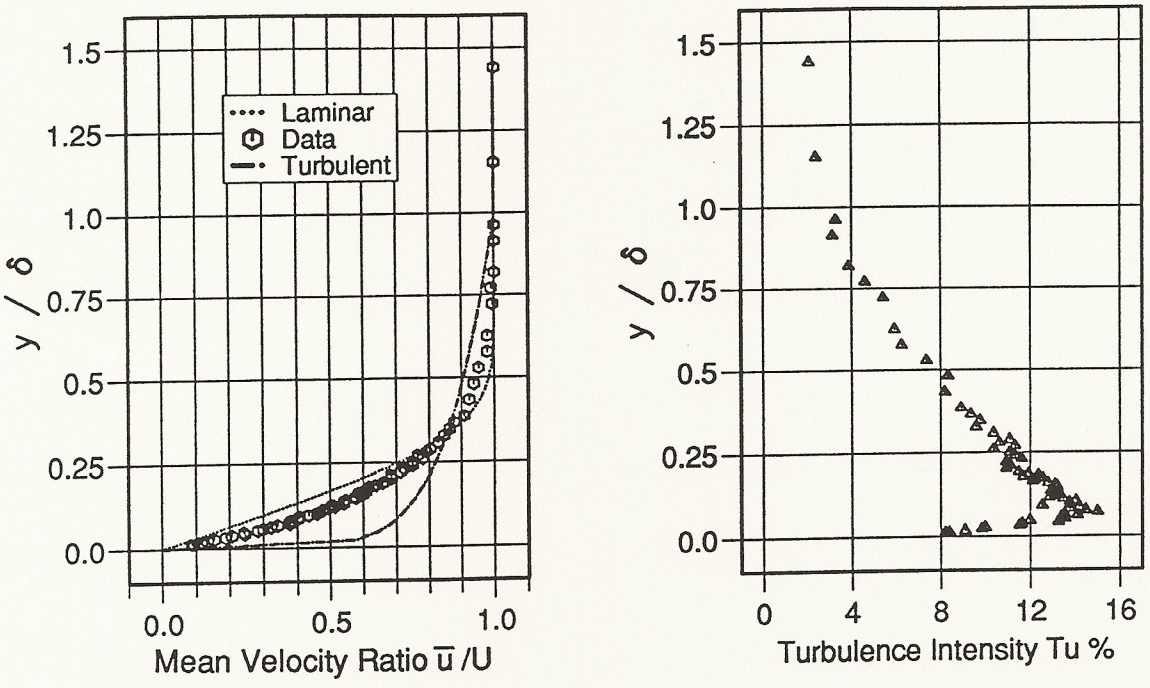


Figure A3.9	Profiles of the Mean Velocity and Turbulence Intensity C4 Plate U_∞ = 15 m/s Tu_∞ = 1.8 % X = 325 mm

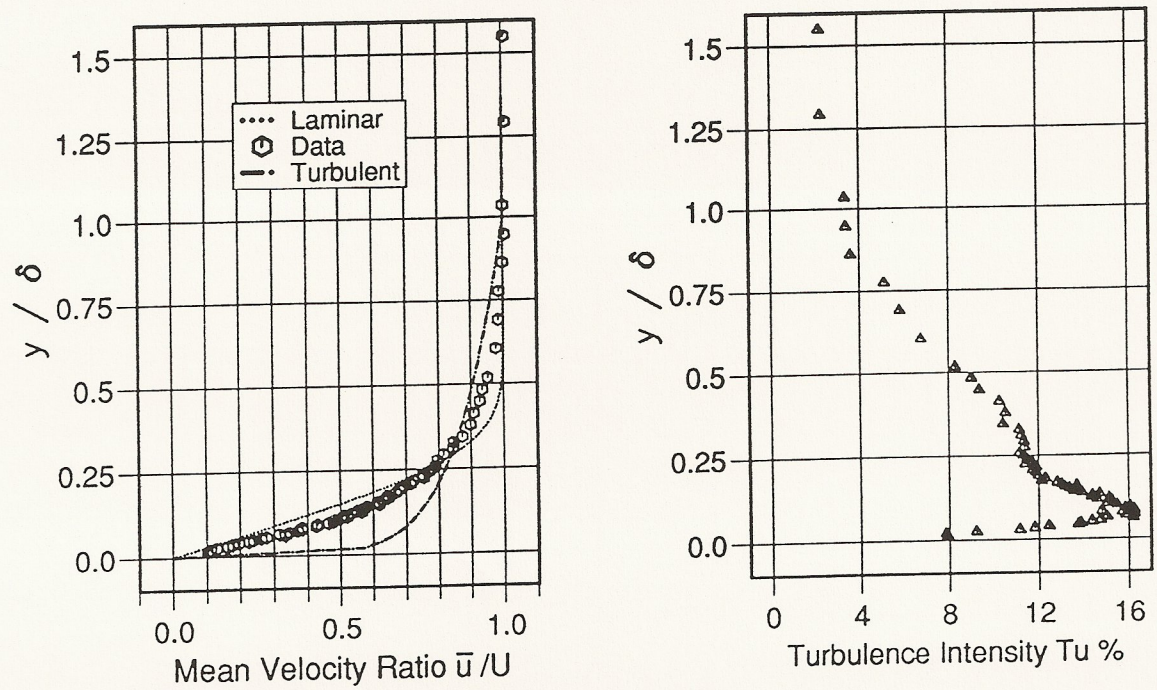


Figure A3.10	Profiles of the Mean Velocity and Turbulence Intensity C4 Plate U_∞ = 15 m/s Tu_∞ = 1.8 % X = 350 mm

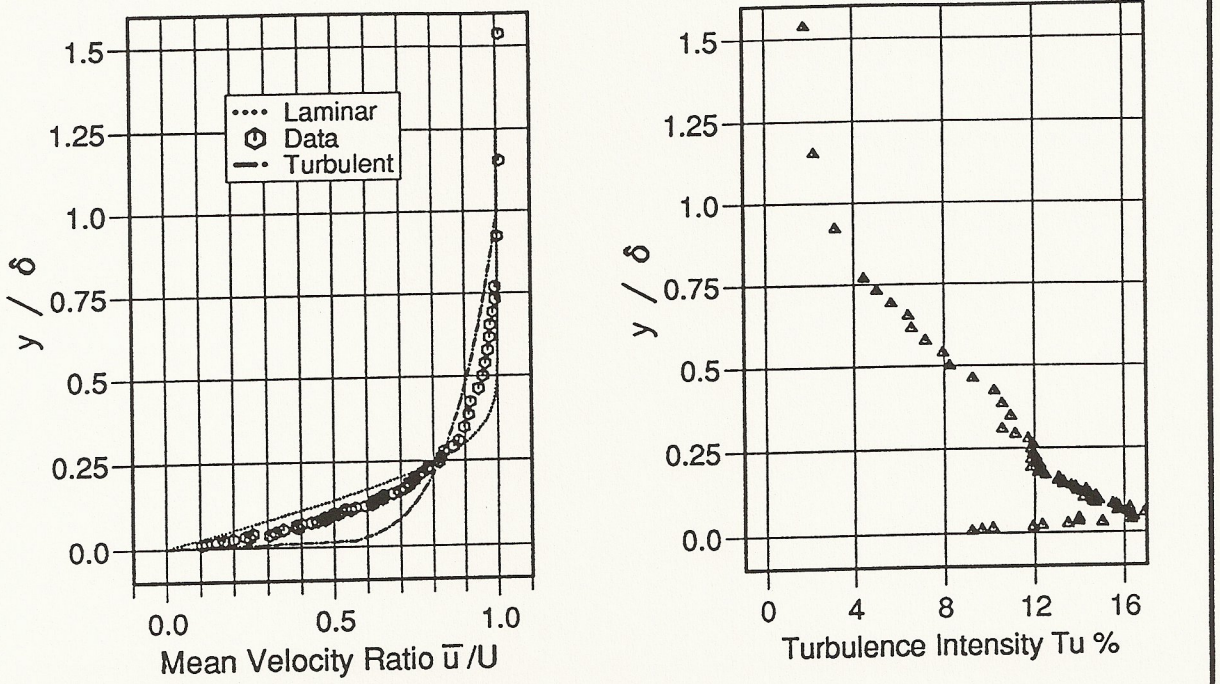


Figure A3.11 Profiles of the Mean Velocity and Turbulence Intensity
C4 Plate U_∞ = 15 m/s Tu_∞ = 1.8 % X = 375 mm

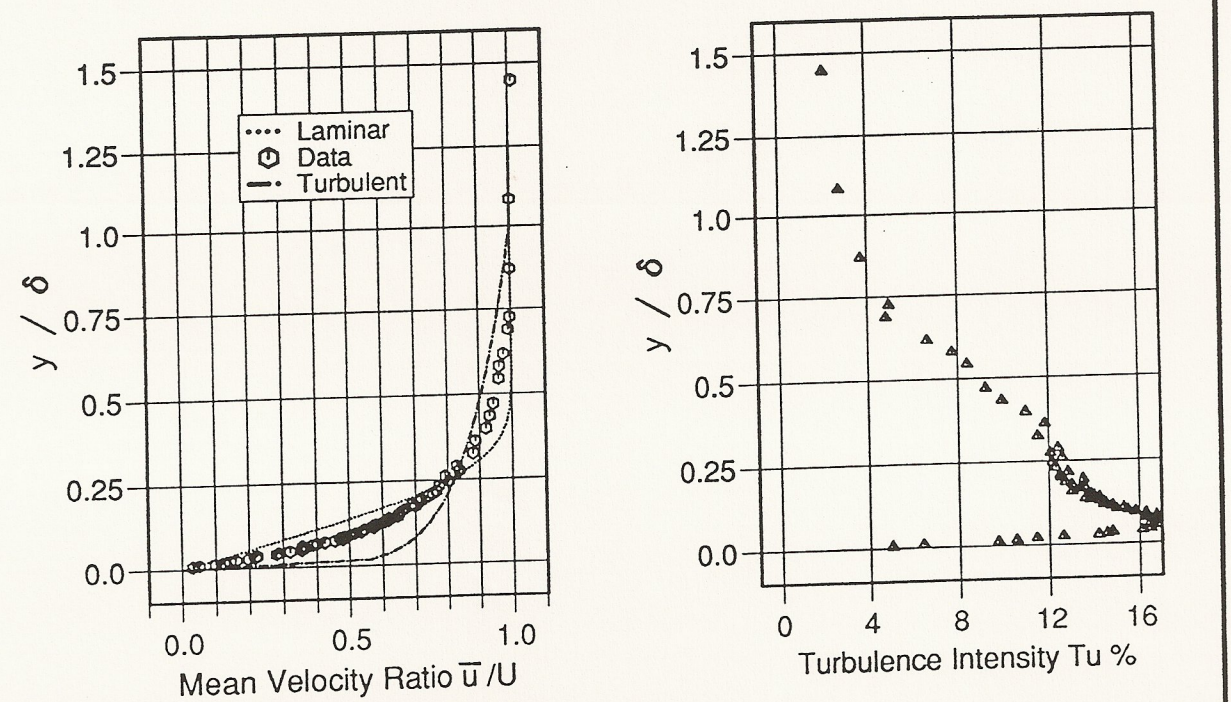


Figure A3.12 Profiles of the Mean Velocity and Turbulence Intensity
C4 Plate U_∞ = 15 m/s Tu_∞ = 1.8 % X = 400 mm

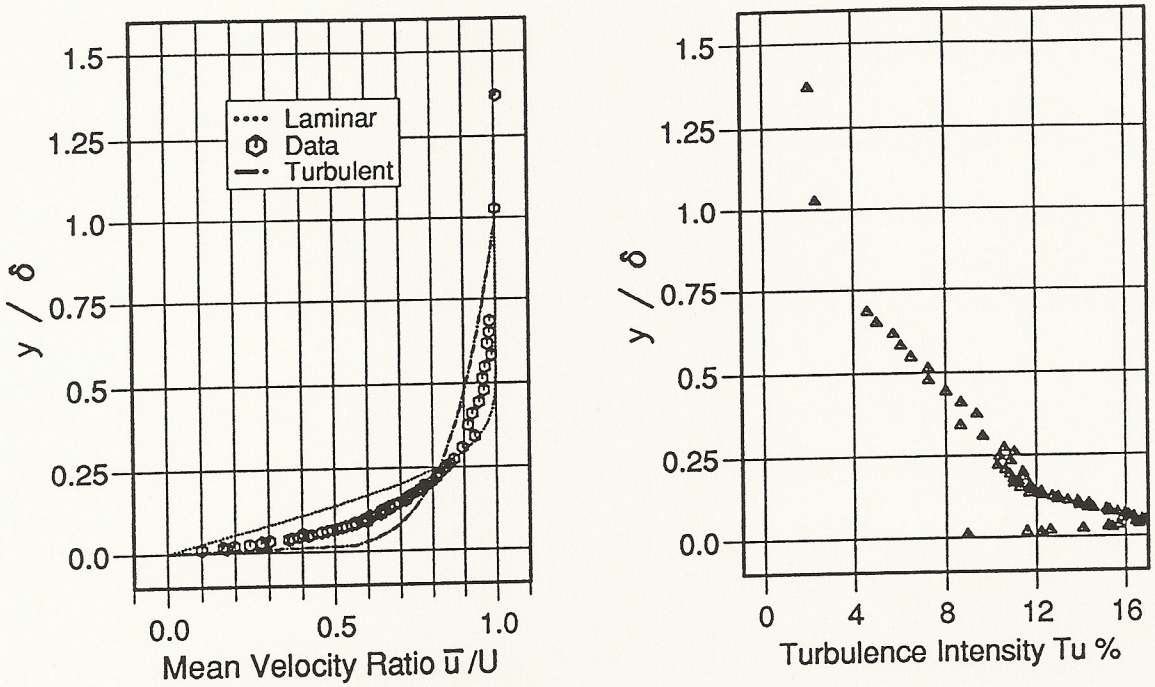


Figure A3.13	Profiles of the Mean Velocity and Turbulence Intensity C4 Plate U_∞ = 15 m/s Tu_∞ = 1.8 % X = 425 mm

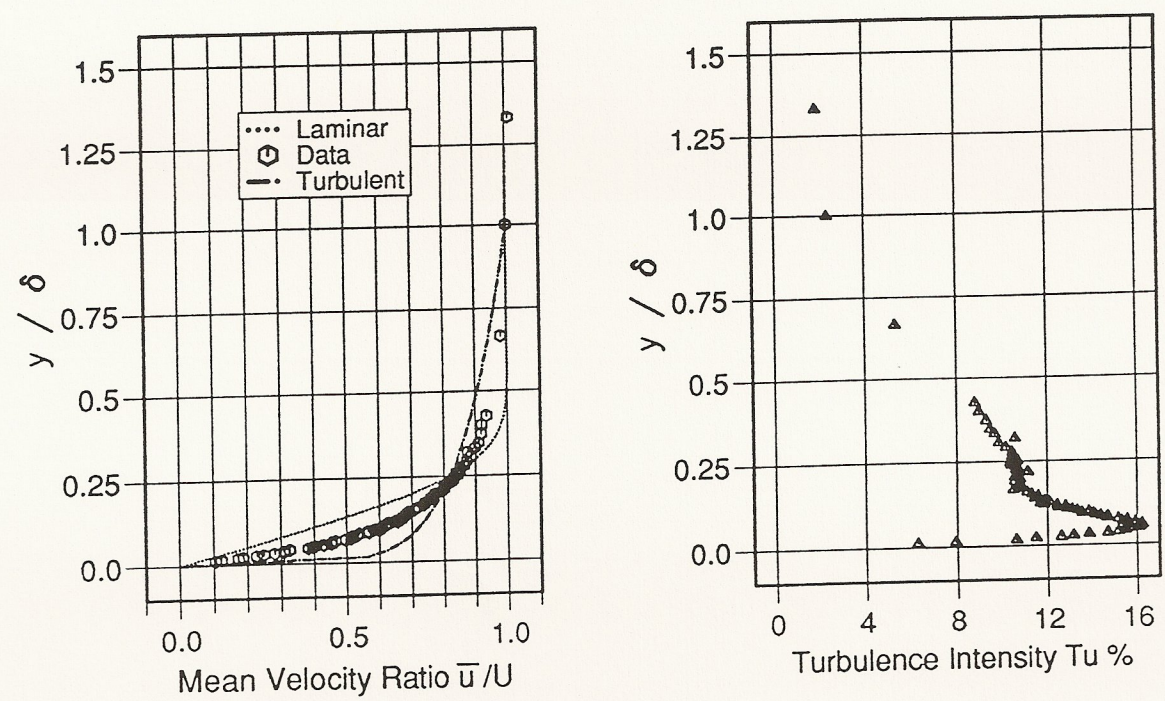


Figure A3.14	Profiles of the Mean Velocity and Turbulence Intensity C4 Plate U_∞ = 15 m/s Tu_∞ = 1.8 % X = 450 mm

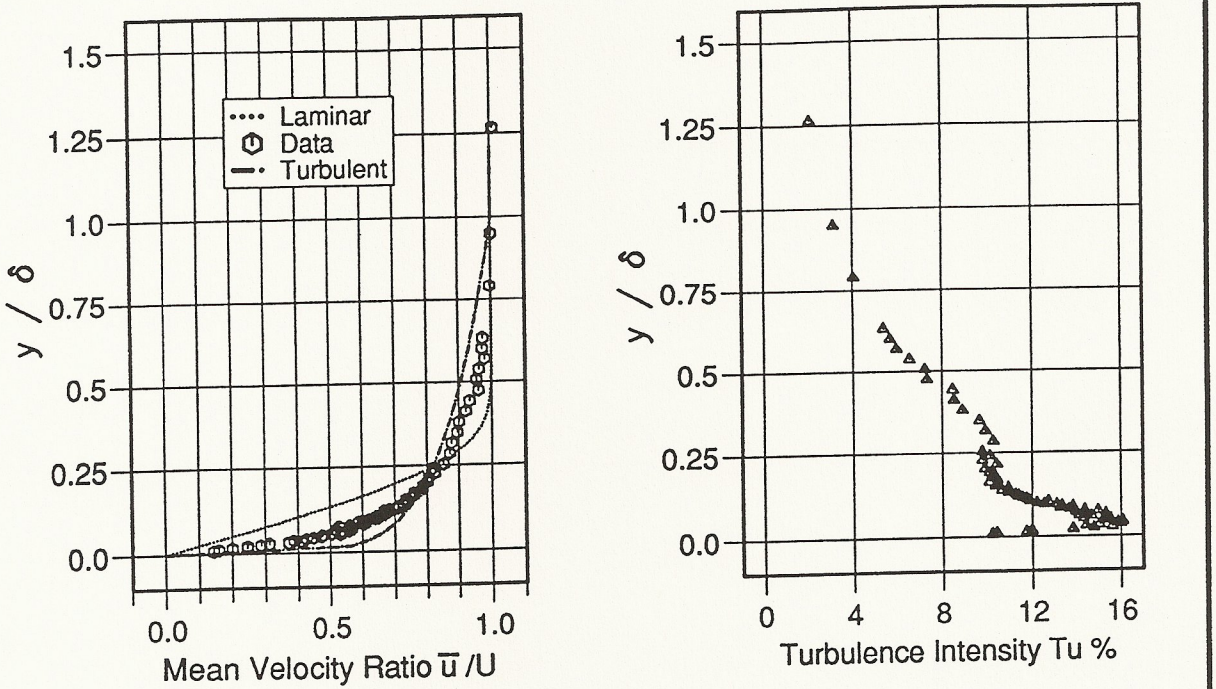


Figure A3.15	Profiles of the Mean Velocity and Turbulence Intensity C4 Plate U_∞ = 15 m/s Tu_∞ = 1.8 % X = 475 mm

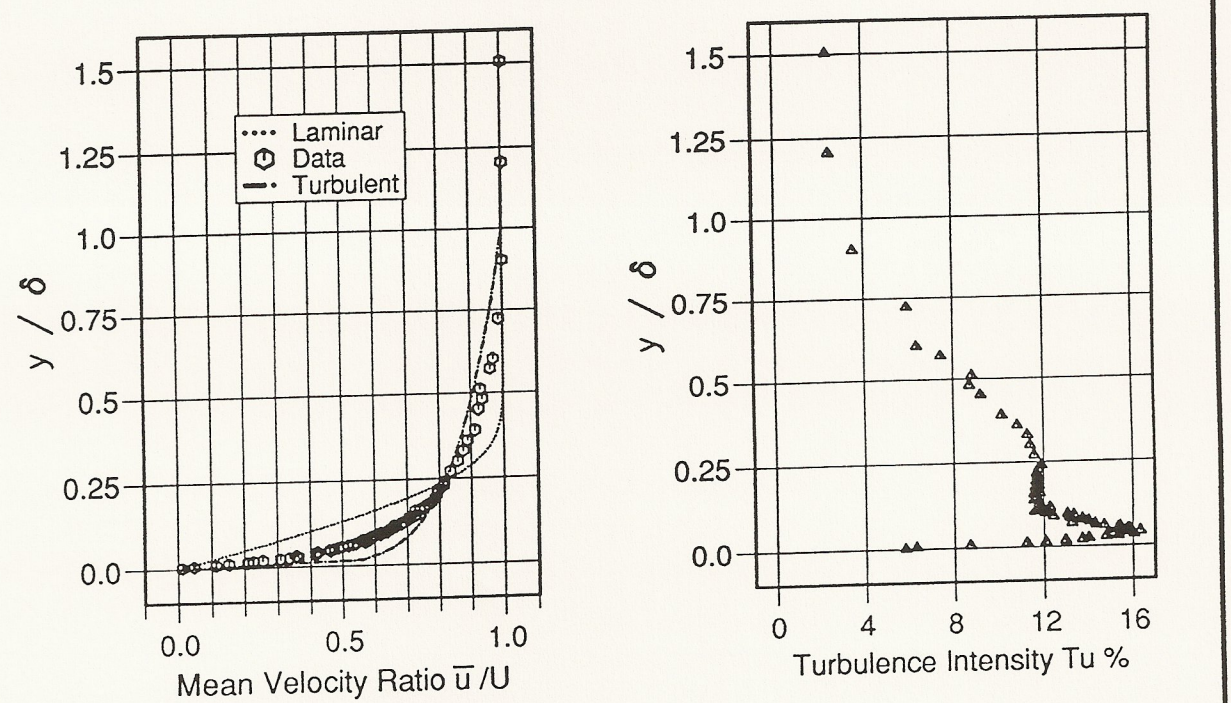


Figure A3.16	Profiles of the Mean Velocity and Turbulence Intensity C4 Plate U_∞ = 15 m/s Tu_∞ = 1.8 % X = 500 mm

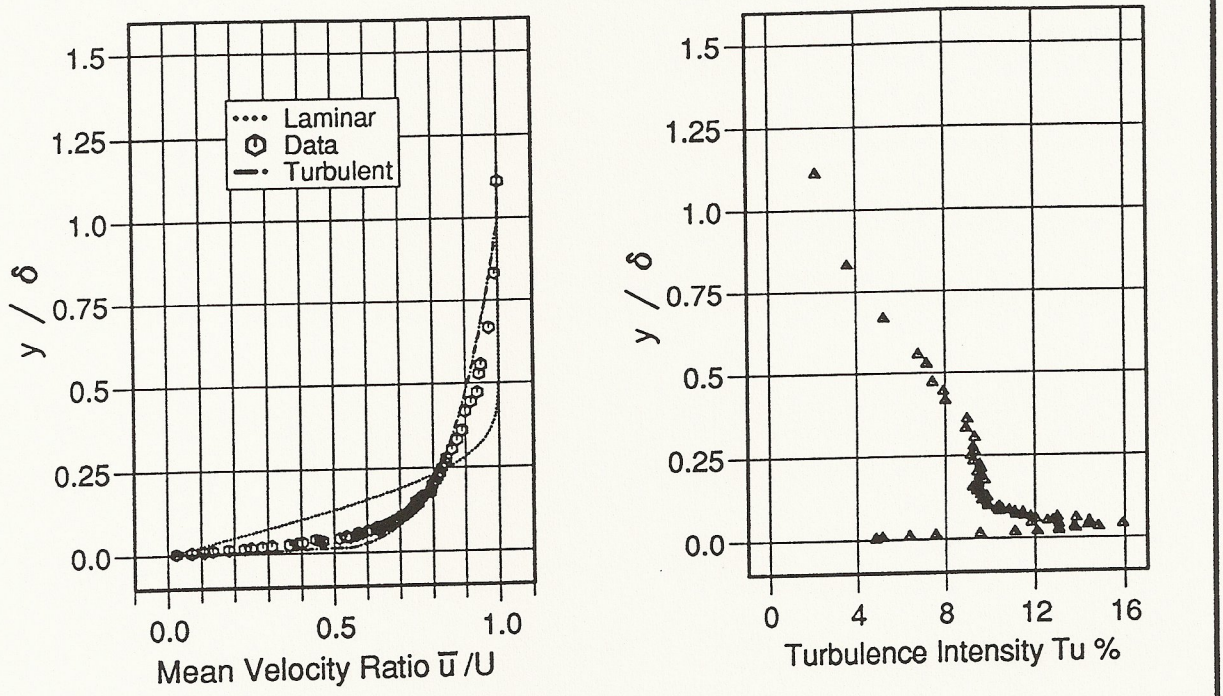


Figure A3.17	Profiles of the Mean Velocity and Turbulence Intensity C4 Plate U_∞ = 15 m/s Tu_∞ = 1.8 % X = 550 mm

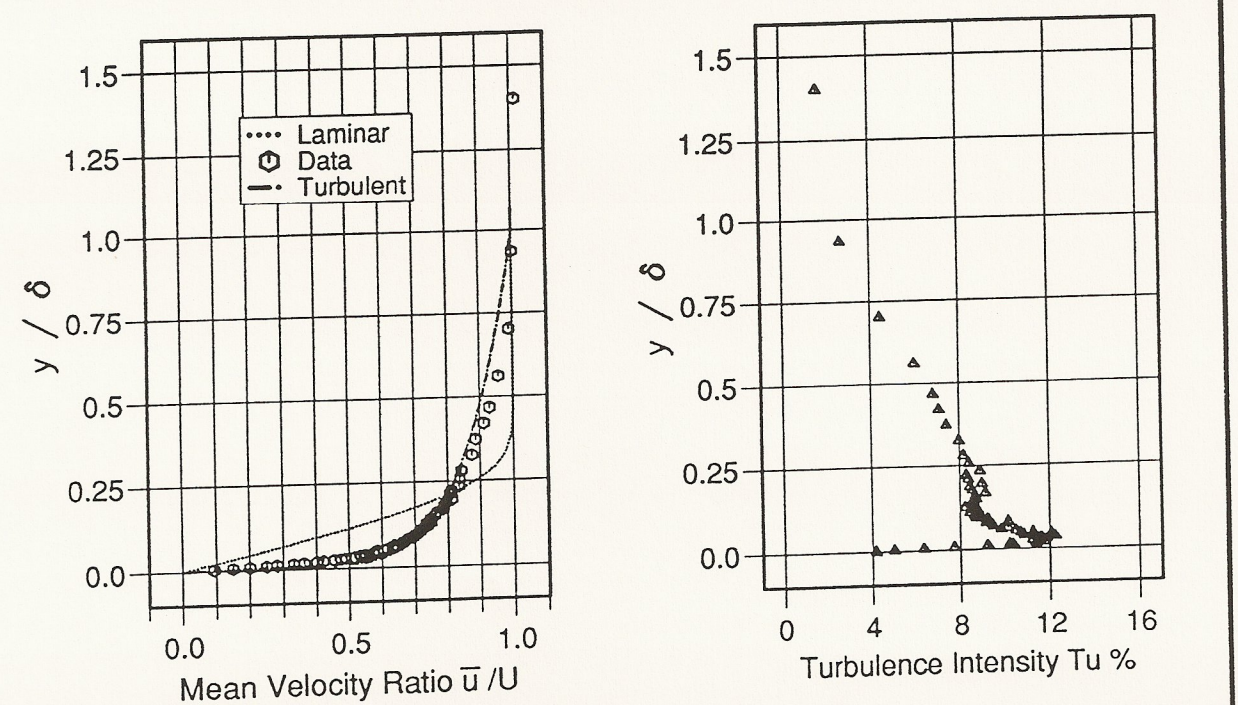


Figure A3.18	Profiles of the Mean Velocity and Turbulence Intensity C4 Plate U_∞ = 15 m/s Tu_∞ = 1.8 % X = 650 mm

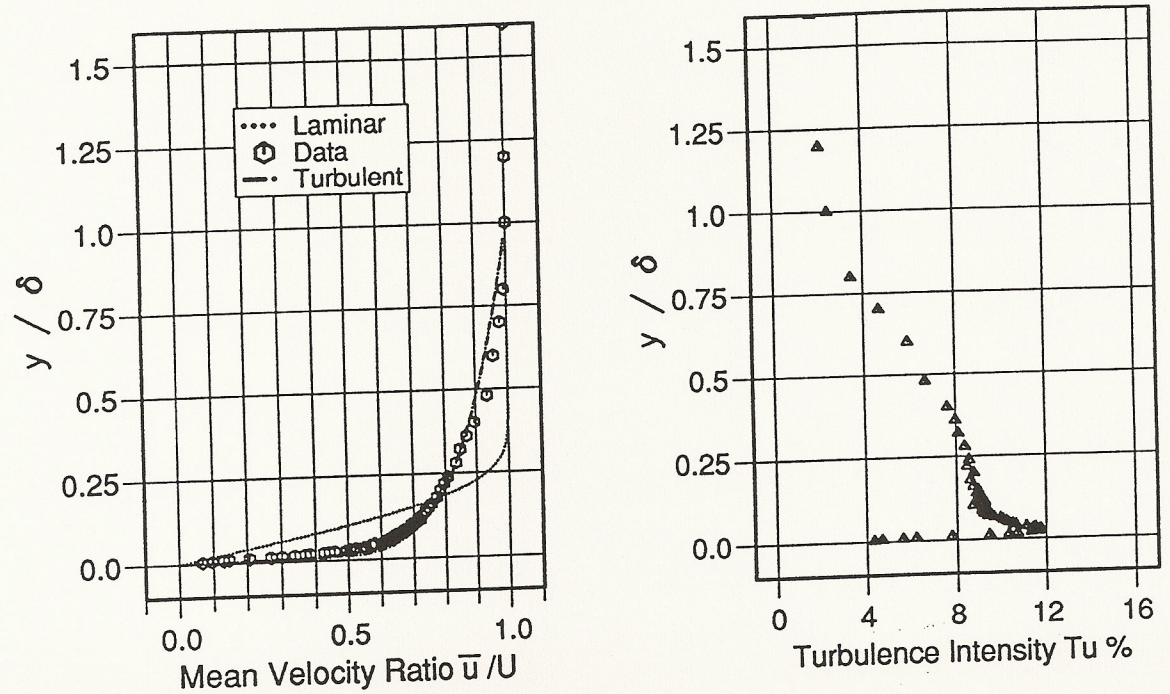


Figure A3.19	Profiles of the Mean Velocity and Turbulence Intensity C4 Plate U_∞ = 15 m/s Tu_∞ = 1.8 % X = 750 mm

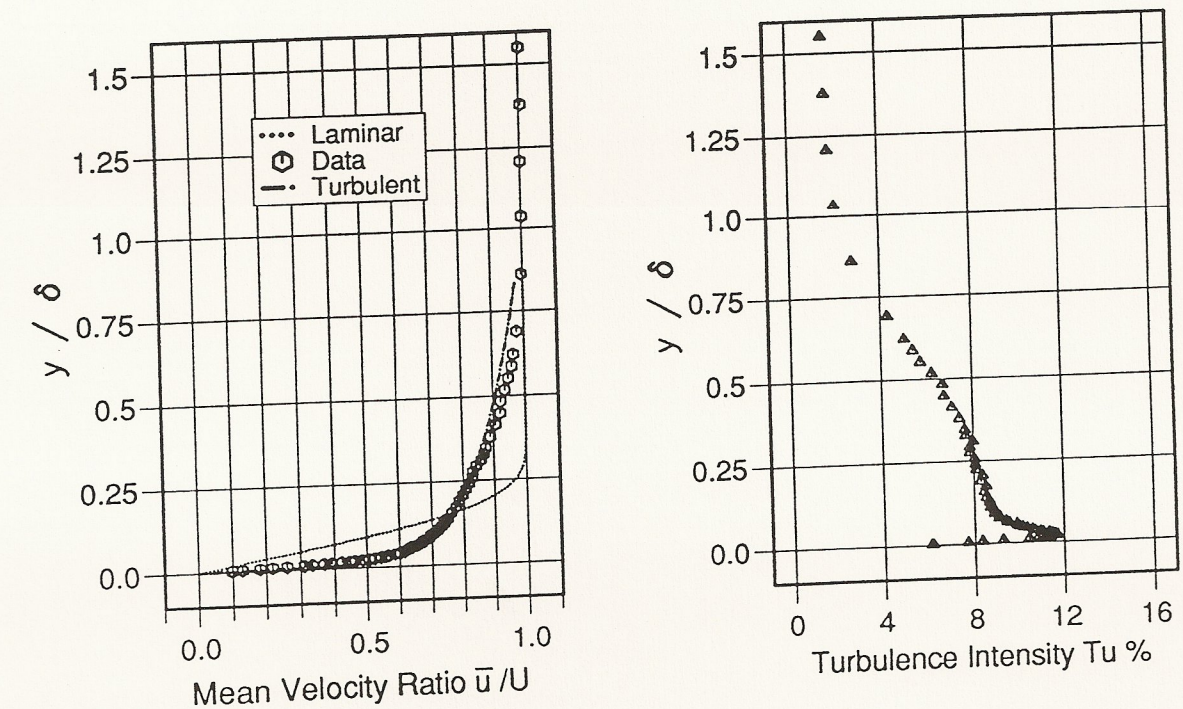


Figure A3.20	Profiles of the Mean Velocity and Turbulence Intensity C4 Plate U_∞ = 15 m/s Tu_∞ = 1.8 % X = 850 mm

APPENDIX B

On the Correction of Hot-wire Measurements for Wall Proximity

APPENDIX B

On the Correction of Hot-Wire Measurements for Wall Proximity

B.1 INTRODUCTION

The hot wire anemometer is considered as the most versatile instrument for the measurement of mean and fluctuating fluid velocities. The small size of the sensing element, the fast response to high frequency fluctuations and the suitability of the output signal for treatment with electronic instrumentation constitute the principal characteristics that make hot wire anemometry adequate for turbulence measurements. Apart from the above described advantages of the hot wire anemometer against other measurement techniques, there are some practical difficulties involved in the manufacturing and use of the hot wire sensors.

The use of hot wire anemometry in the vicinity of a solid boundary involves some potential sources of inaccuracy in the obtained results. The operation of the hot-wire sensor in the vicinity of a infinitely large solid boundary with much higher thermal conductivity than the working fluid results in the alteration of the thermal and velocity fields in the surrounding area. During operation, the hot-wire sensor is kept to a much higher temperature than the neighbouring solid boundary and as a result there is an additional heat loss from the wire. In simple terms, heat is conducted to the solid wall from the surrounding fluid that is heated through the hot wire element.

The above described extra heat loss due to the wall proximity is actually recorded through the electronic instrumentation as an increased velocity in the near wall

area. This effect is increasing rapidly as the wire approaches the wall (see also figure B.2). Finally, it is interesting to note that this phenomenon is often used in order to measure the distance of the sensor from the solid surface using a calibration procedure at zero flow.

In order to obtain reasonably accurate measurements in the near wall area, a suitable correction procedure should be followed. The aim of this appendix is both to briefly review the existing information in the literature, as well as to outline the method employed in this course of study.

B.2 A BRIEF REVIEW OF THE LITERATURE

The vast majority of the investigations of the required correction to the hot wire measurements due to the wall proximity are based on experimental evaluation of the excess heat loss through the conductive material of the solid boundary. Early experimental investigations suggested that the heat loss to the wall at zero velocity can be correlated to the measured velocity difference in normal flow conditions. This approaches assumed that the effect of the wall can be taken into account in terms of an additional heat loss independent of the stream velocity (see also the review paper by Zarić (1972)). A more accurate method has been proposed by Reichardt (1940) (work referred to by Wills (1962) and Bhatia et. al. (1982)). In this case, the hot-wires have been calibrated close to the wall in a laminar flow channel. This calibration was then used in a channel with turbulent flow having the same value of wall shear stress.

The investigation of the appropriate correction scheme for hot-wire measurements in the vicinity of a solid boundary by Wills (1962) obtained a lot of attention. It was noted that Reichardt's approach is also applicable to constant temperature. Very detailed calibration over a wide range of friction velocities was required in order to apply this method to instantaneous velocity measurements. The suggested correction was based on results obtained in laminar flows. This correction method gave an over correction for

turbulent flow that led Wills to suggest that in turbulent flows only half the laminar correction should be applied.

Oka and Kostic (1972) undertook a more practical experimental investigation. Their results suggested that the uncorrected velocity profiles start to deviate from the expected linear velocity profile at approximately $y^+ = 5$. This result has been found in agreement with recent investigations including the work of Van Thinh (1969) who used special wall materials for the investigation of turbulent wall boundary layers. Piercy et al. (1956) carried out a theoretical and experimental investigation of the influence of wall proximity to the heat loss from hot-wires. The heat loss from the hot-wires was found to increase as a result of the increase in the free stream velocity. Finally a comprehensive computational study of the near wall corrections has been presented recently by Bhatia et al. (1982). A collection of further publications relevant to this subject is given in the bibliography.

B.3 THE PRESENT CORRECTION PROCEDURE

The present experimental investigation involved boundary layer measurements using hot-wires as close as 50 μm from the solid boundary. It is also interesting to note that the material of the wall is an aluminium alloy for aeronautical applications that has a quite high thermal conductivity. Using an appropriate correction procedure for the velocity results obtained in the vicinity of the wall, the velocity profiles have been corrected.

The aim of this section of appendix B is to outline the principal correction procedure that has been based on the suggestions of Wills (1962). Dimensional analysis of a wire with infinite length showed that the heat transfer rate from the wire depends on a number of flow parameters, i.e. $Nu = f(Re_w, Pr, Gr, M, y/r)$, where Re_w stands for the Reynolds number based on the diameter of the wire, Pr and M symbolise the Prandtl and Mach numbers respectively and Gr stands for the Grashof number that takes into

account the gravitational effects (free convection). For a variety of test cases the non-dimensional heat transfer number (Nusselt number) has been correlated to the Reynolds number based on the wire's diameter (2 r) and the non-dimensional distance from the wall (y/r), because the rest of the parameters have a minor effect for normal air temperatures and low free stream velocities. It should be noted that the variation of fluid properties with temperature is important. Nevertheless, when constant temperature anemometry is employed for velocity testing in constant free stream conditions, the correction procedure could be simplified significantly because the mean flow field is steady.

Wills proposed that the appropriate correction to hot-wire measurements for wall proximity, is the substraction of a constant K_w, depending on the value of the non-dimensional distance from the wall (y/r), from the value of Re_w^n, where n stands for the exponent involved in the calibration equation (King's law). In order to facilitate the application of the theoretical and experimental considerations presented in the previous sections of this appendix, a chart of the variation of K_w with y/r has been constructed and is reproduced here in figure B.1.

The value of the correction to the measured velocity can be subsequently obtained using the following formulation:

$$u^n = \left[\frac{\nu}{2r}\left(\frac{\theta_w}{\theta_a}\right)^{0.17}\right]^n Re_w^n \qquad \text{(B.1)}$$

where θ_w and θ_a represent the temperature of the wire and the fluid respectively and Re^n_w is the value of the correction obtained from figure B.1. The kinematic viscosity ν of the air is assumed to have a value close to its value at ambient temperature, although the physical properties of the air are affected by temperature variation. Within the limits of this investigation, it can be assumed that the temperature of the air in the vicinity of the hot wire is closer to the ambient rather than the temperature of the wire. The correction applied to the hot wire results obtained in turbulent boundary layer has been decreased to 50% the laminar correction, according to the suggestions of Wills (1962).

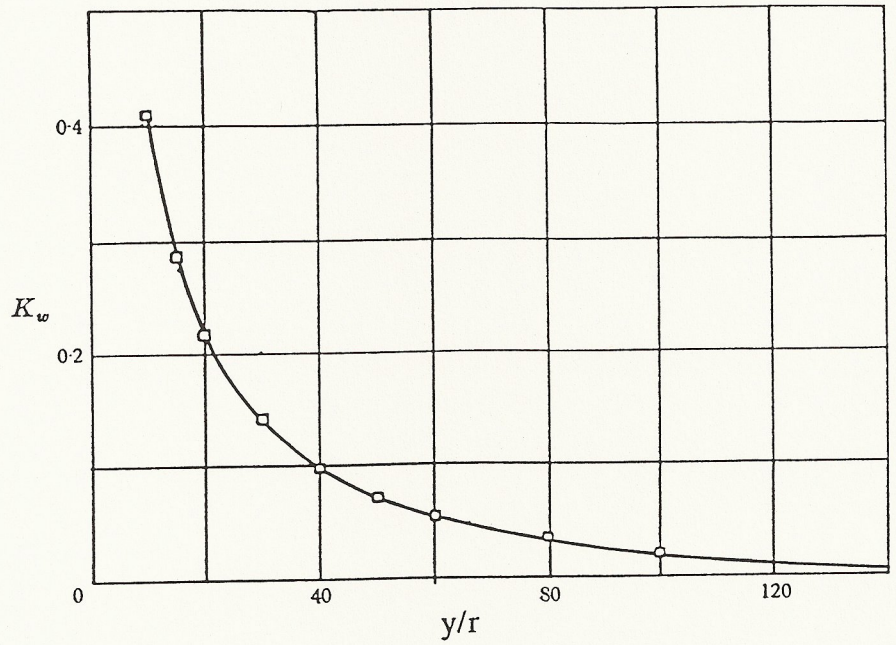


Figure B.1	Correction Chart Applied to the Measured Values of Re_w^n for Wall Proximity (after Wills (1962))

C4 Plate $U_\infty = 5$ m/s $Tu_\infty = 4$ % X = 50 mm

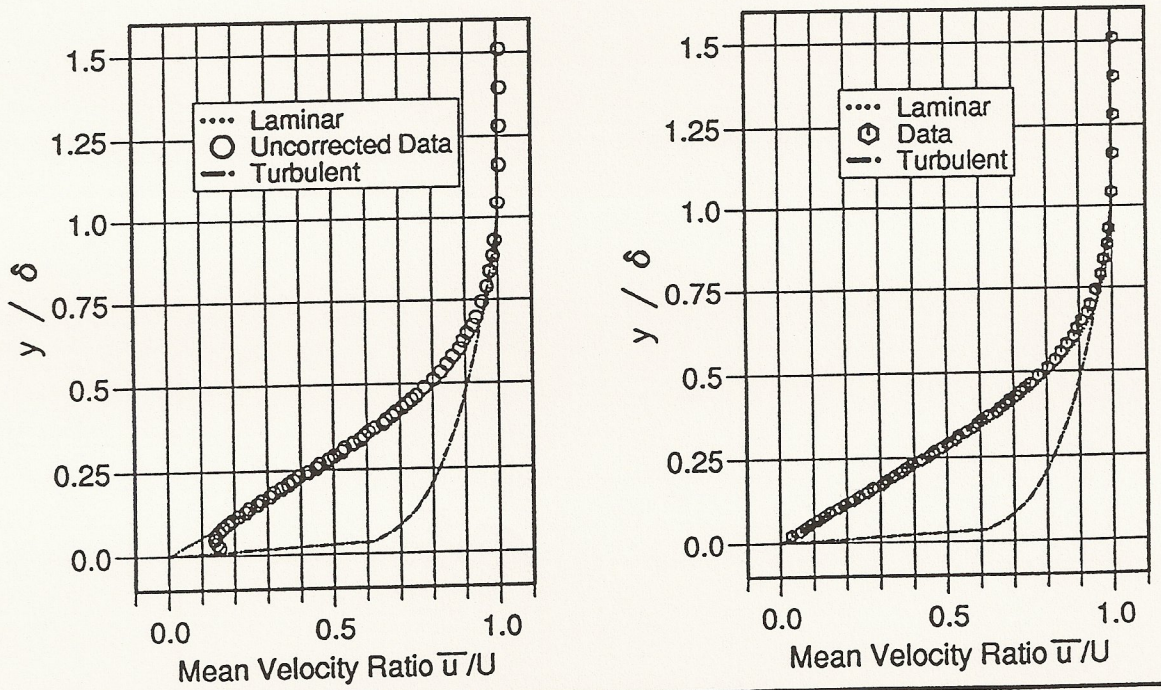


Figure B.2	The Correction Procedure Applied on a Typical Velocity Profile

APPENDIX C

On the Determination of the Skin Friction Coefficient

APPENDIX C

On the Determination of the Skin Friction Coefficient

C.1 INTRODUCTION

The determination of the wall shear stress and consequently the skin friction coefficient, c_f, from experimentally obtained velocity profiles can be considered as one of the most delicate procedures in experimental fluid mechanics. The main reason is that the most commonly used experimental techniques such as hot-wire anemometry, fail to give sufficiently accurate data in the vicinity of solid walls (even when measurements are taken close to the wall as in this study).

The objective of this appendix is to discuss the various details involved in measurement of wall shear stress in this study. In the following sections, the procedure employed in the measurement of skin friction coefficient and wall shear stress is discussed analytically. The peculiarities of the laminar, transitional and turbulent regions of the boundary layer have been taken into account resulting in quite substantial variations in the procedure but before proceeding with the details, a few theoretical considerations are presented.

C.2 THEORETICAL CONSIDERATIONS

The description of the laminar boundary layer has been achieved with remarkable success using the Blasius parameter $y / Re_x^{1/2}$ or simply non-dimensional parameters of the form u/U and y/δ. In 1956, Clauser discussed possible ways of representing the

turbulent boundary layer in a non-dimensional form. It became apparent, that profiles of turbulent boundary layers, having different values of Reynolds numbers and other dynamic characteristics but the same skin friction coefficient, c_f, will have identical non-dimensional velocity profiles. The effect of the skin friction coefficient (non-dimensional shear stress),

$$c_f = \frac{\tau_w}{\frac{1}{2}\rho \bar{u}_e^2} \tag{C.1}$$

is usually taken into account using the, so called, friction velocity,

$$u^* = \sqrt{\frac{\tau_w}{\rho}} \tag{C.2}$$

It would be useful to recall at this point that the wall shear stress is defined as:

$$\tau_w = \mu \left.\frac{\partial u}{\partial y}\right|_w \tag{C.3}$$

Using the above considerations, the dimensionless crosswise distance in wall units, obtains the form:

$$y^+ = \frac{y u^*}{\nu} \tag{C.4}$$

It is interesting to observe that the dimensionless distance y^+ is defined as a Reynolds number using the friction velocity as the velocity scale. By the same token, the boundary layer velocity (instantaneous or mean) has the following non-dimensional form:

$$u^+ = \frac{\bar{u}}{u^*} \tag{C.5}$$

In the following paragraphs the particular characteristics of the laminar, transitional and turbulent boundary layer will be discussed in terms of these dimensionless parameters. In the laminar boundary layer, as well as in the viscous sublayer of the transitional and the turbulent boundary layers, the shear stress is usually assumed to be constant across the width of the layer and in this case the linear relationship $u^+ = y^+$ holds true.

As far as the turbulent boundary layer is concerned, it is understood to consist of four distinct regions, namely: the viscous sublayer, the buffer region, the logarithmic overlap region and the wake region, (fig. C.1). The viscosity forces seem to play a

dominant role in the formation of the viscous sublayer, where (as already mentioned) it is assumed that the following relation holds true:

$$u^+ = y^+ \tag{C.6}$$

The logarithmic law region can be described by the following equation:

$$u^+ = \frac{1}{\kappa} ln y^+ + C \tag{C.7}$$

where κ is usually associated with the von Kármán constant $\kappa = 0.41$ and the integration constant C obtains a value around 5 (see also White (1974)).

In the transitional region, a whole range of cases exist between the laminar and the turbulent boundary layer. As a result, the dimensionless representation of the transitional profiles do not have a universal form (or at least, without the use of the concept of intermittency). However, the linear form (eq. C.6) as well as the universal logarithmic form (eq. C.7) of the law-of-the-wall have been widely used in the literature as a reference for the necessary comparisons with experimentally obtained profiles in the transitional region.

C.3 THE DETERMINATION PROCEDURE

In order to obtain reasonably accurate estimates of the wall shear stress and the skin friction coefficient from velocity profiles measurements, a suitable determination procedure should be followed. This procedure has to be adjusted appropriately for the laminar, the turbulent and the transitional regions of the boundary layer. In principal, the measurement of the wall shear stress τ_w could be obtained from the velocity gradient $d\bar{u}/dy$ at the wall. In this case, the measured values of the velocity profile $\bar{u}(y)$ can be used directly in the wall shear stress determination. In practice, this operation is very delicate because the velocity gradient near the wall is very high.

In the laminar region of the boundary layer, very near the wall, the change in velocity is linear with distance from the wall. Therefore, the approximation of $\Delta u / \Delta y$

has been used to determine the wall shear stress and consequently the friction velocity and the skin friction coefficient.

The determination of the skin friction coefficient in the fully turbulent region has been more involved. In a turbulent boundary layer, it is very difficult to obtain reliable measurements in the region of $y^+ < 3$, where the linear law ($u^+ = y^+$) holds true because the physical extent of the region is very small. On the other hand, the logarithmic law-of-the-wall applies in a region slightly further away from the solid wall where measurements are both easier and more accurate. The measurement of the velocity profile $\bar{u}(y)$ in the logarithmic overlap region can be then used in order to determine the wall shear stress and the skin friction coefficient according to the following procedure which is usually referred to as the Clauser method.

This procedure involves measurements of the velocity profiles ($\bar{u}$ against y) in the logarithmic overlap region (i.e. the region $50 < y^+ < 200$). The Clauser method of measuring the skin friction coefficient is based on the graphical representation of parametric curves of the form $(\bar{u} / \bar{u}_e)$ as a function of $(y\,\bar{u}_e / \nu)$ with the parameter quantity $(c_f/2)^{1/2}$ as a separate variable (fig. C.2) (see also Clauser (1954, 1956)). In this process, the following formula:

$$\frac{\bar{u}}{\bar{u}_e} = \sqrt{\frac{c_f}{2}}\left(\frac{1}{\kappa}\ln\frac{y\bar{u}_e}{\nu}\sqrt{\frac{c_f}{2}} + C\right) \qquad \text{(C.8)}$$

has been used to calculate the set of parametric curves for different values of c_f. The experimental results are overplotted on such data and the value of skin friction coefficient can be then obtained as the value of c_f corresponding to the curve that best fits the experimental data.

The two methods of estimating the skin friction coefficient in the laminar and turbulent boundary layer have been developed using their particular characteristics which can be considered as the two limiting forms of the transitional boundary layer. However, neither of these can be directly applied to the wide variety of forms that the transitional

velocity profiles can take. In this case, a more general approach has been adopted for estimating the skin friction coefficient. In this region, the momentum-integral equation for two dimensional, incompressible boundary layer has been employed (see also Suder et al. (1988)) which has the following form:

$$\frac{\tau_w}{\rho} = \frac{d}{dx}(\bar{u}_e^2 \theta) + \delta^* \bar{u}_e \frac{d\bar{u}_e}{dx} \qquad \text{(C.9)}$$

This equation is general and can be applied to either laminar, turbulent or transitional boundary layers provided that no assumptions are made for the wall shear stress (Schlichting, 1979). However, for a flat plate at zero incidence ($\bar{u}_e$ is constant) the forgoing equation reduces to:

$$\frac{\tau_w}{\rho} = \bar{u}_e^2 \frac{d\theta}{dx} \qquad \text{(C.10)}$$

In this case, the estimation of the wall shear stress can be obtained as a function of the streamwise distribution of the momentum thickness (see also figures 5.29, 5.37 and 5.45). Therefore, the velocity profiles data can be used for defining both the momentum thickness and skin friction coefficient distribution. In the present study, the streamwise distribution of the momentum thickness has been obtained by integration of the velocity profiles data according to the following equation:

$$\theta = \int_0^{\delta} \frac{\bar{u}}{\bar{u}_e}\left(1 - \frac{\bar{u}}{\bar{u}_e}\right) dy \qquad \text{(C.11)}$$

The above procedure has been used in this study for the assessment of skin friction in the transitional region but as a final remark, it is useful to recall the intermittent character of transitional flows and that the mean quantities of the boundary layer can potentially be obtained by decomposing the superposition of their laminar and turbulent counterparts. Following this argument, the value of the skin friction coefficient can be estimated by "conditional analysis" of the intermittent signal (see also sections 1.2.6 and 5.6 of the present document). In this case, the value of the skin friction coefficient at a streamwise location x (within the transitional region) can be estimated by adding the effect of a laminar boundary layer to the effect of a turbulent boundary layer starting at x_t (start of transition according to Narasimha procedure), in the

proportion 1-γ to γ (where γ represents the intermittency factor). Therefore, the skin friction coefficient can be estimated as follows:

$$c_{f_{TR}} = (1-\gamma)\, c_{f_L} + \gamma\, c_{f_T} \qquad \text{(C.12)}$$

The foregoing procedure has not been applied in the present study but in the future additional work could be undertaken in this area.

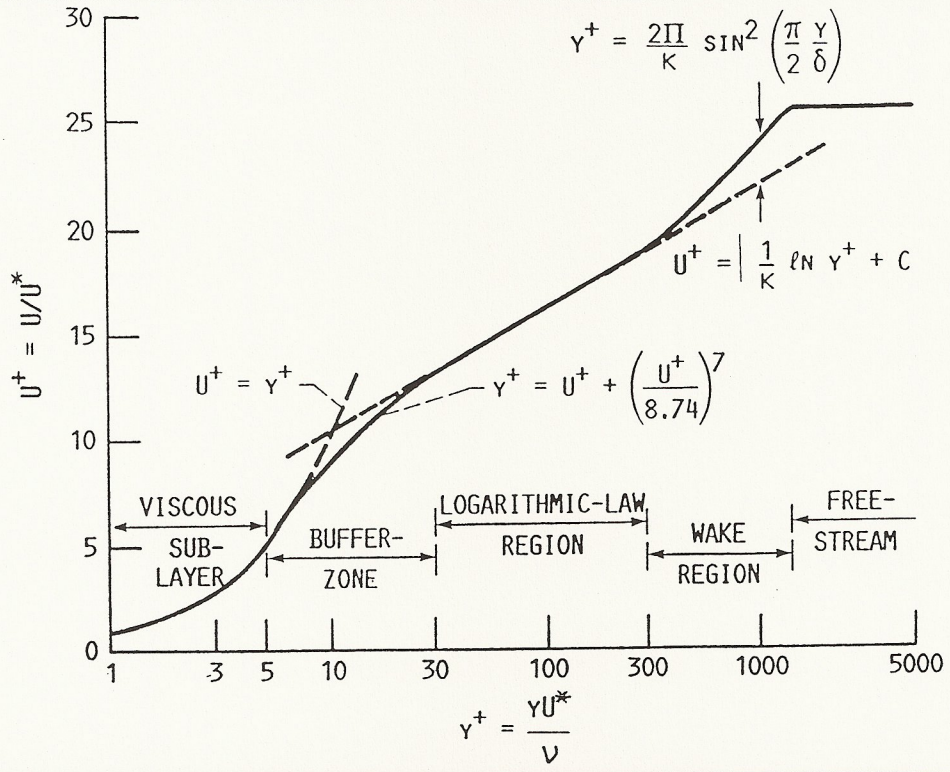


Figure C.1	Dimensionless Representation of the Turbulent Boundary Layer Indicating the Various Regions in the Boundary Layer

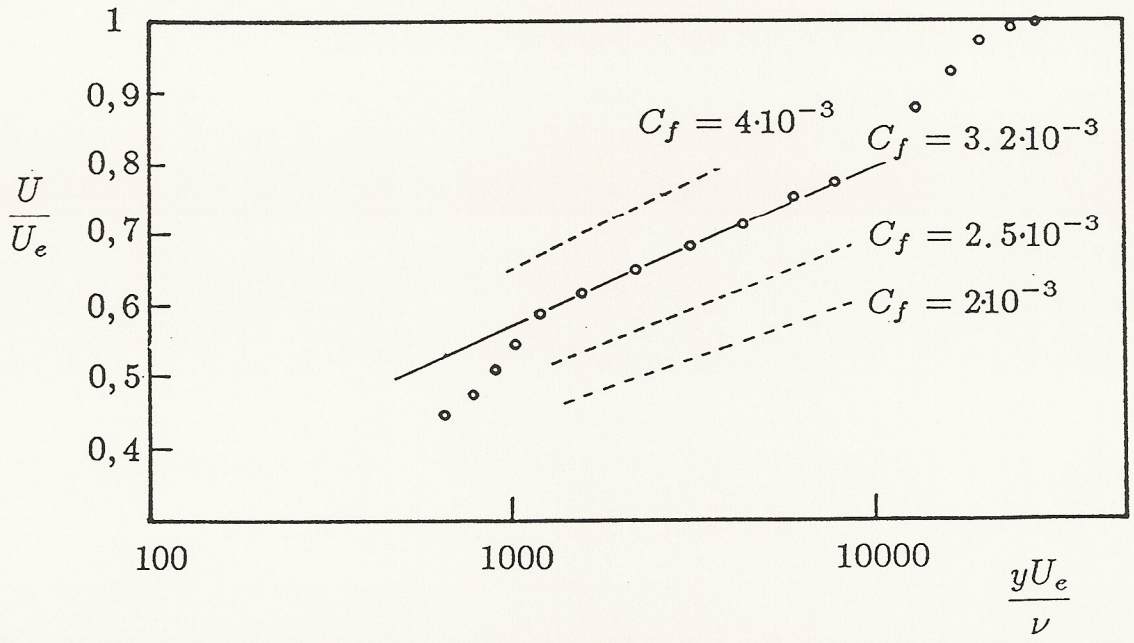


Figure C.2	Determination of the Skin Friction Coefficient According to Clauser Method

APPENDIX D

On the Determination of Turbulence Length Scale

APPENDIX D

On the Determination of Turbulence Length Scale

D.1 INTRODUCTION

In the early decades of this century, a number of scientists including G.I. Taylor (1938), Th. von Karman (1948), F.N. Frenkiel (1948a) and H.L. Dryden (1943), have devoted a considerable amount of research effort to the clarification of various aspects of the statistical theory of turbulence. Since its initial formulation, the statistical theory of turbulence has provided the analytical background for numerous experimental and theoretical investigations.

The turbulent motion of fluid particles is usually characterised using a number of indicative quantities including:

i> the mean-square and higher order values of the turbulent velocity components (turbulence intensity, skewness factor and flatness factor),

ii> the correlation, cross-correlation and autocorrelation coefficients between the components of the turbulent velocities in the space or time domain,

iii> the scales of turbulence (time or length) which are obtained by integrating the correlation distribution with respect to any of the independent time or space variables, and

iv> the spectra of turbulence representing the turbulent energy distribution in the frequency or wave number domain which are obtained by harmonic analysis of the turbulent velocity fluctuations.

These factors have been discussed extensively in the body of the thesis. The objective of this appendix is to examine the various details involved in defining the length scales of turbulence. The present investigation has involved boundary layer measurements under a free stream flow environment dominated by grid generated turbulence and the turbulence length scales have been obtained by integration of the measured distribution of the autocorrelation coefficient (as explained in the following section). In part this is because the alternative method involving cross-correlations using sensors separated in the direction of the mean velocity U, can involve many difficulties because the wake of the upstream probe is liable to interfere with the flow field in the vicinity of the second probe. In the following sections of this appendix, the measurement procedure for length scale of turbulence are also discussed analytically and a few theoretical considerations will be presented.

D.2 THEORETICAL CONSIDERATIONS

In general terms, a value for integral length scale of turbulence, L_x, indicates how far away from the measuring point in the streamwise direction the velocity ceases to be correlated with itself. The physical meaning of the integral length scale can be described as representating the mean size of the vortices travelling with the velocity of the main stream.

By definition (Bradshaw, 1971), the integral length scale is given by the following expression:

$$L = \int_0^\infty R(r)\,dr \approx \int_0^\infty R_{11}(r)\,dr \qquad \text{(D.1)}$$

where R(r) is the spatial correlation coefficient, defined as:

$$R(r) = \frac{\overline{u'(X)u'(X+r)}}{\sqrt{\overline{u'^2(X)}\;\overline{u'^2(X+r)}}} \qquad \text{(D.2)}$$

The correlation coefficient in most turbulence work is approximated by the dimensionless quantity $R_{11}(r)$, defined as:

$$R_{11}(r) = \frac{\overline{u'(X)u'(X+r)}}{\overline{u'^2(X)}} \qquad \text{(D.3)}$$

In practice, many experimentalists prefer to measure the autocorrelation coefficient $R(\tau)$ or the dimensionless quantity $R_{11}(\tau)$, defined as:

$$R_{11}(\tau) = \frac{\overline{u'(t)u'(t+\tau)}}{\overline{u'^2(t)}} \qquad \text{(D.4)}$$

due to the numerous complexities and technical difficulties that are involved in the simultaneous recording of the velocity field in various streamwise locations.

The autocorrelation coefficient could replace the spatial correlation coefficient quite efficiently, using "Taylor's hypothesis". Taylor (1938) argued that the changes in u with time at a fixed measuring point could be assumed to be due to the passage of a "frozen" pattern of turbulent motion past the point, provided that the mean (or free stream) velocity carrying the turbulent eddies was much larger than the turbulent velocity fluctuations. In other words, the velocity field at different instants could be related by the transformation:

$$u(x,t) = u(x - Ut,0) \qquad \text{(D.5)}$$

and hence the local time derivative at the point of measurement could be replaced by the convective derivative:

$$\frac{\partial}{\partial t} \approx -U\frac{\partial}{\partial x} \qquad \text{if } u' << U \qquad \text{(D.6)}$$

The negative sign is necessary because a positive value of $\partial/\partial x$ at a point in space corresponds to a negative value of $\partial/\partial t$ (Hinze, 1975).

Therefore, an accurate measurement of the autocorrelation with time separation τ can provide a good approximation of the spacial correlation with space separation $r = - U \tau$. The physical meaning of this relation is that the measurement, taken at $t_1 = t_0 + \tau$ (in the time domain), corresponds to the area of the "frozen" vorticity field which was situated at distance r behind the measurement point (in the space domain) at the time when the measurement was being undertaken at $t = t_0$ (in the time domain). Consequently, the longitudinal length scale of turbulence can be approximated by:

$$L = \int_0^\infty R_{11}(r)dr \approx U \int_0^\infty R_{11}(\tau)d\tau \qquad \text{(D.7)}$$

The foregoing formulation has been employed in the present study for the estimation of the length scale in a variety of flow conditions. More extensive analysis and global examination of the present results has been incorporated in the following section of this appendix.

D.3 LENGTH SCALE DETERMINATION

A series of measurements has been taken in order to quantify the integral length scale of the background as well as the grid generated turbulence, at a range of locations over the measuring surface. In order to calculate the longitudinal integral length scale of turbulence L_x, the velocity fluctuations have been recorded at various measurement stations. For all the measurements reported in this section, the location of the leading edge (X = 0) has been used as a reference.

The distribution of the autocorrelation coefficient has been measured for a wide range of streamwise locations and Reynolds numbers. Figures D.1 and D.2 present the results obtained behind PXS grid for two streamwise locations. In these figures, the autocorrelation coefficient has been plotted against the non-dimensional form of the time step, η, which is defined as follows:

$$\eta = \frac{\tau U_\infty}{L} \qquad \text{(D.8)}$$

In order to obtain a reasonable frame of reference, the following exponential law:

$$R_{11}(\tau) = e^{-\eta} = e^{-\frac{\tau U_\infty}{L}} \qquad \text{(D.9)}$$

has been employed (Frenkiel, 1948). This inverse exponential formula is quite well accepted in the literature, apart from the region around $\eta = 0$ where the autocorrelation function has a zero derivative ($\partial R / \partial \eta = 0$). It can be observed from figures D.1 and D.2 that the present results are in good agreement with this assumed form.

The aforementioned velocity traces have been statistically analysed, in order to obtain the autocorrelation coefficient and length scale associated with the background turbulence in the mean flow at the working section of the tunnel. The overall value of the integral length scale of the background turbulence was found to be approximately 15 mm, at the inlet of the working section.

The grid design involved the development of five turbulence generating grids based on the suggestions of Roach (1986). Table D.1 summarises the principal characteristics of the turbulence generating grids used in this project together with values of length scale of the turbulence generated by these grids, calculated from the discretised form of equation D.7. These have been calculated using velocity traces acquired at the position of the leading edge without the test plates in position. The turbulence generating grids (as described in chapter 2) have been positioned at the normal operating position (i.e. 650 mm upstream of the leading edge). In this case, the free stream Reynolds number has been $3.3\ 10^5$.

Grid Type	d Diameter or Width of Bar {mm}	M Mesh Length {mm}	S Solidity {%}	L_0 Integral Length Scale {mm}
SMR	0.9 O	4.23	38	14
PR	6.35 O	25	23.8	27
PS	10 □	33.33	27.5	32
PXR	6.35 O	25	42	25
PXS	10 □	33.33	47.4	29

Table D.1 : Integral Length Scale of the Turbulence Generated by the Grids

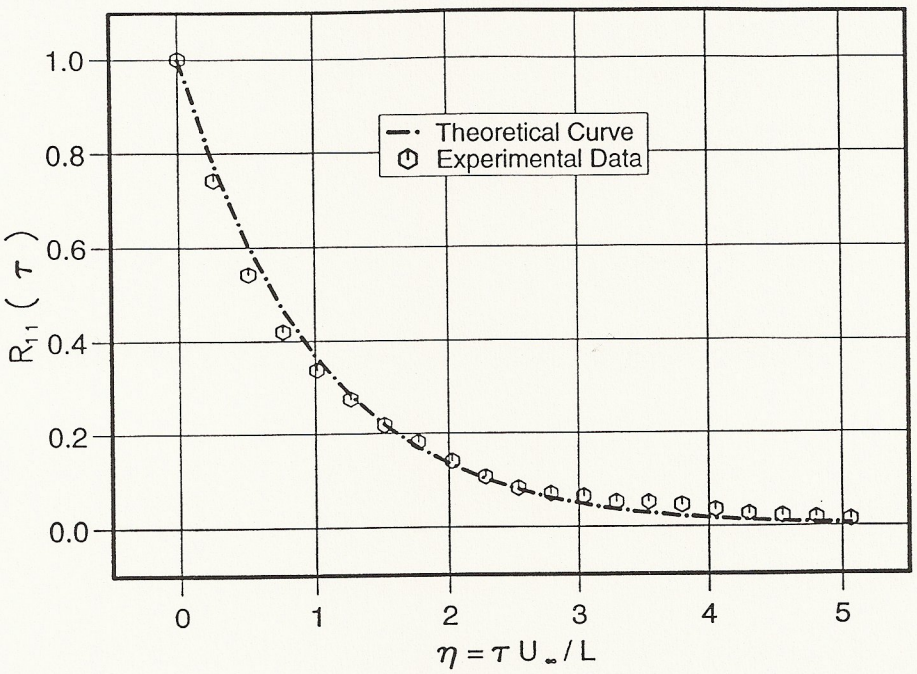


Figure D.1	Autocorrelation of the Axial Turbulence Component C4 Plate U_∞ = 5 m/s Tu_∞ = 4 % X = 50 mm

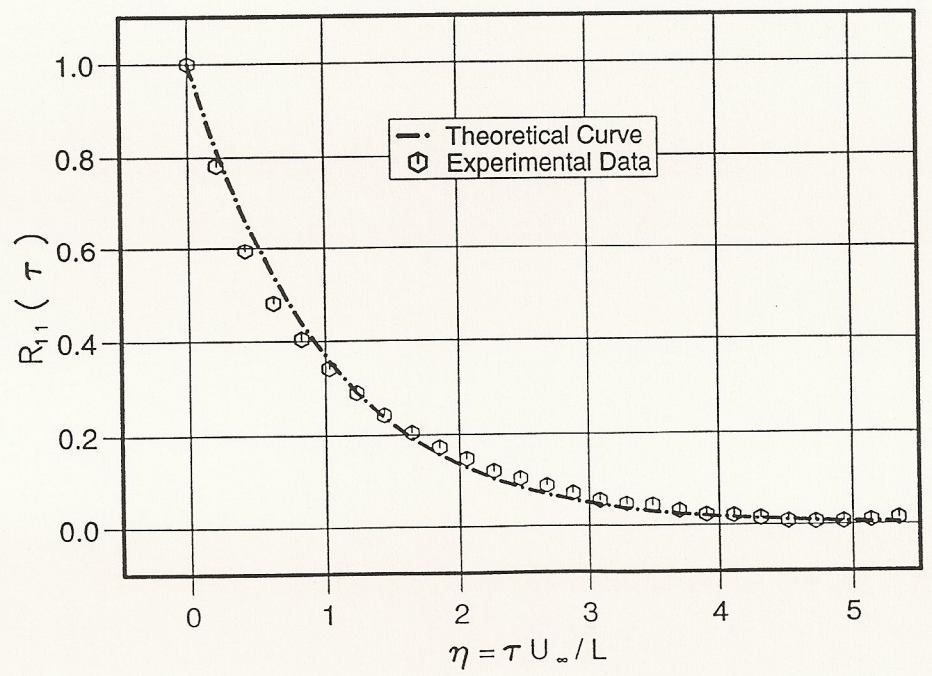


Figure D.2	Autocorrelation of the Axial Turbulence Component C4 Plate U_∞ = 5 m/s Tu_∞ = 4 % X = 425 mm